Wolfgang Osten • Malgorzata Kujawinska (Eds.)

Fringe 2009

The 6th International Workshop on
Advanced Optical Metrology

In Memory of Dr.-Ing. Hans Rottenkolber

(* 12.05.1937 - † 07.03.2008)

Conference Committee

Organizers and Conference Chairs:

Wolfgang Osten (Germany)
Malgorzata Kujawinska (Poland)

Program Committee:

Armando Albertazzi (Brazil)
Oleg Angelsky (Ukraine)
Anand Asundi (Singapore)
Klaus Beckstette (Germany)
Harald Bosse (Germany)
Bernd Dörband (Germany)
Pietro Ferraro (Italy)
Kay Gastinger (Norway)
Marc Georges (Belgium)
Christophe Gorecki (France)
Ulf Griesmann (USA)
Peter J. de Groot (USA)
Igor Gurov (Russia)
Xiaoyuan He (China)
John Huntley (UK)
Gerd Jäger (Germany)
Leszek Jaroszewicz (Poland)
Bahram Javidi (USA)
Ricarda Kafka (Germany)
Guillermo Kaufmann (Argentina)
Richard Kowarschik (Germany)
Peter Lehmann (Germany)
Fernando Mendoza (Mexico)
Andrew Moore (UK)
Yoshiharu Morimoto (Japan)
Thomas J. Naughton (Ireland)
Xiang Peng (China)

Ryszard J. Pryputniewicz (USA)
Eduard Reithmeier (Germany)
Joanna Schmit (USA)
Robert Schmitt (Germany)
Jörg Seewig (Germany)
Chandra Shakher (India)
Mitsuo Takeda (Japan)
Ralph P. Tatam (UK)
Hugo Thienpont (Belgium)
Vivi Tornari (Greece)
Michael Totzeck (Germany)
Satoru Toyooka (Japan)
James D. Trolinger (USA)
Rainer Tutsch (Germany)
Elmar E. Wagner (Germany)
Albert Weckenmann (Germany)
Jacob Woisetschläger (Austria)
James C. Wyant (USA)
Ichirou Yamaguchi (Japan)

Honorary Chairs: Werner Jüptner and Hans Tiziani

Session Chairs:

Session 1:	M. Kujawinska (Poland) P. de Groot (USA) E. Reithmeier (Germany) M. Georges (Belgium)
Session 2:	J. Huntley (GB) Th. Kreis (Germany) C. Koliopoulos (USA)
Session 3:	C. Gorecki (France) A. Asundi (Singapore)
Session 4:	P. Ferraro (Italy)
Session 5:	W. Jüptner (Germany) H. Tiziani (Germany)

Preface

21 years ago it was a joint idea with Hans Rottenkolber to organize a workshop dedicated to the discussion of the latest results in the automatic processing of fringe patterns. This idea was promoted by the insight that automatic and high precision phase measurement techniques will play a key role in all future industrial and scientific applications of optical metrology. A couple of months later more than 50 specialists from East and West met in East Berlin, the capital of the former GDR, to spend 3 days with the discussion of new principles of fringe processing. In the stimulating atmoshere the idea was born to repeat the workshop and to organize the meeting in an olympic schedule. And thus meanwhile 20 years have been passed and we have today Fringe number six. However, such a workshop takes place in a dynamic environment. Therefore the main topics of the previous events were always adapted to the most interesting subjects of the new period. In 1993 the workshop took place in Bremen and was dedicated to new principles of optical shape measurement, setup calibration, phase unwrapping and nondestructive testing, while in 1997 new approaches in multi-sensor metrology, active measurement strategies and hybrid processing technologies played a central role. 2001, the first meeting in the 21st century, was focused to optical methods for micromeasurements, hybrid measurement technologies and new sensor solutions for industrial inspection. In 2005 the fifth workshop was organized in Stuttgart, the capital of the state of Baden-Württemberg and the centre of a region with a long and remarkable tradition in machine construction, vehicle manufacturing and optics. Thus after Berlin 1989, Bremen 1993, 1997 and 2001, Stuttgart was the third Fringe city where international experts met each other to share new ideas and concepts in optical metrology. And this will be continued in 2009.

This volume contains the papers presented during ***FRINGE 2009***. The focus of this meeting is especially directed *to digital wavefront engineering*, *resolution enhanced technologies*, 4D methods addressing applications *from macro to nano considering dynamic changes*, *sensor fusion* and new advances in *the unification of modeling, simulation and experiment*. Since optical metrology becomes more and more important for industrial inspection, sophisticated *sensor systems* and their applications for the solution of challenging measurement problems are chosen again as one of the central topics of the workshop. This extended scope was honored by a great response on our call for papers. Scientists from all

around the world offered more than 150 papers. This enormous response demanded a strong revision of the papers to select the best out of the overwhelming number of excellent papers. The strong limitation of the number of papers which can be presented orally and discussed effectively during a workshop without holding parallel sessions was again an impotant orientation.

The papers presented in this workshop are summarized under 5 topics:

1. New Methods and Tools for Data Acquisition and Processing
2. Application Enhanced Technologies
3. 4D Optical Metrology over a Large Scale Range
4. Hybrid Measurement Techniques
5. New Optical Sensors and Measurement Systems

As in the former workshops, each topic is introduced by an acknowledged expert who gives an extensive overview and a report of the state of the art. The classification of all submitted papers into these topics was again a difficult job which often required compromises. We hope that our decisions will be accepted by the audience. On this occasion we would like to express our deep thanks to the international program committee for helping us to find a good solution in every situation.

The editors would like to express their thanks to all the authors who spent a lot of time and effort in the preparation of their papers. Our appreciation also goes to Eva Hestermann-Beyerle and Birgit Kollmar-Thoni from Springer Heidelberg for providing excellent conditions for the publication. Our deep thanks is directed to the members of the ITO staff. The continuous help given by Katharina Bosse-Mettler, Katja Costantino, Gabriele Grosshans, Heiko Bieger, Valeriano Ferreras Paz, Erich Steinbeißer and Michael Warber was the basis for making a successful *FRINGE 2009*. Finally, our special thanks and appreciation goes to all friends and colleagues for sharing with us again the spirit of the Fringe workshops.

Looking forward to *FRINGE 2013.*

Stuttgart and Warsaw, September 2009

Wolfgang Osten and Malgorzata Kujawinska

Table of Contents

Topic 2: Application Enhanced Technologies

Topic 3: 4D Optical Metrology over a Large Scale Range

Topic 4: Hybrid Measurement Techniques

Topic 5: New Optical Sensors and Measurement Systems

Tutorial

KEY NOTE

Holography in the '60s and '70s
–
A View from the Fringes

Given by

Charles M. Vest
Washington DC
(USA)

Holography in the '60s and '70s – A View from the Fringes

Charles M. Vest
National Academy of Engineering
500 Fifth Street, NW, Washington DC 20001
USA

1 Introduction

It is my hope that the following somewhat random walk through holography in the 1960s and 1970s as I experienced it will give you some sense of the early days of the field and some of the people who invented, discovered, and extended it.

My view of the early days of optical holography is literally and figuratively from the fringes. I came to Willow Run's Radar and Optics Lab to learn to unlock the quantitative information encoded in the fringes of holographic interferometry. My work was not at the heart of the fundamental field of holography, but it followed closely enough after the seminal work on off-axis holography that I was privileged to work with many of the pioneers and appreciate the environment that developed in their laboratory.

I believe I first learned about holography in the 1960s when Robert Powell presented a seminar in the University of Michigan's Department of Mechanical Engineering. At that time I was a graduate student in that department focusing on the thermal sciences, i.e. thermodynamics, heat transfer, and fluid mechanics. Powell described work going on in the Radar and Optics Laboratory. The Radar and Optics Lab was a largely defense-oriented laboratory that had been operated by the University of Michigan on the grounds of Detroit's Willow Run airport, which had been a major facility for producing bombers during World War II. After the war, Michigan leased space there for a nominal amount and established a laboratory focused primarily on missile technology and novel radar systems.

While I was a graduate student, the Radar and Optics Laboratory component of Willow Run was moved to the North Campus of the university in Ann Arbor. This enabled it to draw closer to the academic enterprise and engage more faculty and graduate students in its work. This

was a very satisfactory arrangement, although it became a center of considerable controversy during the Viet Nam War because it was engaged in classified research for the military. It was the target of student protests, and protests were serious business on that campus. In fact, the key national anti-war movement, Students for a Democratic Society, or SDS, was founded at Michigan. I recall with a chuckle the consternation among administrators when a student employee of the Radar and Optics Laboratory who held a security clearance was discovered to be an active member of the SDS. But some things were more serious. The lab was bombed late one night. It was a huge explosion that ripped a gaping hole in a giant metal door in the delivery area. Investigators determined that a very large quantity of explosives had been used, but that those who planted the bomb were rather inept in its placement. This is fortunate because there was one student working very late in his office. Fortunately, he was uninjured.

Be that as it may, the seminar presented by Bob Powell reviewed the fundamental concept of formation of holograms and dramatically showed that interference fringes could be formed by juxtaposing light emanating from the actual light source with holographically reconstructed waves apparently emanating from an image of the same source. Presumably this work was largely that reported in the seminal Optical Society of America paper by Karl Stetson and Robert Powell.

I also attended a major press and public briefing on the new field of three-dimensional holographic images presented by Emmett Leith and Juris Upatnieks in Michigan's Rackham Graduate School Building. The impact on the audience was very strong. Not only was the three-dimensional imagery amazing, but lasers were sufficiently new that many attendees had never seen one before. After the briefing, several now-famous holograms, such as that of the model train, were on display. This was an amazing event, and several of the images subsequently became famous in large part due to the outstanding images of them that the great scientific photographer Fritz Goro published in *Life* magazine.

Later, in 1968, I was in the final stages of my Ph.D. dissertation work on a problem in hydrodynamic stability of natural convection flows when I decided to accept an offer to become an assistant professor of mechanical engineering at the University of Michigan. This work, which was mostly theoretical, was done under the supervision of an excellent mentor, Professor Vedat Arpaci. Because I would be joining the faculty of the same department in which I had studied, I felt it would be important to move into new intellectual territory rather than continue in the same directions that my thesis supervisor was pursuing. Thinking about Powell's seminar, the general excitement of lasers and holography, and the

now somewhat more prevalent work on holographic interferometry, I sought to work half time in the Radar and Optics Laboratory to determine if this new technique could become an important experimental tool for mechanical engineering research, especially in the thermal sciences. Bill Brown, the director of the Willow Run Labs, and Emmett Leith readily agreed and made this possible.

It was in this way that I came close to the early developments of holography, close in both space and time, but certainly not at its center nor at its actual inception.

2 Intersections

The pioneering work in holography at the University of Michigan's Willow Run Laboratories was made possible by *intersections*: intersections of ideas, intersections of technologies, and, above all, intersections of remarkable people, together with a good dose of serendipity.

Most lay people, and indeed scientific and engineering professionals, learned about holography just as I did, i.e. they read or heard about an amazing new technique for producing realistic three-dimensional images of everyday objects using laser light. The reality is that those who developed holography did not intend to make images of everyday objects, and they did their initial work before lasers were available.

The physicist Dennis Gabor first worked out the concept of wavefront reconstruction, or holography, in an attempt to make improved images by electron microscopy. He developed the theory, but did not have a sufficiently coherent source of electrons to actually realize it experimentally. As an analog to electron imaging, he formed a holographic image of a point source of light from a mercury vapor lamp using photographic film. His original papers are remarkably complete and detailed, including details of the appropriate characteristics and processing of the photographic film on which the hologram is recorded.

Today we would refer to Gabor's technique as *in-line holography* and recognize that as an optical imaging technique, it suffered from the fact that the reference wave and the reconstructed object wave propagate along collinear paths. Because of this juxtaposition, holography remained mostly a curiosity; however, the concept and experiment were sufficiently original and potentially important that Gabor received the Nobel Prize in Physics in 1971.

It remained for Emmett Leith and his colleague Juris Upatnieks at Willow Run to separate the reference wave from the reconstructed wave

by placing a substantial angle between the reference wave and the reconstructed wave propagating from the object being imaged. This idea, like many important scientific ideas, seems simple in retrospect, but it was actually quite remarkable.

Like Gabor, Leith and Upatnieks did not set out to do three-dimensional optical imaging. They were radar engineers and were familiar with communication theory. They worked to develop coherent radars capable of high-precision imaging. To develop the necessary concepts, they explored the use of optical analogs to coherent radars. This led them to think about Gabor's technique of optical holography. If they could separate the reference waves from the object waves, they could build a laboratory-scale optical experiment to model coherent radars. This in turn led them to the intersection of optics and communication theory.

Leith and Upatnieks were familiar with the basic techniques of frequency separation in communication theory. They realized that if they thought in terms of angular separation, and therefore used spatial frequencies rather than temporal frequencies, the reconstructed wave could be easily separated from the reference wave, and off-axis holography was born. Soon they successfully formed holographic images. They used a point source of light from a mercury vapor lamp to make their pioneering off-axis holograms.

So the development of off-axis holographic interferometry came from the intersection of optics and communication theory. But if it were not for the serendipitous development and commercialization of He-Ne lasers at just about this time, the limited coherence of mercury vapor light sources would have restricted off-axis holography to being a minor laboratory curiosity. The intersection of lasers and off-axis holography gave us a new tool for science, engineering, and art. It turns out that it also led to a major delay in the availability of holography. Here is why: During this same time period, Leith and others at the Willow Run Laboratory were engaged in developing techniques for optical processing of radar images. This too was truly seminal work that dramatically improved the ability of aircraft-born radars to image objects, e.g. by synthetic aperture techniques. But extracting the image from the raw data was a monumental problem in those days of only minor computing power. Optical data processing techniques, especially after the availability of lasers, was a huge advance, and presumably a major advantage to the U.S. vis a vis the Soviet Union. This was at the height of the Cold War, and because of national security concerns, the fact that radar engineers were working with laser optics was highly classified. For this reason, there was a very substantial time lag between the Leith and Upatnieks work in off-axis holography and its publication in the open literature.

In the late 1960s and early 1970s there were many remarkable people working in the Radar and Optics Lab. I was fortunate to get to know several of them. In addition to Emmet Leith and Juris Upatnieks, I particularly want to note Bill Brown, Adam Kozma, Ken Haines, Al Friesem, Jack Walker, Percy Hildebrand, John Latta, and Ed Champaign, as people from whom I learned many things that one would not expect a mechanical engineer to know. We also had remarkable graduate students in the Lab in the early 1970s such as Rod Alferness, who today is chief scientist of Bell Labs, Don Winter who recently served as the U.S. Secretary of the Navy, and my own student, Don Sweeney, who has had a very productive career at Purdue University and Lawrence Livermore Laboratory and is known especially for his work in ultraviolet lithography.

The holography pioneer who most influenced and enabled my own work is Karl Stetson. Karl had left the Radar and Optics Laboratory prior to my arriving there to work in the settings of industrial labs, most notably the Ford Scientific Laboratory and United Technologies Research Center. His was the most seminal and comprehensive work in the field of holographic interferometry.

3 The View from the Fringes

It was primarily holographic interferometry that brought me to the Radar and Optics Laboratory. Once laser-based off-axis holography was readily accessible as an experimental technique, many people independently discovered that when an object moved slightly, or was strained between exposures of a two-exposure hologram, an image of the object superimposed with dark and bright interference fringes could be seen.

This phenomenon was discovered independently by several investigators including Tony Ennos and Jim Burch at the National Physical Laboratory at Teddington in the UK, Ralph Wuerker at TRW, and, of course, Stetson and Powell at Michigan. Usually, interferometry based on holography was discovered by accident, when the object or optical table was accidentally bumped during an experiment and fringes appeared in the reconstructed image.

These fringes were clearly associated with the slight displacement, rotation, or strain that had occurred, and they had remarkable dynamic properties in that they shifted and changed as one looked at the object from various directions. They often appeared to be detached from the surface of the object. Many scientists and engineers in several countries began to analyze the formation of these fringes and then to solve the important

inverse problem, i.e. given observations of the fringes from several perspectives, estimate the translation, rotation, and strain the object had undergone. This problem was straightforward in several special cases, but a truly general analysis, especially one that explains the apparent localization of fringes in space, requires a sophisticated understanding of the optical physics involved. The deepest and most comprehensive analysis was due to Karl Stetson and formed the basis of the work that earned his doctoral degree at the Royal Institute of Technology in Stockholm.

Nils Abrahmson, also at the Royal institute of Technology in Stockholm, developed a very clever and accessible way of understanding the relation between motion and fringes called the *holodiagram*. Industrial scientists such as Gordon Brown at Ford also pushed forward the state of the art for the practical application of this technique.

Much of this work had been done before I became involved, but these and many other investigators carried the field of holographic interferometry forward, and I was privileged to learn from them and occasionally work with them and many others who followed. Indeed, one of the great pleasures of my life was to participate in sessions of the SPIE and Optical Society of America focused on holographic interferometry, and especially to participate in the occasional informal sessions organized by Werner Juptner, Rich Pryputniewicz, and others in Worpswede, near Bremen, Germany.

When I began doing some of my research at the Radar and Optics Laboratory, my primary interest was not in the motion of solid, opaque objects, but in the measurement of three-dimensional temperature and density fields in transparent fluids. This was not of much interest to the mission of the Laboratory, but the open-minded people who ran the lab enabled me to start this work. To earn my keep, I was assigned to be the principal investigator on a rather large project sponsored by DARPA on the use of optical holographic interferometry for the nondestructive testing of solid objects, especially the detection of subsurface cracks and voids. In 1971, I was sent to a DARPA contractors meeting at the Watertown Arsenal outside Boston, MA. As I was driving along Storrow Drive just across the river from MIT, a local news program I was listening to on my car radio opened with the announcement that Jerome Wiesner, formerly President Kennedy's science advisor, had just been elected the 13th president of MIT. In my wildest dreams I could not have imagined that nineteen years later I would become MIT's 15th president. Karl Stetson, paraphrasing General MacArthur, used to say, “Old holographers never die; they just become incoherent.” As a dedicated teacher and researcher

in 1971, I would have considered such a descent into academic administration to be incoherent indeed. But such is life.

Coincidently, Emmett Leith once took a plunge into administration. Because he was the guiding light of the lab, he was once asked to become its head. He accepted, and in his sole administrative act, cleaned his desk and kept it neat for one or two days. He then decided he was not really an administrator, and, thank goodness for the field of optics, became the chief scientist and continued his long and always productive career as a researcher. He also became a remarkably able and endlessly dedicated teacher and mentor. He developed a unique but very effective lecturing style and always worked side-by-side with his students at all levels as colleagues.

In 1979, Emmett Leith received the National Medal of Science from President Jimmy Carter at the White House. Being an extremely conscientious professor, he arranged for one of his graduate students to teach his undergraduate class that afternoon. But soon after the class started, Emmett walked into the classroom with his presidential medal in his coat pocket. He had been so concerned about missing his class that he had skipped the social events following the ceremony in Washington and flown back to Ann Arbor to teach his class.

Just a few years ago I had the privilege of speaking at a symposium at an Optical Society of America meeting in Baltimore celebrating Emmett's career. He, Don Sweeney, and I had dinner together at a restaurant afterwards. Two things transpired that were pure Emmett. First, as he was nearing completion of a full and excellent meal with us, he noted that in fact he had already eaten dinner, but couldn't pass up the opportunity to visit with Don and me, and since we were in a restaurant, he thought the only decent thing to do was order another dinner. Second, I mentioned to Emmett that a year or two before this, while browsing in a bookstore, I had seen a copy of *Advances in Optics* that included a history of the Radar and Optics Laboratory he had written and wondered if a reprint might be available. He said “Sure,” stood up, reached into his pants pocket, and produced a copy for me. I'm still mulling that over.

I last saw Emmett at a celebration that Nicholas Negroponte and I hosted in honor of Steve Benton at the Media Lab at MIT. Steve, who developed the rainbow hologram, was another remarkably creative pioneer. He also was a teacher's teacher and built important bridges between the holography community and the arts community. The holography/art connection also played a role in the early days of holography, and gave rise to incredible things that could only have happened in the strange era of the 1960s and 1970s. I think especially of Lloyd Cross, who had worked on lasers and masers at the Willow Run

Laboratory and in the defense industry, but went on to work on multiplex holograms and founded the San Francisco Holography School, which was essentially a commune devoted to holography. They didn't like to use metal, or even standard optical components, so they fashioned surprisingly accurate anamorphic lenses by mounting clear plastic pillows filled with silicone in wooden fixtures and painstakingly adjusted until they had the required optical properties. I once visited the School with Emmett and Steve and actually met Pam, the young woman blowing the kiss in the famous cylindrical white-light hologram that is still sold in museum shops and elsewhere around the world.

The symposium to honor Steve Benton took place in 2003 and had been organized in part because he was suffering from a brain tumor. Attendees came from all over the world. Almost all of the early greats of the field were there, including Emmett Leith and Yuri Denysiuk, who had traveled from Russia. But Steve Benton was not there. He died the previous night. Steve's wife Jeannie insisted that the symposium should proceed, and that it should be lively and fun, just as Steve had been. When the group assembled, the atmosphere was solemn and awkward. Then Jeannie rose to speak. She said, “You all know the mantra of the Media Lab is 'Demo or die.' Who but Steve Benton would actually have done it?” This broke the sadness and tension in the room, and we proceeded in a true celebratory spirit. But two years after that, Emmett passed away, as did Densyiuk the following year. So the era of the most central pioneers of holography has passed.

But let me return to the '60s and '70s and the fun I had in research on holographic interferometry. Classical optical metrology, usually the application of Mach-Zehnder interferometers, had been used for many years to measure two-dimensional density fields such as natural convection flows over heated plates, and supersonic flows over airfoils in wind tunnels and shock tubes. The resulting interferograms could be interpreted quantitatively, i.e. be used to measure properties, only if the flows were two-dimensional, or radially symmetric. My goal as a young researcher was to use the three-dimensional images and interferograms made possible by laser holography to measure three-dimensional temperature fields that did not have any particular symmetry. I learned the experimental techniques of making holograms from Al Friesem.

It was my very good fortune to have Don Sweeney as one of my first Ph.D. students, and we worked together on this problem. The inverse problem that must be solved to interpret the fringes in a holographic interferogram of a three-dimensional density field is easy to pose, especially in finite difference form. Solving it, and especially solving it given constrained viewing angles and noisy data is not easy. It was

especially not easy in the early '70s when computing power was modest. But collecting the data was even worse. Don, several undergraduates, and I had to painstakingly record by hand the location of fringes using a viewing scope translated with a micrometer drive, and repeat that for a large number of viewing orientations.

Along the way through this research, Don discovered that his work was not entirely unique, because investigators such as Gabor Herman had been working on this problem in the context of medical X-rays. This gave us some help, but did not detract from the originality of Don's work.

One day I was sitting on a bench in the locker room of the campus recreation center and started talking with the mathematician Wilfred Kaplan. Many scientists and engineers of my generation are familiar with Kaplan's fine textbooks in advanced mathematics. I told Wilfred about our problem, which really was an attempt to computationally reconstruct a field given the values of a large number of line integrals through it.

A few weeks later, Professor Kaplan called me and said that he had been thinking about our problem and had recalled some abstract mathematical work by the Swiss mathematician Radon. It involved the analytical reconstruction of N-dimensional spaces given the set of (N-1)-dimensional projections through it. Sure enough, I tracked down Radon's work, and when it was reduced to the case of one-dimensional projections through a two-dimensional space, it gave the formal solution to the problem of reconstructing a two-dimensional slice of an object given the line integrals through it. Based on Wilfred Kaplan's advice I was able to present what I believe to be the first paper that showed that the Radon transform was the mathematical solution to the problem known today as tomography.

In the context of medical applications, Alan Cormack and Godfrey Hounsfield won the Nobel Prize in Medicine or Physiology in 1979 for solving this problem computationally and reducing it to practice as X-Ray Computer Assisted Tomography. By that time, I had become a friend of Alan Cormack and had come to know many other pioneers of computed tomography.

Thus I encountered another intersection, namely the intersection of holography and tomography, each of which earned the Nobel Prize. But let me assure you that combining two Nobel-winning fields does not produce a third Nobel Prize. But it is a great deal of fun and brings you into contact with lots of interesting people.

4 Closing

As I noted at the outset, my work was not at the heart of the fundamental field of holography, but it followed closely enough after the pioneering advances that I was privileged to work with many of the pioneers at Michigan and appreciate the environment that developed in their laboratory. It also afforded me the opportunity to learn very new things and to interact with many talented scientists and engineers around the world, many of whom are participating in this conference. What an extraordinary legacy of the holography pioneers is to be found in the size, scope, and international breadth of Fringe 2009.

TOPIC 1

New Methods and Tools for Data Acquisition and Processing

Chairs:

Malgorzata Kujawinska
Warsaw
(Poland)

Peter J. de Groot
Middletown
(USA)

Eduard Reithmeier
Hannover
(Germany)

Marc Georges
Liège
(Belgium)

Invited Paper

Coherence Holography: A Thought on Synthesis and Analysis of Optical Coherence Fields

Mitsuo Takeda, Wei Wang*, and Dinesh N. Naik
The University of Electro-Communications, Department of ICE
1-5-1, Chofugaoka, Chofu, Tokyo, 182-8585, Japan
*Heriot-Watt University, School of Engineering and Physical Sciences
Edinburgh, EH14 4AS, UK

1 Introduction

Coherence plays fundamental role in holography and interferometry, and control of coherence is essential in an illumination system for microscopy and lithography. This talk is intended to give a tutorial introduction to the concept, the principle, and the applications of a new technique of unconventional holography, called *coherence holography*, which was developed recently for synthesis and analysis of a spatial coherence function [1]. The basic principle of the new technique was inspired by the fact the coherence function $\Gamma(\boldsymbol{r}_1,t_1;\boldsymbol{r}_2,t_2)$ and the optical field $u(\boldsymbol{r},t)$ bear a formal analogy in the sense that both obey the same wave equation:

$$\begin{pmatrix}\text{Coherence}\\ \text{Function}\end{pmatrix} \quad \nabla^2_{i=1,2}\Gamma(\boldsymbol{r}_1,t_1;\boldsymbol{r}_2,t_2)=\frac{1}{c^2}\frac{\partial^2\Gamma(\boldsymbol{r}_1,t_1;\boldsymbol{r}_2,t_2)}{\partial t^2_{i=1,2}}; \tag{1}$$

$$\begin{pmatrix}\text{Optical}\\ \text{Field}\end{pmatrix} \quad \nabla^2 u(\boldsymbol{r},t)=\frac{1}{c^2}\frac{\partial^2 u(\boldsymbol{r},t)}{\partial t^2}.$$

This formal mathematical analogy suggests that the basic principle of holography already established for the wave of optical field can also be applied for the wave of coherence function. Just as a conventional computer-generated hologram can create an arbitrary 3-D optical field, a computer-generated coherence hologram (CGCH) can synthesize an optical field with a desired 3-D coherence function. Furthermore, the time-space symmetry in the wave equation indicates that the role of a temporal coherence function can be replaced by a spatial coherence function. This leads to a new concept of dispersion-free optical coherence tomography

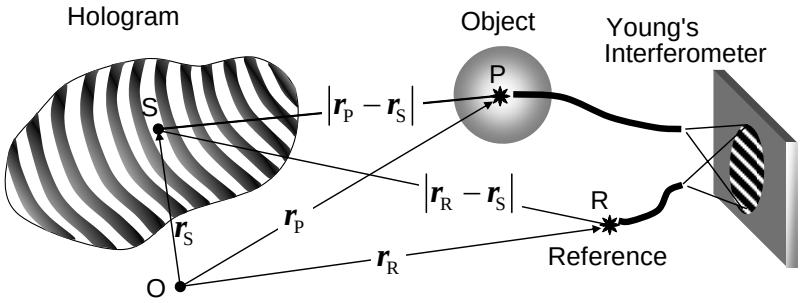

Fig. 1. Schematic geometry for holographic recording and reconstruction of a coherence hologram

and profilometry [2], which makes use of a spatial (rather than temporal) coherence function of quasi-monochromatic light synthesized by CGCH.

2 Principle of coherence holography

2.1 Reciprocity in spatial coherence and hologram recording

The principle of coherence holography can be explained on the basis of reciprocity in spatial coherence and holographic recording. Referring to Fig.1, let us first consider recording of a conventional hologram. We note an arbitrary point P at $\boldsymbol{r}_P$ on a 3-D object recorded with a reference beam from a point source R at $\boldsymbol{r}_R$. Suppose a point S at $\boldsymbol{r}_S$ on the hologram is located on one of the bright fringes resulting from constructive interference between the object and reference beams from points P and R. Then the optical path difference (OPD) between the two beams becomes integer multiples of the wavelength λ:

$$OPD(\boldsymbol{r}_P, \boldsymbol{r}_R; \boldsymbol{r}_S) = |\boldsymbol{r}_P - \boldsymbol{r}_S| - |\boldsymbol{r}_R - \boldsymbol{r}_S| = n\lambda \tag{1}$$

Next we illuminate the hologram with spatially incoherent quasi-monochromatic light. This generates an extended incoherent source with its irradiance distribution proportional to the intensity distribution of the hologram $I(\boldsymbol{r}_S)$. Let us now consider a reciprocal process in which light emitted from point S on the source reaches points P and R to create fields $u(\boldsymbol{r}_P)$ and $u(\boldsymbol{r}_R)$, respectively. From reciprocity of wave propagation and because of Eq. (1), $u(\boldsymbol{r}_P)$ and $u(\boldsymbol{r}_R)$ are always in phase with the

phase difference $2n\pi$, irrespective of the initial phase and the position of the point source S, as far as S is located on one of the bright fringes; this condition is automatically satisfied for all points on the hologram because no lights are emitted from the location of the dark fringes. Thus the incoherently illuminated hologram creates an optical field which is in phase and has high coherence between this particular pair of points at P and R. If we fix one point as a reference at R and move the other point P over the 3-D space with $\boldsymbol{r}_P$ as a variable, we can reconstruct the object as a 3-D distribution of the mutual intensity $J(\boldsymbol{r}_P, \boldsymbol{r}_R) = \langle u(\boldsymbol{r}_P) u^*(\boldsymbol{r}_R) \rangle$, which can be detected with a suitable interferometer. In Fig. 1, a Young's interferometer using an optical fibre is shown just for a conceptually simplest example.

2.2 Formal analogy between the diffraction integral and van Cittert-Zernike theorem

Another explanation of the principle can be made on the basis of formal analogy between the diffraction integral and van Cittert-Zernike theorem. Let us consider a conventional reconstruction process in which the hologram is illuminated from backward with a coherent spherical wave $\exp(-ik|\boldsymbol{r}_S - \boldsymbol{r}_R|)/|\boldsymbol{r}_S - \boldsymbol{r}_R|$ converging into the reference source point R. The reconstructed optical field, which forms a real image of the 3-D object at point P, is given by the diffraction integral for the Fresnel-Huygens secondary waves

$$u(\boldsymbol{r}_P, \boldsymbol{r}_R) = \iint I(\boldsymbol{r}_S) \frac{\exp[ik(|\boldsymbol{r}_P - \boldsymbol{r}_S| - |\boldsymbol{r}_R - \boldsymbol{r}_S|)]}{|\boldsymbol{r}_P - \boldsymbol{r}_S| \cdot |\boldsymbol{r}_R - \boldsymbol{r}_S|} d\boldsymbol{r}_S \tag{2}$$

It should be noted that Eq. (2) has exactly the same form as the formula for mutual intensity given by van Cittert-Zernike theorem

$$J(\boldsymbol{r}_P, \boldsymbol{r}_R) = \iint I(\boldsymbol{r}_S) \frac{\exp[ik(|\boldsymbol{r}_P - \boldsymbol{r}_S| - |\boldsymbol{r}_R - \boldsymbol{r}_S|)]}{|\boldsymbol{r}_P - \boldsymbol{r}_S| \cdot |\boldsymbol{r}_R - \boldsymbol{r}_S|} d\boldsymbol{r}_S \tag{3}$$

except the difference that $I(\boldsymbol{r}_S)$ in Eq. (2) is the amplitude transmittance of the hologram whereas $I(\boldsymbol{r}_S)$ in Eq. (3) is the intensity distribution of the spatially incoherent source. The implication of this formal analogy is that if a hologram, having intensity transmittance $I(\boldsymbol{r}_S)$ proportional to the recorded intensity, is illuminated with spatially incoherent light, an optical field will be generated, for which the mutual intensity between observation

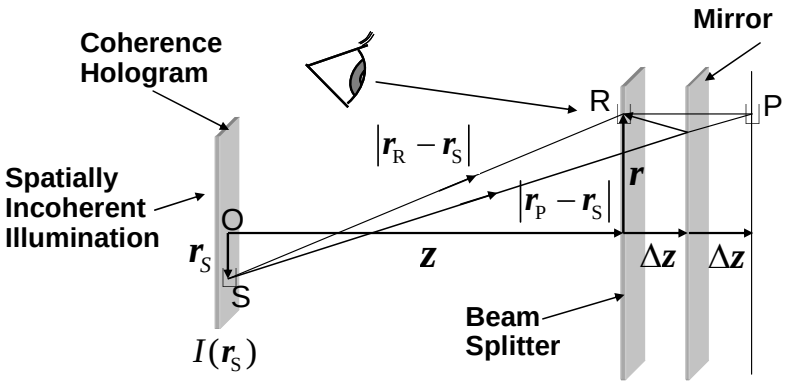

Fig. 2. Schematic geometry for reconstruction of a coherence hologram

point P and reference point R is equal to the optical field that would be reconstructed if the hologram with the same amplitude transmittance were illuminated with a phase-conjugated version of the reference beam. Unlike conventional holography, the reconstructed coherence image is not directly observable. It can be visualized only as the contrast and the phase of an interference fringe pattern by using an appropriate interferometer.

3 Experiment

Detection of coherence image by scanning the probe point of Young's interferometer, as shown in Fig.1, is impractical. We used a simple optical geometry shown in Fig.2, which is in effect a Fizeau interferometer but we realized it with a Michelson interferometer in our experiment. Light from an incoherently illuminated coherence hologram is guided into the interferometer to form interference fringes on the plane of the beam splitter as the result of interference between the fields at point R and point P.

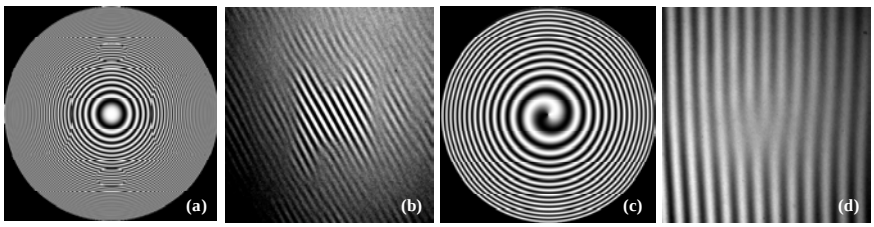

Fig. 3. (a) Computer-generated coherence hologram for a letter H. (b) Coherence image with the high coherence region representing letter H. (c) Computer-generated coherence hologram for generating a coherence vortex. (d) Interferogram of the coherence vortex with phase singularity in the coherence function.

The fringe contrast reflects the mutual intensity between the two points given by van Cittert-Zernike theorem in Eq. (3). Using the position vectors defined in Fig. 2, the mutual intensity is now approximated by

$$\begin{aligned} J(\boldsymbol{r}_P,\boldsymbol{r}_R) &\propto \iint I(\boldsymbol{r}_S)\exp[ik(|\boldsymbol{r}_P-\boldsymbol{r}_S|-|\boldsymbol{r}_R-\boldsymbol{r}_S|)]d\boldsymbol{r}_S \\ &= J(\boldsymbol{r},\Delta z) = \iint I(\boldsymbol{r}_S)\exp\left[ik(|\boldsymbol{z}+2\Delta\boldsymbol{z}+\boldsymbol{r}-\boldsymbol{r}_S|-|\boldsymbol{z}+\boldsymbol{r}-\boldsymbol{r}_S|)\right]d\boldsymbol{r}_S \\ &\approx \exp\left[i\alpha(\Delta z)\right]\iint I(\boldsymbol{r}_S)\exp\left[-ik\left(\frac{\Delta z}{z}\right)\times\frac{|\boldsymbol{r}-\boldsymbol{r}_S|^2}{z}\right]d\boldsymbol{r}_S \end{aligned} \tag{4}$$

where $\alpha(\Delta z)=k(2\Delta z)\left[1-2(\Delta z/z)^2\right]$ and the distance z between the hologram and the observation plane is assumed to be much larger than other parameters. It should be noted that the mutual intensity is given by the Fresnel transform of the incoherently illuminated hologram. If we record a Fresnel hologram with coherent light for an object at distance $\bar{z}=z^2/2\Delta z$ from the hologram, and illuminate the hologram with spatially incoherent light from behind, we will observe on the beam splitter a set of interference fringe patterns whose fringe contrast and phase represent, respectively, the field amplitude and the phase of the original object recorded with coherent light. Just as a computer-generated hologram (CGH) can create a three-dimensional image of a non-existing object, a computer-generated coherence hologram (CGCH) can create an optical field with a desired three-dimensional distribution of spatial coherence function. This CGCH gives a new possibility of optical tomography and profilometry [2] based on a synthesized spatial coherence function, and serves as a generator of coherence vortices [3]. An example of an on-axis (Gabor-type) CGCH for an object of a letter H is shown in Fig.3 (a). Figure 3 (b) shows the reconstructed coherence image, in which the letter H is displayed by the region of high contrast fringes representing the designed high coherence area [1]. Figures 3 (c) and 3(d) show, respectively, a coherence hologram for generating a coherence vortex and an interferogram of the coherence vortex [3].

4 McCutchen theorem and dispersion-free depth sensing with a spatial frequency comb generated by coherence holography

When the incoherent source (representing the coherence hologram in Fig.1) is at a distance very large compared to that between the two

observation points P and R, the mutual intensity $J(\boldsymbol{r}_P, \boldsymbol{r}_R)$ in Eq. (3) can be approximated by a formula in the form of the Debye integral, which we call McCutchen theorem [4]:

$$J(\boldsymbol{r}_P - \boldsymbol{r}_R) \approx \iint I(\boldsymbol{r}_S) \exp\left[-ik\left(\frac{\boldsymbol{r}_S - \boldsymbol{r}_R}{|\boldsymbol{r}_S - \boldsymbol{r}_R|}\right)\cdot(\boldsymbol{r}_P - \boldsymbol{r}_R)\right] \frac{d\boldsymbol{r}_S}{|\boldsymbol{r}_S - \boldsymbol{r}_R|^2}$$
$$= \iint I(\boldsymbol{c}_S) \exp\left[-ik\boldsymbol{c}_S\cdot(\boldsymbol{r}_P - \boldsymbol{r}_R)\right] d\Omega_S \tag{5}$$

where $\boldsymbol{c}_S = (\boldsymbol{r}_S - \boldsymbol{r}_R)/|\boldsymbol{r}_S - \boldsymbol{r}_R|$ is a unit vector pointing from point R toward the source element $d\boldsymbol{r}_S$, $d\Omega_S = d\boldsymbol{r}_S / |\boldsymbol{r}_S - \boldsymbol{r}_R|^2$ is an increment of solid angle subtending the source element $d\boldsymbol{r}_S$ (see, Fig.4). The source distribution projected onto the unit sphere (***c*** sphere) is called a generalized source. MacCutchen theorem can have a more simplified form of 1-D Fourier transform:

$$J(L) = \int_{-\infty}^{\infty} I(l) \exp(-ikLl) dl \tag{6}$$

where $L\boldsymbol{d} = \boldsymbol{r}_P - \boldsymbol{r}_R$ and $l = \boldsymbol{c}_S \cdot \boldsymbol{d}$, with $\boldsymbol{d}$ being a unit vector in the direction of $\boldsymbol{r}_P - \boldsymbol{r}_R$, and $I(l)$ is the projection of the generalized source upon a line oriented in the same $\boldsymbol{d}$ direction in the **c** sphere; $I(l)$ is called the source distribution. McCutchen theorem gives an insight into the new concept of a spatial frequency comb and a spatial coherence comb which can be applied for dispersion-free depth sensing [5]. Suppose a coherence hologram with a Fresnel-zone-plate-like incoherent ring source structure as shown in Fig.5. The thin ring sources are first projected onto the McCutchen ***c*** sphere and then onto a line connecting a reference point R and an observation point R, to form a periodic impulse source distribution with period Δl, expressed by a comb function $I(l) = \mathrm{comb}(l/\Delta l)$. This source distribution is called a spatial frequency comb because the

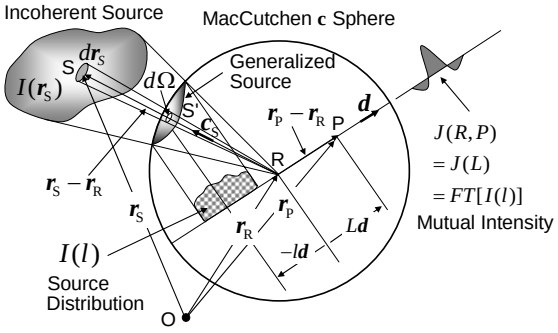

Fig.4. McCutchen theorem for generalized source and mutual intensity

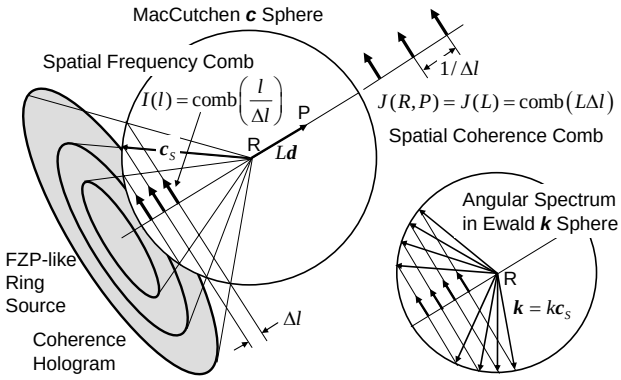

Fig.5. Spatial frequency comb generated by a coherence holography

directional unit vector $\boldsymbol{c}_s$ pointing the ring source can be related to a $\boldsymbol{k}$-vector by $\boldsymbol{k}=k\boldsymbol{c}_s$ which represents an angular spectrum in an Ewald sphere as shown in Fig.5. From the Fourier relation in Eq. (6), the mutual intensity of the optical field between points R and P (separated by L on the line parallel to $\boldsymbol{d}$) becomes a comb function $J(L)=\mathrm{comb}(L\Delta l)$, called a spatial coherence comb, and exhibits a selective high spatial coherence in the direction of $\boldsymbol{d}$ with period inversely proportional to Δl. By controlling the FZP-like ring source in the coherence hologram with a spatial light modulator (SLM), we can scan the coherence comb function in the depth direction $\boldsymbol{d}$ to obtain a 3-D tomography image. Unlike a conventional optical frequency comb (which is composed of equally spaced multiple polychromatic line spectra), the spatial frequency comb is generated by monochromatic light and opens up a new possibility of spatial coherence tomography completely free from dispersion problem [5].

An example of depth sensing with a variable longitudinal spatial coherence comb function created by an SLM-generated tunable spatial frequency comb is shown in Fig.6 [5]. Shown in Fig.6 (a) is a coherence hologram with a FZP-like source distribution, in which each ring source is composed of a same number of point sources to equalize the comb heights. The interval of the spatial coherence comb is varied by SLM, and fringe contrast on the surface of two gauge blocks with a 400 μm height gap was observed with a Michelson interferometer. In Fig. (b), fringe contrast is low because the coherence comb does not match the surfaces of the gauge blocks, whereas high-contrast fringes are observed in Fig. (c) and Fig. (d) because the coherence comb matches the surfaces I and II, respectively.

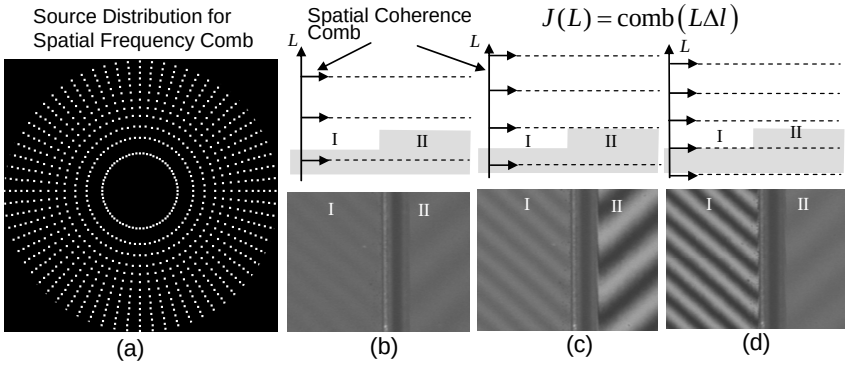

Fig.6. Sensing of the depth of block gauge surfaces by gating with a spatial coherence comb. (a) Source distribution for spatial frequency comb; (b)-(d) spatial coherence gating function is scanned by changing the interval of the spatial coherence comb.

5 Acknowledgment

Part of this work was supported by Grant-in-Aid of JSPS B (2) No. 21360028. We thank Joseph Rosen of Ben-Grion University of the Negev, and Zhihui Duan of Optoelectronics Co., Ltd. for their contributions in the early stage of the research.

6 References

1. Takeda, M, Wang, W, Duan, Z, Miyamoto, Y (2005) Coherence Holography. Opt. Express 13: 9629-9635
2. Rosen, J, Takeda, M (2000) Longitudinal spatial coherence applied for surface profilometry. Appl. Opt. 29: 4107-4111
3. Wang, W, Duan Z, Hanson, S, J, Miyamoto, Y (2006) Experimental study of coherence vortices: Local properties of phase singularities in a spatial coherence function. Phys. Rev. Lett. 96: 073902
4. McCutchen, C, W (1966) Generalized source and the van Cittert-Zernike theorem: A study of spatial coherence required for interferometry. J. Opt. Soc. Am. 56: 727-733
5. Duan, Z, Miyamoto, Y, Takeda, M (2006) Dispersion-free optical coherence depth sensing with a spatial frequency comb generated by an angular spectrum modulator. Opt. Express 14: 12109-12121

The Polarization Approach in Measuring Correlation Properties of Optical Fields

Prof. O. V. Angelsky[1], Dr. C. Yu. Zenkova[2], N. V. Gorodyns'ka[1]
[1]Department of Correlation Optics, Chernivtsi National University,
2, Kotsyubinsky Str., Chernivtsi 58012, Ukraine, angelsky@itf.cv.ua
[2]Optics and Spectroscopy Department, Chernivtsi National University,
2, Kotsyubinsky Str., Chernivtsi 58012, Ukraine, zenkova@itf.cv.ua

1 Introduction

Coherence of electromagnetic waves, including optical ones, manifests itself in their interference resulting in spatial intensity modulation. Visibility of an interference pattern is used for estimating the degree of coherence of the waves causing such distribution [1]. On the other hand, superposition of mutually coherent but orthogonally polarized waves under paraxial approximation results in a spatial variation of the states of polarization of the resulting field; for that, any intensity modulation of the resulting field is absent. It is quite natural in this situation to put in the base of estimation of the degree of correlation of partial waves the parameters characterizing the magnitude of polarization modulation.

The structural diagnostics of objects inhomogeneous from the viewpoint of their polarization state are based on known correlations between the statistical parameters of an object and those of the scattered field [2]. The heaviest volume of information is contained in the near-field pattern, since it is not affected by spatial filtering. The optical field's polarization must be taken into account in this case [3, 4]. The contribution of the longitudinal field component (LFC) then becomes important. Thus we need additional statistical parameters for the diagnostics of such objects. Nowadays, the analysis of these problems shows that in papers [5, 6] the parameter characterizing the degree of mutual polarization in different points of inhomogeneously polarized optical fields has been introduced and accepted. This parameter is invariant to the transformations of the coordinate system and, as a consequence, does not depend on the choice of the state of polarization of the probing beam [5]. Since the degree of mutual polarization contains information about the correlation that exist between the components of the electric field at a pair of points, it might expect that there exist a connection between this parameter and the degree

of polarization that characterizes correlations in a single point. It has been once more theoretically substantiated that the degree of polarization characterizes the level of disorder in each beam, viz. the level of decorrelation of the field components of one beam, and corresponds to the maximum of the autocorrelation function of this beam [7]. In its turn, the intrinsic coherence introduced in the paper [8] characterizes the degree of disorder between interacting beams in different points of a field and at different instants. Henceforth, for the quantitative characteristics of the intrinsic coherence we will use the term degree of cross-correlation of the fields, regarding these terms to be synonyms.

2 Statement of the problem

Let us introduce a normalized mutual coherence matrix $M(\vec{r}_1,\vec{r}_2,t_1,t_2)=\Gamma^{-1/2}(\vec{r}_2,t_2)W(\vec{r}_1,\vec{r}_2,t_1,t_2)\Gamma^{-1/2}(\vec{r}_1,t_1)$, whose singular values $\mu_s(\vec{r}_1,\vec{r}_2,t_1,t_2), \mu_I(\vec{r}_1,\vec{r}_2,t_1,t_2)$ determine the intrinsic degrees of coherence [7]. Here W($\vec{r}_1$, $\vec{r}_2$, t_1, t_2) – is the 3 × 3 mutual coherence matrix, defined by $W(\vec{r}_1,\vec{r}_2,t_1,t_2)=<\vec{E}_i(\vec{r}_1,t_2)\vec{E}_j^{\,*}(\vec{r}_2,t_1)>$, ($i$ = x, z). From mathematical point of view, one uses the property that any matrix can be decomposed in its singular values $\mu_s(\vec{r}_1,\vec{r}_2,t_1,t_2), \mu_I(\vec{r}_1,\vec{r}_2,t_1,t_2)$, such as

$$M(\vec{r}_1,\vec{r}_2,t_1,t_2)=N_2^{*}D(\vec{r}_1,\vec{r}_2,t_1,t_2)N_1 \tag{1}$$

where

$$D(\vec{r}_1,\vec{r}_2,t_1,t_2)=\begin{bmatrix}\mu_s(\vec{r}_1,\vec{r}_2,t_1,t_2) & 0\\ 0 & \mu_I(\vec{r}_1,\vec{r}_2,t_1,t_2)\end{bmatrix} \tag{2}$$

N1 and N2 are unitary matrices and where $\mu_s(\vec{r}_1,\vec{r}_2,t_1,t_2)\geq\mu_I(\vec{r}_1,\vec{r}_2,t_1,t_2)\geq 0$. The matrix $D(\vec{r}_1,\vec{r}_2,t_1,t_2)$ corresponds to the normalized mutual coherence matrix of totally depolarized light described in the basis of the singular value decomposition of $M(\vec{r}_1,\vec{r}_2,t_1,t_2)$. The correlation of collinear components of the interacting beams, for example, $E_{x1}(\vec{r}_2,t_2), E_{x2}(\vec{r}_1,t_1), E_{z1}(\vec{r}_2,t_2), E_{z2}(\vec{r}_1,t_1)$, determines the

degrees of the intrinsic coherence $\mu_s(\vec{r}_1,\vec{r}_2,t_1,t_2), \mu_I(\vec{r}_1,\vec{r}_2,t_1,t_2)$, according to Exp. (1) - (2). We take into consideration the longitudinal field component (z-component) in order to be able to demonstrate the contribution of the polarization modulation into the degree of cross-correlation of optical fields. In our case of the interference of two orthogonally polarized waves $\mu_s(\vec{r}_1,\vec{r}_2,t_1,t_2) = \eta_{xx}(\vec{r}_1,\vec{r}_2,t_1,t_2)$ and it describes the degree of the coherence between x-components of the two initial waves. Correspondingly $\mu_I(\vec{r}_1,\vec{r}_2,t_1,t_2) = \eta_{zz}(\vec{r}_1,\vec{r}_2,t_1,t_2)$ and describes the degree of coherence between z-components. The maximum values of the parameters μ_s and μ_I are unit and correspond to completely correlation of x- and z- components. If the both of these components are equal to one, there exists a polarization modulation of the field that can lead to a unit modulus of the visibility of the interference pattern. That is, in the general case, the correlation of optical fields must be estimated by measuring both the visibility of the resulting distribution and the deepness of modulation, i.e. the degree of polarization of the field. The sum of these two normalized parameters must be equal to unity. It seems that the additive properties of correlations manifests itself just in this manner. In other words, the degree of polarization and the degree of coherence of the field determined by the visibility of the interference pattern are mutually complementary measures of the cross-correlation of two fields. At the same time, the question remains opened: in what way one can experimentally estimate the coherence properties of real optical fields, where the correlation of the fields can manifest both in the spatial modulation of intensity due to interference and in the polarization modulation of the resulting field [9]. The feasibilities of the estimating of the degree of two fields correlation are presented. They are depended on the experimental models:

- interference of identically polarized beams (scalar approximation), when the degree of cross-correlation is estimated by the visibility of the recorded interference pattern;
- superposition of orthogonally polarized interacting beams, when the degree of cross-correlation is estimated by the deepness of polarization state (SOP) modulation, *viz.* the degree of polarization of the resulting field;
- superposition of the beams whose states of polarization (SOPs) are different but not orthogonal, when for the estimating the degree of cross-correlation it is necessary to measure both the visibility of the interference pattern and deepness of modulation of the polarization distribution, i.e. the degree of polarization.

While the results obtained within the scalar approximation are classical and do not require any comments, the other two cases require more detailed consideration. The results, which are presented in this paper show not only the contribution of the polarization component into the correlation of fields, but also directs the way to the quantitative estimation of this correlation. At the registration plane one can analyze the intensity modulation and the polarization modulation which yet must be revealed. It is expediently to use here the interference principle, namely, to introduce perpendicularly to the registration plane the third plane coherent probing beam which is linearly polarized at the figure plane. One can reliably predict that the interference of such three waves will result in changing visibility (deepness of the intensity modulation) of the interference pattern caused by the in-pair interaction of the collinear components of the two initial waves. Usage of the reference wave enables only to illustrate the presence in the field of the spatial polarization modulation (together with the intensity modulation caused by the interference of the collinear field components). In this case**,** we only reveal additional changing of the visibility of the resulting pattern of modulation caused by interference of the collinear components of the SOP distribution and the reference wave. We have used the holographic arrangement (Fig. 1) for the estimation of the degree of coherence of these waves, where for providing "purity" of an experiment an immersion liquid is used, so that the angle of convergence of plane initial superposing waves is 90^0. On the other hand, usage of an immersion provides effective reconstruction of a beam at the readout stage.

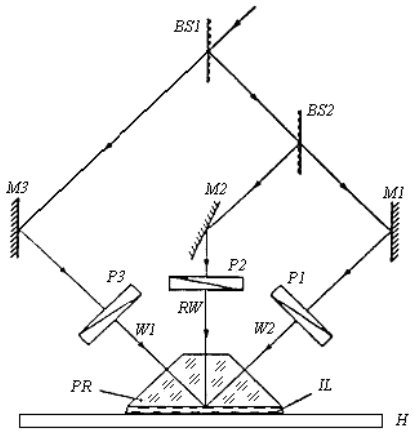

Fig. 1. Optical arrangement for holographic experiment: BS1 and BS2, beam splitters; M1, M2, and M3, mirrors; P1, P2, and P3, polarizers; PR, prism; IL, immersion liquid; H, hologram.

The use of a holographic technique is caused by the necessity of registration of spatial intensity distribution at very high frequencies.

Similarly to the previous case, to diagnostic superposition of the beams whose states of polarization are different but not orthogonal common polarization devices are insufficient for revealing and diagnosing such a modulation. It is expediently to use here the interference principle, namely, to introduce perpendicularly to the registration plane the third plane coherent probing beam which is linearly polarized at the figure plane. The experimental arrangement is shown in Fig. 2. CCD camera is used for the registration of the obtained interference patterns. The angle of convergence of the plane object beams is 10^0, and the angle of each of the plane object beams with the reference beam is 5^0. The intensities of the object beams were equal to each other and intensity and the phase of the reference beam was changed.

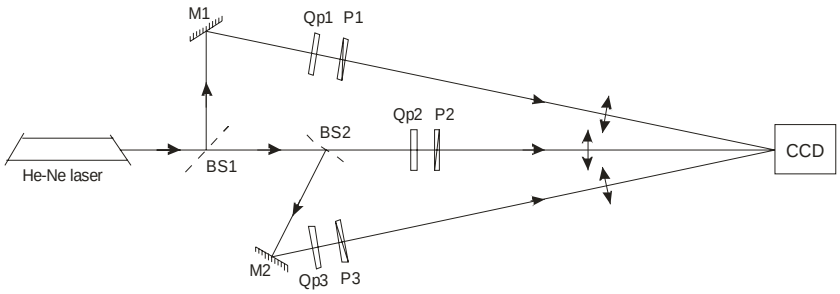

Fig. 2. Optical arrangement of the experiment: BS1, BS2 – beam splitters; M1 and M2 – mirrors; Qp1, Qp2 and Qp3 - quarter-wave plates; P1 – P3 – polarizers; CCD – CCD camera.

The experimental results are presented in the form of interferograms obtained in various polarization situations. If the state of polarization of the reference beam is linear and the electrical vector lies in the figure plane, then the structure (period) of the registered interference pattern is changed, as a rule, it is doubled. The doubling of the period of the interference pattern is the most pronounced in the situation in which the intensity of the reference beam exceeds the intensity of the object beams. Such doubling of a period is of pure polarization nature. Thus, the contribution of the polarization component to the correlation of optical fields has been shown. The differences in the structure of the observed interference patterns are the most pronounced in the situation of a three-beam interference, when the intensity of the reference beam is higher than the intensities of the two object beams. One can certainly assert that only in the pattern of the interference distribution for three beams polarized in

the incidence plane one can observe elements**,** which can be classified as bending or, perhaps, even bifurcations of the interference fringes. This is the unbiased diagnostic sign of the presence of the polarization singularities [10] in the field and shows the contribution of the polarization component in the formation of the structure of the interference distribution and, as a consequence, of a field. The estimations of the visibility of the obtained interference distributions**,** both experimentally and by computer simulation**,** support this conclusion.

3 Conclusions

Thus, the contribution of the polarization component in the correlation of the vector optical fields has been substantiated and experimentally illustrated. It has been noted that the degree of mutual polarization of a field, *viz.* the parameter which by its sense can be referred to as the generalized visibility of a field, is the optimal statistical parameter providing an estimation of the correlation of the complex spatially statistically inhomogeneous fields.

4 References

1. Born, M, Wolf, E (1980) Principles of Optics (Pergamon, Oxford).
2. Rytov, S.M, Kravtsov, Yu.A, and Tatarsky, B.I (1978) Introduction to Statistical Radiophysics, Part II, Random Fields (Nauka, Moscow) (in Russian).
3. Setala, T, Shevchenko, A, Kaivola, M, Friberg, A.T (2002) Degree of polarization for optical near fields. Phys. Rev. E 66: 016615
4. Setala, T, Kaivola, M, Friberg, A.T (2002) Degree of polarization in near fields of thermal sources: effects of surface waves. Phys. Rev. Lett. 88: 123902.
5. Tervo, J, Setala, T, Friberg, A.T (2003) Degree of coherence for electromagnetic fields. Opt. Express 11 (10): 1137-1143.
6. Ellis, J, Dogariu, A (2004) Complex degree of mutual polarization. Opt. Lett. 29 (6): 536-538.
7. Refregier, P, Goudail F (2005) Invariant degrees of coherence of partially polarized light. Opt. Express. 13 (16): 6051-6060.
8. Refregier, P, Roueff, A (2007) Intrinsic Coherence: A new concept in Polarization and Coherence Theory. OPN: 30-35.
9. Tudor, T (1991) Waves. Amplitude waves. Intensity waves. Journal of Optics-Paris (Nouv. Rev. Opt.) 22 (6): 291-296.
10. Angelsky, O.V, Mokhun, I.I, Mokhun, A.I, Soskin, M.S (2002) Interferometric methods in diagnostics of polarization singularities, Physical Review E 65: 036602.

Real-time Coherence Holography

Dinesh N. Naik, Takahiro Ezawa, Yoko Miyamoto, and Mitsuo Takeda
Department of Information and Communication Engineering,
Laboratory for Information Photonics and Wave Signal Processing,
The University of Electro-Communications,
1-5-1, Chofugaoka, Chofu, Tokyo 182-8585, Japan

1 Introduction

Coherence holography capable of real-time recording and reconstruction is proposed and experimentally demonstrated for the first time. The coherence holography is an unconventional holographic technique which has a unique characteristic that a recorded object is reconstructed with a 3-D coherence function [1]. The recording process of a coherence hologram is same as that of a conventional hologram, but the reconstruction process is completely different, as a suitable interferometer is used to correlate the field at two different locations in 3-D space to find the coherence function.

2 Principles

Because of the formal analogy between the diffraction integral and the formula of van Cittert-Zernike theorem [2,3], when a hologram is illuminated with a spatially incoherent light, the coherence function or the mutual intensity between a pair of points separated by a length $\delta \boldsymbol{r} = \boldsymbol{r}_2 - \boldsymbol{r}_1$ on the image plane is proportional to the optical field which would be observed at a point $\boldsymbol{r} = \delta \boldsymbol{r}$ by conventional holography if the hologram were illuminated by a coherent light source.

For an object with its Fourier spectrum given by $G(\hat{x}, \hat{y})$, the Fourier transform hologram is given by $\left|H(\hat{x}, \hat{y})\right|^2$ where $H(\hat{x}, \hat{y})$ is the interfering optical field resulting from the superposition of a reference beam with unit amplitude (see Eq.1.).

$$H(\hat{x}, \hat{y}) = G(\hat{x}, \hat{y}) + 1 \tag{1}$$

In conventional holography we can realize the reconstruction of coherently illuminated hologram by taking an inverse Fourier transform (see Eq.2.).

$$g'(x,y;z) = \iint \left|H(\hat{x},\hat{y})\right|^2 \exp\left[ik_z(\hat{x},\hat{y})z\right]\exp\left[i\frac{2\pi}{\lambda f}(x\hat{x}+y\hat{y})\right]d\hat{x}d\hat{y} \tag{2}$$

where

$$k_z(\hat{x},\hat{y}) = \frac{2\pi}{\lambda}\sqrt{1-\left(\frac{\hat{x}}{f}\right)^2-\left(\frac{\hat{y}}{f}\right)^2} \tag{3}$$

Here λ is the wavelength of light and *f* is the focal length of lens used to perform inverse Fourier transform. The term $\exp\left[ik_z(\hat{x},\hat{y})z\right]$ propagates the field in z direction by distance *z*. When z=0, we are in the inverse Fourier transform plane.

Instead of recording the hologram, if we display the interference fringes on a rotating ground glass, it destroys the spatial coherence by adding a random phase $\Phi_R(\hat{x},\hat{y})$ for the field in that plane. The scattered optical field is given by

$$g(x,y;z) = \iint H(\hat{x},\hat{y})\exp\left(i\Phi_R(\hat{x},\hat{y})\right)\exp\left[ik_z(\hat{x},\hat{y})z\right] \exp\left[i\frac{2\pi}{\lambda f}(x\hat{x}+y\hat{y})\right]d\hat{x}d\hat{y} \quad (4) \tag{4}$$

This field by itself does not reconstruct the object. We correlate the field and find the mutual intensity or coherence function $\Gamma(\Delta x,\Delta y;\Delta z)$ between a pair of points. Now it can be clearly seen that the 3-D coherence function reconstructs the object in the same way the optical field reconstructs the object in conventional holography (see Eq.6.).

$$\Gamma(\Delta x,\Delta y;\Delta z) = \left\langle g^*(x_1,y_1;z_1)\,g(x_2,y_2;z_2)\right\rangle \tag{5}$$

$$= \iint \left|H(\hat{x},\hat{y})\right|^2 \exp\left[ik_z(\hat{x},\hat{y})\Delta z\right] \times \exp\left[i\frac{2\pi}{\lambda f}\left(\hat{x}\Delta x+\hat{y}\Delta y\right)\right]d\hat{x}d\hat{y} \tag{6}$$

where $\Delta x = x_2 - x_1, \Delta y = y_2 - y_1, \Delta z = z_2 - z_1$

In principle the mutual intensity between any two points can be detected by means of a Young's interferometer, but such sequential point probing is impractical. To reconstruct the image in coherence holography simultaneously we need a suitable interferometer that gives us a 2D correlation map in real time for the entire correlation lengths covering the full image field. A reconstructed image, represented by a coherence function, can be visualized with a controllable magnification by our new technique, which opens up a new possibility of a coherence-zooming microscope with variable magnification. For this purpose, we use a modified Sagnac radial shearing interferometer with a geometric phase shifter.

3 Experiments

In our new experiment, a lensless Fourier transform hologram of a transmission object is generated with the help of a Mach-Zehnder interferometer as shown in Fig. 1. We used a numeral 3 with a size about a millimeter as object in this case. The polarizing beam splitter 1 (PBS1) splits the incoming He-Ne laser beam into two orthogonally polarized beams. Inside the interferometer, a half wave plate 2 (HWP2) rotates the polarization to make it same as that of the other beam.

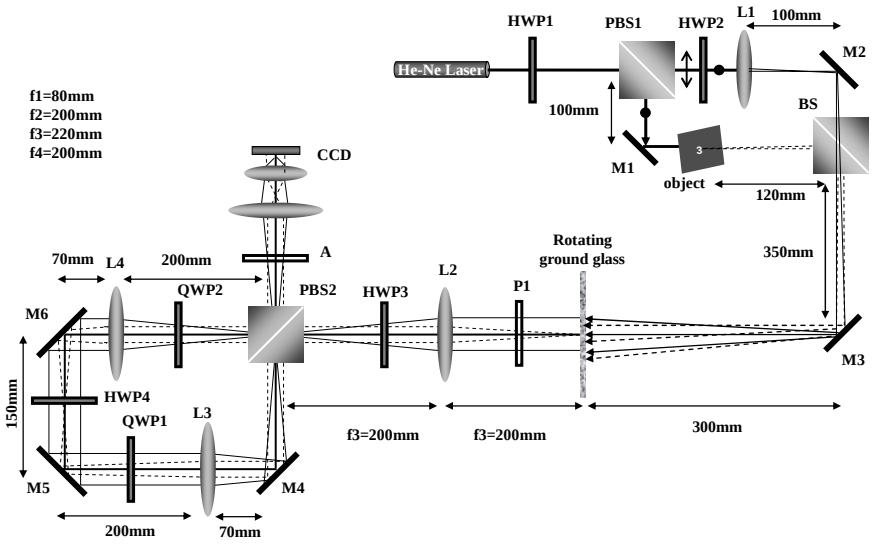

Fig. 1. The experimental set up for real-time coherence holography

Inside the Mach-Zehnder interferometer, one of the beams coherently illuminates the object and the other beam generates a point source with the help of lens L1. Looking from the output of the interferometer, we have an off axis object with a point source at the centre that generates a lensless Fourier transform of the object. Instead of recording interference fringes of the hologram, we directly displayed the fringe pattern on a rotating ground glass so that the hologram is represented in real time by the irradiance distribution of a spatially incoherent extended source. The relative intensity of the superposing fields can be controlled by rotating the half wave plate 1 (HWP1) kept at the input of the Mach-Zehnder interferometer.

The field distribution of the incoherently illuminated hologram is Fourier transformed by lens L2 with a focal length 200mm and introduced into the interferometer through a half wave plate 3 (HWP3). A polarizer P1 placed after the ground glass nulls any depolarization of the scattered light due to birefringence or multiple scattering in the ground glass material. A polarizing beam splitter (PBS2) splits the incoming beam into two counter propagating beams. The telescopic system with magnification $\alpha = 1.1$, formed by lenses L3 (focal length 220mm) and L4 (focal length 200mm), gives a radial shear between the counter propagating beams as they travel through interferometer before they are brought back together and imaged by CCD. At any location **r** on the image plane, the interference is due to the superposition of fields at the locations $\mathbf{r}\alpha$ and $\mathbf{r}/\alpha$ of the original beam [4]. Thus, at point **r** on the image plane, we have a cross-correlation of the fields between two points separated by $\delta\mathbf{r}$ proportional to **r** scaled by the factor $(\alpha - \alpha^{-1})$. The resulting interference gives a 2-D correlation map that reconstructs the image as a coherence function represented by the fringe contrast. The magnification of the reconstructed image can be suitably chosen with the proper choice of the amount of shear. In our present setup with α =1.1, the magnification for reconstruction becomes 5.23 so that the reconstructed image size fits the field aperture of the CCD camera. The half-wave plate 3 (HWP3) is aligned such that the radially sheared interfering beams at the output of the interferometer have equal amplitudes. To detect the reconstructed coherence image represented by the fringe visibility, we need to introduce a phase shift into the common-path Sagnac interferometer. Because of its common path nature, the Sagnac interferometer is insensitive to the conventional PZT-based mechanical mirror movement. We therefore introduced the required phase shift by means of a geometric phase shifter. Inside the interferometer we made use of two quarter wave plates (QWP1 and QWP2) to turn the linearly polarized light into a circularly polarized light and back to linearly

polarized light. By rotating a half wave plate 4 (HWP4), placed between QWP1 and QWP2, we introduced a geometric phase into the counter propagating beams [5], which is used to find the fringe visibility. With an analyzer A with its axis kept at 45^{o} to the orientation of the polarization of the two beams, interference between the two beams was achieved.

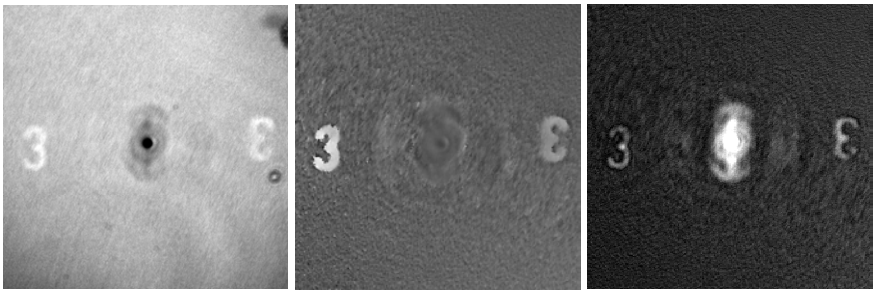

(a) (b) (c)

Fig. 2. Reconstructed images: (a) Raw intensity image resulted from shearing interference in real time; (b) phase image and (c) contrast image jointly representing the complex coherence function

Fig. 2(a) shows the image captured by CCD at the interference output. Figures 2 (b) and (c) show, respectively, the phase map and the fringe visibility calculated by using the model based nonlinear least squares fitting method [6] which solves the over determined equations generated from the image data for the parameters of the model.

4 Conclusions

We proposed and experimentally demonstrated object reconstruction using coherence holography in real-time. Because of the fact that Sagnac common path interferometer is very stable to the surrounding vibrations and air turbulences, the reconstruction process is highly reliable which means that what ever changes occurring for the object only will reflect in reconstructed image. In our present experiment we have used a 2-D object because the lensless Fourier transform method is used for the generation of hologram. But the reconstruction method using Sagnac radial shearing interferometer is also capable of reconstructing 3-D objects or objects placed at different depths with out any further modification. For 3-D object reconstruction, we only need to image a different depth location at the output of Sagnac radial shearing interferometer on to the CCD camera. The radial shear introduced in the transverse direction is same for field at

different depths that allows the reconstruction of objects at different depths with same magnification and quality. The choice of magnification of the reconstructed image paves the way for using it as a coherence imaging microscope.

5 Acknowledgment

Part of this work was supported by Grant-in-Aid of JSPS B (2) No. 21360028.

6 References

1. Takeda, M, Wang, W, Duan, Z, Miyamoto, Y (2005) Coherence Holography. Opt. Express 13: 9629-9635
2. Born, M, Wolf, E (1970) *Principles of Optics*, 4th ed. (Pergamon, London): Chap. 10.
3. Goodman, J. W (1985) *Statistical Optics*, 1st ed. (Wiley, New York): Chap. 5.
4. Murty, M. V. R. K (1964) A compact radial shearing interferometer based on the law of refraction. Appl. Opt. 3: 853-857
5. Hariharan, P, Roy, M (1992) A geometric-phase interferometer. J. Mod. Opt. 39: 1811-1815
6. Handel, P (2000) Properties of the IEEE-STD-1057 four-parameter sine wave fit algorithm. IEEE Trans. Instrum. Meas 49, No.6: 1189–1193

Coherence and Correlation in Digital Holography

Ichirou Yamaguchi
Toyo Seiki Seisaku-sho
1-2-6 Funado, Itabashi-ku, Tokyo 174-0041, Japan

1 Introduction

Digital image processing has widely extended capability and practicablity of interferometry applied to mirror surfaces. In holography and speckle metrology aiming at diffusely reflecting surfaces digital approaches are even more useful because diffraction integrals and/or correlation analysis that were difficult to carry out by analog processing can be performed accurately and flexiblly. Advanced digital memory and communication channels have realized storage and transmission of versatile amounts of image information reliablly and quickly. The biggest challenge in coherent metrology is suppression of speckle noise altough speckles work as information carriers. Both holography and speckle can measure 3-dimensional objects because the former has capability of 3-dimensional imaging and the latter is distinct everywhere in 3-dimensional space. They can provide qunatitative information on shape and deformation of diffusely reflecting surfaces. The information is carried by spatially fluctuating but temporally stationary light field generated by diffuse reflection of laser light, which leads to interference of a number of light with random phase differences introduced by surface roughness. Only the interference between identical surface point is extracted to provide the desired information. It means that the optical path change arising from displacement of each object point can be observed as deterministic interference fringes or speckle displacement. Speckle displacement is related with the gradient of the change in the optical path. Although analytical relationships between holographic interferometry and speckle metrology have been already discussed on the basis of correlation properties of scattered fields [1,2], it has not been clarified how the specifications of detectors recording holograms or speckle patterns affect the final results of measurement for general shape and deformation of surfaces. In this paper we derive the observed qunantities by numerical simulations that can treat genreral cases for evaluating performance of particular measurement systems.

2 Basic relations

We start from a digital holographic system represented by the 2-dimensiona coordinate system shown in Fig.1. A diffuse object is illuminated by a point monochromatic source S with the wave number $k=2\pi/\lambda$. An object point P[x,$h(x)+r(x)$] where $h(x)$ and $r(x)$ mean the initial mean surface and the random roughness profile, respectively, is assumed to be displaced to P'[$x+a_x(x)$, $h(x)+r(x)+a_z(x)$] with the displacement vector $\boldsymbol{a}$ (a_x,a_z). The complex amplitudes at the hologram plane are represented by superpositions of spherical waves scattered by each object point P or P'. The distribution of $r(x)$ is represented by random numbers whose range is characterized by the maximum surface roughness. At the hologram plane the complex amplitude from each point is added with macroscopic amplitude but with random phase differences introduced by the surface roughness such as

$$U(s:a)=\sum_{xi}\sqrt{I_O(x_i+a_x)}\exp\left\{ik\left[L(\mathrm{S},\mathrm{P}')+L(\mathrm{P}',\mathrm{Q})\right]\right\}, \tag{1}$$

where $I_o(x)$ is the macroscopic intensity distribution at the object and $L(A,B)$ the distance between A and B. At the CCD plane distant from the object by L_H the complex amplitude is combined with the reference beam having the complex amplitude $U_R=A_Re^{i\delta}$ to yield the intensity

$$I_H(s:a:\delta)=\left|A_R\exp(i\delta)+U(s:a)\right|^2, \tag{2}$$

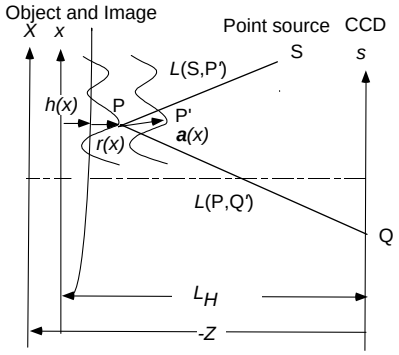

Fig. 1. Coordinate system for simulating image formation by digital holography

Each pixel of the image detector with the pitch p, the width w, and pixel number N supplies the output

$$S(m:a:\delta)=\int_{(m-1)p}^{(m-1)p+w} I_H(s:a:\delta)ds \qquad (m=1\ \sim N), \tag{3}$$

In phase-shifting digital holography at least three holograms are recorded after phase shifts of the reference beam. In the case of three-steps algorithm the complex amplitude of the object wave is derived such as

$$U(m:a)=S(m:0)-S(m:\pi)+i\left[S(m:0)-2S(m:\pi/2)+S(m:\pi)\right], \tag{4}$$

where the dependence on *a* has been omitted on the right-hand side. The image reconstruction is conducted by the angular spectrum method. It is appropriate here because of no limitation on the distance between the object and the reconstruction plane as well as the constant sample pitch equal to *p* of the reconstructed image. First we calculate the Fourier transform of the above complex amplitude

$$\hat{U}(n:a)=\sum_{m=1}^{N} U(m:a)\exp(-i2\pi mm), \tag{5}$$

from which the complex amplitude at the plane *z* is calculated as

$$U(n,Z:a)=\sum_{m=1}^{N}\tilde{U}(m:a)\exp\left[i2\pi\left(nm+Z\sqrt{\frac{1}{\lambda^2}-\left(\frac{m}{Np}\right)^2}\right)\right], \tag{6}$$

For measurement of surface deformation we calculate the complex coherence factor defined by an average of the conjugate product of the complex amplitudes before and after object deformation on the reconstruction plane

$$\Gamma(n,Z:a)=\sum_{m=-M}^{M} U(n+m,Z:0)U^*(n+m,Z:a), \tag{7}$$

We can also derive speckle displacement at the observation plane from the cross-correlation function of the reconstructed intensity given by

$$C(m,Z:a)=\sum_{n=1}^{N-m}\left|U(n,Z:0)\right|^2\left|U(n+m,Z:a)\right|^2 \Big/ C(0,Z:a), \tag{8}$$

whose peak position and height mean speckle displacement and decorrelation due to object deformation, respectively.

Digital holography thus provides both the phase change and speckle displacement in the 3-d space by recording the complex amplitude at the CCD plane.

3 Computer simulations for deformation measurement

The above algorithm was programmed by using Mathematica 5.1 to simulate deformation measurements as well as surface contouring using dual-wavelengths or two sources [3]. Optical systems and CCD specifications for hologram recording can be chosen arbitrarily. Even effects of recording bit depths and phase-shifting error can be analyzed. These situations are difficult to investigate analytically.

In the following we present the results for deformation measurement. The object is a plate with the size of 10 mm. The mean object surface is assumed to be flat and the maximum surface roughness given by Max(r) is equal to 10 μm. Object deformation is represented by a superposition of in-plane translation and tilt with the displacement expressed by

$$a_x = a_{xo} \quad \text{and} \; a_z = \Omega_z x, \tag{9}$$

where a_{xo} is in-plane translation and Ω_z is an angle of tilt. We assume the collimated illumination with normal incidence of wavelength 657 nm. The CCD is located at a distance of L_H=200 mm from the surface and has the pixels of pitch p=5 μm with a width of photosensitive region w=5 μm and the number N=512.

Figure 2 shows the output of the CCD S(m: 0, δ) for the 3 step algorithm before object deformation. These phase-shifted outputs were substituted into Eq.(4) to yield the amplitude and phase of U(m:0) presented by Fig.3. After object deformation the CCD outputs exhibits similar appearance although details are different.

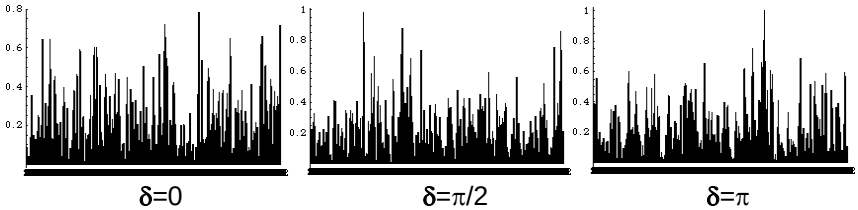

Fig.2. CCD outputs during phase-shift with a step of π/2 of the reference beam in phase-shifting digital holography

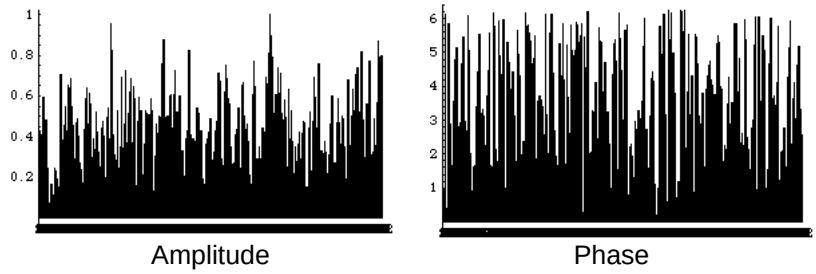

Fig.3. Amplitude and phase of the object wave derived from the phase-shifted signals shown in Fig.2

After the numerical reconstruction using Eqs.(5) and (6) we obtained the X-Z cross-sections of intensity before and after tilt of Ω_z=0.0004 radians as shown in Fig.4. Here no in-plane translation is added, that is, a_x=0. The scale of x-axis is equal to the sensor pitch 5 μm and that along z-axis is taken to be the axial speckle size given by $\Delta Z = \lambda(L_H/Np)^2$.

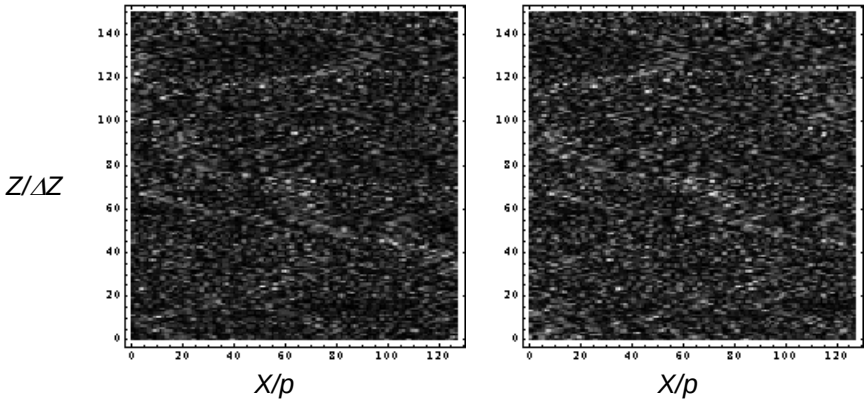

Fig.4. Cross-sections of the reconstructed intensity before and after object tilt of 0.0004 radians

For deformation measurement we calculated the cross-section of the coherence factor given by Eq.(7). Its phase that is directly proportional to a_z is shown in Fig.5 where (a) is without averaging (M=0) and (b) with averaging with M=3. We note that the averaging is very effective for noise reduction. The figures also exhibit localization of the fringe pattern at the object plane. It takes place at the plane of zero speckle displacement, called speckle boiling [1,2]. The cross-section of the intensity cross-correlation given by Eq.(8) to deliver speckle displacement is plotted in Fig.6.

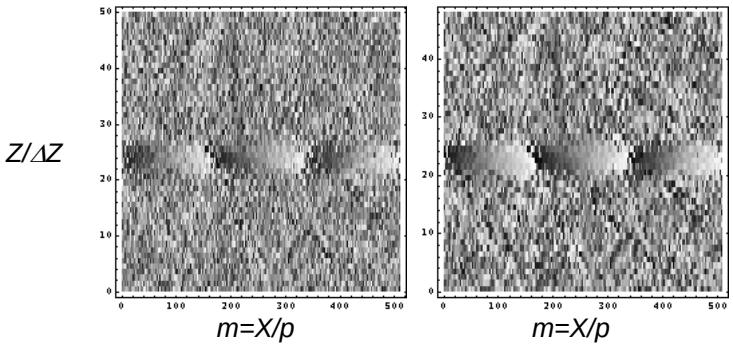

Fig.5. Cross-sections of the phase of coherence factor before and after averaging

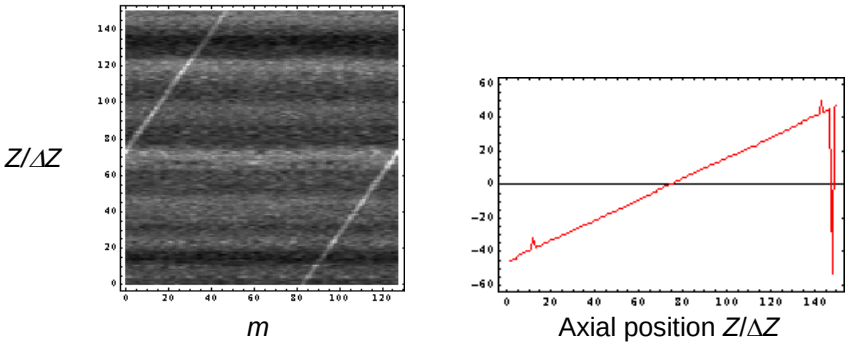

Fig.6. Cross-correlation of intensity cross-section and axial dependence of speckle displacement

The function was calculated by means of 1-d FFT along *X*-axis with the grid *m* and wrapped about *m*=0. The unwrapped position of correlation peak corresponds to real speckle displacement whose axial dependence is also plotted in Fig.6.

If we add in-plane translation a_x=50 μm to the object tilt the cross-section of the phase of the averaged coherence factor changes to that shown in Fig.7 where the localization position is shifted from the object plane as expected from a theory. The dependence of speckle displacement is also shown in Fig.7 where only the correlation values higher than 0.6 are plotted. Here we see again that the fringe localization occurs at the plane of no speckle displacement.

The plane of fringe localization can be used for detection of the surface position [4] but we find that the same measurement can be accomplished from detection of speckle displacement caused by surface tilt with higher resolution.

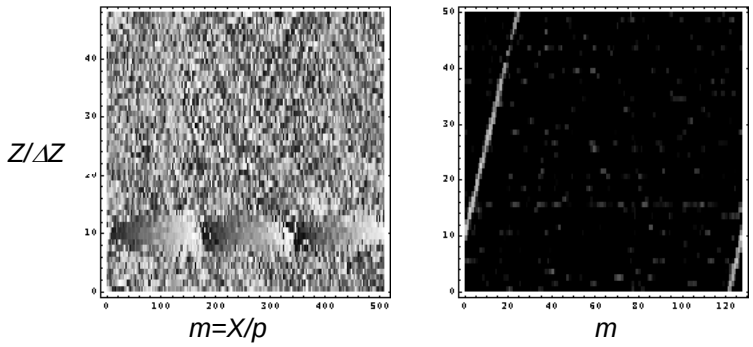

Fig.7. Cross-sections of the phase of the averaged coherence factor and the intensity cross-correlation in the presence of tilt and in-plane translation

4 Conclusions

We have reported the method and results of numerical simulation of deformation measurement by phase-shifting digital holography applied to general optical systems and hologram recording conditions. Surface roughness was represented by random numbers and we obtained the results that agree well with analytical approaches. It enables, however, to evaluate quantitatively the resolution and range of measurements, especially, their dependence on specifications of CCD that are difficult by analytical approach. The present program can also be applied to almost all kinds of coherent measurement of diffusely reflecting surfaces.

5 References

1. Yamaguchi, I (1985) Fringe formations in deformation and vibration measurements using laser light, Progress in Optics. Vol.22 : 271-340
2. Yamaguchi, I (2003) Holography, speckle, and computers. Opt. Lasers in Eng., 39: 411-429
3. Yamaguchi, I, Ida, T, Yokota, M, Yamashita, K (2006) Surface shape measurement by phase-shifting digital holography with a wavelength shift, Appl. Opt., 45: 7610-7616
4. Yamaguchi, I, Ida, T, Yokota M (2008) Measurement of surface shape and position by phase-shifting digital holography, Strain, 44: 349-356

Analysis of fringe formation and localization in optical interferometry using optical coherence

C S Narayanamurthy,
Department of Physics, Indian Institute of Space Science and Technology (IIST), ATF Campus, VSSC, ISRO (PO), Thiruvananthapuram – 695 022, India

1 Introduction

Fringe formation and localization in holographic interferometry, speckle interferometry, and *Michelson* interferometry is very important to understand the nature of interfering waves and the perturbation involved in one of the waves. The fringes of optical interferometry [1] can be classified into two parts and they are i) Localized and ii) Non localized. The localized fringes are obtained in Michelson interferometer, irrespective of coherence of sources, if the two mirrors are tilted with respect to each other. On the other hand if they are parallel, then fringes never localize at any plane. The non localized fringes will be formed, if the interfering beams from two arms of the interferometer have path length variation within the coherence length of source. Unlike fringe formations in classical interferometric systems, localization of fringes in holographic interferometry, speckle interferometry depends on the reflected or transmitted object waves as the other interfering waves could be plane laser beam. In such cases the fringes localize only at planes where the phases remain constant and the plane is normal to the direction of interference. This condition can not be satisfied for most of the interferometric experiments which in turn may introduce error in measuring the cause of interference. For example if, we want to measure the tilt of an object or any other motion of an object in holographic interfreometry, it will not be possible to accurately compute the amount of motion without the fringes being localized at a particular plane. The fringe formation and localization also depends upon coherence of optical waves, interfering medium, polarization etc. In this paper we report detailed analysis about the formation and localization of interferometric fringes under various conditions.

42 Fringe formation and localization

Interference fringes are formed whenever light from a source is made to reach points in a region of space via two different paths. Following [1], if *P* be a point in this region, and

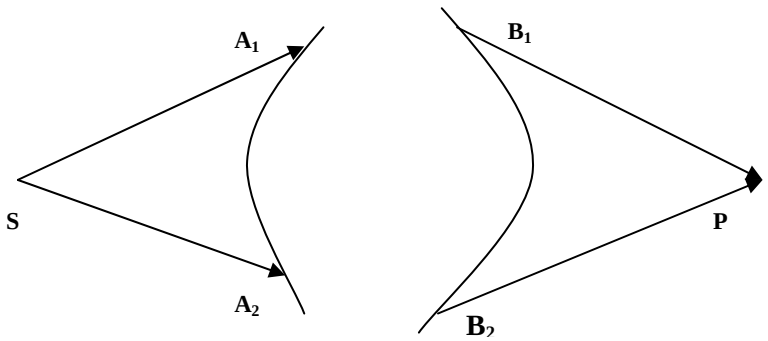

Fig. 1. Shows the interference of two waves from source via the path SA_1B_1P and SA_2B_2P at point P

light originates from a quasi-monochromatic point source S of wave length λ, then the phase difference at point *P* is,

$$\delta = \frac{2\pi}{\lambda}\{[SA_2B_2P] - [SA_1B_1P]\} \tag{1}$$

The value of δ depends upon the position of *P* and the interference fringes are formed over any plane in the region common to two paths from source *S* and along loci of all points where it (phase difference δ) remains constant . Such fringes are called as nonlocalized fringes and their visibility depends only on the relative intensities of two interfering waves. On the other hand, if the primary source is quasi monochromatic and extended about *S* then the phase difference at point *P* is not same for all loci of points and the visibility of interference fringes reduces. Such types of fringes are called as localized fringes. The relation between visibility of interference fringes from extended sources can be explained in terms of maximum (δ_{max})or minimum (δ_{min}) values of phase differences at point *P*(Fig.1). If (δ_{max} - δ_{min}) < π/2 , then the loss of visibility is negligible and if (δ_{max} - δ_{min}) > π then the loss of visibility will be maximum.

3 Michelson Interferometric fringes :

3.1 Non-localized Fringes

Michelson interferometer is one of the basic interferometers where, the temporal coherence behavior of interfering beams play important role. Fig.1 shows a typical *Michelson* interferometer experimental arrangement in which a diverging laser beam from the pinhole of the spatial filtering assembly falls on the beamsplitter which, splits it into two parts. These two waves recombine at the CCD camera plane after getting reflected from mirrors1,2 respectively to produce non-localized circular fringes (Fig.1) which never localizes at any plane[2].

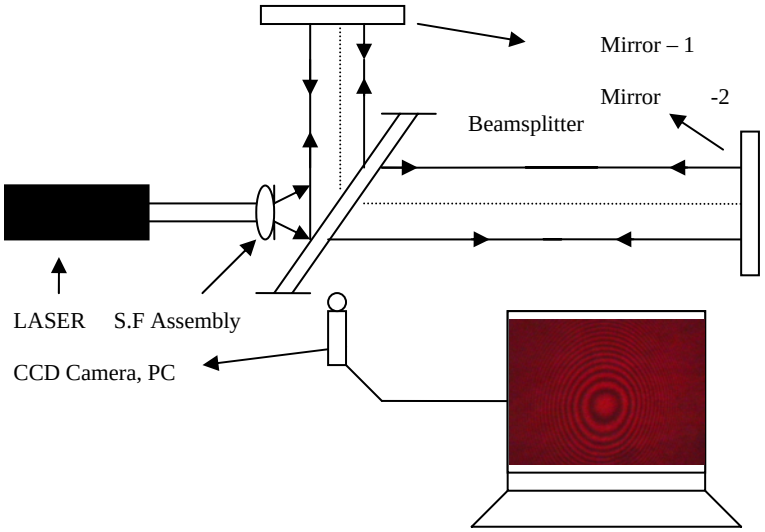

Fig. 2. Michelson Interferometer setup showing the interference pattern in the monitor

In fact if the two mirrors are parallel then the fringes localizes every where in space and the coherence length of the source limits the liberty of position of mirrors M_1 and M_2. Instead of long coherent laser sources, sodium lamp is used as a source then, the liberty is only about the distance between two mirrors i.e $(l_1 - l_2) = d$ and it has to be within 5cm and for a mercury lamp it has to be within few microns (which are respective coherence lengths). But, once fringes are formed in *Michelson Interferometer* it, localizes every where in detector plane. The equation governing fringe formation in Michelson Interferometer is,

$$I_D(P) = I_{01}(P) + I_{02}(P) + K_1^* K_2 \Gamma_{12}\left(\frac{2d}{c}\right) + K_1 K_2^* \Gamma_{21}\left(\frac{-2d}{c}\right) \tag{2}$$

Where, Γ_{12} is called the mutual coherence function and K_1 and K_2 are purely imaginary numbers of the form $i|K_1|$ and $i|K_2|$, respectively and we see that $K_1 K_2^* = K_1^* K_2 = |K_1||K_2|$. Now equivalently the (See Eq.2) can be written as,

$$I_D(P) = I_{01}(P) + I_{02}(P) + 2|K_1 \| K_2| \Gamma_{12}\left(\frac{2d}{c}\right) \tag{3}$$

With a slight change of notation, if $\Gamma_{11}(0)$ and $\Gamma_{22}(0)$ as the intensities of the spherical beams from the virtual sources S_1 and S_2 which are due to mirrors 1 and 2 respectively.

Also, assuming $I_{01}(P) = K_1^2 \Gamma_{11}(0)$ and $I_{02}(P) = K_2^2 \Gamma_{11}(0)$ we can rewrite the (See Eq.3) as,

$$I_D(P) = I_{01}(P) + I_{02}(P) + 2\sqrt{I_{01}(P) I_{02}(P)}\,\mathrm{Re}\,\mu_{12}\left(\frac{2d}{c}\right) \tag{4}$$

In the above (See Eq.4), the first two terms represent the intensities of the diverging light beams at the detector from the virtual sources S_1 and S_2 respectively, and the last two terms represent the cross correlation terms of the two wave fronts from the two virtual sources S_1 and S_2 respectively. With these values the visibility of the interference pattern at the detector plane will become,

$$\gamma(P) = \frac{2\sqrt{I_{01} I_{02}}}{I_{01} + I_{02}}\,\mathrm{Re}\left[\mu\left(\frac{2d}{c}\right)\right] \tag{5}$$

(See Eq.5) represents the visibility equation in terms of complex degree of mutual coherence function for a time delayed two diverging light beams interfering at the detector plane of a *Michelson* interferometer. Thus by moving one of the mirrors, and analyzing the visibility *γ(P)* of fringes we can determine collimation of light beams, coherence factor of the source.

In the same *Michelson Interferometer* set up one can obtain localized fringes of equal thickness if, the mirrors M_1 and M_2'(image of mirror M_2) are close together but mutually inclined to form a wedge of small angle.

4 Holographic interferometric fringes

4.1 Double exposure conventional holographic interferogram

Fringes are formed in doubly exposed holographic interferometer due to the interference of two time delayed wave fronts which, are similar to *Michelson* interferometer but the difference is that in holographic interferometer one of the interfering waves is the scattered diffuse waves from the object surface. Depending upon the nature of object motions, fringes are formed in holographic interferometer and these fringes can be localized on a particular plane or non-localized. In conventional holographic interferometry, using photographic plates for recording, one has to reconstruct separately,

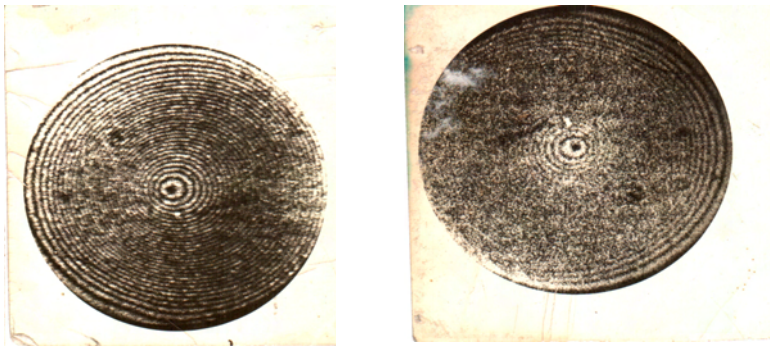

Fig.3. Shows old photographs of fringes formed at focal plane(left) and defocus plane(right) of doubly exposed hologram of centrally loaded diaphragm.

and take a photograph of it from appropriate localization plane of the interferogram. Fig.3 shows old type photographs of fringes of doubly exposed image plane hologram of a centrally loaded diaphragm which undergone an out of plane displacement at the center. In that two photographs are shown with the first fringe system(left) was taken when the reconstruction was done at image plane and the other one(right) at the defocus plane. It is clear from these two photographs that fringes localize exactly at the image plane of hologram where the phases of interfering beams remain constant. The fringes localize depending on the motion of object and for lens less holography the analysis is different and in that case the fringes never localize at any plane and can behave like circular *Michelson* interferometric fringes. As most of applications in holographic

interferometry with opaque objects, use imaging geometry we restrict the discussion to image plane holographic interferometry. The equation governing fringe localization is [3],

$$d\delta = \frac{\partial \delta}{\partial x} dx + \frac{\partial \delta}{\partial y} dy = 0 \tag{6}$$

$$\delta = \frac{2\pi}{\lambda} \left(\hat{k}_2 - \hat{k}_1 \right) \vec{L} = \tilde{\vec{K}} . \vec{L} \tag{7}$$

Where, $\hat{k}_2$ and $\hat{k}_1$ are unit vectors, and $\tilde{\vec{K}} = \hat{k}_2 - \hat{k}_1$. The cartesian coordinate components of these vectors are denoted by,

$$\hat{k}_1 = (k_{1x}, k_{1y}, k_{1z}), \hat{k}_2 = (k_{2x}, k_{2y}, k_{2z}), \tilde{\vec{K}} = (k_x, k_y, k_z), L = (L_x, L_y, L_z)$$

The terms *dx* and *dy* (see Eq.6) represent differential changes in the object point. So for getting maximum visible fringes, the differential change of phase difference δ at the localization plane must be equal to zero. Considering the localization of fringes in Fig.3 for focal and defocus planes, the fringes localize if the recording is done at image plane and not at the defocus plane that is the phase difference δ remains constant at focus plane of hologram.

4.2 Double exposure photorefractive holographic interferometry

Fig.4 shows the schematic of photorefractive hologram in which a BSO/BTO crystal sandwiched between crossed polarizers are used as recording medium instead of conventional 10-E 75/10-E 85 Agfa Gaevert photographic plates. In this type of set up, holographic interferometry is done dynamically in real time as wet processing is not required. In fact object under test, a white card board (diffuse object) is not imaged on to the recording photorefractive BSO/BTO crystal, instead a phase object (plastic ruler) is imaged on to the crystal and is captured in the monitor via CCD (Charge Coupled Devise) camera (Fig.4). In this setup the moment laser beam is switched on, a dynamic hologram of plastic ruler is formed in real-time on the crystal due to photorefractive effect [4,5]. Now, when the object under test is given an out of plane tilt, fringes are formed in real time in the photorefractive crystal and such fringes are shown in Fig.4. In fact high visible fringes are seen and they are formed at defocus plane as the object (card board) is not imaged on to the crystal.

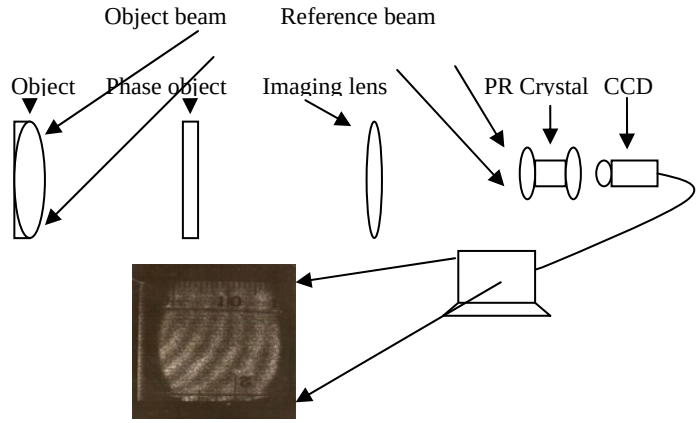

Fig. 4. Shows the schematic and photorefractive holographic fringes of an arbitrarily tilted diffuse object

Comparing with fringes in Fig.3, where high visible fringes are formed only at image plane of hologram, the fringes shown in Fig.4 are formed due to out of plane tilt of diffuse object at the defocus plane of hologram. The main difference in both cases is the thickness of recording medium. Another important fact is that the fringes formed in PR hologram is non localized and the fringes formed due to out-of plane tilt or motion in conventional double exposure holographic interferometer with photographic plate as recording medium is localized. For a dynamic hologram inside photorefractive crystal the equation governing fringe localization changes to,

$$\int_0^l d\delta dz = \int_0^l \left(\frac{\partial \delta}{\partial x} dx + \frac{\partial \delta}{\partial y} dy \right) dz = 0 \tag{8}$$

In this case, the fringes do not localize at any plane due to increase of coherence length inside the photorefractive media.

5 Speckle photography / interferometry

The fringes due to object motions are localized in case of speckle interferometry/photography except for the fringes due to longitudinal motions of diffuse objects in speckle photography without any imaging lens [6,7]. The fringes formed due to the

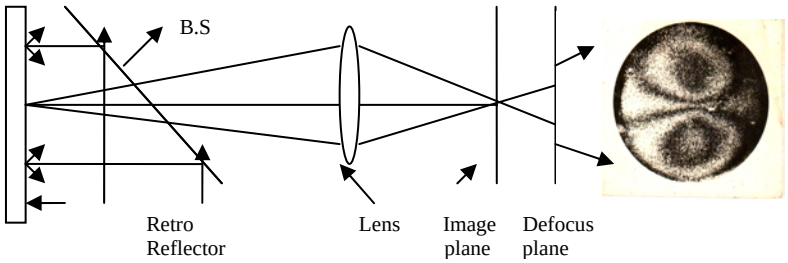

Fig. 5. Shows the schematic of speckle photography/interferometry set up with slope fringes at defocus plane

longitudinal motion of diffuse objects in lensless speckle photography never localizes at any plane like circular fringes of *Michelson* interferometer [7]. On the other hand, in double exposure speckle interferometry/electronic speckle interferometry/digital speckle interferometry fringes are localized only at image plane and the interfering speckle beams will be decorrelated at the defocus plane. De-correlation of speckles affect the visibility of fringes. Fig.5 shows a speckle interferometry/photography geometry used for recording out of plane displacements. If speckle photography of a diaphragm is recorded before and after out of plane displacement at defocus plane only slope fringes are formed and not displacement fringes as shown in Fig.5. This results show that speckle waves from diffuse objects produce high visible fringes at image plane only and not any other plane. One can produce non-localized high visible circular interference fringes in lens less laser or white light speckle photography. Whenever two speckle patterns are made to interfere at image plane, the interference occur at this plane due to correlation of these two speckle patterns and elsewhere it de-correlation occurs. Also, true is that laser beam loses its coherence property once it passes through or reflected back by diffuse objects.

6 Conclusion

A detailed analysis of fringe formation and localization is given for i) Michelson interferometer, ii) Holographic interferometer iii) Photorefractive holographic interferometer iv) Speckle Photography/Interferometer. Both localized and non localized fringes were analyzed using the interference properties of interfering beams. The important conclusion is that it appears from our analysis that the random linear speckle patterns, produced due to reflection of laser beam by the

diffuse object gains coherence length when passing through non-linear medium like photorefractive crystals. However detailed analysis is yet to be carried out.

7 References

1. Max Born and Emil Wolf, (1999) Principles of Optics, Cambridge University Press, Seventh (expanded) edition,
2. Narayanamurthy C S, (2009), Analysis of the localization of Michelson interferometer fringes using Fourier optics and temporal coherence, Eu. Jl.Phys., 30: 147-155
3. Vest,C M (7) Holographic Interferometry, John Wiley & Sons, New York
4. Solymer L, Webb D J, Grunnet-Jepsen A (1996),The physics and applications of photorefractive materials, Oxford series in optical and imaging sciences, Clarendon Press, Oxford,
5. Narayanamurthy C S, Dainty J C, (1992), Real-time holographic metrology using BSO, Optics Communications(Elsevier*)*, 91 : 23-28
6. Narayanamurthy C S , Joenathan C (1988), Speckle pattern fringes produced by longitudinal motion of the diffuse object : Sensitivity dependence and multiple exposures, Optics Communications(Elsevier*)*, 65: 179-184
7. Joenathan C, Narayanamurthy C S, Sirohi R S (1988), Localization of fringes in speckle photography that are due to axial motion of the diffuse object, Jl.Opt.Soc.Am `A'.5: 1035-1040

Invited Paper

Quantitative Phase Imaging in Microscopy

Colin JR Sheppard, Shan S Kou and Shalin Mehta
Division of Bioengineering
National University of Singapore
Singapore 117574

1 Introduction

There are many different alternative methods that can be used for phase contrast imaging of objects at a microscopic scale [1]. Some of these are more amenable than others to obtaining quantitative information. The most important methods are:

Digital holographic microscopy (DHM)
Defocus
Transport of intensity equation (TIE)
Differential Interference Contrast (DIC)
Differential phase contrast (DPC)
Interference microscopy
Optical coherence tomography (OCT)

Phase imaging can be used in a reflection or transmission geometry. In biology it has the advantage of being marker-free. It can measure physical shape, and refractive index variations, ideally in three dimensions (3D). In transmission, phase is related to optical path difference. The phase difference after travelling through a thickness t in a medium with refractive index n as compared with the ambient refractive index n_0 is $\phi = (n - n_0)k_0 t$, where k_0 is the free-space wave number $2\pi / \lambda_0$. Thus optical path can be used to determine the thickness if we know the refractive index, or the refractive index if we know the thickness. Refractive index is important in biology because it can be used to determine concentration or dry mass [2]. In reflection, phase is also related to optical path, and can be used to reconstruct surface profiles or the optical thickness of layers. Note that refractive index also influences the amplitude of the reflected beam, by the Fresnel equations.

In tomography, in the first Born approximation the object scatters with a scattering potential given by [3]

$$F(\mathbf{r}) = -k_0^2 \left[n^2(\mathbf{r}) - n_0^2 \right] \tag{1}$$

Note that here we have replaced the background refractive index by n_0. It is well-known that the Born approximation can be invalid for many practical samples, e.g. in biology. The Rytov approximation can be an improvement [4]. For imaging in reflection, another approach based on the Kirchhoff approximation gives a scattering potential [5, 6]

$$F(r) \propto \nabla^2 \left\{ \ln\left[\frac{n(r)}{n_0} \right] \right\} \tag{2}$$

It is seen that in this model the signal comes from the changes in refractive index, rather than the refractive index itself.

2 Coherent methods

Imaging methods can be simply classified into coherent and partially-coherent methods. The main coherent method is digital holographic microscopy (DHM). A major advantage of DHM performed in an off-axis arrangement, is that the complete phase and amplitude information can be recovered from a single hologram. According to the Abbe theory of microscope image formation, an object can be resolved into grating components, which are filtered by the aperture stop of the imaging lens. It is well-known that imaging in a coherent system can be analyzed in terms of a coherent transfer function (CTF), which is a scaled version of the pupil function. For an in-focus circular pupil, all spatial frequencies less than the cut-off $(n_0 \sin\alpha)/\lambda$, where we take n0 to be the immersion medium, are imaged perfectly. These principles can be extended to the case of 3D imaging, and the CTF now becomes a 3D CTF. As was shown by Wolf [3], the 3D CTF for coherent imaging is given by the cap of a sphere of radius $n_0 k$, the Ewald sphere of x-ray diffraction theory, with the angle subtended by the cap being equal to the semi-angular aperture α of the imaging lens. The sphere passes through the origin of Fourier space. Then the only grating vectors present in the object that can be imaged are those that lie on the surface of the sphere. Thus we recognize that holography, and other forms of coherent imaging, result in some 3D information including surface height information, sometimes called $2\frac{1}{2}$D, but not complete 3D volume information [7]. The 2D hologram is, in fact,

not large enough to contain the full 3D information. Different paprts of the hologram contain information on different views, but full resolution (given by the size of the complete hologram) is not present for the different views.

3 Partially coherent methods

Incoherent imaging is described by an optical transfer function (OTF), given by the scaled autocorrelation of the pupil function. As is well known the spatial frequency cut-off of an incoherent system is twice that of a coherent system. For a weak object, spatial frequencies twice as large can be imaged in an incoherent as compared with a coherent imaging system. However, it is not completely fair to say that imaging is superior in an incoherent system, as the OTF decreases in value for no-zero spatial frequencies, and higher spatial frequencies are present in the intensity object. For 3D imaging, the 3D OTF is given by a toroidal pass-band, which now includes a volume of imaged spatial frequencies, but exhibits a missing cone of information around the longitudinal spatial frequency axis. Incoherent imaging systems, however, cannot image phase information.

Partially-coherent imaging systems are, unfortunately, much more difficult to analyze. In general, we have to introduce a partially coherent transfer function, or transmission cross-coefficient, that depends on spatial frequency pairs. For the simpler case of a weak object, such that we neglect interference of diffracted light with diffracted light, the 3D transfer function was presented by Streibl [8]. The form of the weak object transfer function (WOTF) depends on the aperture of the condenser lens. In the limit of a small condenser aperture, it tends to the normal CTF for a coherent system, while if the condenser aperture is equal to that of the objective, it has the same form as the OTF. In general the WOTF is not symmetric about the origin of axial spatial frequencies, the even part imaging amplitude information and the odd part imaging phase information.

3.1 Defocus

This suggests that phase information can indeed be present in a partially coherent image, but that defocus is necessary to obtain this information. In fact defocus was used many years ago as a way of imaging phase information. A way to make this quantitative is to take two images at

opposite defocus settings [9]. This phenomenon is based on the fact that the image wave field must satisfy the wave equation.

3.2 Transport of intensity equation

The above method is based on the assumption that the object is weakly scattering, but even if it is not the phase can be recovered using the transport of intensity equation [10, 11]. However, the method recovers the phase of the wave-field rather than the phase of the object, and extracting the phase for the partially-coherent case is not so simple, especially for a 3D object [12].

3.3 Differential interference contrast (DIC)

One of the most used methods for phase imaging is differential interference contrast (DIC). This uses a shearing interferometer to compare two closely-spaced images of the sample. The images are added with a relative phase difference called the bias. Theory for imaging based on diffraction theory which takes account of vignetting effects has been developed [13-16]. By using different values of bias, a phase-shifting algorithm can be used to extract the phase gradient, and by measuring phase gradient in two directions the phase can be recovered [15].

3.4 Differential phase contrast (DPC)

Differential phase contrast (DPC) was first introduced for scanning microscopy, and uses a pair of semicircular detectors. The two images are subtracted to produce a DPC image and summed to give an amplitude contrast image [17]. A similar method can be used in the conventional microscope, by using condenser pupil masks and processing the images digitally [18]. We call this technique asymmetric illumination DPC (AIDPC). Fig. 1 shows an example, where the object exhibits strong amplitude and phase information that can be separated by the technique. The middle row of the figure shows the partially coherent transfer function, that is useful to investigate the imaging properties of the system.

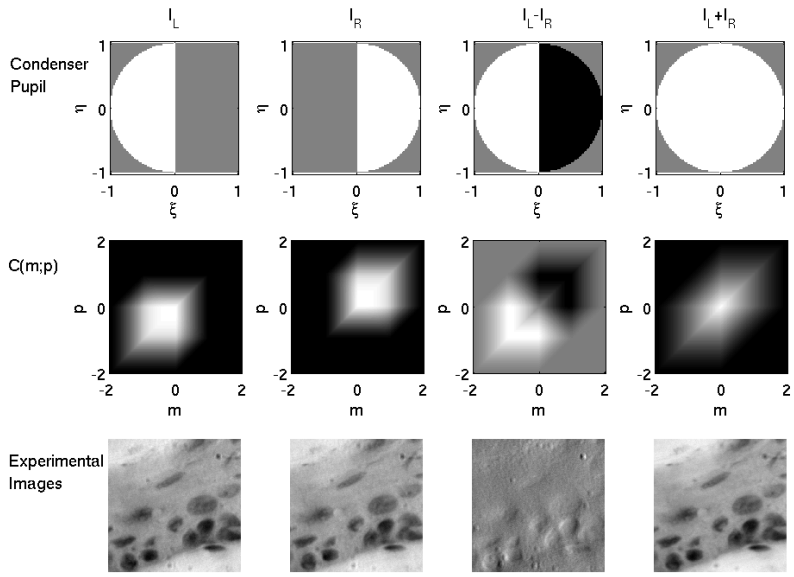

Fig. 2. Condenser pupil structures (top row), partially coherent transfer function in direction of differentiation (middle row), and experimental images (bottom row) obtained with AIDPC. The sample is skin H&E stained section courtesy Graham Wright, TLL and Declan Lunny, IMB.

3.5 Interference microscopy

Holographic microscopy when performed as image plane holography can be regarded as a form of interference microscopy. A special feature of DHM is that the illumination is spatially coherent, or close to spatially coherent. When interference microscopy is performed with a spatially incoherent source and an appreciable condenser aperture, the imaging properties become very different [13]. The 3D imaging properties depend on the aperture of the condenser in a similar way to partially coherent imaging considered earlier [19]. In reflection there is an optical sectioning effect, similar to that in confocal imaging, that results from the correlation of the object and reference waves [20]. The 3D CTF is thus also similar to that in confocal imaging [7]. Using a source of low temporal coherence can also be used to improve image formation in the depth direction [21, 22]. This is, of course, also the basis of optical coherence tomography, which is usually performed in a scanning modality.

4 Acknowledgments

The authors acknowledge support from Singapore Ministry of Education Tier 1 funding (grant R397000033112).

5 References

1. Sheppard, CJR (2004) Phase contrast microscopy, *Encyclopedia of Modern Optics*, RD Guenther, DG Steel, L Bayvel, eds, Elsevier, Oxford, Vol. 3, pp. 103-110
2. Barer, R (1952) Interference microscopy and mass determination. Nature 169: 366-367
3. Wolf, E. (1969) Three-dimensional satructure determination of semi-transparent objects from holographic data. Opt. Comm. 1: 153-156.
4. Sheppard, CJR (1994) Modeling of 3-D brightfield microscope images. *Proc. SPIE* 2302: 352-358.
5. Sheppard CJR (2006) Scattering and the spatial frequency representation, *Light Scattering and Nanoscale Surface Roughness*, AA Maradudin, ed., Springer, Berlin, pp. 60-91
6. Sheppard CJR and Aguilar F (1999) Fresnel coefficients for weak reflection, and the scattering potential for three-dimensional imaging. *Opt. Commun.* 162: 182-186
7. Kou, SS and Sheppard, CJR (2007) Imaging in digital holographic microscopy. Optics Express 15: 13640-13648
8. Streibl N (1985) Three dimensional imaging by a microscope. J. Opt. Soc. Am. A 2: 121-127
9. Sheppard, CJR (2004) Defocused transfer function for a partially coherent microscope, and application to phase retrieval. J. Opt. Soc. Am. A 21: 828-831
10. Streibl, N (1984) Phase imaging by the transport equation of intensity. Opt. Comm. 49: 6-10
11. Barty, A, Nugent, K.A, Paganin, D. and Roberts, A. (1998) Quantitative optical phase microscopy, Opt. Lett. 23: 817-819
12. Sheppard, CJR (2002) Three-dimensional phase imaging with the intensity transport equation, Appl. Opt. 41: 5951-5955
13. Sheppard CJR, Wilson T (1980) Fourier imaging of phase information in conventional and scanning microscopes, *Phil. Trans. Roy. Soc. A* **295**, 513-536

14. Cogswell CJ, Sheppard CJR (1992) Confocal differential interference contrast (DIC) microscopy: including a theoretical analysis of conventional and confocal DIC imaging. J. Microsc. 165: 81-101
15. Arnison MR, Larkin KG, Sheppard CJR, Smith NI, Cogswell CJ (2004) Linear phase imaging using differential interference microscopy. J. Microscopy, 214: 7-12
16. Mehta SB, Sheppard CJR (2008) Partially coherent image formation in differential interference contrast (DIC) microscope. Optics Express, 16: 19462-19469
17. Hamilton DK, Sheppard CJR (1984) Differential phase contrast in scanning optical microscopy. J. Microsc. 133: 27-39
18. Mehta, S, Sheppard, CJR (2008) Asymmetric illumination based differential phase contrast (AI-DPC) for full-field transmission imaging of phase information in biological specimens, Focus on Microscopy FOM08, Awaji Island, Japan, 13-16 April, p. 33
19. Sheppard, CJR, Roy, M, Sharma, MD (2004) Image formation in low-coherence and confocal interference microscopes. Appl. Opt. 43: 1493-1502
20. Corcoran, VJ (1965) Directional characteristics in optical heterodyne detection processes. J. Appl. Phys. 36: 1819-1825.
21. Davidson, M, Kaufman, K, Mazor, I and Cohen F (1987) An application of interference microscopy to integrated circuit inspection and metrology. Proc. SPIE 775: 233-247
22. Roy, M, Svahn, P, Cherel, L, Sheppard, CJR (2002) Geometric phase-shifting for low coherence interference microscopy. Optics and Lasers in Engineering, 37: 631-641

Comparison and unification of speckle-based phase retrieval and holography with applications in phasefront alignment and recognition

P. F. Almoro[1], G. Pedrini[2], F. Zhang[3], A. M. S. Maallo[4], A. Anand[5], P. N. Gundu[1], W. Wang[6], A. Asundi[7], W. Osten[2] and S. G. Hanson[1]
[1]DTU Fotonik, Department of Photonics Engineering, Denmark
[2]Institut für Technische Optik, Universität Stuttgart, Germany
[3]Department of Electronic and Electrical Engineering, University of Sheffield, United Kingdom
[4]National Institute of Physics, University of the Philippines, Philippines
[5]Applied Physics Department, Faculty of Technology & Engineering, The MS University of Baroda Vadodara, India
[6]Department of Mechanical Engineering, School of Engineering and Physical Sciences, Heriot-Watt University, United Kingdom
[7]Precision Engineering and Nanotechnology Centre, Nanyang Technological University, Singapore

1 Introduction

Comparisons between various wavefront reconstruction methods such as wavefront curvature sensing and phase diversity [1] have been reported in the literature. These comparative studies highlight the differences, similarities, relative advantages, operating regimes and main applications of the various reconstruction methods. For coherent light metrological applications, especially on rough objects, Digital Holography (DH) is considered one of the established interferometric methods because of its sub-wavelength accuracy. For investigations of smooth surfaces, Phase Retrieval (PR) or the non-interferometric approach offers a simple setup since no reference beam (RB) is required. In PR, recent trends favour the use of multiple intensity images, rather than a few images, due to its robustness against quantization error. Recently, a multiple speckle-pattern PR method was utilized in the interferometric analysis of object rotation and deformation [2] and in the numerical correction of aberrations [3], indicating a point of convergence between the two, traditionally parallel, reconstruction methods. To the best of our knowledge, no comparative study has been done between PR and DH. Recognition of test objects has been carried out by correlation with a reference object wavefront obtained

through DH [4]. Since no RB is used, PR may offer a more robust recognition method. The objectives of this study are: 1) compare off-axis DH and PR in terms of setup and reconstruction algorithm; 2) present a new model for the PR method interpreting it as a special case of holography called “phase-shifting broadband DH”; 3) describe a novel method for phasefront alignment of uncorrelated laser beams using PR; and, 4) describe a novel method for object recognition using PR.

2 Recording setups and reconstruction algorithms

Figure 1 shows the setups for off-axis DH and the speckle-based PR method in both transmission and reflection modes. In off-axis DH, the test wavefront is interfered with a RB, usually a plane wave with an offset angle, to be recorded as the hologram [5]. The twin-image problem may be addressed by shifting the hologram carrier frequency before reconstruction or through the phase shifting technique where three or more holograms are recorded [6]. It is remarked that a comparison with in-line DH, where the object beam (OB) is interfered with an in-line reference wave, is beyond the scope of the present study. For PR (Fig. 1(c) and 1(d)), the object is illuminated with a partially-developed speckle field (PDSF) from a diffuser and the transmitted/reflected wavefront is sampled at 20 planes [4]. PDSF can be decomposed into components: unperturbed plane wave and scattered wave [8, 9] resulting in a rapid axial intensity variation. It has to be emphasized that rapid intensity variation is essential to keep the following PR iterative algorithm from stagnation. Wave propagation is simulated iteratively between the detection planes using the recorded speckle intensities as constraints. Wave propagation is carried out using the angular spectrum method of solving the Rayleigh-Sommerfeld (RS) equation because of the small distances involved (millimeters). The sampled hologram or speckle patterns are represented as $m \times n$ matrices.

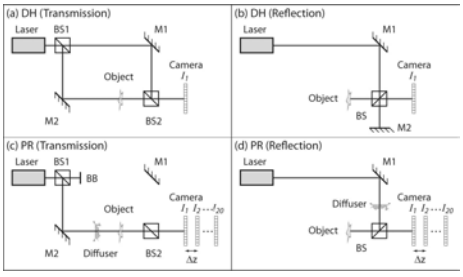

Fig. 1. Setups for DH and PR. BS: beam splitter; M: mirror; BB: beam block

For DH, the spatial carrier frequency is first removed and the resulting spectrum is multiplied with the free-space transfer function. The product is then inverse Fourier transformed to yield the complex field (U_O) at object plane. The RS equation in discrete form is given by

$$U_O\left(k\Delta x', l\Delta y', z\right) = \Im^{-1}\left(\left[\Im\left\{I_H\left(m\Delta x, n\Delta y\right)\right\}\right]_c \cdot \exp\left[\left(-i2\pi z/\lambda\right)\left(1-\frac{\lambda^2 m^2}{\Delta x^2}-\frac{\lambda^2 n^2}{\Delta y^2}\right)^{1/2}\right]\right) \tag{1}$$

where $(k\Delta x', l\Delta y')$ and $(m\Delta x, n\Delta y)$ are the coordinates at the object and hologram planes, respectively; $\Delta x \times \Delta y$ are the dimensions of the camera pixels; and, $\Im$ indicates Fourier transform. For the PR method, the complex field (U_{p+1}) calculated at the $(p+1)$ plane is given by

$$U_{p+1}\left(k\Delta x', l\Delta y', z\right) = \Im^{-1}\left(\Im\left\{\left[I_p\left(m\Delta x, n\Delta y\right)\right]^{1/2}\exp\left[i\phi_p\left(m\Delta x, n\Delta y\right)\right]\right\} \times \exp\left[\left(-i2\pi z/\lambda\right)\left(1-\frac{\lambda^2 m^2}{\Delta x^2}-\frac{\lambda^2 n^2}{\Delta y^2}\right)^{1/2}\right]\right) \tag{2}$$

where $p = 1\ldots19$; I_p and ϕ_p are the speckle intensity and phase estimate, respectively, at p^{th} plane. The algorithm starts from a random guess of ϕ_1. From the experimental verification, the obtained results are shown in Fig. 2. For the transmission mode, the off-axis hologram is shown Fig. 2(a) and a depiction of the removal of the carrier frequency is shown in Fig. 2(b). Figure 2(c) is the reconstructed phase revealing the details of the photoresist test object. Figure 2(d) shows a stack of recorded speckle patterns. The reconstructed phase with speckle noise is shown in Fig. 2(e). The desired object wavefront (Fig. 2(f)) after spatial filtering (filter size, $(1/0.042)\,mm^{-1}$) exhibits high correlation (0.78). For the reflection mode, the test object is a pattern (smiley) displayed on a phase-only spatial light modulator (Holoeye, 8.1 μm × 8.1μm pixel size, 3π maximum phase stroke). The high correlation (0.85) between the reconstructed phases (Fig. (i) and (l)) indicates that for the samples used, both PR and DH yield similar results, tacitly pointing towards a possible unification of the two parallel reconstruction approaches.

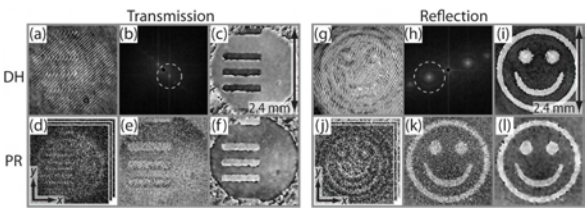

Fig. 2. Recordings and reconstructions using DH and PR

3 Properties of the phase diffuser

Figure 3 shows the properties of the photoresist (refractive index, $n = 1.65$ at λ = 0.633 nm) diffuser. The surface line scan (Fig. 3(a)) reveals a maximum roughness height of 0.44 μm, which corresponds to a phase shift $\phi = (2\pi/0.633)([1.65-1]\cdot 0.44) = 0.9\pi$ and a lateral scale of σ = 16.12 μm (Fig. 3(b)). Both the phase shift values and feature size are favourable for the generation of a PDSF. Figure 3(c) shows the 3D view of a small section (50 μm × 50 μm) that visualizes the surface terrain and scale.

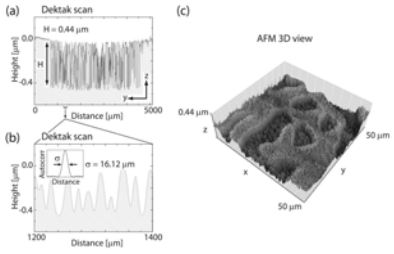

Fig. 3. Properties of phase diffuser

4 Object-perturbed speckle pattern as hologram

Figure 4 depicts the unperturbed plane wave (broken lines) and a scattered wave (oblong shapes), illumination of the object and the speckle patterns. The object-modulated plane wave is the OB. The ubiquitous scattered wave is considered as a weighted superposition of angularly-displaced plane waves based on Fourier optics. These act as reference waves (RB1, .., RBN) interfering with the OB and contributing a spectrum of spatial carrier frequencies. The speckle pattern may, therefore, be considered as a spatial broadband hologram. For the multiple recordings, an analogy is made with phase-shifting DH. The Nth broadband hologram is considered to be phase-shifted by $\phi_N = (2\pi/\lambda)(N \cdot \Delta z)$, where $\Delta z = 3mm$. The algorithm, then, sweeps through the holograms and reconstructs OB and RBN. Removal of the broadband spatial carriers is done after the reconstruction

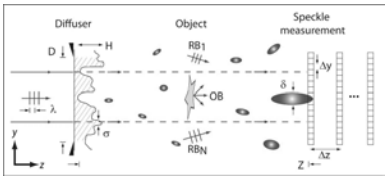

Fig. 4. Broadband holography model schematic

5 Complementary advantages

In DH, single hologram recording means fast processing time but requires that the OB and RB be temporally coherent. Hence, optical elements are necessary to split and combine the laser beams. Speckle-based PR requires multiple recordings. Figure 5 depicts the alignment of beams from two different lasers (A and B) and the subtraction of retrieved phases to evaluate rotation. The fringe spacing of the resulting interferogram (Fig.5, third column) decreases as the angle $\Delta\theta$ between wavefronts increases [4]. The benefit of the PR technique is that it allows the comparison of uncorrelated beams with a simpler setup yet achieving the same interferometric accuracy as in DH.

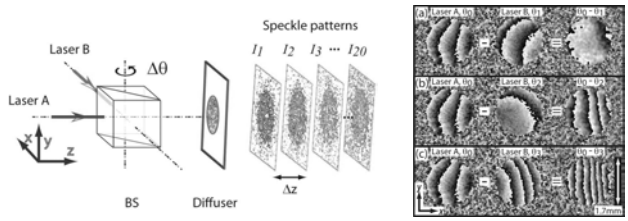

Fig. 5. Setup and results of interferometric alignment of two uncorrelated beams

6 Application in phase object recognition

Figure 6 demonstrates the influence of the beam illuminating the object on the phase recognition via PR. Even if the test object (Fig. 6(b)) is the same as the master object (Fig. 6(a)), recognition may fail (low correlation (Fig. 6(f))) due to a small aberration. In this demonstration, a lens (f = 200 mm) to defocus is positioned in the path of the object illumination. To correct for the aberration, a phase factor (Fig. 6(c), 6(g)) is subtracted yielding the object phase (Fig. 6(d)) and re-establishing a high correlation (Fig. 6(h)). The main benefit of phase recognition by PR, compared to DH, is robustness against aberrations that may arise from the use of a RB.

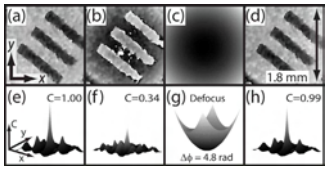

Fig. 6. Effects of illumination beam curvature on recognition

7 Summary and Conclusions

A unifying model for DH and PR is proposed, where the speckle-based PR technique is represented as “phase-shifting broadband DH”. For the smooth test objects used, the reconstructions are highly similar. The original ideas of off-axis holography by Leith and Upatnieks are rediscovered in the context of PR using partially-developed speckles. The fundamental principles behind the recording and reconstruction of the broadband holograms are shown to be similar with those in DH, thus, unifying the two reconstruction approaches. P.F. Almoro and S.G. Hanson acknowledge the financial support from the Danish Council for Technology and Innovation under the Innovation Consortium CINO (Centre for Industrial Nano Optics). P. Almoro acknowledges Peter John Rodrigo and Darwin Palima of DTU Fotonik for the fruitful discussions, as well as the University of the Philippines for the financial support.

8 References:

1. Fienup, J, Thelen, B, Paxman, R, Carrara, D (1998) Comparison of phase diversity and curvature wavefront sensing. Proc. SPIE 3353: 930
2. Almoro PF, Pedrini G, Anand A, Osten W, Hanson, SG (2009) Angular displacement and deformation analyses using a speckle-based wavefront sensor. Appl. Opt. 48: 932-940
3. Almoro PF, Gundu PN, Hanson SG (2009) Numerical correction of aberrations via phase retrieval with speckle illumination. Opt. Lett. 34: 521-523
4. Javidi B, Tajahuerce E (2000) Three-dimensional object recognition by use of digital holography. Opt. Lett. 25: 610-612
5. Xu L, Peng X, Guo Z, Miao J, Asundi A (2005) Imaging analysis of digital holography. Opt. Express 13: 2444-2452
6. Yamaguchi I (2008) Phase-Shifting Digital Holography. Optics & Photonics News 19: 48-53
7. Almoro PF, Hanson SG (2008) Random phase plate for wavefront sensing via phase retrieval and a volume speckle field. Appl. Opt. 47: 2979-2987
8. Wang W, Hanson SG, Takeda M (2006) Complex amplitude correlations of dynamic laser speckle in complex ABCD optical systems. J. Opt. Soc. Am. A 23: 2198-2207

High Precision Object Phase Reconstruction with Modified Phase Retrieval

Sandro Förster, Herbert Gross
Carl Zeiss AG
Carl-Zeiss-Str. 22, 73447 Oberkochen
Germany

1 Introduction

The recovering of phase information out of intensity measurements through focus image stacks is an interesting topic for a long time. This so called phase retrieval avoids expensive and environmental sensitive direct phase measurement. The method is applicable to the imaging of phase objects [1], to the layout and optimization of phase structures for desired illumination distributions in beam shaping setups [2] and for metrology of systems [3]. The reconstruction of the phase is a nonlinear inverse problem and the corresponding computation is critical concerning convergence and accuracy. In the past a large variety of algorithms is proposed in the literature to deal with this problem [4], [5], [6], [7]. Usually, the performance of the algorithms can be improved, if several images are taken into account, which are diversified by at least one parameter. The most prominent and easiest choice to get information out of the system is to gather the images in several defocussed planes.

If the situation is analyzed form a Fourier optical viewpoint, only those spatial frequencies of the wave front can be reconstructed, which have a considerable support by the diversification. In the case of defocussing, especially low frequencies have only minor contributions and can not be calculated with high accuracy. This means, that for a defocussing technique, the parts of the object phase with a shallow profile are not reconstructed well. In practice a high precision phase reconstruction for smooth phase areas and steep edges are desired. Therefore alternative diversifications with a more comfortable spectral behavior are proposed in the literature. In this work, one special method and the corresponding results are discussed.

2 Classical Phase Retrieval Approach

A first approach to the phase retrieval method was presented by Gerchberg and Saxton [8]. The principle of the underlying idea is shown in figure 1. In the simple error-reduction algorithm, the field in one or several defocussed planes in the image space is calculated from the pupil plane. In the images planes, the intensities are substituted by the measured distribution. These fields are back propagated into the pupil plane, where the boundary conditions are applied. This simple calculation scheme is also called IFTA (iterated Fourier transform algorithm).

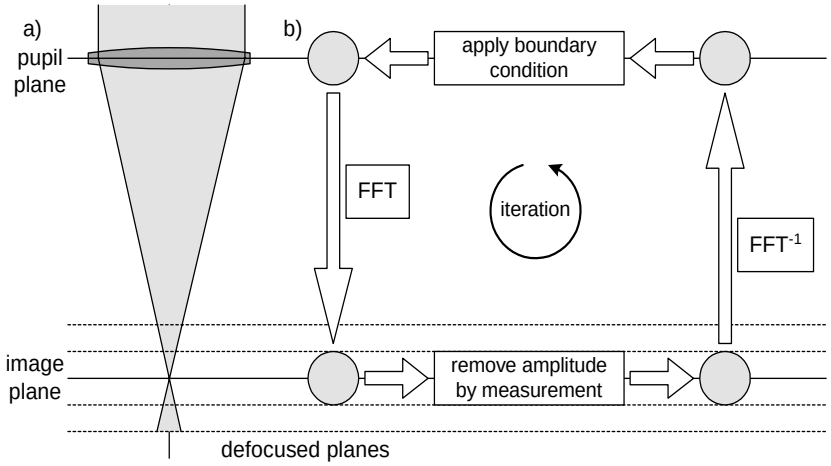

Fig. 1. Principle of the conventional phase retrieval calculation with the Gerchberg-Saxton algorithm by analyzing an image stack. Part a) on the left side shows the optical system with pupil and image plane, part b) is a sketch of the data processing in the algorithm

If the generation of the image amplitude A(x) is written in the simple Fourier description in one dimension as

$$A(x) = H(x) * O(x) \tag{1}$$

with the complex object transmission O(x) and the complex amplitude transfer function H(x), the diversification of the imaging conditions corresponds to a change of the transfer function H(x) in order to reconstruct the object phase W(x)

$$O(x) = T(x) \cdot e^{iW(x)} \tag{2}$$

with the object amplitude transmission T(x). This means, the set of equations

$$A_j(x) = H_j(x) * T(x) \cdot e^{iW(x)} \tag{3}$$

with index j to indicate the diversification must be solved to get the phase W(x). In the case of a defocus diversification, the function $H_j(x)$ is given by

$$H_j(x) = H_{image}(x) \cdot e^{\frac{i\pi x^2 \cdot \Delta z_j}{\lambda R^2}} \tag{4}$$

where R is the radius of curvature of the reference sphere in the pupil, λ is the wavelength and Δz_j is the defocus of the jth plane relative to the image plane with transfer function $H_{image}(x)$ of the system.

If equation (3) is Fourier transformed, we get a representation of the system of equations in the spectral domain

$$A_j(\nu) = H_j(\nu) \cdot \left(T(\nu) * \hat{F}\left[e^{iW(x)}\right]\right) \tag{5}$$

This equation shows, that the object phase can only be reconstructed for those spatial frequencies ν, which are well supported by at least one of the diversification transfer functions $H_j(\nu)$.

3 Modified Phase Retrieval with Pupil Masks

If one recapitulates the main properties of the classical Gerchberg-Saxton algorithm, one can summarize, that the phase reconstruction process is based on selective intensity measurements of free space field propagation. With knowledge of the mathematical propagation according to the Helmholz equation, it is possible to recover the original complex amplitude distribution. In the past most proposals of partial improvement of the original approach, according to section 2, are focused on treating the ill-conditioned problem of reverse reconstruction.

The classical defocussing has only limited support for low spatial frequencies [9]. Therefore, several other possibilities of diversification are proposed in the literature. Among others, a sliding sub-aperture [10], a scanning slit [11], a transversely moved structured illumination [12] or an exploited dielectric slab [13] are options to improve the spectral support.

Our method of a modified phase retrieval algorithm presented here which uses variable pupil masks goes another way. Instead of measuring

the field intensity on different positions during free space propagation, we use changeable pupil masks, to create several free definable measurement conditions. This means that in equation (4) not the second defocus factor is used, but the first term is changed by diversification. The main advantage of such a strategy is the possibility to avoid strong spatial-frequency dependencies of the diversification.

In the iterative retrieval approach, which propagates the lightfield distribution between image and pupil plane and make constraints in each of this planes, it is very important, that these constraints have an significant impact on each iteration. This means the replacements of measured amplitudes in the image plane and the enforcement of spatial frequency limitation in the pupil plane in a qualified sense should achieve noticeable changes of the field. In a first approximation a large size of modification accelerates the convergence speed, because in the interpretation of the steepest decent approach, this is equivalent to the chosen step size. In this context it is also clear, that a strong change of the field in each iteration is no guarantee to get the desired result. For defocus as diversification function this means that an attempt to recover a low frequency structure in relation to the maximal spatial resolution of the system needs a high defocus value to produce intensity differences in the considered frequency range.

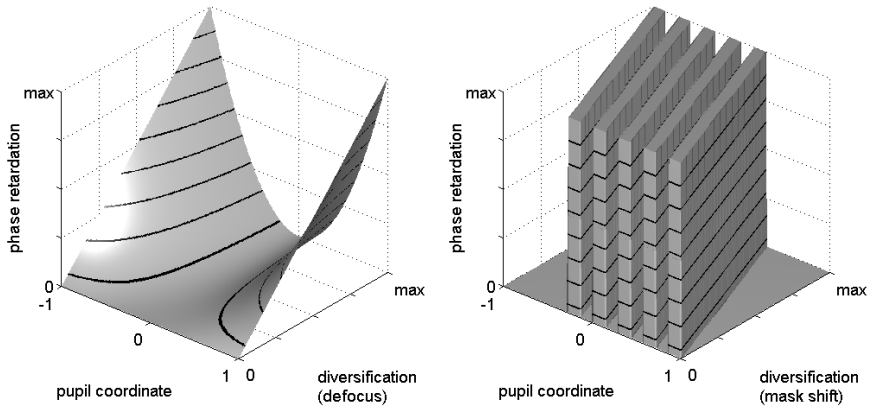

Fig. 2. Support of phase changes in pupil plane for two examples of phase diversification methods. Case (a) defocus with weak effect on low spatial frequencies and (b) shifted grating with frequency independence

Figure 2 illustrates the difference of defocus diversification and use of e.g. one-dimensional phase mask with grid structure. As one can see the

defocus function has a small impact to low spatial frequencies even for high phase retardation values. On the other hand, the depicted phase grating has no such frequency dependency. All spatial frequency components have notable phase retardation while shifting the mask.

In reality we have discrete diversification steps, which correspond to the index j in equation (5). If P_j describes the pupil transmission and Φ_j is the chosen profile of the phase mask, the diversification transfer function has the following form.

$$H_j(\nu) = P_j(\nu) \cdot e^{i\Phi_j(\nu)} \tag{6}$$

If this support function is applied for all diversification steps for every frequency ν there is at least one case, where the maximum value of H_j is valid.

In the following discussion we present three different phase masks avoiding the described disadvantages. Figure 3 shows the shape of the phase masks.

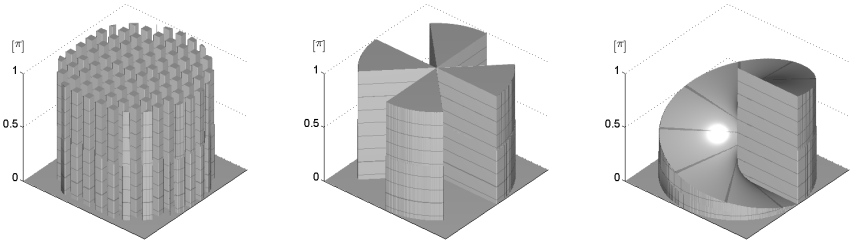

(a) (b) (c)

Fig. 3. Possible phase mask profiles (a) binary grid (b) binary Siemens star (c) spiral mask. The first mask has to be shifted in each direction the others have to be rotated

The first one is a binary phase mask, which has a chessboard like profile. This mask has to be shifted in each direction to diversify the phase distribution of arbitrary specimens. Size and number of steps are typically free parameters, but it is reasonable to choose these two parameters in a way that a periodic section of the pupil mask is separated in *n* equidistant steps.

The next two masks, a Siemens star and a spiral mask have to be rotated to vary the system aberration. Again, the selection of the rotational step sizes should be determined as *n* equidistant rotation angles of full circle. The additional combination with original defocusing is always possible, but there is no need to do this. However it is conceivable to design a pupil

filter which does not cover the high-frequency components of the specimen. In this case a combination of moving pupil filter and variable defocus could be reasonable.

4 Results and Discussion

In the following section we want to present some simulation results for the evaluation of the performance of the proposed mask types. As a test pattern a synthetic binary phase mask with phase retardation of π is used, which has a size of 64µm in square and is shown in figure 4.

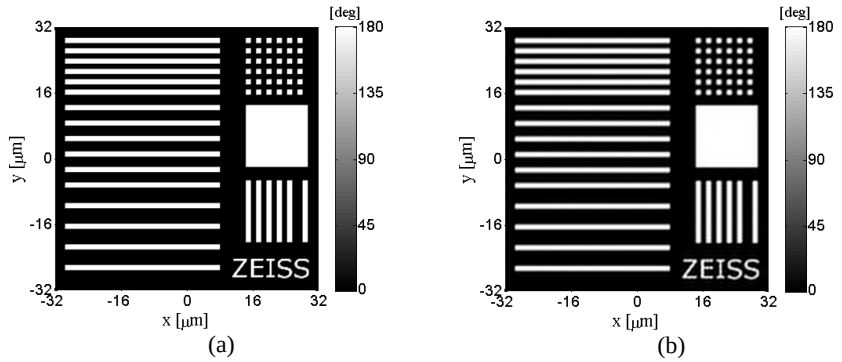

Fig. 4. Original phase function of the object (a) and phase function of the image (b), which is the reconstructible distribution of the test sample. Picture (b) shows a small loss of resolution

The optical test setup has a coherent illumination with a wavelength of 500 nm. The numerical aperture is 0.5 and there are no aberrations in addition to the phase mask implemented the in pupil plane. Apart from the restriction to an ideal optical system we also ignore other degrading effects, e.g. noise, centering errors, and jitter of mask or sensor. The reason of this restriction to ideal conditions is the goal to show the pure performance improvement of phase retrieval with the use of pupil masks. Three different phase masks, which are already described in last section and depicted in figure 3, are used. The number of images and iterations as input parameters were chosen equally to make the calculation results comparable. In every case 8 images with different positions of pupil filter or defocus positions were calculated. As reference case the original Gerchgerg-Saxton algorithm with 4 Rayleigh units defocus range was used.

Figure 5 shows the result of a phase retrieval after 25 iterations over the whole image stack. The error distribution of the remaining deviation of the correct phase in the image plane is shown for the four cases of diversification.

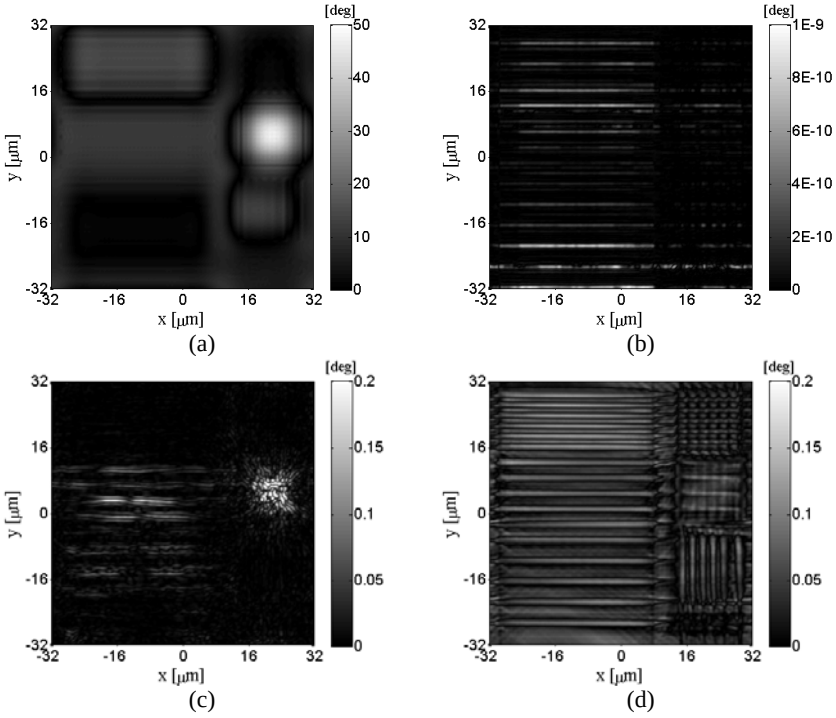

Fig. 5. Error plot of retrieval results with (a) original method with defocusing (b) binary grid (c) binary Siemens star (d) spiral mask. Plotted is the spatial resolved phase difference between the exact image phase and the reconstructed phase distribution. The different gray scales has to be noted, therefore the pictures are not comparable directly

The scales are adapted to the residual errors for the different cases. In contrast to the good phase reconstruction results in cases with phase masks, the classical retrieval with defocus diversification shows larger false phase values. The maximum local error is about 47 degrees and therefore approximately 100 times higher than the error of the most inconvenient pupil masks application. In the best case with the binary grating mask, the reconstruction accuracy reaches nearly perfect results not far from machine precision. At this point it is important to emphasize, that this is the peak-to-valley error over the whole image size. For defocus diversification it is highly located in low frequency structure of the sample with constant phase.

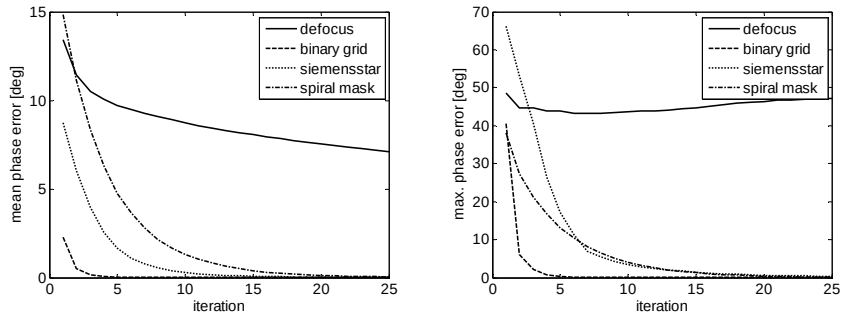

(a) (b)

Fig. 6. Error of the phase retrieval: (a) mean value and (b) peak–to-valley value as a function of iteration steps for original Gerchberg-Saxton approach and different moveable pupilmasks

Figure 6 shows the convergence behaviour of the different retrieval calculations. Both the mean phase error and the maximum phase error are considered. In table 1 the remaining reconstruction errors after 25 iterations over the whole image stack are listed. One can see that the use of adequate pupil filter helps to improve convergence speed and reconstruction accuracy as well.

Table 1. Reconstruction errors after 25 iterations

Error	Defocus	Binary mask	Siemens star	Spiral mask
Mean phase error [deg]	7.123	5e-11	0.01	0.04
Max. phase error [deg]	47.256	1e-9	0.35	0.13

5 Conclusions

In this paper we presented a modified phase retrieval approach, which uses changeable phase masks in the pupil plane instead of defocus. We formulated the most important requirements to the shape and mode of operation of the masks and presented three possible types. The simulation results clearly indicate an improvement of the phase reconstruction accuracy and the speedup of numerical calculation. The improvement depends on the chosen parameters, like defocus range, shape of pupil filters and their movement, number of images and number of iterations. Especially for industry application the reliability and reproducibility of

retrieval results play an important role. To investigate these issues one has to take external perturbations like noise and jitter into account but also sensor properties. This could be a topic of further work.

6 References

1. Fienup, J.R. (1978) Reconstruction of an object from the modulus of its Fourier transform. Opt. Lett. 3:27-29
2. Wu,R., Shu, F., Zhang, W., Zhang, X., Li, Y. (2007) Extended algorithm for the design of diffractive optical elements around the focal plane. Appl. Opt. 46:5779-5783
3. Möller,B., Gross,H. (2005) Characterization of complex optical systems based on wavefront retrieval from point spread function. Proc. SPIE 5905.
4. Marchesini, S. (2007) A unified evaluation of iterative projection algorithms for phase retrieval. Rev. of Sci. Inst. 78:011301
5. Brady, G.R., Fienup, J.R. (2006) Nonlinear optimization algorithm for retrieving the full complex pupil function. Opt. Express 14:474-486
6. Fienup,J.R., Wackerman, C.C. (1986) Phase-retrieval stagnation problems and solutions. JOSA A 3:1897-1907
7. Fienup,J.R. (1982) Phase retrieval algorithms: a comparison. Appl. Opt. 21:2758-2769
8. Gerchberg G. W., W. O. Saxon, D. (1972) Practical algorithm for the determination of phase from image and diffraction plane pictures. Optik (Stuttgart) 35, 237–246
9. Dean, B., Bowers, C.W. (2003) Diversity selection for phase-diverse phase retrieval. JOSA A 20:1490-1504
10. Brady, G. R., Guizar-Sicairos, M., Fienup, J. R. (2009) Optical wavefront measurement using phase retrieval with transverse translation diversity. Opt. Express 17:624-639
11. Nakajima, N. (2005) Phase retrieval from diffraction intensities by use of a scanning slit aperture. Appl. Opt. 44:6228-6234
12. Guizar-Sicairos, M., Fienup, J.R. (2008) Phase retrieval with transverse translation diversity: a nonlinear optimization aproach. Opt. Express 16:7264-7278
13. Soldovieri, F., Leone, G., Pierri, R. (2008) A novel phase retrieval technique based on propagation diversity via a dielectric slab. Opt. Express 16:7418-74427

Phase retrieval with an LCoS display: characterization and application

C. Kohler **) *)
*) Institut für Technische Optik
Pfaffenwalding 9, 70569 Stuttgart
Germany
**) LABMETRO: Laboratório de Metrologia e Automatização,
Universidade Federal de Santa Catarina,
CEP 88040-970, Florianópolis, Santa Catarina, Brazil
F. Zhang ***) *)
***) Kroto Research Institute, University of Sheffield, Broad Lane S3 7HQ Sheffield, United Kingdom
W. Osten *)

1 Introduction

We recently reported about a new phase retrieval method that employs a movable phase plate as modulator [1]. In this paper, as a practical demonstration we first apply this method for the characterization of a reflective Liquid Crystal on Silicon Display (LCoS). In turn, we show how to use the calibrated LCoS display as the modulator required in this method. Using a display as the modulation device offers several advantages over a phase plate: flexibility in selecting the optimal phase distribution for objects and easy adaptation to different wavelengths. The most important advantage is that the disposal of moving parts makes this method very suitable for the use with instantaneous fields. The measurement speed will be only limited by the switching time of the display and the acquisition time of camera.

Phase retrieval methods provide a solution to the phase problem by directly deriving the unknown phase from recorded intensities [2,3]. Many different kinds of phase retrieval methods have been proposed in literature. Among them, methods originated from the Fienup's HIO (hybrid input output) algorithm [4] are most widely used. Those need only single diffraction intensity and work well for a small isolated object illuminated by a big beam. For extended objects that are not able or reasonable to make small, these methods have difficulties to give a unique answer. To overcome the inability for extended objects, especially when objects

introduce a strong phase shift, various methods employing multiple recordings have been conceived. The diversities that have been exploited are recording distance variation, illumination area overlapping [5], wavelength of radiation [6] as well as tilting and curvature modification of the illumination beam [7].

Our recently presented method [1] is another multiple recording based method inspired by the spread-spectrum modulation techniques that are widely used in mobile communication industry [8]. In Spread Spectrum methods, information contained in a certain bandwidth is deliberately spread out in the frequency domain, resulting in a signal with a much broader bandwidth. In our optical case, Spread Spectrum is carried out by putting in a spatial modulator between the object and the image sensor. Due to this similarity we call the method presented "Spread-Spectrum Phase Retrieval" (SSPR).

2 Using the SSPR method for the characterization of an LCoS display

LCoS displays have been widely used in many applications in which they usually act as a projection device operating in amplitude modulation mode. Recently, there is also increasing interest of using LCoS displays as a phase modulator. In comparison to transmissive displays, the increasing popularity of LCoS displays is due to their high fill factor and therefore better light and diffraction efficiency. To use an LCoS display as a phase modulator, a good knowledge about its phase shifting properties is required [9, 10]. A number of methods for display characterization have been reported but most are not capable of delivering pixel-resolvable characterization. Although some methods are able to provide laterally resolved characterization, they are usually time-consuming and have strict requirement on system stability. The pixel-resolvable capability is important for the investigation of important issues like non-uniformity and cross-talk effects of a display. The SSPR method is able to provide laterally resolved characterization in short time. Its feasibility and accuracy are confirmed by comparing results with that obtained from a standard phase shift measurement method, as described in [9, 11].

As a first step we shortly describe the setup used for the display characterization here. The experimental setup consists of two main parts. One is the display illumination including state of polarization generation and the other one is the phase plate and an image sensor used to record the intensity patterns. One aim of an enhanced display characterization is to

observe the phase distribution within one LCoS pixel, to detect potentially present cross talk effects between pixels. Therefore we introduced an imaging system with a 5 times magnification. A telescope type optics was used, to image the display onto the phase modulator. In addition to a magnification the optics offers another advantage, as the LCoS display is imaged onto the modulator no final propagation to the LCoS plane is necessary after the iterative phase retrieval procedure. [1]

In figure 1 the setup used is shown. The display is illuminated over a beam splitter which is possible because we used a planar nematic display in eigenpolarization [12]. Accordingly no change of polarization is caused by the display which otherwise has to be considered in the experiment. Additionally no analyzer is needed behind the display, facilitating the optical setup and avoiding problems that might occur due to reflection on the analyzer surface. In figure 2 (a) the results of a conventional phase shift measurement and in figure 2 (b) the results of the SSPR method are shown. In fig. 2 (a) the double slit like method was used and all gray values were measured sequentially [9, 11]. In fig. 2 (b) a blazed grating with a period of 12 pixels was addressed to the display, eight diffraction intensities were recorded for retrieving the phase.

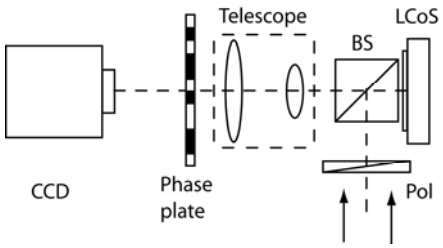

Fig. 1. SSPR setup used for the characterization of an LCoS display. The display is illuminated using a beam splitter, a telescope type imaging optics is used to image the display onto the phase plate.

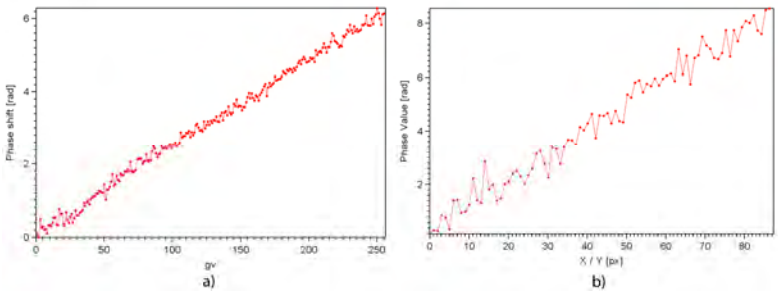

Fig. 2. Results of the display characterization. In (a) the phase shift measured with a double slit method is shown, (b) is the result obtained with the SSPR method.

The results of both methods agree well. The larger noise in the SSPR result may result from imperfections in the phase of the phase plate used and the camera noise. Note that for the results shown in Fig 2(a) a number of 8 camera images have been averaged. This averaging can also be used to for SSPR result to reduce the noise but were not used in this case in favour of a shorter data acquisition time.

3 Using an LCoS display as a modulator for the SSPR method

As we could successfully verify the phase shifting properties of the LCoS display with the SSPR method, we now aimed to use the display as a modulator for the method itself. Because the LCoS display is reflective and the modulator used before is transmissive the optical setup had to be modified.
At first problems were caused by reflections of the modulators cover glass, they overlayed the recorded diffraction patterns and hindered convergence seriously. Hence the LCoS display was tilted by an angle and because the modulator and the camera chip have to be aligned in parallel, the camera is tilted by the same angle. To maintain light transmission the optical axis of the display and the camera must be offset be a certain distance. The final setup is shown in figure 3, the distance of the optical axis is denoted with the letter "*l*" in the figure.

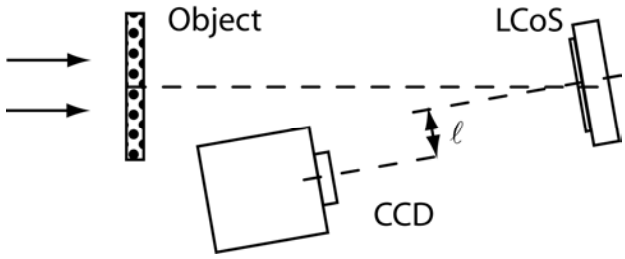

Fig. 3. Setup for the SSPR method with the LCoS display as a modulator. Due to reflections on the modulator's cover glass, both the modulator and the camera are tilted by the same angle.

Results of a first test measurement with the LCoS display as modulator are shown in figure 4: a) the recovered intensity distribution and b) the recovered phase map of a mount plate. Due to pixel cross talk within the LCoS display a phase pattern with a quick change in the addressed phase values is spread out and altered by the display which largely reduces the

convergence. Only with a binning of at least 3 by 3 LCoS pixels we started getting convergence again. Besides the reduced convergence the recovered phase maps and intensity distributions show a strong grid overlayed, which is probably caused by the modulator fill factor. In addition to binning modulator pixels the use of low pass filtered version of the phase patterns within the retrieval process slightly improved the convergence, but the quality is still inferior to that using phase plate.

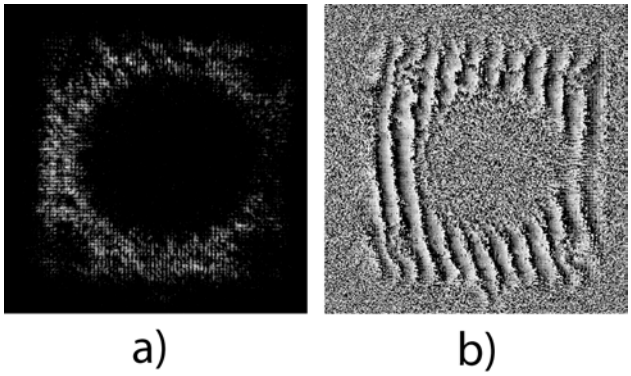

Fig. 4. First results obtained with the LCoS displayed used as a modulator within the SSPR method. Except the reduced convergence strong grid like artefacts are present in the results.

4 Summary

The recently presented phase retrieval method could successfully be used for the characterization of the phase shifting properties of an LCoS display. The result obtained agrees well with the result of a standard method. First experiments were made, using the characterized LCoS display as a modulator for the SSPR method. The results show the principle feasibility but still suffer from strong artefacts caused by the modulator properties. Further research is needed to create a robust and flexible measurement setup.

5 Acknowledges

We thank the Deutsche Forschungsgemeinschaft (DFG) for supporting this research under the grant number OS-111/23-1.

6 References

1. Zhang, F., Pedrini, G., Osten, W. (2007) Phase retrieval of arbitrary complex-valued fields through aperture-plane modification. Phys. Rev. A 75:043805
2. Gerchberg, R.W., Saxton, W.O. (1971) Phase determination for image and diffraction plane pictures in the electron microscope. Optik 34:275-284
3. Gecherberg, R.W., Saxton, W.O. (1972) A practical algorithm for the determination of phase from image and diffraction plane pictures . Optik 35:227-246
4. Fienup, J.R., (1982) Phase retrieval algorithms a comparison. Appl. Opt. 21:2758-2769
5. Rodenburg, J.M., Faulkner, H.M.L. (2004) A phase retrieval algorithm for shifting illumination. Appl. Phys. Lett. 85:4795-4797
6. Bao, P., Zhang, F., Pedrini, G., Osten, W. (2008) Phase retrieval using multiple wavelengths. Opt. Lett. 33 309-311
7. Nugent, K.A., Peele, G., Quiney, H.M., Chapman, H.N. (2005) Diffraction with wavefront curvature a path to unique phase recovery. Acta Cryst. A61: 373-381
8. Dixon R.C. (1984) Spread spectrum Systems, John- Wiley and Sons
9. Kohler, C., Schwab, X., Osten, W. (2006) Optimally tuned spatial light modulators for digital holography. Appl. Opt. 45: 960-967
10. Kohler, C., Haist, T., Osten, W. (2009) Modell-free method for measuring the full Jones matrix of reflective liquid-crystal displays. Opt. Eng. 48:044002
11. Bader, G., Bürkle, R., Lüder, E., Frühauf, N., Zeile, C. (1997) Fast and accurate techniques for measuring the complex transmittance of liquid crystal valves. Proc. SPIE 3015:93-104
12. Pezzaniti, J.L., Chipman, R.A. (1993) Phase-only modulation of a twisted nematic liquid-crystal TV by use of the eigenpolarization states. Opt. Lett. 18:1567-1569

Digital dynamic-fringe pattern processing without frequency carrier, using wideband phase-shifting algorithms.

Julio C. Estrada, Fernando Mendoza-Santoyo, Manuel de la Torre
Centro de Investigaciones en Óptica, León Guanajuato, México
Tonatihu Saucedo
Universidad Autónoma de Zacatecas, Zacatecas, México

Abstract

Here, we will show a method to recover the phase of a temporal sequence of interferograms, without knowing its carrier frequency. To accomplish this, we will use algorithms that we call wideband phase-shifting algorithms. The underlying idea is to combine first and second order quadrature filters to obtain wideband phase-shifting algorithms. This first and second order quadrature filters are analogous to the first and second order filters commonly used in communications engineering. The method presented here is very useful in areas where transient events are analised, and a high performance demodulation method is needed to recover the phase of the interferograms without frequency carrier, i.e., when one does not know the phase shift or the frequency carrier. In general, the approach presented here gives a powerful and robust frequency analysis and design tool for detuning phase-shifting algorithms for interferometry.

1 Introduction

It is assumed in few-steps *Phase-Shifting Interferometry* (PSI) that the phase throughout the interferogram temporal sequence remains constant, e.g., the object under test is static and that the phase shifting is linear. The interferogram sequences obtained in PSI, can be seen as a finite discrete-time interferometric signals where each element (x, y) can be modeled as:

$$s(t) = a_{x,y} + b_{x,y}\cos(\phi_{x,y} + \omega_0 t), \tag{1}$$

The integer index $t \in \{0,1,2,\ldots,N-1\}$ refers to the n-th interferogram taken at time t , $a_{x,y}$ is the background illumination, $b_{x,y}$ the contrast, $\phi_{x,y}$ the modulating phase that we want to recover, and ω_0 the frequency carrier, or as called in the PSI parlance, the phase shifting. All these variables are defined for any site (x,y) of the interferogram image.

In PSI, the usual number of interferometric images varies from 3 to about 11, and to recover the phase from these few-step interferometric signals, there are dozens of algorithms (See Refs. [6 ,5 ,4 ,3 ,2]. In this class of PSI algorithms, the order of the algorithm is the same as the number of interferograms taken. For example, if we have 7 interferograms then we have a 7-steps phase-shifting algorithm. This phase-shifting algorithm uses the information of the 7 interferograms to obtain the phase for only one interferogram, e.g., the center one. The phase shifting algorithms can be seen as convolution quadrature filters. For example, for a 3-steps phase-shifting algorithm its quadrature filter impulse response would be

$$h(t) = [\,2\delta(t) - \delta(t-1) - \delta(t+1)]\sin(\frac{\alpha}{2}) + i[\delta(t-1) - \delta(t+1)]\cos(\frac{\alpha}{2}), \qquad (2)$$

where, and in order to recover the phase from (1), α must be equal to the carrier frequency ω_0 from the interferometric signal given in (1). Thus, when $\alpha = \omega_0$ it is said that the algorithm is tuned. Then, to recover the modulating phase $\phi_{x,y}$ from (1), we must to know the value of its carrier frequency ω_0 , or phase shift.

In what follows, we will show how to construct a wideband quadrature filter for PSI like that shown in Eq. (2), but it will be a 9-steps wideband phase shifting algorithm. Using this quadrature filter we do not have to know the value of the carrier frequency from the interferometric signal. An interesting application of this wideband quadrature filter is its application to demodulate the phase of a dynamic fringe pattern. In this case, the interferogram sequence is taken under normal circumstances, for instance, while the object under test is moving. The only restriction imposed is that the local temporal frequency must be greater than the maximum variation of the phase.

2 Method

The problem to obtain a digital quadrature filter for signals like that given by Eq. (1), could be stated as follows: Find an operator that given a few samples of the signal given in Eq. (1), results in a complex value given by:

$$\hat{s}(t) = c \cdot \exp[-i(\phi_{x,y} + \omega_0 t)], \tag{3}$$

where $i = \sqrt{-1}$, and c is a constant related to the response of the quadrature filter. To find this, let us first analyze the frequency response of Eq. (1). If we take its Fourier transform we obtain the following:

$$S(\omega) = \frac{b_{x,y}}{2}\delta(\omega + \omega_0)e^{i\phi_{x,y}} + a_{x,y}\delta(\omega) + \frac{b_{x,y}}{2}\delta(\omega - \omega_0)e^{-i\phi_{x,y}}, \tag{4}$$

considering that $\phi_{x,y}$, $a_{x,y}$, and $b_{x,y}$, are all constants. $\delta()$ is the Dirac delta function, and ω is the transformed frequency space. Its power spectrum can be seeing as three weighted Dirac delta functions, one located at $\omega = -\omega_0$, another at $\omega = 0$, and the last one at $\omega = \omega_0$. Given this and to obtain the complex signal shown in Eq. (3), we must obtain a filter that removes the Dirac delta at $\omega = \omega_0$, and at $\omega = 0$.

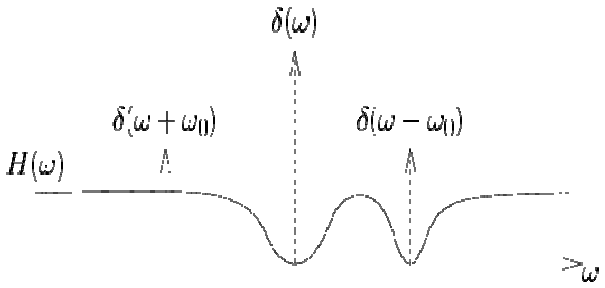

Fig. 1. Illustration of a quadrature filter that removes the Dirac delta functions located at $\omega = \omega_0$, and $\omega = 0$.

For illustration purposes, in Fig. 1, we show the shape of a quadrature filter $H(\omega)$ that removes these frequency components. The principal properties of the quadrature filter are such that $H(0) = 0$, $H(\omega_0)$, and

$H(-\omega_0) \neq 0$. To obtain a filter with these properties, we propose the following first and second order derivative operators:

$$h_1(t) = \frac{i}{2}[\delta(t-1) - \delta(t+1)], \tag{5}$$

and

$$h_2(t) = 2\delta(t) - \delta(t-1) - \delta(t+1), \tag{6}$$

respectively. At this point the reader may wonder why $h_1(t)$ is complex; we define it as complex only because we want its frequency response to be *real*. Thus, the Fourier transform of these filters is the following:

$$H_1(\omega) = -\sin(\omega) \tag{7}$$

and

$$H_2(\omega) = 2 - 2\cos(\omega), \tag{8}$$

respectively. If we see their graphics, Figs. 2(a) and 2(b), we see that both operators remove the frequency components at $\omega = 0$. But now, we want to remove the frequency component at $\omega = \omega_0$. To do this, we simply

$$\begin{aligned} H(\omega) &= H_1(\omega)H_2(\omega - \omega_0) \\ &= -\sin(\omega)[2 - 2\cos(\omega - \omega_0)]. \end{aligned} \tag{9}$$

displace these operators to the frequency ω_0 as shown in Figs. 2(b) and 2(d). Then, the quadrature filter with the properties that we are looking for is obtained as a combination of these filters in the following way:

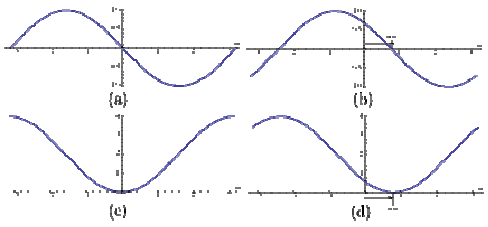

Fig. 2. Graphic (a) shows the graphic of Eq. (7); (b) shows the graphic of Eq. (8). Graphs (c) and (d) show the graphs of Eqs. (7) and (8), shifted (tuned) at $\omega = \omega_0$, respectively.

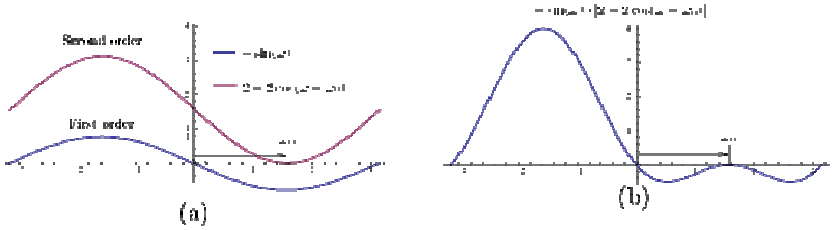

Fig. 3. Graphic (a) shows the first order and the displaced second order filters, and (b) shows the product of these building blocks. We can see in (b) that the quadrature filter obtained removes the DC term at $\omega = 0$, and the frequency component at $\omega = \omega_0$.

Up to this point we have presented only the frequency analysis to obtain a quadrature filter for signals like the one given in Eq. (1). However, we want the mathematical formula to apply this quadrature filter to the samples of a signal in Eq. (1). For this we take the inverse Fourier transform of (9) to obtain the following:

$$\begin{aligned} h(t) &= [2\delta(t) - \delta(t-2) - \delta(t+2)]\sin(\omega_0)/2 \\ &+ i[2\delta(t-1) - 2\delta(t+1)]/2 \\ &- i[\delta(t-2) - \delta(t+2)]\cos(\omega_0)/2 \end{aligned} \qquad (10)$$

which can be applied over 5 samples of the. Then assuming that $s(-2)$, $s(-1)$, $s(0)$, $s(1)$, and $s(2)$ are the five samples from the signal, we can apply (10) to these samples by means of convolutions to obtain the following complex response:

$$\begin{aligned} \hat{s}(0) &= [2s(0) - s(-2) - s(2)]\sin(\omega_0)/2 \\ &+ i[2s(-1) - 2s(1)]/2 \\ &- i[s(-2) - s(2)]\cos(\omega_0)/2, \end{aligned} \qquad (11)$$

from which, the phase $\phi_{x,y}$ can be recovered (modulus 2π) as:

$$\phi_{x,y} = \tan^{-1}\left[\frac{2s(-1) - 2s(1) - [s(-2) - s(2)]\cos(\omega_0)}{[2s(0) - s(-2) - s(2)]\sin(\omega_0)}\right]. \qquad (12)$$

We call this last equation the phase-shifting algorithm. In this case is a 5-step phase-shifting algorithm. A particular case that the reader can

recognize is when $\omega_0 = \pi/2$. In this case by taking $\omega_0 = \pi/2$ directly, we obtain the well known formula:

$$\phi_{x,y} = \tan^{-1}\left[\frac{2s(-1) - 2s(1)}{2s(0) - s(-2) - s(2)}\right], \tag{13}$$

reported by Hariharan [3]. However, the formula given in (12) is more general since in this case ω_0 can take any value. Now, let us extend this new concept to obtain wideband quadrature filters for phase-shifting interferometry. As shown before, we can design our quadrature filter by using the operators given in (7) and (8). In this case, we are going to locate our filter operators not only to remove the frequency components at $\omega = 0$ and $\omega = \omega_0$, but also with the aim of extending the bandwidth of the resulting filter: we are going to attach the filter operators in frequencies $\omega = 0$, $\omega_0 = \frac{\pi}{4}$, $\omega_1 = \frac{\pi}{2}$, and $\omega_2 = 3\frac{\pi}{4}$. We show this in Fig. 4.

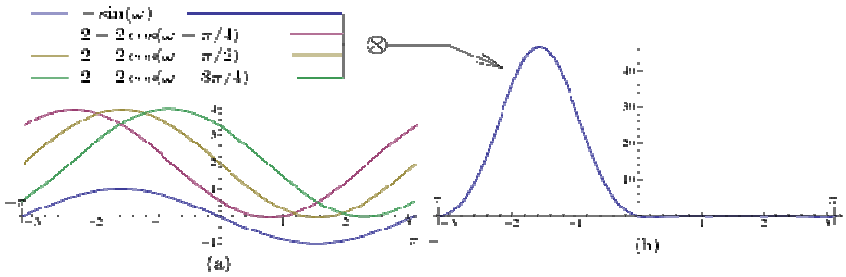

Fig. 4. (a) shows the frequency locations of the basic filters used to construct the wideband quadrature filter shown in graph (b). The quadrature filter thus obtained is the product of these filters.

The resulting quadrature filter shown in Fig. 4(b). It removes, or makes approximately zero, a wide range of frequencies hence we call this a wideband quadrature filter. Mathematically we obtain this in the following way:

$$H(\omega) = H_1(\omega)H_2(\omega - \omega_0)H_2(\omega - \omega_1)H_2(\omega - \omega_2), \tag{14}$$

where $H_1(\cdot)$ and $H_2(\cdot)$ are the first and second order quadrature filters from Eqs. (7) and (8). Now, taking the inverse Fourier transform of Eq. (14), we get:

$$\begin{aligned} h(t) &= \frac{1}{2}\delta(t-4) - (2\sqrt{2}+3)\delta(t-2) + (4\sqrt{2}+5)\delta(t) - (2\sqrt{2}+3)\delta(t+2) + \frac{1}{2}\delta(t+4) \\ &- i[(\sqrt{2}+1)\delta(t-3) - (3\sqrt{2}+5)\delta(t-1) - (3\sqrt{2}+5)\delta(t+1) - (\sqrt{2}+1)\delta(t+3)]. \end{aligned} \tag{15}$$

Finally, to obtain the mathematical formula for the wideband phase-shifting algorithm, we convolve this quadrature filter with 9 samples of the signal given in Eq. (1), and take its angle to obtain the following 9-steps wideband phase-shifting algorithm:

$$\phi_{x,y} = \tan^{-1}\left[\frac{(\sqrt{2}+1)s(-3)-(3\sqrt{2}+5)s(-1)+(3\sqrt{2}+5)s(1)-(\sqrt{2}+1)s(3)}{\frac{1}{2}s(-4)-(2\sqrt{2}+3)s(-2)+(4\sqrt{2}+5)s(0)-(2\sqrt{2}+3)s(2)+\frac{1}{2}s(4)}\right]. \quad (16)$$

3 Tests and results

Let us now test the wideband phase-shifting algorithm obtained in Eq. (16). As a first test, we use a simulated signal whose frequency is varying between 0 and π radians.

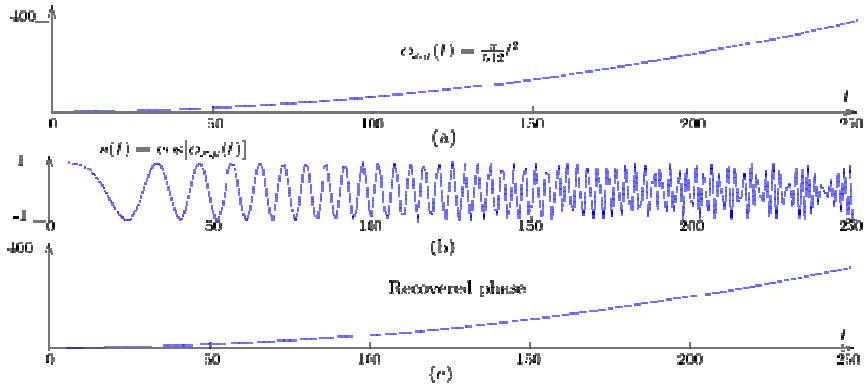

Fig. 5. (a) shows the ground true phase, (b) is the generated signal, and (c) the absolute phase error of the estimated phase using the wideband phase shifting algorithm in Eq. (16). Note: *Plot (b) suffers of aliasing due to the limited resolution of the software used to generate it.*

In fig. 5(a) we show the phase used to generate the signal. If we take its derivative, its frequency is 0 for $t = 0$ and π for $t = 256$. Fig. 5(b), shows the signal generated. It is necessary to remark, that the presentation of the signal's plot suffers from aliasing due to the limited resolution of the software used to generate it. Given this signal, we estimated its phase with Eq. (16), and in Fig. 5(c) the absolute phase error of the estimated phase is plotted, that is $\left|\phi_{x,y}(t)-\hat{\phi}_{x,y}(t)\right|$, where $\phi_{x,y}(t)$ is the ground true phase,

and $\hat{\phi}_{x,y}$ is the estimated phase previously unwrapped. There we can see that the absolute phase error close to the frequencies 0 and π is almost 0.3 radians, and at least zero between frequencies $\frac{\pi}{5}$ and $4\frac{\pi}{5}$. This is expected if we see the frequency response of the algorithm used in Fig. 4.
The test presented above, was made with the aim to numerically illustrate the behavior of the wideband phase-shifting algorithm in Eq. (16). Now, let us test it with a sequence of interferograms taken from *Electronic Speckle Pattern Interferometry* (ESPI) fringe patterns. We used an old original video from a VHS tape containing fringe patterns from a vibrating plate using an in-plane sensitive ESPI. From this video we took a sequence of 13 interferograms and applied the wideband phase-shifting algorithm in Eq. (16). With these 13 interferograms we were able to recover the phase for the 5 middle interferograms.

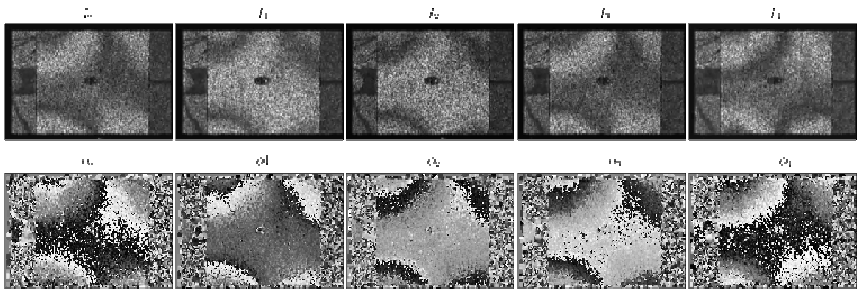

Fig. 6. Here we show an experimental interferometric signal, above, and below are their corresponding demodulating phase maps.

In Fig. 6, we show the result of this test, where the interferograms where the phase was obtained are depicted. As we can see, the obtained phase is the expected from the interferograms given. The reader may want to compare these phase maps with the ones obtained in Ref [7]. The phase of each interferogram shown is obtained without knowing its temporal frequency carrier, or as said in the PSI parlance, without knowing its phase shift.

4 Summing up

In this work we presented a wideband phase-shifting algorithm, Eq. (16). The algorithm presented is suitable for processing dynamic fringe patterns

where the temporal carrier frequency is not known. The only restriction is that the temporal frequency carrier must exist, although we do not require to know it. These wideband phase-shifting algorithms were first published in Ref. [1].

5 References

1. J. C. Estrada, M. Servin, and J. A. Quiroga. Easy and straightforward construction of wideband phase-shifting algorithms for interferometry. Optics Letters, 34(4):413–415, 2009.
2. John E. Greivenkamp. Generalized data reduccion for heterodyne interferometry. Optical Engineering, 23(4):350–352, July 1984.
3. P. Hariharan, B. F. Oreb, and T. Eiju. Digital phase-shifting interferometry: a simple error-compensating phase calculation algorithm. Appl. Opt., 26(13):2504–2506, 1987.
4. C. J. Morgan. Least-squares estimation in phase-measurement interferometry. Opt. Lett., 7(8):368, 1982.
5. Johannes Schwider, Oliver R. Falkenstoerfer, Horst Schreiber, Andreas Zoeller, and Norbert Streibl. New compensating four-phase algorithm for phase-shift interferometry. Optical Engineering, 32(8):1883–1885, 1993.
6. J. C. Wyant. Use of an ac heterodyne lateral shear interferometer with real-time wavefront correction systems. Appl. Opt., 14(11):2622, 1975.
7. F. Mendoza Santoyo, M. C. Shellabear, and John R. Tyrer, "Whole field in-plane vibration analysis using pulsed phase-stepped ESPI," Appl. Opt. 30(7):717, 1991.

Error-compensating phase-shifting Fizeau interferometry with a wavelength-tunable laser diode

Yukihiro Ishii, Sayaka Idoi, Hayato Fujita, and Hideki Funamizu
Department of Applied Physics, Tokyo University of Science
1-3 Kagurazaka, Shinjuku-ku, Tokyo 162-8601, JAPAN

1 Introduction

Laser diodes (LDs) are useful light sources in phase-shifting interferometry (PSI) because of their direct frequency tunability [1]. The phase of the interference fringe on an unbalanced Fizeau interferometer can be shifted by a frequency change in the LD [1]. The phase shifts introduced by the wavelength changes of a LD become equal in both axial and off-axial rays at a Fizeau interferometer but it is impracticable with a PZT movement.

A 16 -sample phase-extraction algorithm in a phase-shifting Fizeau interferometer [2,3] is newly developed from Fourier analysis [4,5] and a wanted surface profile of a test object can be measured suppressing all noises due to an alignment error of a test object, the power changes of a LD [6] and multiple-beam interferences. A wavelength-tunable LD causes power changes. Many interference fringes by changing LD currents are successively captured with a high-speed camera. Sixteen $\pi/3$ phase shifts are measured from all captured fringes by using a heterodyne method, and are used to an experiment. A surface profile of a cylinder lens can be measured with an error-compensating 16-step algorithm if many unwanted interference fringes are superimposed on a wanted fringe.

2 Error-compensating 16-step algorithm

In a Fizeau interferometer in Fig. 1 with an unbalanced optical path difference (OPD) d, the multiple interference intensity with *j*-th phase-shift δ_j, i.e., $\delta_j = 2\pi\nu_1 t_j$ with *j*-th harmonic frequency ν_j is given by

$$I(t_j) = I_0(1+\rho\nu_1 t_j)\{1+\gamma_1\cos(\phi'_1+2\pi\nu'_1 t_j) + \gamma_2\cos(\phi'_2+2\pi\nu_2 t_j)+\gamma_3\cos(\phi'_3+2\pi\nu'_3 t_j)\} \quad (1)$$

where I_0 is the bias intensity, $\rho=\Delta I/I_0$ those ΔI is the intensity change by the current variation for a phase-shift interval of 2π, γ_k is the visibility of the k-th frequency, and ϕ_1 is a phase of the measured profile, ϕ_k is given by $\phi_k=kl_k$ (for k=1,2,3), l_k is the k-th OPD, l_1 is an OPD between a reference and the measurement plate, l_2 is an OPD between the front and rear surface of the measurement, and l_3 is an OPD between a reference and the rear measurement. The phase ϕ'_1 differing from an actual phase ϕ_1 is written as $\phi'_1(x,y)=\phi_1(x,y)+\phi_\varepsilon$, where ϕ_ε is a constant phase due to an alignment error ε that corresponds to a detuning error. Here the wave number k is changed to $k+\Delta k$ by varying the LD currents, a wave-number change Δk is $\Delta k = -2\pi\Delta\lambda/\lambda^2$ with a wavelength diversity $\Delta\lambda$. The relations of the harmonic frequency ν_j with a wave-number change Δk and an alignment error ε are written as $2\pi\nu'_1 t = 2(d+\varepsilon)\Delta k(t)$, $2\pi\nu_2 t = 2nt_h\Delta k(t)$, and $2\pi\nu'_3 t = 2(d+\varepsilon+nt_h)\Delta k(t)$. Here an index and a thickness of a plane-parallel glass plate in Fig. 1 are n and t_h, respectively.

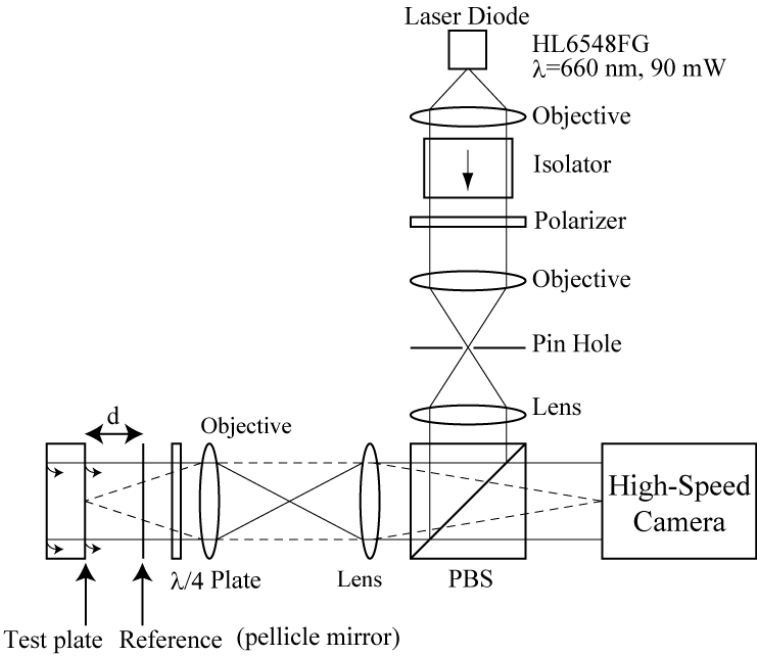

Fig. 1. A laser-diode phase-shifting Fizeau interferometer with a pellicle mirror

An N-th sample phase-extraction algorithm with sampling amplitudes a_j and b_j can be given as

$$\phi_1(x,y) = \tan^{-1}\frac{\sum_{j=1}^{N} a_j I(x,y,t_j)}{\sum_{j=1}^{N} b_j I(x,y,t_j)} = \tan^{-1}\left[\frac{c_1}{c_2}\right]. \tag{2}$$

In Eq. (2), two phase-stepping functions c_n is given by the correlations of the Fourier tranform of the intensity $I(t_j)$ with the filter function $F_n(\nu)$ corresponding to the Fourier transform of the coefficients a_j and b_j.

For the extraction of the coefficients a_j and b_j at a fundamental frequency ν_1 in FT[$F_n(\nu)$], the following conditions for zero amplitudes at higher harmonics should be satisfied [7]: $F_1(\nu_k)=F_2(\nu_k)=0$ (k=0,2,...,10) for an equal phase-shift interval of $\delta_j=\pi/3$ and a thickness setup of $nt_h=3d$. Two filter functions, $F_1(\nu_1)$ and $F_2(\nu_2)$ must satisfy an in-quadrature condition of a $\pi/2$ change to another, i.e., $F_1(\nu_1)=iF_2(\nu_2)$. Error-compensating algorithm can be derived from the added conditions by setting a small deviation equal to zero with a Taylor expansion in a function $F_n(\nu)$ and its derivative $dF_n(\nu)/d\nu$,

$$\left(\frac{\partial F_1^*}{\partial \nu}\right)_{\nu_k} = 0, \quad \left(\frac{\partial F_2^*}{\partial \nu}\right)_{\nu_k} = 0 \quad (\nu_k = 0, \nu_1, \nu_2, \nu_3) \tag{3}$$

for an elimination of the phase error due to the laser-power change of a LD, and

$$\left(\frac{\partial^2 F_1^*}{\partial \nu^2}\right)_{\nu_k} = 0, \quad \left(\frac{\partial^2 F_2^*}{\partial \nu^2}\right)_{\nu_k} = 0 \quad (\nu_k = \nu_1, \nu_3) \tag{4}$$

for the suppression of an alignment error ε in a test plane-parallel plate.

The phase ϕ_1 to be measured is equal to the arctangent of the ratio c_1/c_2 in Eq. (2). The coefficients a_j and b_j in the Fourier transforms of the filter functions $F_n(\nu)$ are solved by simultaneous linear algebraic equations with Eqs. (3) and (4) where sixteen (N=16) unknowns exist. The coefficients a_j and b_j are odd and even properties those Fourier transformations give the relative amplitudes of the filter functions $F_n(\nu)$ in Fig. 2. Filter functions have equal amplitudes at the fundamental frequency ν_1. Note that both $F_1(\nu)$ and $F_2(\nu)$ have zeros at $\nu=2\nu_1$, $3\nu_1$ and $4\nu_1$. It is clear from the figures that $F_1(\nu_1)$ and $F_2(\nu_1)$ are 90-degree out of phase and equal in magnitude. An enlarged portion of Fig. 2(a) is shown in Fig. (b) in which

zeros of 1st.-order and 2nd.-order differentiation are evident at a normalized frequency $\nu/\nu_1=1$. From Fig. 2(b), the filter functions $F_n(\nu_1)$ are almost flat within $0.95 \leq \varepsilon/d_1 \leq 1.05$ so that a 16-step algorithm tolerates an allowable alignment error $\varepsilon=0.3$ mm for an OPD d=6.1 mm.

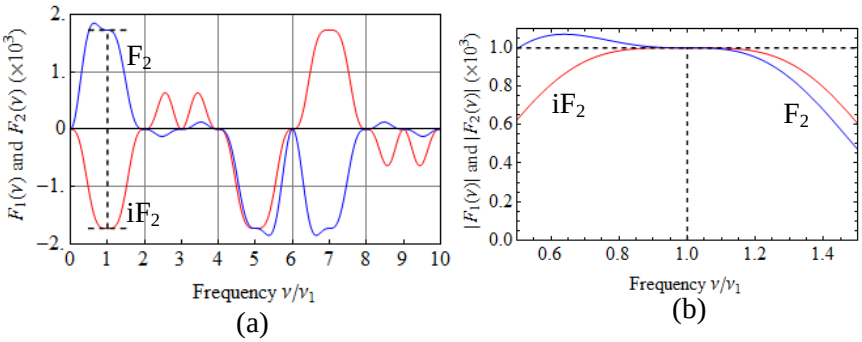

Fig. 2. (a) Filter functions F_1 and F_2 in a 16-step algorithm. (b) Enlarged portion of (a)

3 Results

As shown in Fig. 1, a LD collimated beam through an isolator is incident on a polarizing beam splitter (PBS). A reflected light from a PBS is incident on a reference pellicle mirror and a test plate. A test surface is imaged onto a high speed CMOS camera through an objective lens (5x, NA=0.14). While an active current of a 90-mW LD at λ=660 nm is ranged from 67 to 102 mA causing a 30-% power change of a LD, ρ=0.3, a wavelength change is 0.2 nm by tuning the current including a mode hop. 1000 interference fringes are captured for 2 sec with a total phase shift of 6π.

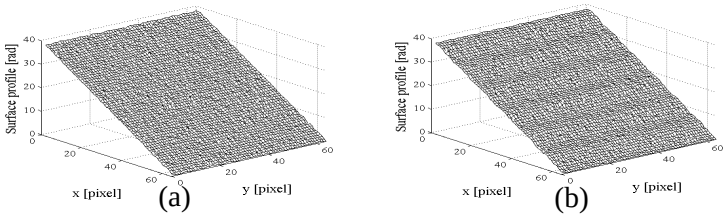

Fig. 3. Numerical phases of a tilted plane calculated from 16 step (a) and 6 step (b)

Phase shifts are measured from a heterodyne beat signal at a fixed sample point,

$B\cos(2\pi\nu_1 t_n+\phi_0)$ (n=1,…,1000) generated by a FMCW technique with the changes in LD currents. A Fourier transform of a beat signal gives $(B/2)\exp(i\phi_0)\delta(\nu-\nu_1)$. An inverse Fourier transform of this function becomes $(B/2)\exp(i\phi_0)\ \exp(i2\pi\nu_1 t_n)$ after filtering the spectra at a frequency ν_1. A n-th phase shift $2\pi\nu_1 t_n$ can be measured at a n-th time sequence, and then sixteen $\pi/3$ phase shifts used in a 16-step algorithm are chosen from all phase-shift measurements. A wide tunability including a mode hop has been used for measurement in the calibration.

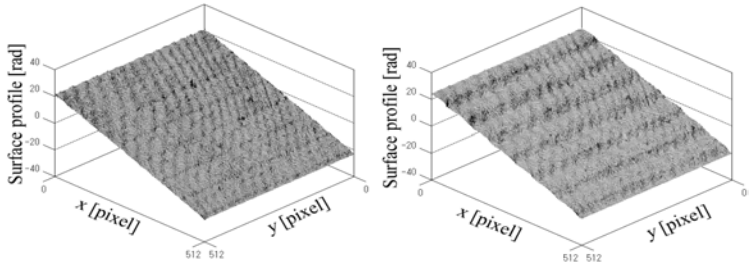

(a) (b)

Fig. 4. Experimental phases of a tilted plane calculated from 16 step (a) and 6 step (b)

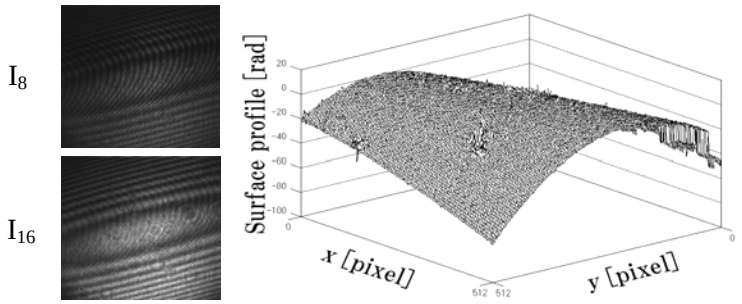

(a) (b)

Fig. 5. (a) Fringe patterns I_8 and I_{16}. (b) Measured surface profile of a cylindrical lens

Figs. 3 and 4 show numerical and experimental results of a test surface measurement suffering from a LD power variation ρ=0.3 and an alignment error ε =0.3 mm for d=6.1 mm with ε/d=0.05. A 6-step algorithm [1] only suppresses the phase error due to the multiple interference noises. Additive gaussian noises in the simulation of Fig. 3 are used as 8.4 % by the comparison of the experimental noisy interference fringes to the low-pass

filtered fringes. The experimental rms phase errors are reduced to 2.9×10^{-1} rad by a 16-step algorithm in Fig. 4(a) from 4.5×10^{-1} rad by a 6-step algorithm in Fig. 4(b). The rms phase accuracy by 16 step increases 1.5 times as 6 step. The numerical phase errors in Fig. 3 are the same behaviors as the experiment. Both figures in Fig. (b) in 3 and 4 show a 2π periodic phase error caused by intensity modulation of the LD [6]. Fig. 5(b) is a measured surface of a cylindrical lens with an error-compensating 16-step algorithm. A saddle surface profile can be extracted even if many interference fringes shown in Fig. (a) are superimposed. A 16-th phase-stepped fringe pattern I_{16} is brighter than I_8 due to the LD power increase.

4 Conclusion

A newly developed 16-step phase-shifting Fizeau interferometry acts to eliminate the multiple-beam interference noise, the measurement errors due to the LD power variations and the setup misalignment in an object surface. A convex-to-flat depth in a cylindrical lens is less than an allowable misalignment length so that a surface profile measurement demonstrates without phase error.

5 References

1. Ishii, Y (2004) Laser-diode interferometry. Prog. Opt., 46, E.Wolf Ed, Elsevier: 243-309
2. Hibino, K (1999) Error-compensating phase measuring algorithms in a Fizeau interferometer. Opt. Rev., 6: 529-538
3. de Groot, P (2000) Measurement of transparent plates with wavelength-tuned phase-shifting interferometry, Appl. Opt., 39: 2658-2663
4. Fraischlad, K, Koliopoulos C. L (1990) Fourier description of digital phase-measuring interferometry, J. Opt. Soc. Am. A, 7: 542-551
5. Larkin, K. G, Oreb, B. F (1992) Design and assessment of symmetrical phase-shifting algorithms, J. Opt. Soc. Am. A, 9: 1740-1748
6. Onodera, R, Ishii, Y (1996) Phase-extraction analysis of laser-diode phase-shifting interferometry that is insensitive to change in laser power, J. Opt. Soc. Am. A, 13: 139-146
7. Hibino, K, Oreb, B. F, Fairman P. S (2003) Wavelength-scanning interferometry of a transparent parallel plate with refractive-index dispersion, Appl. Opt., 42: 3888-3895

Lateral Shearing Interferometer based on a Spatial Light Modulator in the Fourier Plane

Claas Falldorf[1], Reiner Klattenhoff[1], Achim Gesierich[2],
Christoph v. Kopylow[1] and Ralf Bergmann[1]
[1]BIAS - Bremer Intitut für Angewandte Strahltechnik
Klagenfurter Str.2, 28359 Bremen
[2]VEW - Vereinigte Elektronik Werkstätten
Edisonstr.19, 28357 Bremen
Germany

1 Introduction

Shearing interferometry is based on the coherent superposition of two mutually shifted representations of the same wave field, where the term *shear* refers to the lateral shift. The resulting interference pattern can be recorded by a camera sensor for further evaluation [1]. Since both of the interfering wave fields travel almost along the same path, shearing interferometry makes low demands regarding the coherency of the light and at the same time provides enhanced stability and robustness compared to conventional interferometric methods.

During the past decades a number of techniques to invoke the lateral shift have been reported ranging from wedge prisms to diffraction gratings, Michelson interferometers and birefringent components. Recently, a set of different configurations have been proposed which make use of a spatial light modulator (SLM) as shearing element [2,3,4]. This approach allows for the realization of a large variety of lateral and/or radial shears without the requirement of moving parts. Moreover, the spatial light modulator can additionally be used to add constant phase steps to one of the wave fields in order to apply phase shifting techniques.

In this report we present an integrated shearing interferometer which is based on a SLM in the Fourier domain of a classical 4f-arrangement. In contrast to existing setups, this approach provides a pure lateral shift in the spatial domain, where the camera sensor is located. The presented configuration is explained in detail and an analytical model based on the scalar diffraction theory and the Jones matrix formalism is derived. Finally, experimental results are presented in order to verify the scheme.

2 Working principle of the proposed interferometer

Figure 1a shows a photograph of the shearing interferometer presented in this work. It is based on the scheme shown by Fig.1b which will be discussed throughout this section. Let us assume that the lens objective LO provides the complex amplitude U_{img} with the linearly polarized real amplitude A_{img} across its image plane $\{\boldsymbol{u}\}$:

$$\mathrm{U}_{\mathrm{img}}(\mathbf{u}) = \mathrm{A}_{\mathrm{img}}(\mathbf{u}) \cdot \exp\left[-\mathrm{i}\phi_{\mathrm{img}}(\mathbf{u})\right]. \tag{1}$$

Here, $\boldsymbol{u}=(u_i,u_j)$ is a position vector in the image plane. The lenses L_1 and L_2 have equal focal length f and are arranged in a 4f-configuration with a spatial light modulator in the corresponding Fourier plane $\{\boldsymbol{\xi}\}$. This configuration enables optical filtering in the frequency plane while projecting the image onto the sensor located in the camera plane $\{\boldsymbol{x}\}$. The effect of a tilt of α=15° is observed to be negligible and will not be addressed here.

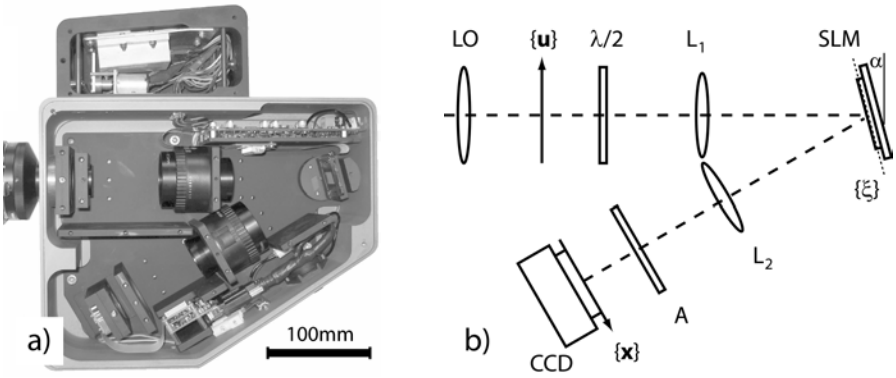

Fig. 1. a) Integrated system with attached laser module on top; b) sketch of the proposed scheme: LO = lens objective, L_1 and L_2 = lenses, $\lambda/2$ = $\lambda/2$-plate and A = polarizer

Throughout the following paragraph it will be shown that this filtering setup can be used to realize a shearing interferometer by adding a $\lambda/2$-plate and a polarizer as shown by Fig.1b. In preparation to the following discussion, it will be convenient to describe the Fourier transform property of either of the lenses [5] by means of the projection operator P:

$$\mathrm{P}\{\mathrm{U}\}(\boldsymbol{\eta}) = \frac{1}{\mathrm{i}\lambda \mathrm{f}} \mathrm{F}\{\mathrm{U}\}\left(\frac{\boldsymbol{\eta}}{\lambda \mathrm{f}}\right). \tag{2}$$

Here, F{} denotes the Fourier transform and $\boldsymbol{\eta}=(\eta_i,\eta_j)$ is an arbitrary position vector in the back focal plane.

The employed light modulator is a reflective panel based on nematic cells which are organized in a matrix like structure. It has birefringent properties and allows for manipulating the lateral phase of the reflected light in accordance with an electrically addressed distribution. However, only light which is polarized along the slow axis will be modulated whereas light being oriented towards the fast axis will not be affected at all. Therefore, since polarisation has to be considered, the wave field incident on the SLM may be described according to the Jones matrix formalism [6]:

$$\mathrm{U}_{\mathrm{slm}}(\boldsymbol{\xi})\cdot\mathbf{e}_{\mathbf{P}} = \mathbf{J}_{\mathbf{0}}(\boldsymbol{\xi})\cdot\exp\left[-\mathrm{i}\phi_{\mathrm{slm}}(\boldsymbol{\xi})\right] = \mathrm{P}\left\{\mathrm{U}_{\mathrm{img}}\right\}\cdot\mathbf{e}_{\mathbf{P}} \tag{3}$$

Here, the unit vector $\boldsymbol{e_P}$ specifies the orientation of the linearly polarized field amplitude perpendicular to the optical axis and $\boldsymbol{J_0}(\boldsymbol{\xi})=A_{slm}(\boldsymbol{\xi})\boldsymbol{e_P}$ indicates the Jones vector, which describes the real amplitude in case of polarized light. Please note, that the state of polarization and therefore the orientation of $\boldsymbol{e_P}$ can be adjusted by rotating the $\lambda/2$-plate. Let us assume that the fast and the slow axis of the SLM coincide with the base of the $\{\boldsymbol{\xi}\}$ plane and that the $\lambda/2$-plate is configured to set the polarization to 45° with respect to the ξ_i-axis, i.e. $\boldsymbol{e_P}=(\cos\pi/4,\sin\pi/4)$. In this case, the effect of the SLM can be described within the Jones formalism by means of a modulation matrix $\boldsymbol{M}$:

$$\mathbf{M} = \begin{pmatrix} \mathrm{t}_{\mathrm{slm}} & 0 \\ 0 & 1 \end{pmatrix} \tag{4}$$

Here, $t_{slm}(\boldsymbol{\xi})$ denotes the complex transmittance of the light modulator. Consequently, the complex amplitude of the reflected light is given by:

$$\mathbf{U}_{\mathbf{mod}}(\boldsymbol{\xi}) = \mathrm{U}_{\mathrm{slm}}(\boldsymbol{\xi})\cdot\mathbf{M}\cdot\mathbf{e}_{\mathbf{P}} = \frac{1}{\sqrt{2}}\begin{pmatrix} \mathrm{t}_{\mathrm{slm}} \\ 1 \end{pmatrix}\cdot\mathrm{U}_{\mathrm{slm}}(\boldsymbol{\xi}) \tag{5}$$

As seen from Eq.5, it will be convenient and means no loss of generality to regard the wave field $\boldsymbol{U_{mod}}(\boldsymbol{\xi})$ as being composed of two orthogonally and linearly polarized wave fields, with the individual polarization states being oriented towards the corresponding birefringent axes of the SLM. The wave field $\boldsymbol{U_S}$ in the sensor plane $\{\boldsymbol{x}\}$ can be determined by applying the operator P to the individual components of $\boldsymbol{U_{mod}}$. Regarding Eq.3 and considering the identity $\mathrm{P}\{\mathrm{P}\{U(\boldsymbol{x})\}\}= -U(-\boldsymbol{x})$ yields:

$$\mathbf{U}_S(\mathbf{x}) = \frac{-1}{\sqrt{2}}\begin{pmatrix} i\lambda f \cdot P\{t_{slm}\} \otimes U_{img}(-\mathbf{x}) \\ U_{img}(-\mathbf{x}) \end{pmatrix}. \tag{6}$$

The polarizer in front of the camera sensor is set to 45° with respect to the x_i-axis, i.e. it has the same orientation like $\boldsymbol{e_P}$. Hence, its effect on the wave field can be described by the projection matrix $\boldsymbol{M_P}$:

$$\mathbf{M_P} \cdot \mathbf{U}_S = \frac{1}{2}\begin{pmatrix} 1 & 1 \\ 1 & 1 \end{pmatrix} \cdot \mathbf{U}_S = -\mathbf{e_P}\frac{1}{2}\left[U_{img} + i\lambda f \cdot P\{t_{slm}\} \otimes U_{img}\right]. \tag{7}$$

Since $\boldsymbol{e_P}$ is a unit vector, the scalar field U_S in the sensor domain is found to be given by:

$$U_S(\mathbf{x}) = -\frac{1}{2}\left[U_{img}(-\mathbf{x}) + i\lambda f \cdot P\{t_{slm}\} \otimes U_{img}(-\mathbf{x})\right]. \tag{8}$$

Eq.8 is an important intermediate result, because it relates the complex amplitude U_S in the sensor plane to the complex transmittance t_{slm} displayed by the SLM and the wave field U_{img} in the image plane of the lens objective. Let us consider the specific case in which t_{slm} is selected to be a phase grating with blazed structure:

$$t_{slm}(\xi) = t_\varphi \cdot \exp[i2\pi\mathbf{g} \cdot \xi]. \tag{9}$$

Here, $\boldsymbol{g}=(g_i,g_j)$ is a grating vector in the $\{\boldsymbol{\xi}\}$ plane and $t_\varphi=\exp[i\varphi]$ is a constant phasor. It is straightforward to show that $P\{t_{slm}\}i\lambda f=\delta(\boldsymbol{\xi}-\lambda f\boldsymbol{g})t_\varphi$ and thus Eq.8 becomes:

$$U_S(\mathbf{x}) = -\frac{1}{2}\left[U_{img}(-\mathbf{x}) + t_\varphi \cdot U_{img}(-\mathbf{x} + \lambda f\mathbf{g})\right]. \tag{10}$$

From Eq.10 it is seen that in case of a blazed grating being displayed by the SLM, the proposed setup shares the characteristics of a shearing interferometer with the corresponding shear set to $\boldsymbol{s}=\lambda f\boldsymbol{g}$. Furthermore, phase shifting techniques can be applied by selecting different values for t_φ in consecutive measurements.

3 Experimental investigations and discussion

Figure 2 presents experimental results obtained using the integrated system introduced in Fig.1a.

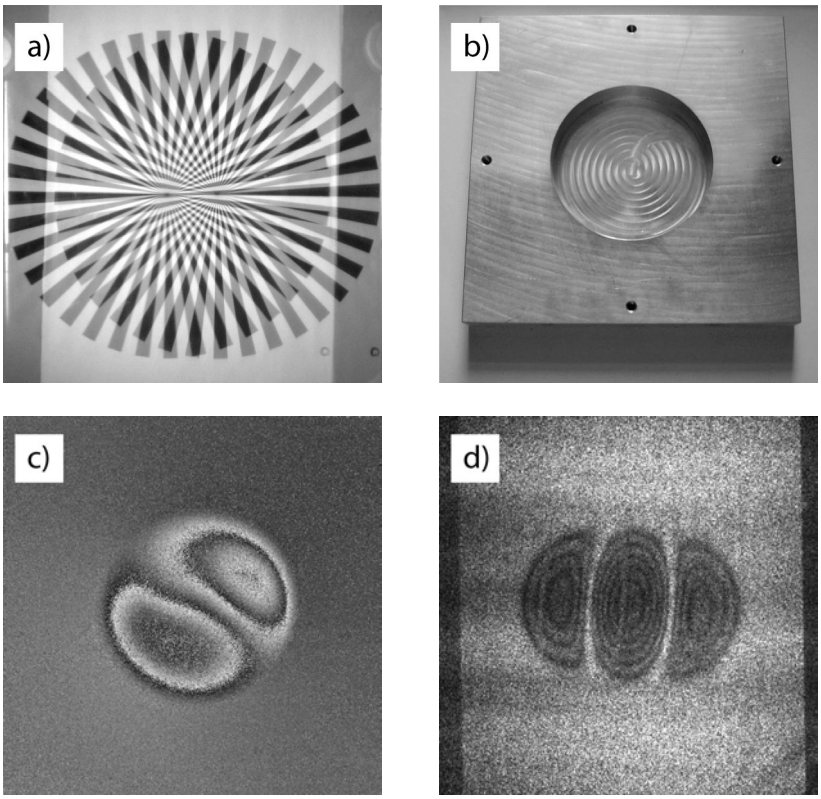

Fig. 2. Experimental results: a) Twin image of a Siemens star with incoherent illumination; b) backside of the demo object; c) phase difference corresponding to deformation of the objects surface because of thermal excitation; d) the time averaged intensity measured across the front side of the object while inducing a vibration of 1.960kHz

Exemplarily, Fig.2a shows the twin image of a Siemens star illuminated by an incoherent light source. The diameter of the star is 200mm and the shear is set to s=35mm in the horizontal direction. In order to demonstrate the applicability in regards to non destructive testing, the deformation of a sample object has been investigated. The object is a massive metallic plate of which the backside is seen from Fig.2b. The milled region has a diameter of 100mm and represents a local inhomogeneity of the objects thickness. The front side of the object was investigated by means of phase shifting speckle shearography and both thermal and mechanical loading [1]. Fig.2c shows the phase difference obtained from a thermal load of ΔT=3K. A diagonal shear was set with an absolute value of 25mm on the objects surface. A typical butterfly like structure is observed due to the milled region in the backside. Fig.2d shows the result of a vibration analysis. In this case the shear was set to 20mm in horizontal direction. A

Piezo shaker has been attached to the surface in order to invoke a dynamic load of 1.960kHz. As seen from Fig.2d, the inclusion is well observed from the time averaged intensity.
The experimental investigations proof the applicability of the presented shearing interferometer to typical cases in the field of non destructive testing. However, effects arising from the discreteness of the SLM such as higher diffractions orders and modulation effects [7] due to the finite size of the pixels have not been considered throughout this treatise and are required to be addressed in further discussions.

4 Acknowledgements

The authors would like to thank the *Deutsche Forschungsgemeinschaft* (DFG) for supporting the presented work under the grant no. KO 2894/6-1 (project WeSer).

5 References

1. Hung, YY, Ho, HP (2005) Shearography: An optical measurement technique and applications. Materials Science and Engineering 49:61-87
2. Zhao, S, Chung, PS (2006) Digital speckle shearing interferometer using a liquid-crystal spatial light modulator. Optical Engineering, 45:105606
3. Falldorf, C, Kopylow, C, Jüptner, W (2007) Compact Lateral Shearing Interferometer to Determine Continuous Wave Fronts. 3DTV Conference 2007, DOI: 10.1109/3DTV.2007.4379400
4. Moreno, I, Davis, JA (2008) Polarization-splitting common-path interferometer based on a zero-twist liquid crystal display. Appl. Opt. 47:1797-1801
5. Goodman, JW (1996) Introduction to Fourier Optics. 2. McGraw-Hill
6. Jones, RC (1941) A new Calculus for the Treatment of Optical Systems. J. Opt. Soc. Am., 31:488
7. M. Agour, C. Falldorf, C. von Kopylow (2009) Complementary Filtering Approach to Enhance the Optical Reconstruction of Holograms from a Spatial Light Modulator. In Proc. of Fringe 2009: 6th International Workshop on Advanced Optical Metrology

Digital phase shifting holography and holographic interferometry

M. Kujawińska, N. Kumar, A. Michalkiewicz
Warsaw University of Technology, Institute of Micromechanics and Photonics, 02-525 Warsaw, 8 Sw. A. Boboli St., Poland

1 Introduction

Phase shifting digital holography (PSDH) technique was introduced for the first time in 1997 by I. Yamaguchi [1]. It was successfully applied to reduce unwanted zero and conjugated (twin image) terms in the reconstruction plane (Fig.1a,b) and therefore allows to reconstruct on-line holograms and use efficiently the bandwidth of a matrix detector. Also it is proven that the object phase reconstruction performed by "ideal" PSDH brings a perfect phase (the RMS and P-V errors at the level 10^{-14} (digitization errors)), while a phase from a single hologram reconstruction suffers significant P-V and RMS errors (Fig.1c).

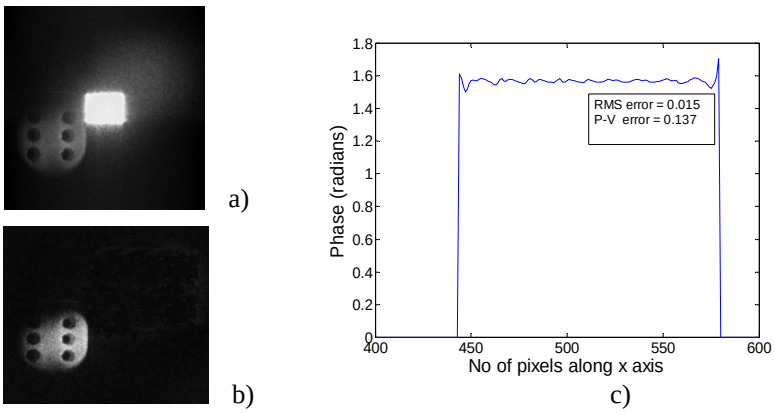

Fig. 1. The exemplary results of numerical reconstruction of off- axis Fresnel holograms a) single, b) PSDH of an intensity of a real object and c) the crossection of a constant object phase reconstructed from a single computer generated hologram

PSDH realizes a new flexibility of quantitative acquisition, processing and reconstruction of digital holograms. At the images acquisition stage PSDH is similar to temporal phase shifting interferometry TPSI [2] and

requires capturing of at least three phase shifted holograms. Let us consider an object phase reconstruction (Fig.2). In the TPSI method a phase is calculated directly from a series of phase shifted interferograms (one step process), while in PSDH at first the phase of an object wavefront ϕ_H at the detector plane is calculated by the conventional phase shifting method and than an image of an object (its intensity and phase) is reconstructed by propagation of the complex amplitude U to an object plane by one of the digital holography reconstruction methods [3]. So in the case of PSDH two step reconstruction procedure is implemented. It was proven [1] that in the case of diffusely reflecting objects the phase distribution ϕ_H is enough to reconstruct images of almost the same quality.

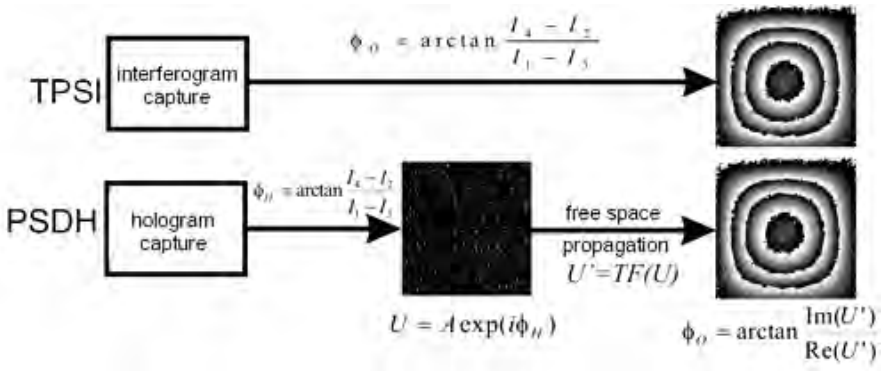

Fig. 2. The scheme of an object phase reconstruction by a) temporal phase shifting interferometry TPSI and b) phase shifting digital holography PSDH

The influence of the errors which may appear during registration of the sequential interferograms/holograms on the reconstructed object phase is well known in TPSI [2]. However in the case of PSDH they refer to the hologram phase ϕ_H but object one ϕ_O. The calculated complex wavefront U with possible errors in ϕ_H is propagated, during numerical reconstruction, between hologram and object planes and these errors will influence the errors appearing in the final reconstructed object phase. However the values and character of these errors may be different than in classical PSI. Therefore below we present the extended investigation of the influence of typical PSI errors on the phase determined by PSDH.

2 Comparison of the errors in PSI and PSDH

The most important sources of errors in the phase shifting interferometry include: miscalibration of a phase shifter, nonlinearities due to detector and air turbulences and vibrations. Those and many other errors were studied by several researchers and are well described [2,4]. In order to compare the influence of these errors on the accuracy of phase reconstruction by PSI and PSDH we choose a flat reflective object with $\phi_O = \pi/2$. The considered linear ε_p and quadratic ε_n phase shift errors and the nonlinearity of detector error are in the range +/-20% [2]. Additionally we will compare the performance of 3-, 4- and 5-frame phase shifting algorithms. The object phase retrieval in the second step of PSDH is performed by the angular plane waves spectral decomposition method [5].

At first the influence of the linear phase-shift error ε_p (Fig.3a)

$$\varphi' = \varphi(1 + \varepsilon_p) \tag{1}$$

and the non-linear phase shift error ε_n (Fig.3b)

$$\varphi' = \varphi(1 + \varepsilon_n \varphi) \tag{2}$$

have been investigated.

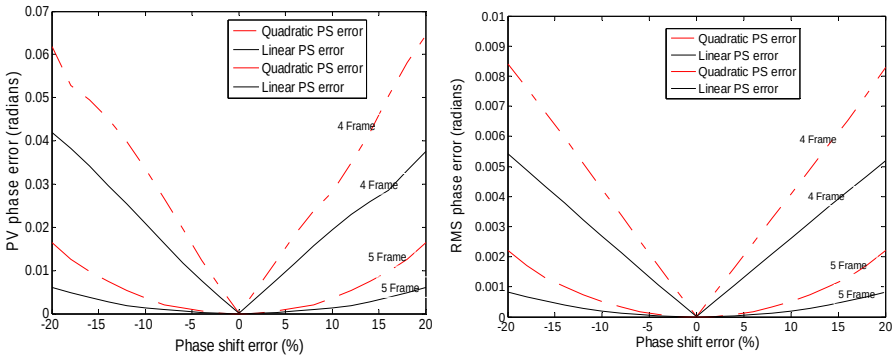

a) b)

Fig. 3. Object phase errors due to linear and nonlinear phase shift error obtained in 4-frame and 5-frame PS algorithms: a) P-V values and b) RMS values

In both cases we can conclude that the object phase errors (both RMS and P-V) are much smaller (more than one order of magnitude) than in the case of PSI, however they maintain similar character. Also the values of errors obtained for significant phase shift error (20%) are much smaller than in the case of the object phase reconstruction from a single hologram (compare with Fig.1c). In the case of second order nonlinear detector errors the object phase reconstructed by 4- and 5-frame algorithms have,

like in the case of PSI, negligible errors, while three frame algorithm generate three times smaller errors than in PSI [6].

Finally we can conclude that in the case of a reflective (transmissive) object (e.g. the case of DH microscopy) PSDH is less sensitive to typical errors which may be introduced during capturing of phase shifting holograms. As in the case of PSI the five frame algorithm is most favorable to obtain high accuracy reconstruction of an object phase. However even the four frame and three algorithms give considerable improvement over the accuracy of phase reconstructed from a single hologram.

3 PSDH for arbitrary object phase reconstruction and phase shifting digital holographic interferometry

The analysis performed in Section 2 presents the results for a very simple object. In practice objects have complex phases and, most often, scattering properties (diffuse objects). For these reasons we investigate the errors in PSDH for the following cases:

- the reflective objects with linear phases introduced in the range from $\pi/2$ to 7π rad (Fig.4),
- the scattering object (random phase added) with linear phase 0- $\pi/2$ rad (Fig.5).

The numerical simulations were performed for 4-frame algorithm, which is commonly used in DH. The 5-frame algorithm errors will be smaller, so we can use it if the highly accurate measurements are required.

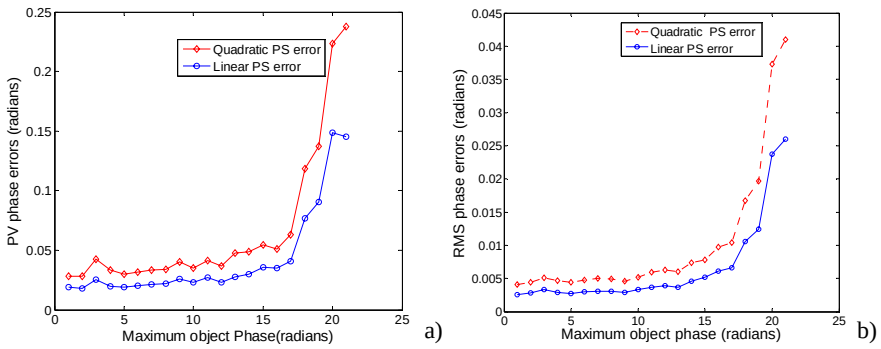

Fig. 4. The reflected object phase error in the function of the maximum value of object linear phase: a) P-V phase error and b) RMS phase error calculated for the case of 10% linear and quadratic phase shift error

It is clearly seen from Fig.4 that the object phase error is nearly constant up to a certain phase gradient value (here up to 15rad), for bigger phase gradients the error increases significantly. This fact has to be taken into account in the case of an measurement uncertainty determination of an object with complex phase.

The second case considers the PSDH applied for determination of the phase of a scattering object. The numerical analysis (with known model of theoretical object phase values with the random phase) allows to determine the reconstructed object phase errors for different values of linear and quadratic phase shift errors (Fig.5).

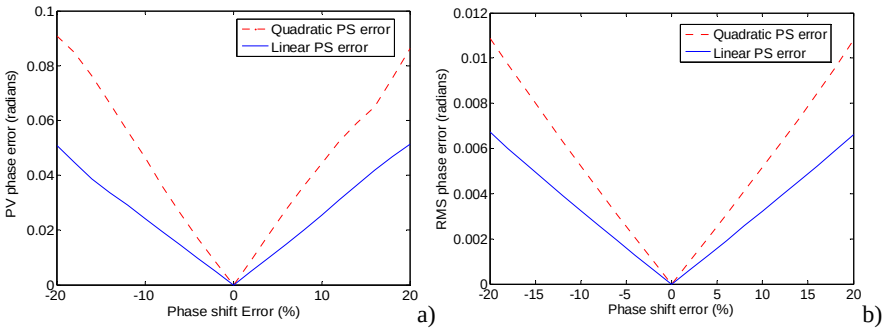

Fig. 5. The scattering object phase error in the function of linear and quadratic phase shift error: a) P-V phase error and b) RMS phase error calculated for the case of linear object phase ($\phi_{Omax}=\pi/2$).

The reconstructed object phase errors have in this case bigger values, when compared with those obtained for a reflective object, however still these values are smaller than in PSI. Of course in a real experiment the phase obtained from a scattering object cannot be used directly as it contains a random phase. In the metrology of scattering object we use holographic interferometry. In the digital holographic interferometry, the initial phase of an object is subtracted from the sequential phases of the object under load [3]. The result of such subtraction between two linear object phases ($\phi_{O1max}=\pi/2$, $\phi_{O2max}=3\pi$) are shown in Fig.6 while the crossections of the phase error maps are presented in Fig.7. The single phases were calculated by 4-frame PS algorithm and for the 10% linear and quadratic phase shift errors.

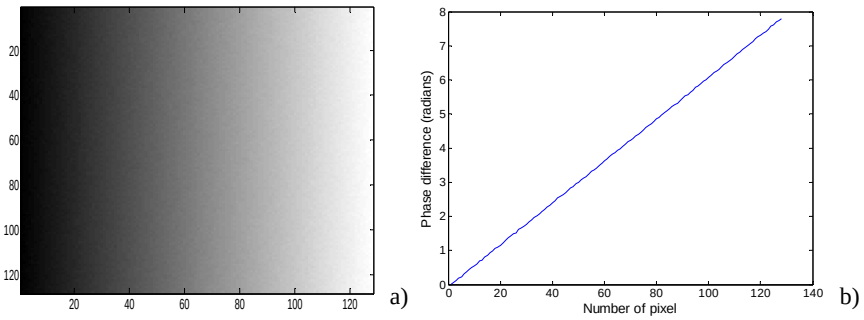

Fig. 6. The result of the phase shifting digital holographic interferometric procedure: a) the object phase difference and b) its horizontal crossection.

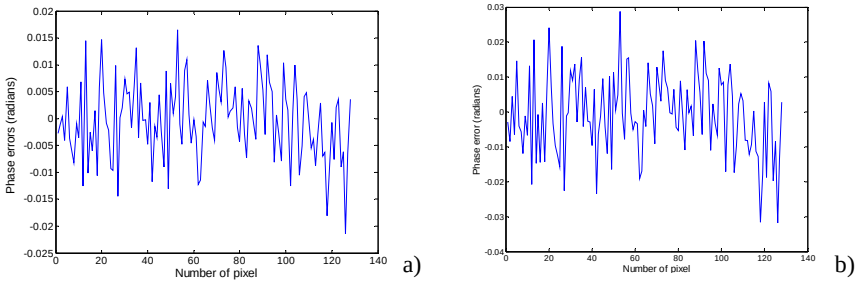

Fig. 7. The crossections of the object phase difference errors: a) for 10% linear PS error and b) 10% quadratic PS error

The theoretical RMS and P-V errors of the reconstructed phase difference are at the very similar level as those obtained for a single phase reconstruction by PSDH (compare with Fig.5). However in real holographic interferometry experiments we can expect higher level of errors especially due to the random phase term caused by an environmental instability.

4 Conclusions

The phase shifting digital holography PSDH provides an excellent improvement of both digital holography and digital holographic interferometry. It allows to obtain a high quality object phase reconstruction without influence of the zero and conjugate terms. It was shown that, due to the two step process in an object phase reconstruction,

PSDH has much smaller sensitivity to the typical PSI errors. It refers to both reflective/transmissive and scattering objects, therefore it can be successfully applied for high accuracy quantitative phase analysis in digital holographic microscopy and digital holographic interferometry.

5 Acknowledgments

The research leading to these results has received funding from the European Community's Seventh Framework Programme FP7/2007-2013 under grant agreement n° 216105 (“Real 3D” Project).

6 References

1. Yamaguchi I and Zhang T (1997) Phase-shifting digital holography, Opt. Lett., 22:1268–1270
2. Creath K (1993) Temporal phase measurement methods, in *Interferogram analysis*, Robinson D W and Reid G T (eds), Inst. of Physics Pub.
3. Kreis T (2005) “Handbook of Holographic Interferometry” WILEY VCH Verlag GmbH
4. Schwider J et al. (1983) Digital Wavefront Measuring Interferometry: Some Systematic Error Sources, Appl. Opt., 22: 3421-3432
5. Kozacki T (2008) Numerical errors of diffraction computing using plane wave spectrum decomposition, Optics Comm., 281: 4219-4223
6. Michalkiewicz A (2009) Digital holography systems for mechanical elements investigation, PhD dissertation, Warsaw University of Technology

Fourier-transform method with high accuracy by use of iterative technique narrowing the spectra of a fringe pattern

S. Nakayama[1], H. Toba[1], N. Fujiwara[1], T. Gemma[1], M. Takeda[2]
[1]NIKON CORPORATION, 6-3, Nishi-ohi 1-chome, Shinagawa-ku, Tokyo 140-8601, Japan
[2]THE UNIVERSITY OF ELECTRO-COMMUNICATIONS, 1-5-1, Chofugaoka, Chofu, Tokyo 182-8585, Japan

1 Introduction

The Fourier-transform method (FTM) [1] is widely used for a single-shot fringe pattern analysis in interferometry and fringe-projection topography. Because of the spatial carrier fringe, the Fourier spectrum of the fringe pattern splits into the signal spectrum to be reconstructed, its Hermite conjugate spectrum and the unwanted DC component. The phase distribution can be reconstructed from the isolated signal spectrum by inverse Fourier transform. This method is insensitive to the vibration and can be applied for the moving objects, because only a single-shot fringe pattern is needed to determine a phase distribution.

However, for a phase distribution having large slope compared with the spatial carrier frequency, the bandwidth of the signal spectrum and its Hermite conjugate spectrum become wide and overlap each other. Then these spectra can not be separated perfectly, and give rise to a large ripple-shaped phase error.

In this paper, we propose a new iterative model-based technique which can effectively narrow the bandwidth of the Fourier spectra and improve the accuracy of fringe pattern analysis relative to FTM.

2 Method

An intensity distribution of a fringe pattern can be described by

$$g_0(x,y) = a(x,y) + b(x,y)\cos[\phi(x,y)], \tag{1}$$

with

$$\phi(x,y) = 2\pi(f_x x + f_y y) + \phi_s(x,y), \tag{2}$$

where the phase $\phi_s(x,y)$ contains the desired information, $a(x,y)$ and $b(x,y)$ represent unwanted irradiance variation, and where f_x and f_y are the carrier frequencies. In order to reduce errors in phase determination, the proposed technique implements three functions making use of a model phase distribution. The first function narrows the conjugate spectrum and filters it out with a narrow band-rejection filter. After removing the DC component (see procedure 3 described later.), we multiply the fringe pattern with $\exp[i\phi_m(x,y)]$, where $\phi_m(x,y)$ is a model phase distribution [2]. The resulting complex amplitude distribution is described approximately by

$$\begin{aligned} g_1(x,y) \approx\ & b(x,y)\exp[i\phi(x,y) + i\phi_m(x,y)] \\ & + b(x,y)\exp[-i\phi(x,y) + i\phi_m(x,y)]. \end{aligned} \tag{3}$$

As can be seen in Eq. (3), if $\phi_m(x,y)$ is close to $\phi(x,y)$, the phase variation in the second term is nearly cancelled and the conjugate spectrum obtained from the second term by performing Fourier transform becomes narrower. Therefore, the unwanted conjugate spectrum can be removed and the leakage of the signal spectrum can be reduced. The second function narrows the signal spectrum and extracts it perfectly with a suitable band-pass filter. After removing the conjugate spectrum (see procedure 5 described later.), we multiply the complex amplitude distribution with $\exp[-i2\phi_m(x,y)]$. The resulting complex amplitude distribution is approximated by

$$g_2(x,y) \approx b(x,y)\exp[i\phi(x,y) - i\phi_m(x,y)]. \tag{4}$$

Here, if $\phi_m(x,y)$ is close to $\phi(x,y)$, the signal spectrum obtained by performing Fourier transform becomes narrower. The third function is an iterative process in which the model phase distribution is replaced with a newly determined phase distribution each time. Consequently, we can determine the phase distribution accurately even if we do not know the approximate distribution at the beginning of analysis.

The procedures are as follows.

1. Compute the average DC intensity of the fringe pattern and subtract the average DC value from the fringe pattern intensity.
2. Determine the phase distribution with conventional FTM as an initial solution.
3. Fourier transform the fringe pattern obtained in procedure 1, filter out the DC component, and inverse Fourier transform.

4. Extract the model phase distribution from the determined phase distribution by use of polynomial fitting.
5. Narrow the conjugate spectrum, filter it out with a narrow rejection-band filter and perform an inverse Fourier transform.
6. Narrow the signal spectrum, extract it with a suitable band-pass filter and perform an inverse Fourier transform.
7. Compute the phase distribution from the complex amplitude distribution obtained in procedure 6.
8. Set the phase distribution determined above as the new model.

We repeat procedures from 4 to 8 until the determined phase distribution converges. In procedure 4, polynomial fitting is performed to prevent $\phi_m(x,y)$ from containing large errors. At the first iteration, the model is extracted from the phase distribution obtained in procedure 2.

Furthermore, we used an additional technique to correct the determined phase distribution [3]. In this technique, we create a virtual fringe pattern numerically with the determined phase distribution and analyze the pattern through the same procedures. The error of analysis to be removed can be estimated by subtracting the given phase distribution from that obtained by analyzing the virtual pattern.

3 Simulations

The fringe patterns that would be obtained in interferometric testing of aspheric wavefronts were simulated and analyzed. The data window was a square with N=512. In this paper, frequencies are given in the number of cycles per length of the data window, and in this simulation the carrier frequencies f_x, f_y were set to 64. In the first simulation, the irradiance variation was not taken into consideration, namely, $a(x,y)=1$ and $b(x,y)=1$ and the given wavefront was described by the 9-th term of Zernike polynomial (primary spherical) with the coefficient of 1λ. The cross-section intensity distribution of the fringe pattern and the Fourier spectrum of the pattern are shown in Fig. 1, where the data on the line from lower-left to upper-right in the data window are shown. The cross-section intensity distribution of the Fourier spectra calculated in procedure 5 and 6 are shown in Fig. 2. The conjugate spectrum shown in Fig. 2(a) and the signal spectrum shown in Fig. 2(b) are centred at the origin. The rejection-band filter used in procedure 3 and 5 was a circle with a radius of 10 cycles which was selected to minimize error for this fringe pattern. The narrower rejection-bands are presumably caused by the effect of narrowing spectrum and preventing signal spectrum from leaking.

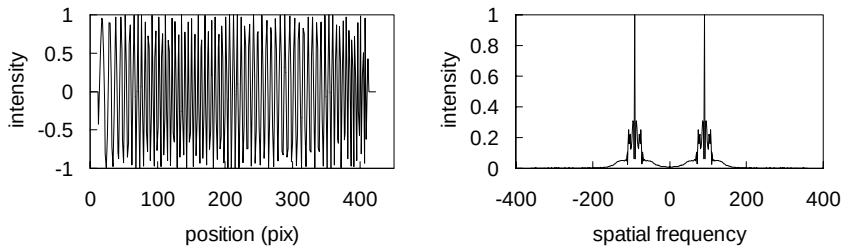

Fig. 1. Simulated interferogram. (a) Cross-section intensity distribution of the fringe pattern; (b) Fourier spectrum of the pattern.

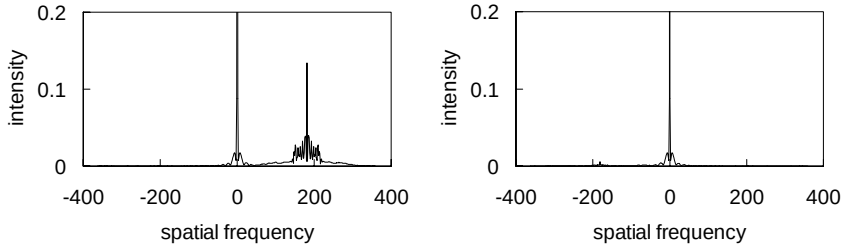

Fig. 2. Cross-section intensity distribution of Fourier spectra calculated in our technique. (a) calculated in procedure 5; (b) calculated in procedure 6.

Zernike polynomials under 36-th term (quaternary spherical) were used in the fitting process in procedure 4. After that, we used the same rejection-band filter and fitting polynomials. The estimation error with conventional FTM and our proposed technique are shown in Fig. 3. The band-pass filter used in both analyses was a circle with a radius of 64 cycles. In the analysis with our technique, the determined phase distribution converged within 3 cycles of iteration. As can be seen in Fig. 3(b), the error of analysis was reduced with our proposed technique compared to the large error with conventional FTM shown in Fig. 3(a). The RMS error of analysis is 7mλ with conventional FTM and 1.0mλ with our technique.

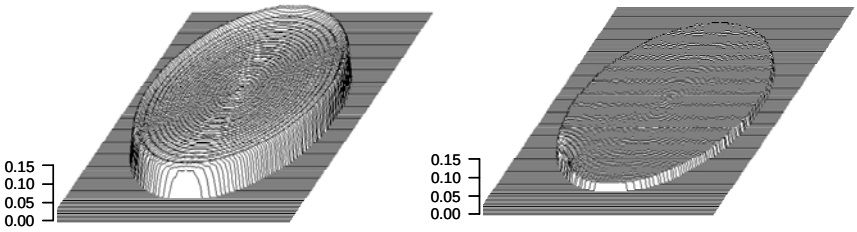

Fig. 3. Error of analysis. (a) with conventional FTM; (b) with our proposed technique.

Furthermore, the slight error seen in Fig. 3(b) was completely removed by performing the correction of phase distribution mentioned in Sec. 2.

We performed simulations with different phase distributions and irradiance variations. In the case of pure phase variation, we obtained good results showing that the error was reduced to less than 0.2mλ rms. But in the cases where irradiance variations were included, slight ripple shaped errors remained. For example, the RMS error of analysis in the case of a uniform random irradiance variation of 10%, the RMS error of analysis was 1.6mλ. The remaining errors are presumably caused by the deviation from our analysis model, which considered only phase distributions.

4 Experiment

The validity of our proposed technique was experimentally examined with a Fizeau interferometer for spherical surface testing. In order to obtain a distorted fringe pattern, we shifted the test surface slightly along the optical axis. The data window was a square with N=512 and the carrier frequencies f_x, f_y were about 50 cycles. The cross-section intensity distribution of the interferogram is shown in Fig. 4. The phase distribution was almost composed of power component of 5.4λ p-v. For comparison, we measured the phase distribution with phase shifting method and performed low-pass filtering to the data to be adapted to the pass-band of FTM. In this experiment, we regarded the difference between the phase distributions determined with our technique and phase shifting method as an error of analysis with our technique. The error of analysis with conventional FTM and with our proposed technique are shown in Fig. 5. The band-pass filter used in both analyses was a circle with a radius of 50 cycles. We can see the large error with conventional FTM in Fig. 5(a) and the calculated RMS error is 25mλ. As can be seen in Fig. 5(b), the error of analysis was reduced with our proposed technique. The RMS error of analysis decreased to 1mλ. We believe that the remaining ripple shaped error was caused by irradiance variation.

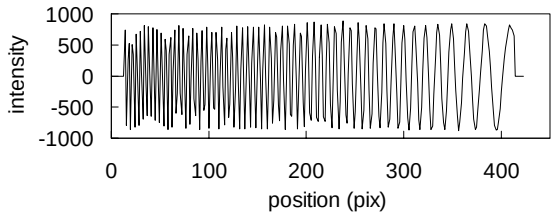

Fig. 4. Cross-section intensity distribution of the fringe pattern obtained in the experiment.

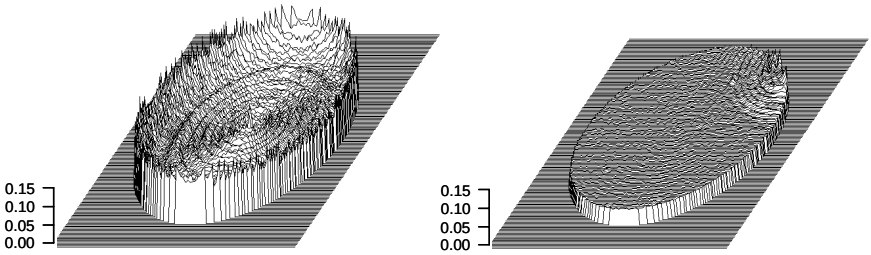

Fig. 5. Errors of analyses. (a) with conventional FTM; (b) with our proposed technique.

5 Conclusion

In order to reduce the errors of analysis in the determination of phase distributions with large slope, we propose a new iterative model-based technique for narrowing the bandwidth of the spectrum. Experiment showed that the RMS error of our proposed technique was 1mλ compared to 25mλ in the conventional Fourier transform method. We conclude that our proposed technique is effective under real measurement conditions.

6 Acknowledgments

We wish to thank D. Smith and Y. Zhu for their great help.

7 References

1. M. Takeda, H. Ina, and S. Kobayashi, ”Fourier-transform method of fringe-pattern analysis for computer-based topography and interferometry,” J. Opt. Soc. Am. 72, 156-160 (1982).
2. D. Malacara, M. Servin, and Zacarias Malacara, Interferogram Analysis for Optical Testing (Marcel Dekker, New York, 1998), Ch.8, p.300-302.
3. H. Toba, Z. Liu, S. Udagawa, N. Fujiwara, S. Nakayama, T. Gemma, M. Takeda, “Phase analysis error reduction in the Fourier transform method using a virtual interferogram,” Proc. SPIE 7389 (to be published).

Fringe pattern processing using a new adaptive and steereable asynchronous algorithm

J.A. Quiroga[1], J.A. Gómez-Pedrero[1], M. Servín[2]
[1]Departamento de Óptica, Universidad Complutense de Madrid, Facultad de Ciencias Físicas, Ciudad Universitaria s/n, 28040, Madrid, Spain
[2]Centro de Investigaciones en Óptica A.C., León, Guanajuato, 20036, México

Abstract

We present a new asynchronous algorithm for the demodulation of single image fringe patterns with wide frequency content based on a five-step asynchronous algorithm which has been steered using the fringe direction to deal with closed fringe patterns. Numerical and experimental results show the good behaviour of the proposed algorithm for a number of different experimental set-ups.

1 Introduction

In many optical measurement setups, the information is extracted through a fringe pattern [1]. Usually, a fringe pattern can be described by the following equation

$$I(\mathbf{r}) = b(\mathbf{r}) + m(\mathbf{r})\cos\phi(\mathbf{r}), \tag{1}$$

where I is the irradiance, b the background, m the modulation and ϕ the phase (which is related with the quantity to be measured) of the fringe pattern. In the general case [2] $\mathbf{r}$ is an n-dimensional vector which stands for the appropriate spatial and temporal coordinates describing the problem. The task of fringe pattern demodulation algorithms is to get the phase from the irradiance of the fringe pattern (1).

In the past years, a number of demodulation techniques for single fringe patterns with closed fringes have been proposed [3-5]. This problem is of paramount importance when dealing with dynamic phenomena for which the fringe pattern varies with time. For single fringe pattern demodulation, the main goal is to get accurate algorithms with the lowest processing time

possible (at the end it would be desirable to have processing times faster enough to process fringe pattern at video frame rates).

In this way, Larkin *et al*. [3] proposed the phase extraction by the spiral quadrature transform, which was generalized by Servin *et al*. [2] for *n*-dimensional fringe patterns. These algorithms employ Fourier transform so could be limited if the fringe pattern is not defined on a rectangular region. Other algorithms work within a phase propagation scheme such as the RPT algorithm [4] or similar ones [5], but they are usually complex and computationally expensive.

In this work we present an alternative for the existing closed fringe pattern demodulation algorithms which can be employed to demodulate fringe patterns with high frequency variability using an exact adaptive algorithm. In this way, we can avoid the complications of the algorithms based on phase propagation and we can, also, demodulate fringe patterns defined on an irregular spatial domain where the algorithms based on Fourier technique will fail.

2 Theoretical foundations

Let us suppose that we have a fringe pattern described by equation (1). In our case, we would deal with bi-dimensional fringe patterns, so $\mathbf{r} \in \mathbf{R}^2$. Taking the first order of the Taylor serial expansion of the phase ϕ, we get

$$I \cong b + m \cdot \cos\left(\phi_o + \nabla\phi \cdot \mathbf{r}\right). \tag{2}$$

So we can assume that, locally, the phase present a spatial carrier in the direction given by the phase gradient. As it is shown in [6], to demodulate this kind of local-monotonically fringe patterns, we can generalize a 1D complex filter $g(I)$ given by

$$g(I) = f(I) + i \cdot h(I). \tag{3}$$

Being $f(I)$ a low pass filter and $h(I)$ a quadrature filter. According to [6], if we know the fringe direction angle $\beta(\mathbf{r})$ for each point of the fringe pattern, it is possible to get the wrapped phase using the following expression

$$\tan\phi = \frac{h_x(I)\cos\beta + h_y(I)\sin\beta}{f_x(I) + f_y(I)}. \tag{4}$$

Where f_x denotes the filter f acting in the x direction, f_x is the filter f acting in the y direction and the same applies to h_x, h_y. Therefore equation (4) constitutes a general expression to generalize 1D filters to demodulate bidimensional fringe patterns.

In this paper, we propose to generalize an adaptive five step Spatial Phase Shifting (SPS) algorithm [7]. To describe this filter, let us suppose that we have a 1D irradiance signal and we define, for each point of this signal, five irradiance samples as:

$$I_l(k) = I(k + (l-3)\Delta), \quad {}_{l=1,2...,5}, \tag{5}$$

being k a discrete spatial variable, and Δ an integer that stands for a decimation factor whose role will be explained in the following paragraphs. In these conditions, the adaptive SPS filter components are given by:

$$\begin{aligned} h_\Delta(I) &= sign(I_2 - I_4)\sqrt{4(I_2 - I_4)^2 - (I_1 - I_5)^2}, \\ f_\Delta(I) &= 2I_3 - (I_1 + I_5), \end{aligned} \tag{6}$$

where the spatial dependence has been removed for simplicity. Note that, for each value of the decimation factor Δ, we will have a different filter. We can compute the frequency response of these filters by the following expression

$$m_\Delta(\omega) \equiv \sqrt{{f_\Delta}^2 + {h_\Delta}^2} = 4b\sin^2(\omega\Delta). \tag{7}$$

From equation (8), we can see the role played by the decimation factor. As it is depicted in Fig. 1, the decimation factor Δ changes the frequency response of the SPS algorithm. The adaptive SPS algorithm determines [7] for each point of the fringe pattern, the best decimation factor (as the one which gives the best frequency response) so the overall frequency response of the adaptive SPS algorithm is greater than the response function of the original SPS algorithm (see Fig. 1). Therefore, the adaptive SPS algorithm is able to deal with fringe patterns which present wider frequency ranges.

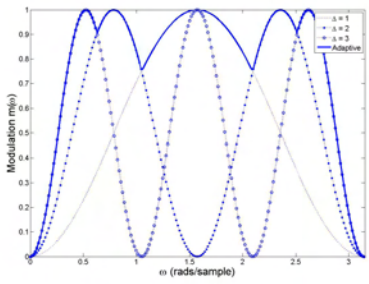

Fig. 1. Frequency response of the SPS five step algorithm for several values of the decimation factor and frequency response of the adaptive algorithm

To summarize, we propose to use the adaptive five step SPS algorithm "steered" by equation (5) to demodulate single fringe patterns with closed fringes. To do this it is necessary to calculate the fringe direction which can be obtained using the algorithm described in reference [2]. In next section we will show the performance of the proposed technique when applied to both synthetic and real fringe patterns.

3 Experimental results

In order to show the performance of our algorithm, we have demodulated first a synthetic fringe pattern consisting in a circular chip signal of 256×256 pixels. In Fig. 2a we have represented this fringe pattern, while in Fig. 2b and 2c we have represented the result obtained after applying the adaptive SPS algorithm to both horizontal and vertical directions. After "steering" these contributions using the information provided by the fringe direction angle using equation (4) we get the wrapped phase of Fig. 2d. As it can be seen in this figure, the algorithm has been able to demodulate properly a pattern with close fringes presenting a wide range of spatial frequencies.

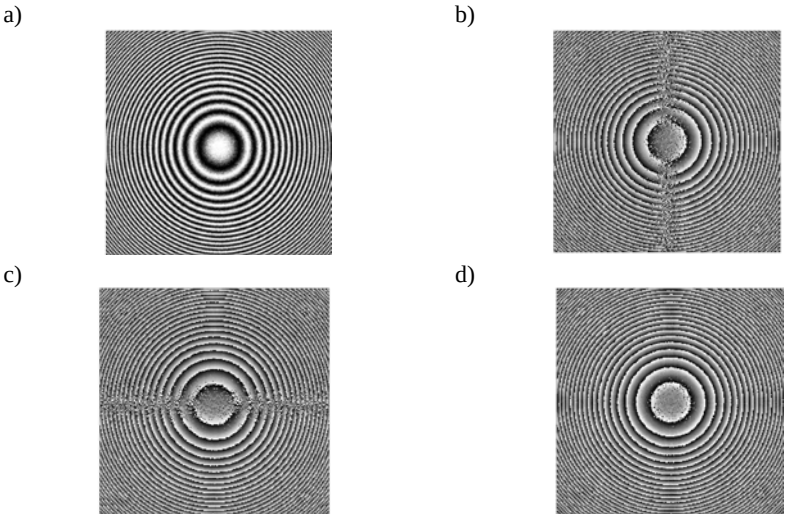

Fig. 2. a) Computer generated closed fringe patterns, b) Phase demodulated using the SPS algorithm in the horizontal direction, c) Phase demodulated using the SPS algorithm in the vertical direction, d) result obtained after steering the phase maps of Fig. 2a and 2b.

In Fig.3a we represent a real fringe pattern given by an interferomer. Due to the set up, the fringe spatial frequency presents a wide variation along the pattern's field and the pattern presents a mixture of open and closed fringes. It can be also appreciated a considerable amount of noise through the whole field. In Fig. 3b we can see the unwrapped phase obtained by the SPS adaptive algorithm showing how the algorithm has been able to demodulate properly the fringe pattern.

4 Conclusions

We present a new algorithm to demodulate single fringe patterns. The algorithm is based on a 1D five step spatial phase shifting technique "steered" to deal with closed fringe patterns. The algorithm is based on an exact non-linear SPS algorithm so it does not suffer from algebraic errors and, also, due to the adaptive nature of the algorithm it presents a high response for a wider range of spatial frequencies than similar algorithms.

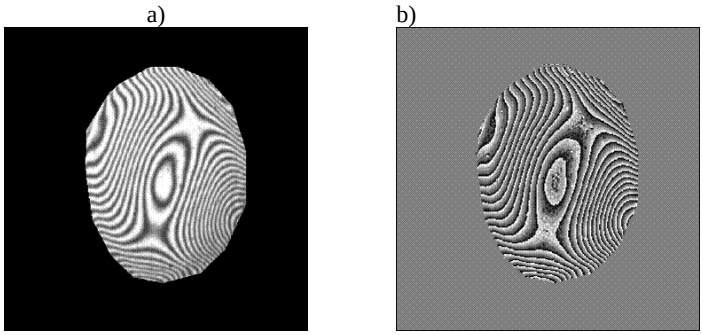

Fig. 3. a) Fringe pattern obtained through an interferometry experiment, b) wrapped phase obtained after applying the proposed algorithm.

5 References

1. Malacara D., Servin M., Malacara Z., "Interferogram analysis for optical testing", Marcel Dekker, (1998)
2. Servin, M, Quiroga, JA, Marroquin, JL (2003) A general n-dimensional quadrature transform and its applications to interferogram demodulation. JOSA A 20:925-934
3. Larkin, K, Bone, DJ, Oldfield, MA, (2001) Natural demodulation of two-dimensional fringe patterns. I General background. JOSA A, 18:1862-1870
4. Servin M., Marroquin, JL, Cuevas, F, (2001) Fringe-follower regularized phase tracker for demodulation of closed-fringe interferograms, JOSA A, 18: 689-695
5. Rivera M, (2005), Robust phase demodulation of interferograms with open or closed fringes, JOSA A, 22:1170-1175
6. Quiroga, JA, Servin, M, Estrada, JC, Gomez-Pedrero, JA, (2009) Steereable spatial phase shifting applied to single-image closed fringe interferogramas, Appl.Opt, 48:2401-2409
7. Gómez-Pedrero, JA, Quiroga, JA, Servin, M, (2008) Adaptive asynchronous algorithm for fringe pattern demodulation. Appl. Opt., 47:3954-3961

Invited Paper

Synthetic Aperture Digital Holography

Joseph Rosen* and Barak Katz
Department of Electrical and Computer Engineering
Ben Gurion University of the Negev, P.O Box 653, Beer-Sheva 84105, Israel
*Corresponding author: rosen@ee.bgu.ac.il

1 Introduction

Synthetic aperture is a well-known super-resolution technique which extends the resolution capabilities of an imaging system beyond the theoretical Rayleigh limit dictated by the system's actual aperture. Using this technique, several patterns acquired by an aperture-limited system, from various locations, are tiled together to one large pattern which could be captured only by a virtual system equipped with a much wider synthetic aperture.

The use of optical holography for synthetic aperture is usually restricted to coherent imaging [1-3]. Therefore, the use of this technique is limited only to those applications in which the observed targets can be illuminated by a laser. Synthetic aperture carried out by a combination of several off-axis incoherent holograms in scanning holographic microscopy has been demonstrated by Indebetouw *et al* [4]. However, this method is limited to microscopy only, and although it is a technique of recording incoherent holograms, a specimen should also be illuminated by an interference pattern between two laser beams.

We present a new lensless incoherent holographic system operating in a synthetic aperture mode. Spatial resolution exceeding the Rayleigh limit of the system is obtained by digital tiling several Fresnel holographic elements into a complete Fresnel hologram of the observed object. Each element is acquired by the limited-aperture system from different point of view. This method is demonstrated experimentally by combining three holographic elements recorded from white light illumination which is emitted from a binary grating.

The proposed holographic method in this study is based on the recently invented system of a single-channel incoherent interferometer for generating digital Fresnel holograms [5]. In this non-scanning holographic technique, white light is reflected or emitted from a three dimensional (3-

D) object, then propagates through a spatial light modulator (SLM), and is finally recorded by a digital camera. The SLM is used as a diffractive beam splitter of the incoherent interferometer, so that each spherical beam, originated from each object point, is split into two spherical beams with two different curve radii. Accumulation of the entire interferences within all of the couples of spherical beams creates the Fresnel hologram of the observed object. Three holograms are recorded sequentially, each for a different phase factor of the SLM. The three holograms are superposed in the computer, so that the result is a complex-valued Fresnel hologram that does not contain the twin image and the bias term.

2 Synthetic aperture with Fresnel elements

In this paper we demonstrate a different scheme, dubbed a synthetic aperture with Fresnel elements (SAFE), for holographic imaging of incoherently illuminated objects. The proposed lensless system contains only an SLM and a digital camera. This holographic system has an extended synthetic aperture in order to improve the transverse and axial resolutions beyond the classic limitations. The term synthetic aperture, in the present context, means time (or space) multiplexing of several Fresnel holographic elements captured from various viewpoints by a system with a limited real aperture. The synthetic aperture is implemented by shifting the SLM-camera set, located across the field of view, between several viewpoints. At each viewpoint a different mask is displayed on the SLM, and a single element of the Fresnel hologram is recorded (See Fig. 1). The various elements, each of which is recorded by the real aperture system during the capturing time, are tiled together so that the final mosaic hologram is effectively considered as captured from a single synthetic aperture which is much wider than the actual aperture.

An example of such system with the synthetic aperture, which is three times wider than the actual aperture, can be seen in Fig. 1. For simplicity of the demonstration, the synthetic aperture was implemented only along the horizontal axis. In principle this concept can be generalized for both axes and for any ratio of synthetic to actual apertures. Imaging with the synthetic aperture is necessary for cases where the angular spectrum of the light emitted from the observed object is wider than the numerical aperture of a given imaging system. In SAFE shown in Fig. 1, the SLM and the digital camera, move in front of the object. The complete Fresnel hologram of the object, located at some distance from the SLM, is a mosaic of 3 holographic elements, each of which is recorded from a different position

by the system with the real aperture of the size $A \times A$. The complete hologram tiled from the 3 holographic Fresnel elements has the synthetic aperture of the size $3 \cdot A \times A$ which is 3 times larger than the real aperture at the horizontal axis.

The method to eliminate the twin image and the bias term is the same as has been used before [5]; three elemental holograms of the same object and for each point of view are recorded, each of holograms has a different phase constant of the SLM's phase mask. The final holographic element is a specific superposition of the three recorded elements. The digital reconstruction of the final complex-valued mosaic hologram is conventionally computed by Fresnel back propagation.

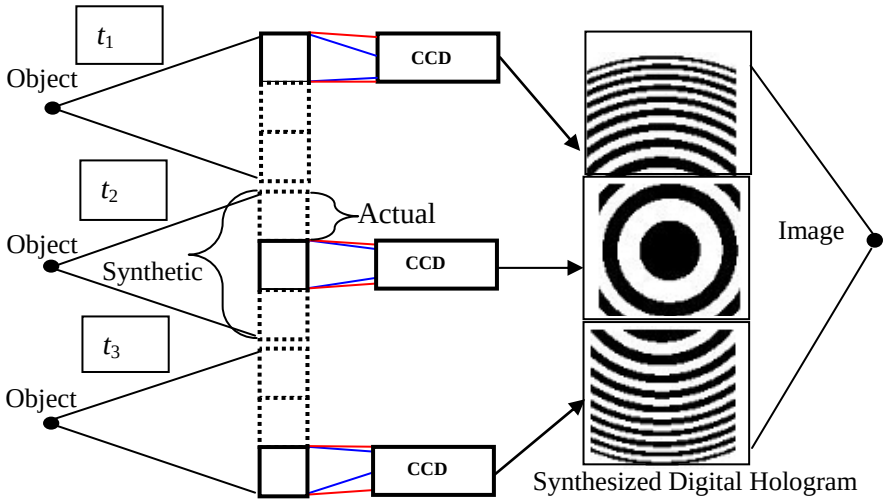

Fig. 1. Scheme of SAFE operating as synthetic aperture radar to achieve super-resolution

3 Experimental results

SAFE has been tested in the lab by the system shown in Fig. 1. The object in this experiment is a binary grating with cycle length of 11 lines per one cm. The distance from the binary grating to the SLM has been 17 cm, and between the SLM and the CCD camera (PCO, Scientific 230XS) 8 cm. The results of the experiments are summarized in Fig. 2. In the first experiment we have recorded a hologram only by the actual aperture without shifting the system, in the setup shown in Fig. 1 at the time t2. Fig. 2(a) shows one of the three masks displayed on the SLM (Holoeye, PLUTO) in this experiment. Each of the three masks has had one of the

three different phase factors: 0o, 120o or 240o. As mentioned above, these three phase masks with different phase constants are required in order to eliminate the bias term and the twin image from the holographic reconstruction. The SLM is a phase-only modulator, and therefore the sum of two pure phase functions is no longer a pure phase. Our solution [5] of this problem is to distribute randomly the phase values of the two quadratic functions among the SLM pixels. The three recorded holograms are superposed according to the same superposition equation given in Ref. [5]. Figs. 2(b) and 2(c) are the magnitude and the phase of the superposed hologram, respectively. The resolution along the horizontal direction of the reconstructed image shown in Fig. 2(d) is damaged in the sense that the image is lacking the original horizontal gratings because of the limited aperture used in this case.

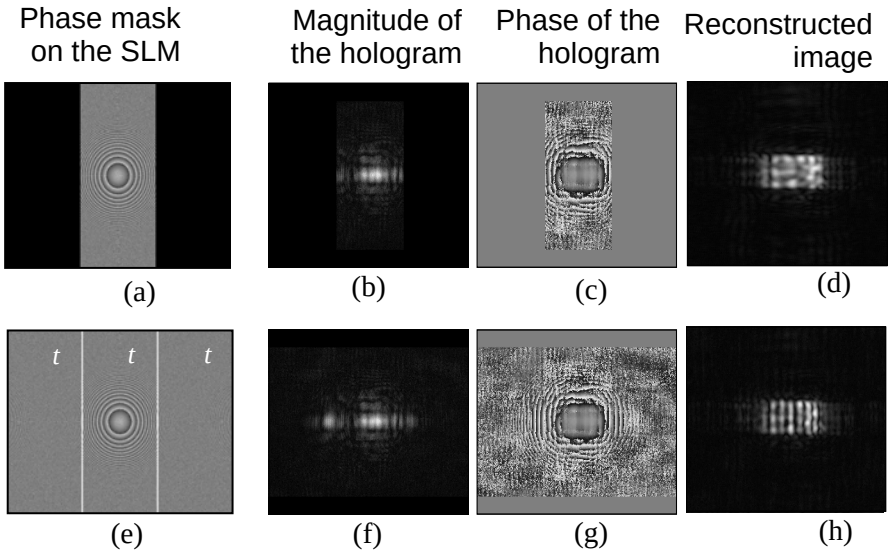

Fig. 2. Results of SAFE with the narrow aperture (Top) and with the synthetic aperture (Bottom).

In the second experiment nine different phase masks were displayed on the SLM, three for each location of the SLM-camera set; left, central and right. Each of the masks has had an actual aperture of 640×1080 pixels. Each of the three masks at every location has had one of the three different phase factors: 0^o, 120^o or 240^o. For each location of the system, the three recorded holograms have been superposed as mentioned before. Fig. 2(e) represents three masks, out of nine, each of which has been displayed at different time (indicated on each mask by t_n, n=1,2,3) and at a different

location of the setup along the horizontal axis. The superposed complex-valued holographic element from each system's viewpoint is stored in the computer. Upon completing the system movement along the entire synthetic aperture, all three holographic elements are tiled to a single mosaic hologram. Figs. 2(f) and 2(g) represent the magnitude and the phase of the complete mosaic hologram, respectively. The reconstruction result of the mosaic hologram is depicted in Fig. 2(h). All of the gratings of the observed object are seen well in the reconstructed image, indicating that the synthetic aperture is wide enough to acquire most of the spectral information of the object.

4 Conclusions

In conclusion, we have proposed and demonstrated a process of recording incoherent holograms in the synthetic aperture mode. The synthetic aperture of SAFE considerably increases both the transverse and the axial resolving power. This experiment is a demonstration of a synthetic aperture radar in the visible light where the observed scene is illuminated by white light. The concept of the present system can be applied to all regimes of imaging from microscopy to telescopes, and either for 2-D or 3-D imaging.

5 References

1. Beck, S M, Buck, J R, Buell, W F, Dickinson, R P, Kozlowski, D A, Marechal, N J, Wright, T J (2005) Synthetic-aperture imaging laser radar: laboratory demonstration and signal processing. Applied Optics 44:7621-7629
2. Mico, V, Zalevsky, Z, García-Martínez, P, García, J (2006) Synthetic aperture superresolution with multiple off-axis holograms. Journal of Optical Society of America A 23:3162-3170
3. Martínez-León, L, Javidi, B (2008) Synthetic aperture single-exposure on-axis digital holography. Optics Express 16:161-169
4. Indebetouw, G, Tada, Y, Rosen, J, Brooker, G (2007) Scanning holographic microscopy with resolution exceeding the Rayleigh limit of the objective by superposition of off-axis holograms. Applied Optics 46:993-1000
5. Rosen, J, Brooker G (2007) Digital spatially incoherent Fresnel holography Optics Letters 32:912-914

A new application of the Delaunay triangulation: The processing of speckle interferometry signals

Sébastien Equis and Pierre Jacquot
STI-NAM, Ecole Polytechnique Fédérale de Lausanne
1015 Lausanne
Switzerland

1 Introduction

It is now more than thirty years that speckle interferometry (SI) finds growing applications fields, and continuously arouses the interest of researchers. One topical line of research deals with decorrelations, intrinsically linked to speckle fields. Decorrelations impose a lower bound to the variance of the extracted phase – which is the sought-after quantity in SI – and at the same time, an upper bound to the available measurement range. The temporal approach which proved to be the choicest method for dynamic and long range experiments [1-4], allows to get rid of the measurement range limitation, but of course not of the decorrelation-induced phase error. SI signals obey the well-known two-beam equation (Eq.1):

$$I(r,t) = I_o(r,t) + I_m(r,t) \cdot \cos(\varphi_p(r,t) + \varphi_s(r,t)), \tag{1}$$

where Io and Im are respectively the background and modulation intensities, φp is the measurand, φs is the speckle phase, and r and t designate respectively the spatial and the temporal coordinates. Io, Im and φs are random variables, making tricky and prone to errors phase extraction procedures. Several strategies aiming at reducing or eliminating the phase errors are available. The first one consists in compensating the decorrelations by appropriate adjustments of the setup. It is also possible to split the recorded data set into several batches, in each of which the displacement is confined to a fraction of the correlation length, and to finally concatenate the results. Another successful way is to use filtering methods, where the kernel coefficients depend on the confidence levels of the measurements [5]. The method we propose here, namely the 3DPP method – standing for 3 dimensional piecewise processing – is a still completely different approach. It consists in discarding, purely and simply,

the regions, within each temporal pixel history, where the phase extraction is likely to be unreliable, according to a predefined criterion. The so-built regions of missing data, of random length and location, are filled by the information carried by reliable well-modulated neighbouring pixels, using an interpolation operation based on the Delaunay triangulation (DT).

We present in this paper a comprehensive description of the 3DPP method, only briefly outlined in [4]. The two main steps are detailed: *i)* the classification of the pixel signals based on their modulation which provides non-uniformly sampled maps of phase increment at each instant, and *ii)* the DT of the so-build scattered data associated to a triangle-based interpolation procedure to obtain the phase maps at each instant of the experiment. Finally, a first experimental result illustrates the implementation and the soundness of the method.

2 Random phase measurement errors in SI and the concept of pixel signal reliability

Due to the intrinsic randomness of the intensity and the phase of a speckle field, the temporal SI signal will experience strong fluctuations of modulation and local mean (respectively Im and Io in Eq. 1). In [4], we vindicated the use of the Empirical Mode Decomposition (EMD) [6] to remove efficiently the local mean to give to the signals the required shape for a meaningful subsequent phase computation [4]. However, when the modulation of the centred signal drops to zero, the derivative of the phase or instantaneous frequency (IF) [7] does not reflect the underlying physical phenomenon. In addition, in the vicinity of those areas of null modulation, noise – due to the electronic chain of acquisition, or to laser power fluctuations, or also to mechanical disturbances – becomes preeminent and the EMD and, as a consequence, the phase extraction tend to be very inaccurate – as any other method would be, by the way. Due to the 1D unwrapping operation, the error will propagate and corrupt the whole phase dataset. The statistics of these phase errors are actually quite complex [5, 8, 9]. In [5], the standard deviation of this error is computed with respect to the decorrelation amount for different pixel modulations. The conclusion is that the higher the modulation, the lower the phase error, reaching of course the maximum value of $\pi/\sqrt{3}$ at total decorrelation (standard deviation of a random variable uniformly distributed in the range $[-\pi, \pi]$). Interestingly, the phase error does not depend on the number of speckle grains per pixel. Those results have been derived analytically for a smooth-reference-wave interferometer and the trickier case of speckle-

reference-wave interferometer follows presumably the same trend. It is thus reasonable to consider the modulation of the temporal pixel signal as a good indicator of reliability (Fig. 1).

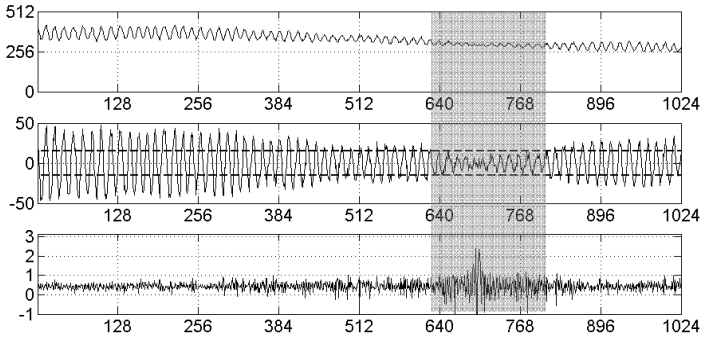

Fig. 1. A temporal SI signal (top) with 1024 time samples, experimentally obtained and processed with the EMD, yields a centered signal (middle) with a fluctuating modulation (the chosen threshold is shown in dashed line in the middle graph), whose IF (bottom in plain line) obtained through the use of the Hilbert transform [4] exhibits high noise level in the low-modulation discarded region (highlighted by the gray strip in the three graphs).

In the reliable areas, *i.e.* where the pixel modulation is higher than a chosen threshold, the phase will be obtained up to an additive constant. The computation of the discrete IF – temporal derivative of the phase – allows of course to get rid of this constant, leaving a meaningful exploitable result. The IF values in the under-modulated regions are discarded. Each pixel being independent, when we gather again the temporal sets to form frames (see Fig. 2), we obtain arrays of valid discrete IF sampled on a fluctuating non-uniform grid. An interpolation step has then to take place to obtain arrays of discrete IFs uniformly sampled. A final discrete integration step yields the phase maps at each instant.

3 Scattered data interpolation with Delaunay triangulation and triangle-based cubic interpolation

Given a set of points, randomly spread over a portion of space, it is convenient in many instances (from terrain surveying to graphics rendering, robotics, and crystal structures modelling [10]) to construct a smooth surface, containing these points and obeying definite properties, which can be furthermore sampled on a uniform mesh. With this aim in view, a natural approach is to construct first a triangulation in the plane,

then assign a weight to each point of the mesh, i.e. the IF value here, and finally, build a piecewise polynomial surface over it.

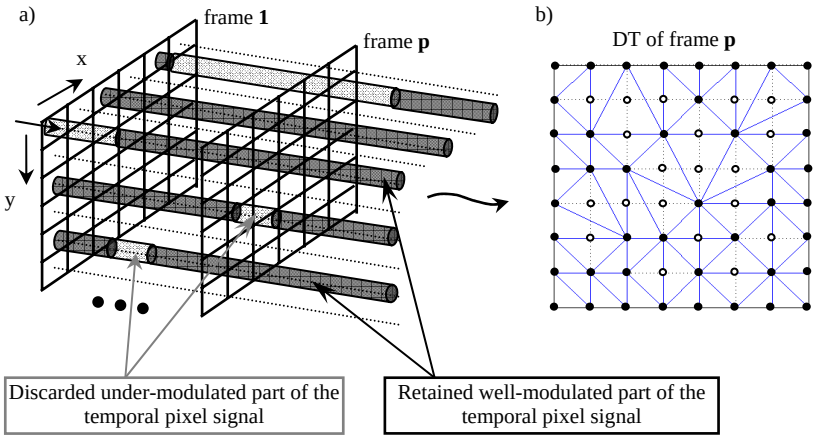

Fig. 2. Data classification: a) the irrelevant parts of the temporal signals are highlighted by bright tubes while the dark ones show the parts on which the interpolation step will rely; b) the non-uniform sampling grid computed for an arbitrary frame with the associated DT.

Considering our set of points irregularly placed in a plane, lines may be drawn between these points to create a complete set of non-overlapping triangles (triangulation) with the outer boundary being the convex hull of the point set. The convex hull in 2D might be seen as a rubber band surrounding a set of nails driven in a wooden board, the latter ones representing our mesh of valid data. Once the convex hull of the point set is defined, facets have to be built following some criteria. It is actually desirable to build a triangulation which minimizes the size of the facets. In other words, we should obtain a triangulation where each facet is as close as possible to an equilateral triangle. Indeed, it sounds natural to expect from the triangulation-interpolation process that each interpolated point is computed by relying on the closest data.

The DT actually fulfils this criterion by maximizing the smallest angle of all the triangles of the mesh, avoiding this way skinny triangles. So equivalently said, the DT generates the least stretched facets and thus preserved at best the spatial resolution.

At this point, three questions must be raised: *i)* does the definition of the DT ensure its uniqueness, *ii)*, how to compute this triangulation and finally

iii) what about the boundaries management in our very specific application?

i) The DT is unique for point sets containing no subsets of four co-circular points. Solutions have been proposed (see [11] and references therein) to resolve this non-uniqueness problem. If valuable in some applications, the uniqueness is not of great concern in our case.

ii) There is another well-known geometrical entity, worthy of interest for practical implementation of the DT: the Voronoi diagram (VD) [9]. Given a set of points in the plane, each point – or site – is associated with a Voronoi cell, consisting of all points closer to this point than to any other one. The frontiers of those Voronoi cells are all segments of the plane equidistant to two sites and also the perpendicular bisectors of the triangles sides of the associated DT. The VD is actually the dual graph of the DT (Fig. 3). There is moreover a close relationship between planar VD and convex hulls in space, which cannot be made plain here though lack of space [12]. This connection between those geometrical structures led to the design of improved algorithms for fast computations of VD or equivalently DT. In our case, the DT is implemented using the Quickhull algorithm [13] and followed by a triangle-based cubic spline interpolation [14] step to obtain the wanted uniformly sampled smooth IF frames.

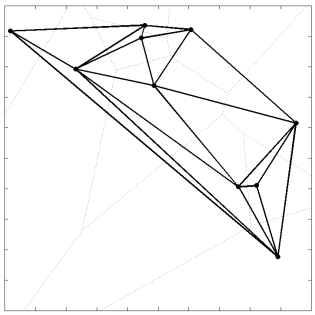

Fig. 3. The Voronoi diagram (thin dashed lines) of a random point set (black circles), jointly shown with the DT (thick lines).

iii) We have mentioned that the triangulation is constructed inside the convex hull of the data set, which does not guarantee a constant definition of the boundaries of our area of interest (AOI). It is thus mandatory to have at each instant fixed points on which the convex hull will be constructed. The triangulation will then be computed within this fixed framework, and the interpolating surface as well. To do so, we simply make sure that the AOI is always surrounded by pixels, naturally or artificially, labelled as

valid with values of IF, either imposed by a priori knowledge or computed by averaging the values of the AOI border.

4 Experimental results

A SI setup with in-plane sensitivity (Leendertz configuration) has been built to follow the rotation of an octagonal diffusing metallic plate (1 dm^2) around its center [4]. In this particular experiment, the central part of the metal plate undergoes the largest phase errors due to the small number of displacement fringes. We report in Fig. 4 the non-uniform sampling grid at one instant of the dynamic experiment, jointly with the corresponding DT. For the construction of the fixed convex hull, the simplest way for this particular example of in-plane rotation was to assign to the points surrounding the AOI *a priori* known IF values. It appears clearly that the size of the facets increases noticeably in the middle part of the plate. Indeed, the higher the threshold, the more discriminative the test and as a consequence, the sparser the DT.

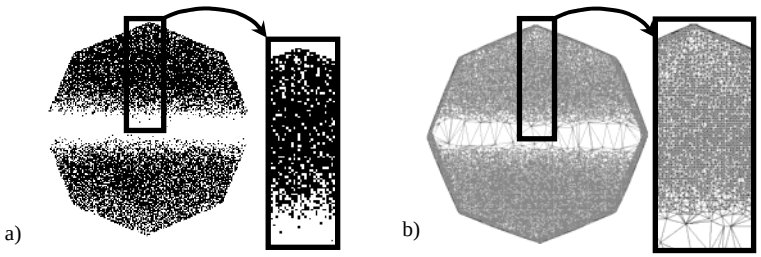

Fig. 4. a) Non uniform sampling grid experimentally obtained. Black pixels are valid while the white pixels are not; b) the corresponding DT is shown on the right side.

Where the triangulation yields large facets, the spatial resolution is consequently degraded. A trade-off has thus to be found between noise removal and spatial resolution conservation. For three different modulation thresholds, the area of each triangle is computed at the same state of the motion and reported in Fig. 5.

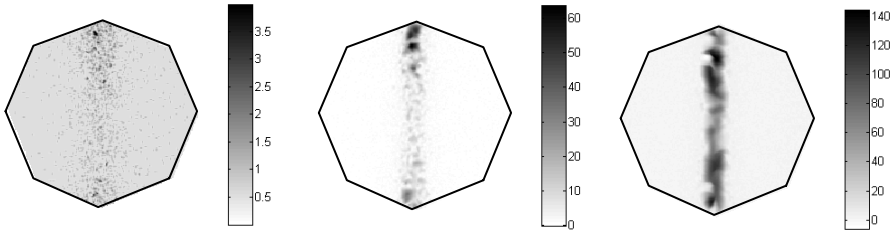

Threshold = **10** gray levels
95% of valid points

Threshold = **20** gray levels
73% of valid points

Threshold = **40** gray levels
58% of valid points

Fig. 5. Maps of triangle area for the DT of non-uniform meshs obtained with three different thresholds. The areas are expressed in (pixel)2 unit.

For the threshold value of 10 gray levels, we discard only few pixels and the triangles areas are mainly equal to 0.5 $(\text{pixel})^2$. However, it is not straightforward to accurately quantify the spatial resolution loss, as the grids are fluctuating. Indeed, at one point of the probed surface, the spatial resolution, or in other words the density of relevant pixels, changes at each frame and except for areas with almost no activity, a pixel always features enough modulation somewhere in its history to allow meaningful IF extraction. It is clear that the under-modulated parts of the temporal pixel signals lead to a phase, computed with the Hilbert transform, strongly polluted by salt noise (especially in the areas with low activity).

The phase maps of Fig. 6 show the complete displacement obtained after 4640 frames (1000×1000 encoded on 10 bits) taken at a rate of 48 fps, and processed by blocks of 1024 frames with an overlapping of 120 frames between them to reduce the boundaries errors. The total rotation, equal to 0.25°, represents for the points of higher displacement four times the pixel size, *i.e.* the correlation length. In this experiment, we do not use an optical temporal carrier – mandatory to find out the direction of the deformation – in order to have the largest measurement bandwidth (which otherwise would have to be shared with the carrier frequency) and to assess the method with a very wide range of deformation rates. The temporal pixel signals of half the plate are considered and processed. All temporal pixel signals are processed with a specific EMD algorithm and the Hilbert transform [4] to provide temporal phase signals. All those phase signals are then interrogated at the same time to build 2D phase frames at each instant. The 3DPP technique is furthermore applied to obtain 4640 smooth phase frames where the random phase errors have been greatly reduced. The benefit of the 3DPP technique is obvious and greatly extends the measurement bandwidth, except again in the central

part of the plate, which cannot be characterized without the adjonction of a temporal carrier.

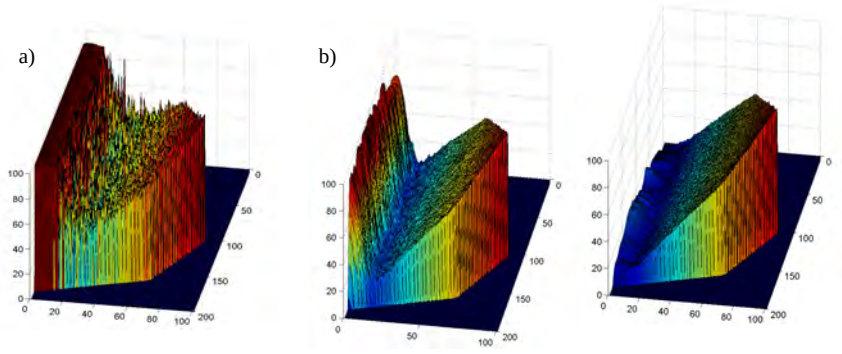

Fig. 6. Phase extraction results corresponding to the rotation of 0.25°: a) raw phase, b) phase resulting from the 3DPP with a threshold of b) 20 gray levels and of c) 40 gray levels.

5 Acknowledgments

This work is supported by the Swiss National Science Foundation.

6 References

1. Huntley, J.M., Saldner, H. (1993) Temporal phase-unwrapping algorithm for automated interferogram analysis. Appl. Opt. 32: 3047-3052.
2. Colonna de Lega, X., Jacquot, P. (1996) Deformation measurement with object-induced dynamic phase shifting. Appl. Opt. 35: 5115-5121.
3. Cherbuliez, M., Jacquot, P., Colonna de Lega, X. (1999) Wavelet processing of interferometric signals and fringe patterns. Proc. SPIE 3813: 692-702.
4. Equis, S., Jacquot, P. (2009) The empirical mode decomposition: a must-have tool in speckle interferometry? Optics Express 17: 611-623.
5. Lehmann, M. (2001) “Speckle statistics in the context of digital speckle interferometry” in Digital Speckle Pattern Interferometry and Related Techniques, John Wiley & Sons, Ltd, Chichester, Chap. 1.
6. Huang, N.E., Shen, Z., Long, S.R., Wu, M.C., Shih, H.H., Zheng, Q., Yen, N.-C., Tung, C.C., Liu, H.H. (1998) The empirical mode

decomposition and the Hilbert spectrum for nonlinear and non-stationary time series analysis. Proc. R. Soc. Lond. A 454: 903-995.
7. Boashash, B. (1992) Estimating and interpreting the instantaneous frequency of a signal. Proc. IEEE 80: 520-568.
8. Goodman, J.W. (2007) Speckle phenomena in optics, theory and applications. Roberts and Company Publishers.
9. Huntley, J.M. (1997) Random phase measurements errors in digital speckle pattern interferometry. Opt. Laser Eng. 26: 131-150.
10. Aurenhammer, F. (1991) Voronoi diagrams – a survey of a fundamental geometric data structure. ACM comp. surveys 23: 345-405.
11. Dyken, C., Floater, M.S. (2006) Preferred directions for resolving the non-uniqueness of Delaunay triangulations. Comput. Geom. 34: 96-101.
12. De Berg, M., Van Kreveld, M., Overmars, M., Schwarzkopf, O. (2008) Computational Geometry: Algorithms and Applications. Springer-Verlag.
13. www.qhull.org.
14. Isaac, A. (2002) Scattered data interpolation methods for electronic imaging systems: a survey. Journal of Electronic Imaging 11: 157-176.

Phase analysis of interference signal with optical Hilbert transform based on orthogonal linear polarization phase shifting

Violeta Dimitrova Madjarova, Hirofumi Kadono, Naoaki Kurita
Saitama University, Faculty of Engineering, Department of Environmental Science
338-8570, Saitama-ken, Saitama-shi, Sakura-ku, Shimookubo 255
Japan

1 Introduction

Digital optical interferometry is a whole-field technique for deformation measurements with high temporal and spatial resolution and with possibility for in-situ measurements of dynamic events. Quantitative evaluation of the deformation field is obtained by analysing the phase of the interference signal. To accurately calculate the phase, at least three phase-shifted interference patterns are required. Consequently, majority of the phase-analyzing algorithms that were proposed in the past were applicable only for static events [1]. For dynamic events, there is a different approach, in which each point in the image is considered independently, and the interference signal in time domain is analyzed [2, 3]. In our previous studies, we proposed a Hilbert transform (HT) method for phase analyses [3]. The method has the advantage of low noise level in the signal, in a fully automated manner. One disadvantage of HT method, however, is the accumulation of huge three-dimensional data sets that requires considerable amount of computer memory. In addition, the processing is carried out after the experiment, which does not allow in-situ measurements of deformation fields. To overcome these problems, we proposed a method that uses both temporal and spatial interference signal, where HT is carried out optically by spatial phase-shifting, which is achieved by separation of orthogonal components of polarized light. Similar methods have also been proposed in the past [4-7]. In the present method, only one measurement is necessary to calculate the phase distribution. For dynamic events, the temporal information of the interference signal can used to determine the bias intensity and to unwrap the phase in time domain.

2 Principle of the method

The optical setup of optical Hilbert transform based on orthogonal linear polarization phase shifting is illustrated in Fig. 1.

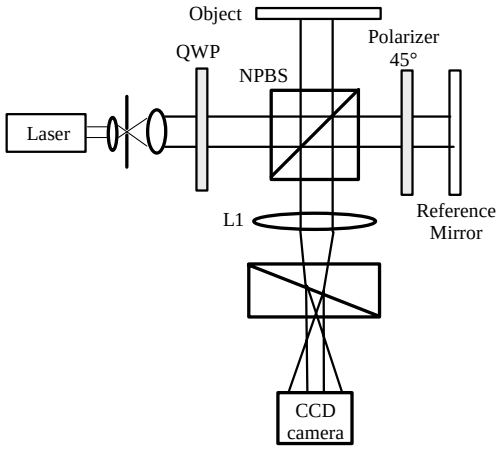

Fig. 1. Schematic of the optical setup. QWP – quarter-wave plate, YAG Laser λ=532 nm, L1 – imaging lens f=100 mm.

Linearly polarized light from the laser passes through a quarter-wave plate (QWP) which is adjusted so that the linearly polarized light is converted to circularly polarized light after the QWP. The light beam is equally split into a reference and a sample beams by a non-polarizing beam splitter (NPBS). A polarizer at +45° with respect to the horizontal direction is introduced in the reference arm. The light beam after the polarizer is linearly polarized. The reference and sample beams are recombined at the NPBS, and there is a $\pi/2$ phase difference between the two orthogonal p and s components of the sample beam with respect to the reference beam. The two orthogonal components of light beam are spatially separated by Wollaston prism, and two images which represent the sine and cosine interference patterns are captured in one single frame using CCD camera.

In order to confirm the cosine and sine distributions on the camera we used Jones matrices formalism for describing the state of polarised light. The Jones vector of the light after the QWP is given by,

$$E = E_0 \begin{pmatrix} 1 \\ i \end{pmatrix}. \tag{1}$$

The Jones vector of the sample beam after it is reflected from the beam splitter, reflected form the sample and passed through the beam splitter is,

$$E_S = \frac{E_o}{4}\begin{pmatrix}1\\ i\end{pmatrix}\exp\left(i\Delta\varphi\right), \tag{2}$$

where Δφ represents the phase difference between the sample and reference beams. The Jones vector of the reference beam after it passed through the beam splitter, passed through the polarizer, is reflected form the reference mirror, passed through the polarizer and is reflected by the beam splitter is,

$$E_R = \frac{E_o}{8}\begin{pmatrix}1+i\\ 1+i\end{pmatrix}. \tag{3}$$

After the beam splitter, the two beams are recombined and their sum can be expressed as

$$E_R + E_S = \frac{E_0}{4}\exp\left(i\Delta\varphi\right)\begin{pmatrix}1\\ i\end{pmatrix} + \frac{E_o}{8}\begin{pmatrix}1+i\\ 1+i\end{pmatrix}. \tag{4}$$

At the Wollaston prism the two components of the above Jones vector are separated spatially and are detected on one frame by the CCD camera. Intensities of the two components can be expressed as;

$$I_{si} = \frac{I_o}{64}(3 + 2\sqrt{2}\sin(\Delta\varphi - \pi/4) = I_{bias} + I_m \sin(\Delta\varphi - \pi/4), \tag{5}$$

$$I_{co} = \frac{I_o}{64}(3 - 2\sqrt{2}\cos(\Delta\varphi - \pi/4) = I_{bias} - I_m \cos(\Delta\varphi - \pi/4). \tag{6}$$

Bias intensity is evaluated by averaging all the acquired frames in time. From the sine and cosine images the phase distribution is obtained as follows;

$$\Delta\varphi - \pi/4 = \tan^{-1}\left(\frac{I_{si} - I_{bias}}{I_{bias} - I_{co}}\right). \tag{7}$$

3 Experimental results and discussions

To confirm the proposed method, an optical interferometric system (illustrated in Fig. 1) was constructed. The linearly polarised light from a

SHG-YAG laser at wavelength of 532 nm was incident to the quarter wave plate (QWP). The QWP and the polarizer were adjusted so that there is a $\pi/2$ phase difference between the two orthogonal p and s components of the sample beam with respect to the reference beam. As a spatial separation device, Wollaston prism, is used, which splits the two orthogonal polarisations into two separate fringe patterns which were captured in one frame by a CCD camera (Sony XCL-U1000) with resolution of 1200x1600 pixels and acquisition rate of 15 frames/s. Frames were taken consecutively as the sample was translated by a sinusoidal signal with a frequency of 1 Hz and peak-to-peak amplitude of 266 nm. The object that was imaged on the camera with a lens of focal length of 100 mm was with radius 6.75 mm. Fig. 2 presents one of the frames taken by the CCD camera.

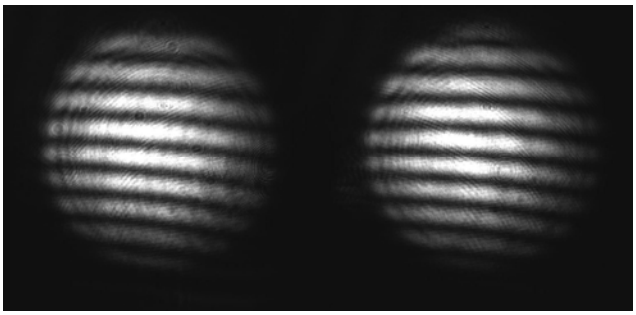

Fig. 2. Frame acquired by camera representing cosine and sine fringe patterns.

In order to apply the proposed method, the identical point on each image has to be assured. Two additional frames, before sample was displaced, were taken. The first frame was taken when the sample arm was blocked, and the second frame was taken when the reference arm was blocked. These two frames are summed and binarized by giving a threshold. The translation vector of one of the image towards the other was determined by using the autocorrelation function for the binarized image. This translation vector is used consecutively for all the frames which were taken while the sample was displaced. After adjusting the position of cosine and sine fringe patterns so that they overlap correctly, the bias intensity was estimated by taking the average over all frames in time. The intensities of the cosine and the sine functions were obtained by subtracting the bias intensity from the cosine and sine fringe patterns and normalized in time domain so that two components have the same amplitude. The phase was calculated using Eq. 7 and finally unwrapped in time and in space domain. Figure 3 presents two-dimensional spatial distribution of the object phase.

A circular mask was used to select the region of interest. The unwrapped phase is smooth with no phase jumps. Figure 4 represents a temporal signal at several points. The measured peak-to-peak displacement amplitude of 210 nm gives difference of λ/9.7 in comparison with the displacement given by the PZT. Errors in the correct estimation of the phase values can be divided in two. The first types of the error sources are due to the imperfect overlapping of the two fringe patterns which represent the since and the cosine functions. The correct estimation of phase value is especially sensitive to those types of error. The second types of error sources are due to imperfections of the polarizing elements including QWP, polarizer and Wollaston prism.

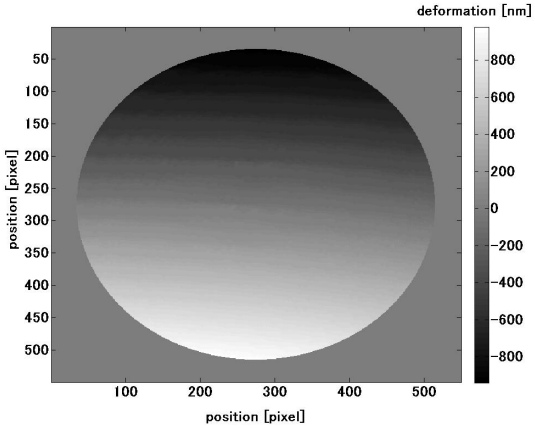

Fig. 3. Two-dimensional phase map of the sample taken at frame number 15.

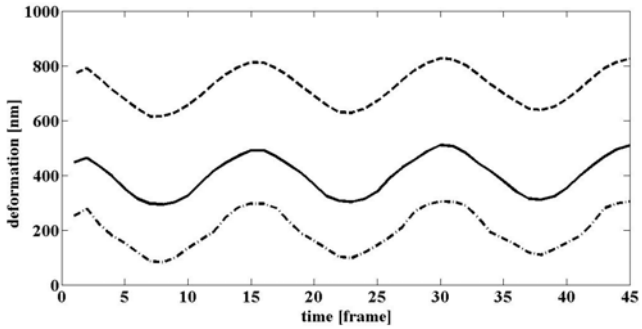

Fig. 4. Displacement of object in time for three different points.

4 Conclusion

In this study, we proposed a method for phase analysis which uses an optical Hilbert transform based on orthogonal linear polarization phase shifting. The method gives possibility for studying dynamic events continuously. Experiment was carried out to demonstrate the feasibility of the proposed method. The accuracy of the method was determined to be $\lambda/9.7$. This accuracy can me improved by wore finer algorithm for superimposing the sine and cosine fringe patterns.

5 References

1. Robinson D.W. and Read C.R. (Ed.) (1993) Interferogram Analysis: Digital Fringe Measurement Techniques, Institute of Physics, Bristol.
2. C. Joenathan, B. Franze, P. Haible, H.J. Tiziani (1998) Large in-plane displacement in dual-beam speckle interferometry using temporal phase measurement J. Mod. Optics 44:1975-1984
3. V. Madjarova, H. Kadono, and S. Toyooka (2003) Dynamic electronic speckle pattern interferometry (DESPI) phase analyses with temporal Hilbert transform Opt. Express 11: 617-623
4. Kiire T., S. Nakadate and M. Shibuya (2008) Simultaneous formation of four fringes by using a polarization quadrature phase-shifting interferometer with wave plates and diffraction grating. Applied Optics 47: 4787-4792
5. Rodriguez-Zurita G., C. Meneses-Fabian, N-I Toto-Arellano, J.F Vazques-Castillo, C. Robledo-Sanchez (2008) One-shot phase-shifting phase grating interferometry with modulation of polarization: case of four interferograms. Optics Exxpress 16:9806-9817
6. Hettwer A., J. Kranz, J. Shwider (200) Three channel phase-shifting interferometer using polarization-optics and a diffraction grating. Optical Engineering 39:960-966
7. Shaked N.T,, M.T. Rinehart and A. Wax (2009) Dual-interference-channel quantitative-phase microscopy of live cell dynamics. Optics Letters 24:767-769

Digital Fourier-transform processing for analysis of speckle photographs

Karl A. Stetson
Karl Stetson Associates, LLC
2060 South Street
Coventry, CT 06238

1 Introduction

Laser speckle photography[1] arose as an alternative to holographic interferometry as a method of measuring object displacements by measuring the displacements of laser speckles. Originally, speckles were recorded on photographic plates, which required chemical development and fixing and were analyzed by optical Fourier transforms. Digital photography has been used for specklegram analysis for quite some time,[2,3] however, speckle displacements have been analyzed mainly by image correlation. While this method is powerful, rapid, and well suited to digital processing, a method more strictly analogous to optical processing offers an interesting alternative. The purpose of this paper is to present work done to apply digital photography and digital Fourier transforms to the measurement of speckle displacements.

2 Procedure for digital Fourier processing

To begin, the object is photographed with a digital camera. The optical axis of the lens should be aligned along the surface normal and the camera should have black and white pixels in a square format. Photographs captured before and after the object is perturbed are designated as A and B. For simple displacement analysis, an entire camera image can be used; however, for strain analysis, the image must be divided into segments for separate processing. The next step is to compute the digital Fourier transforms, FAnm and FBmn, for each photograph or segment thereof. Unlike optical Fourier transforms, digital Fourier transforms allow calculation of the phase of the pixels in the transform. The values range randomly from $-\pi$ to π; however, a speckle displacement generates a linear phase change across the transform plane whose slope is proportional to the

displacement and whose gradient is in the direction of displacement as described by the shift theorem of Fourier transforms. This function is obtained by subtracting the phases of the two transforms and wrapping the result into the range of $-\pi$ to π. The phase difference must then be unwrapped and fit to a linear function of the spatial frequencies, ωx and ωy, the slopes of which correspond to the x and y translations of the speckles. If strain analysis is being performed, the image will be divided into segments and the changes in slope between neighboring segments is used to calculate the average strains between the segments as described below.

3 Mathematical Analysis

The digital Fourier transform is described by the following equation:

$$F(j,k) = \sum_{m=0}^{m=M-1} \sum_{n=0}^{n=N-1} f(m,n)\exp[-i2\pi(\frac{jm}{M} + \frac{km}{N})], \quad (1)$$

where f(m,n) is the pixel function whose transform is being calculated, m and n are the pixel indices in the x and y directions, M and N are the number of pixels in the x and y directions of the image or sector thereof, j and k are the horizontal and vertical indices of the coordinates of the transform, and F(j,k) is the Fourier transform of f(m,n) with respect to the variables j and k.

The y axis, represented by n, is positive downward as is consistent with television usage. We may calculate the effect of a one pixel displacement in the x or y directions, d_{px} and d_{py}, for the pixel function f(m,n) by substituting m-1 for m or n-1 for n in Eq.(1). This generates phase functions $\Phi_{\omega x}$ or $\Phi_{\omega y}$ in the transform plane, where

$$\Phi_{\omega x} = \exp(i2\pi j/M), \text{ and } \Phi_{\omega y} = \exp(i2\pi k/N). \quad (2)$$

The slopes of these phase functions, s_{j1} and s_{k1} per increment of j or k, are

$$s_{j1} = 2\pi/M, \text{ and } s_{k1} = 2\pi/N. \quad (3)$$

If d_x and d_y are the actual displacements of the image pattern, and s_k and s_j are the corresponding measured phase changes per pixel of their transforms, then the corresponding fractions of pixel displacements, d_x/d_{px} and d_y/d_{py}, will equal the corresponding fractional changes in slope of the transform function, s_k/s_{j1} and s_k/s_{k1}.

$$d_x/d_{px} = s_j/s_{j1}, \text{ and } d_y/d_{py} = s_k/s_{k1} \tag{4}$$

Substituting from Eqs.(3) gives

$$d_x = d_{px}s_jM/2\pi, \text{ and } d_y = d_{py}s_kN/2\pi, \tag{5}$$

where the units of s_j and s_k are radians per pixel in the Fourier transform plane. Equations (5) allow calculation of the object displacement in terms of the pixel spacing, the transform plane slope, and the total number of pixels in the direction considered. The products, $d_{px}M$ and $d_{py}N$, are the physical sizes in x and y of the camera array or the segments of the array. If the object is magnified relative to its image on the camera, the object displacements from equations 5 must be multiplied by that amount.

For strain analysis, we need to analyze neighboring M by N segments as follows. Identify four sectors by subscripts in a rectangular array:

11 12
21 22

The relative displacements of these sectors may be defined as:

$\Delta_{xx} = (d_{x12} - d_{x11} + d_{x22} - d_{x21})/2$, the x expansion in the x direction. (6a)

$\Delta_{yy} = (d_{y21} - d_{y11} + d_{y22} - d_{y12})/2$, the y expansion in the y direction.(6b)

$\Delta_{xy} = (d_{x21} - d_{x11} + d_{x22} - d_{x12})/2$, the x expansion in the y direction. (6c)

$\Delta_{yx} = (d_{y11} - d_{y12} + d_{y21} - d_{y22})/2$, the y expansion in the x direction.(6d)

The sectors are separated in x by M pixels and in y by N pixels, the x strain, y strain, and shear are defined as:

$$\varepsilon_{xx} = \Delta_{xx}/d_{px}M \tag{7a}$$

$$\varepsilon_{yy} = \Delta_{yy}/d_{py}N \tag{7b}$$

$$\varepsilon_{xy} = (\Delta_{yx}/d_{px}M + \Delta_{xy}/d_{py}N)/2 \tag{7c}$$

Eqs. (3) and (4) are substituted into Eqs. 6a-6d, and the results substituted into Eqs. 7a-7c, and the factors of p_xM and p_yN cancel. Equations 7a-7c may be rewritten as

$$\varepsilon_{xx} = (s_{j12} - s_{j11} + s_{j22} - s_{j21})/4\pi \tag{8a}$$

$$\varepsilon_{yy} = (s_{k21} - s_{k11} + s_{k22} - s_{k12})/4\pi \tag{8b}$$

$$\varepsilon_{xy} = (s_{j21} - s_{j11} + s_{j22} - s_{j12} + s_{k12} - s_{k11} + s_{k22} - s_{k21})/8\pi \tag{8c}$$

4 Experimental Study

An experimental study was carried out to determine the effectiveness of the process described above. The details are described elsewhere4 and are summarized here. For displacement measurement, 8-bit laser specklegrams of 640x480 pixels were recorded at x displacements of 0, 10, 20, 40, 80, 160, 320, and 640 micrometers. Displacement analysis via Eqs (5) gave RMS errors of approximately 6 to 10 μm, and it was shown that variations in f/number did not improve accuracy nor did using 12 bit digitization. For comparison, a random speckle pattern was computer generated, printed, fastened to the object surface, illuminated with incoherent light, and the same set of x displacements recorded. For these recordings, the RMS error was approximately 2 μm. Closer examination of the live specklegram images revealed that, with laser speckles, the pattern showed a cyclic fluctuation with displacement. This appears to come from the fact that the CCD TV camera detector has a fill factor in the order of 35% of its area. The recorded pattern is perfectly replicated, therefore, only when the speckle pattern shift is exactly by one pixel spacing. This was less of a problem with incoherent speckles.

Strain of the object was simulated by translating it toward the camera so that its image appeared to grow in size, giving equal x and y apparent strains. The images were divided into 12 segments, 3 vertical by 4 horizontal, of 160x160 pixels each. The best results for this were obtained with the incoherent speckle pattern, and for a simulated strain of 2817E-6, the resulting measurements were accurate with a standard deviation of about 30E-6.

5 References

1. E. Ennos, Speckle Interferometry, in Progress in Optics Vol. XVI, Emil Wolf, Ed. North-Holland, Amsterdam, 1978, Chap. 4, pp. 235-290.
2. Mikael Sjödahl, Digital Speckle Photography in Digital Speckle Pattern Interferometry and Related Techniques, P. K. Rastoji, (Ed.), J. Wiley & Sons, New York, 2001, Chap. 5.
3. J. M. Huntley, Automated Analysis of Speckle Interferograms in Digital Speckle Pattern Interferometry and Related Techniques, P. K. Rastoji, (Ed.), J. Wiley & Sons, New York, 2001, Chap. 2, pp. 89-95.
4. K. A. Stetson, Digital Fourier-transform processing for analysis of speckle photographs, (Submitted to Applied Optics).

Wavefront evaluation in phase shifting interferometry based on recurrence fringe processing with 3D prediction

Igor Gurov, Alexey Karpets, Elena Vorobeva
Saint Petersburg State University of
Information Technologies, Mechanics and Optics
49 Kronverksky ave., Saint Petersburg, 197101, Russia

1 Introduction

The phase shifting interferometry (PSI) techniques allow accurate evaluating fringe phase [1, 2] and are usually implemented by controllable changing the path length of the reference wave in interferometer with recording of a set of phase shifted fringe patterns. Conventional phase evaluation algorithms involve arctangent transformation and recover wrapped fringe phase (see, *e.g.* [1, 2]). The disadvantages of conventional PSI methods consist in necessity to record full set of fringe patterns before their processing and to apply additional phase unwrapping algorithms to recover full phase of a wavefront. To overcome the former disadvantage, recurrence processing algorithms were developed [3], in which fringe intensity value is predicted from previous fringe pattern to next pattern taking into account the fringe signal model. The prediction error is used to correct fringe parameters at current step. Dynamic recurrence data processing methods are based on statistical characteristics of fringe signals with correct evaluation of fringe phase errors [4]. Recently, the method to overcome the latter disadvantage was reported [5], which is based on the Kalman filtering algorithm with 3D spatial-temporal prediction and dynamic recovery of full unwrapped fringe phase.

In the present paper, a developed variant of the method [5] is reported, which provides increased processing speed when recovering unwrapped phase of wavefront in dynamic mode.

2 Principle of the method

In PSI, the following interferometric signal model is used

$$s(k) = b + a\cos(\varepsilon + 2\pi fk\Delta z)\,, \tag{1}$$

where fringe background component b and amplitude a are supposed to be unknown constants. Fringe frequency $f = 1/\lambda$ is defined by known wavelength λ, and $2\Delta z$ is the optical path difference (OPD) change step, $k = 0, \ldots, K\text{-}1$. It is required to assess the fringe phase ε with highest accuracy by processing fringe signal samples series $s(k)$. The number of phase steps K within single fringe is typically selected as $K = 3\ldots 11$ depending on PSI algorithm (see, *e.g.* [2, 6, 7]).

The model Eq. (1) can be rewritten in the parametric form $s(k) = s(k, \boldsymbol{\theta})$, where vector of parameters of the model can be set as $\boldsymbol{\theta} = (b, a, \Phi, f)^T$, $\Phi(k) = \varepsilon + 2\pi fk\Delta z$ is full phase. If phase step $4\pi f\Delta z$ is non-stable, *e.g.*, due to external disturbances of OPD, it can be interpreted by an observer as fringe frequency variations, *i.e.* $f = f(k)$. In this case, dynamic estimates of both $\Phi(k)$ and $f(k)$ must be obtained using signal samples series Eq. (1). This problem can be solved using the non-linear (extended) Kalman filtering method [3, 4, 8].

In Kalman filtering algorithm, input signal sample $s(k)$ is compared with predicted signal value $s(k/k\text{-}1)$ from previous signal sample $(k\text{-}1)$ at the sample k using known signal model $s(k, \boldsymbol{\theta})$, Eq. (1). The difference (prediction error) is used to correct dynamically the vector of parameters at each step. The basics of the Kalman filtering method described in detail in [9].

When evaluating a wavefront, the model Eq. (1) should be rewritten by introducing lateral discrete coordinates (i, j) in the form

$$\begin{aligned} s(i, j, k) &= b(i, j) + a(i, j)\cos[\varepsilon(i, j) + 2\pi fk\Delta z] + n(i, j, k) \\ &= h(i, j, k, \boldsymbol{\theta}) + n(i, j, k), \end{aligned} \tag{2}$$

where $h(i, j, k, \boldsymbol{\theta})$ is three-dimensional observation function, $n(i, j, k)$ is observation noise. In this case, the vector of parameters is

$$\boldsymbol{\theta}(k) = (b, a, \Phi, f_H, f_V, f_t)^T\,, \tag{3}$$

where f_H, f_V are spatial frequencies in horizontal direction (discrete variable i) and in vertical direction (discrete variable j), accordingly, f_t is temporal fringe frequency (discrete variable k). To recover 3D full phase $\Phi(i, j)$ characterizing a wavefront shape, unwrapping of fringe signal phase over the range of 2π is required. Note that it is possible if the phase difference between neighbor pixels in lateral directions is less than π.

In the suggested method [5], the system equation describing evolution of the vector of parameters $\boldsymbol{\theta}(i, j, k)$ is presented in the form

$$\begin{aligned}\boldsymbol{\theta}(i,j,k) &= \mathbf{A}(i,j,k)\boldsymbol{\theta}(i-1,j,k) \\ &+ \mathbf{B}(i,j,k)\boldsymbol{\theta}(i,j-1,k) + \mathbf{C}(i,j,k)\boldsymbol{\theta}(i,j,k-1) + \mathbf{w}(i,j,k),\end{aligned} \quad (4)$$

where **A**, **B** and **C** are the known transition matrices, $\mathbf{w}(i,j,k)$ is "forming" noise [9].

Following to Eq. (4), prediction of the vector of parameters at *k*-th phase shifting step is calculated as

$$\begin{aligned}\bar{\boldsymbol{\theta}}(i,j,k) &= \mathbf{A}(i,j,k)\tilde{\boldsymbol{\theta}}(i-1,j,k) \\ &+ \mathbf{B}(i,j,k)\tilde{\boldsymbol{\theta}}(i,j-1,k) + \mathbf{C}(i,j,k)\tilde{\boldsymbol{\theta}}(i,j,k-1),\end{aligned} \quad (5)$$

where $\tilde{\boldsymbol{\theta}}(i-1,j,k)$, $\tilde{\boldsymbol{\theta}}(i,j-1,k)$ and $\tilde{\boldsymbol{\theta}}(i,j,k-1)$ are the *a posteriori* estimates obtained at neighbor pixel of (*i*-1)-th row of fringe pattern, at neighbor pixel of (*j*-1)-th column of fringe pattern and at (*k*-1)-th phase shifting step, correspondigly. Transition matrices in Eq. (5) can have simple form

$$\mathbf{A} = \frac{\alpha}{2}\begin{pmatrix} 1 & 0 & 0 & 0 & 0 & 0 \\ 0 & 1 & 0 & 0 & 0 & 0 \\ 0 & 0 & 1 & 2\pi\Delta x & 0 & 0 \\ 0 & 0 & 0 & 1 & 0 & 0 \\ 0 & 0 & 0 & 0 & 1 & 0 \\ 0 & 0 & 0 & 0 & 0 & 1 \end{pmatrix}, \quad \mathbf{B} = \frac{\alpha}{2}\begin{pmatrix} 1 & 0 & 0 & 0 & 0 & 0 \\ 0 & 1 & 0 & 0 & 0 & 0 \\ 0 & 0 & 1 & 0 & 2\pi\Delta y & 0 \\ 0 & 0 & 0 & 1 & 0 & 0 \\ 0 & 0 & 0 & 0 & 1 & 0 \\ 0 & 0 & 0 & 0 & 0 & 1 \end{pmatrix},$$

$$\mathbf{C} = (1-\alpha)\begin{pmatrix} 1 & 0 & 0 & 0 & 0 & 0 \\ 0 & 1 & 0 & 0 & 0 & 0 \\ 0 & 0 & 1 & 0 & 0 & 4\pi\Delta z \\ 0 & 0 & 0 & 1 & 0 & 0 \\ 0 & 0 & 0 & 0 & 1 & 0 \\ 0 & 0 & 0 & 0 & 0 & 1 \end{pmatrix},$$

where Δx and Δy are discretization steps in lateral directions, $\alpha \in [0,1]$ is the coefficient defining degree of influence of neighbor pixels in lateral directions with respect to temporal prediction. This coefficient is set taking into account a character of concrete evaluated 3D wavefront shape.

Dynamic estimates of fringe parameters are obtained by the Kalman filtering algorithm:

$$\tilde{\boldsymbol{\theta}}(i,j,k) = \bar{\boldsymbol{\theta}}(i,j,k) + \mathbf{P}(i,j,k)[s(i,j,k) - h(i,j,k,\bar{\boldsymbol{\theta}})], \quad (6)$$

where $\mathbf{P}(i,j,k)$ is the Kalman filter amplification factor [5].

If the phase shifts are stable and known *a priori* with high accuracy, it is possible to omit dynamic estimates of temporal fringe frequency f_t, and the algorithm provides 3D spatial phase unwrapping automatically.

To increase data processing speed, in difference with the algorithm [5] fringe data are processed in parallel in four quadrants *I-IV* (see Fig. 2) with their borders merger to recover full wavefront.

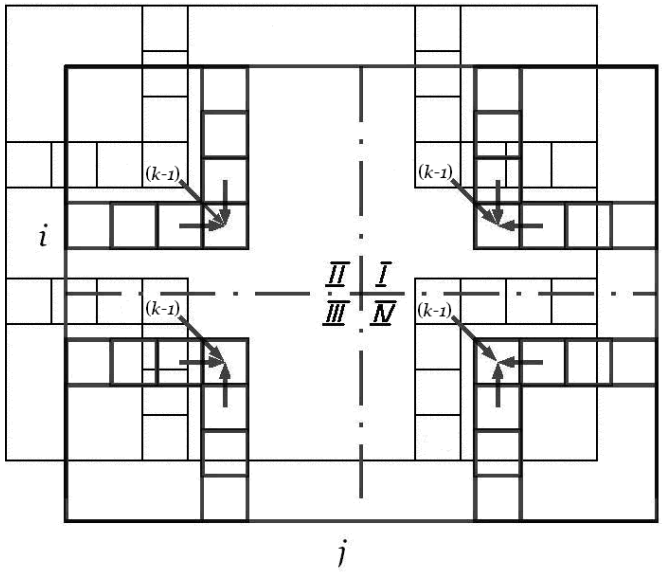

Fig. 1. Schematic diagram of 3D prediction procedure: current frame (bold lines), previous frame (*k*-1) and 3D prediction indicated by arrows in four quadrants *I-IV*

3 Experimental results

To investigate properties of the suggested algorithm, the initial wavefront was modeled by Zernike polynomial of the form

$$\Phi(x,y)=\frac{4\pi}{\lambda}(3y-12x^2y+10x^4y-12y^3+20x^2y^3+10y^5)\,. \qquad (7)$$

Fig. 2 shows examples of fringe patterns corresponding to the wavefront shape Eq. (7) with introduced phase shifts between them.

Full range of the phase change Φ is equal approximately to 140 radians being defined by the total number of fringes inside the fringe pattern Fig. 2. Dynamically recovered 3D phase distributions are illustrated in Fig. 3. The fringe patterns and phase distributions were modeled by 200 × 200 pixels in lateral directions.

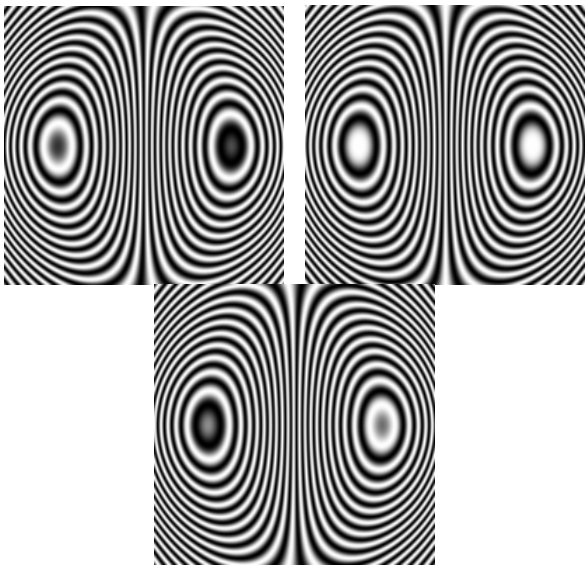

Fig. 2. Fringe patterns corresponding to the modeled wavefront

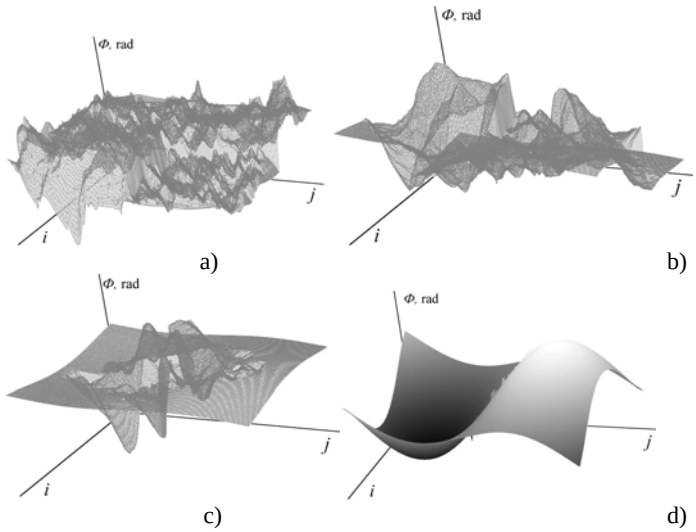

Fig. 3. Reconstruction of 3D wavefront after (a) 2 steps, (b) 10 steps, (c) 25 steps, (d) 60 steps of phase shifts using the suggested algorithm

It is important to note that following to the Nyquist condition the introduced phase shift between two neighbor fringe patterns should not

exceed the value corresponding to phase change of π in lateral direction at the pixel placed within narrowest fringe.

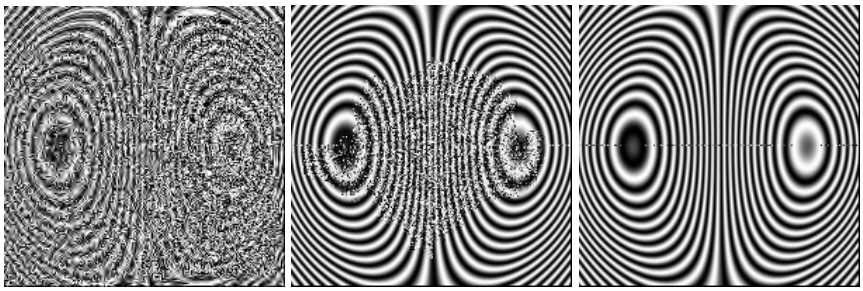

Fig. 4. Fringe patterns corresponding to the recovered full fringe phase Fig. 3 (a), (c), (d)

Fig. 4 illustrates fringe patterns calculated using the values of recovered full phase (Fig. 3). It is seen that phase deviations in Fig. 3 are defined mainly by uncertainty of integer number of phase cycles.

The convergence speed of phase estimates to true phase values depends on the phase shift step. Curves in Fig. 5 represent RMS errors of phase estimates obtained with different value of phase step. The RMS error at initial step is defined by the wavefront deviation from plain form supposed as initial condition. Recovery of true values of unwrapped fringe phase is achieved within the range of accumulated introduced phase shift equal to 2π. Investigation results of phase accuracy of the Kalman filtering algorithm applied to processing of fringe signals in PSI were presented in [4]. It has been shown that phase accuracy of the algorithm achieved without phase unwrapping can be $2\pi/1000$ or higher. Such high potential accuracy of full phase recovery over the range of 2π is provided also by the considered recurrence fringe processing algorithm with 3D prediction, if phase shift value meets to the Nyquist condition for lateral spatial sampling mentioned above.

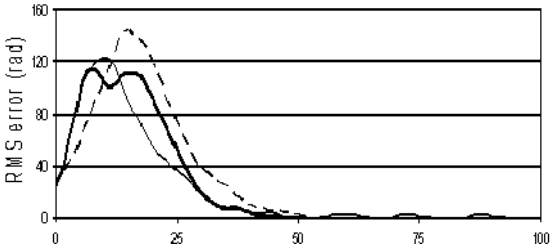

Fig. 5. Convergence of the algorithm of full phase recovery with different phase shifts: $2\pi/40$ (thin solid line), $2\pi/50$ (bold solid line) and $2\pi/120$ (dotted line)

4 Conclusions

The results obtained demonstrate the possibility to recover unwrapped full phase of wavefront in dynamic mode using the suggested method of recurrence fringe processing with 3D prediction. The convergence of the full phase dynamic estimates to true values depends on the phase shift step. The total number of phase shifts is defined by spatial resolution of photo sensitive array in lateral directions. Full phase recovery of wavefront with phase deviations exceeding 2π is provided by the suggested algorithm in PSI mode within accumulated phase shift range of 2π.

5 References

1. Bruning, JH, Herriott, DR, Gallagher, JE, Rosenfeld, DP, White, AD, Brangaccio, DJ (1974) Digital wavefront measuring interferometer for testing optical surfaces and lenses. Applied Optics 13: 2693–2703.
2. Patil, A, Rastogi, P (2005) Approaches in generalized phase shifting interferometry. Optics and Lasers in Engineering 43: 475–490.
3. Gurov, I, Zakharov, A (2005) Dynamic evaluation of fringe parameters by recurrence processing algorithms. Proc. FRINGE'2005, the 5th Int. Workshop on Automatic Processing of Fringe Patterns. Stuttgart: Springer-Verlag: 118-125.
4. Gurov, I, Zakharov, A, Voronina, E (2004) Evaluation of interference fringe parameters by recurrence dynamic data processing. Proc. ODIMAP IV, the 4th Topical Meeting on Optoelectronic Distance/Displacement Measurements and Applications (University of Oulu, Oulu, Finland, 16-18 June 2004): 60-71.
5. Gurov, I, Karpets, A (2008) Surface shape evaluation in phase shifting interferometry based on the Kalman filtering method with 3D prediction. Proc. OSAV'2008, the 2nd Int. Topical Meeting on Optical Sensing and Artificial Vision (Saint Petersburg, Russia, 12-15 May 2008): 212-217.
6. Schwider, J, Burow, R, Ellsner KE, Grzanna J, Spolaczyk R, Merkel K (1983) Digital wave-front measuring interferometry: some systematic error sources. Applied Optics 22: 3421-3432.
7. Creath, K (1988) Phase measurement interferometry technique. Progress in Optics 26: 349-383.
8. Gurov, I, Zakharov, A (2004) Analysis of characteristics of interference fringes by nonlinear Kalman filtering. Optics and Spectroscopy 96: 175-181.
9. Kalman, RE (1960) A new approach to linear filtering and prediction problems. Transactions of the ASME, Journal of Basic Engineering 82: 35-45.

White-light fringe analysis with low-cost CCD camera

Zdeněk Buchta, Petr Jedlička, Milan Matějka, Vladimír Kolařík,
Břetislav Mikel, Josef Lazar and Ondřej číp
Institute of Scientific Instruments AS CR, v.v.i.
Královopolská 147, 612 64 Brno
Czech Republic

1 Introduction

Using of length measuring instruments is a usual part of everyday life. The accuracy of a length measuring instrument is ensured and verified by instrument calibration process. In works practice branch of mechanical engineering, gauge blocks are at the end of the calibration chain.

Gauge blocks are made of stainless steel or ceramics. In both cases, gauge blocks wear away because of the mechanical contact between the gauge block and the calibrated instrument. Because of this reason, the regular gauge blocks calibration is necessary and it is hot-topic for fundamental and industrial metrology.

We describe in this paper a pilot experiment of a white-light fringe analysis with a low-cost color CCD camera. The used detection technique employs the phase-crossing algorithm. The experimental setup is designed to be a crucial part of the complex system for automatic contactless diagnostic and calibration of gauge blocks.

2 White-light interferometry and phase-crossing algorithm

White-light interferometry (low-coherence interferometry) is a powerful diagnostic technique which has become attractive and useful method for fast and accurate 3D inspection of macroscopic object. Typical branch of application of white-light interferometer is contactless surface diagnostics of macroscopic objects, surface roughness and quality assurance, thickness of thin film measurement and also in medicine in branch of optical tomography [1-4].

The principle of white-light interferometry comes out from classical laser interferometry. In case of white-light interferometry, a low-coherent

light emitter (halogen lamp, Xenon lamp, superluminescent LED diode) instead of a coherent laser is used.

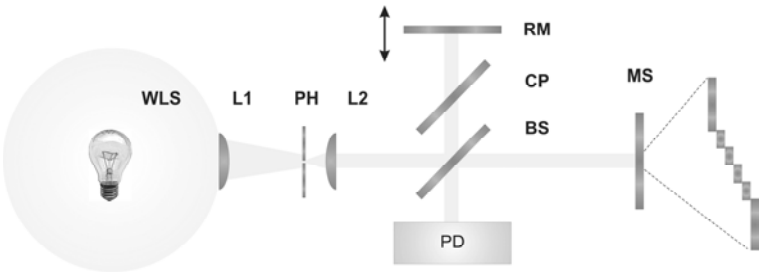

Fig. 1. Michelson interferometer with white-light source. WSL is a source of white-light (e.g. halogen bulb), L1 and L2 are lenses, PH is pinehole (100 μm), BS is beam splitter, CP is compensation plate, RM is reference mirror, MS is monitored surface and PD is photodetector.

Typical white-light interferometer employs the Michelson setup (Fig. 1). In contrast with the laser interferometer, there is a compensation plate placed in reference arm of the white-light interferometer. The compensation plate is used for compensation of light dispersion caused by the passage of the white-light beam throw the beam splitter [5].

The principle of white-light interferometry is given by the white light source. Its coherence length is only a few micrometers (typically from 1 μm to 5 μm). This feature predestines the white light interferometer to be an indicator of balance of the white-light interferometer.

There are several techniques and algorithms for interference fringe central point detection [6]. For the pilot experiments we decided to use a phase-crossing algorithm as a detection technique [7]. The algorithm takes advantage of a color CCD camera usage.and makes comparison of the phase difference between interference fringes monitored by selected pixels and identifies the point where the phase difference between the red, green and blue part of the white-light interference fringe becomes equal to zero. The phase crossing point given by relevant color pixels represents the point of the measured surface.

3 Experimental setup and results

The experimental setup is illustrated by the block diagram in Fig. 1.

As a source of white light, the superluminescent LED diode LUXEON (3 W) is used. The color CCD camera is used as a photodetector. Using single CCD camera instead of three-CCD one influences the space

resolution of the measurement. The three-CCD system assures perfect pixel-by-pixel registration of the red, green and blue interference fringe components and the detection technique resolution limit is given by pixel size. As for single CCD camera, at least two pixels are necessary for the phase crossing point determination and the detection technique resolution limit is given by this fact. On the other hand, for the purpose of contactless diagnostics gauge blocks, the assumed method resolution is sufficient and its low price is important for possible commercial use.

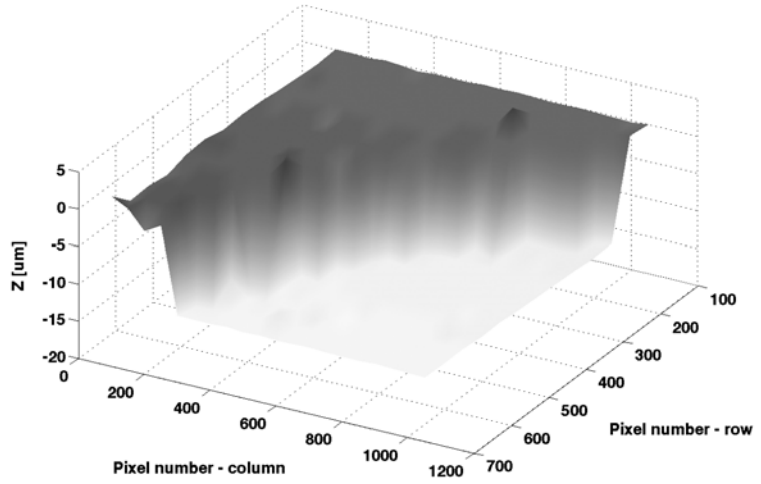

Fig. 2. Raw data of monitored sector of the hollow roundel recorded with ImagingSource CCD camera DFK 41BU02. The measured roundel depth is 12.01 µm.

For our experiments, we used two low-cost single CCD cameras. The first one was the webcam i-tec with ¼" SONY CCD sensor with resolution 1280 x 960 pixels (pixel size is 3.5 µm x 3.5 µm) and the second one was the ImagingSource CCD camera DFK 41BU02 with ½" SONY CCD sensor with resolution 1280 x 960 pixels (pixel size is 4.65 µm x 4.65 µm).

The main advantage of the ImagingSource camera against i-tec webcam is that the Y800 (RAW) image format is here in option. It means that uncompressed data from each single pixel are available and could be processed as needed.

By the anisotropic etching technique, the artificial surface with four hollow roundels (diameter about 10 mm) were made for the pilot experiment and Fig. 2 shows raw data of monitored sector of the hollow roundel. The measured roundel depth is 12.01 µm. This value was checked by a profile gauge TALYSTEP (Taylor Hudson) with the result 12.00 µm.

4 Conclusion

A pilot experiment of a white-light interference fringe analysis using the phase-crossing algorithm and a low-cost color CCD camera is described in this paper. We realized an experimental arrangement based on superluminescent LED diode. By the designed experimental arrangement, the hollow roundel depth was measured. The measured value 12.01 μm was succesfuly checked by a profile gauge TALYSTEP.

5 Acknowledgment

The authors wish to express thanks for support to the grant projects no. LC06007, 2C06012, KAN311610701, 2A-1TP1/127, FT-TA3/133, 2A-3TP1/113, GA102/07/1179, GP102/09/P293, GP102/09/P630, GA102/09/1276.

6 References

1. Fournoy, P A, McClure, R W, Wyntjes, G (1972) White light interferometric thickness gauge. Applied Optics 11:1907–1915
2. Yanli, D, Huimin, Y, Yongjun, N, Zhang, X, Zheng, M (2006) New data-processing technique for measurement of metallic foil thickness with differential white-light interferometry. Optics and Lasers in Engineering 45:240–244
3. Itoh, M, Tian, R, Yatagai, T (1992) Absolute measurement of 3-D shape using white light interferometer. Proceedings of SPIE 1755:24–28
4. Lee, B S, Strand, T, (2007) Profilometry with a coherence scanning microscope. Applied Optics 29:3784–3788
5. Hlubina, P, Gurov, I, Chugunov, V (2003) Slightly dispersive white-light spectral interferometry to measure distances and displacements. Optik 114:389–393
6. Ailing, T, Chunhui, W, Zhuangde, J, Hongjun, W, Bingcai, L (2008) Study on key algorthm for scanning white-light interferometry. Proceedings of SPIE 7155:71552N–1 - 71552N–8
7. Pawlowski, M E, Sakano, Y, Miyamoto, Y, Takeda, M (2006) Phase-crossin algorithm for white-light fringes analysis. Optics Communications 260:68–72

Design and assessment of Differential Phase-Shifting Algorithms by means of their Fourier representation

Marta Miranda and Benito V. Dorrío
Applied Physics Department, University of Vigo
Campus Universitario, 36310 Vigo
Spain

1 Introduction

Most metrology applications code data from what is being measured in the $\phi(\mathbf{r})$ phase of a two-dimensional fringe pattern $s(\mathbf{r},\phi,\alpha)$ that can be conveniently modulated with an additional phase α

$$s(\mathbf{r},\phi,\alpha)=\sum_{k=0}^{\infty}a_k(\mathbf{r})\cos\left[k\left(\phi(\mathbf{r})+\alpha\right)\right]=\sum_{k=0}^{\infty}\frac{a_k(\mathbf{r})}{2}\left[e^{jk[\phi(\mathbf{r})+\alpha]}+e^{-jk[\phi(\mathbf{r})+\alpha]}\right] \tag{1}$$

where a_0 refers to average local irradiance and a_1 is the modulation amplitude of the fundamental harmonic. The main values for phase $\phi(\mathbf{r})$ can be calculated with an appropriate composition of $M\geq 3$ irradiance values in the argument of an inverse trigonometric function

$$\phi(\mathbf{r})=\arctan\frac{N_1\{s_m(\mathbf{r},\phi,\alpha_m)\}}{D_1\{s_m(\mathbf{r},\phi,\alpha_m)\}}=\arctan\frac{\sum_{m=1}^{M}n_m s_m(\mathbf{r},\phi,\alpha_m)}{\sum_{m=1}^{M}d_m s_m(\mathbf{r},\phi,\alpha_m)}=\arctan\frac{\sum_{m=1}^{M}g_N(u_m)s_m(\mathbf{r},\phi,\alpha_m)}{\sum_{m=1}^{M}g_D(u_m)s_m(\mathbf{r},\phi,\alpha_m)} \tag{2}$$

where $N_1\{s_m(\mathbf{r},\phi,\alpha_m)\}$ and $D_1\{s_m(\mathbf{r},\phi,\alpha_m)\}$ are linear combinations of the irradiance values weighted by constants (n_m,d_m) that define the Phase Shifting Algorithm (PSA) [1] and that can also be expressed as a discretization of the irradiance signal with Sampling Functions $g_{N,D}(u_1)$ [1] at each point u_m where $\alpha_m=2\pi f_s u_m$ with f_s its fundamental frequency. In most cases values are obtained for the 2π module phase which need a further delicate unwrapping process [1] in order to obtain their continuous values.

But there are many other situations that require direct calculation of the phase difference $\Delta\phi(\mathbf{r})$ between the original pattern $s(\mathbf{r},\phi,\alpha)$ (see eq. 1) and another modified pattern $t_p(\mathbf{r},\phi+\Delta\phi,\beta)$ (with harmonic amplitudes b_g and

additional phase β_p). This phase difference $\Delta\phi(\mathbf{r})$ can be calculated by using PSAs – with $N_2\{t_p(\mathbf{r},\phi+\Delta\phi,\beta_p)\}$, $D_2\{t_p(\mathbf{r},\phi+\Delta\phi,\beta_p)\}$ and (n_p,d_p) similarly in eq. 2 – duplicating evaluation and unwrapping processes for this and subtracting the results obtained). However, $\Delta\phi(\mathbf{r})$ can be obtained directly if Differential Phase Shifting Algorithms (DPSAs) are used, and continuous values for the phase can even be recovered when this modification $\Delta\phi(\mathbf{r})$ does not reach a complete period. Of particular note for being computationally simple are Generic DPSAs (GDPSAs) whose design involves a non-linear combination of the irradiance arguments from their PSA predecessors – where the PSAs of the original and modified patterns can be different – in an inverse trigonometric function [2]:

$$\Delta\phi(r)=\arctan\frac{D_1\{s_m(\mathbf{r},\phi,\alpha_m)\}N_2\{t_p(\mathbf{r},\phi+\Delta\phi,\beta_p)\}-N_1\{s_m(\mathbf{r},\phi,\alpha_m)\}D_2\{t_p(\mathbf{r},\phi+\Delta\phi,\beta_p)\}}{N_1\{s_m(\mathbf{r},\phi,\alpha_m)\}N_2\{t_p(\mathbf{r},\phi+\Delta\phi,\beta_p)\}+D_1\{s_m(\mathbf{r},\phi,\alpha_m)\}D_2\{t_p(\mathbf{r},\phi+\Delta\phi,\beta_p)\}} \quad (3)$$

The potential of these algorithms is currently unknown [3], as is their sensitivity to the main sources of systematic error: calibration errors in the additional phases (α_m,β_p) and undesired appearance of harmonics in the signal (a_k, b_g with $k>1$ and $g>1$). This work proposes a qualitative characterisation of GDPSAs by following a similar procedure to that used for PSAs [4].

2 Frequential DPSA analysis

The heterodyne differential process that directly provides $\Delta\phi(\mathbf{r})$ can be described by a correlation quotient $H_{N,D}$ of the complex auxiliary function $s_m(\mathbf{r},\phi,\alpha_m)t_p(\mathbf{r},\phi+\Delta\phi,\beta_p)$ with each of the Differential Sampling Functions $g_{N,D}(u_1,u_2)$ in $M+P$ (with $M\geq 3$ and $P\geq 3$) values of

$$\arctan\frac{H_N}{H_D}=\arctan\frac{\sum_{m=1}^{M}\sum_{p=1}^{P}s_m(\mathbf{r},\phi,\alpha_m)\,t_p(\mathbf{r},\phi+\Delta\phi,\beta_p)g_N(u_m,u_p)}{\sum_{m=1}^{M}\sum_{p=1}^{P}s_m(\mathbf{r},\phi,\alpha_m)\,t_p(\mathbf{r},\phi+\Delta\phi,\beta_p)g_D(u_m,u_p)}+\Delta\phi_0 \quad (4)$$

where $u_{1,2}$ are the sampling values for the original and modified signals respectively, thus making it possible to express the modified additional step at the point analysed u_p as $\beta_p=2\pi f_t u_p$, where f_t is its reference frequency and $\Delta\phi_0$ indicates the possible distance from the first maximum of the complex auxiliary pattern to the origin of the coordinates where it was evaluated.

These correlations are moved to reciprocal space, using the central ordinate theorem and the convolution theorem and thus evaluating the required phase $\Delta\phi(\mathbf{r})$ at the origin $(f_1,f_2)=(0,0)$

$$TF\left[s_m(r,\phi,\alpha_m)t_p(r,\phi+\Delta\phi,\beta_p)\right]_{f_1=0,\,f_2=0} * TF\left[g_{N,D}(\alpha_m,\beta_p)\right]_{f_1=0,\,f_2=0} = \\ = \sum_{k=-\infty}^{\infty}\sum_{l=-\infty}^{\infty}\frac{a_k b_g}{2}\left[G^*_{N,D}(kf_s,gf_t)e^{j[k\phi+g(\phi+\Delta\phi)]} + G^*_{N,D}(-kf_s,gf_t)e^{j[-k\phi+g(\phi+\Delta\phi)]}\right] \tag{5}$$

thus $G_{N,D}(f_1,f_2)=|G_{N,D}(f_1,f_2)e^{j\gamma_{N,D}(f_1,f_2)}|$ filters certain spectral components of the signal. Eq. 5 can be valid for calculating both the sum phase $2\phi(\mathbf{r})+\Delta\phi(\mathbf{r})$ and the phase difference $\Delta\phi(\mathbf{r})$ between both patterns, in this latter case the Differential Characteristic Spectra $G_{N,D}(f_1,f_2)$ must meet the following conditions:

C1. They must not have continuous term: $G_{N,D}(0,0)=0$.

C2. Undesired harmonics must not interfere, nor for $\Delta\phi(\mathbf{r})$, $G_{N,D}(-kf_s,gf_t)=G_{N,D}(-kf_s,gf_t)=0$, nor for $2\phi(\mathbf{r})+\Delta\phi(\mathbf{r})$, $G_{N,D}(kf_s,gf_t)=G_{N,D}(kf_s,gf_t)=0$, in both cases for $k>1$ and $g>1$.

C3. They must cancel at (f_s,f_t).

C4. They must be orthogonal at $(-f_s,f_t)$: $G_N(-f_s,f_t)=G_D(-f_s,f_t)e^{\mp j\pi/2}$, i.e. $\gamma_D(-f_s,f_t)=\Delta\phi_0$ y $\gamma_N(-f_s,f_t)=\Delta\phi_0\pm\pi/2$.

C5. They must have equal magnitudes at $(-f_s,f_t)$: $|G_N(-f_s,f_t)|=|G_D(-f_s,f_t)|$.

Restricting ourselves to the case of Differential Phase Shifting Interferometry, where the original signal is uniformly sampled in a single signal period every $2\pi(m-1)/M$ and the modified one every $2\pi(p-1)/P$, the Differential Sampling Functions are defined by

$$g_N(u_1,u_2)=\sum_{m=1}^{M}\sum_{p=1}^{P} n_{m,p}\,\delta(u_1-u_m,u_2-u_p) \tag{6a}$$

$$g_D(u_1,u_2)=\sum_{m=1}^{M}\sum_{p=1}^{P} d_{m,p}\,\delta(u_1-u_m,u_2-u_p) \tag{6b}$$

whose transformation to reciprocal space provides the Differential Characteristic Spectra

$$G_N(f_1,f_2)=\sum_{m=1}^{M}\sum_{p=1}^{P} n_{m,p}e^{-j2\pi u_m f_1}\,e^{-j2\pi u_p f_2}=\sum_{m=1}^{M}\sum_{p=1}^{P} n_{m,p}e^{-j\alpha_m\frac{f_1}{f_s}}\,e^{-j\beta_p\frac{f_2}{f_t}} \tag{7a}$$

$$G_D(f_1, f_2) = \sum_{m=1}^{M}\sum_{p=1}^{P} d_{m,p} e^{-j2\pi u_m f_1}\, e^{-j2\pi u_p f_2} = \sum_{m=1}^{M}\sum_{p=1}^{P} d_{m,p} e^{-j\alpha_m \frac{f_1}{f_s}}\, e^{-j\beta_p \frac{f_2}{f_t}} \tag{7b}$$

where $(n_{m,p},d_{m,p})$ are the differential sampling amplitudes whose value can be derived from the othogonality condition (C4), with obligatory compliance to

$$\sum_{m=1}^{M}\sum_{p=1}^{P} \left(d_{m,p} \mp j n_{m,p}\right) e^{-j\alpha_m}\, e^{-j\beta_p} = 0 \tag{8}$$

To solve the equation system given in 8 the orthogonality condition must be resorted to, which maintains the sampling amplitudes of a GDPSA, to finally obtain

$$\sum_{m=1}^{M}\sum_{p=1}^{P} n_{m,p} = \mp \sum_{m=1}^{M}\sum_{p=1}^{P} sen\left(\beta_p - \alpha_m\right) \tag{9a}$$

$$\sum_{m=1}^{M}\sum_{p=1}^{P} d_{m,p} = \sum_{m=1}^{M}\sum_{p=1}^{P} \cos\left(\beta_p - \alpha_m\right) \tag{9b}$$

The previous conditions (C1-C5) tell us how some multi-frequential patterns affect calculation of the optical phase difference $\Delta\phi(\mathbf{r})$. In order to find out the influence of error in the calibration of additional phase shifters [5], we introduce the additional disturbed steps into the Differential Characteristic Spectra,

$${}^{E}\alpha_m = \alpha_m + E\alpha_m = \alpha_m + \sum_{q=1}^{\infty} \varepsilon_q \frac{\alpha_m^q}{q\pi^{q-1}} \tag{10a}$$

$${}^{E}\beta_p = \beta_p + E\beta_p = \beta_p + \sum_{r=1}^{\infty} \chi_r \frac{\beta_p^r}{r\pi^{r-1}} \tag{10b}$$

with ε_q and χ_r the error coefficients for the q^{th} and r^{th} terms for the original pattern $s_m(\mathbf{r},\phi,\alpha_m)$ and the modified one $t_p(\mathbf{r},\phi+\Delta\phi,\beta_p)$ respectively

$$
\begin{aligned}
{}^{E}G_{N,D}(f_1,f_2) = G_{N,D}(f_1,f_2) &+ \sum_{q=1}^{\infty} \varepsilon_q \frac{f_1 f_s^{\,q}}{q}\left(\frac{\mathrm{j}}{\pi}\right)^{q-1} \frac{\partial^q G_{N,D}(f_1,f_2)}{\partial f_1^{\,q}} + \\
&+ \sum_{r=1}^{\infty} \chi_r \frac{f_2 f_t^{\,r}}{r}\left(\frac{\mathrm{j}}{\pi}\right)^{r-1} \frac{\partial^r G_{N,D}(f_1,f_2)}{\partial f_2^{\,r}} + \\
&+ \sum_{q=1}^{\infty}\sum_{r=1}^{\infty} \frac{\varepsilon_q \chi_r}{qr} f_1 f_2 f_s^{\,q} f_t^{\,r}\left(\frac{\mathrm{j}}{\pi}\right)^{(q-1)(r-1)} \frac{\partial^r}{\partial f_2^{\,r}}\left(\frac{\partial^q G_{N,D}(f_1,f_2)}{\partial f_1^{\,q}}\right)
\end{aligned}
\tag{11}
$$

As we saw in condition C4 insensitivity to errors in the phase step is influenced by the orthogonality that must be maintained at $(-f_s,f_t)$. By applying this condition to the Characteristic Spectra with error, we obtain

$$
\begin{aligned}
&[G_N(-f_s,f_t) + jG_D(-f_s,f_t)] + \sum_{q=1}^{\infty}\left(\frac{j}{\pi q}\right)^{q-1} \varepsilon_q f_s^{\,q+1}\left[\left.\frac{\partial^q G_N(f_1,f_2)}{\partial f_1^{\,q}}\right|_{(-f_s,f_t)} + j\left.\frac{\partial^q G_D(f_1,f_2)}{\partial f_1^{\,q}}\right|_{(-f_s,f_t)}\right] + \\
&+ \sum_{r=1}^{\infty}\left(\frac{j}{\pi r}\right)^{r-1} \chi_r f_t^{\,r+1}\left[\left.\frac{\partial^r G_N(f_1,f_2)}{\partial f_2^{\,r}}\right|_{(-f_s,f_t)} + j\left.\frac{\partial^r G_D(f_1,f_2)}{\partial f_2^{\,r}}\right|_{(-f_s,f_t)}\right] + \\
&+ \sum_{q=1}^{\infty}\sum_{r=1}^{\infty} \varepsilon_q \chi_r \frac{f_1 f_2 f_s^{\,q} f_t^{\,r}}{qr}\left(\frac{j}{\pi}\right)^{(q-1)(r-1)}\left[\left.\frac{\partial^r}{\partial f_2^{\,r}}\left(\frac{\partial^q G_N(f_1,f_2)}{\partial f_1^{\,q}}\right)\right|_{(-f_s,f_t)} + j\left.\frac{\partial^r}{\partial f_2^{\,r}}\left(\frac{\partial^q G_D(f_1,f_2)}{\partial f_1^{\,q}}\right)\right|_{(-f_s,f_t)}\right] = 0
\end{aligned}
\tag{12}
$$

that is, it must be that for arbitrary values of ε_q and χ_r the Differential Characteristic Spectra, besides having coinciding values at the reference frequency $(-f_s,f_t)$ (C5), must also have them at their respective q^{th} and r^{th} partial derivatives and at their cross derivatives.

Errors in the steps (α_m,β_p) can lead to the appearance of undesired high order harmonics in the signal, thus if conditions C1 and C2 are considered, then the disturbed multi-frequential Characteristic Spectra (see eq. 11) should be cancelled at frequency zero and at the k-harmonics and g-harmonics of the fundamental frequency $(-f_s,f_t)$, which in this latter case means not only the cancellation of the Differential Characteristic Spectra but also of their partial derivatives.

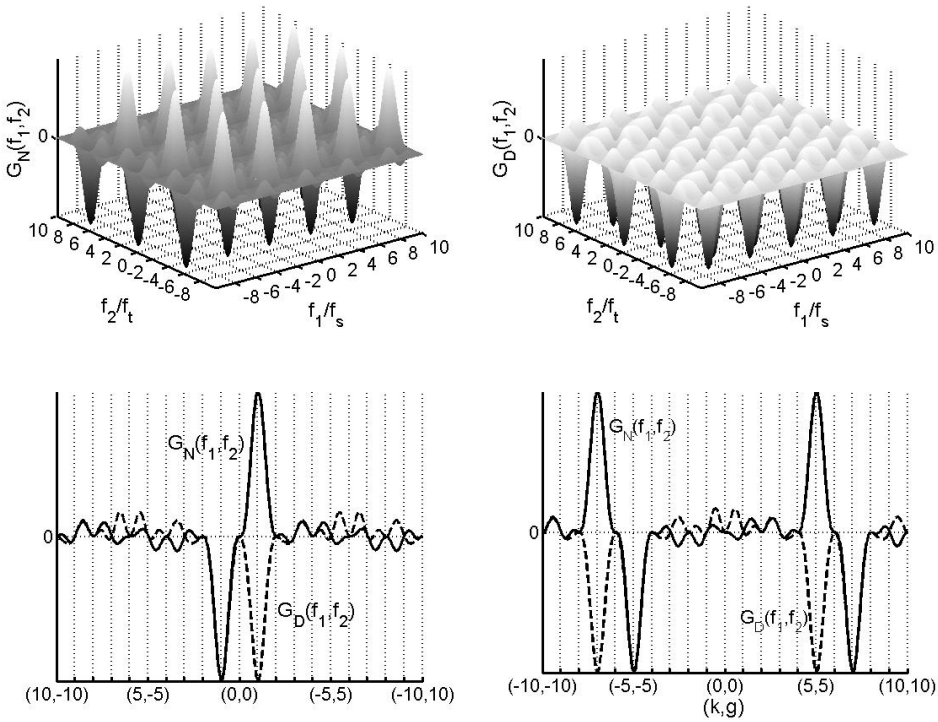

Fig. 1. Differential Characteristic Spectra for the Schwider-Hariharan – Symmetrical 6+1 GDPSA (above) with diagonal cross-section (below) according to $N_1=2(s_2-s_4)$, $D_1=2s_3-s_1-s_5$, $N_2=-\sqrt{3}(t_2+t_3-t_5-t_6)$ and $D_2=t_1+t_2-t_3-2t_4-t_5+t_6+t_7$ (see eq. 3).

By way of example, Figure 1 shows the Schwider-Hariharan [6] – 6+1 Symmetrical [6] GDPSA where the first undesired harmonic contribution at $\Delta\phi(\mathbf{r})$ is to third order for, although $G_{N,D}(-f_1,f_2)$ are null at $(k,g)=(-3,3)$ (C2), their partial derivatives are not so, with regard to the harmonics of $2\phi(\mathbf{r})+\Delta\phi(\mathbf{r})$ now at first order, they interfere in the calculation of $\Delta\phi(\mathbf{r})$ and an immunity to harmonic pairs can be observed in both cases. The error does not inherit the Schwider-Hariharan GPSA compensation as, although they are orthogonal at all frequencies, including $(-f_s,f_t)$ (C4), they do not have equal magnitudes at $(-f_s,f_t)$ (C5).

3 Conclusions

Fourier analysis is presented as a powerful error characterisation and design tool for errors associated with GDPSAs. New conditions related with main error sensibilities are obtained

4 Acknowledgments

The authors are grateful for funding received from Xunta de Galicia (07DPI002CT) and Ministerio de Ciencia e Innovación (DPI2008-06818-C2-01/DPI).

5 References

1. Dorrío, BV, Fernández, JL (1999) Phase-evaluation methods in whole-field optical measurement techniques. Meas. Sci. Technol 10:33-35.
2. Huntley, JM (1998) Automated fringe pattern analysis in experimental mechanics: a review. J. Strain Anal. 33:105-125
3. Miranda, M, Dorrío, BV (2008) Error behaviour in Differential Phase-Shifting Algorithms. SPIE: Optical Fabrication, Testing, and Metrology III 7102:71021B-1-71021B-9
4. Freischlad, K, Koliopoulos, CL (1990) Fourier description of digital phase-measuring interferometry. J. Opt. Soc. Am. A 7:542-551
5. Hibino, K (1999) Error-Compensating Phase Measuring Algorithms in a Fizeau Interferometer. Opt. Rev. 6:529-538
6. 6. Malacara, D, Servín, M, Malacara, Z (2005) Interferogram Analysis for Optical Testing. Taylor&Francis Group: Florida.

A Nonlinear Technique for Automatic Twin-Image and Zero-Order Term Suppression in Digital Holographic Microscopy

Nicolas Pavillon[1], Chandra Sekhar Seelamantula[2], Michael Unser[2], and Christian Depeursinge[1]
[1]Advanced Photonics Laboratory, [2]Biomedical Imaging Group, Ecole Polytechnique Fédérale de Lausanne (EPFL), 1015 Lausanne, Switzerland

1 Introduction

Digital holography enables the encoding of complex wavefronts with an intensity measurement, making it possible to recover the quantitative phase for phase-contrast imaging [1] or profilometry [2]. Encoding the wavefront in this fashion leads, however, to the generation of artifacts such as the so-called zero-order, which is the sum of the intensities of the object and reference waves, and the so-called twin-image, which corresponds to the complex conjugate of the desired imaging order.

Since the first developments, efforts have been made to suppress the artifacts either by separation in the spatial Fourier domain in the so-called off-axis configuration [3], or by temporal separation through phase-shifting algorithms [4]. The spatial separation method has the advantage of making it possible to reconstruct the hologram from a single measurement, but at the cost of loss of bandwidth for the imaging terms.

We propose here a technique based on non-linear filtering to suppress the zero-order artifact for off-axis digital holographic microscopy (DHM). The advantages of the proposed method are: (1) it can potentially increase the spatial bandwidth for the imaging terms; (2) it is non-iterative; and (3) it keeps the one-shot feature of DHM.

2 Principle

The technique is based on the use of a non-linear operator during hologram filtering. The fundamental equation of interference on a detector is:

$$i = (r+o)(r+o)^* = |o|^2 + |r|^2 + r^* o + r o^* , \qquad (1)$$

where all functions are defined in the (x, y) plane, r is the reference wave, o is the object wave, and $(*)$ denotes the complex conjugate.

By rearranging the terms in Eq. 1, and using the logarithm operator, we get that:

$$\ln\left[\frac{i}{|r|^2}\right] = \ln\left[1+\frac{o}{r}\right] + \ln\left[\left(1+\frac{o}{r}\right)^*\right]. \tag{2}$$

It can be shown that under the condition that the reference intensity is stronger than that of the object, the spectral supports of the two terms on the right-hand side of Eq. 2 are non-overlapping. This implies that the wavefront reconstruction method based on Fourier filtering [5] can be employed, by applying it to the so-called *cepstrum* domain [6]. The reconstruction equation for the object wavefront becomes:

$$\begin{aligned} o'(x,y) &= C \cdot D(x,y) \cdot \left[\exp\left(i'_F\right) - 1\right], \\ i'_F &= F^{-1}\left\{F\left\{\ln\left[\frac{i(x,y)}{|r(x,y)|^2}\right]\right\} \cdot W\left(\omega_x, \omega_y\right)\right\}, \end{aligned} \tag{3}$$

where F is the Fourier transform operator, C is a real constant, and $W\left(\omega_x, \omega_y\right)$ is a window function in the spectral domain. The variable $D\left(x, y\right)$ is a phase mask for hologram demodulation.

One can observe from Eq. 3 that the knowledge of the reference intensity is required. It is either possible to use a measurement of the reference by blocking the object wave, or by employing a model such as a plane wave as an estimator of the reference wave. For practical reconstruction, a discrete version of Eq. 3 is implemented.

3 Experimental results

In order to demonstrate the performance of the method, we made measurements on a transmission DHM setup, employing a Mach-Zehnder interferometer. The sample, a solution containing yew pollens, is illuminated with a laser diode (λ = 652.5 nm), and the image is recorded in the Fresnel zone with an 8-bit charge-coupled device (CCD) camera ($\Delta x = 6.45$ μm) with 10x magnification. The hologram is reconstructed with the standard spatial filtering method applied to a quadrant of the image, as well as with the non-linear technique. The complex wavefront is

then digitally propagated into focus (d = 4.4 cm) with a numerical implementation of the Fresnel integral.

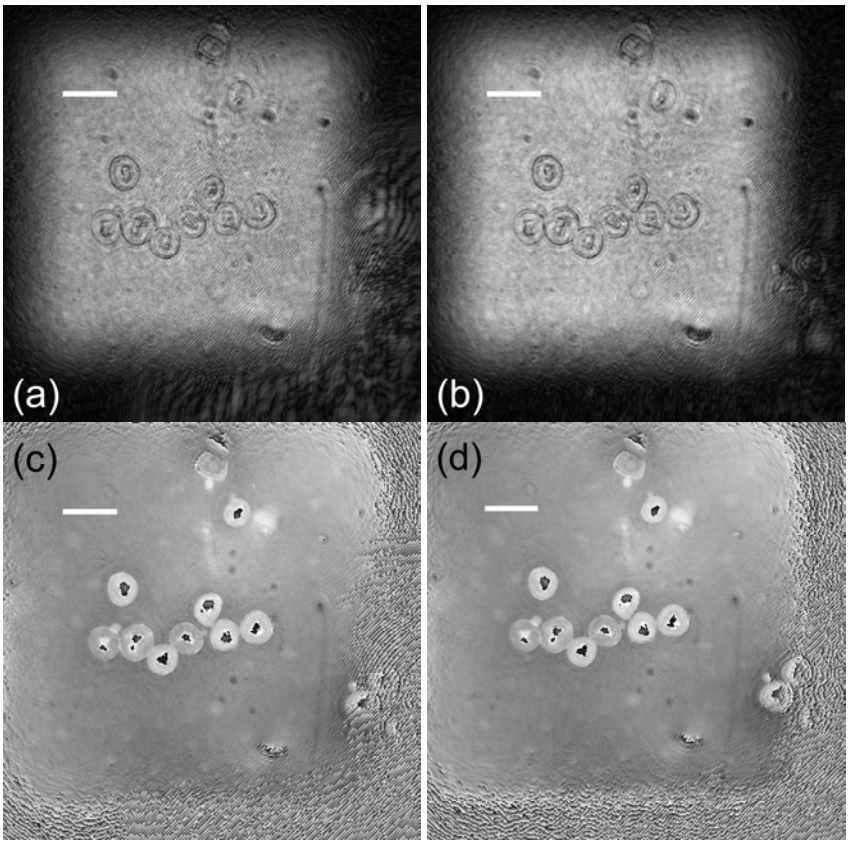

Fig. 1. Image of a yew pollens hologram reconstructed with (a, c) standard spatial filtering and (b, d) non-linear method, where artefacts at the bottom right are suppressed both in amplitude (a, b) and in phase (c, d) images. The scale bars are 20 μm long.

The intensity ratio is controlled by using a neutral density filter in the path of the object arm of the interferometer. The mean of the reference intensity divided by the object intensity in this case is 12.1. The reconstructions are shown in Fig. 1, for the standard method (Fig. 1.(a, c)) and the non-linear technique (Fig. 1.(b, d)), respectively. The suppression of the residues of the zero-order can be readily identified in both amplitude (Fig. 1.(a, b)) and phase (Fig. 1.(c, d)) at the bottom-right of the images. Some remnants of the zero-order are still present in the reconstruction, because of quantization and measurement noise.

4 Conclusion

We presented the principle of a new non-linear filtering method for artifact-free reconstruction in digital holography. This method intrinsically suppresses the so-called zero-order, and thus increases the available bandwidth for the imaging orders in off-axis holography. We provided experimental results to validate the technique.

5 Acknowledgements

N. Pavillon and C. Depeursinge were supported by the Swiss National Science Foundation (SNSF) grant #205320-120118. C.S. Seelamantula and M. Unser were supported by the Center for Biomedical Imaging (CIBM) of the Geneva-Lausanne universities and the EPFL, Hasler, Leenards, and Louis-Jeantet foundations. The authors would like to thank their colleagues in the MVD Group and at Lyncee Tec SA (www.lynceetec.com) for their cooperation and fruitful discussions.

6 References

1. Marquet, P, Rappaz, B, Magistretti, P J, Cuche, E, Emery, Y, Colomb, T, Depeursinge, C (2005) Digital holographic microscopy: a noninvasive contrast imaging technique allowing quantitative visualization of living cells with subwavelength axial accuracy. Optics Letters 30:468-470
2. Schnars, U, Jüptner, W P O (2002) Digital recording and numerical reconstruction of holograms. Measurement Science and Technology 13:R85-R101
3. Leith, E N, Upatnieks, J (1962) Reconstructed Wavefronts and Communication Theory. Journal of the Optical Society of America 52:1123-1130
4. Yamaguchi, I, Zhang, T (1997) Phase-shifting digital holography. Optics Letters 22:1268-1270
5. Cuche, E, Marquet, P, Depeursinge, C (1999) Simultaneous amplitude-contrast and quantitative phase-contrast microscopy by numerical reconstruction of Fresnel off-axis holograms. Applied Optics 38:6994-7001
6. Oppenheim, A V, Schafer, R W (2004) From frequency to quefrency: a history of the cepstrum. Signal Processing Magazine, IEEE 21:95-106

Modified two-step phase-shifting algorithm: analysis, demonstration, and application

Xiang-Feng Meng[1], Xiang Peng[1], Lu-Zhong Cai[2], A-Meng Li[1], Ji-Ping Guo[1], Yu-Rong Wang[2]
[1]Key Laboratory of Optoelectronics Devices and Systems of Education Ministry of China, Shenzhen University, Shenzhen, 518060, P. R. China
[2]Department of Optics, Shandong University, Jinan, 250100, P. R. China

1 introduction

As a powerful means of accurate phase measurements, phase-shifting interferometry (PSI) has been applied in many fields of optical non-contact and non-destructive testing. Conventional phase-shifting algorithms require a minimum of three fringe patterns shifted in phase with respect to one another [1, 2].

To simplify the computation process, Wizinowich developed a two-plus-one (2 + 1) phase-shifting algorithm, in which two fringe patterns with $\pi/2$ phase shift are captured, and a third flat image is collected which is the average of two patterns with a phase shift of π [3]. Recently Zhang et al. have modified 2 + 1 algorithm and applied for fringe projection system, in which the 3rd pattern is directly captured instead of indirectly averaging two π-phase-shifted images [4]. Recently, Yang *et al* utilized two deformed fringe patterns with a phase-shift increment of $\pi/2$ to measure the 3-D object shape [5]; Quan et al. proposed a method in which two π-phase-shifted patterns are used in fringe projection system [6].

Independently, we have proposed a two-step algorithm in PSI [7, 8], however, the following two additional measurements are needed: (1) measuring the intensities of both object wave and reference wave [8], (2) measuring the reference wave intensity and then solving a related equation [7]. In this paper, we will address this issue by modifying and improving the two-step phase-shifting algorithm mentioned above, in which only two phase-shifted fringe patterns with removal of direct current (DC) component and an arbitrary phase shift δ ($0 < \delta < \pi$) can be utilized.

2 Theoretical analysis

In general, two interferograms I_1 and I_2 with a phase-shift increment of δ ($0 < \delta < \pi$) in PSI can be written as [7]

$$I_1(x, y) = A_o^2(x, y) + A_r^2(x, y) + 2A_o(x, y)A_r(x, y)\cos\varphi(x, y), \tag{1}$$

$$I_2(x, y) = A_o^2(x, y) + A_r^2(x, y) + 2A_o(x, y)A_r(x, y)\cos[\varphi(x, y) - \delta], \tag{2}$$

where $A_o(x, y)$ and $A_r(x, y)$ represent the amplitudes of object wave and the reference wave, respective, $\varphi(x, y)$ is the phase distribution of the object wave. After some deduction shown in Ref. 7, the reconstructed complex amplitude $U'(x, y)$ can be expressed as

$$U'(x, y) = \frac{I_1 - a}{2A_r} + i\frac{(I_2 - a) - \cos\delta(I_1 - a)}{2A_r \sin\delta}, \tag{3}$$

where $a(x, y) = A_o^2(x, y) + A_r^2(x, y)$, is the sum of object wave intensity and reference wave intensity, represents the DC term or background intensity of the interferograms.

The DC term $a(x, y)$ can be obtained by direct measurement (measuring the intensities of both two waves [8], the background intensity [4], etc.) or indirect measurement (introducing a third π-phase-shifted intensity [3], measuring the reference wave intensity and then solving a related equation [7], etc.), however, these operations mentioned all increase greater experimental effort due to the additional measurements required. Therefore, to avoid the aid of additional measurements and increase the convenience in optical experiments, here we introduce two methods to extract the DC term $a(x, y)$ from the two intensities I_1 and I_2:

(1) Averaging technique in the spatial domain [9]

Since the third terms in Eq. (1) and (2) is statistically varying between $\pm 2A_oA_r$ from pixel to pixel in the CCD, by employing an average operation in spatial domain, the average intensity I_{1a} or I_{2a} can be regarded as the DC term a [9]

$$a = I_{ia} = \frac{1}{MN}\sum_{n=0}^{N-1}\sum_{m=0}^{M-1} I_i(m\Delta x, n\Delta y), \quad i = 1,2; \quad m = 0,1...M-1, \quad n = 0,1...N-1 \tag{4}$$

where Δx and Δy are the pixel sizes in horizontal and vertical directions, respectively, M and N denote the corresponding pixel numbers [9].

(2) Low-pass filtering technique in the frequency domain [10]

The other way to extract the DC term a is the low-pass filtering technique in the frequency domain, which consists of the following steps [10]: (a) Calculate $F(u, v)$, the discrete Fourier transform (DFT) of the input intensity $I(x, y)$; (b) multiply $F(u, v)$ by a low-pass filter function $H(u, v)$; (c)compute the inverse Fourier transform (IFT) of the result in (b); (d) extract the real part of result in (c), and then obtain the DC term $a(x, y)$.

Two common types of low-pass filter: ideal and hanning filter are introduced here. A 2-D ideal low-pass filter (ILPF) is the simplest low-pass filter, and its filter function can be expressed as [10]

$$H(u, v) = \begin{cases} 1 & \text{if } D(u, v) \le D_0 \\ 0 & \text{if } D(u, v) > D_0 \end{cases} \tag{5}$$

where, $D(u, v)$ is the distance from point (u, v) to the center of the Fourier frequency, and D_0 is a specified nonnegative quantity.

In a 2-D hanning filter, the hann filter function of which can be expressed below

$$H(u,v) = 0.25\left[1-\cos\left(\frac{2\pi u}{K}\right)\right]\left[1-\cos\left(\frac{2\pi v}{L}\right)\right], \quad 0 \le u \le K-1, \;\; 0 \le v \le L-1, \tag{6}$$

where, both K and L are specified nonnegative quantities, denote the window widths of the filter in horizontal and vertical directions, respectively.

After obtain the DC term $a(x, y)$ by the averaging or filtering techniques mentioned above, we can subtract this result a from each stored intensity value, yielding the DC-term-suppressed phase-shifted intensities $I_{1s} = I_1 - a$ and $I_{2s} = I_2 - a$, respectively, therefore, the complex amplitude $U'(x, y)$ in Eq. (3) can be rewritten as

$$U'(x,y) = \frac{I_{1s}}{2A_r} + i\frac{I_{2s} - I_{1s}\cos\delta}{2A_r \sin\delta}, \tag{7}$$

where, A_r exists only in denominators, and it has no essential effect on the wavefront reconstruction. The corresponding wrapped phase information can be expressed as

$$\Phi'(x,y) = \tan^{-1}\left(\frac{I_{2s}}{I_{1s}\sin\delta} - \cot\delta\right), \tag{8}$$

from Eqs. (7) and (8), we can see that the object field can be successfully retrieved by using only two DC-term-suppressed intensities with arbitrary phase shift δ ($0 < \delta < \pi$), not using the additional intensity(s) to be measured any more.

3 Computer simulations

In case of phase-shifting digital holography, a series of computer simulations have been made to test the effectiveness of our proposed method. An irregular wavefront with uniform amplitude and the optical path function

$$W(x,y) = 3(x+10\Delta x)[(x-60\Delta x)^2 + (y+5\Delta y)^2] - 4.375\times10^{-4}(x-400\Delta x) - 1.438\times10^{-4}(y+200\Delta y) \tag{9}$$

is generated as the test object information in the object plane (x, y), where arg [·] is a phase extraction operator; $k = 2\pi/\lambda$. All the images in this simulation have $M \times N = 511 \times 511$ pixels of 256 gray levels, the other system parameters are $\lambda = 632.8$ nm, $\delta = \pi/4$, $\Delta x = \Delta y = 60$ μm.

In Fig. 1(a) we show the phase map φ of the original object wavefront, after simulating the process of two-step PSI with a constant A_r according to Eq. (1) and (2), two generated interferograms (I_1, I_2) are shown in Figs. 1(b) and (c), respectively. According to the averaging technique in spatial domain, two DC terms of interferograms I_1 and I_2 can be computed by the algorithm described in Eq. (4), subtracting DC term from each interferograms yields two dc-term-suppressed interferograms I_{1s} and I_{2s}, which are shown in Figs. 1(d) and (e), respectively. The reconstructed wrapped phase is displayed in Fig. 1(f), the CC (correlation coefficient) [8] between this retrieved phase and the original one in Fig. 1(a) is as high as 0.996, it is obvious that the modified two-step phase-shifting algorithm can retrieve the original wavefront without doubt.

4 Optical experiments

We made an optical experiment to measure the 3-D shape of a telephone by sinusoidal fringe projection technique. Two π/2-phase-shifted sinusoidal fringes generated by a computer are loaded into a projector (SAMSUNG SP400, 800 × 600), and projected onto the surface of a telephone to be tested, then a CCD camera (Imagingsource DMK21BF04, 640 × 480) is used to capture the two reflected fringe patterns I_1 and I_2, which are shown in Figs. 2(a) and (b) (only the useful central parts) respectively. The two corresponding Fourier spectrums after log transform [10] are shown in Figs. 2(c) and (d), respectively, a 2-D 64 × 64 hanning filter is utilized to extract the DC term, and the filtered results in the frequency domain are given in Figs. 2(e) and (f), respectively. After IFT, and subtraction operation, two DC-term-suppressed intensities I_{1s} and I_{2s}

are obtained and displayed in Figs. 2(g) and (h), respectively. Following the procedures of wavefront reconstruction, phase extraction, phase unwrapping, system calibration, Gaussian smooth and noise reduction, Fig. 3 shows the recovered 3-D geometry in wireframe mode, evidently, the 3-D shape can be well acquired by the modified two-step phase-shifting algorithm.

5 Conclusion

In conclusion, we have modified and improved the two-step phase-shifting algorithm, in which, only two DC-term-suppressed intensities are required to realize wavefront reconstruction and 3-D shape measurement. The advantages of this method lie in its simplicity, increase in processing, and decrease storage burden.

6 Acknowledgement

This work is supported by the National Natural Science Foundation of China (grant 60775021 and 60777008), and China postdoctoral Science Foundation funded project.

7 References

1. Yamaguchi, I, Zhang, T (1997) Phase-shifting digital holography. Optics Letters 22: 1268-1270
2. Quan, C, He, X, Y, Wang, C, F, Tay, C, J, Shang, H, M (2001) Shape measurement of small objects using LCD fringe projection with phase shifting. Optics Communications 189: 21-29
3. Wizinowich, P, L (1990) Phase shifting interferometry in the presence of vibration: a new algorithm and system. Applied Optics 29: 3271-3279
4. Zhang, S, Yau, S, T (2007) High-speed three-dimensional shape measurement system using a modified two-plus-one phase-shifting algorithm. Optical Engineering 46: 113603
5. Yang, F, J, He, X, Y (2007) Two-step phase-shifting fringe projection profilometry: intensity derivative approach. Applied Optics 46: 7172-7178

6. Quan, C, Y, Tay, C, J, Kang, X, He, X, Y, Shang, H, M (2003) Shape measurement by use of liquid-crystal display fringe projection with two-step phase shifting. Applied Optics 42: 2329-2335
7. Meng, X, F, Cai, L, Z, Xu, X, F, Yang, X, L, Shen, X, X, Dong, G, Y, Wang, Y, R (2006) Two-step phase-shifting interferometry and its application in image encryption. Optics Letters 31: 1414-1416
8. Meng, X, F, Cai, L, Z, Wang, Y, R, Yang, X, L, Xu, X, F, Dong, G, Y, Shen, X, X, Cheng, X, C (2008) Wavefront reconstruction by two-step generalized phase-shifting interferometry. Optics Communications 281: 5701-5705
9. Schnars, U, Jüptner, W (2002) Digital recording and numerical reconstruction of holograms. Measurement Science and Technology 13: R85-R101
10. Gonzalez, R, C, Woods, R, E (2002) *Digital image processing (2nd edition)*, Prentice Hall

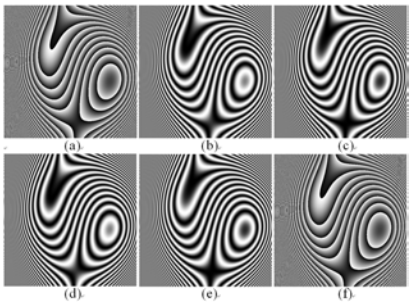

Fig. 1. (a) Phase map of the original object wave; (b) and (c) interferograms I_1 and I_2, respectively; (d) and (e) DC-term-suppressed interferograms I_{1s} and I_{2s}, respectively; (f) retrieved wrapped phase map.

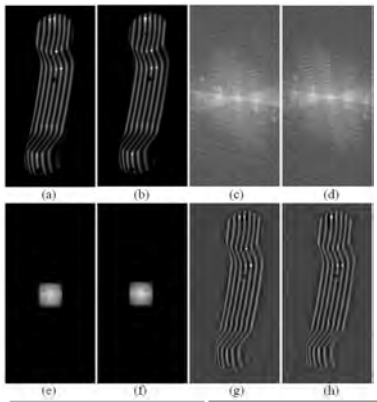

Fig. 2. 3-D shape measurement of a telephone: (a) and (b) captured two phase-shifted sinusoidal fringe pattern images I_1 and I_2; (c) and (d) Fourier spectrums of (a) and (b), respectively; (e) and (f) the filtered DC-term in the frequency domain by hanning filter technique; (g) and (h) two DC-term-suppressed phase-shifted patterns I_{1s} and I_{2s}.

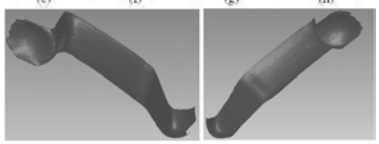

Fig. 3. Experimental results using the proposed method: some typical 3-D geometries of the telephone in wireframe mode

.

The Used of Reference Wave for Diagnostics of Phase Singularities

Oleg V. Angelsky, Alexander P. Maksimyak, Peter P. Maksimyak
Department of Correlation Optics, Chernivtsi National University
2 Kotsyubinsky St., Chernivtsi 58012
Ukraine

1 Introduction

Scattering of coherent optical radiation of inhomogeneous objects and media leads to formation of complex spatial distribution of the field due to interference imposing of partial waves with random amplitudes and phases. Intensity distributions of such fields are referred to as speckle-patterns [1]. The points where amplitude of the field equals zero and, as a consequence, the phase is undetermined are present at the transversal cross-section of such field. These points are referred to as the phase singularities, or amplitude zeroes, or optical vortices [2,3].

Imposing of the off-axis coherent reference wave on the studied field (the interference technique) is the reliable tool for diagnostics of amplitude zeroes [4]. Interference fringe at the vicinity of amplitude zero bifurcates and forms so-called interference “forklet” that is easily diagnosed visually. However, detection of amplitude zeroes by locations of interference forklets at complex speckle fields is complicated and is hardly automated. Furthermore, the forklet is shifted in respect of the amplitude zero point by a half-period of the interference pattern.

We propose the optical correlation techniques for diagnostics of amplitude zeroes at the fields scattered by random rough surfaces.

2 Modeling

We have carried out the computer simulation and physical modeling of optical fields with the phase singularities scattered by a rough surface, which is the most instructive example of light-scattering objects. Heights of inhomogeneities of random object have been specified by the generator of random digits with the Gaussian distribution. To provide good approximation of the modeled at the computer random surfaces to the real

ones we use the procedure of two-dimensional smoothing of height inhomogeneities by the Gaussian law with various dispersions [5].

Amplitude and phase distributions of the field resulting from scattering of a plane wave at the phase relief of a rough surface can be found using the double Rayleigh-Sommerfeld diffraction integral [6].

At the center of the optical vortex intensity of the field vanishes. That is why, it seems that measuring of the field intensity is a simple and reliable technique for determination of the vortex coordinates. However, such measurements are not unambiguous, while the field contains the points where intensity approaches zero but the phase does not undergo singularity (intensity distribution $I(x,y)$ in Fig. 1a. Experimental discrimination of such points from the zero amplitude points is difficult. For example, the coordinate distribution of the intensity minima for the field represented in Fig. 1a is shown in Fig. 1b.

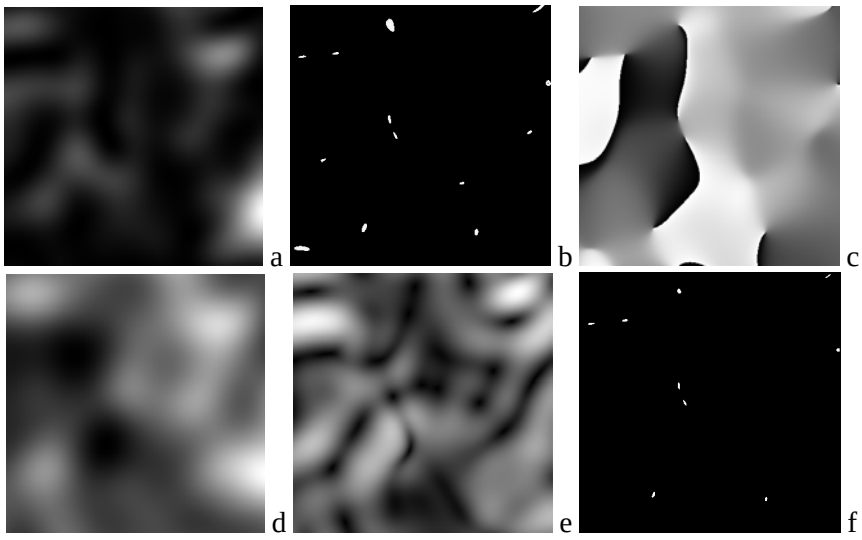

Fig. 1. Distributions of the parameters of the field scattered at rough surface: intensity distribution $I(x,y)$ a); coordinate distribution of intensity minima (b); phase distribution $\Phi(x,y)$ (c); intensity distribution of the resulting field $U(x,y)+U_0$ (d); distribution of the intensity gradient modulus of the resulting field $\left|\nabla\left|U(x,y)+U_0\right|^2\right|$ (e); coordinate distribution of the phase singularities $S(x,y)$ (f).

Analyzing the phase distribution of this field, $\Phi(x,y)$, (Fig. 1c) one can see that the number of intensity minima is larger (13) than the number of singular points (9).

For determination of the amplitude zero coordinates we impose at the optical field $U(x,y)$ strictly coaxial reference wave U_0 (Fig. 1 d). Phase delay between the fields in this case can be arbitrary. As a result, non-zero gradient of intensity arises at the amplitude zero points, while intensity gradient at the intensity minima points without phase singularity is in practice zero (Fig. 1 e). For pixel-by-pixel division of the distribution of the resulting field gradient by the intensity of the input field one obtains the maximal magnitudes of the distribution:

$$F(x,y)=\frac{\left|\nabla\left|U(x,y)+U_0\right|^2\right|}{I(x,y)}. \tag{1}$$

Normalizing this function by its maximal value,

$$F^n(x,y)=\frac{F(x,y)}{F_{max}}, \tag{2}$$

and using the condition

$$S(x,y)=\begin{cases}1, (F(x,y)+\delta\geq 1)\\ 0, (F(x,y)+\delta<1)\end{cases} \tag{3}$$

provide obtaining of the coordinate distribution of amplitude zeroes (Fig. 1f), which strictly coincides with the amplitude zero distribution obtaining from the phase distribution in Fig. 1c. Here δ is a noise of CCD-camera in experiment or computing errors in computer simulation. Increasing δ results in increasing the area within which the coordinates of amplitude zero lie.

The considered above technique for diagnostics of amplitude zeroes occurs applicable also out of the validity of the model on infinite random phase object, *viz.* in the case of limited aperture.

Determining the coordinate distribution of phase singularities occurs useful in the problem of recognition of strongly scattered objects. So, in the intensity distribution of a field (size 3x3 mm^2) scattered by a strongly rough surface (size 1x1 mm^2) and registered at the distance 40 mm from the object within its geometrical shadow the contours of the objects are not visualized (Fig. 2a).

We have established that the distribution of amplitude zero density at the field with coaxially imposed plane reference wave provides visual diagnostics of the object contours (Fig. 2b).

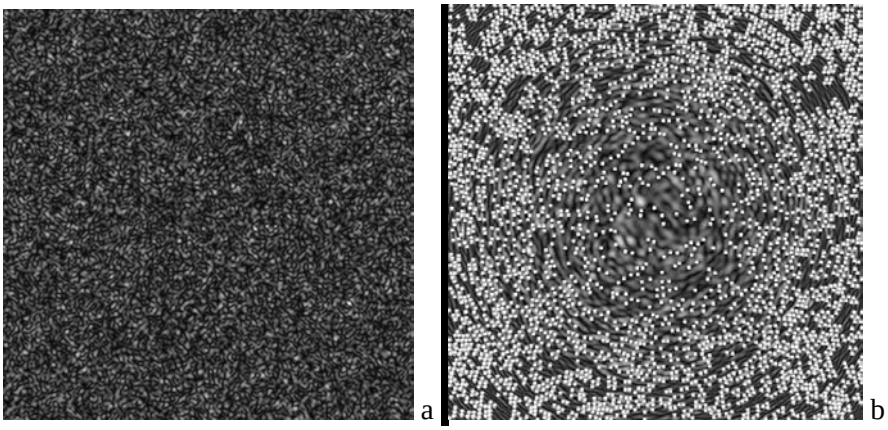

Fig. 2. Intensity distribution of the field (a), distribution of amplitude zero density at the field with coaxially imposed plane reference wave (b).

3 Conclusions

Thus, the coordinate distribution of the phase singularities at the field with coaxially imposed reference wave provides visualization of strongly scattering objects.

4 References

1. Golgfischer, L.I, (1975) Laser speckle and Related Phenomena J. Opt. Soc. Am. 55: 247
2. Nye, J.F, Berry, M (1974) Dislocations in wave trains. Proc. R. Soc. Lond. A 336: 165-190
3. Nye, J.F, (1981) The motion and structure of dislocations in wave fronts Proc. R. Soc. Lond. A 378: 219-239
4. Baranova, N.B, Mamayev, A.V, Pilipetsky, N.F, Shkunov, V.V, Zeldovich, B.Ya (1983) Wavefront dislocations: topological limitations for adaptive systems with phase conjugation J. Opt. Soc. Am. A73: 525-528,.
5. Angelsky, O. V, Maksimyak. P. P, Hanson, S (1999) The Use of Optical-Correlation Techniques for Characterizing Scattering Object and Media, Bellingham: SPIE Press PM71: 194 p
6. Angelsky, O. V, Maksimyak. P. P, Ryukhtin, V.V Hanson, S (2001) New Feasibilities for Characterizing Rough Surfaces by Optical-Correlation Techniques Applied Optics 40: 5693-5707

New convolution algorithms for reconstructing extended objects encoded in digitally recorded holograms

Pascal Picart[1], Patrice Tankam[1], Denis Mounier[2], Zu-jie Peng[1], Jun-chang Li[1]
[1]LAUM CNRS, Université du Maine, Avenue Olivier Messiaen, 72085 LE MANS Cedex 9, France
[2]LPEC CNRS, Université du Maine, Avenue Olivier Messiaen, 72085 LE MANS Cedex 9, France

1 Introduction

In digital holography, the numerical reconstruction of the object encoded using optical interferences is usually based on the discrete version of the Fresnel transform, on the computation of the convolution formula of diffraction [1-2] or on the angular spectrum method [3]. The discrete Fresnel transform is very well adapted to large objects, i.e. objects with lateral dimensions quite greater than that of the recording area. With this method, the sampling pitches in the reconstructed plane depend on the wavelength of the light used for the recording, on the diffraction distance and on the dimension of he reconstructed field. However, such algorithm is not suitable for digital color holography except if one uses a zero padding adapted to the wavelength [4]. With convolution, the field of view conserves the same physical dimension as that of the recording. Thus this approach is limited to very small objects and a convolution algorithm designed for large object has not been proposed in the literature. This paper proposes two new alternative algorithms based on the convolution approach, and allowing the reconstruction of a large object size variety.

2 Principle of the algorithms

The algorithms are based on the use of a virtual spherical wave as a reconstructing wave whereas classically a plane wave is considered. So, the reconstruction distance d_R that must be put into the algorithm is modified and depends on the physical distance between object and sensor

and on the curvature radius of the virtual wave according to $1/d_R=-1/d_0+1/R_c$ (d_0 physical distance, R_c curvature radius). The reconstructing wave can be chosen to be a Rayleigh-Sommerfeld spherical wave as explicated in Eq. 1:

$$w(x,y,R_c)=\frac{iR_c}{\lambda}\frac{\exp\left[2i\pi\,\mathrm{sgn}(R_c)/\lambda\sqrt{R_c^2+x^2+y^2}\right]}{R_c^2+x^2+y^2} \tag{1}$$

Here, sgn(…) is the sign function, $i=\sqrt{-1}$ and λ is the wavelength of the light. The main consequence of this is that the object bandwidth becomes adapted to that of the reconstruction kernel. The choice of the curvature radius is governed by the transversal magnification, γ, between the reconstructed object and the extended physical object and it is found to be given by $R_c=\gamma d_0/(\gamma-1)$. Furthermore the transversal magnification between reconstructed object and real one is given by $\gamma=-d_R/d_0$. Since the convolution approach imposes the size of the reconstructed horizon, consider that it is (Lp_x,Kp_y). The transversal magnification γ must be chosen according to the ratio $Lp_x/\Delta A_x$ (or $Kp_y/\Delta A_y$), where $\{\Delta A_x,\Delta A_y\}$ are respectively the object sizes along the x and y directions. The transfer function associated to the spatial spectral filtering can be chosen in two ways: the first is based on the use of a modified version of the angular spectrum transfer function and the last is based on the spatially phase biased Fresnel impulse response of free space propagation. In the first case, we chose a transfer function as a modified version of the angular spectrum transfer function according to Eq. 2 (u_0, v_0 spatial frequencies of the reference wave):

$$\tilde{H}(u,v,d_R)=\begin{cases}\exp\left[2i\pi\,d_R/\lambda\sqrt{1-\lambda^2(u-u_0)^2-\lambda^2(v-v_0)^2}\right] \\ \qquad\text{if } |u-u_0|\le|\gamma|\Delta A_x/2\lambda d_R \\ \qquad\text{and } |v-v_0|\le|\gamma|\Delta A_y/2\lambda d_R \\ 0 \qquad \text{elsewhere}\end{cases} \tag{2}$$

In the last case, the transfer function is the Fourier transform of the spatially phase biased Fresnel impulse response of free space propagation which is given according to Eq. 3. Basic synoptic of the proposed algorithms is given in Fig. 1. These two algorithms allow the reconstruction of any horizon starting from that of the sensor to zero-padded horizons, such as 2048×2048 pixels.

$$h(x,y,d_R)=\begin{cases}\exp\left[\dfrac{i\pi}{\lambda d_R}\left(x^2+y^2\right)+2i\pi\left(u_0x+v_0y\right)\right] \\ \quad \text{if } |x|\le|\gamma|\Delta A_x/2 \quad \text{and } |y|\le|\gamma|\Delta A_y/2 \\ 0 \qquad \text{elsewhere}\end{cases} \tag{3}$$

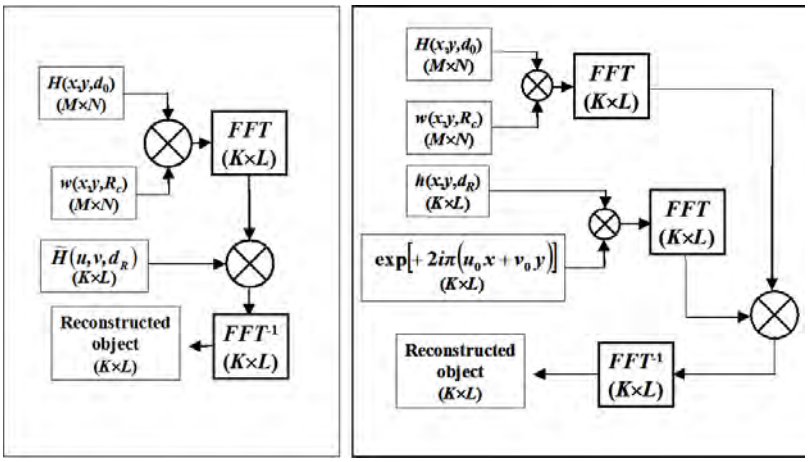

Fig. 1. Synoptic of the two proposed convolution algorithms (left: modified angular spectrum transfer function, right: spatially phase biased Fresnel impulse response)

3 Experimental setup and results

Proof of the validity of the concept is performed through an experimental off axis digital holographic setup, based on a Mach-Zehnder architecture (Fig. 2). The detector is a 12-bit digital CCD with 1024×1360 pixels with 4.65μm pitches (PCO Pixel Fly). In the setup, the laser is a 2ωNdYAG and the reference wave is smooth and plane and the curvature radius of the numerical reconstructing wave is adjusted according to the wanted transversal magnification. As a first illustration, the object under consideration is the bronze medal of the running race "20km de Paris 2000" which is 60mm in diameter. The distance for the recording is set to d_0=1500mm and the object is translated perpendicularly to the optical axis of quantities (x_0=53.6mm,y_0=–51.9mm) thus producing off axis spatial frequencies $(u_0,v_0)=(x_0/\lambda d_0, y_0/\lambda d_0)\approx(67.2\text{mm}^{-1},-65.1\text{mm}^{-1})$. Fig. 3 shows the reconstructed object obtained with algorithm of Fig. 1 (left) with

K=L=2048, γ=0.158 (left) and γ=0.14 (right). For γ=0.158, parameters are R_c=−281.4mm, d_R=−237mm and for γ=0.14 they are R_c=−244.2mm, d_R=−210mm.

Since the algorithms are also suitable for digital color holography, experimental results are provided in the case of digital two-color holograms and simultaneous two-dimensional measurements. The set-up is modified to include a second Mach-Zehnder interferometer using a HeNe laser. Now each laser beam illuminates the object under interest with illuminating angles θ_R and θ_G respectively for the red and green lines (θ_R=−θ_G). The smooth and plane reference waves are produced through the two spatial filters (SF1 and SF2). Since the monochrome sensor is not able to record the two colors simultaneously at each pixel, the spatial frequencies of the reference waves (R and G) are adjusted so that the two-color holograms are spatially multiplexed in the field of view. Thus, the off-line holographic recording is carried out using the two spatial filters in which each collimating lens is displaced out of the afocal axis by means of two micrometric transducers. Using algorithm of Fig. 1 (right), Fig. 4 shows two-color holographic reconstructions of objects with various shapes, simultaneously illuminated with the HeNe laser and the 2ωNdYAD laser. Fig. 4 also shows CCD images of the two objects illuminated in the same conditions with the two lasers. It is satisfactorily faithful pictures compared to the ordinary pictures, taken by the CCD with an imaging lens. Fig. 5 shows that the proposed method is of general interest since it also increases the signal to noise ratio in phase measurements giving a more contrasted phase map in the case of application of the method to simultaneous two-dimensional deformation measurements.

4 Conclusion

The paper has presented two numerical methods for reconstructing large objects using a convolution method with an adjustable magnification based on the use of a virtual spherical reconstructing wave. The filtering is realized using a modified version of the angular spectrum transfer function or using the spatially phase biased Fresnel response of free space propagation. Experimental results presented in the case of monochrome and two-color recordings confirm the suitability of the proposed methods.

5 References

1. Kreis, Th, Adams, M, Jüptner, W (1997) Methods of digital holography: a comparison. Proceedings SPIE 3098:224-233
2. Mas, D, Perez, J, Hernandez, C, Vazquez, C, Miret, JJ, Illueca, C (2003) Fast numerical calculation of Fresnel patterns in convergent systems. Optics Communication 227:245-258
3. Yu, L, Kim, MK (2005) Wavelength-scanning digital interference holography for tomographic three-dimensional imaging by use of the angular spectrum method. Optics Letters 30:2092-2094
4. Ferraro, P, De Nicola, S, Coppola, G, Finizio, A, Alfieri, D, Pierattini, G (2004) Controlling image size as a function of distance and wavelength in Fresnel-transform reconstruction of digital holograms. Optics Letters 29:854-856

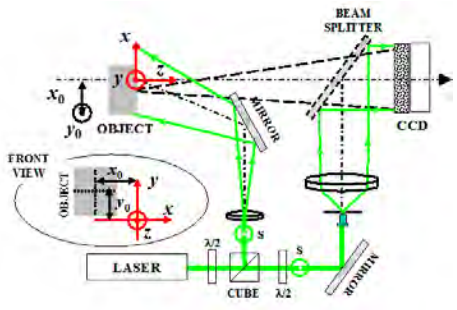

Fig. 2. Experimental setup

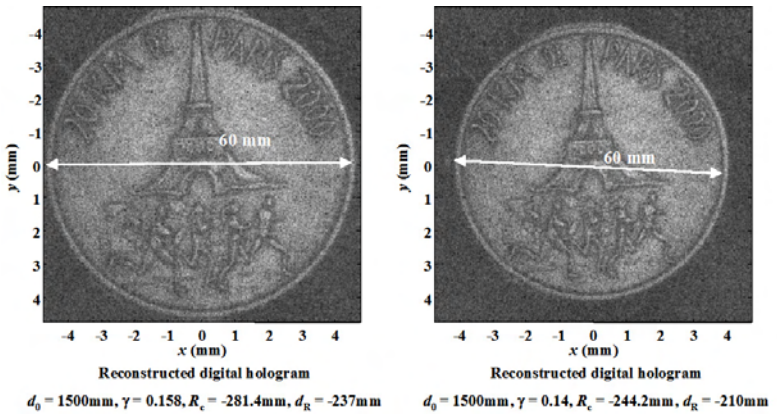

Fig. 3. Example for monochrome digital hologram of a medal 60mm in diameter (λ=532nm)

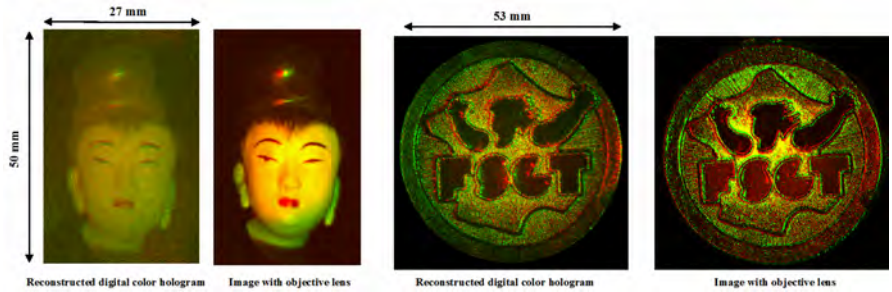

Fig. 4. Example for 2-color digital holograms of large objects (λ=532nm and λ=632.8nm)

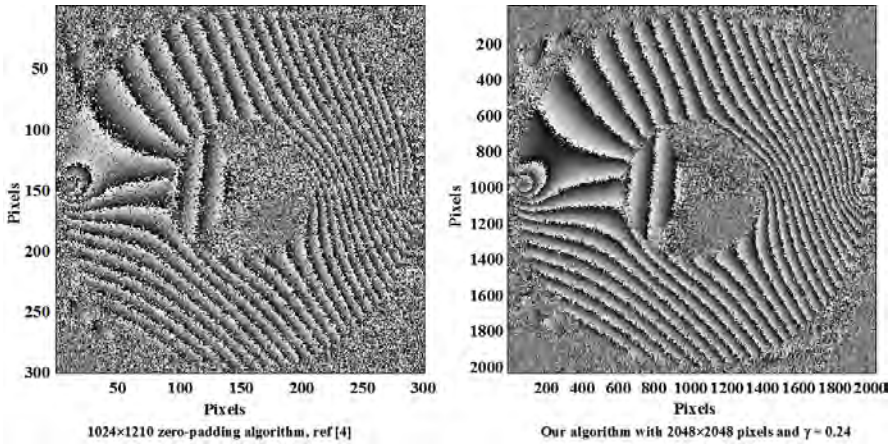

Fig. 5. Comparison between zero-padding algorithm [4] and one of the proposed algorithms (λ=532nm, object size: 40mm)

Reconstruction of noisy measured sharp edges at thin sheet metal components

J. Weickmann, A. Liedl, P.-F. Brenner, A. Weckenmann
Chair QFM, University Erlangen-Nuremberg,
Naegelsbachstrasse 25, 91052 Erlangen
Germany

1 Introduction

Fringe projection systems are increasingly used in industry for the inspection of workpieces due to short measurement duration and laminar data acquisition. Fringe projection sensors are very well suited for the inspection of free form surfaces, whereas sharp edges of thin sheet metal components generate certain problems. When those – in reality distinctive sharp – edges are measured, the resulting edge looks always more or less 'frayed' (Fig.1a) due to overshooting [1]. Thus it is challenging to reconstruct the real position, orientation and shape of an edge with an acceptable measurement uncertainty by performing only a single measurement. This leads to additional efforts when components are reverse engineered. Besides, the range of application for fringe projection is limited, as e.g. trimmings of sheet metal parts are usually not inspected.

In this paper a method for the reconstruction of sharp edges is introduced, assuming that the body structure of a coarse measured edge depends only on few systematic influences.

2 Influences on measurements of sharp edges

Measurement series, planned and interpreted with DoE [2], were performed at a thin sheet metal strip (width 60.10mm) in order to identify the main influences on the shape and position of a sharp edge. For these test series the position of the measured sharp edge was assumed at the position of the arithmetic mean of the 'frayed' measured edge. Three main influences are responsible for 95% of the effects at sharp edges (Fig. 1&2):

- Inclination angle β between sensor and the measured surface
- Height z of the sharp edge above the ground,
- Alignment angle α between fringe direction and sharp edge.

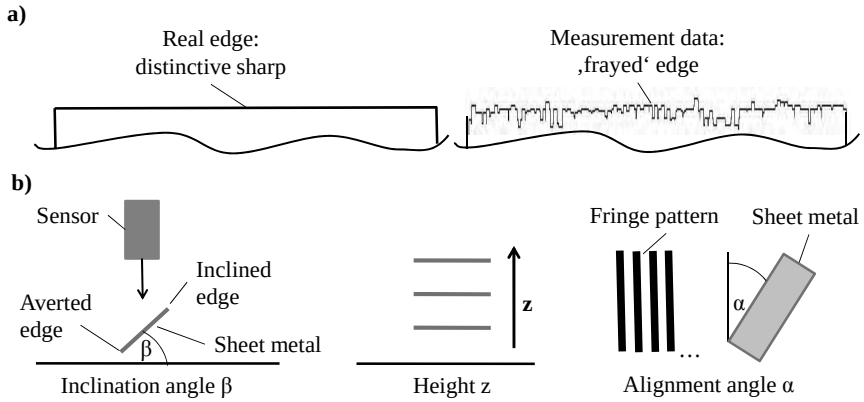

Fig. 1. a) Nominal sharp edge and measured sharp edge; b) Main Influences

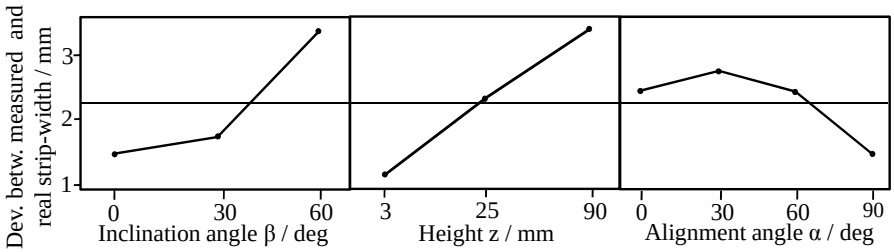

Fig. 2. Analysis of DoE experiments: Main Effects

Other influences, e.g. measuring mode (phase shift/gray code) or material are either insignificant or constant.

Another result of the test series is that the datasets of the sensor-inclined and of the sensor-averted sharp edge behave differently. The mean average of the inclining sharp edge is always closer to the real edge than the averted sharp edge, but the exact distance depends on β (Fig. 2).

By use of regression analysis, the equations for the reconstruction of the real edge positions were found. Eq. (1) is used for sensor-inclined edge, Eq. (2) for sensor-averted edge:

$$\left|\vec{v}\right| = (0.79 + 0.0123 \cdot z + 0.00261 \cdot \beta - 0.00925 \cdot \alpha) mm \tag{1}$$

$$\left|\vec{v}\right| = (0.557 + 0.0142 \cdot z + 0.0115 \cdot \beta - 0.00558 \cdot \alpha) mm \tag{2}$$

These equations are valid for GFM TopoCam mobile 500. The factors have to be determined for each sensor individually.

3 Reconstruction method

Steps for the reconstruction of the real sharp edge in 3D-space (Fig. 3):

- Detect all edge points P_i;
- Determine for each P_i the local surface plane S_i of the sheet metal;
- Determine offset vector $\vec{v}$ in the sheet metal plane for each point P_i rectangular to the edge by analysis of the neighbouring edge points;
- Calculate the offset distance by use of Eq. (1)/(2) and draw R_i;
- Reconstruct the real edge shape by use of a smoothing function.

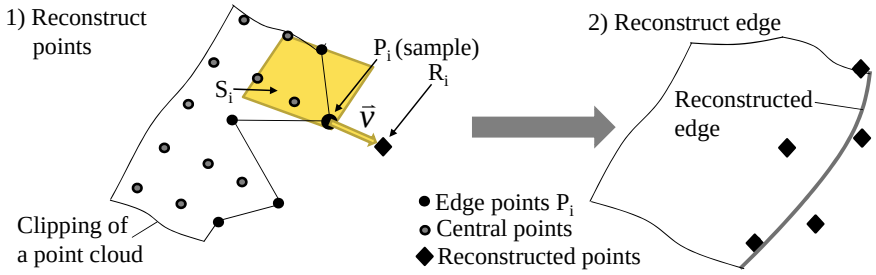

Fig. 3. Reconstruction method

4 Evaluation of method

Fig. 4 depicts an early sample for the efficiency of the edge reconstruction method. Here, a free form edge at a deep drawn longitudinal beam of a car is reconstructed. The black dots represent the measured points; the dashed line represents the floating average of the un-reconstructed edge. The black line represents the successfully reconstructed edge, which corresponds very well with the real edge shape (grey line).

With the described method we reach a mean deviation between real and reconstructed sharp edge of 0.2 mm. Experimental verifications at different components lead to similar results. For comparison: In the original data was no possibility to inspect edge shape or edge position at all.

The reconstructed edge can be used to correct known influences and minimize deviations. Thus measurement uncertainty is reduced. Already in this early experiment the resulting (experimentally determined and GUM-conform [3]) measurement uncertainty for the reconstruction of the sharp edge is calculated to U = 0.33 mm (k=2) by use of Eq. (3):

$$U = k \cdot \sqrt{{u_{cal}}^2 + {u_p}^2 + {u_w}^2} + |b| \tag{3}$$

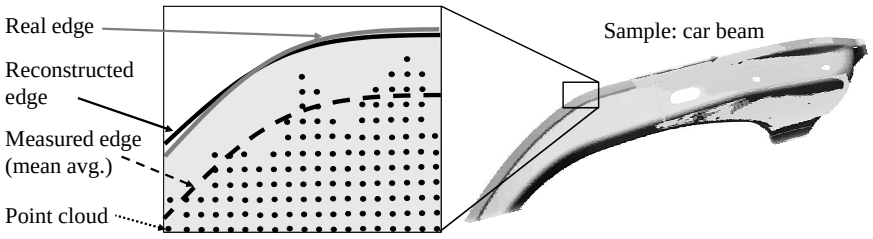

Fig. 4. Sample reconstruction of a free form sharp edge

5 Conclusion

The introduced analytical method allows the reconstruction of sharp edges at sheet metal components in consideration of the major influences on the measurement. Thus the range of application for fringe projection sensors is widened, e.g. for the inspection of trimmings. The model is universal so that reconstruction of a wide range of sharp edges at sheet metal components with any fringe projection sensors is possible.

The focus of future investigation lies on the minimization of method uncertainty to $U < 0.1$ mm. Another aim is the implementation of the method in reengineering-software, so that the corrected measurement data of the edges is displayed automatically. Thus there will be the possibility to reverse engineer a CAD-model of a sheet metal component with good quality by a reduced number of fringe projection measurements.

6 Acknowledgements

The underlying research is gratefully funded within the DFG SFB/TR73.

7 References

1. Kohler, C, Droste, U, Körner, K, Osten, W (2006) Reduction of overshooting in 3D fringe projection measurements by inverse filtering. Technisches Messen 73:595-602
2. Kleppmann, W (2008) Taschenbuch Versuchsplanung. Hanser Verlag, München Wien
3. International Organization for Standardization (1995) Guide to the Expression of Uncertainty in Measurement. ISO, Geneva (Switzerland)

Reduction of speckles in digital holographic interferometry

S. Hertwig, H. Babovsky, A. Kiessling, R. Kowarschik
Institute of Applied Optics, Friedrich-Schiller-University Jena
Fröbelstieg 1, 07743 Jena
Germany

1 Introduction

Reconstructed images of digital holograms are often strongly covered by speckles. A hologram of an object taken under coherent illumination shows objective speckles which size depends on the objects dimensions and its distance from the hologram plane (CCD-camera). These speckles can reach the size of camera pixels and therefore strongly influences the quality of the numerically reconstructed hologram.

In the past, a number of suggestions were made for the reduction of speckles by filtering processes or by multiplexing of several images [1]. Mathematical filtering processes have the disadvantage of a lower lateral resolution. Therefore, the image sharpness decreases and, in the case of holographic interferometry, the accuracy of measurement is deteriorated sharply.

A possible solution is the averaging of a series of reconstructed images of the same object with different speckle distributions. The speckle distribution depends among others on the angle of observation and on the phase structure of the illuminating wave.

We show that the multiple recording of an object by simultaneous phase encoding of the illuminating wave enables to average the n-times reconstructed holograms. This improves the reproduction of the hologram without decreasing the lateral resolution.

2 Experimental setup

The setup shown in Fig.1 consists of an illumination laser which radiation is split by a beam splitter (BS) in a reference beam and an object beam. The object beam will be reflected by a liquid crystal on silicon device [2] (LCoS) controlling the phase distribution. An additional fixed scattering

plate is used optional to randomise the phase. The polarizers define the intensity ratio between the object wave and the reference wave and its polarisation state.

The interference pattern (hologram) is recorded by a CCD camera.

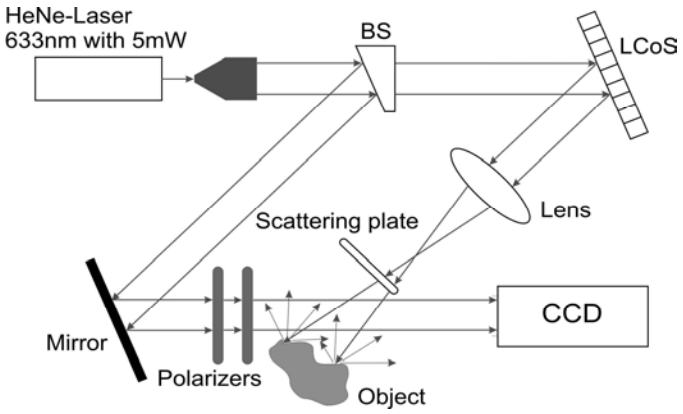

Fig. 1. Setup for reducing speckles in digital holography

3 Speckle-measurement

To characterize the speckles on an image it was necessary to create a value to describe the quality of pictures. We called it the “speckle rate” (SR). The SR is the ratio of the number of the “pixels identified as speckles” SP and the total number of image-pixels TP (Eq. 1). One pixel is “identified as a speckle”, if the sum of the absolute value of the difference between the mean value of a pixel and its eight neighbours and those nine grey-scale values divided by nine is bigger than a certain intuitive number p.

$$SR = \frac{SP}{TP} \tag{1}$$

The SR yields no information about size, quantity or other properties of the speckles! But it has shown, that it is a good size to characterize the degree of speckles in a picture.

Fig. 2. Examples of SR-values left SR = 45.57, right SR = 3.99

4 Measurements

As described we can change the speckle-patterns with the scattering plate or the LCoS.

Several measurements gave us the result that using the scattering plate is the best method to reduce speckles. Unfortunately it can not be used in digital holographic interferometry because one would have to restore each single position of the scattering plate exactly for both states of the object we want to compare. By using the LCoS this problem is annihilated, because it able to create defined states of the phase distribution.

Naturally the improvement in speckle reduction depends on the used pattern on the LCoS (see Fig.3). Contrary to our first expectations statistically LCoS-patterns do not lead to the best reached results. To ensure that this is not a result of a small average phase shift we also tested binary statistically matrices (also called statistic 0/255 in Fig.3). According to the image processing in computer sciences we used Hadamard-matrices.

This resulted in lower SR-values, almost reaching the results while employing the scattering plate in a fixed state in the optical path like shown in Fig.1. The difference in both SR-values can be explained by a smaller grain size of the scattering plate compared to a pixel of the LCoS.

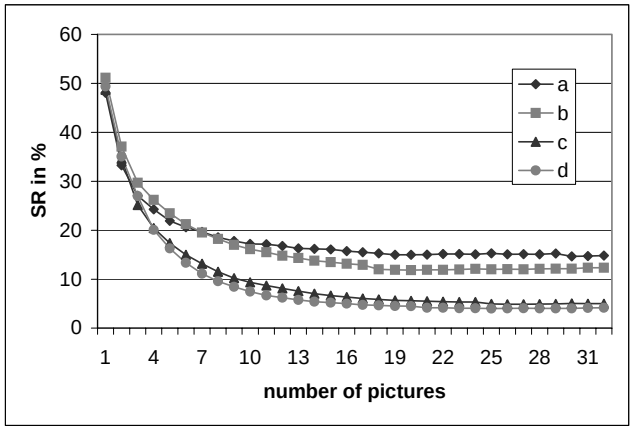

Fig. 3. Comparison of SR with different methods: a: statistic 0/255, b: Hadamard-matrices, c: Hadamard-matrices + scattering plate, d: scattering plate

Like mentioned before the LCoS enables us to reduce the SR in interferomety, too. These results have been tested by observing a object in two tilted states with the methods of digital holographic interferometry.

Reconstructing the holograms of two different states of an object the coherent overlay results in interference fringes in the speckled picture of the object.

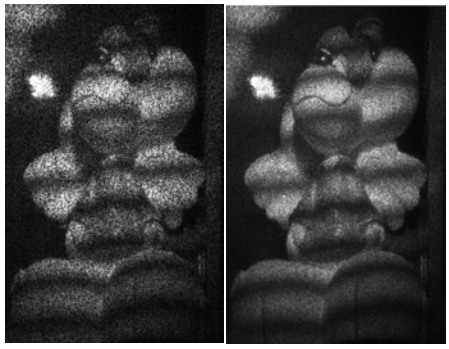

Fig. 4. Speckle reduction in holographic interferometry left: one picture,

right: average of 5 pictures

By now using the LCoS we generate different defined phase distributions. This enables us to record a series of reconstructed images with the same interference fringes but different speckle distributions.

Averaging the pictures of this series we gain interference pictures with reduced SR like the example shown in Fig.4.

The main problem we observed is realizing a system with sufficient stability. The positions of all components have to be exact at least in the range of $\lambda/10$ to get pictures with the same interference fringes. Averaging pictures with just similar interference-patterns reduces the contrast of the fringes dramatically.

5 Conclusion

We demonstrated that in digital holography by averaging N pictures with different speckle statistics, the speckles can be suppressed in the resulting picture. To characterize the image quality we made an expression called speckle rate SR which allows us to compare the achieved results. The best results were reached with a scattering plate (SR = 0.05). Moreover, by the combination with a LCoS we could show that the procedure can be also applied for the digital holographic interferometry. The still insufficient temporal stability of the optical setup limits the number of the pictures we are able to use.

6 References

1. U. Schnars, W. Jueptner Digital Holography, 2005 Springer Verlag
2. Hai Tao Dai et al. Characteristics of LCoS Phase-only spatial light modulator and ist applications, Optics Communications 238 (2004) p. 269–276

Normalization and denoising in a multi-source and multi-camera profilometric system

Elena Stoykova[1], Atanas Gotchev[2], Ventseslav Sainov[1]
[1]Central Laboratory of Optical Storage and Processing of Information, Bulgarian Academy of Sciences, Acad. G. Bonchev Str. 101, 1113 Sofia, Bulgaria [2]Department of Signal Processing, Tampere Institute of Technology, P.O.Box 553**,** 33101 Tampere, Finland

1 Introduction

The goal of the work is to develop reliable phase retrieval in a single-shot pattern projection profilometric system which has been built for real time implementation of the phase-shifting algorithm [1]. The system projection module includes four identical projection elements irradiated by four near-infrared diode lasers emitting at different wavelengths for simultaneous projection of four phase-shifted at $\pi/2$ fringe patterns. The registration module consists of four CCD cameras for simultaneous recording. A sinusoidal phase grating has been chosen to act as a projection element due to its easy manufacturing and good reproducibility of the desired modulation and spacing, high efficiency, and independence of the lateral spatial period of the diffraction pattern on the wavelength [2]. The phase shift between the patterns is introduced by mechanical displacement of the gratings with respect to each other. Two challenges should be overcome for successful operation of such multi-source and multi-camera system due to inherent limitations of the phase-shifting algorithm. First of them is the requirement for a sinusoidal fringe profile while the second is the necessity to ensure equal background and contrast of fringes in the recorded fringe patterns. As a first task, we analyze the systematical errors due to the combined influence of the higher harmonics and multi-wavelength illumination in the Fresnel diffraction zone. The second important task is evaluation of the degrading effect of the speckle noise and the spatially varying fringe modulation at non-uniform illumination on the overall accuracy of the profilometric measurement. Finally, the third task is to develop a reliable phase retrieval procedure which includes denoising/smoothing of the recorded fringe patterns, background removal and normalization. The developed phase retrieval procedure is applied to the simulated and measured fringe patterns obtained for a dome surface.

2 Phase retrieval – simulation and experiment

In general, fringe patterns created by a thin sinusoidal phase grating are not sinusoidal. At plane-wave illumination, the diffraction pattern along transversal (x) and longitudinal direction (z) consists of alternating zones with a phase-reversed contrast that are separated by the so called Talbot planes in which self-imaging occurs and the contrast of fringes is zero. However, divergent illumination ensures occurrence of only one Talbot plane in the Fresnel zone and small variations of the fringe contrast with z. The contrast of fringes increases with grating modulation but the same is true for the higher harmonics in the fringe pattern. To evaluate the influence of higher harmonics and multi-wavelength illumination on 3D reconstruction accuracy we simulated a profilometric measurement of a dome with a height h for a conventional cross-axes optical arrangement [3] of the four-wavelength system in the absence of noise for the case when each of the four gratings was illuminated by a spherical wave in paraxial approximation. The intensity profile of the projected fringes was determined by solution of the Fresnel diffraction integral in [2]:

$$I(x,z,\lambda,m)=\frac{2A_0^2 d}{z\lambda(z+d)}\left\{I_0(z)+I_V(z,\lambda,m)\sin\frac{2\pi x d}{L(z+d)}+\Theta(x,z,\lambda,m)\right\} \quad (1)$$

where λ is the wavelength, m is the modulation of the phase grating [4], L is the grating pitch, d is the distance between the illuminating point source and the grating, and A_0 is a constant amplitude. The expressions for the background $I_0(z)$, the contrast $I_V(z,\lambda,m)$ and the non-sinusoidal term $\Theta(x,z,\lambda,m)$ are given in [2]. Hence, in general, the background and contrast vary with the wavelength. Figure 1 (left) shows a non-uniform negative bias in reconstruction of the dome with h = 7 mm for noiseless non-normalized fringes with a contrast of about 40%, L = 0.25 mm, d = 1 m, and an illumination angle 30°. The fringe patterns were simulated as 8-bit encoded 256×256 arrays with equal sampling steps along X and Y axes $\Delta_x = \Delta_y$ = 0.2 mm in the plane of the object at wavelengths 790nm, 810 nm, 850 nm, and 910 nm. The phase retrieval was performed with a four-step algorithm [3] without preprocessing of the fringe patterns. The bias substantially decreases with the grating phase modulation as well as with increasing the distance from the grating or illumination angle. The usage of different wavelengths may lead to non-correlated impacts of disturbing factors in the recorded fringe patterns, which may severely ruin the phase retrieval process.

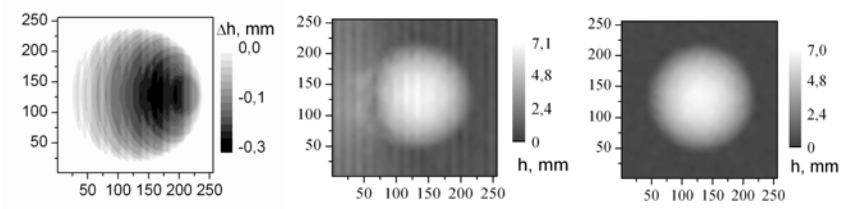

Fig.1 Simulation of the multiwavelength profilometric measurement of a dome with a height 7 mm at 790 nm, 810 nm, 850 nm and 910 nm: (left) – reconstruction error due to multiwavelength illumination and higher harmonics; (middle) –reconstruction from speckled fringe patterns after James-Stein filter with 3×3 window; (right) – reconstruction from speckled fringe patterns with non-uniform illumination after normalization.

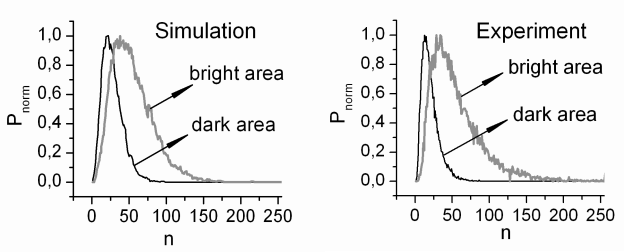

Fig.2 Normalized histograms of intensity distribution in bright and dark fringe areas.

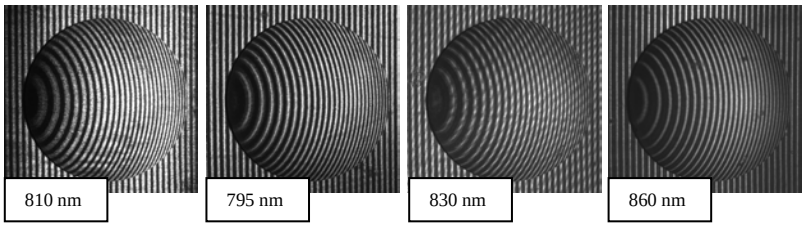

Fig.3 Four phase-shifted at π/2 fringe patterns (experiment).

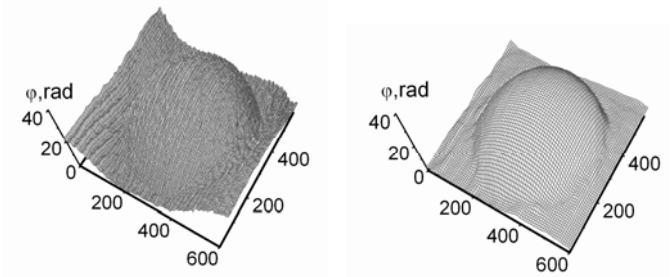

Fig.4 Reconstruction of a dome with a four-step algorithm applied to fringe patterns in Fig.3: (left) – phase retrieval without preprocessing; (right) – phase retrieval after smoothing and normalization.

We adopted a signal dependent multiplicative noise model for the speckle noise. The differences between the used wavelengths permit to model it as an independent circular Gaussian process in the four channels of the system with subsequent integration by the CCD cameras. Figure 4 gives the normalized histograms of intensity which are built from the bright and dark sections of simulated and experimental fringes. Each histogram corresponds to a constant illuminating intensity and a given wavelength. For speckle denoising we applied a James-Stein filter after performing a homomorphic transformation of the patterns [5]. The result for a 3×3 filter window is depicted in Fig.2 (middle). Increase of window size worsens the accuracy of 3D reconstruction. A systematic error due to higher harmonics is clearly visible. The result in Fig.2 (right) is much better. In this case the preprocessing of fringe patterns included normalization and smoothing which were performed using the Fourier transform filtering proposed in [6]. It is performed by rotation of a semiplane passband filter at steps of $2\pi/N$ in the frequency domain. We used $N = 12$ both for simulated and experimental data. The background removal and smoothing are accomplished through an annular passband filtering. The experimental phase-shifted fringes which are projected using the multi-source and multi-camera system are presented in Fig.3. The non-correlated disturbances in the recorded patterns are large enough to deteriorate the 3D reconstruction (Fig.4, left). The normalization and smoothing of the patterns in Fig.3 leads to substantial improvement (Fig.4, right). The achieved accuracy of 0.08 mm in the 3D dome reconstruction guarantees good performance of the built real-time profilometric system.

3 References

1. Stoykova, E, Harizanova, J, Sainov, V (2009) Pattern Projection with a Sinusoidal Phase Grating, EURASIP J. Adv. Sign. Proc., vol. 2009, Article ID 351626, 10 pages
2. Stoykova, E, Minchev, G, Sainov, V (2009) Fringe projection with a sinusoidal phase grating, Appl.Opt., in press
3. Gasvik, K (2002) Optical Metrology, Wiley
4. Goodman, J (1996) Introduction to Fourier Optics, McGraw-Hill
5. Terrillon, J.-C. (1996) Image preprocessing for rotation-invariant pattern recognition in the presence of signal-dependent noise**,** Appl.Opt. 31**:** 1879-1893
6. Ochoa, N (2008) Normalization and smoothing algorithm for electronic speckle-pattern interferometry fringes, Opt.Eng. 47 (4), 045601

Automated Phase Map Referencing Against Historic Phase Map Data

Roger M. Groves[1,2], Dominique Derauw[3], Cédric Thizy[3], Igor Alexeenko[2], Wolfgang Osten[2], Marc Georges[3], Vivi Tornari[4]
[1]Faculty of Aerospace Engineering, Delft University of Technology, Kluyverweg 1, 2600 GB, Delft, The Netherlands;
[2]ITO Institut für Technische Optik, Universität Stuttgart, Pfaffenwaldring 9, 70569 Stuttgart, Germany;
[3]Centre Spatial de Liège – Université de Liège, Liège Science Park, B-4031 Angleur, Belgium;
[4]Foundation for Research and Technology-Hellas, Institute of Electronic Structure and Laser, Vassilika Vouton, Voutes, 71110 Heraklion-Crete, Greece

1 Introduction

Holography and shearography techniques are in common use for precise measurements in high technology industries, such as aerospace, automotive, precision manufacturing and for the structural diagnostics of artwork. The phase map data generated by these instruments allows precise measurements of parameters such as displacement, strain and shape. The comparison of data from different measurement campaigns is useful for null testing components and for studying changes. However, the comparison of data with previous measurements is non-trivial due to the sensitivity of these techniques to alignment and to sample loading parameters. This paper addresses image and phase registration issues for holography and shearography. This manuscript describes 2D spatial co-registration to compensate for differences between the field of view between the measurements and a phase referencing to calculate the difference between the phase maps for comparison of data with previous measurements. These techniques are implemented after following a standardised measurement procedure.

2 Standardised Measurement Procedure

The standardised measurement procedure developed for the instrument described in is detailed below. The sensor distance and camera lens parameters control the field of view of the sensor. As optimum parameters, the field of view of the reference and re-measured images should overlap as much as possible, approximately the same number of pixels should be used and out-of-plane image tilt and image rotation differences should be minimised. Acquisition parameter variations, even under optimum conditions, are sufficient to induce phase measurements that are not perfectly superimposable, leading to an incorrect phase comparison. For this reason the sub-pixel accuracy co-registration, detailed in Section 3 is necessary. Samples are thermally loaded using infra-red lamps. To reduce phase differences due to differences in loading parameters, infra-red lamp power, distance to sample, illumination angles and illumination direction are specified by the measurement procedure.

3 Spatial Co-Registration

Co-registration is the computation of the transform that should be applied to a slave image to make it superimposable onto a master image. In this work, computation is limited to an affine transform which takes account translation, rotation, magnifications and out-of-plane tilt variations. Once found, the transform must be applied through proper interpolation process. Mathematically, the affine transform is expressed as:

$$x_2 = A_x + B_x x_1 + C_x y_1 \quad (1)$$

$$y_2 = A_y + B_y x_1 + C_y y_1 \quad (2)$$

where (x_1,y_1) and (x_2,y_2) are the coordinates in the first and second images, respectively. The parameters of the affine transform are determined from white light reference and re-measured images. The co-registration and interpolation procedure were adapted from processes developed for SAR interferometry. Co-registration in itself is conducted through correlation of imagettes taken from the master and the slave images. The process leads to a list of anchor points in the master image for which corresponding anchor points can be found in the slave image. The affine transform parameters are then found by a mean square calculation, fitting the transform through the list of anchor point pairs. The transform obtained must then be applied to the image in order to make it superimposable to the reference one and to allow for correct phase difference computation.

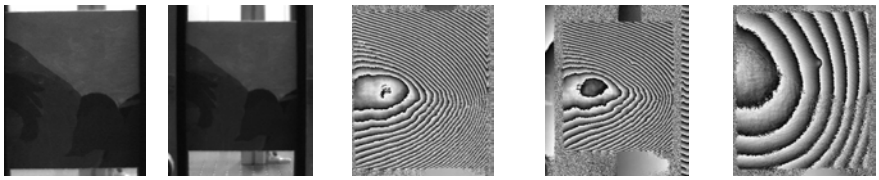

(a) (b) (c) (d) (e)

Fig. 1. (a) and (b) are images of a wooden panel painting, recorded using different camera positions. (c) and (d) are phase maps recorded using these camera positions. (e) is the difference phase map after co-registration and subtraction of the phase maps

To apply the transform, a complex interpolator, based on the Chirp-Z transform, was used. As the viewing geometries are identical, the same transform can be applied to both the intensity image and to the re-measured phase maps. For this latter one, phase is first converted to complex interferograms to allow complex interpolation, then the phase is recalculated from the interpolated complex phase values. Results showing the co-registration of phase maps recorded from a wooden panel painting using dynamic holography are shown in Fig. 1.

4 Phase Referencing

The first step of this procedure is to identify the reference phase map with the most similar time after heating. This time information is obtained from phase map file names. The phase maps selected are unwrapped and divided into sub-images. The size of the sub-image should be small enough to be considered as a planar surface in 3D space and be large enough to smooth variations due to speckle noise. A typical size is 7x7 pixels. The next step is to correct for phase offsets between the reference and re-measured phase maps. These phase offsets may be introduced by the phase-shifting algorithm, deviations in the sample loading and the co-registration procedure. The sub-images are rescaled by calculating the mean intensity and setting this value to 128 intensity. The final stage is to compare these sub-images using the matching-ratio (M-ratio) formula:

$$M = \frac{\left\{\sum I_1 + \sum I_2\right\}}{\left\{\sum \left(I_1(x,y) - I_2(x,y)\right)\right\}} \tag{3}$$

where M is the Matching ratio, I_1 and I_2 are images are the reference and re-measured phase maps respectively. x and y refer to columns and rows in the phase maps. The meaning of the M-value was empirically determined. Values less than 1.2 indicating a highly-significant change and values greater than 1.7 indicating an insignificant change.

5 Discussion and Summary

The co-registration application shown here demonstrates how spatial co-registration can be successfully applied to holography when measurement parameters are carefully controlled. The phase referencing described could, in principle, provide fully automated phase analysis and provide the instrument user with clear information on pass or fail. Current work is to refine these empirical M-ratio values using a larger data set. In summary, the manuscript describes an automated procedure for comparing phase maps with historic data, using spatial co-registration algorithms and an empirical matching ratio.

This research was supported by the European Union funded MULTI-ENCODE (Multifunctional Encoding System for the Assessment of Movable Cultural Heritage) FP6 Project (006427 SSPI).

6 References

1. Vest, CM (1979) Holographic Interferometry. Wiley, New York
2. Steinchen, W, Yang, L (2001) Digital shearography. SPIE Press, Bellingham
3. Fotakis, C, Anglos, D, Zafiropulos, V, Georgiou, S, Tornari, V (2006) Lasers in the Preservation of Cultural Heritage; Principles and applications. Brown, RGW, Pike, ER, Eds. Taylor and Francis, New York
4. Osten, W, Pedrini, G, Schwab, X, Baumbach, Th (2007) Null test in speckle light by comparative digital holography. Proc. of the 13th International Conference on Experimental Mechanics, Gdoutos, EE, Ed. Springer, pp. 603-604
5. Tornari, V, Bernikola, E, Hatziyannakis, K, Osten, W, Groves, RM, Georges, M, Thizy, C, Hustinx, G-M, Rochet, J, Kouloumpi, E, Doulgeridis, M, Green, T, Hackney, S (2009) Multifunctional encoding system for assessment of movable cultural heritage and resulted prototype device, Proc. FRINGE 2009.
6. Derauw, D, Roose, S (1995) Co-registration and complex interpolation. Proc. SPIE 2584:326-331
7. Lemaire, Ph, Georges, M (2006) Dynamic holographic interferometry: devices and applications in Photorefractive Materials And Their Applications 3: Applications, Günter, P, Huignard, J-P, Eds., Springer Series in Optical Sciences 115

Numerical multiplexing and de-multiplexing techniques for efficient storage and transmission of digital holographic information

M. Paturzo[1], P. Memmolo[1,2], A. Tulino[2], A. Finizio[1] , L. Miccio[1] and P. Ferraro[1]
[1]CNR - Istituto Nazionale di Ottica Applicata & Istituto di Cibernetica, via Campi Flegrei 34,80078-Pozzuoli (NA), Italy
[2]DIET, Università di Napoli "Federico II", Via Claudio 21, 80125 Napoli, Italy

1 Introduction

Digital Holograms can be multiplexed by encoding the information of two or more holograms in a single one. Multiplexing of digital holograms has been used to measure some object properties, as the state of polarization, by a single image acquisition [1]. Other applications of multiplexing techniques in holography regard the investigation of ultra-fast events [2], or experiments in which a diffraction grating is used to get super-resolved images increasing synthetically the numerical aperture of the image sensor [3].

Actually, in the most of the above mentioned approaches, spatial multiplexing of digital holograms is obtained optically, that means recording simultaneously more then one fringe pattern on the same sensor array. All the holograms are superimposed in one composite CCD frame, and each of them can be independently reconstructed after the digital spatial filtering in the Fourier spectral domain of the multiplexed hologram.

However, the multiplexing operation can be carried out also by numerical techniques by combining numerically digital holograms to obtain a single synthetic hologram. Recently, we demonstrated that an efficient storage and/or transmission of a large number of digital holograms can be attained by numerical multiplexing (NM) method [4]. The results obtained are reported in the section 3.

2 Experimental set-up

The multiplexed holograms are acquired by means of a Mach-Zehnder interferometric microscope, shown in Fig.1. The laser wavelength is 532 nm and the microscope objective is a 20 X objective with a focal length *f* =9.0 mm and a NA=0.40. The CCD detector has 1280 X 1024 square pixel which size P_{CCD} = 6.7 μm. To obtain the multiplexed hologram, we exploit the single capability of DH to manage numerically the complex wavefronts, to reconstruct the object wave field at an intermediate plane, that is, essentially, the back focal plane (BFP) of the imaging lens

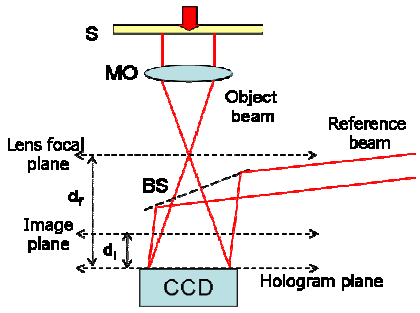

Fig. 1. Sketch of the DH setup; S: sample; BS: beam splitter; MO: microscope objectives.

In the BFP of the imaging lens, the complex-value array, corresponding to the object wavefield, is proportional to the Fourier transform of the complex amplitude of the wave at an input plane. Therefore, we obtain only the spectrum of the object wave field, removing the contribution of the carrier frequencies.

3 Numerical multiplexing and de-multiplexing

Here we described the method we use for the numerical multiplexing and de-multiplexing of up to 100 digital holograms. Firstly, we will show how the holograms are multiplexed and, then, how the multiplexed hologram is processed in order to reconstruct all one hundred amplitude and phase maps. Finally, these reconstructed images are compared with those one obtained by the original holograms and the distortions caused by the multiplexing are evaluated.

The specimen is an in vitro mouse preadipocyte 3T3-F442A cell. It has been monitored for 25 hours to investigate its activities and one hundred holograms have been recorded with an acquisition rate of 4frame/ hour.

Moreover, a reference hologram is acquired in a area of the sample far from the cell in order to calculate the phase retardation caused only by the cell subtracting the phase shift due to the interferometer and the culture medium. Each of the hologram is reconstructed in the BFP of the MO. The amplitude reconstruction of one hologram in the BFP is shown in Fig.2(a).

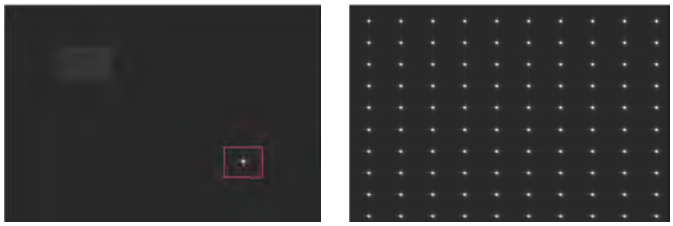

(a) (b)

Fig. 2. (a) Amplitude reconstruction of one hologram in BFP. The red frame indicates the used filtering window around the carrier frequency of the object spectrum. (b) Amplitude of the synthetic spectrum obtained by the numerical multiplexing in the BFP of 100 digital holograms.

Then, we choose a mask to filter each hologram in the BFP. The red frame in Fig.2(a) indicates the shape and the dimension of the used filtering window, that is 50 X 50 pixels around the carrier frequency of the object spectrum, whose position depends on some geometrical parameters of the experimental setup. The transmittance of the mask is 1 within the frame and 0 outside. Obviously, reducing the dimension of the filtering window will increase the number of holograms we can encode in one single hologram. On the other hand, the size of the filtering window should be larger than the object bandwidth in order to retain the spectral information. To properly multiplex the holograms in the BFP, we join together the 100 filtered spectra. The amplitude of the synthetic spectrum obtained in this way is shown in Fig.2(b). This complex-value array contains the information about the phase and amplitude of all one hundred holograms.

In the de-multiplexing process, the hologram composed in the BFP is filtered selecting one by one the single holograms that, then, are numerically reconstructed in the image plane.

In Fig. 3 are shown the phase reconstructions of one hologram as acquired by the CCD (a) and after the multiplexing/de-multiplexing process (b). Comparing the two reconstructions, the distortion caused by the filtering process is not evident. In Fig.3 (c) we have plotted the difference between the two phase reconstructions in order to evaluate the distortion.

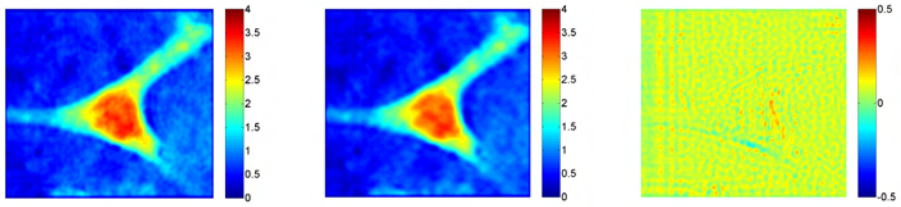

(a) (b) (c)

Fig. 3. Phase reconstructions of one hologram as acquired by the CCD (a) and after the multiplexing/de-multiplexing process (b). Difference between the two phase reconstructions in Fig. 3(a) and 3(b).

Then, we calculated the mean value of the 2D distribution of this phase difference that results 0.068 rad with a variance of 1 * 10-3 rad, while the maximum value is 0.23 rad. The maximum phase difference is situated on the cell border. This result is caused by the use of the filtering window that acts as a band-pass filter with limited bandwidth, cutting the high frequencies due to the edges.

In conclusion, we proposed an all numerical technique to multiplexed and de-multiplexed correctly up to 100 DHs. This technique could be useful to perform an efficient storage and/or a fast transmission of DHs from the recording head to the display unit.

4 References

1. Colomb, T., Dürr, F., Cuche, E., Marquet, P., Limberger, H. G., Salathé, R.-P. and Depeursinge, C. (2005) Polarization microscopy by use of digital holography: application to optical-fiber birefringence measurements. Appl. Opt. 44: 4461-4469
2. Liu, Z., Centurion, M., Panotopoulos, G., Hong, J. and Psaltis, D. (2002) Holographic recording of fast events on a CCD camera Opt. Lett. 27: 22-24
3. Paturzo, M., Merola, F., Grilli, S., De Nicola, S., Finizio, A. and Ferraro, P. (2008) Enhanced super-resolution in digital holography by a dynamic phase grating. Opt. Express 16: 17107-17118
4. Paturzo, M., Memmolo, P., Miccio, L., Finizio, A., Ferraro, P., Tulino, A. and Javidi, B. (2008) Numerical multiplexing and demultiplexing of digital holographic information for remote reconstruction in amplitude and phase. Opt. Lett. 33: 2629-2631

Fringe Pattern Normalization Using Bidimensional Empirical Mode Decomposition and the Hilbert Transform

María Belén Bernini
Instituto de Física Rosario
Blvd. 27 de Febrero 210 bis, S2000EZP Rosario
Alejandro Federico
Electrónica e Informática, Instituto Nacional de Tecnología Industrial
P.O. Box B1650WAB, B1650KNA San Martín, Argentina
Guillermo H. Kaufmann
Instituto de Física Rosario and Centro Internacional Franco Argentino de Ciencias de la Información y de Sistemas
Blvd. 27 de Febrero 210 bis, S2000EZP Rosario
Argentina

1 Introduction

Phase extraction techniques in fringe analysis are very sensitive to noise but also to modulation defects mostly due to non-uniform illumination. For this reason, in many cases the fringe pattern modulation must be normalized before the phase map is extracted in order to avoid the introduction of large errors in the demodulated phase.

The application of a normalization method can be also of great utility in Digital Speckle Pattern Interferometry (DSPI). When it is necessary to smooth the DSPI fringes with a denoising technique previous to phase extraction, frequently the smoothing process reduces the visibility of the fringes. Therefore, a normalization algorithm must be used to pre-process the smoothed DSPI fringes before the extraction of the phase distribution.

Various fringe normalization techniques have been proposed, such as the one presented by Quiroga et al. [1]. Even though this method has been successfully applied in fringe normalization, its efficiency is reduced in images presenting regions with very low modulation or stepped contrast changes.

In this paper we describe an approach to normalize fringe patterns based on the Bidimensional Empirical Mode Decomposition (BEMD) method adapted to DSPI in Ref. [2] and the partial Hilbert transform (PHT).

2 The Bidimensional Empirical Mode Decomposition

The BEMD method decomposes an image into a small set of orthogonal sub-images called intrinsic mode functions (IMFs), which represent the high and low frequency components of the original image. The IMFs are obtained using a fully data-driven sifting process clearly described in Refs. [2] and [3]. We introduced a pre-processing of the input fringe patterns in order to avoid boundary effects which consist in applying a circular symmetric and gaussian shaped window to the original fringe pattern, so that the amplitude and frequency of the borders tend smoothly to zero, while the central part remains unchanged. After the decomposition, only the central part of the IMFs that were not altered by the pre-processing is used and the boundaries are discarded.

3 Normalization Method

The normalization is performed by decomposing a fringe pattern with the BEMD method in order to obtain the first significative IMFs. Then, the amplitude of each selected IMF is calculated using the partial Hilbert transform. The PHT is applied to each row and column of the selected IMFs, and the amplitude of each of these signals is calculated using the absolute value of its Hilbert transform. The full amplitude image is reconstructed by averaging the previously obtained results. The normalized pattern is obtained by adding the selected IMFs, each one divided by its corresponding amplitude. The background suppression is achieved keeping only the first significative IMFs, since the dc component information is on the last modes of the decomposition.

The number of significative IMFs to be selected is the only step of the normalization procedure that needs external supervision. This number can vary depending on the fringe patterns to be normalized. In most cases, the first IMF is enough to perform the normalization.

4 Numerical Results

The computer simulated fringe patterns used to evaluate the proposed normalization technique were generated with added illumination defects in the form of gaussian shaped dc components and modulation distortions. The gaussian defects had different variance and were centered at various regions of the fringe patterns. The fringes were generated with a resolution

of 512 × 512 pixels with 256 gray levels. After the BEMD boundary processing, the central part extracted from the IMFs had a resolution of 128 × 128 pixels. The performance of the proposed normalization technique was obtained by calculating a figure of merit named quality index Q described in Ref. [2], which compares the normalized patterns with the defect-free ones and has a dynamic range of [-1,1] .

The normalized fringe patterns obtained using the BEMD and the Hilbert transform were compared with those generated by the application of the technique proposed by Quiroga et al. In order to make the comparison more accurate, this last method was also applied to fringe patterns with 512 X 512 pixels pre-processed by the application of the circular symmetric gaussian shaped window used in the BEMD method to avoid boundary conditions and only the 128 × 128 central part was used.

Satisfactory Q index values were obtained in all the tested examples analyzed with the proposed technique. As a typical example, Fig. 1(a) shows the central region of a computer simulated fringe pattern with a gaussian dc component and a modulation defect. Figure 1(b) displays the same region of the normalized image obtained with the technique proposed in this paper, using only the first IMF. The result of applying the Quiroga et al. method is shown in Fig. 1(c).

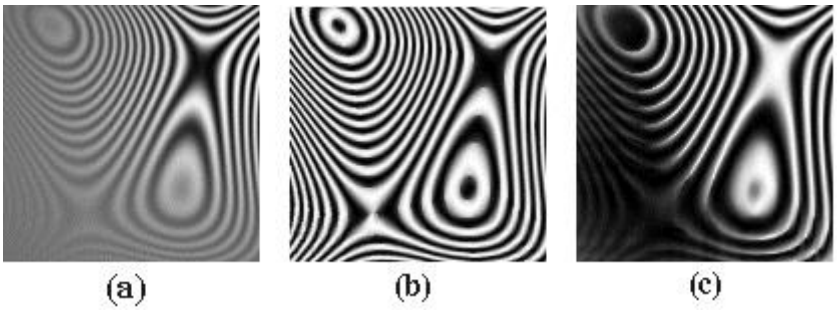

Fig. 1. (a) Fringe pattern with high fringe density and low modulation area; (b) normalized with the BEMD method; (c) result obtained using the Quiroga et al. technique

While Fig. 1(c) presents some serious defects in the low modulated region of the original image, the pattern normalized using the technique proposed in this work is almost free of defects. This improvement can also be seen by comparing the Q values calculated for both images (Q = 0.845 for Fig. 1(b) and Q = 0.160 for Fig. 1(c)).

5 Conclusions

This work presents a novel normalization procedure to be used in fringe pattern analysis. The proposed technique is based in the BEMD method and the partial Hilbert transform. The performance of the normalization procedure was tested in computer simulated fringe patterns with varying fringe densities. Illumination defects of varying intensities were added at various locations of different fringe patterns to evaluate the background suppression and the modulation normalization of the proposed method. The accuracy of the proposed normalization approach was evaluated using a parameter called the quality index Q.

Satisfactory results were obtained in all the evaluated cases, even in fringe patterns with very low modulation regions and stepped contrast changes, improving the results of other normalization techniques.

6 Acknowledgments

The authors would like to thank the financial support provided by Fundación Josefina Prats of Argentina.

7 References

1. Quiroga, J A, Gómez Pedrero, J A, García Botella, A (2001) Algorithm for fringe pattern normalization. Optics Communications 197:43-51
2. Bernini, M B, Federico, A, Kaufmann, G H (2008) Noise reduction in digital speckle pattern interferometry using bidimensional empirical mode decomposition. Applied Optics 47:2592-2598
3. Huang, N E, Sheng, Z, Long, S R, Wu, M C, Shih, H H, Zheng, Q, Yen, N C, Tung C. C., Liu H (1998) The empirical mode decomposition and the Hilbert spectrum for non-linear and non-stationary time series analysis. Proceedings of the Royal Society A 454:903-995

Complementary Filtering Approach to Enhance the Optical Reconstruction of Holograms from a Spatial Light Modulator

Mostafa Agour,[1,2*] Claas Falldorf,[2] Christoph von Kopylow[2]
[1]Department of Physics, Aswan Faculty of Science, South Valley University,81528 Aswan, Egypt
[2]Department of Optical Metrology, Bremer Institut für angewandte Strahltechnik, Klagenfurter Str. 2, D-28359 Bremen, Germany
[*]Corresponding author: agour@bias.de

1 Introduction

Electrically-addressed spatial light modulators (SLMs) are programmable diffractive optical elements (DOE), which are capable to modulate the amplitude and/or the phase of the incident light through a matrix structure. They are organized in a two-dimensional array of discrete pixels, which is geometrically specified by pixel pitch and pixel gap. Pixel pitch is the distance between the centres of neighboring pixels and pixel gap is the non-active area between them. The ratio of the SLM active area to its total area is referred to as its fill factor [1].

SLMs can be used to optically reconstruct the complex amplitude of a wavefield [2,3]. However, the reconstructed wavefield in the far field is corrupted by effects arising from the discrete nature, the finite pixel size and the limited fill factor of nowadays light modulators. One of the principal drawbacks is the appearance of unwanted laterally shifted replicas which are called higher diffraction orders. Another is the modulation of the wavefield in the reconstruction domain by an envelope function that affects the quality of the recovered signal.

In this report, a complementary two-step filtering process is described to enhance the quality of the signal in the reconstruction plane. Firstly, the high diffraction orders are filtered by means of a limiting aperture in the Fourier domain of a classical 4*f*-arrangement. The second filter is digitally applied by changing the signal to be encoded into the SLM in order to compensate the effect of the envelop function.

2 Complex amplitude in the Fourier domain of an SLM

In this work we focus on devices which modulate the phase distribution of incident light by a complex transmittance $t(x,y)$. If such a SLM is illuminated by a plane wave with constant amplitude u_0, the complex amplitude in the Fraunhofer diffraction plane $U(u,v)$ is proportional to the Fourier transform of $t(x,y)$ [4]:

$$U(u,v) \propto u_0 \cdot T(u,v) \tag{1}$$

Here, functions with capital letters denote the Fourier transform. The SLM's transmittance is characterized by the contribution of the active and the non-active regions and it is given by:

$$t(x,y) = a(x,y) \cdot t_{el}(x,y). \tag{2}$$

The expression $t_{el}(x,y)$ is the complex field behind the SLM, and $a(x,y)$=rect($x/M\Delta d$, $y/M\Delta d$) defines the SLM's aperture, where Δd is the corresponding pixel pitch and M is the total number of pixels. Due to its structure, the SLM only displays a discrete representation of a continuous complex transmittance $t_C(x,y)=\exp[i\varphi(x,y)]$. In addition, the non-active area is a light reflecting or transmitting region causing a constant phase shift of the incident light $b=\exp(i\varphi_c)$. Therefore, the term $t_{el}(x,y)$ may be modeled according to the sampling theory:

$$t_{el} = \left[(t_c \cdot s) \otimes \Pi_d\right](x,y) + \left[(b \cdot s) \otimes \Pi_{\Delta d - d}\right](x,y), \tag{3}$$

where d is the pixel size, $\prod_d$ and $\prod_{\Delta d\text{-}d}$ are rect-functions and $s(x,y)$ is the comb-function [4]:

$$\Pi_d = \mathrm{rect}(x/d, y/d), \Pi_{\Delta d - d} = \mathrm{rect}(x/\Delta d, y/\Delta d) - \mathrm{rect}(x/d, y/d), \tag{4}$$

and

$$s(x,y) = \sum_{n,m=-\infty}^{\infty} \delta(x - m\Delta d, y - n\Delta d). \tag{5}$$

If there is no specific reason to define it outside the area given by the aperture of the SLM, it will be convenient to regard $t_C(x,y)$ as a two dimensional periodic function, which is extended to infinity. By employing the convolution theorem and the properties of the comb-function [4], the spectrum of a plane wave illuminating the SLM is proportional to:

$$U(u,v) \propto u_0 \cdot T(u,v) = u_0 \cdot A \otimes \left[(T_C \otimes S) \cdot W_1 + (B \otimes S) \cdot W_2\right], \tag{6}$$

where,

$$S(u,v) = \sum_{m,n=-\infty}^{\infty} \delta(u - m/\Delta d, v - n/\Delta d), \tag{7}$$

$$W_1(u,v) = F\{\Pi_d\} = d^2 \,\mathrm{sinc}(d\,u, d\,v), \tag{8}$$

$$W_2(u,v) = F\{\Pi_{\Delta d - d}\} = \Delta d^2 \,\mathrm{sinc}(\Delta d\,u, \Delta d\,v) - d^2 \,\mathrm{sinc}(d\,u, d\,v). \tag{9}$$

The term $S(u,v)$ generates a set of laterally shifted replicas [5] of the diffracted complex amplitude which are called higher diffraction orders. They disturb for example the visual impression in the development of 3D-TV based on holographic concepts [6]. The term $W_1(u,v)$ arises due to the finite size of pixels which disturbs the diffracted complex amplitude by a sinc envelop. The term $W_2(u,v)$ is another envelop which modulates the dc-term. Here, we suggest to enhance the quality of the reconstructed complex amplitude by applying a complementary filtering process thus reducing the disturbing influence of $S(u,v)$ and $W_1(u,v)$.

3 Complementary Filtering

The suggested 4*f*-arrangement is shown by Fig.1. The SLM is placed in the front focal plane of the first lens. The complex amplitude at the corresponding back focal plane is proportional to the Fourier transform of the complex transmittance encoded into the SLM. Here, a limiting aperture is placed in order to block the high diffraction orders, where the spacing, $\Delta S_L=\lambda f/\Delta d$, between the orders depends on the wavelength λ, the focal length f of the lens and the pixel pitch Δd of the SLM [2].

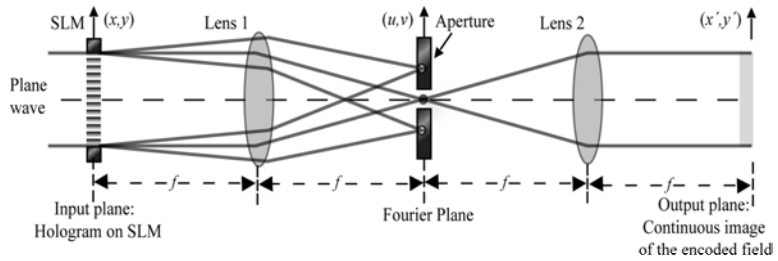

Fig. 1. Optical Fourier filtering process

The second lens provides another Fourier transform thus completing the filtering process. The whole filtering operation may be characterized by a linear system with a rectangular window function $H(u,v)$=rect(Δdu, Δdv) as transfer function. The complex amplitude $u'(x',y')$ in the back focal plane of the second lens is a continuous representation of the encoded signal which will not produce higher diffraction orders in the further propagation:

$$u'(x',y') = F\{U(u,v)\cdot H(u,v)\} = u_0 \cdot \left(t^* \otimes h\right)(x',y') . \qquad (10)$$

Although the high diffraction orders are blocked, the complex amplitude in the far field will still be distorted by the modulation term $W_1(u,v)$, see Eq. 6. In order to compensate this, a digital pre-filtering method is

proposed. The method is based on changing the complex transmittance in a way, that it compensates the modulation in the Fourier plane. This could be done in two different ways. If methods like the iterative Fourier transform algorithm (IFTA) are employed in order to design a signal $T(u,v)$ in the diffraction plane, it may be directly substituted by a shift invariant linear filter as follows, where proper sampling is assumed:

$$T_c'(u,v) = T_c(u,v) \cdot \left\{ \frac{H(u,v) \cdot W_1^*(u,v)}{\left| W_1(u,v) \right|^2} \right\}. \tag{11}$$

Alternatively, the corresponding signal $t'_C(x,y)$ could be designed in the spatial domain:

$$t_c'(x,y) = \left[t_c \otimes F^{-1} \left\{ H(u,v) \cdot W_1^*(u,v) / \left| W_1(u,v) \right|^2 \right\} \right](x,y). \tag{12}$$

Please, note that $t'_C(x,y)$ is a periodic function since $t_C(x,y)$ is assumed to be periodic as well. It is straight forward to show that inserting $t'_C(x,y)$ into Eq. 3 compensates $W_1(u,v)$ within the area defined by $H(u,v)$. The window function $H(u,v)$ is applied in accordance with the sampling, which occurs when $t_C(x,y)$ is inserted into Eq. 3. Due to this reason, $W_1(u,v)$ cannot be compensated outside $H(u,v)$ by any choice of $t'_C(x,y)$. However, this problem is of little significance since the corresponding region in the Fourier domain will be blocked by the 4*f*-setup.

4 Experimental results and conclusions

The experiment which was used to verify the presented filtering approach was based on the same principle assumptions as the numerical model in the previous section: A phase only liquid crystal on silicon (LCOS) display with high reflectance supplied by Holoeye is used in a set-up based on a 4*f*-configuration as shown in Fig. 1. It has a resolution of 1920 ×1080 pixels with a pixel size of 8 µm. For the optical reconstruction, the setup was configured in the phase mode. The SLM was configured to display a phase distribution generated from a rectangular white blank object which is disturbed by a logo using the IFTA method [7]. The hologram was illuminated with a coherent beam at wavelength λ = 532 nm.

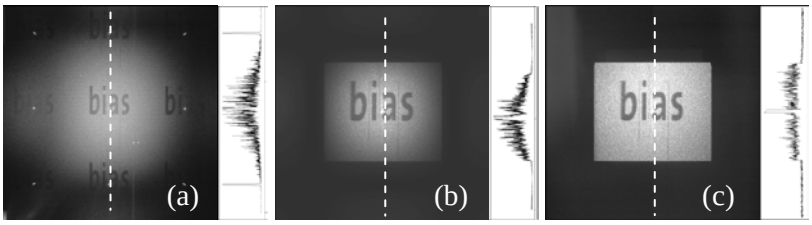

Fig. 2. Amplitude of the optically reconstructed complex amplitude a) without filtering, b) after optical and c) after digital and optical filtering

However, the reconstructed object is surrounded by multiple copies and superposes with a bright spot arising from the non-active area of the modulator as seen by Fig. 2a. The gray scale of this figure is scaled to show the diffraction orders. Figure 2b shows the amplitude of the optically filtered complex amplitude in the far-field. The diffraction orders are suppressed but still the modulation $W_1(u,v)$ is regarded as shown in Fig. 2b. To compensate $W_1(u,v)$, a new distribution $T'_C(x,y)$ using the definition of the pre-filtering Eq. 11 is generated which replaces the old one $T_C(x,y)$. Figure 2c shows the amplitude of the filtered wavefield after applying both the optical and digital filtering processes. It can be seen in Fig. 2c that the optical reconstruction the complex amplitude is clearly improved compared to the non-filtered one in Fig. 2a.

As a conclusion a complementary two-step filtering process has been demonstrated to enhance the quality of the signal and the visual impression in the reconstruction plane. One is a digital pre-filtering to compensate the signal distortion caused by the finite pixel. Another is to suppress the high diffraction orders by an optical filtering process.

5 Acknowledgement

This work is supported by DFG SFB747 B3 and EC within FP6 under Grant 511568 with the acronym 3DTV.

6 References

1. Efron, U Spatial Light Modulator Technology (Marcel Dekker, New York, NY, 1994).
2. Reicherter, M, Haist, T, Wagemann, E U, Tiziani, H J (1999) Optical particle trapping with computer-generated holograms written on a liquid-crystal display. Opt. Lett. 24:608-610

3. Baumbach, T, Osten, W, von Kopylow, C, Jüptner, W (2006) Remote metrology by comparative digital holography. Appl. Opt. 45:925-934
4. Goodman, J W Introduction to Fourier Optics (McGraw-Hill, San Francisco, 1968).
5. Arrizon, V, Carreon, E, Testorf, M (1999) Implementation of Fourier array illuminators using pixelated SLM: efficiency limitations. Optics comm. 16:207-213
6. Kreis, T (2007) Digital holography methods in 3DTV. In Proceedings of IEEE Conference on 3DTV
7. Gerchberg R W, Saxton, W O (1972) A practical algorithm for the determination of the phase from image and diffraction plane pictures. Optik 35:237-246

Combination of Phase Stepping and Fringe Tracking to Evaluate Strain from Noisy DSPI Data

Erwin Hack
Empa, Laboratory Electronics/ Metrology/ Reliability
CH-8600 Dübendorf
Switzerland

1 Introduction

Phase-stepping Digital Speckle Pattern Interferometry (DSPI) is known to suffer from speckle phase noise. In most cases this is the dominant source of measurement uncertainty, even more so, when a series of phase patterns is added up to increase the measurement range [1]. In order to obtain quantitative strain values from DSPI displacement data numerical differentiation is applied which decreases the signal to noise ratio further. Many techniques to filter the original unwrapped phase data have been reported in the literature, including low pass filtering, Gaussian convolution, image moments, power series expansions, or Fourier techniques. All these methods work satisfactorily when a smoothly varying, continuous strain field may be assumed. In presence of interfaces or object boundaries where a sudden change of strain values occur, such an assumption might not be valid. Filtering along a line of evaluation would obscure the very effect of strain transfer or peak strain values of interest. This is due to the fact that in transition zones the fringe density is changing rapidly, and strain values cannot be filtered out by low-pass techniques. Hence, both smoothing the data over a sub-window as well as filtering the data along a line of interest inevitably blurs object boundaries and transition zones. Smoothing along the line of interest is only possible if a mathematical model assumption of the displacement or strain values is made *a priori*. This model can either be motivated from a physical law or an analytical solution, or be a purely phenomenological model such as a polynomial ansatz. However, without *a priori* knowledge, a justification of the model is difficult.

Our approach relies on the observation that the quantity of interest, the strain, is coded in the fringe density or fringe gradient, i.e. along lines perpendicular to the fringes. While there is a lack of modelling phase values along the line of interest, the phase values are constant along the

lines of constant phase. Although this seems to be a trivial statement, it allows for using a parametric modelling of the fringe contour. Fringe contours are defined for each phase value or grey-level, although they are not easily extracted due to the phase noise. Filtering along the fringe contours is expected to preserve the fringe density and hence the quantity of interest [2]. Therefore, strain transfer across a transition zone can be identified reliably.

2 Experiment

An I-section steel beam was strengthened in flexure by adhesively joining a CFRP plate to its bottom surface [3]. Fig. 1 shows the measurement area of approximately 16 x 11 mm^2 at plate end where stress concentrations are expected. The area was illuminated with a Nd:YVO-laser (λ = 532 nm) sequentially from three directions. At each load level, DSPI phase maps for the three illumination directions were taken using a 3D-DSPI system (Steinbichler) with OPTOCAT Software (Breuckmann). A standard four-frame phase-stepping algorithm was applied. The phase maps were transformed to Cartesian displacement components (u, v, w) using the appropriate transformation matrix that was calculated from the geometry of the experimental set-up. The resulting phase map after elimination of rigid body in plane translation and in-plane rotation fringes is displayed in Figure 2. While the stress transfer through the adhesive layer is clearly seen in the x-displacement field, there is little evidence of increasing fringe density in the v-field.

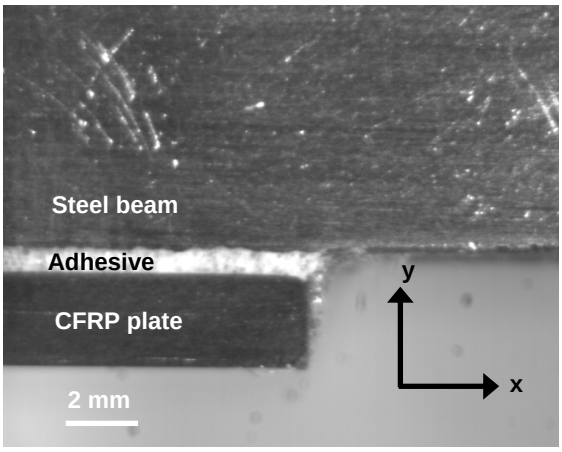

Fig. 1. Optical measurement area, 16x11 mm^2, at the CFRP plate end.

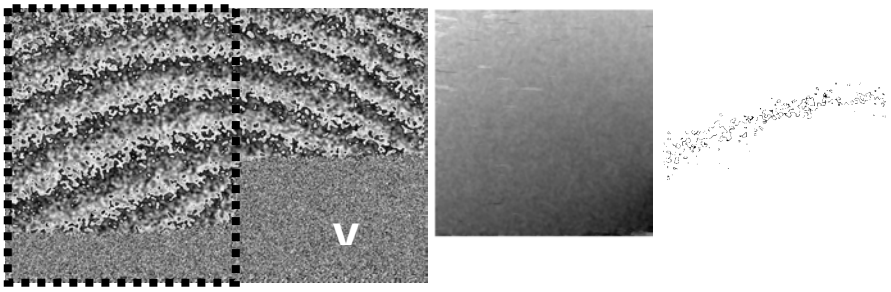

Fig. 2. Noisy fringe pattern with 0.39 μm/fringe for in-plane displacement in y-direction and area of interest (left). Demodulated phase map (middle), and pixels of equal greylevel (GL = 128, right) showing the noise level of the data.

3 Evaluation Procedure

The demodulated phase map is first binarized for a specific grey-level (phase value), as exemplified in Fig. 2, resulting in a scattered point cloud. Then either a local or a global interpolation through the point cloud is performed resulting in a smooth curve that follows the fringe. First, a second order fit is used to identify and discriminate outliers, then, a third order fit is performed on the reduced data set. Note that the fringes show no kink so that a low order polynomial fitting is sufficient. Iterating the procedure for all grey-levels provides a dense set of curves each representing the average fringe of a given phase value (Fig.3).

Although this set of curves does not completely cover the image, and intersections of individual smoothed lines are unavoidable, the resulting smoothed data allow a reliable evaluation of strain. To fill the gaps between the interpolated points, cubic splines or piecewise cubic Hermite interpolating polynomials are used.

Fig.4 shows the result for compressive strain across the adhesive zone at plate end. A simple difference quotient over 8 pixels has been taken for both the original and interpolated data sets to show the increase of quality. Note that much less variation in strain level, notably no tensile strain is obtained after interpolation with our method.

When combined with fringe tracking or segmenting methods, the technique can also be applied to unwrapped phase maps. Hence, in a sense, the method expands the fringe tracking methods that are normally used on intensity correlation data rather than unwrapped phase maps.

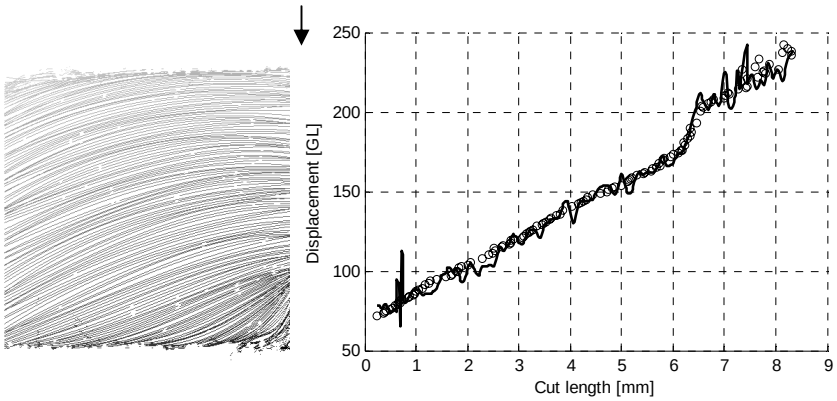

Fig. 3. Family of curves for each greylevel (left). Original data (solid line) and interpolated data (bullets) for a cut along the arrow near to the right border (right).

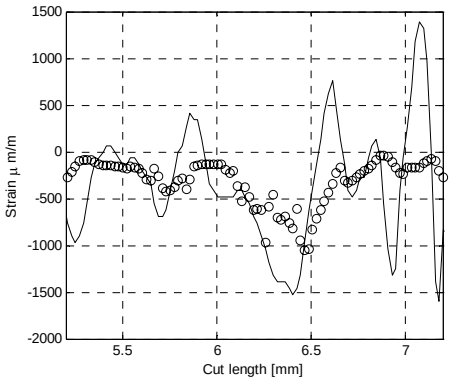

Fig. 4. Strain evaluation across the interface based on original data (solid line) and interpolated data (bullets) for the cut shown in Fig.3.

4 References

1. Hack, E., Schumacher, A. (2007). DSPI strain measurement on an externally reinforced bending beam: A comparison of step-by-step addition and pixel shift correlation. Optics and Lasers in Engineering, 45(5): 589-595.
2. O. Marklund (2001), Robust fringe density and direction estimation in noisy phase maps, J. Opt. Soc. Am. A 18, 2717-2727
3. Schumacher, A., Hack, E. (2008). Comparison of measured and calculated interfacial strains at CFRP plate end. Fourth International Conference on FRP Composites in Civil Engineering (CICE2008)

Influence of filter operators on 3D coordinate calculation in fringe projection systems

Christian Bräuer-Burchardt, Matthias Heinze, Christoph Munkelt, Peter Kühmstedt, Gunther Notni
Fraunhofer Institute for Applied Optics and Precision Engineering
Albert-Einstein-Straße 7, 07745 Jena, Germany

1 Introduction

Modern 3D measuring systems using fringe projection provide robust measurements even under measuring conditions such as low fringe contrast and high noise. In order to give reliable statements about the measuring accuracy, a well-founded error analysis should be performed as e.g. suggested by Notni [1].

Reduction of measuring errors and small gap filling can be achieved by use of filtering operators applied to rough intensity or phase images. In this work a number of linear and nonlinear filters applicable to phase value images was developed and analyzed concerning their influence on measuring accuracy.

2 Filters

In case of bad recording conditions (e.g. poor illumination, not diffuse reflections, shaded areas, incidence angles near 90°) typical errors in the phase images occur (e.g. poor modulation) resulting in incomplete areas, high noise, and measuring artefacts. These influences lead to errors in the Gray-Code determination, false positive correspondences, and missing values. According to these error sources three types of filter operators applicable to the phase images have been constructed, implemented, and analyzed: masking, correcting, and smoothing filters. All operators use information of an $n \times n$ neighborhood of the considered point.

In order to illustrate the filters impact we selected a cast teeth model as measuring object and an intraoral 3D scanner [2] as measuring device. For data production a *n*-image Gray-Code (GC) sequence [3] together with a four-image-(1+cos)-fringe sequence is used. Our aim is to obtain complete and undistorted measuring data with low noise. Here, illumination is no

problem, and measuring artefacts only occur because of shaded areas, reflections, and steep incidence angles resulting from the object shape.

In principle, the following chain of filtering will be performed: elimination or correction of probable false values, noise reduction, and reconstruction of missing values. Accordingly two groups of filter operators have been constructed: masking and correcting ones.

An example for a filter of the first group is e.g. the background masking operator *F1*. It rejects points without information of interest concerning measurement. These points have two major properties: low modulation and high noise in the close neighborhood. Points are rejected if the actual modulation is below and the phase noise above a certain threshold.

Operator *F2* corrects errors of the Gray-Code (GC) and performs a median filtering of the GC, which is used to obtain the uniqueness of the phase values. When the modulation is poor, errors in the GC determination may occur. The idea to remove these errors is the assumption of an error rate in the neighborhood of a point of below 50%. Otherwise, the disturbance is too strong and a false GC determination remains. The implementation is as follows: median of the period's number in the $n \times n$ neighborhood according to the selected kernel size is determined and used for phase calculation. Figure 1 shows an image of the reconstruction result without and with application of operators *F1* and *F2*.

Next filter operator is a Gaussian, well known in image and signal processing applications. We utilize the Gaussian operator denoted by *F3* as a two dimensional $n \times n$ filter mask which is applied to the phase image by convolution. Finally, missing phase values are completed by inter- and extrapolation filter (*F4*), when enough additional information is available. It is only applicable when the surface in the considered region may be sufficiently approximated by a plane or a second order surface.

Figure 2 shows a phase image section and resulting 3D data after Gaussian filtering and final interpolation in a certain image area, fig.3 shows an example of the effects of all applied filters to the 3D data of a cast tooth.

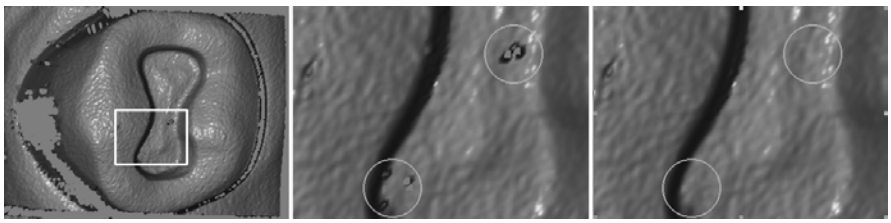

Fig. 1. Application effect of Gray-Code filtering operator *F2* (right), in a section (left) of the 3D measurement, unfiltered result (left and middle), relevant areas in the circles

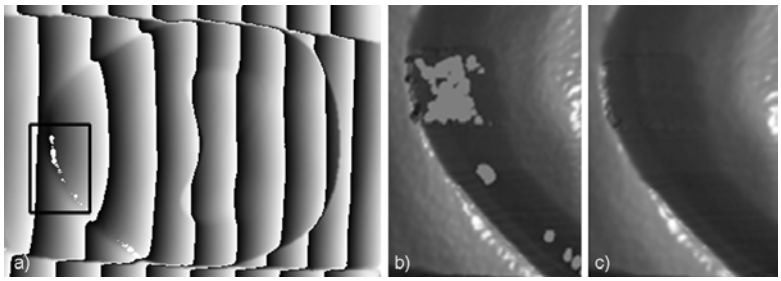

Fig. 2. Phase image with undefined white pixels (a) and section of 3D data after *F3* (b) and after *F3* + *F4* filtering (c). Notice the spreading of holes because of bad incidence angle.

Additionally, several filter operators were realized which delete certain points which are probable erroneous. For example, one operator deletes phase values with too high deviation. Another operator deletes values obtained under a high angle of incidence (e.g. > 80°). This operator, however, additionally uses preliminary estimated 3D information.

3 Influence of the Filter Operators on Measuring Accuracy

The applied filter operators influence the measuring accuracy mainly by rounding of sharp edges and a reduction of the resolution. Masking operators as *F1* do not influence the accuracy. The application of the *F2* operator also does not influence the accuracy but the completeness of the measurement. In the case of false Gray-Code determination in more than the half in the $n \times n$ neighborhood the *F2* operator may fail.

Edge rounding radius *ER* is defined as the expectation value of the measured circle radius of a sharp edge between perpendicular planes (plane cut perpendicular to both planes, see fig.4a). It should be noticed that initially the given spatial resolution leads to an edge rounding value bigger than zero.

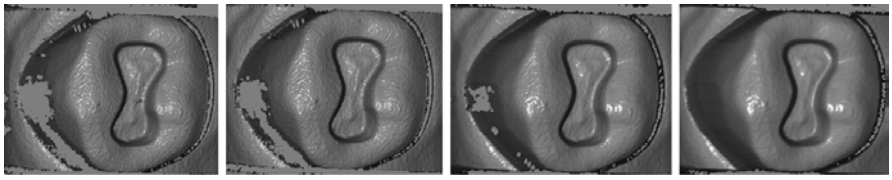

Fig. 3. Effects of the application of the filter operator chain to the 3D data of a cast tooth: without filtering, after background masking and Gray-Code correction (*F1* and *F2*), after Gaussian (*F3*), and after Interpolation (*F4*) operator (from left to right)

Resolution reduction is defined as $RR = sr(F) / sr()$, where $sr(F)$ is the structural resolution [4, 5] of filtered and $sr()$ the structural resolution of unfiltered data. A gap structure of the same depth D as width W is resolved, when it holds for the ratio $D'/D > 0.63$ (D' is the measured depth).

Interpolation usually leads to a blunting of structures and leads to edge rounding and resolution reduction. Masking operators indirectly influence the accuracy because subsequent filtering (*F3* or *F4*) is necessary.

Simulations were performed in order to quantify the edge rounding effect. A data set of intensity and phase images including an optimal edge and rectangular structures was produced. For analysis of resolution reduction effect a gap structure with same depth as width was generated.

The quantities *ER* and *RR* were determined depending on the kernel size of the Gaussian. Figures 4 and 5 show the filtering effects, results are given in table 1.

Then a set of real data of a prism with plane surfaces and sharp edges was taken as the input of a 3D data determination using different sets of filter parameters. Here the quantities *ER* (at the "sharp" edges) and signal noise *SN* (on the "plane" areas), which is defined as standard deviation of the distance of the points to a fitted plane, were determined. Results are given in table 1. Image size was 516 x 778 pixels. A measuring area of about 15 x 22 mm² was observed (1 pixel $\hat{=}$ 30 µm² in the object space).

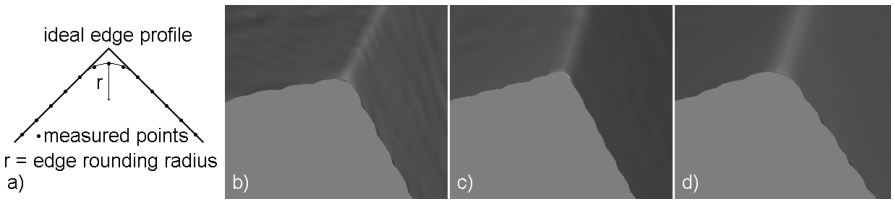

Fig. 4. Sketch concerning edge rounding radius (a) and effect of *F3* operator at different kernel sizes: without *F3* (b), 5x5 (c), and 7x7 (d) to a sharp 3D edge (simulated data)

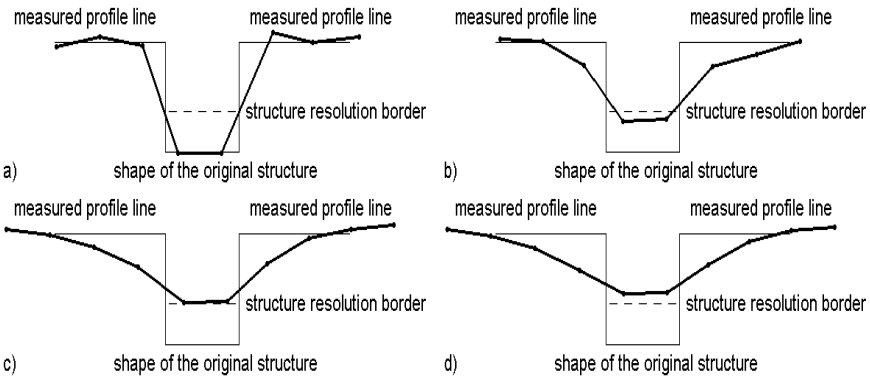

Fig. 5. Resolution reduction of simulated data by decreasing of structural resolution at different kernel sizes: without (a), 3x3 (b), 5x5 (c), and 7x7 (d). Edge rounding is visible, too.

Table 1. Results for *ER* and *RR* (simulation) and *ER* and *SN* (real data) by *F3* application

Measuring quantity / kernel size	unfiltered	3 x 3	5 x 5	7 x 7
ER in µm (simulated)	24	38	42	58
RR (simulated)	1,2	1,5	1,7	2,0
ER in µm (real)	not measurable	36	47	59
SN in µm (real)	29,7	8,2	4,8	3,0

Results show that simulated and real date provide similar results in edge rounding. Resolution reduction is significant. Signal noise decreases approximately proportionally by square root of number of kernel pixels.

4 Summary, Discussion and Outlook

From the experiments and theoretical analysis two main declarations can be made. First, filtering of phase images improves 3D measurements concerning completeness, removal of artefacts, and reduction of noise. Second, especially noise reduction can be only obtained at the expense of edge rounding and resolution reduction. Here a reduction of the accuracy depending on the shape of the measuring object must be accepted.

Optimal solution for a given task means maximal suppression of noise together with minimal edge rounding. Optimal parameters for the Gaussian depend on the measuring conditions and the shape of the object and should be estimated before filter application.

Future work should be focussed on the improvement of the Gaussian operator concerning edge preserving and on the detailed analysis of the interpolation filter influence on the accuracy.

5 References

1. Notni, GH, and Notni, G (2003) Digital fringe projection in 3D shape measurement – an error analysis. Proc SPIE Vol.5144: 372-80
2. Kühmstedt, M, Bräuer-Burchardt, C, Munkelt, C, Heinze, M, Schmidt, I, Hintersehr, J, Notni, G (2007) Intraoral 3D-Scanner. Proc. SPIE vol. 6762, 67620E
3. Gray, F (1953) Pulse code communication. US-Patent Nr. 2.632.058
4. VDI/VDE 2617 Blatt 6.2 (2005) Verein Deutscher Ingenieure, p 27
5. Carmignato, S (2006) Tests and artefacts for determining the structural resolution of distance sensors for coordinate measurements. Proc 6 th Euspen Int Conf

Polarization interferometry of singular structure of organic crystal polarization properties.

S.B.Yermolenko, M.P.Gorsky, Yu.A.Ushenko and A.G. Pridiy
Correlation Optic Dept., Chernivtsi National University,
2 Kotsybunsky Str, 58012 Chernivtsi
Ukraine

1 Introduction

The investigation of the optical geometric structure of the human skin is one of the topical directions in biological tissue optics [1]. An additional information in the matter of the skin structure is obtained by means of the optical coherent tomography methods (OCT) and its newest branch of the polarization sensitive OCT (PSOCT) which allows to accomplish the interference picture contrasting of the optically anisotropic heterogeneities of the biological tissues [1]. But the capabilities of such methods are limited by the speckle modulation of the polarization heterogeneous biological images and their singularities formation, i.e. the coordinately distributed amplitude zeros. That's why the topical task for now is searching the contrast interconnections of the polarization heterogeneous interference skin images as well as the coordinate distributions of their singular points with its physiological condition, what makes the main subject of this work.

2 Theoretical simulation

The process of the formation of such interference pattern in general case for the elliptically polarized oscillations in an arbitrary point (r) of the skin image could be presented in the following way

$$\begin{cases} E_x(r) + E_y(r)\exp(-i\delta); \\ E_{0x} + E_{0y.} \end{cases} \quad (1)$$

Here E_x, E_y are the amplitudes of the orthogonal components of the polarization ellipse, δ is a phase shift in between them; E_{0x}, E_{0y} are the

orthogonal components of E_0 amplitude of the linearly polarized supporting wave with the azimuth of the polarization Θ.

$$\begin{cases} E_{0x} = E_0 \cos\Theta; \\ E_{0y} = E_0 \sin\Theta. \end{cases} \tag{2}$$

The result of the interference addition of two fields (1), (2) is described by the following interference equations

$$\begin{cases} E_x^*(r) = E_{0x} + E_x(r) + 2\sqrt{E_{0x}E_x(r)}\cos\varphi; \\ E_y^*(r) = E_{0y} + E_y(r) + 2\sqrt{E_{0y}E_y(r)}\cos(\varphi - \delta(r)). \end{cases} \tag{3}$$

Here φ is a geometric difference of the phases in between the supporting wave and the image point with the coordinate (r).

The analysis of the equations (3) helps to reveal that the conditions of a simultaneous '0' formation of the corresponding orthogonal amplitudes (E_x^*, E_y^*) could not be reached for the elliptically polarized points of the skin interference pattern at none phase values of the supporting wave φ

$$\begin{cases} E_x^*(r) = 0 \Leftrightarrow \begin{cases} E_0 = E_x(r); \\ \varphi = (2k+1)\pi, k = 0,1,2,... \end{cases} \\ E_y^*(r) = 0 \Leftrightarrow \begin{cases} E_0 = E_y(r); \\ \varphi = \delta(r) + (2k+1)\pi, k = 0,1,2,... \end{cases} \end{cases} \tag{4}$$

It may be proved that the absolute zero of the skin object field amplitude could be reached for the points with linearly polarized oscillations.

3 Experimental results and discussion

Two groups of the histological sections were used as the examination objects, they are the physiologically normal skin (fig. 1a) and the pathologically changed skin (fig. 1b). Pathological changes of skin structure are connected with a progressive disorganization of connective tissue, namely collagen disease – dermatosclerosis.

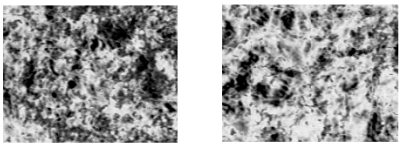

(a) (b)

Fig. 1. The polarization images of the physiologically normal (a) and pathologically changed skin specimens (b).

The examination of the interference structure of the laser skin images was done by Mach - Zehnder interferometer, its optical scheme is given in the fig. 2. This device consists of He-Ne laser 1 with a wave length of λ = 0.6328 μm; the collimator 2; polarizers 3, 7, 11; a quarter-wave plate 4; the skin biological tissue specimen 8; beam splitters 5, 12; mirrors 6, 9; the piezoelectric element 10; the microscope objective 13; CCD-camera 14; the processor 15. The polarization illuminator 3, 4 forms the circular polarization of a laser wave. The light divider 5 divides the beam into a lightening and a reference one, the polarization azimuths of which are formed by the polarized filters 7 and 10. The beam splitter 12 accomplishes the mixing of the supporting wave and the skin speckle image 8. The phase shift value φ is determined by a mirror linear displacement 9 with a help of the piezoelectric element 10. The skin interference pattern is projected by the lens 13 into the plane of the light sensitive area of CCD-camera 14.

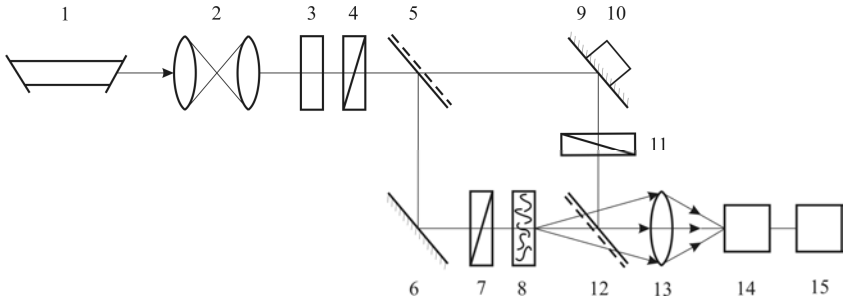

Fig. 2. The optical scheme of investigation.

The examination of the singular points in the skin interference patterns registered in Fresnel diffraction field discovered the optional possibilities involved into the problem of the skin specimens differentiation. The histograms $M(\Delta)$ of the singular points quantity are given in the fig. 3 and determined with $\Delta = 5\,pixel$ step for two registering areas in the distance of 1mm (fragments “a”, “b”) and 5mm (fragments “c”, “d”) from the plane of the physiologically normal (fragments “a”, “c”) and pathologically changed skin specimens (fragments “b”, “d”).

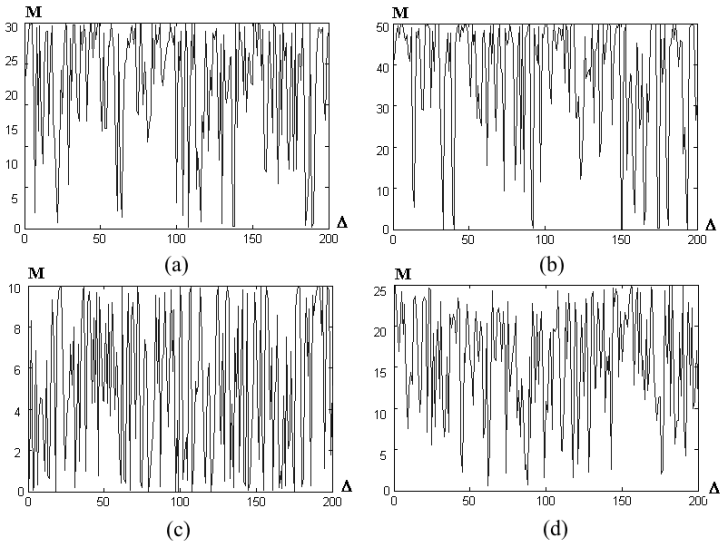

Fig. 3. The histograms of the singular points distributions of the physiologically normal skin object field (left column) and pathologically changed skin (right column) registered in Fresnel diffraction field in 1mm [(a), (b)] and 5 mm [(c), (d)] distances.

4 Conclusions

The comparative analysis of the statistics of the 1st-4th orders of the coordinate singular points distributions of the skin interference pattern registered in Fresnel diffraction field discovers an essential difference in their values. For the physiologically normal skin the skewness S_3 is two-three times less then the similar parameter for the interference patterns of the pathologically changed skin specimens. The kurtosis values S_4 differ in five-six times.

5 References

1. Handbook of coherent domain optical methods. Biomedical diagnostics, environmental and material science (Ed. Valery V. Tuchin), Kluwer Academic Publishers, Boston/Dodrecht/London (2004).

Zero order interferometry technique for measuring the Lyapunov's maximal index in optical fields

Gavrylyak M.S., Maksimyak A.P. and Maksimyak P.P.
Department of Correlation Optics, Yuri Fedkovych Chernivtsi National University, 2 Kotsyubinsky Str., Chernivtsi 58012, Ukraine

1 Introduction

Correlation, spectral, and other methods commonly used to analyze random fields usually give little or no information on nature of system generating the field. For example, one cannot determine whether the field is generated by a random object or by a deterministic but complex system.

Any optical scatter or object can be considered as a system that can generate both time and space-time chaos. For a time-independent case, a notion of optical field dimension can be introduced by analogy with the time-dependent case. In spatially extended systems, the problem of characterizing the evolution of infinitesimal perturbations becomes more complex.

We propose here an optical method for determining the largest Lyapunov exponent of an optical field that is based on the interference real-time measurement of intensity transverse correlation function.

2 Interference method for measuring the largest Lyapunov exponent field's intensity

For a dynamical system, sensitivity to initial conditions is quantified by the Lyapunov's maximal index. If d_0 – initial distance between two initial points of phase trajectories, the distance between trajectories, coming off these points, in time t will be as follows:

$$d(t) = d_0 e^{\lambda_1 t} \quad (1)$$

The value λ is called the Lyapunov's maximal index [1]. The positive value of the Lyapunov's maximal index gives the possibility of chaos existence in system, and the value of this index characterizes chaosity intensity. To calculate the largest Lyapunov exponent for a single

generalized coordinate, namely for the object field's intensity $I(r)$, we construct the dynamic systems, so that

$$I_i^{(m)} = \left[I_i, I_{i+1}, \ldots, I_{i+m-1} \right] \tag{2}$$

where I_i are the field intensities at the points, x_i.

The numerical "distances" from the i^{th} to j^{th} points are given by

$$d_j(i) = \left| I_i^{(m)} - I_j^{(m)} \right| = \left[\left(I_i - I_j \right)^2 + \left(I_{i+1} - I_{j+1} \right)^2 + \ldots + \left(I_{i+m} - I_{j+m} \right)^2 \right]^{1/2} \tag{3}$$

Point $I_i^{(m)}$ is nearest "neighbor" for each trajectory point $I_j^{(m)}$, as a nearest "neighbor" is regarded point $I_i^{(m)}$ with minimum distance $d_j(0)$ from it to the basic point $I_j^{(m)}$.

For a single generalized coordinate field's intensity $I(r)$, we construct relation, which is given by Eq.(4) and which a slope is proportional to λ_1.

$$y(i) = \frac{1}{\delta r} \langle \ln \; d_j(i) \rangle \tag{4}$$

Where <…> means the average value at all *j*, δr being the interval over which the field intensity is measured.

However, a direct application of this procedure to a real physical system having a high embedding dimension is difficult, because it requires a large number of sampling points.

To by pass the difficulties associated with digital processing, we propose to perform some operations in analog mode. The Lyapunov exponent λ_1 appears to be closely related to some correlation characteristics of an optical field, particularly the structure function [2]

$$D_I(r_1, r_2) = \left\langle \left| \tilde{I}(r_1) - \tilde{I}(r_2) \right|^2 \right\rangle \tag{5}$$

For locally uniform and isotropic fields, the intensity structure function is related to the intensity correlation function, $I_\perp(\rho)$, by

$$D_I(r_1, r_2) = D_I(\rho) = 2\left[\Psi_I(0) - \Psi_I(\rho) \right] \tag{6}$$

where $\Psi_I(\rho)$ and $\Psi_I(0)$ are the transverse intensity correlation functions for $\rho = |r_1 - r_2|$ and $\rho = 0$, respectively.

Consider the numerical "distances" Eq. (3), and define an expression for the separation between two points in the *m*-dimensional space,

$$\left| I_i^{(m)} - I_j^{(m)} \right| = \left[\sum_{k=0}^{m-1} \left(I_{i+k} - I_{j+k} \right)^2 \right]^{1/2} \tag{7}$$

Apparently, for large m expression (7) will be approximately equal to the square root of the structure function $D_I(\rho)$, where $\rho = (j-i)\delta r$.

Figure 1 shows the algorithm for calculating the Lyapunov exponent λ_1 from a plot of the structure function $D_I(\rho)$.

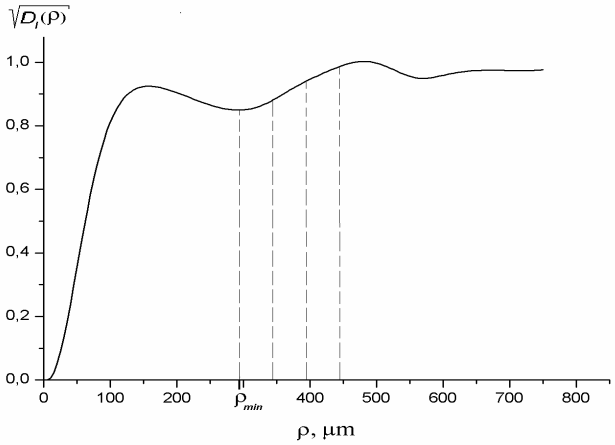

Fig. 1. The algorithm for determination of the largest Lyapunov exponent from the plots of the structure function.

We first find the $\rho_\perp$ to equal the lag where the structure function drops to 1/*e* of its initial value. For $\rho > \rho_\perp$ we find locates the nearest neighbor of each point on the trajectory for which $d_j(0)$ is minimum. This transverse displacement on Fig.1 is corresponds to $\rho_{\min}$ and is greater than the mean period of the spatial intensity field fluctuations.

Distance between trajectories, in the *m*-dimensional space, (7) will be as follows: $d(1) = \sqrt{D_I(\rho)}$ for different values $l = i - j = \rho/\delta r$. Then, the largest Lyapunov exponent λ_1 can be easily found from the slopes of the curves of l versus $y(l) = y(\rho - \rho_{\min}) = \frac{1}{\delta r}\left\langle \ln \sqrt{D_I(l)} \right\rangle$. The curve $D_I(\rho)$ can be obtained from a measured or a calculated function $[D_I(\rho)]^{1/2}$, from which the curve $y(l) = f(\ln \sqrt{D_I(l)})$ is constructed for the number of points used in calculating the structure function equal $m = N/2$ and which

are shown on Fig.2. The largest Lyapunov exponent field's intensity $I(r)$ calculated using the above procedure (λ_1=0.187) is in a good agreement with those obtained by the commonly used method (λ_1=0.191), but the processing time is reduced by about two orders of magnitude.

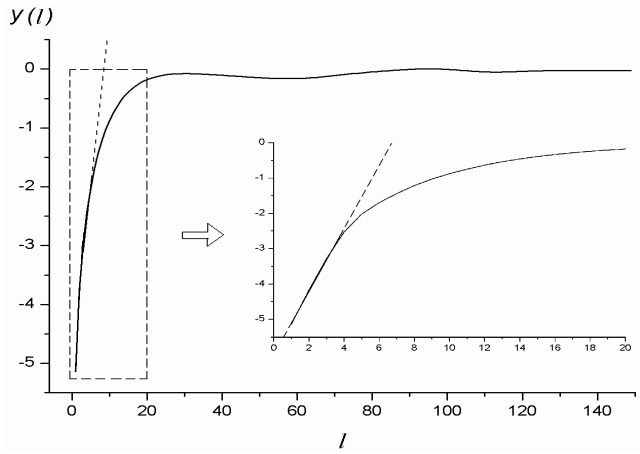

Fig.2. Calculation results *y(l)* for optical field.

Another possibility is to measure the transverse intensity correlation function using an intensity correlator and then substitute the data into Eq. (8). It can also be evaluated by measuring the field correlation function using a shearing interferometer with subsequent determination of the intensity structure function, $D_I(\rho)$, and the relation [3].

$$D_I(\rho) = 8\Gamma_\perp(0)\left[1 - |\Gamma_\perp(\rho)|^2\right] \tag{8}$$

where $\Gamma_\perp(\rho)$ and $\Gamma_\perp(0)$ are the transverse field correlation functions for displacement ρ and for zero displacement, respectively.

In summary, we have proposed the interference approach for measurement of the largest Lyapunov exponent in coherent chaotic optical fields. We have applied for high-speed real time correlation techniques and the largest Lyapunov exponent field's intensity calculated that using the above procedure is in good agreement with those obtained by the commonly used method.

3 References

1. Wolf, A, Swift, J, Swinney, H, and Vastano, J (1985) Determining Lyapunov exponents from a time series. Physica D 16: 285-317.
2. Rytov, S, Kravtsov, Yu, and Tatarsky, V (1989) Principles of Statistical Radiophysics. Berlin: Springer: 320.
3. Angelsky, O, Maksimyak, P, Perun, T (1993) Dimensionality in optical fields and signals. Appl. Opt. 32: 6066-6071.

Orientation-selective spiral-phase contrast microscopy

Guohai Situ, Michael Warber, Giancarlo Pedrini, and Wolfgang Osten
Institut für Technische Optik, Universität Stuttgart
Pfaffenwaldring 9, 70569 Stuttgart
Germany

1 Introduction

Recently it has been shown that a spiral phase plate (SPP), $\exp(i\phi)$, where ϕ is the azimuthal angle, can be used as a Fourier plane filter for edge enhancement [1-5]. When using a SPP with the above symmetric phase structure as a filter, one usually obtains orientation-independent edge-enhancement of an input image, i.e., all its edges are enhanced to a degree with respect to the local phase and amplitude gradients regardless of their local orientations. It has been shown that a slight modification of the phase structure of the SPP turns the filtered output into a relief-like pattern (shadow effect) [5], in a manner similar to the Nomarski microscopy. In contrast to the Nomarski microscopy, spiral phase contrast microscopy does not need to rotate the specimen in order to enhance the edges of required local orientation but, for example, replaces the phase singularity and its vicinity with a uniformed phase of a certain value [4,5]. In this work we demonstrate two alternative methods to achieve orientational phase-contrast enhancement in standard microscopes.

2 Experimental setup

The proposed spiral-phase contrast microscopy is schematically shown in Fig.1. An LED (Diamond Dragon LR-W5AP, Osram) emitting light with the wavelength of 633 nm ($\Delta\lambda$=18 nm) was used to illuminate the microscope after passing through a bandwidth filter $\Delta\lambda$=1 nm. All the imaging lenses in the system have a focal length equal to 200 mm. The scattered light from the specimen was collected using a microscopic objective (Zeiss, 20×) and brought to the input plane of a followed 4*f* filtering system. A phase only spatial light modulator (SLM, PLUTO-VIS, Holoeye) was placed at the Fourier plane to represent the spatial filter. The

spiral phase is encoded into a phase grating by multiplying with a plane wave, in a way so that the grating period is equal to 32 μm, occupying 4 pixel lines. At the output plane of the filtering system a CCD camera (AVT Pike F-145B) was used to record the first order diffraction of the grating.

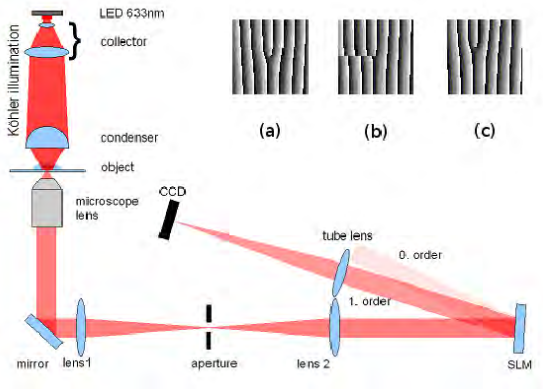

Fig.1. Optical setup of the spiral phase contrast microscopy. The grating in (a) represents the spiral phase exp(iϕ); the one in (b) represents a fractional SPF and the one in (c) represents an off-axis SPF.

3 Results

The specimens used are the microtome of taste buds of a rabbit on a glass slide. Figure 2 shows the part of the specimen in the field of view under investigation without any phase filtering. Depending on the phase structure of the filter, one can obtain contrast enhancement of different degree and orientation for a given input image. Two techniques are employed here to modify the phase structure.

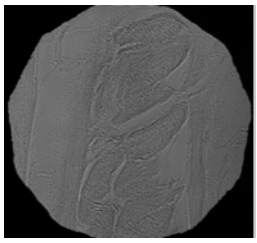

Fig. 2. The image of the biological specimen under investigated: the microtome taste buds from a rabbit.

The first method is based on the fractional SPP [6], exp(i$p\phi$), where, in this case, $0 < p < 1$ is a fractional number. For the application in filtering, the

Fourier spectrum of the SPP, especially the position of the vortex core, plays a very important role. It has been shown that the vortex core lies in a radial line orthogonal to the starting angle, ϕ_0, of the spiral phase [3]. It is therefore expected to find the orientation of enhancement along this radial line. Figure 3(a) is obtained by filtering the spectrum of the specimen using a SPF with p=0.6 and ϕ_0=0. It is clearly seen that the filtered image has a pseudo three-dimensional shadow view, which results in a significant enhancement of contrast so that the details are more visible. When rotating ϕ_0 to be $\pi/2$, π and $3\pi/2$ and keeping p unchanged, the corresponding filtered outputs are plotted in Fig. 3(b)-(d), from which we can see that the orientation of enhancement rotates accordingly over an angle $\pi/2$, π and $3\pi/2$, respectively.

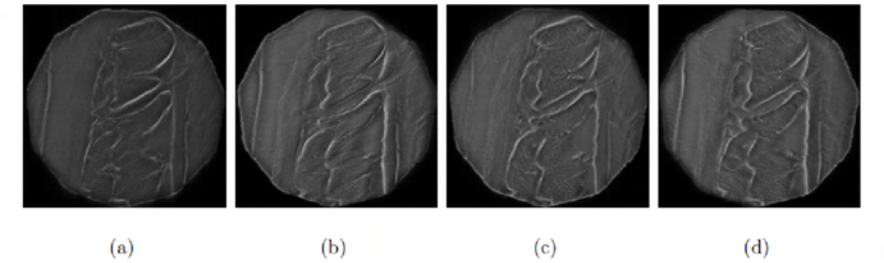

Fig. 3. The effect of the starting angle to the orientation of edge enhancement. In the figures p=0.6, and the starting angles are (a) 0, (b) $\pi/2$, (c) π, and (d) $3\pi/2$, respectively

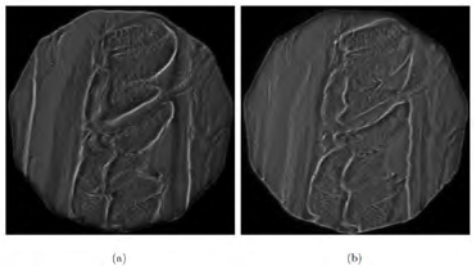

Fig. 4. The effect of the position of the singularity to the orientation of edge enhancement. θ is equal to (a) 0 and (b) π.

The second method is to use an off-axis SPF. An interesting consequence is that the vortex core in the diffraction field is not located on the axis. This leads to a shadow effect similar to the one obtained with the above method. Explicitly, the orientation of enhancement is determined by its polar angle, θ, of the vortex core. This is also suggested by the experimental results shown in Fig. 4, in which the images filtered by use of

a SPF with θ equal to 0 and π are plotted. Both the two images resemble a relief-like surface structure of the cell, but the one obtained with θ=0 seems to have a negative relief rendering, whereas the other one has a positive rendering. By continually shifting the singularity along the circle with a certain radius, we can obtain anisotropic contrast enhancement of the input specimen of arbitrary azimuthal orientation.

4 Conclusion

In conclusion, we have proposed two methods to achieve anisotropic spiral phase contrast microscopy. Both these methods are based on filtering the specimen frequency using a spiral phase plate in the Fourier domain in a 4*f* system. For the method using the fractional SPP, one can control the enhancement by changing the value of the topological charge and the starting angle of the filter. For the method using an off-axis SPP, the enhancement can be controlled by the off-axial position of the singularity. Both these methods can render the phase specimen into a relief-like view.

5 Acknowledgement

G. Situ acknowledges the support of the Alexander von Humboldt Foundation.

6 References

1. Khonina, S N, Kotlyar, V V, Shinkaryev, M V, Soifer, V A. and Uspleniev, G V, (1992) Journal of Modern Optics 39, 1147-1154
2. Davis, J A, McNamara, D E, Cottrell, D M, and Campos, (2000) J, Optics Letters 25, 99-101
3. Situ, G, Pedrini, G, and Osten, W, (2009) submitted to J. Opt. Soc. Am. A
4. Fürhapter, S, Jesacher, A, Bernet, S, and Ritsch-Marte, M, (2005) Optics Express 13, 689-694
5. Jesacher, A, Fürhapter, S, Bernet, S, and Ritsch-Marte, M, (2005) Physical Review Letteres 94, 233902
6. Berry, M V, (2004) Journal of Optics A 6, 259-26

TOPIC 2

Application Enhanced Technologies

Chairs:

Jonathan M. Huntley
Loughborough
(GB)

Thomas Kreis
Bremen
(Germany)

Chris L. Koliopoulos
Tucson
(USA)

Invited Paper

Model-based white light interference microscopy for metrology of transparent film stacks and optically-unresolved structures

Peter de Groot, Xavier Colonna de Lega, and Jan Liesener
Zygo Corporation
Laurel Brook Road, Middletown, CT USA

1 Introduction

Surface form and roughness evaluation by interferometry is a highly-evolved practical science, encompassing a wide range of tools from the laser Fizeau to the interference microscope sketched below as Fig. 1.

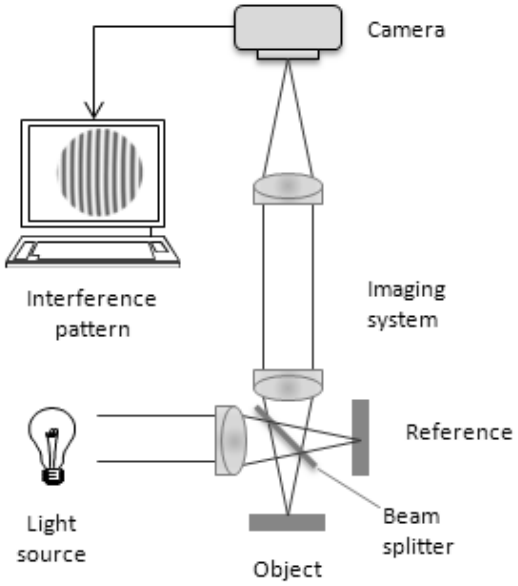

Fig. 1. A Michelson-type interference microscope for 3D surface profiling.

The present work considers the current revolution in white-light interference microscopy, in which the fairly simple pairing of interference phase to surface height has given way to more complex and powerful techniques that extract *surface structure* details, such as transparent film

characteristics and the shape of optically-unresolved surface features. These new capabilities rely on a *model-based* interpretation of the interference signals, using methods and optical geometries that are still in rapid development.

2 Model-based analysis

Let us begin with the signal shown in Fig. 2, with its characteristic interference fringes and white-light contrast envelope. A significant industry has developed around the idea that the phase of the interference fringes varies linearly with the surface height, at a rate inversely proportional to the wavelength. In spite of advances in enabling technologies for interferometry, the principles of 3D surface metrology today are about the same as they have been for 100 years, relying on this linear phase-height relationship with perhaps an equally simplified, generic formula for the fringe contrast envelope.

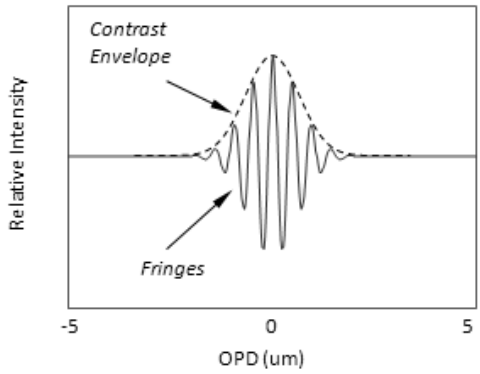

Fig. 2. A white-light interferometry signal as a function of optical path difference (OPD).

From the earliest days of commercial white-light interferometry in the 1990's, it has been understood that there is more about the surface structure that could be extracted from the signal if we use a more detailed model of the interference effect [1]. The signal in Fig. 3, for example, looks very different from the simple model represented by Fig. 2. The differences relate to surface structure—in the case of Fig. 3, a transparent thin film of silicon dioxide on a silicon substrate. This signal is not so easy to interpret as the one in Fig. 2, particularly as the film gets thinner and the overlapping signals coalesce.

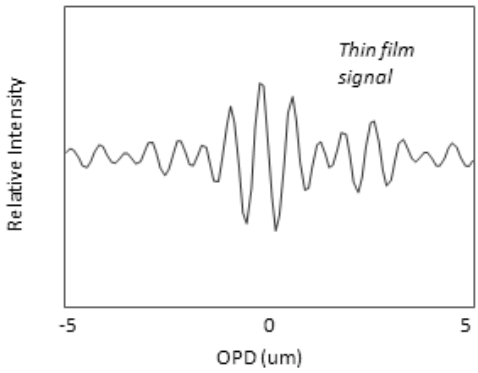

Fig. 3. Signal for an object having a transparent film coating of approximately 1 micron thickness.

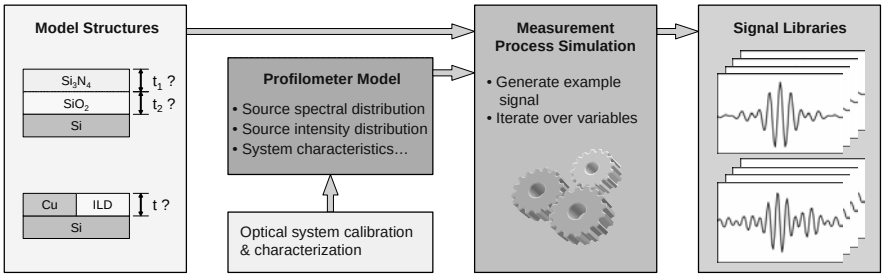

Fig. 4. Schematic flowchart of model-based interferometry. A comparison of the experimental signal with the signal library entries leads to the determination of a surface structure characteristic such as film thickness.

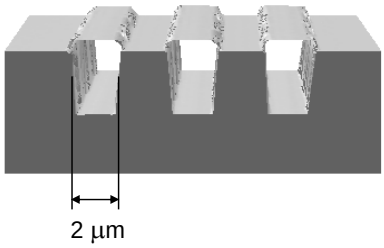

Fig. 5. Example model-based white light interference 3D profiling of film thickness measured with a 100X objective, showing simultaneously the top surface and underlying substrate profiles of a sample related to semiconductor processing. Here the Si substrate has trenches that are 480 nm deep, filled with SiO_2 that protrudes 70 nm above the surface of the wafer. From ref. [2]

The essence of a model-based approach is to begin with a more complete and accurate model of the interferometer and how the light interacts with the object surface [3]. Next, we solve the *inverse problem* to discover parameters such as film thickness by comparing of experimental and theoretical signals (or the Fourier Transforms) over a range of possible surface structures [2][4].

The first and most well-documented application of model-based white light interferometry has been 3D profiling of transparent film thickness and topography, as illustrated in Fig. 5. This is a capability difficult to match in any other tool—reflectometry may provide film thickness profiles but not topography, while tactile gages provide topography over films but without film thickness. Here we have both, in a non-contact, high-speed instrument with high data density.

3 Pupil-plane interferometry

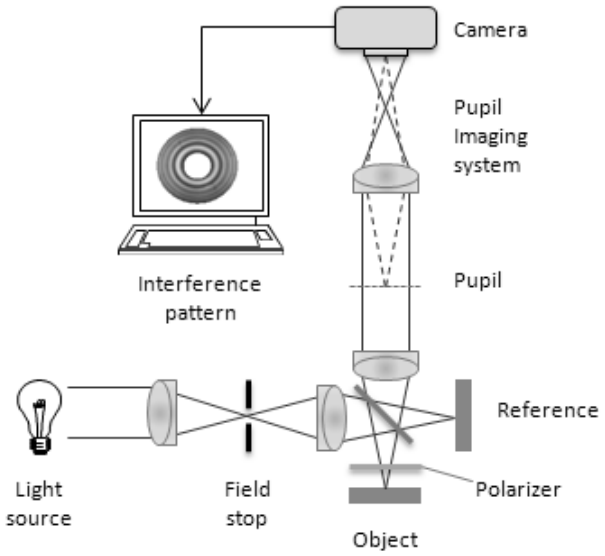

Fig. 6. White-light nterferometer for detailed surface structure analysis at a single point on the object surface.

For a higher-performance, advanced films capability (AFC), we adopt the geometry of Fig. 6, which shares some features with traditional conoscopy [5], microellipsometry [6] and monochrome interferometric techniques [7]. A field stop reduces the view to a single, 10-micron diameter spot on the

object surface, and a special lens relays the pupil image to the camera in place of the object image [8][9]. The addition of a polarizer enables complex surface reflectivity analysis as a function of polarization and angle of incidence. Fourier analysis of the white-light interferometer signals adds the dimension of wavelength, as shown in the data example of Fig. 7. A model-based interpretation of these multiple-wavelength, multiple-angle ellipsometric data provides the desired information about surface structure.

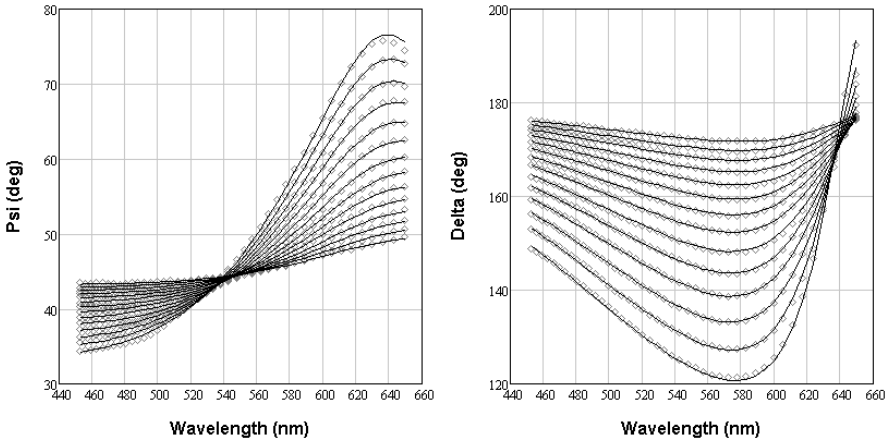

Fig. 7. Plot of ellipsometric parameters Delta and Psi measured as a function of wavelength and angle of incidence for a two-layer film stack of 56 nm Diamond Like Carbon (DLC) on 5 nm alumina over a metal alloy, using the AFC interferometer of Fig. 6. Markers represent experimental data points computed from a single measurement. Lines correspond to Delta and Psi computed using an optimized model of the film stack. Each line maps to a different angle of incidence, covering a 20° to 46° range. See Ref.[10].

Because the geometry of Fig. 6 relies on a platform that is very close to the conventional 3D imager of Fig. 1, it is straightforward to switch between the two modes using a simple exchange of imaging lens. We have reported several applications of this combination instrument in Ref. [10]and related papers.

4 Sub-wavelength surface structures

Transparent films are not the only surface structure characteristics that can influence white-light interference effects. Features ten times smaller than the source wavelength can leave a record of their presence in the

interference signal shape that can be related to parameters such as width, height, edge shape and other optically-unresolved critical dimensions.

We use rigorous coupled wave analysis (RCWA) to model these effects and determine their influence on the interferometer signals. In collaboration with the Institut für Technische Optik at the University of Stuttgart, we employ a version of RCWA developed for high-NA white light interferometry [11]. RCWA is most effective with regular patterns or grating-like structures. The compromise is that we do not directly image individual sub-wavelength features, but rather to infer critical dimensions from the aggregate interaction of white light with these grating structures specifically designed for this purpose.

A first approach involves measurements of trench depth using a simple 3D step-height measurement using an interference microscope in imaging mode. For the example shown in Fig. 8, the unresolved grating manifests itself as an overall change in measured profile, which can be compared to theoretical expectations to determine the substrate etch depth. For simple structures with only one or two variable parameters, this method is a rapid and effective means of parameter control with a repeatability for individual measurements of 0.1nm rms and a validated correlation to AFM measurements, as detailed in Ref.[12].

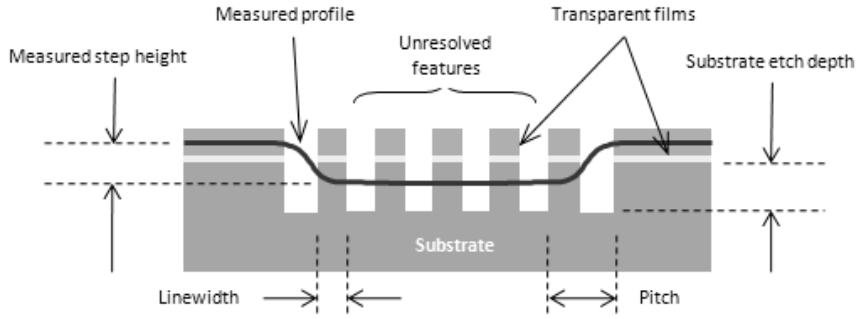

Fig. 8. Optical step-height measurement on a surface structure that includes transparent film layers with optically unresolved features. The measured profile does not resolve the features but is influenced by linewidth and etch depth.

For more complex structures or a multi-parameter analysis, we again call upon the pupil-plane geometry of Fig. 1. This is a more sensitive method with correspondingly greater complexity in the analysis, comparable to classical scatterometry but using an interferometer in place of the traditional reflectometer or ellipsometer. We call our technique Interferometric Critical Dimension analysis or ICD [8][9].

Fig. 9 shows a cross section of a periodic, 160-nm pitch structure that was measured using the ICD approach at a mean wavelength of 500nm. Seven parameters define the structure shape, including film thickness, side-wall angle (SWA), lateral width or critical dimension (CD), and height. Comparison with theoretical modeling using 4 wavelengths, 4 angles of incidence between 30° and 50°, and the complete 0 to 2π azimuth range available to the pupil-plane geometry provides simultaneous measurement of all of these sub-wavelength feature parameters in a few seconds. The cross section determined experimentally by ICD shown to the left in Fig. 9 is in good agreement with the scanning-electron microscope (SEM) cross section image shown on the right. The 3 sigma reproducibility for the 7 parameters over 3 days range between 0.25nm and 0.75 nm for dimensions and 0.25° and 0.35° for angles.

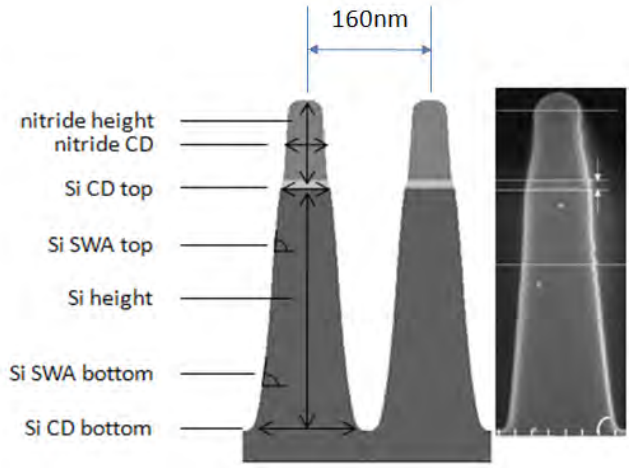

Fig. 9. Seven-parameter critical-dimension analysis (ICD) of an optically-unresolved, sub-wavelength grating-like structure using pupil-plane white-light interferometry.

5 Summary and conclusion

The field of application for white-light and related coherence-based interferometric techniques significantly increases with model-based methods; particularly when these techniques are combined with variations in optical geometry such as the pupil-plane geometry (Fig. 6) of our AFC and ICD instruments. Interference microscopes are now capable not only of high-quality 3D topography measurements, but detailed parameter

analysis of transparent films and sub-wavelength structures relevant to state-of-the art, high-technology devices and systems.

6 References

1. de Groot, P (1995) Method and apparatus for surface topography measurement by spatial-frequency analysis of interferograms. US Patent No. 5,398,113.
2. Colonna de Lega, X, de Groot, P (2005) Optical Topography Measurement of Patterned Wafers. AIP ULSI Proceedings 788:432
3. de Groot, P, Colonna de Lega, X (2004) Signal modeling for low coherence height-scanning interference microscopy," Appl. Opt., 43:4821
4. Kim, S-W, Kim, G-H (1999) Thickness-profile measurement of transparent thin-film layers by white-light scanning interferometry. Appl. Opt. 38:5968
5. Pluta, M (1993) Advanced light microscopy. Vol.3, Elsevier, Amsterdam: 265
6. Shatalin, S V, Juškaitis, R; Tan J B, Wilson, T (1995) Reflection conoscopy and microellipsometry of isotropic thin film structures. J. Microsc. 179:241
7. Feke, G D, Snow, D P, Grober, R D, de Groot, P, Deck, L (1998) Interferometric back focal plane microellipsometry. Appl. Opt. 37:1796
8. Davidson, M, (2006) Interferometric back focal plane scatterometry with Koehler illumination. US Patent 7,061,623
9. Colonna de Lega, X, de Groot, P (2008) "Interferometer for determining characteristics of an object surface," US patent 7,446,882
10. Colonna de Lega, X, Fay, M, de Groot, P, Kamenev, B, Kruse, J R, Haller, M, Davidson, M, Miloslavsky, L, Mills, D (2009) Multi-purpose optical profiler for characterization of materials, film stacks and for absolute topography measurement. SPIE 7272:paper 163
11. Totzeck, M (2001) Numerical simulation of high-NA quantitative polarization microscopy and corresponding near-fields. Optik 112:381
12. de Groot, P, Colonna de Lega, X, Liesener, J, Darwin, M (2008) Metrology of optically-unresolved features using interferometric surface profiling and RCWA modeling. Opt. Express 16:3970
13. Raymond, C J, (2001) Scatterometry for Semiconductor Metrology. Handbook of Silicon Semiconductor Metrology, A. J. Deibold, ed., (Marcel Dekker, Inc., New York)

Limitations and Optimization of Low-coherence Interferometry for High Precision Microscopic Form Measurement

Peter Lehmann, Jan Niehues
Dept. of Electrical Engineering, University of Kassel
Wilhelmshöher Allee 71, 34109 Kassel
Germany

1 Introduction

Optical areal measurement represents an efficient way to produce 3D-topography data sets. These are taken in parallel and with low requirements concerning mechanical axes. Well-established instruments for measuring microscopic objects such as micro-lenses or etched silicon structures are based on interference microscopy, e.g. white-light interferometry (WLI) or phase-shifting interferometry (PSI).

These instruments achieve nanometer accuracy of the measured height data. However, there are some limitations, especially if complex surface structures involving flanks, height steps and curved areas are to be measured with high precision.

In certain cases, optical effects occur that distort measurement results systematically. Erroneous, invalid, or inaccurate topography data will be the consequence.

In this contribution, we discuss some of the limiting phenomena by means of test objects with well-defined geometry such as sinusoidal standards. The relevant effects are analysed using a simplified model of a Mirau interferometer, which is the most common type of interference microscope in industrial applications.

A well-known extension of white-light interferometry utilizes both, the estimation of the height position obtained from the coherence peak (also called envelope or contrast evaluation) and the evaluation of the phase of the interference component of the signal at the peak's position.

Considering the signal's phase yields an accuracy, which is comparable to PSI but without the restriction of the 2π ambiguity: The fringe order is obtained from the envelope's maximum position.

Problems arise from objects with height steps if a step height of less than the coherence length of the light is to be measured. In this situation,

light waves originating at different height levels and the reference wave interfere. Therefore, the envelope of the resulting signals will be shifted in a characteristic way, thus leading to the well-known batwing effect [1, 2].

Furthermore, the position of the envelope's maximum can also systematically shift if the surface of a specularly reflecting object shows some tilt or curvature [3, 4]. This results in a deviation of a height value obtained from the envelope's position with respect to the height position resulting from the phase. If this deviation exceeds a quarter of the light wavelength, the fringe order is no longer obtained correctly. Consequently, this leads to phase jumps corresponding to virtual height steps of half the wavelength. We proposed a dual-wavelengths technique, which allows us to overcome some of the current limitations of with-light interferometry, namely batwings and phase jumps caused by tilts or curvatures of specularly reflecting objects [5].

However, as the flanks of an object become steeper, further effort may be necessary in order to reduce phase jumps. This can be demonstrated by a novel PTB chirp standard showing a maximum slope of nearly 18° [6].

The limitations discussed here affect almost all white-light interferometers commercially available today [7].

It depends on the surface parameters whether the curvature or the slope effect dominates. We demonstrate this in the following section by measurements of sinusoidal surfaces of different spatial frequency.

2 Experimental Results

The experimental results shown in this section were obtained by different white-light interferometers equipped with Mirau objectives. Fig. 1 depicts two-dimensional surface profiles calculated from the same set of interferograms. While the socalled depth-scan was carried out, i.e. a 20x Mirau objective moves along the optical axis towards the measuring object, these interferograms were taken at equidistant axial positions. The plotted profiles are related to a single line of the CCD camera. The measuring object was a polished silicon wafer with some pores on the surface. These pores were produced from a contamination of the wafer surface with droplets of the etching medium.

However, if only the envelope of the WLI signal is evaluated, the measured profile shows a strong peak instead of a pore. The height of this peak is approximately 150 nm. If the phase of the WLI signals is taken into consideration, an erroneous fringe order is determined close the peak's maximum. Obviously, this leads to a 2π-phase jump in the corresponding

curve. The phase jump can be easily eliminated, for example by phase unwrapping or by use of the dual-wavelength technique mentioned above. As it can also be seen in Fig. 1, after elimination of the 2π jump the measured profile shows a pore instead of a peak. In the following, we try to find an explanation for this phenomenon.

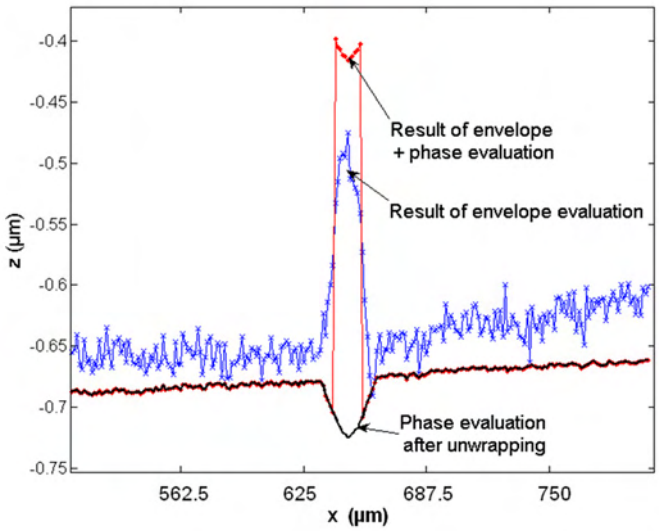

Fig. 1. Profile measured by WLI showing a strong dependence on the evaluation

It is well known, that WLI is quite sensitive to chromatic aberrations [7]. Consequently, for further studies an optical imaging system with an improved chromatic correction was used. With this system, a sinusoidal standard of 0.1 µm amplitude and 8 µm cycle length was measured by use of a 50x Mirau objective. Fig. 2 shows the result. The amplitude of the sinusoid obtained from the position of the coherence peak deviates significantly from the nominal amplitude. A correct determination of the sinusoidal geometry requires the evaluation of the phase of the interference signal. Due to the improved optical design of the system, in comparison with Fig. 1 both profiles in the upper diagram of Fig. 2 show peaks and valleys at the same locations.

However, the lower diagram in Fig. 2 exhibits significant differences between the results of envelope and phase evaluation. These differences are at a minimum close to the optical axis of the interferometer and increase continuously with the distance from the optical axis. The maximum amplitude error resulting from the envelope evaluation is approximately 100% close to the edges of the diagram in Fig. 2.

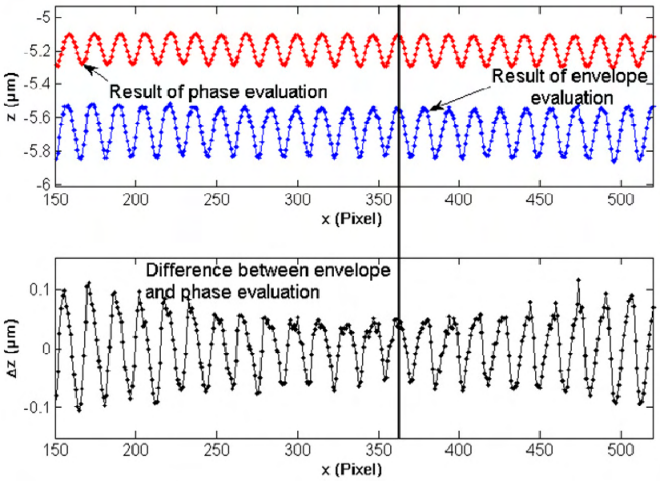

Fig. 2. Sinusoidal profile measured by a chromatically corrected WLI system: comparison of envelope and phase evaluation results (lateral distance corresponding to pixel pitch: 0.5 µm)

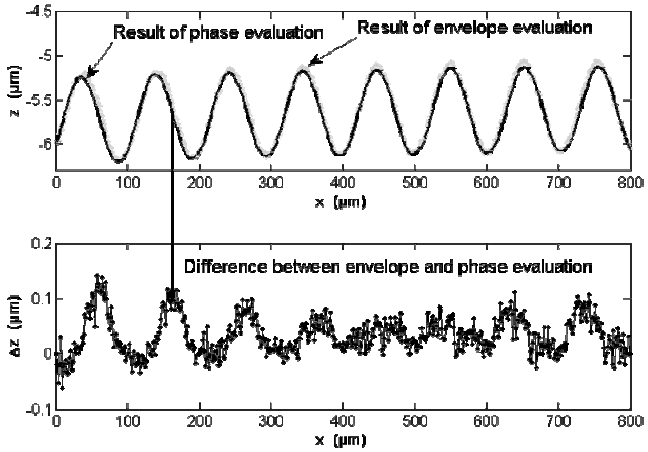

Fig. 3. Sinusoidal profile measured by a chromatically corrected WLI system: comparison of envelope and phase evaluation results

An important point in this context is that the maximum errors occur at the locations of the peaks and valleys, where the curvature of the profile is at a maximum, too. For the standard according to Fig. 2, the minimum radius of curvature is 16.2 µm. For comparison, we carried out measurements on a different sinusoidal sample showing an amplitude of 0.5 µm and a cycle length of 100 µm resulting in a minimum radius of curvature of 506.6 µm. Fig. 3 shows profiles obtained by use of a 20x

Mirau objective. In this case, the results of envelope and phase evaluation are close together in the upper diagram. However, the difference plotted in the lower diagram again exhibits systematic errors. In contrast to Fig. 2, the maximum deviation appears at the flanks of the sinusoid, where the slope reaches its maximum. In all cases of deviation between envelope and phase evaluation phase jumps occur if these deviations increase a quarter of the wavelength of light. Again, the phase jumps can be first identified and then eliminated, for example by use of the dual wavelength method.

3 Discussion and Physical Model

The measuring results shown in Figs. 1 to 3 demonstrate that although white-light interferometry is a well-established tool in micro metrology, systematic measuring errors appear in certain situations. Especially the position of the coherence peak is sensitive to height steps as well as surface slope and curvature. The batwing problem is well understood and documented in this context [1, 2].

Hence, in this paper only the slope and curvature effects are discussed. We state that the resulting systematic errors in the cases of slope and curvature are primarily related to dispersion effects [8]. Therefore, they strongly dependent on chromatic aberrations of the optical system.

In order to explain the experimental effects according to Figures 1 to 3 we analyse how the pupil of the Mirau objective is illuminated by light rays travelling towards the image plane. The case of a tilted object point as it is shown in Fig. 4 d) agrees to the situation described by Berger et al. [4].

If a concave object area is imaged, the cone of the reflected light will be cut at two opposite edges as shown in Fig. 4 b). Otherwise, if the surface area shows a convex shape, the inner cone arising from the reference mirror will be broadened according to Fig. 4 c). In all cases except for the ideal situation shown in Fig. 4 a) different averaged ray pathes in the measuring and the reference arm appear. In combination with chromatic aberrations, dispersion differences will be the consequence. It is well known, that dispersion influences the position of the coherence peak dramatically [3, 8]. However, a quantitative analysis of the limiting effects mentioned above requires a detailed physical model of the interferometer. Usually, in microscopic imaging a satisfying correction of axial chromatic aberrations is achieved, if the rays of different wavelength converge within the depth of focus of the imaging system. A further reduction of these

aberrations in low-coherence interferometers seems to be a promising approach for future instrumental developments.

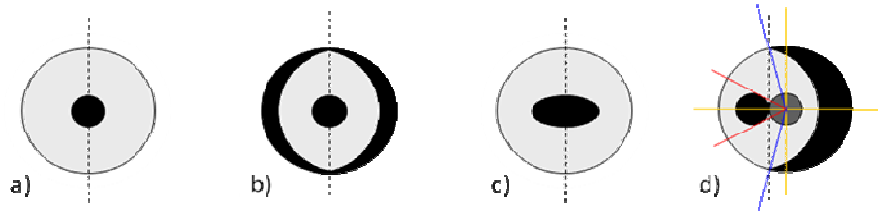

Fig. 4. Illumination of the pupil of a Mirau interference objective a) for an ideally aligned specularly reflecting plane object, b) for an object with concave curvature in horizontal direction, c) for an object with convex curvature in horizontal direction, and d) for a plane surface tilted in horizontal direction.

4 References

1. De Groot, P, Colonna de Lega, X, Kramer, J, Turzhitsky, M (2000) Determination of fringe order in white-light interference microscopy. Appl. Opt. 41: 4571-4578
2. Harasaki, A, Wyant, J C (2000) Fringe modulation skewing effect in white-light vertical-scanning interferometry. Appl. Opt. 39: 2101-2106
3. Lehmann, P (2006) Systematic effects in coherence peak and phase evaluation of signals obtained with a vertical scanning white-light Mirau interferometer. SPIE Proc. 6188: 11-1 – 11-11
4. Berger, R, Sure, T, Osten, W (2007) Measurement errors of mirrorlike, tilted objects in white-light interferometry. SPIE Proc. 6616: 2E-1–8
5. Niehues, J, Lehmann, P, Bobey, K (2007) Dual-wavelength vertical scanning low-coherence interferometric microscope. Appl. Opt. 46: 7141-7148
6. Krüger-Sehm, R, Bakucz, P, Jung, L, Wilhelms, H (2007) Chirp-Kalibriernormal für Oberflächenmessgeräte. Technisches Messen 95: 572-576
7. Gao, F, Leach, R K, Petzing, J, Coupland, J M (2008) Surface measurement errors using commercial scanning white light interferometers. Meas. Sci. Technol. 19: 015303, 13
8. Pförtner, A, Schwider, J (2001) Dispersion error in white-light Linnik interferometers and its implications for evaluations procedures. Appl. Opt. 40: 6223-62

Instantaneous Wavelength Detection by a Whole-Field k-space Method

A. Davila[1], J. M. Huntley, P. D. Ruiz and J. M. Coupland
Loughborough University
Loughborough, Leics. LE11 3TU, UK
[1] On sabbatical leave from the Centro de Investigaciones en Optica, Loma del bosque 115, Leon Gto. 37150 Mexico.

1 Introduction

Wavelength scanning interferometry (WSI) and swept source optical coherence tomography (OCT) are techniques for providing absolute 1-D range maps at each camera pixel. 3-D volumes of both structure and displacement within scattering media can be obtained from the magnitude and phase fields measured by a 2-D array of such pixels [1,2]. The image reconstruction algorithms depend however on accurate knowledge of the changes in wavenumber, k, over time, denoted here Δk.

Wavelength detection methods with high sensitivity have been available for some time. The most precise are based on measurement of the fringe patterns from a Michelson interferometer. For increased precision the fringes are compared with a wavelength-stabilized reference. Wavelengths are measured to a resolution of ± 0.2 ppm by counting fringes whilst an internal mirror is displaced. However, the need for temporal scanning makes it unsuitable for instantaneous wavelength measurements.

In this work we describe an alternative method, capable of instantaneous wavelength measurement, based on whole-field detection of a wavefront. An interference pattern generated by an array of wedges is measured by a camera. Phase maps are computed within each wedge by the Fourier transform method. By choosing the wedge thicknesses to follow a reversed exponential sequence, the temporal unwrapping algorithm described in [3] can be implemented to provide absolute Δk measurement to high precision from the one interferogram. Although simple Fizeau interferometers with a single wedge have been reported in the literature [4], and with a set of wedges [5], our new approach based on a set of wedges with specific heights allows the reduction of k-space errors. The details of the technique are presented along with sample simulation results.

2 Wedge design

Consider a transparent wedge of angle α, refractive index n and centre thickness d_j that is imaged onto a photodetector array. The phase difference ψ between light reflected from front and back surfaces at normal incidence may be written [6]

$$\psi_j = k(2nd + \lambda/2), \tag{1}$$

where $d = d_j + \alpha x$ is the local wedge thickness, k is the wavenumber ($=2\pi/\lambda$, where λ is the wavelength), and x is a spatial coordinate. Changes in k induce changes in ψ, denoted Δk and $\Delta\psi$, respectively, where

$$\Delta\psi_j = 2nd_j\Delta k\,. \tag{2}$$

In WSI the target Δk value between two adjacent frames is one which induces a phase change of $\pi/2$ between the waves reflected respectively from the front and back of a sample of thickness t. If t = 3 mm, for example, one requires a wedge thickness of order 6 mm to produce a $\Delta\psi$ value of π. Unfortunately, laser mode hops can cause $\Delta\psi$ values to fall well outside the range $-\pi$ to π and since only the wrapped phase is measured, Δk is not then estimated correctly. This problem can be reduced by reducing d_j, however the sensitivity is correspondingly diminished. The solution proposed here is to use a set of wedges of varying thicknesses to achieve simultaneously a high Δk resolution and a wide operating range.

The choice of centre wedge thicknesses then becomes the main issue to be resolved. One strategy is to choose d_j to grow exponentially with wedge index j. A phase value estimated at the centre of each wedge by the Fourier transform method could then be unwrapped straightforwardly by application of the forward exponential phase unwrapping algorithm[3]. The problem with this approach is that the thinnest wedges are then only a few hundred μm thick and so are very difficult to manufacture.

The approach proposed here is instead to *reduce* the thicknesses between adjacent wedges by an exponentially growing amount. In this way the thinnest wedge can still be several mm thick. The forward exponential phase unwrapping algorithm can still be applied, but operating this time on the *differences* in phase between the thickest wedge and all the other wedges.

We denote the wedge thickness differences by t_j (j = 1,2,..,s) where

$$\begin{aligned} t_j &= d_1 - d_{j+1}, \qquad j = 1,2,..,s-1 \\ t_s &= d_1 \end{aligned}, \tag{3}$$

and where d_1 and d_s refer to the centre thicknesses of the thickest and thinnest wedges, respectively. Provided the d_j are chosen according to the following rules:

$$\begin{aligned} d_1 &= d_0 r^{s-1} \\ d_j &= d_1 - d_0 r^{j-2} \qquad j = 2,3,..,s, \end{aligned} \tag{4}$$

where d_0 and r are constants, then the t_j values, and hence the differences between $\Delta\psi$ values from adjacent wedges, grow exponentially with j with a constant factor r between successive t_j values. An example of a set of d_j and corresponding t_j values for a four-wedge system (s = 4), with an r-factor of 4 and d_0 = 0.2 mm, is shown in Table 1 below.

Table 1. Centre thicknesses and their differences for a 4-wedge system

j	1	2	3	4
d_j [mm]	12.8	12.6	12.0	9.6
t_j [mm]	0.2	0.8	3.2	12.8

Apart from the lateral dimensions of the wedge, which are determined by the size of the wavefront and imaging lens magnification, the remaining parameter is the wedge angle α. This can be specified in terms of the number of fringes, N, across a wedge of width W as follows:

$$\alpha = N\lambda/2nW \tag{5}$$

3 Forward exponential phase unwrapping algorithm

By making the variable transformations

$$\begin{aligned} \Phi(j) &= \Delta\Psi_1 - \Delta\Psi_{j+1}, \qquad j = 1,2,3,..,s-1 \\ \Phi(s) &= \Delta\Psi_1, \end{aligned} \tag{6}$$

and

$$\omega = 2nd_0\Delta k\,, \tag{7}$$

the unwrapping problem reduces to the standard forward exponential temporal unwrapping form [3] in which the unwrapped phase values, which are proportional to the t_j calculated in Eq. 3, follow the sequence

$$\Phi(j) = r^{j-1}\omega, \qquad j = 1,2,3,\ldots,s. \tag{8}$$

Provided the true (unwrapped) value of ω lies in the range $-\pi$ to π, i.e. the value of Δk is known to lie in the range $-\pi/2nd_0$ to $\pi/2nd_0$, the Φ sequence can be unwrapped according to Eqs. (25) and (26) of [3] as follows:

$$\begin{aligned} \Delta\Phi_u(j, j-1) &= U\{\Delta\Phi_w(j, j-1), (r-1)\Delta\Phi_u(j-1,0)\} \\ \Delta\Phi_u(j,0) &= \Delta\Phi_u(j, j-1) + \Delta\Phi_u(j-1,0), \end{aligned} \tag{9}$$

where

$$\Delta\Phi(i, j) = \Phi(i) - \Phi(j). \tag{10}$$

Subscripts w and u represent respectively wrapped and unwrapped quantities, and $U\{\Phi(i), \Phi(j)\}$ represents the unwrapping operator which subtracts an integral multiple of 2π from $\Phi(i)$ such that $\Phi(i) - \Phi(j)$ lies within the range $-\pi$ to π, that is

$$U\{\Phi(i), \Phi(j)\} = \Phi(i) - 2\pi\mathrm{NINT}\left(\frac{\Phi(i) - \Phi(j)}{2\pi}\right), \tag{11}$$

where NINT denotes rounding to the nearest integer.

Once unwrapping has been completed, the required wavenumber change Δk is computed as follows

$$\Delta k = \Delta\Phi_u(s,0) / 2nt_s. \tag{12}$$

4 Computer simulations

A four-wedge design with thickness values defined in Table 1 has been manufactured from fused silica. The wedge angle α is 2 min, and each wedge has dimensions 7.5 × 30 mm^2 where x is parallel to the long wedge axis. The four wedges are aligned adjacent to one another to form a 30 × 30 mm^2 wavefront sensor. At the time of writing, the tunable laser for which they were designed was not available. Sample results using simulated data are presented to illustrate the basic principle. For clarity of presentation the wedge angle has been reduced to the value 0.05 mrad. The refractive index n takes the value 1.45332 for fused silica. Figure 1 shows four fringe patterns for k corresponding to λ = 810 nm and Figure 2 shows a second set where a shift in wavenumber of Δk = 180.14 m^{-1} is introduced.

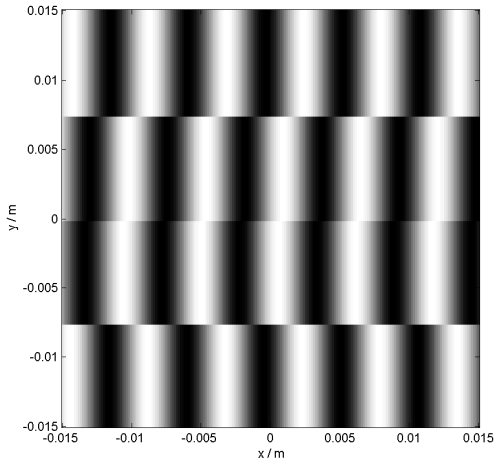

Fig. 1. Simulated wedge fringe patterns for λ = 810 nm. Wedge index j increases up the page

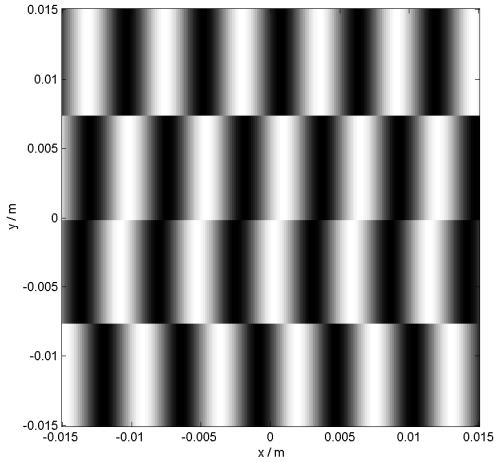

Fig. 2. Wedge fringe patterns after a wavenumber shift Δk = 180.14 m-1

The phase values at the wedge centrelines (x = 0) from Figures 1 and 2 are shown in rows 2 and 3 of Table 2, together with the wrapped Φ values defined by Eq. 6 in row 4. Row 5 shows the results of unwrapping by the forward exponential method (Eq. 9). The correct Δk value is recovered by using Eq. 12 with $\Delta\Phi_u(4,0) = \Phi_u(4) = 6.7021$.

Table 2. Phase values at the 4 wedge centres before and after unwrapping

j	1	2	3	4
$\psi_j(k)$	-2.5831	-0.6283	-1.0472	-2.7227
$\psi_j(k+\Delta k)$	-2.1641	-0.3141	-1.0471	2.3039
$\Phi_w(j)$	0.1047	0.4189	1.6755	0.4190
$\Phi_u(j)$	0.1047	0.4189	1.6755	6.7021

5 Summary

A method for measuring changes in wavenumber, Δk, of a wavefront has been proposed. By measuring phase values from the interference patterns from a set of wedges with exponentially growing thickness differences, the forward exponential temporal phase unwrapping algorithm can be used to unambiguously calculate Δk. The use of multiple wedges provides simultaneously fine Δk resolution and an extended Δk range along with single shot capability.

6 References

1. Ruiz, P D, Huntley, J M, Wildman, R D (2005) Depth-resolved whole-field displacement measurement by wavelength-scanning electronic speckle pattern interferometry. Applied Optics 44:3945-3953
2. Fercher, A F, Drexler, W, Hitzenberger, C K, Lasser, T (2003) Optical coherence tomography - principles and applications. Reports on Progress in Physics 66:239-303
3. Huntley, J M, Saldner, H O (1997) Shape measurement by temporal phase unwrapping: comparison of unwrapping algorithms. Measurement Science and Technology **8**:986-992
4. Alipieva, B, Stoykova, B and Nikolovac, V (2001) Wavemeter with Fizean interferometer for CW lasers. Proceedings of SPIE 4397:129-133
5. Lee, L S, Schawlow, A L (1981) Multiple-wedge wavemeter for pulsed lasers. Optics Letters 6:610-612
6. Françon, M (1966) Optical interferometry. Academic Press, New York

Limiting aspects in length measurements by interferometry

René Schödel
Physikalisch-Technische Bundesanstalt
Bundesallee 100, 38116 Braunschweig
Germany

1 Introduction

Since 1983 the metre, one of the seven base units of the SI, is defined as the length of the path travelled by light in vacuum during a time interval of 1/299 792 458 of a second. This definition is based on the availability of primary frequency standards (atomic clocks) highly accurately defining the second. Interferometry is the most accurate method for the realization of this definition by means of plane electromagnetic waves of frequency f. The length along an interferometer's axes can be expressed as a multiple of the wavelength of light:

$$L = \frac{\lambda}{2} \times \tfrac{1}{2\pi}\phi = \frac{\lambda}{2} \times (i + q), \tag{1}$$

in which i is an integer and q the fractional order of interference.

The attainable uncertainty of interferometric length measurements performed under vacuum and under air conditions is different. In the latter case the wavelength is scaled down by the refractive index of air, n, limiting the uncertainty. Empirical equations may be used for its evaluation. As an example for applying such approach [1], the input parameters: pressure, 10^5 Pa, temperature, 20 °C, CO_2-content, 400 ppm, relative humidity, 50% lead to a refractive index of n = 1.0002693982, which is sensitive to the these parameters as shown in Tab. 1.

Table 1. Sensitivity of the air refractive index to changes of environmental parameters [1]

influence	sensitivity
temperature	- 9.23 x 10^{-7} / K
pressure	+2.70 x 10^{-9} / Pa
CO_2 content	+1.44 x 10^{-10} / ppm
rel. humidity	- 8.58 x 10^{-7} / %

Under vacuum conditions, the wavelength of light is directly obtained from $\lambda = c_0 / f$ (c_0 = 299 792 458 m s^{-1}), i.e. for achieving sub-nanometer uncertainties in 1 m length measurements the frequency must be known at a relative level smaller than 10^{-9}. There exists a growing list of laser radiations recommended by the CIPM [2] which meets this demand. However, even when the relative uncertainty of the light frequency is in the order of 10^{-12} it is important to take into account the detailed physical relationship between the interference phase and the geometrical length to be determined. Besides the availability of monochromatic light sources it is important to take into account for additional aspects, among them:

- quality and alignment of plane waves entering the interferometer
- the possible existence of parasitic interferences
- appropriate technique for extracting the interference phase

In addition to these points widely discussed in the literature [3], in the context of length measurements one point was less discussed, namely:

- the effect of wavefront distortion induced by the optics error of the interferometer and the measuring faces itself

In flatness measuring interferometers the optics error was extensively studied and there exist a number of self calibration methods in order to extract a relevant additive correction (see [4] and references therein). In this type of imaging interferometers the plane at which such additive correction is extracted is unique and the same as in the flatness measurements. In length measuring interferometers there exist several planes at which the interference phase is of interest. Consequently, the concept of an additive optics error correction is not able to completely remove the effect of wave front distortions. In fact, measurements in PTB's gauge block interferometers reveal that the phase topography of an optical reference flat is slightly influenced by the position along the measurement pathway. This effect can simply be explained by the progression of the wave front which is distorted by the existence of the optics error. In this paper the effect of wave front distortion onto the measured length is investigated theoretically and experimentally for the most simple case. Conclusions are of general relevance for length measuring interferometers, i.e. the effect in imaging interferometers as well as in non-imaging interferometers is discussed.

2 Expected effect of a curved face that is shifted

In Fig. 1 a plane wave propagates along *z*-direction and is reflected at a spherical mirror (solid grey) of radius *R* whose apex is located at $z = R/2$. At this point the reflected wave front (solid black) is given by $z_1(y) = \sqrt{(R/2)^2 - y^2}$ which will be considered as a reference. A shift of the mirror by the amount of Δz (dashed grey) generates a reflected wave front (dashed black) propagating to the reference position, $z = R/2$, at which it is given by $z_2(y) = \sqrt{(R/2 - \Delta z)^2 - y^2} + \Delta z$. The difference between both can be expressed in good approximation by:

$$\delta z := z_2(y) - z_1(y) \overset{y << R}{\cong} \frac{y^2 \Delta z}{R\Delta z - R^2/2} \tag{2}$$

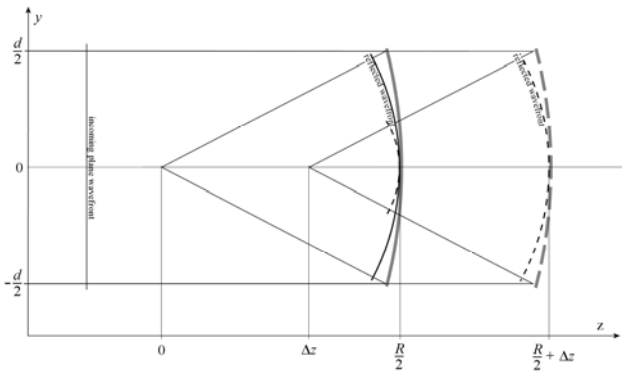

Fig. 1. Illustration of wave propagation in the presence of a spherical mirror.

Considering non-imaging interferometry the effect of wave propagation is mediated via the average of δz across the beam resulting in:

$$\overline{\delta z} = \frac{1}{\tilde{d}} \int_{-\tilde{d}/2}^{\tilde{d}/2} \delta z \, dy = \frac{\tilde{d}^2 \Delta z}{12\left(R\Delta z - R^2/2\right)}, \tag{3}$$

in which $\tilde{d}$ may be replaced by the beam diameter *d* for $d << R$.

3 Experimental setup

Fig. 2 shows a scheme of PTB's Ultra-Precision Interferometer (UPI) whose measurement principle is described in more detail in [5]. In the present paper the UPI is used to investigate the effect of wave front propagation as predicted by Eq. (2). For this purpose a convex mirror with $R = 2$ m was inserted that can be moved along z-axes. The direction of the movement was adjusted to be parallel to the beam direction within 1 arc minute. The reference position $\Delta z = 0$ is set to the position which is imaged to the camera via the output collimator and the lens in front of the camera. It is mentioned that this position is identical with the front face position of a gauge block shaped sample which length is of interest in the "normal" case of measurements.

Fig. 3 shows the wrapped phase topography (left) measured using $\lambda \cong 532$ nm at $\Delta z = 0$ from which the unwrapped phase topography (right) of the convex mirror is evaluated. Without going in more detail, diffraction at the output aperture (see Fig. 2) slightly affects the measured phase for axial distances larger 3 mm from the centre of the mirror. In the central region of the mirror, i.e. within ± 2 mm from the centre, the measured topography multiplied with $\lambda/2$ can be fitted to a sphere within 1.5 nm (RMS) setting the radius to $R = 2.004$ m.

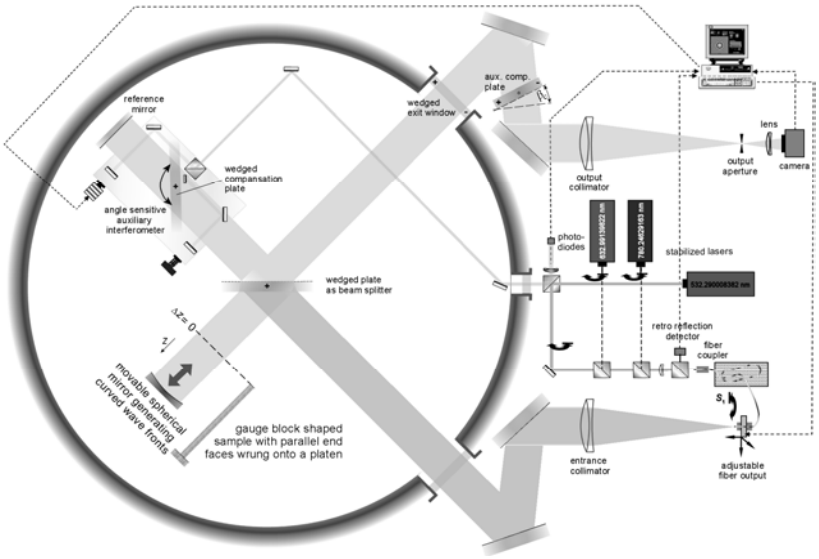

Fig. 2. Scheme of PTB's Utra-Precision Interferometer (UPI) in which a gauge block shaped sample is replaced by a movable convex mirror with $R = 2$ m.

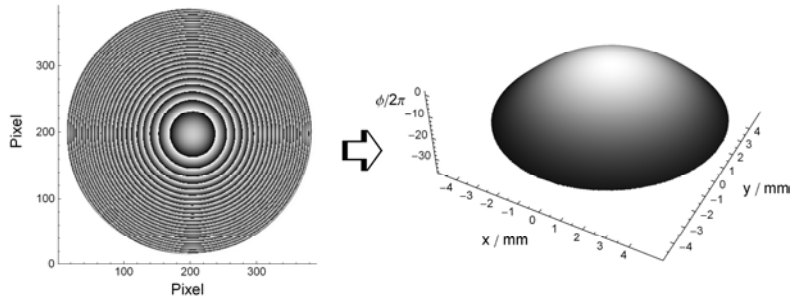

Fig. 3. Measured wrapped phase frame (left) and resulting unwrapped phase at $z = 0$.

4 Results

In order to validate Eq. (2) experimentally, phase topographies as in Fig. 3 have been recorded at discrete z-positions, and the difference phase topographies with respect to $\Delta z = 0$ were calculated. Multiplication with $\lambda \cong 532$ nm transfers such differences to the length unit as expressed in Eq. (3). Fitting a polynomial surface of the degree 2 results in data sets of curvatures for x and y direction which coincide within 0.0025 m^{-1} (RMS). At each z-position the mean of these curvatures are monitored in Fig. 4 (data points). For illustration, the insert shows the difference phase topography at maximum Δz (0.15 m). The solid line in Fig. 4 shows the theoretical curvature derived from Eq. (2), i.e. $\delta z'' = 2\Delta z \big/ \left(R\Delta z - R^2/2 \right)$. Here the radius R was used as a parameter for fitting the data points derived experimentally. The resulting $R = 2.03$ m is in good agreement with the radius derived above from the phase topography itself at $\Delta z = 0$.

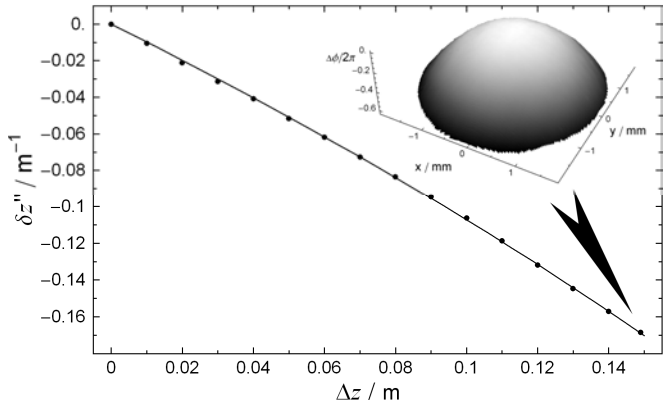

Fig. 4. Measured curvature (data points) of difference phase topographies as a function of the displacement of the spherical mirror and theoretical curve (solid line).

5 Conclusions

The main conclusion is that deviations from flatness of optical components within a length measuring interferometer (optics error) lead to length dependent errors due to the propagation of the deformed wave front. In case of a single spherical face the theoretically expected virtual deformation as a function of displacement could be confirmed experimentally. Accordingly, the effect of a curved face onto a length measurement can be estimated by using Eq. (2) in the case of imaging interferometers (e.g. gauge block interferometers) and Eq. (3) in the case of non-imaging interferometers. In reality, the optics error in length measuring interferometers is a sum of contributions from flatness deviations of all optical components involved. This leads to a more complicated influence. On the other hand Eqs. (2, 3) may be used in order to estimate a limit for the attainable uncertainty at a given specification of optical components. For illustration of such approach, Tab. 2 shows the relative effect of the optics error onto the measured length via Eq. (3) in different measurement ranges at $d = 5$ mm and values of R. Accordingly, only when the total optics error is surely less than $\lambda/20$ the measured length is affected less than $10^{-9}\,L$. For "normal" optics the length is affected to more than $10^{-8}\,L$.

Table 2. Relative effect of the optics error onto the measured length

measurement range [m]	effective radius R [m]	optics error (PV = $d^2/8R$, λ = 633 nm)	rel. effect to the length via Eq. (3)
1	25	λ/5	1.1×10^{-8}
1	100	λ/20	4.2×10^{-10}
10	25	λ/5	3.3×10^{-8}
10	100	λ/20	5.2×10^{-10}

6 References

1. Bönsch, G. and Potulski, E. (1998) Measurement of the refractive index of air and comparison with modified Edlen's formulae. Metrologia 35:133-139
2. http://www.bipm.org/en/si/si_brochure/appendix2/mep.html
3. Haitjema, H. (2008) Achieving traceability and sub-nanometer uncertainty using interferometric techniques. Meas. Sci. Technol. 19:084002
4. Bitou, Y., Takatsuji, T. and Ehara, K. (2008) Simple uncertainty evaluation method for an interferometric flatness measurement machine using a calibrated test flat. Metrologia 45:21–26
5. Schödel, R. (2008) Ultra high accuracy thermal expansion measurements with PTB's Precision Interferometer. Meas. Sci. Technol. 19:084003

Aspects of design and the characterization of a high resolution heterodyne displacement interferometer

Ch. Weichert[1], J. Flügge[1], R. Köning[1], H. Bosse[1], R. Tutsch[2]
1: Physikalisch-Technische Bundesanstalt (PTB), Bundesallee 100, 38116 Braunschweig
2: Technische Universität Braunschweig, Germany
christoph.weichert@ptb.de

1 Introduction

Due to current evolutions in positioning technology the uncertainty of the length measurement has to decrease continuously. Nowadays the PTB is developing measurement capabilities, which intend to reach uncertainties in sub-nanometer range. Interferometeric measurement systems are in some cases the only choice due to their direct traceability to the definition of the length unit [1]. As part of a multinational EU supported Project [2], the PTB is developing a high resolution heterodyne interferometer aiming at an accuracy level of 10 pm. Therefore an interferometer setup with a spatial separation of the input beams of different frequencies will be used, similar to the one of the Nanometer Comparator [3], to avoid periodic nonlinearities. Furthermore a phase meter with a noise level and long term stability in the pm range is necessary as well. To allow the use in different measurement setups the phase meter must be able to work at measurement speeds up to 10 mm/s. Up to now, there is no heterodyne interferometer phase meter with these specifications commercially available. Therefore we develop a phase meter based on a lock-in principle using a 100 MHz VME based ADC board with integrated FPGAs. For high resolution phase measurement in heterodyne interferometry digital lock-in amplifiers were already applied successfully [4, 5] in the past. But the currently available digital lock-in amplifiers are limited by their data acquisition capabilities. Some measurement applications and digital control loops require a continues data rate of some 10 kHz and more with a minimal time delay.

The noise level and the long term stability of the new phase meter were determined at first using a synthetic signal of a function generator. Additionally the phase difference of the two output beams of a Mach-Zehnder interferometer is used to determine the influence of the beat

frequency generation electro optics, of the transmission over optical fibers and of the beam splitter at which the beams interfere. But a Mach-Zehnder setup is not able to measure length variations, because it consists only of the minimal number of components of a fiber based heterodyne interferometer with spatially separated input beams.

2 Performance of the phase meter

The phase measurement, necessary to interpolate the interference period, is realized using a fast ADC board from the company Struck Innovative Systeme. The VME board consists of eight 16 bit ADC's operating at a data acquisition rate of 100 Msamples/sec, four Spartan 3 FPGAs performing the high speed calculation of the lock-in algorithm and 512 MByte memory to store the measurement results. The phase measurement results will be available with a rate up to 100 ksamples/sec. Tightly coupled ADC clocks are required, because the phase values are defined here as differences of the phases of the measurement channel and the one of the reference channel.

At the moment the lock-in algorithm has not been implemented on the FPGA. Only the ADC values are stored in the memory and phase values are calculated off-line at the PC. Therefore only time periods of 83.9 ms can be acquired continuously before a longer transfer time is required. Hence, the long term stability is determined by analyzing the average of these data sets of 8192 phase values. One of the data sets is shown in figure 1. In this case the measurement and reference channel of the ADC board were fed with the signal of a function generator (Tektronix AFG 3101) with an amplitude of 40 % of the ADC full range.

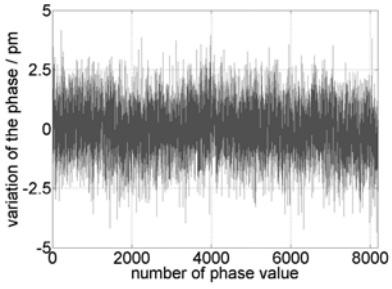

Fig. 1. Array of 8192 phase values for the phase meter fed with a function generator

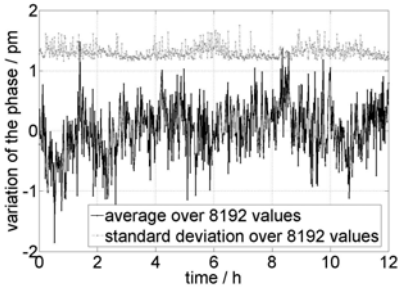

Fig. 2. Stability of the phase meter over 12 hours fed with a function generator

The phase values of one set is nearly Gaussian distributed, so the standard deviation of these data sets is an indicator for the noise level of the phase meter. Due to the use of the phase meter in combination with the single path interferometer used at a wavelength of 532 nm, all variations of the phase are converted to displacements and presented in pm.

The variation of the average of this 8192 phase value sets as function of the time is presented in figure 2. Over a time period of 12 hours a peak to peak stability of 3.3 pm was observed.

3 Setup of the Mach-Zehnder interferometer

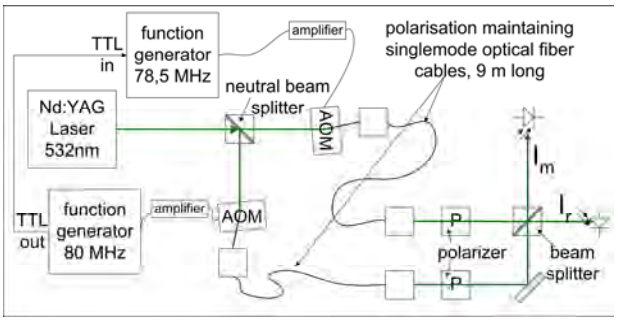

Fig. 3. Schematical setup of the Zehnder interferometer used to measure the phase stability

The Mach-Zehnder setup used to investigate the phase stability, which is shown in figure 3, includes the minimal number of parts of a heterodyne interferometer with spatially separated input beams. The light from a single mode, frequency doubled, unstabilized Nd:YAG laser is divided and the frequencies of the two beams are shifted by acousto-optic modulators (AOM). Preliminary experiments had shown an optimal performance at a beat frequency of 1.5 MHz. To avoid sidebands, the AOMs are fed by two function generators (harmonic distortion -37 dBc and phase noise -47 dBc). These function generators are synchronized by a 10 MHz TTL signal. To separate the heat dissipated by the laser and the AOMs from the optical setup, the light is transferred over 9 m long polarization maintaining single mode fibers. After passing polarizers the two beams are recombined by a beam splitter. The output beams of the beam splitter should exhibit a stable phase difference of π, due to the principle of conservation of energy. The phase of one output of the beam splitter is not stable to a synthetic reference. Variations of more than 19 nm in 84 ms introduced by thermal and vibrational influences on the fibers were observed.

According to some references, the noise level of the phase measurement depends on the quality of the signals of the function generators [6-8]. In this setup the imperfect synchronization of the function generators and mainly the optical fibers contribute phase variations between the two incoming beams of the Mach-Zehnder interferometer in a frequency range of some kHz. By additionally added amplitude or frequency modulations of the output signals of the function generators it could be shown, that the influence of these phase variations on the interference phase determination can be neglected.

4 Long term stability

Two possible reasons for a deviation of the phase difference between the two outputs of the Zehnder setup from π might be assumed. The first one is a different delay between the two signals behind the beam splitter, caused by different distances of the detectors to the beam splitter, by different delays of the photo detectors and their integrated amplifiers, by different cable lengths and by different delays in the ADC triggers. The second possible reason is, that not the same parts of the input beams interfere at the exits of the Mach-Zehnder setup, which could be caused by polarization effects. However, for displacement interferometry only variations in time are of interest, because every measurement is referenced to the initial phase difference.

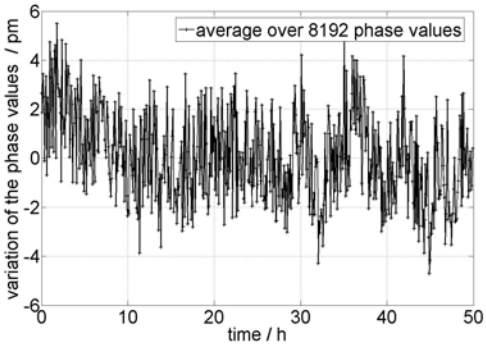

Fig. 4. Stability of the averages of a well-aligned Zehnder setup over 50 hours

The standard deviation of a single phase data set increases by a factor of three to five for a well-aligned Mach-Zehnder setup in comparison to the results obtained by the use of the function generator (compare figure 1).

Possible reasons for this increase could be the additional noise introduced by the detectors and their amplifiers, the smaller contrast and influences of the frequency generation and of the AOMs and of the optical fibers. The stability of the averages increases also at least by the factor of five, as shown in figure 5. For the Mach-Zehnder setup using a neutral beam splitter, a beam aperture of 10 mm (beam diameter of 5 mm) and the same linear polarization state (s-polarization) of the interfering beams at the neutral beam splitter, a phase stability of ± 5 pm over 50 hours was reached. These average values are not Gaussian distributed and their variation is much larger than the standard deviation of the mean, which indicates, that they are caused by systematic effects.

As described above, not only the phase, but also the polarization of the light varied permanently, although polarization maintaining fibers [9] are used. At the exit of the fibers the different polarization states exhibit different phases. The neutral beam splitter at the exit of the Zehnder setup has different reflection ratios and different phase shifts for s- and p-polarized light. Therefore the phase difference between the outputs of the Zehnder setup varies with the polarization states at the fiber outputs. This effect remains, when a polarization beam splitter instead of the neutral one is in use due to the imperfect extinction ratio [10]. With linear under 45° to the s- polarization polarized light we only reach a phase stability of the averages of ± 30 pm over 12 hours. The described effect is shown quite clearly in figure 5, where we left the polarizers behind the fibers away. In this case the averages the phase vary in the nanometer- instead of the picometer range.

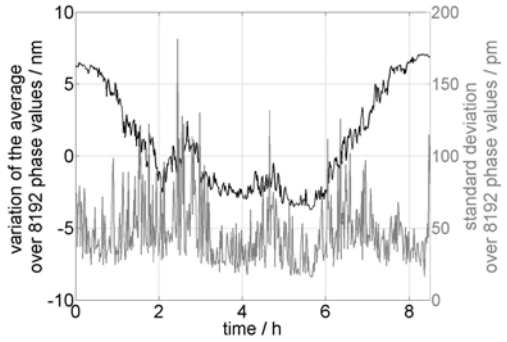

Fig. 5. Stability of averaged values over 8.5 hours, without polarizers behind the fibers

5 Conclusions

In the course of developing a heterodyne interferometer with an uncertainty of 10 pm we are realizing a new phase meter and have demonstrated experimentally its stability and noise level to be in the picometer range. With the aid of this phase meter and a Mach-Zehnder setup we analyzed the influence of the basic components of a heterodyne interferometer with spatial separated input beams. Motivated by the experimental results we like to accent the influence of the polarization on the phase stability and conclude that at every beam splitter of an interferometer setup the beams should have the same linear polarization state to reach an uncertainty in the range of 10 pm.

Further factors influencing the stability might be the driver electronics of the AOMs, the aperture of the beam together with a jitter of the beam position and the amplifiers of the detectors. All these influences are still under investigation.

6 References

1. Quinn, T, 2003, Practical realization of the definition of the metre, including recommended radiations of other optical frequency standards (2001), Metrologia 40, 103-133
2. Matus, M, et al, 2009, Optical interferometry with 10 pm level accuracy - the Project Nanotrace, Proceeding of Nanoscale 2008, to be published
3. Flügge, J, et al, 2008, Interferometry at the PTB Nanometer Comparator – design, status and development, SPIE Vol. 7133
4. Wu, C, Lawall, J, Deslattes, R.D., 1999, Heterodyne interferometer with subatomic periodic nonlinearity, Appl. Optics, 38, 19
5. Eom, TaeBong, et al, 2002, A simple method for the compensation of the nonlinearity in the heterodyne interferometer, Meas. Sci. Technol. 13:222-225
6. Heinzel, G, et al, 2004, The LTP interferometer and phasemeter, Class. Quantum Grav. 21:581-587
7. Robertson, D, et al, 2005, LTP interferometer – noise sources and performance, Class. Quantum Grav. 22:155-163
8. Heinzel, G, et al, 2006, Interferometry for LISA technology package LTP: an update, Journal of Physics: Conference Series 32, 132-136
9. Knarren, B, Cosijns, S, Haitjema, H, Schellekens, P, 2005, Validation of a single fibre- fed heterodyne laser interferometer with nanometre uncertainty, Prec. Eng. 29, 229-236
10. Cosijns, S, 2004, Displacement laser interferometry with sub-nanometer uncertainty, ISBN 90-386-2656-8

The femtosecond optical synthesizer as a tool for determination of the refractive index of air in ultra-precise measurement of lengths

Ondrej Cip, Radek Smid, Bretislav Mikel, Martin Cizek, Bohdan Ruzicka and Josef Lazar
Institute of Scientific Instruments, Academy of Sciences of the Czech Republic, Kralovopolska 147, 612 64 Brno, Czech Republic

1 Introduction

In production of semiconductor microchips, nano-components like MEMS, or optical lithography, an even more precise length measuring devices are necessary for a reliable fabrication [1]. Modern high-resolution laser interferometers are considered in this field as these more precise measuring length sensors. They use a wavelength of the laser light like a fundamental length unit [2]. If the interferometers measure distances in atmospheric conditions, the absolute value of the laser wavelength fluctuates in linear form with a refractive index of air [3]. It causes a distortion of the measured values of the length, so that, the repeatability of controlled dimensions can be degraded. On the other hand, if we know the value of the refractive index of air we are able to compensate the measured length value obtained by the laser interferometer easily. But techniques of direct measurement of the index are not solved sufficiently now.

Presently, the progress in the field of optical frequency standards is oriented to femtosecond mode-lock lasers stabilized by a technique of the optical frequency comb [4]. Such a laser produces a supercontinuum light, which is composed of a cluster of coherent frequency components in certain interval of wavelengths. A value of the repetition rate (frequency) of femtosecond pulses determines (in the frequency domain) spacing of these coherent components. If we control the mode-lock laser by means of i.e. atomic clocks we ensure frequency of these components very stable. The comb spectrum plays a role as a frequency rule which is suitable for the metrology of length in various branches: it can be used as a tool for generation of precise distance and at the same time as a length measuring device with the atomic clock as the fundamental reference.

2 Frequency comb in dimensional metrology

The optical frequency comb is based on laser source periodically generating a train of femtosecond pulses. The train is characterized by the central wavelength, period of pulses, pulse shape and pulse to pulse phase shift. The train produces a frequency spectrum of comb lines around the central optical frequency (wavelength). The frequency f_i of one selected spectral component of the comb is expressed as:

$$f_i = f_{ceo} + i \cdot f_{rep} \tag{1}$$

where i is the number of a comb line (typically in the order of 10^6) and f_{rep}, and f_{ceo} are frequencies typically set in RF domain, called repetition and offset frequency, respectively. The repetition frequency f_{rep} is indirectly proportional to the period of the train pulses and the offset frequency f_{ceo} describes phase-shift between envelope of pulses and their carrier wave. For free running femtosecond laser both frequencies (f_{rep} and f_{ceo}) are typically stable only up to 10^{-7}. Therefore its better stabilization is necessary to generating precise and stable frequency comb spectrum. On basis of Eq. 1. the stability of the repetition frequency f_{rep} affects stability of i-th component of the comb multiplicatively and the offset frequency f_{ceo} additively. The repetition frequency is very intensively present in RF spectrum and could be then easily retrieved and phase locked to i.e. a division of an atomic clock RF signal (typically 10 MHz) by phase-lock servo-loop [5]. The offset frequency is derived by self-referencing method called as the f-to-2f technique. It is based on broadening of 100 nm approx. wide spectrum of the femtosecond laser (with central wavelength λ = 1541 nm) by means a photonics crystal fibre. In the fibre a four-wave mixing technique produces very broad comb spectrum which cover at least one octave of optical frequencies (in our case an interval from 1000 nm to 2000 nm). Longer wavelengths (frequency f_i) are frequency doubled by non-linear crystal to shorter wavelengths (frequency $2f_i$). Doubled longer wavelengths are optically mixed with short wavelengths (frequency f_{2i}) and the offset frequency is obtained:

$$2 f_i - f_{2i} = f_{ceo} \tag{2}$$

This beat-frequency is also phase locked to the atomic clock RF signal by servo-loop. The result of the method is the comb frequency spectrum with stability of all of frequency components with degree of relative stability of atomic clocks (thus more than 10^{-14}).

3 Fabry-Perot cavity as a generator of precise length

Fabry-Perot cavity (FPC) consists of two mirrors separated by the geometrical distance L_{cav}. The FPC is an instrument which transfers precise frequencies characterized from the optical path to a distance between mirrors [6]:

$$\nu = \frac{c}{2nL_{cav}} = \frac{c}{2L_{opd}} \tag{3}$$

where ν is the free spectral range (FSR), c is speed of the light, n is the refractive index of the cavity environment, and L_{opd} is the optical path distance between mirrors ($L_{opd} = n \cdot L_{cav}$). A frequency of m-th longitudinal mode transmitted through the FPC can be expressed:

$$f_m = \frac{mc}{2nL_{cav}} \tag{4}$$

where f_m is optical frequency of m-th mode of the FPC. If the cavity is inserted into the vacuum chamber then the refractive index n equals 1.0 and $L_{opd} = L_{cav}$ (geometrical and optical length of the cavity is the same). Then for generation of the precise length L_{opd} is necessary to stabilize only one of frequency modes f_m of the cavity to a stable optical frequency f_i. For this purposes the femtosecond laser deals such a stable frequency spectrum. As we express in Chapt. 2, each i-th component of the comb is perfectly stable. If we hold the cavity length L_{cav} at the "right" position the optical frequency of the i-th component of the comb equals to the optical frequency of m-th mode of the FPC. Then:

$$f_i = f_m = f_{ceo} + i \cdot f_{rep} = \frac{mc}{2nL_{cav}} \tag{5}$$

$$L_{cav} = \frac{mc}{2n\,(f_{ceo} + i \cdot f_{rep})} \tag{6}$$

Because i and m are integer constant and c is speed of the light then the stability of the cavity length L_{cav} is determined only by stability of the repetition and offset frequency.

4 The frequency comb like a measuring sensor for direct detection of the refractive index of air

The FPC can be used like a distance measuring sensor in cooperation with the femtosecond comb too. If we cancel the servo-loop lock of the repetition frequency f_{rep} to the atomic clock RF signal the spectrum of the comb stays free running. But if we control the repetition frequency for condition that the *m*-th frequency line of the FPC equals to *i*-th component of the frequency comb, it leads to expression:

$$f_{rep} = \frac{c}{2nL_{cav}} \frac{m}{i} - \frac{f_{ceo}}{i} \tag{7}$$

If we monitor the repetition frequency by a counter which is referenced to RF signal derived from atomic clocks then we are able to determine the L_{cav} very precise on basis of Eq. 6. If the cavity length is stable but the refractive index of air changes the optical length of the cavity L_{opd} then we monitor the refractive index *n* by following expression:

$$n = \frac{mc}{2L_{cav}(f_{ceo} + i \cdot f_{rep})} \tag{8}$$

The optical setup of the novel method for the refractive index of air measurement by means of frequency comb is in Fig. 1.

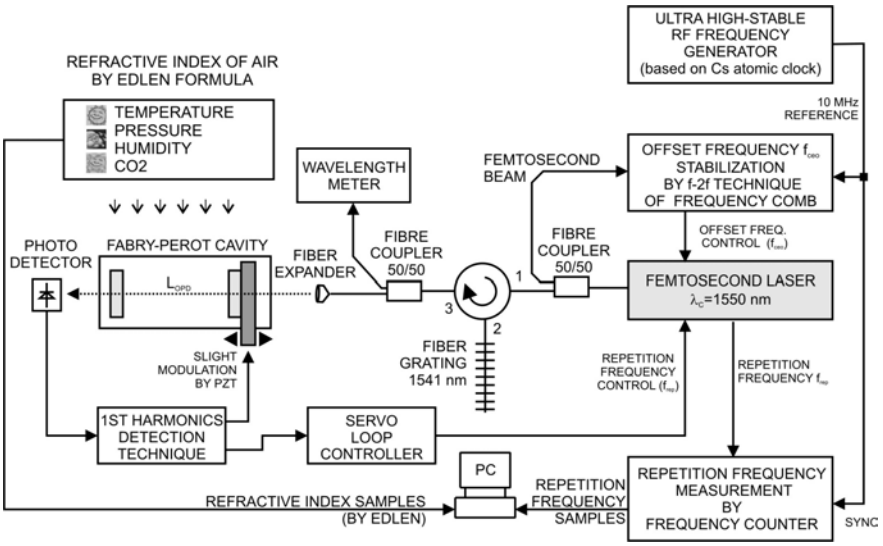

Fig. 1. Detailed scheme of the optical setup for measurement of the refractive index of air by means of the femtosecond laser equipped with optical frequency comb technology.

Because the character of the comb light is broad optical spectrum with thousands narrow lightwaves (supercontinuum) it is impossible to use such a light to direct illumination of the FPC. We have to firstly to separate *i*-th component from the femtosecond comb and to illuminate the FPC by only this component with respect to Eq. 5. It can be done i.e. by supporting tunable laser diode (DFB) which is frequency locked to *i*-th component by special servo-loop. But due to poor signal-to-noise ratio of the beat-note we proposed and verified other technique which uses a passive filtering of only several components of the frequency comb by means of an ultra narrow-band fibre Bragg grating. As is presented in Fig. 1, the output of the femtosecond laser is equipped by a fibre circulator which prevents back-reflection from the long period fibre Bragg grating and FPC into the laser. The group of several components about *i*-th line of the comb is transmitted to the tap 3 of the circulator. This light is sent to the FPC through the fibre expander. The FPC is constructed with a fixed length L_{cav} = 75 mm. The body of the FPC is made from low-expansion material (zerodur). The position of one of the cavity mirrors is modulated by a piezoelectric transducer. It is suitable for the first harmonic detection technique used in the servo-loop lock of the repetition frequency of the femtosecond laser to the cavity length of the FPC. The stabilization of the offset frequency f_{ceo} by means of f-2f technique of the frequency comb is remaining.

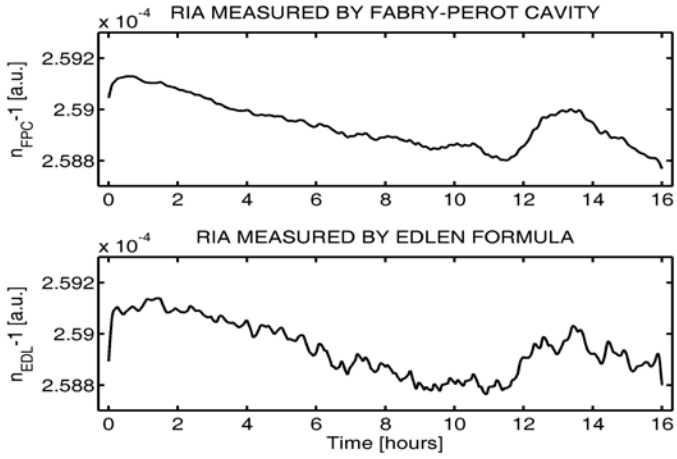

Fig. 2. The example of a measurement of the refractive index of air by combination of the femtosecond comb and stable FPC vs. Edlen formula indirect method.

The locked repetition frequency f_{rep} is monitored by a high-resolution frequency counter which has RF signal from atomic clocks as the

reference. In this setup the repetition frequency express changes of the refractive index of air, see Eq. 8. Thanks to performed novel method we determined the refractive index for more than 16 hours with help of the femtosecond laser, the FPC, and atomic clock ultra-stable frequency reference. This result was done with the pilot experimental setup presented in Fig. 2. For verification of this result we used the non-direct measurement of the refractive index by Edlen formula. Note, the indirect measurement by Edlen method is determined on basis of knowledge of temperature, pressure, and humidity of the air and concentration of CO_2 and NO_2 [7]. The absolute difference between these two measurements is $\approx 0.3 \times 10^{-7}$ and the standard deviation of this difference lies about 2×10^{-7} approx. We consider the result of the pilot experiment as very promising for next research in this field.

5 Acknowledgements

The authors wish to express thanks for support to the grant projects from Ministry of Education, Youth and Sports of CR, projects No.: LC06007, 2C06012, the AS CR, projects No.: AV0 Z20650511, Ministry of Industry and Commerce, projects No: 2A-1TP1/127, FT-TA3/133, 2A-3TP1/113 and GA CR, projects: GA102/09/1276, GA102/07/1179.

6 References

1. Misumi I et al (2005) Sub-hundred nanometre pitch measurements using an AFM with differential laser interferometers for designing usable lateral scales. Meas. Sci. Technol, 16: 2080-2090
2. Quinn TJ (2003) Practical realization of the definition of the metre. (2001) Metrologia, 40: 103-133
3. Eickhoff ML, Hall JL (1997) Real-time precision refractometry: new approaches. Applied Optics, 36: 1223-1234
4. Udem T, Holzwarth R, Zimmermann M, et al (2004) Optical frequency-comb generation and high-resolution laser spectroscopy. Topics in Applied Physics, 95: 295-316
5. Bauch A (2003) Caesium atomic clocks: function, performance and applications. Meas. Sci. Technol, 14: 1159-1173
6. Cip O, Smid R, Lazar J (2007) An ultra-stable generator of absolute length based on femtosecond mode-lock laser and optical resonator. Proc. of the 2007 IEEE Int. Freq. Control Symposium, 1-4: 659-662
7. Edlen B (1966) The refractive index of air. Metrologia, 2: 71-80

Invited Paper

Digital holographic microscopy with a simultaneous phase-shifting interferometer for measuring the angular spectrum generated by micro-optical structures

Byoungho Lee, Joonku Hahn, Yongjun Lim, Hwi Kim, and Eun-Hee Kim
National Creative Research Center for Active Plasmonics Application Systems, Inter-University Semiconductor Research Center and School of Electrical Engineering, Seoul National University, Gwanak-Gu Gwanakro 599, Seoul 151-744, Korea

1 Introduction

Recently, digital holographic measurement technique receives lots of interests in applications for biological and environmental sensing since it has outstanding benefits of measuring both amplitude and phase profiles [1-3]. With the help of numerical reconstruction method, the optical wave can be calculated at any position from measured optical wave profile. Then, the positions of diffractive objects can be identified by analyzing the change of diffracted wave according to propagation. Moreover, it is possible to solve the angular spectrum of optical wave by the numerical reconstruction in spatial frequency domain.

In this digital holographic measurement technique, phase-shifting interferometry is a well-known method which has the benefit to eliminate ambiguities in both autocorrelation and twin terms. This phase-shifting interferometry method can be divided into temporal and spatial phase-shifting interferometries. Spatial phase-shifting interferometry has a potential to measure the fast varying objects, since it can acquire interferograms with different phase steps simultaneously [4-6]. Recently, this method is applied to pixelated phase-mask on CCD [7, 8]. In this paper, we present an approach to analyze the geometric errors and compensate them with three CCDs.

As applications of the proposed measurement technique, some experimental results are presented, which are measured with holographic microscopy. Especially our holographic microscopy is designed to analyze the angular spectrum of object waves by the use of high numerical-aperture objective lens.

2 Temporal and spatial phase-shifting interferometries

For digital holographic measurement, phase-shifting interferometry, one of the temporal measurement methods, is preferred. This technique induces an object wave by plural interferograms with the relative phase-shift with respective to the reference wave. However, this technique has disadvantages in measuring fast-moving objects since the failure in synchronization of every interferogram results in the error in the object wave. Therefore, there have been previous studies on the spatial measurement methods based on phase-shifting interferometry. In this paper, the spatial measurement configuration with three CCDs is proposed where reference waves are combined with object waves in front of each CCD. And there is relatively large mechanical freedom. With our proposed system, a simultaneous phase-shifting interferometer can be realized.

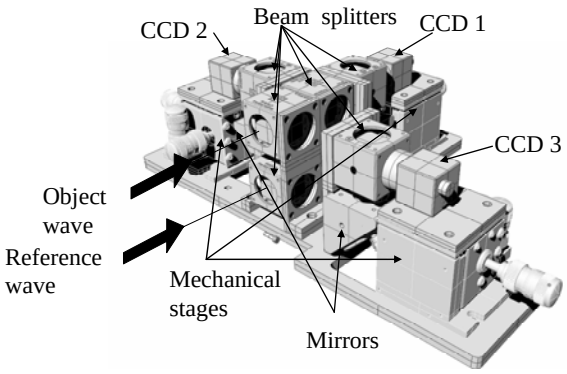

Fig. 1. Schematics of interferometry with three CCDs.

Fig. 1 shows the proposed intereferometry with three CCDs. In this system, object and reference waves enter different apertures. These waves are split into three paths after passing through beam splitters. Then, in front of the individual CCD, object and reference waves are combined and intereference patterns are recorded on each CCD. The optical path length is different from each other and spatial phase-shift interferograms are obtained simultaneously.

The alignmet processes are executed by following two steps. First, the position of the CCD is measured with the use of an alignment target with the imaging optics in front of the proposed interferometry. Second, the relatively tilted angle of each CCD is measured by recording interferograms with collimated object and reference wave. Fig. 2 shows the captured images as for alignment. Figs. 2(a), (b), and (c) show

alignment target images on three CCDs respectively. Figs. 2(d), (e), and (f) show intereference patterns between collimated object and reference waves on individual CCDs.

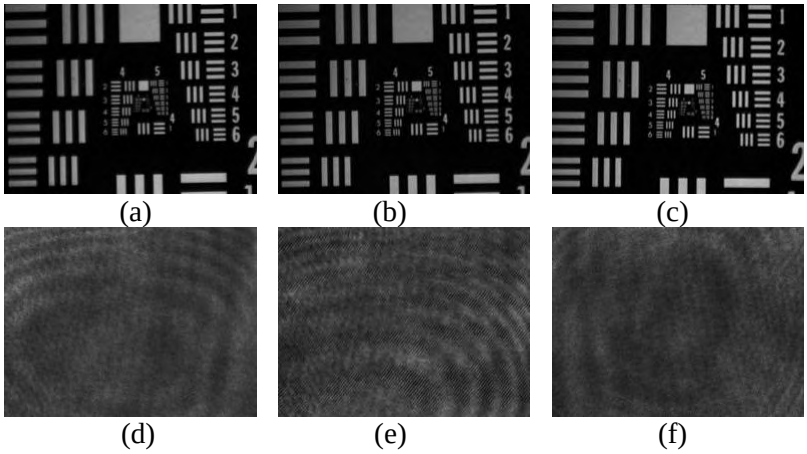

Fig. 2. Captured images for alignments. Figs. 2(a), (b), and (c) show alignment target images on 1st, 2nd, and 3rd CCDs, respectively. Figs. 2(d), (e), and (f) show the corresponding intereference patterns between collimated object and reference waves on individual CCDs.

Fig. 3 shows the reconstruction images by the use of our proposed intereferometry with different shutter speed. The object is hanging on a string. This is not fixed but swinging back and forth. Therefore, it is impossible to measure hologram with slow shutter speed. As it can be expected, the object is recognized with the hologram measured with relatively high speed.

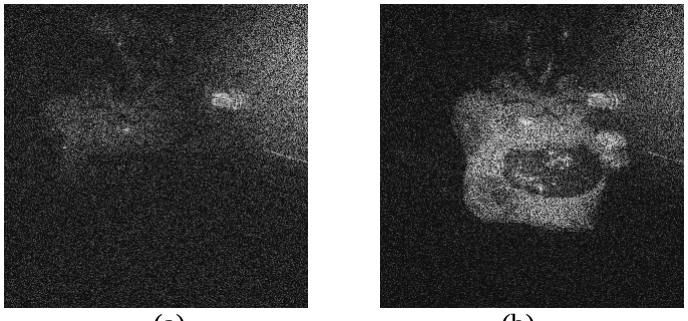

Fig. 3. Reconstructed images with shutter oprning time of (a) 5.02ms and (b) 0.21ms, respectively.

3 Geometric errors in phase-shifting interferometry

In digital holographic measurement, there is a troublesome problem, that is, twin image. In general, this twin image results from phase-shift errors and the twin image is represented as a conjugate wave of the original object wave [9]. In temporal measurement methods, since only one phase-shifter is used, this phase-shift errors are originated from the miscalibration of the phase-shifter or vibrations of optical systems [10]. However, in spatial measurement methods, there also exist phase-shift errors resulting from the misalignment of optical devices. Then on this account, twin image occurs frequently. Moreover, the plane of CCD can be tilted around the lines perpendicular to the optical axis in comparison of each others and there are more complicated noises in spatial measurement methods than simple twin image. These noises are classified into longitudinal displacements and transversal displacements [11]. The properties of these two displacements are discussed in the following.

The phase-shifting digital holography records the object wave by measuring the interferograms. The *i*th interferogram with phase shift is given by

$$I_i = \left|U_O + U_{R,i}\right|^2 = A_O^2 + A_R^2 + 2A_O A_R \cos\left(\varphi - \alpha_i\right), \tag{1}$$

where the object wave and the reference wave are defined by U_O and $U_{R,i}$, respectively. Conventional phase-shifting holography with four steps is represented as

$$U_O' = I_{31} + jI_{24} \ . \tag{2}$$

If there are the longitudinal errors, Eq. (2) should be changed into the formula with different coefficients. These errors result in the well-known noise, twin image. On the other hand, the transversal errors result in the different effects in reconstructing images. The transversal error on the i^{th} interferogram can be represented as

$$I_i'\left(x, y\right) = I_i\left(x + \Delta_x, y + \Delta_y\right), \tag{3}$$

where Δ_x and Δ_y are the amount of displacement of the interferogram. This transversal errors are orignated from both the displacements of CCD and also the tilts of opitcs.

Fig. 4 shows the effects of geometrical errors in reconstructing images. Fig. 4(a) shows the original image without geometric errors, and Figs. 4(b) and (c) show the reconstruction images respectively with longitudinal and transversal displacements of interferograms. In general, the longitudinal displacement results in twin image but the intensity of the twin image is uniform, while on the other hand, the transversal displacement results in

alternating intensities in the original and twin images. And the periods of this alternation depends on the amount of transversal displacements.

(a) (b) (c)

Fig. 4. Reconstruction images (a) without geometric errors and with (b) longitudinal and (c) transversal displacements of interferograms.

4 Applications of phase-shifting holographic microscopy

As an application of the holographic measurement techniques, the holographic microscopy can provide the measurement of diffracted waves from micro-optical structures [12-14]. Especially the holographic microscopy is designed for analyzing the angular spectrum of object waves [15]. In our holographic microscopy system, a local angular spectrum is to be analyzed since this analysis helps us to obtain the inclination of surfaces or to filter diffracted waves within the narrow bandwidth of angular spectrum. Fig. 5 shows our holographic microscopy configuration to detect angular spectrum.

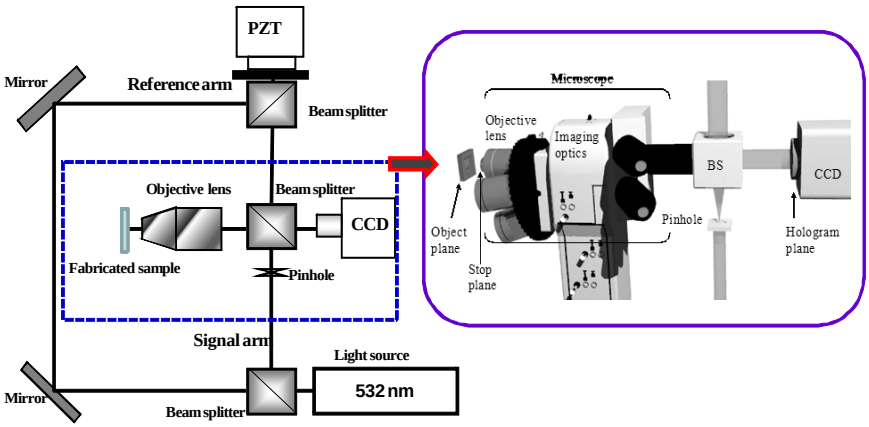

Fig. 5. Schematic diagram of our phase-shifting holographic microscopy.

To fabricate the micro structure, focused ion beam (FIB) machining (FEI Quanta 200 3D) is used. Fig. 6(a) shows the design of micro structure for the FIB fabrication. This pyramid-shaped structure is devised to understand and demonstrate the capability of our microscopy system in detecting angular spectrum from the fabricated micro-structure. The fabricated pyramid is structured with 24 stairs due to the condition of fabrication process. The width between each stair is 1.0 . And on each face of the pyramid, one capital letter is marked by FIB milling.

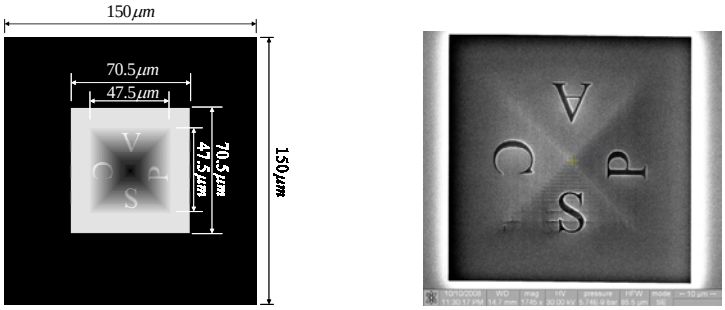

(a) (b)

Fig. 6. (a) is the design of the target micro-structure and (b) is the SEM image (top view) of the structure fabricated by FIB milling.

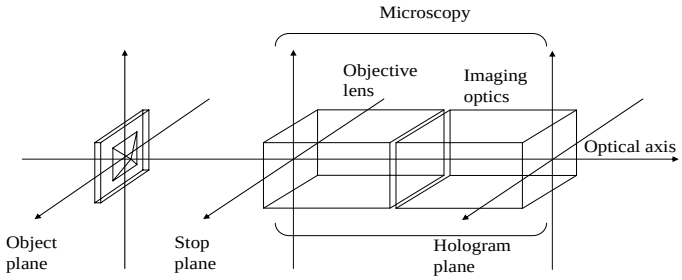

Fig. 7. Schematic diagram for designing the Fresnel domain filter.

Additionally, in our holographic microscopy system, the stop plane is located at the entrance pupil of objective lens, and this stop defines the bandwidth of angular spectrum which can pass through the system. The object wave at the boundary of the stop is diffracted and makes noise on the hologram plane. Since this noise is originated from the entrance pupil of the objective lens, it is necessary to filter out the error at the stop plane. Hence, we use the Fresnel domain filter, and the corresponding schematic diagram is shown in Fig. 7. With the help of the Fresnel domain filter, we can remove unwanted noise. With the proposed holographic microscopy

system, we could reconstruct either the whole hologram or selected angular spectrum hologram of Fig. 6. Correcponding to the selected angular spectrum, each face of the pyramid-shaped structure can be reconstructed, as shown in Fig. 8.

(a) (b)

Fig. 8. (a) shows the reconstructed image of the whole hologram and (b) shows a selected region of the hologram.

5 Conclusions

In this paper, we proposed spatial phase-shift intereferometry and discussed the geometrical errors. By using the holographic microscopy with the high numerical apeture objective, experimental results on some micro-structure objects are presented where analyses on angular spectrum are significant.

6 Acknowledgment

This work was supported by Ministry of Education, Science and Technology of Korea and Korea Science and Engineering Foundation through the Creative Research Initiatives Program (#R16-2007-030-01001-0).

7 References

1. Yamaguchi, I. Phase-shifting digital holography in Digital Holography and Three-dimensional Display, T.-C. Poon, ed. (Springer, 2006) 145-171.
2. Zel'dovich, B. Y., Mamaev, A. V., Shkunov, V. V. Speckle Wave Interactions in Application to Holography and Nonlinear Optics (CRC Press, 1995).

3. Javidi, B., Moon, I., Yeome, S. (2006) Real-Time 3D Sensing and Identification of Microorganisms Optics & Photonics News 17:16-21.
4. Creath, K. “Temporal phase measurement methods,” in Interferogram Analysis, Digital Fringe Pattern Measurement Techniques, D. W. Robinson and G. T. Reid, eds. (Taylor & Francis, 1993), 94–140.
5. Millerd, J., Brock, N., Hayes, J., North-Morris, M., Novak, M., Wyant, J. C. (2004) Pixelated phase-mask dynamic interferometer. Proceedings of SPIE (SPIE, Bellingham, WA), 5531:304.
6. Hrebesh, M. S., Watanabe, Y., Sato, M. (2008) Profilometry with compact single-shot low-coherence time-domain interferometry. Optics Communications, 281:4566-4571.
7. Awatsuji, Y., Sasada, M., Kubota, T. (2004) Parallel quasi-phase-shifting digital holography. Applied Physics Letters, 85: 1069-1071.
8. Millerd, J. E., Brock, N. J., Hayes, J. B., Wyant, J. C. (2004) Pixelated phase-mask dynamic interferometer. Proceedings of SPIE (SPIE, Bellingham, WA), 5531:264.
9. Hahn, J., Kim, H., Cho, S.-W., Lee, B. (2008) Phase-shifting interferometry with genetic algorithm-based twin image noise elimination. Applied Optics 47:4068-4076.
10. Waller, L., Barbastathis, G. (2007) Error analysis of phase-shifting for phase and amplitude tomographic reconstruction in Signal Recovery and Synthesis. OSA Technical Digest, paper CTuB5.
11. Hahn, J., Kim, H., Kim, E.-H., Park, J., Lee, B. (2008) Adaptive phase-shifting digital holography compensating positional inaccuracy and tilting of optics. Proceedings of SPIE, 7056:70561N-70561N-8.
12. Mann, C., Yu, L., Lo, C., Kim, M. (2005) High-resolution quantitative phase-contrast microscopy by digital holography. Optics Express 13:8693-8698.
13. Antkowiak, M., Callens, N., Yourassowsky, C., Dubois, F. (2008) Extended focused imaging of a microparticle field with digital holographic microscopy. Optics Letters 33:1626-1628.
14. Kou, S. S., Sheppard, C. J. (2007) Imaging in digital holographic microscopy. Optics Express 15:13640-13648.
15. 15. Hahn, J. (2009) Holographic measurement and synthesis of optical field using a spatial light modulator. (Doctoral dissertation, Seoul National University, 2009).

Resolution enhancement in digital holography by a two-dimensional electro-optically tunable phase grating

M. Paturzo, A. Finizio , S. De Nicola and P. Ferraro
CNR - Istituto Nazionale di Ottica Applicata & Istituto di Cibernetica, via Campi Flegrei 34,80078-Pozzuoli (NA), Italy

1 Introduction

Digital Holography (DH) provide coherent imaging in microscopy for a variety of applications such as characterization of silicon MEMS, three dimensional imaging [1,2], particle image analysis [3,4]. The potential applications of DH have been extended to a wide spectral range, from far IR [5] to deep UV [6]. The computational image reconstruction from a digital hologram has many advantages compared to the traditional optical holography, including amplitude and phase imaging, 3D imaging and the digital wavefront manipulation. On the other hand, some disadvantages also exist. In fact, no electronic device is able to compete with the high resolution (up to 5000 lines/mm) of the photographic emulsions used in optical holography. Therefore, in most cases, the resolution achieved in DH is too low and not qualified for practical applications.

Recently, important results have been achieved for increasing the optical resolution in DH imaging. The resolution of the optical systems is limited by the numerical aperture (NA). In fact, because of the finite aperture of the imaging system, only the low frequency parts of the object spectrum are transmitted and then recorded by the sensor. Therefore, the corresponding reconstructed images are band limited in the frequency domain. Different approaches have been tested to increase the NA of the optical system in order to get super-resolution. Massig et al. increased the NA by recording nine holograms with a camera (CCD array) translated to different positions and by recombining them in a single synthetic digital hologram [7]. Alexandrov et al. were able to break the diffraction limit by rotating the sample and recording a digital hologram for each position in order to capture the diffraction field along different directions [8]. Recently, an approach that allows superresolved imaging of 3-D samples by numerical refocusing has been presented in the field of digital holographic microscopy [9]. A different method based on the use of a

diffraction grating to obtain super-resolved images was demonstrated in ref. [10,11]. Essentially, the technique allows to collect parts of the spectrum diffracted by the object, which otherwise would fall outside the CCD array. This was achieved by inserting in the recording DH set-up a diffraction grating. Basically, three digital holograms are recorded and spatially multiplexed onto the same CCD array. Super-resolved images can be obtained by the numerical reconstruction of those multiplexed digital holograms, by increasing up to three times the NA. Although the working principle has been demonstrated in [10], it is important to highlight that some limitations wait to be overcome in that approach, because they used a 1D amplitude grating in the recording process. In ref.11 a novel approach is presented where a particular diffraction grating is used. It has two important characteristics that allow to improve the optical resolution behind the limit imposed by the recording system: 1) the grating has 2D hexagonal geometry that allows to obtain super-resolution in two dimensions; 2) since our phase grating is made of an electro-optic substrate it has a tuneable diffraction efficiency. The diffraction tuneability allows to adjust the relative intensities of the multiplexed holograms that, indeed, depend on the diffraction efficiency of the grating itself. Such relative intensities can affect the quality of the super-resolved image obtained by the superimposition of the reconstructed holograms. In addition we will demonstrate that, thanks to the flexibility of the numerical reconstruction process, it is possible to use only the diffraction orders that contribute significantly to increase the spatial resolution discarding those not carrying useful information.

2 Description of the experimental set-up

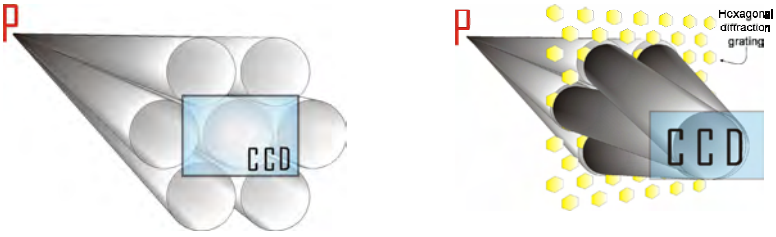

(a) (b)

Fig. 1. Scheme of the ray diagrams of the object waves: (a) without the grating in the setup and (b) with the grating in the setup.

The recording process was carried out by using a Fourier configuration in off-axis mode. The laser source is a He-Ne laser emitting at 632nm. The

specimen is illuminated with a collimated plane laser beam, and a spherical laser beam from a pinhole is used as the reference beam. The CCD array has (1024 × 1024) pixels with 7.6 micron pixel size.
The diffraction grating G is inserted in the optical path between the object and the CCD. The diffraction grating consisted of a 2D array of hexagonally shaped periodic reversed domains in a lithium niobate (LN) substrate with a pitch of 35 μm. After poling, transparent ITO (indium tin oxide) electrodes were deposited on both *z* faces of the sample in order to apply an external field across the crystal preserving the optical transmission along the *z* axis. The phase step between opposite ferroelectric domains can be varied by changing the applied voltage across the *z*-axis of the crystal. When no voltage is applied to the crystal, no diffraction occurs. When voltage is applied, the grating becomes active (*switched-on*) and it is able to generate different diffraction orders. Essentially, each diffraction order produces a corresponding digital hologram and all of the holograms are spatially multiplexed and recorded simultaneously by the CCD. The schematic view of the object waves is shown in Fig. 1(a), (b) where only one point object P is discussed. The holographic system in Fig. 1(b) clearly exhibits higher NA compared to that in Fig. 1(a). In fact, the CCD aperture augments up to three times along each of the three diffraction directions. Consequently, the reconstructed image of the point P has a resolution enhanced up to three times compared to the usual DH system without the diffraction grating.

3 Numerical reconstruction of the spatially multiplexed digital holograms

The numerical reconstruction of the multiplexed digital hologram was divided into two steps. In the first one the wavefield is propagated back in the plane just behind the grating. Then, this complex amplitude distribution is multiplied by the transmission function of the grating to obtain the wavefield in the plane immediately before the grating. Finally, propagating back to the object plane this complex wavefield, we obtained the final reconstructed image with the enhanced resolution. As the grating transmission function we use

$$T(x_1, y_1) = 1 + a\cos(2\pi x_1 / p) + b\cos\left(\left(x_1 + \sqrt{3}y_1\right)\pi / p\right) + c\cos\left(\left(x_1 - \sqrt{3}y_1\right)\pi / p\right) \quad (1)$$

3.1 Experimental results

Figure 2(a) shows the amplitude reconstruction of the digital hologram of the object when no voltage is applied to the electro-optic grating. The object is a microscopy target with different spatial frequencies ranging from 12.59 to 100 lines/mm. The resolution is limited up to the maximum value of 31.6 lines/mm, as evidenced in Fig. 2(b), while pitches with 25.1 μm, 20.0 μm, 15.8 μm are clearly below the resolution limit of the system.

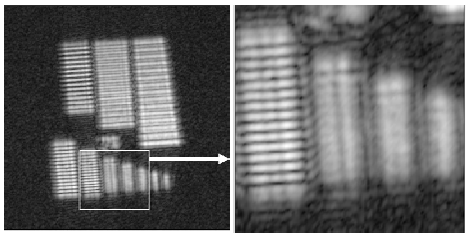

Fig. 2. (a) Amplitude reconstruction of the digital hologram when no voltage is applied to the electro-optic grating; (b) magnified view showing the reticules with the shortest pitches (31.6 μm, 25.1 μm, 20.0 μm, 15.8 μm).

When the phase grating is switched-on, seven spatially multiplexed digital holograms are recorded by the CCD array simultaneously. Figure 3 shows the amplitude reconstruction of the multiplexed digital hologram when a voltage is applied (2.5 kV). The numerical reconstruction is performed without introducing the transmission function T(x,y) of the phase grating.

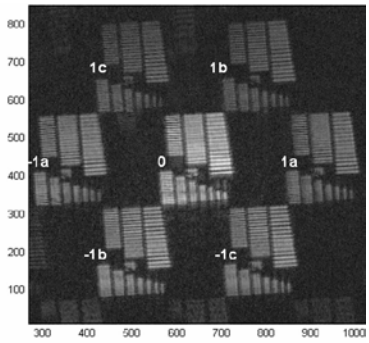

Fig. 3. Amplitude reconstruction of the multiplexed digital hologram when the phase grating is switched-on (applied voltage of 2.5 kV). This numerical reconstruction has been obtained without introducing the transmission function of the phase diffraction grating in the reconstruction algorithm (i.e. T(x,y)=1). The labels of the reconstructed images indicates the corresponding diffraction orders.

The resolution enhancement can be obtained by selectively superimposing the different reconstructed images obtained by the digital holograms. In this way, we can increase the NA of the optical system and therefore the optical resolution of the resulting image. According to the particular geometry of the object, it is also possible to superimpose only some of the reconstructed images that effectively carry the useful information with the aim at resolving the details of the tested object. In fact, the numerical reconstruction algorithm can be considered for one, two or all of the three directions, simply assigning appropriate values to the diffraction efficiency coefficients in the Eq.(1) (i.e a, b, c, respectively).

We found that for the used object, the signal/noise ratio in the super-resolved image is increased when the two orders **±1b** and **±1c** have the same weight in the superimposition. This depends on the particular geometry of the object which has spatial frequencies all along the vertical direction, that is exactly along the bisector of the angle between the directions of the diffraction orders b and c. In Fig.4 (c) is shown the profile calculated along the ruling with 25.1 μm pitch (white line in (b)) completely blurred in Fig.2 concerning the measure with the grating *switched off*.

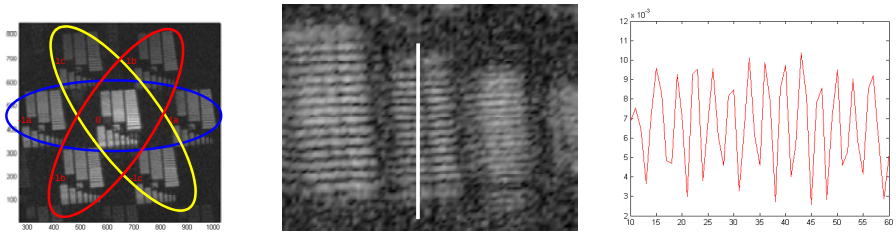

(a) (b) (c)

Fig.4 The coloured ellipses encircle the reconstructed images along the three typical directions of the hexagonal grating. (b) magnified view of the image obtained by superimposing only the 0^{th} and **±1b** and **±1c** orders (red and yellow ellipses); (c) corresponding profiles calculated along the ruling with 25.1 μm pitch (white line in (b)).

As to the diffraction efficiency, we did different measurements varying the voltage applied across the phase grating. The results presented above are obtained when the voltage was 2.5 kV. In fact, we found that this value allows to optimize the relative intensities of the different multiplexed holograms and, therefore, to improve the quality of the super-resolved image obtained by the superimposition of the reconstructed holograms.

4 References

1. Xu, L, Peng, X, Miao, J, Asundi, A K (2001) Studies of Digital Microscopic Holography with Applications to Microstructure Testing. Appl. Opt. 40: 5046-5051
2. Ferraro, P, Grilli, S, Alfieri, D, De Nicola, S, Finizio, A, Pierattini, G. Javidi, B, Coppola, G, and Striano, V (2005) Extended focused image in microscopy by digital Holography. Opt. Express 13:6738-6749
3. Dubois, F, Callens, N, Yourassowsky, C, Hoyos, M, Kurowski, P, Monnom, O (2006) Digital holographic microscopy with reduced spatial coherence for three-dimensional particle flow analysis. Appl. Opt. 45: 864-871
4. Park, Y, Popescu, G, Badizadegan, K, Dasari, R, Feld, M S (2007) Fresnel particle tracing in three dimensions using diffraction phase microscopy. Opt. Lett. 32:811-813
5. De Nicola, S, Ferraro, P, Grilli, S, Miccio, L, Meucci, R, Buah-Bassuahc, P K, Arecchi, F. T (2008) Infrared digital reflective-holographic 3D shape measurements. Opt. Commun. 281:1445-1449
6. Pedrini, G, Zhang, F, Osten, W (2007) Digital holographic microscopy in the deep (193 nm) ultraviolet. Appl. Opt. 46: 7829-7835
7. Massig, J H, (2002) Digital off-axis holography with a synthetic aperture. Opt. Lett. 27:2179–2181.
8. Alexandrov, S A, Hillman, T R, Gutzler, T, Sampson, D (2006) Synthetic Aperture Fourier Holographic Optical Microscopy. Phys. Rev. Lett. 97: 168102
9. Mico, V, Zalevsky, Z, Ferreira, C, García, J (2008) Superresolution digital holographic microscopy for three-dimensional samples. Opt. Express 16: 19260-19270
10. Liu, C, Liu, Z, Bo, F, Wang, F, Zhu, J (2002) Super-resolution digital holographic imaging method. Appl. Phys. Lett. 81: 3143
11. Paturzo, M, Merola, F, Grilli, S, De Nicola, S, Finizio, A, Ferraro, P, (2008) Super-resolution in digital holography by a two-dimensional dynamic phase grating. Opt. Express 16:17107-17118

Resolution improvement in lensless digital holographic interferometry

Daniel Claus[1], Marco Fritzsche*, Dr. Brenda Timmerman, Prof. Peter Bryanston-Cross
Optical Engineering Laboratory, School of Engineering, University of Warwick, CV4 7AL Coventry, UK
*Visiting Student, Mechanical Engineering Department, Technische Universität Ilmenau, 98693, Germany
[1]Corresponding author: daniel.claus@gmx.net

1 Introduction

In digital holography the sinusoidal interference pattern resulting from the interference between reference and object-wave is stored on a digital receiver, such as CCD or CMOS cameras. The maximum resolution of such receivers (typically 500 lp/mm) is small compared to the typical resolution of photographic plates (3000 lp/mm) originally used in optical holography, which limits the maximum angle between reference and object-wave. Furthermore, the sensor size of digital receivers is small compared to photographic plates. Therefore, the numerically reconstructed hologram possesses larger speckles and the smallest resolvable object detail according to Abbé's theorem is much larger than in optical holography. The equation for the average speckle-size, taken from [1], and the smallest resolvable object details are represented in Eq. 1. and Eq. 2.

$$D_{speckle} = \frac{2.44\lambda d}{N\Delta x'} \tag{1}$$

$$\delta = \frac{\lambda d}{N\Delta x'} \tag{2}$$

With $D_{speckle}$ the speckle size in the reconstructed hologram, λ the wavelength, d the recording distance, N the pixel-number and Δx' the pixel-size.
This paper describes two different methods to improve the resolution in digital holography, the *synthetic aperture* and *sub-pixel* method.

Both methods are demonstrated using a lensless 6.6 Megapixel CMOS camera (C-Cam, BCi4-6600) with a pixel-size of 3.5 µm and a fill factor of 35%. CMOS cameras are less expensive and have a smaller pixel-size than CCD cameras, but the signal read out of CMOS sensors is less homogeneous and the fill factor is smaller than for CCD cameras. The homogeneity of the read out can be improved by dark measurement and hot pixel elimination prior to the measurement. The small fill factor can be overcome by the sub-pixel method described in this paper. For both methods the resolution improvement has been demonstrated on a reconstructed intensity and double exposure phase map. The signal to noise ratio SNR was calculated for these images to prove the image quality improvement, see Eq. 3. taken from [2].

$$\mathrm{SNR} = 20\log\left(\frac{\overline{X}}{\sigma}\right) \tag{3}$$

With $\overline{X}$ the mean value of a population and σ the standard deviation.
Assuming that the noise is evenly distributed over the reconstruction, only a small region of interest of approximately 200x200 pixels with ideally constant grey level needs to be considered for the SNR measurement. Grey level changes in that region should then solely be due to noise. Almost all the grey levels are apparent in a 2π phase jump discontinuity of a double exposure phase map. Thus the SNR calculation needed to be adopted to calculate σ alongside the fringe orientation and then to average all values.
Both methods have been evaluated using the USAF1951 test target in order to demonstrate the resolution improvement, which is shown in the last section.

2 Synthetic aperture method

The camera sensor is shifted by a motorized PI M150.11 x-y stage with a linear resolution of 8.5 nm in order to generate an increased sensor area. The total shift is in the range of the sensor dimension with a small overlap between adjacent holograms to enable pixel precise alignment by means of cross-correlation. The setup used is shown in Fig. 1. Polarized laser light is split into its vertical and horizontal component by a polarization beam splitter cube. The polarization of the reference-wave is adapted to the one of the object-wave by two quarter wave plates ensuring a good contrast. Lensless Fourier holograms are recorded by locating the origin of the spherical reference-wave and the object at the same distance to the camera.

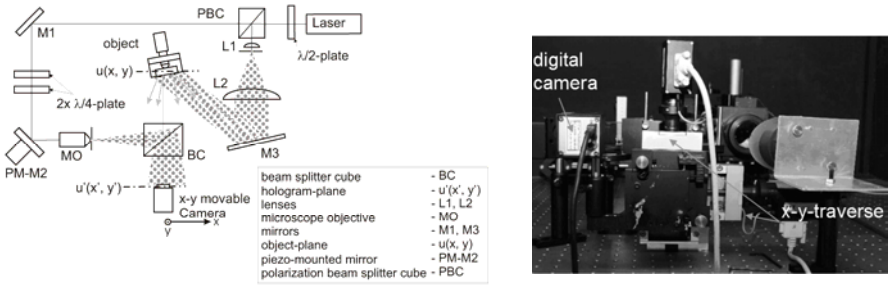

Fig. 1. sketch and realized setup for recording a Fourier-hologram

Fourier holograms have an almost homogenous fringe distribution over the entire sensor. The highest spatial frequency recorded is independent from the pixel-number, which makes them suitable for synthetic aperture holography. The numerical reconstruction, shown in Eq. 4., requires only a two dimensional Fourier transform with an additional phase factor, which means that the numerical effort is less than for alternative reconstruction methods such as the Fresnel- or Convolution approach.

$$u(x,y) = \frac{i\exp(ikd)}{\lambda d}\exp\left[-\frac{i\pi}{\lambda d}\left(x^2 - y^2\right)\right]\Im^{-1}\left\{u\left(x',y'\right)\right\} \tag{4}$$

The investigated object is a cantilever, which allows precise deformation by an attached micrometer screw. The camera has been moved in a 4x3 grid to twelve different positions to generate an increased sensor area of 8800x8800 pixels.

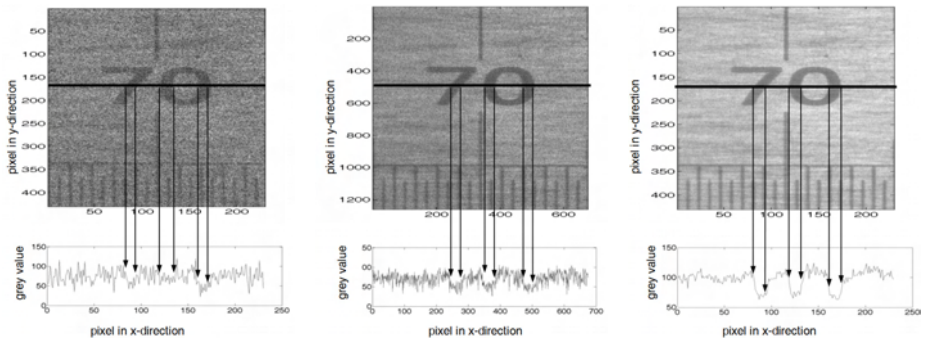

Fig. 2. segment of reconstructed hologram with profile line (a) 3000x3000 pixels, (b) 8800x8800 pixels and (c) 3000x3000 pixels averaging approach

The results obtained for the intensity reconstruction of the cantilever, shown in Fig. 2.(b), demonstrate an increase in SNR from 24.06 dB for a reconstructed 3000x3000 pixels hologram to 26.66 dB for a reconstructed 8800x8800 pixels hologram.

The results obtained for the double exposure phase map applying the synthetic aperture approach are less well defined. The 2π phase jumps appear washed out, which might be due to a less accurate alignment of camera and motorized stage in the z-direction. Moreover, it was found that the camera sensor possesses a slight curvature, which results into scanning at different axial positions of the incoming speckle field. Both effects lead to axial speckle de-correlation. Since the phase is highly sensitive to misalignment the results obtained with double exposure holography are not useful for further interpretations. The averaging approach described by [3], which is not sensitive for axial misalignment, has been slightly modified and applied to address this problem. This approach is based on reconstructing each hologram at its position. Due to the shift $\delta x'$ and $\delta y'$ an additional phase factor, see Eq. 5, arises in the reconstruction formula.

$$\delta\varphi(x,y) = \frac{\pi}{\lambda d}\left(2x\cdot\delta x' + 2y\cdot\delta y'\right) \tag{5}$$

This phase factor can be cancelled out for double exposure deformation measurement since the position is the same for both deformation states. A constant phase offset is still apparent between the phase maps $\Delta\varphi_k$ calculated at each position. This constant offset can be determined in an iterative approach by taking for instance the phase map at the first position as a reference phase map and then subtract the difference from the phase map at the corresponding positions. In order to avoid smearing the phase maps are then added up in an exponential manner Eq. 6. The double exposure phase maps obtained for a single position, the synthetic aperture method and the averaging approach are represented in Fig. 3.

$$\exp\left[i\Delta\varphi_{average}(x,y)\right] = \sum_{k=1}^{n}\exp\left[i\Delta\varphi_k(x,y)\right] \tag{6}$$

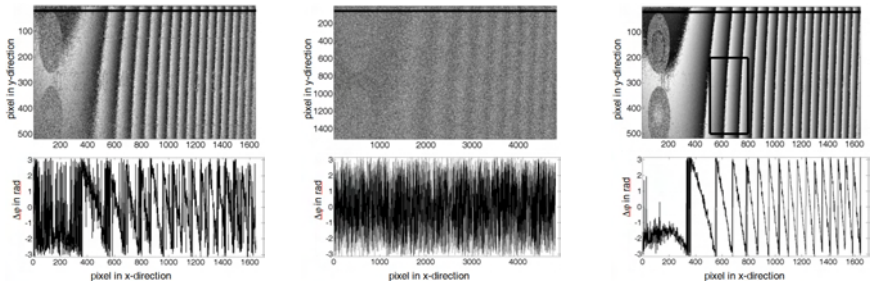

(a) (b) (c)

Fig. 3. segments from double exposure phase maps with indicated profile-scan line and profile for, (a) reconstructed 3000x3000 pixels hologram, (b) reconstructed 8800x8800 pixels hologram, (c) averaging approach

A significant image improvement between the synthetic aperture method and the averaging approach is demonstrated. The SNR was calculated for the region shown in Fig. 3.(c) at the same position for all three phase maps. The values obtained are 17.22 dB, 11.47 dB and 25.57 dB respectively. The averaging approach has also been applied to intensity reconstructions, Fig. 2.(c) shows a segment of the reconstructed intensity image with an SNR of 36.61 dB. Additionally, the influence on the image quality with respect to the position of the holograms used in the averaging approach has been investigated for both the intensity reconstruction and the double exposure phase map, respectively. Considering both graphs in Fig. 4. two aspects become clear, the relationship between number of holograms and the image quality follows to a good approximation a logarithmical curve with R^2-values of 0.98 and 0.99 for reconstructed intensity and phase map respectively. Moreover the more distant the holograms used in the averaging approach are the better is the image quality.

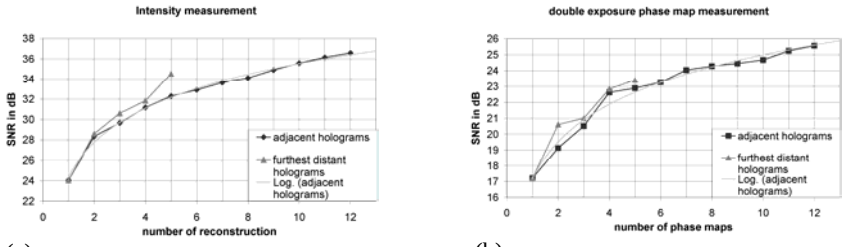

(a) (b)

Fig. 4. (a) SNR for intensity reconstruction versus number of images and their position, (b) SNR for phase map versus number of images and their position

3 Sub-pixel method

The setup used in this case is similar to the one shown in Fig. 1., but the spherical reference-wave has been replaced by a plane reference-wave. The object of investigation is once again a ruler fixed at one end serving as a cantilever, which has been subjected to a much stronger tilt of 2 mm in order to generate a high density of fringes in the double exposure phase map. In order to increase the resolution of the numerically reconstructed hologram, the camera sensor is now moved in x- and y-direction by half the pixel-size. Phase stepping is applied at each camera position to minimize environmental influences which cause the fringes to move slightly around a centred location. Phase stepping is implemented in the setup by a piezo-mounted mirror in the reference-beam. The additional effort for the phase stepping setup is rewarded by enabling an on-line setup

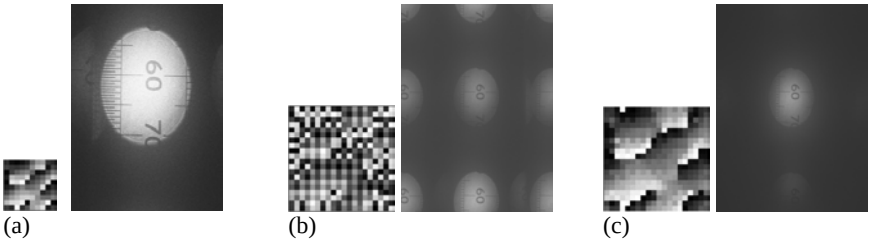

Fig. 5. segment of phase holograms recorded and their reconstruction at 191 mm (a) 10x10 pixels hologram at first position, (b) 20x20 pixels combined hologram without phase correction, (c) 20x20 pixels combined hologram with phase correction

with a further reduced object-camera distance. The phase stepping algorithm used was firstly proposed by [4]. It is based on recording at least three phase stepped holograms. The precision of the phase steps is checked and small phase step errors are cancelled out. The four different phase maps corresponding to each camera position are combined into a common phase map. The initial phase among the four phase maps might differ, which would result in sudden phase jumps between adjacent pixels in the combined phase map**.** If one reconstructs the common phase map without changing the initial phase for each of the four phase maps, higher orders, which cause a splitting of the object information, appear in the reconstructed hologram, see Fig. 5.(b). This can be overcome by resizing a part of the first phase-hologram to twice its size. The interpolated phase value between the original phase values are used to calculate the phase offset for the other three phase maps. The final combined phase map possesses a smooth phase transition, which to a high extent suppresses higher orders in the reconstructed hologram, see Fig. 5. (c). Double

exposure holography was performed without and with applying the sub-pixel method for a recording distance of 191 mm. Their corresponding reconstructed intensity images are shown in Fig. 5. In this case the Nyquist-criterion is violated for the hologram of 3.5 µm pixel-size without applying the sub-pixel method, which leads to aliasing and the appearance of ghost images, see Fig. 5.(a).

Due to the high density of fringes only small segments of the double exposure phase maps are shown in Fig. 6. The fringes are more defined for the sub-pixel method with phase correction than they are for the reconstruction without phase correction and for the reconstruction with 3.5 µm. This is also represented by the SNR values of 11.07 dB, 10.98 dB and 10.96 dB respectively. Additionally to recording at 191 mm a hologram was recorded at 300 mm where the Nyquist-criterion is not violated for 3.5 µm. In that case the image quality improvement becomes very obvious. The intensity reconstructions are shown in Fig. 7.(b) and (c), which are the corresponding segments for Fig. 5(b) and (c). The SNR values for the reconstructions shown in Fig. 7.(a), (b) and (c) are 22.71 dB, 24.94 dB and 25.18 dB respectively.

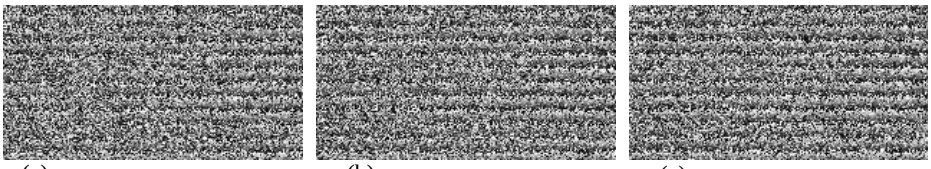

(a) (b) (c)

Fig. 6. segment of double exposure phase maps for 191 mm recording distance (a) 3.5 µm pixel-size, (b) 1.75 µm pixel-size and without phase correction, (c) 1.75 µm pixel-size and with phase correction

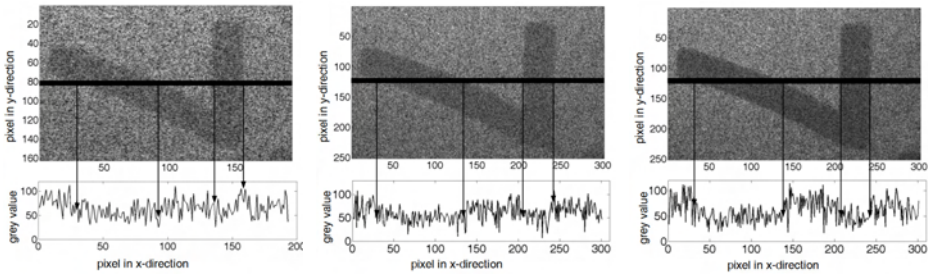

(a) (b) (c)

Fig. 7. segment and their profile lines for (a) reconstructed hologram without sub-pixel method and at 300 mm recording distance, (b) reconstructed sub-pixel hologram at 191 mm recording distance, (c) reconstructed phase corrected sub-pixel hologram at 191mm

4 Combination of synthetic aperture and sub-pixel method

The advantages of both methods were combined and the resolution improvement demonstrated on an USAF1951 test target. The setup used is the same as shown in Fig.1. apart from using a transparent object. Small alignment errors for the location of reference source point and object would result in a slightly out of focus reconstruction. This problem can be solved by introducing a numerical lens, as proposed by [5] and [6], in the reconstruction prior to the two dimensional Fourier transformation.

$$L\left(x', y', d_r, d_o\right) = \exp\left[\frac{i\pi}{\lambda}\frac{\left(d_r - d_o\right)}{d_r d_o}\left(x'^2 + y'^2\right)\right] \tag{7}$$

The numerical lens represented in Eq. 7. enables refocusing as it is a function of the reference point source distance d_r and the object distance d_o. Fig. 8. shows the reconstruction results, the black ring encircles the horizontal resolution and the white ring the vertical one. The theoretically possible resolution was calculated with Eq. 2 and it was found that the recorded holograms exceed it. This might be due the free space propagation between object and camera, meaning that there is no optical imaging device which might insert aberrations. Furthermore, Fourier holograms have been recorded allowing a reduction in the object-camera distance and thus enabling the recording of higher spatial frequencies which results in a higher resolution reconstruction.

Table 1. theoretical and practically achieved resolution

reconstruction	3000x3000 @295 mm	8000x8000 @295 mm	sub-pixel 6000x6000 @185.5 mm	combined 10,000x10,000 @185.5 mm
theoretical resolution	17.8 µm	6.7 µm	11.2 µm	6.7 µm
achieved vertical resolution	17.5 µm	5.5 µm	9.8 µm	7.0 µm
achieved horizontal resolution	17.5 µm	6.2 µm	9.8 µm	5.5 µm

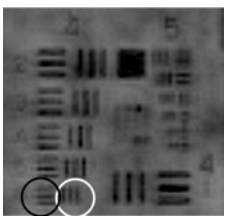

(a)

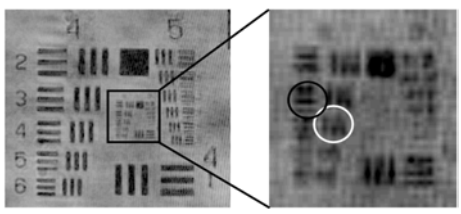

(b)

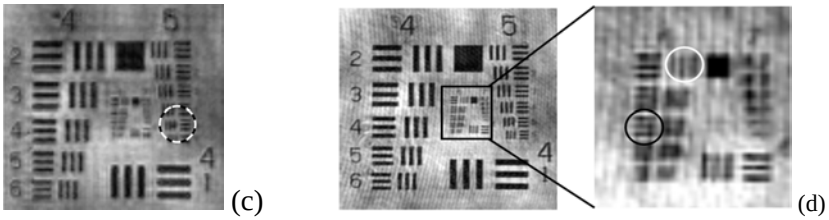

Fig. 8. segment of reconstructed USAF1951 test target (a) 3000x3000 @295 mm distance, (b) 8000x8000 @295 mm distance, (c) sub-pixel 6000x6000 @185.5 mm distance, (d) synthetic aperture and sub-pixel combined for 10,000x10,000 @185.5mm distance

5 Acknowledgment

I would like to thank my supervisors Prof. Peter Bryanston-Cross and Dr. Brenda Timmerman for their helpful advices and for making this project possible. Furthermore, I need to express my thanks to the Socrates-Erasmus foundation and the Optical Institute at the Technische Universität Ilmenau, which made Mr. Marco Fritzsche's stay at the OEL at Warwick possible. Last but not least, I would like to thank IMRC for their financial support of this project and the School Of Engineering technicians for their help manufacturing the necessary devices needed to perform these experiments.

6 References

1. Kreis, T., Handbook of holographic interferometry: optical and digital methods. 2005: Wiley-VCH. 542.
2. Smith, S.W., The scientist and Engineer's Guide to Digital Signal Processing. 2002: California Technical Pub.
3. T. Baumbach, E.K., V. Kebbel, and W. Jüptner, Improvement of accuracy in digital holography by use of multiple holograms. Appl. Opt., 2006. 45(24): p. 6077-6085.
4. L. Z. Cai, Q.L., and X. L. Yang, Generalized phase-shifting interferometry with arbitrary unknown phase steps for diffraction objects. Opt. Lett., 2004. 29(2): p. 183-185.
5. Goodman, J.W., Introduction to Fourier Optics second ed. 1996, San Francisco: McGraw-Hill. 441
6. W.S. Haddad et al., Fourier-transform holographic microscope. Appl. Opt., 1991. 31(24): p. 4973-4978.

Digital holography catching up with analogue holography both in resolution and in field of view with a bottom-line camera

F. Gyímesi, V. Borbély, Z. Füzessy and B. Ráczkevi*
Budapest University of Technology and Economics, Budapest University of Technology and Economics, Department of Physics
Department of Physics
Budafoki út 8., 1111 Budapest,
Hungary
*Institute for Particle and Nuclear Physics of the Hungarian Academy of Sciences
Konkoly-Thege Miklós út 29-33, 1121 Budapest
Hungary

1 Introduction

Analogue holography uses a relatively permanent recording material for recording the interference fringes of an aerial hologram and subsequently for providing a real materialized hologram-grating for the reference light wave to diffract on it at reconstruction. Therefore, from our present point of view, it could be called quite rightfully as “material holography”, too. Digital holography, on the other hand, replaces this permanent recording material with electronic light sensitive matrix detector which relatively instantly converts the interference fringes of the aerial hologram into digital information for a computer. No materialized grating is produced instead the reconstruction is performed purely numerically. On one side, digital holography has the great advantage of the really unique flexibility of the numerical reconstruction but on the other side it suffers from the basic physical shortcomings of the converting electronic matrix detector.

A CCD or CMOS camera has a very limited resolution in comparison with the photographic recording materials of analogue holography, and the detector target of the camera has a size, as well, much smaller than the possible size of these photographic plates. The limited resolution restricts the field of view of the reconstruction; while the limited size restricts the resolution in the reconstructed holographic image. Since the invention of digital holography, many attempts have been made to overcome these two basic limitations.

As for the limited size of the detector target, scanning the larger aerial hologram somehow with the small matrix detector is the most straightforward approach. Although there are important other methods, as well, to build up some type of a synthesized aperture, this mostly means the relative motion of the camera and the object with respect to each other [1-6]. The synthesized aperture can be in the real hologram plane directly [3-6] or somewhere before it in the Fourier plane of an intermediate optical system [1] or in a virtual calculation-transformed hologram plane, too [2]. In most cases [2,5,6] the camera is the only moving element. In [1] some part of the optical setup moves together with the camera, and in [2] separate fixed cameras are used. Besides, there is an opposite possibility of moving the object instead of the camera, as well [3].Both on-axis [5,6]and off-axis [1-4]optical arrangements are practiced. Phase shifting procedure is applied in on-axis arrangement [5] or at moving reference case [1]. The stitching of the holograms is usually performed by correlation calculation on their overlapping side areas.

The present paper reports results in probably the simplest version possible of the synthetic aperture approach which does not seem to have been directly exploited up to now. An optics-free small bottom line camera is moved directly in the aerial hologram plane in a conventional off-axis arrangement - up to 10(20) times to its original size. The increase in resolution is at a factor of 6(14).

As for the limited size of the detector pixels, the application of some magnification at the readout of the fine-structured aerial hologram, is again another most straightforward approach. Nevertheless, according to the best knowledge of the authors of this paper, no attempts have been made at all in this direction up to now.

The authors of the present paper would like to report the results achieved by the modified version of their previously described synthetic aperture approach, where the otherwise optics-free camera is already equipped with a commercial microscope objective to take a magnified image of the aerial hologram. The increase in the maximum size of the object which can be reconstructed in one step is at a factor of 7 without loss in the image resolution – and at factor 4 with a concurrent increase in image resolution of factor 3, too.

2 Scanning the aerial hologram – for better resolution

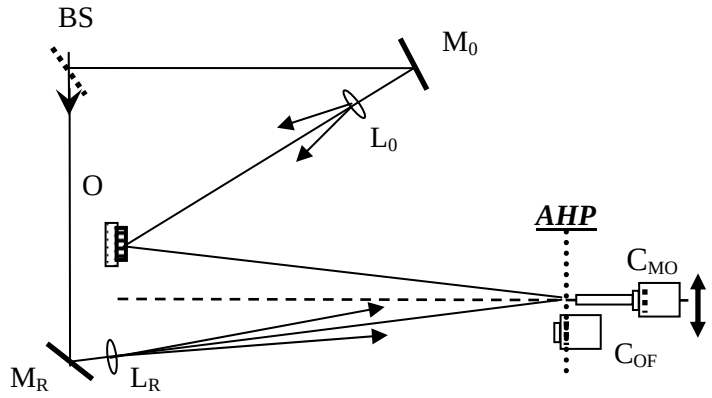

Fig. 1. Optical arrangement for scanning and magnifying the aerial hologram

Scanning was performed by moving the optics-free CCD camera C_{OF} in x and y directions on a meander path - directly in the AHP plane of the off-axis aerial hologram (Fig. 1.). The small bottom line camera was simulated by cutting out a 512x512 pixel portion from a larger camera of pixel size 7,4x7,4 μm^2. The camera motion was controlled only with 0.1 mm accuracy. Overlapping recordings were matched by correlation calculation.

Aperture size	LENSE image	MATERIAL HOLOGRAM reconstructed image	**DIGITAL HOLOGRAM** ***calculated image***
BASIC APERTURE 512x512 pxl 3,8x3,8 mm^2	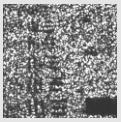 2,52 lp/mm	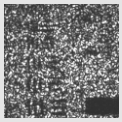 2,24 lp/mm	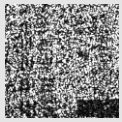 2,24 lp/mm
10x10 Synthesized Aperture 4096x4096 pxl 30,3x30,3 mm^2	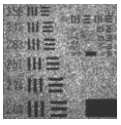 7,13 lp/mm	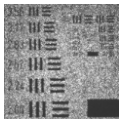 6,35 lp/mm	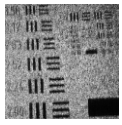 **12,7 lp/mm**

Fig. 2. Results of scanning the aerial hologram – and the comparison of the achievement of digital holography with material holography and with imaging by lens

A 10x10 synthesized aperture of 4096x4096 pxl (30,3x30,3 mm^2) can produce 12.7 line-pair/mm resolution at an USAF Resolution Test Chart from 1 m distance (Fig. 2.).This is 6 times better than what can be provided by the non-scanning basic aperture. The 10x10 synthesized aperture results even better resolution than the resolution provided by a large photo objective or by a photographic material hologram of the same aperture size. (The material hologram, as well, requires a lens to reconstruct a real image for the photo and thus it is affected by the same aberration problems as the photographic lens itself at this relatively large aperture.)

3 Magnifying the aerial hologram – for larger field of view

The magnification of the aerial hologram is equivalent to the demagnification of the detector target – which in itself is small enough originally. In a magnified case, therefore, a viable method of hologram readout can not exist without a concurrent robust application of some synthetic aperture approach. (This need for the combined application may be the reason, perhaps, for the seeming lack of this line.)

In the previous arrangement (Fig. 1.), the optics-free camera C_{OF} was transformed into camera C_{MO} where a microscope objective of magnification of 4 or 10 was attached to the camera house with a proper tube extension. The microscope objective produces a sharp image of the aerial hologram in the AHP plane directly onto the camera target. The 4x objective reduces the pixel size to 1,85x1,85 μm^2 and increases the observable object size by a factor 4 from 17 to 64 mm (Fig. 3.). To withhold the original resolution of 2,24 line-pair/mm from 1 m, a concurrent application of a 5x5 synthetic aperture was needed. If instead of that a a 20x20 is used and the extrem large 8192x8192 pxl virtual pixel number is generated then even the original resolution can be increased simultaneously with a factor 3.

The 10x objective reduces the pixel size to 0,74x0,74 μm^2 and increases the observable object size by a factor of 7 to 120 mm (Fig. 3.). To withhold the original resolution of 2,24 line-pair/mm from 1 m, a concurrent application of a 10x10 synthetic aperture was needed. (With preference for maximum increase of field of view, even an increase of a factor 20 can be reached for it – on the cost of a resolution decrease to the half of the original value.)

Pixel Demagnification (Virtual pixel size)	***Synthesized aperture size***	**DIGITAL HOLOGRAM** **Object size**	**DIGITAL HOLOGRAM** **Resolution**
1x (7,4x7,4 μm^2)	512x512 pxl 3,8x3,8 mm^2	 17 mm	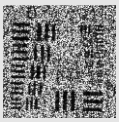 2,24 lp/mm
4x (1,85x1,85 μm^2)	***5x5 Synthesized aperture*** 2048x2048 pxl 3,8x3,8 mm^2	 **64 mm**	 **2,24 lp/mm**
4x (1,85x1,85 μm^2)	***20x20 Synthesized aperture*** 8192x8192 pxl 15,2x15,2 mm^2	 **64 mm**	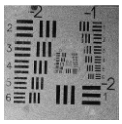 **7,13 lp/mm**
10x (0,74x0,74 μm^2)	***10x10 Synthesized aperture*** 4096x4096 pxl 3,03x3,03 mm^2	 **120 mm**	 2,24 lp/mm

Fig. 3. Results of magnifying the aerial hologram – and the results of the combination of magnifying with scanning at the aerial hologram

4 Summary

Digital holography seems not to have exploited fully or at all the two most straightforward possibilities of overcoming the basic physical shortcomings of the electronic cameras. The limited detector target size can be extended by producing a synthesized aperture with camera scanning - directly in the aerial hologram plane and in the conventional off-axis

arrangement, too. On the other hand, the limited pixel size can be extended by a demagnifying microscope objective – although it has to be combined immediately with some synthesized aperture extension, too.

With a 10x10 synthesized aperture of 4096x4096 pxl, 12.7 line-pair/mm resolution could be reached from 1 m distance with a basic 512x512 pxl camera – which is extension by factor 6. On the other hand, a 4x microscope objective magnification could provide an extension of the observable object size by a factor 4 - and a concurrent resolution increase by factor 3. could be reached with a 20x20 synthesized aperture of 8192x8192 pxl. A 10x microscope objective could provide an extension even by factor 7, up to an object size of 120 mm – without resolution loss.

5 Acknowledgments

The work has been performed within the scope of the Hungarian GVOP project No. 3.1.1.-2004-05-0403/3.0, supported by the EU Structural Fund, too. The authors wish to acknowledge A. Czitrovszky and A. Nagy at RISSPO (Hungarian Acadamy of Sciences), Gy. Molnárka and H. Abdelhakim at Széchenyi István University, D. Szigethy at Technoorg-Linda ScTD Ltd. for their important contributions.

6 References

1. Le Clerc, F., Gross, M., Collot L. (2001) Synthetic-aperture experiment in the visible with on-axis digital heterodyne holography. Optics Letters 26: 1550-155211
2. Massig, J. (2002) Digital off-axis holography with synthetic aperture. Optics Letters. 27: 2179-2181
3. Binet, R., Colineau, J., Lehureau J-C. (2002) Short-range synthetic aperture imaging at 633 nm by digtital holography. Applied Optics 41:4775-4782
4. Kreis, T., Adams, M., Jüptner, W., (2002) Aperture synthesis in digital holography. Proc. SPIE 4774:69-76
5. Nakatsuji, T., Matsushima, K. (2008) Free-viewpoint images captured using phase.shifting synthetic aperture digital holography. Applied Optics 47: D136-143
6. Martínez-León, L., Javidi, B. (2008) Synthetic aperture single-exposure on-axis digital holography. Optics Express 16:161-169

Fresnel and Fourier digital holography architectures: a comparison.

Damien P. Kelly, David S. Monaghan, Nitesh Pandey,
Bryan M. Hennelly.
Department of Computer Science,
National University of Ireland, Maynooth,
Co. Kildare, Ireland.

1 Introduction

In this manuscript we examine the characteristics of holograms that are captured using both Fresnel and lens-less Fourier digital holographic systems. We begin by introducing some of the fundamental equations describing the intensity distribution captured by the camera. Naturally this captured intensity will vary depending on whether the system used is a Fourier or a Fresnel due to the different reference field in each case, however as we shall see with appropriate numerical processing it is possible to obtain similar performance from both systems. We discuss a reconstruction algorithm for changing the focus depth in Fourier holograms and examine how it effects the twin image and dc terms. A theoretical comparison with Fresnel holograms is made. Experimental results are provided to support our analysis. We finish with a brief conclusion.

2 Theory and Experimental Results

A typical optical setup for capturing both Fresnel and lens-less Fourier digital holograms was built. The object is illuminated with a plane wave. Light scattered from this object then propagates to the camera plane where it is combined with our reference wave and the resulting intensity pattern recorded. A lens in the reference arm is used to vary the curvature of the reference field and may be removed in order to capture a Fresnel hologram. The intensity recorded by the camera may be expressed as [1]

$$H(x) = \left| u_z(x) + u_R(x) \right|^2 \tag{1 a}$$

$$H(x) = I_z + I_R + u_z(x)u_R^*(x) + u_z^*(x)u_R(x) \tag{1 b}$$

where I_z and I_R represent the intensities of the object and reference fields respectively, while the latter two terms in Eq. (1 b) correspond to the real and twin image fields. We use a lens of focal length, f, to produce a spherical reference field $u_R(x)$ for our Fourier holography setup,

$$u_R(x) = \exp\left(\frac{j\pi x^2}{\lambda f}\right) \tag{2 a}$$

wheras for Fresnel holography the reference is a flat unit amplitude plane wave and can be written as

$$u_R(x) = \exp(j\alpha) \tag{2 b}$$

where α is some arbitrary constant phase. We may relate the field $u_z(x)$ to the field in the object plane, $U(X)$ using a Fresnel transform which we define as,

$$u_z(x) = \Im_z\{U(X)\}(x) \tag{3 a}$$

$$u_z(x) = \exp\left(\frac{j\pi x^2}{\lambda z}\right)\int U(X)\exp\left(\frac{j\pi x^2}{\lambda z}\right)\exp\left(\frac{-j2\pi xX}{\lambda z}\right)dX \tag{3 b}$$

Note that for simplicity in this manuscript we ignore: (i) the finite extent of the camera, (ii) the reduction in power of higher spatial frequencies due to an averaging introduced by the finite pixel size, and (iii) sampling introduced by pixels spaced uniformly at fixed intervals from each other [1, 2].

We now wish to consider numerical reconstruction of both Fourier and Fresnel holograms. We may recover our Fresnel hologram numerically using the Direct Method [3]. This entails multiplying $H(x)$ by a quadratic phase factor, $\exp\left(j\pi x^2/\lambda z_R\right)$, (where z_R is the desired reconstruction distance), and performing a numerical Fourier transform on the result. By varying z_R we can change the reconstruction distance. Performing such a numerical operation on the real image term from Eq. (1 b) produces the following result, see Fig. 1. The image in Fig. 1 corresponds to a Fresnel hologram

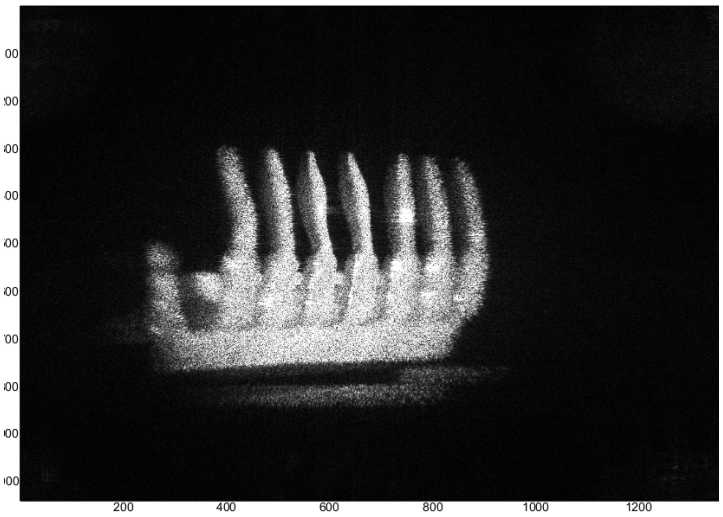

Fig. 1. Numerical reconstruction of a digital hologram captured using a Fresnel geometry. Both the DC terms and the twin image have been removed in this example using a PSI technique.

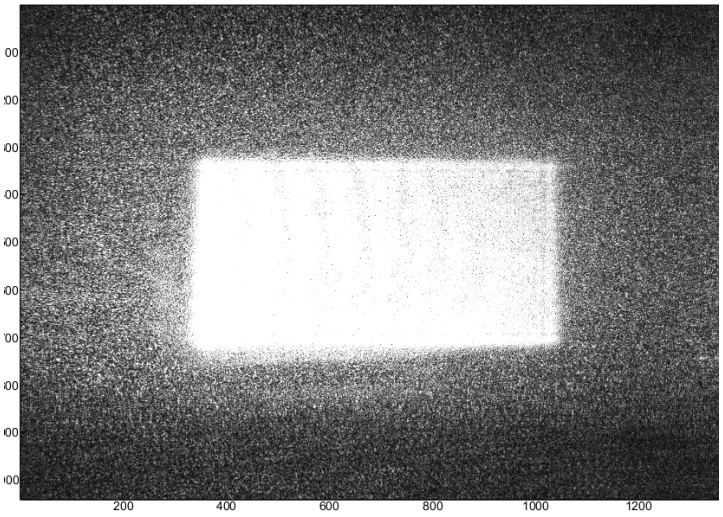

Fig. 2. Numerical reconstruction of a digital hologram captured using a Fresnel geometry. In this case the neither the twin nor DC terms have been removed and both act to significantly reduce the quality of the reconstructed hologram.

where the twin image and DC terms have been removed using a phase shifting interferometric technique (PSI). If the twin image term is not removed from Eq. (1 b) we see that it overlaps with the real image in the

reconstruction plane reducing the quality of the reconstructed hologram. This can be seen in Fig. 2. Note the DC terms will also contribute negatively to the image quality. We now wish to examine how we may reconstruct our real image term [term 3 in Eq. (1 b)] assuming that our incident reference field is now described by Eq. (2 a),

$$u_z u_R^* = \exp\left[\frac{j\pi x^2}{\lambda}\left(\frac{1}{z}-\frac{1}{f}-\frac{1}{z_R}\right)\right] \times \int U(X)\exp\left(\frac{j\pi x^2}{\lambda z}\right)\exp\left(\frac{-j2\pi xX}{\lambda z}\right)dX \quad (4)$$

If $z = f$ in the equation above (we set $z_R = 0$ for the moment) then the leading quadratic phase term drops out and we can relate $u_z u_R^*$ to $U(X)\exp\left(j\pi x^2/\lambda z\right)$ by a Fourier transform. A similar analysis holds for the twin term. In Fig. 3 we present a typical Fourier reconstruction, see figure caption for details.

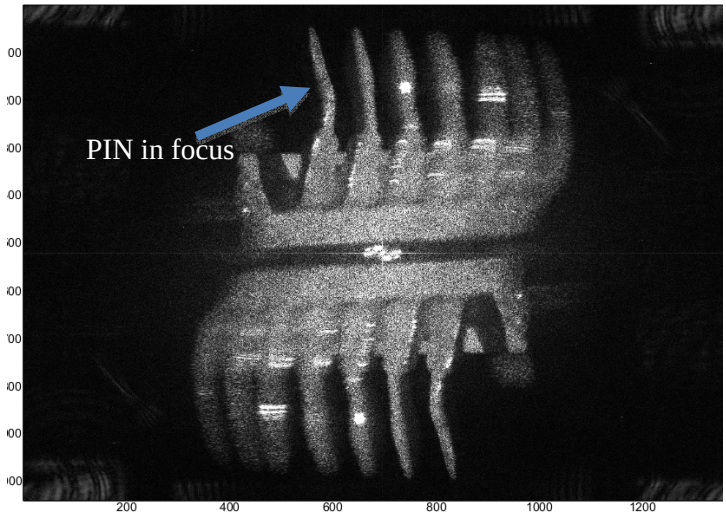

Fig. 3. Numerical reconstruction of a digital hologram captured using a Fourier geometry. Both the twin and real image terms are in focus. The DC term is roughly mapped to a spot in the center of the digital reconstruction. Note that the first PIN is in sharp focus.

To focus on a different section of the Fourier hologram we now change the value of z_R in Eq. (4) by multiplying with a numerical quadratic phase factor and perform a Fourier transform on the result (a similar approach is

also discussed in Ref. [4]). Note the increased blurring of the DC and twin terms in Fig. 4 when compared to Fig. 3, also note the change in focus.

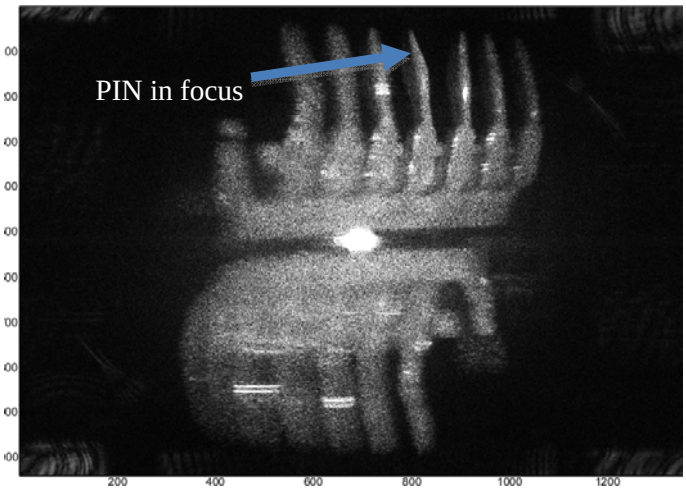

Fig. 4. Numerical reconstruction of a digital hologram captured using a Fourier geometry. Here we have re-focused using a numerical algorithm. The effect of the focusing is to blur the twin term and smear the DC term.

3 Conclusion

We have shown that both Fourier and Fresnel holograms can be refocused using numerical techniques however this focusing operation will effect the twin and DC terms differently in each case.

4 References

1. Kreis M. T, (2002) Frequency analysis of digital holography. Optical Engineering 41:771-778
2. Kelly P. D, Hennelly M. B, Pandey N, Naughton J. T, Rhodes T. W, (2009) Resolution limits in practical digital holographic systems. Under Review Optical Engineering
3. Kelly P. D, Hennelly M. B, Rhodes T. W, Sheridan T. J, (2006) Analytical and numerical analysis of linear optical systems. Optical Engineering 088201:1-12
4. Pedrini G, Froening P, Tiziani J. H, Mendoza Santoya F, (1999) Shape measurement of microscopic structures using digital holograms. Optics Communications 164:257-268

The last Word on Three-Flat Calibration – are we there yet?

Jan Burke and Bob Oreb
Australian Centre for Precision Optics
CSIRO Materials Science and Engineering
PO Box 218, Lindfield, NSW 2070
Australia

1 Introduction

Laser interferometry, paired with phase-shifting, is a magnificent non-contact measurement tool that responds to changes on the nanometre scale. However, interference fringe patterns, such as those produced in a Fizeau interferometer, only ever give the difference between two surfaces, not the absolute shapes. The so-called 3-flat calibration is based on the idea that 3 nominally flat surfaces $A(x,y)$, $B(x,y)$, $C(x,y)$, when combined in 3 different pairs, define an equation system yielding solutions for all the flats' surface maps. The 3-flat problem then arises from the fact that one of the flats (here: B), with its co-ordinate system, has to be flipped during the measurements, as shown in Fig.. Solutions always involve ways to reduce the number of unknowns, by additional measurements, symmetry decompositions, co-ordinate transformations, recursion relations, or a combination of these.

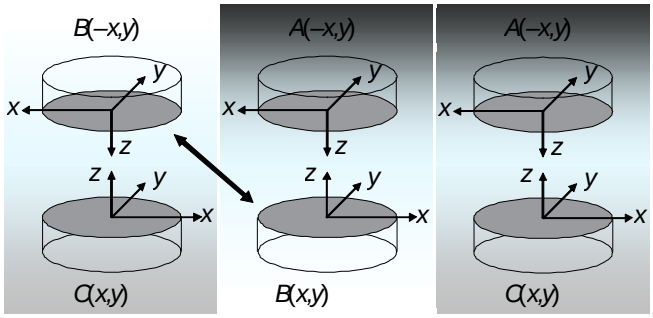

Fig. 1. Optical set-up for absolute calibration of three flats A, B, and C. The arrowed line marks reversal of the *x* co-ordinate of flat B; one such reversal is inevitable in the test

The measurements in Fig. will yield a valid generic calibration only along the *y*-axis. However, it was realised in 1967 that only two intersecting lines of this type are sufficient to define a plane, and the problem was solved by adding two measurements, namely with one of the flats rotated by ±60º [1]. In the same year, a recursion formula was presented that used only one extra measurement with a rotation of either a rational or irrational fraction of 360º, and then allowed to solve along a finite or (in principle) infinite number of meridians by building on the known points from the previous step [2]. Practical problems with interpolation and accuracy were, however, pointed out even then, and lateral shifts were introduced to make the technique more amenable for use with CCD cameras [3]. Shifts will decrease the calibrated aperture however [4], and it is therefore better to work with rotations only. Besides computing absolute data on meridians (the radial co-ordinate), one can also isolate the angular co-ordinate instead to obtain complete solutions [5,6]. All of the above methods involve some degree of interpolation and thereby increased uncertainties. This restriction has been overcome by replacing the software rotations with as many physical rotations as necessary and using only mirroring operations about the *x* and *y* axes on the data [7,8]. Since the original data set involves only mirroring about *y*, the approach has been further simplified [9]. With the matrix notation introduced in [8], new and customised solutions can be developed quickly, which shows that the theory is now well understood. Practical problems to be dealt with include variable distortions [10,11], system functions [11] and fine-structure uncertainty [12]. We will show how a method can be developed and implemented for our custom interferometer.

2 The Large Aperture Digital Interferometer (LADI)

For high-performance metrology, CSIRO's Australian Centre for Precision Optics uses a custom-built wavelength-shifting Fizeau interferometer [4], whose layout is shown in Fig.. This realisation introduces a few particular variables:

(i) the test and reference flats will sag under gravity;

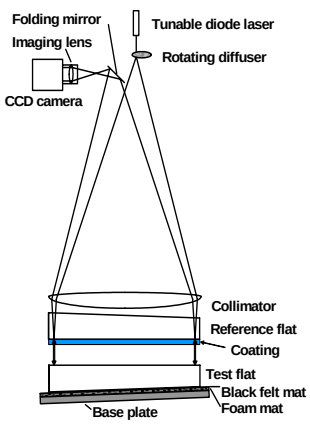

Fig. 2. Wavelength-shifting Fizeau interferometer with vertical optical axis

(ii) if they are supported, they must be supported uniformly;

(iii) the dedicated reference surface has an absorptive coating, so it can be used in the reference position only;

(iv) there is a slight off-axis angle between incoming and reflected beam;

(v) since the tilt axes for the test flat are not in its surface, each tilt to remove fringes will also result in a sub-pixel image displacement.

2.1 Gravity sag

As can be seen in Fig., one of the flats (here: B) must be flipped for the calibration measurements, whereby a flat surface would become concave in the test position (unless we support its bottom surface uniformly) and convex in the reference position (where we cannot support the bottom surface as we need the transmitted wavefront). The other flats are not flipped, so that their sags can be ignored. Recording an accurate sag map for the flipped flat is very important for a successful calibration of this type of instrument, and implies the assumption that the magnitude of the sag does not depend on whether the test surface is pointing up or down. We have designed specialised flat mounts which hold each flat in its neutral plane to achieve this. The sag maps are generated by comparing a measurement of a flat supported by a foam mat to a measurement of the same flat suspended in its kinematic mount. To confirm our data, we can also use flat C in the reference position and B in the test position, to test our symmetry assumption by reversing the way gravity pulls on the flats. Fig. shows what has been achieved.

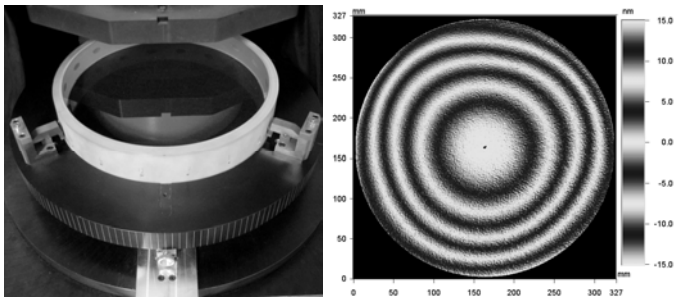

Fig. 3. Left: test flat in custom collar; right: sag map between supported and suspended state (pseudo-fringes, –15 - +15 nm)

2.2 Customised measurement sequence

To make the measurement sequence practical, we have to design it so that we measure flat A (our designated reference flat) only in the reference position, and also leave it in place after the calibration measurements. The arrangement in Fig. fulfils this condition. However, we must take at least one extra measurement to resolve the symmetry issues and carry out our calibration.

It has been suggested to build an averaged measurement by rotating one of the flats (in theory continuously, in practice by a certain number of discrete steps) [8]. This creates a measurement file in which one of the flats is represented only as a rotational average, which has no odd symmetry components. Thus we gain access to the odd symmetry components of the other (stationary) flat and are able to solve the equation system. The extended measurement sequence is shown in Fig., where we have written $B_s(-x,y)$ to indicate where we cannot support flat B against gravitational sagging.

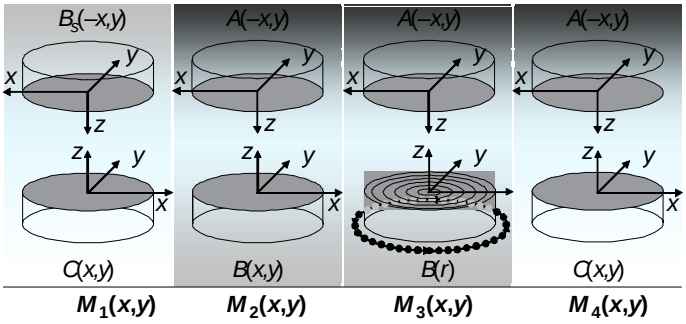

Fig. 4. Customised measurement sequence with rotational average. The sag map needs to be determined only for flat B, as flats A and C are not flipped; but flat A has sag as well

2.3 Instrument error

Generally, Fizeau interferometers have no instrument error; however our glass flats have refractive index inhomogeneities that will be detected as phase variations during wavelength-shifting, do not cancel out because of the slight off-axis configuration of the LADI, and create an extra phase function specific to each flat in the reference position. Fig. presents an example.

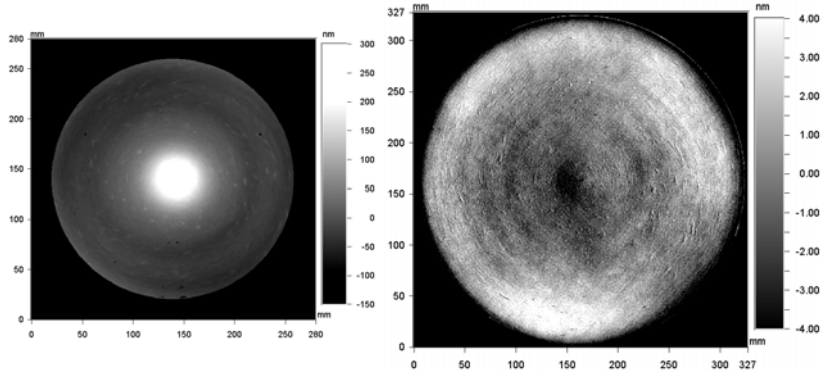

Fig. 5. Measurement of flat B in reference position against C in test position. Left: Optical path variation through centre of flat B (–150 to +300 nm); right: resulting phase profile, with optical power subtracted to show the differentiation effect more clearly (–4 to +4 nm)

The slight offset in x direction between rays returning from reference and test surfaces in effect creates a shear which differentiates the refractive index map. (Consequently, we must keep the air gap between the measured surfaces constant in all measurements, as this gap determines the shear.) In Fig., we can ignore this effect for flats A and C: for flat A, we can simply interpret the error as part of the flat itself, and flat C is only used in the test position. However, flat B is used in the reference and test positions and therefore we must account for the change.

We can model the extra phase function by adding a system function $S(-x,y)$ to the measurement sequence $M(x,y)$ which is present only in $M_1(x,y)$ but not in the other measurements. Our system of measurement equations thus reads

$$\begin{aligned} M_1(x,y) &= B(-x,y) + S(-x,y) + C(x,y) \\ M_2(x,y) &= A(-x,y) + B(x,y) \\ M_3(x,y) &= A(-x,y) + B(r) \\ M_4(x,y) &= A(-x,y) + C(x,y), \end{aligned} \tag{1}$$

where $B(r)$, the rotational average, varies only radially on the circular aperture. This set of four equations contains six variables and is therefore solvable only if the variables are not independent.

3 Solution strategy

The problem has been treated in a multitude of related ways, for which we offer the following generalisation. The ubiquitous approach is that we try

to take advantage of symmetry properties to eliminate variables; e.g. $B(-x,y) = B(x,y)$ if we look at the part that is even in x, and $B(-x,y) = -B(x,y)$ for the odd part in x, and so on [7,8]. It is also possible to optimise the statistical robustness of the linear combinations with regard to random noise [8]. We can express the surface functions in four parts of different symmetries: odd (in x) and odd (in y), denoted by the subscript *oo*, even-odd (*eo*), odd-even (*oe*) and even-even (*ee*). Starting with the odd-odd contributions,

$$\begin{aligned} M_{1,oo}(x,y) &= -B_{oo}(x,y) + S_{oo}(-x,y) + C_{oo}(x,y) \\ M_{2,oo}(x,y) &= A_{oo}(-x,y) + B_{oo}(x,y) \\ M_{3,oo}(x,y) &= A_{oo}(-x,y) \\ M_{4,oo}(x,y) &= A_{oo}(-x,y) + C_{oo}(x,y). \end{aligned} \tag{2}$$

We have used $B_{oo}(-x,y) = -B_{oo}(x,y)$ and $B_{oo}(r) = 0$, i.e. $B(r)$ contains no odd-odd parts, so that the odd-odd parts in $M_3(x,y)$ are from flat A only. Hence, the number of variables is reduced to 4 and Eq. 2 is solvable. Likewise,

$$\begin{aligned} M_{1,eo}(x,y) &= B_{eo}(x,y) + S_{eo}(-x,y) + C_{eo}(x,y) \\ M_{2,eo}(x,y) &= A_{eo}(-x,y) + B_{eo}(x,y) \\ M_{3,eo}(x,y) &= A_{eo}(-x,y) \\ M_{4,eo}(x,y) &= A_{eo}(-x,y) + C_{eo}(x,y)\,, \end{aligned} \tag{3}$$

where we have used $B_{eo}(-x,y) = B_{eo}(x,y)$ and $B_{eo}(r) = 0$. The latter is only valid if a full 360° radial average is taken. It has been suggested in [8] that a half-turn is sufficient, but this eliminates only the odd-odd parts from the average and Eq. 3 does not hold. Only with a full turn can we create purely even-even symmetry in the rotational average, label it $B(r)$, drop it from all symmetry components other than even-even, and simplify the equations considerably. Alternatively, the full average can be synthesised [6,13]. Next, we have

$$\begin{aligned} M_{1,oe}(x,y) &= -B_{oe}(x,y) + S_{oe}(-x,y) + C_{oe}(x,y) \\ M_{2,oe}(x,y) &= A_{oe}(-x,y) + B_{oe}(x,y) \\ M_{3,oe}(x,y) &= A_{oe}(-x,y) \\ M_{4,oe}(x,y) &= A_{oe}(-x,y) + C_{oe}(x,y)\,, \end{aligned} \tag{4}$$

and for the even-even parts we get

$$
\begin{aligned}
M_{1,ee}(x,y) &= B_{ee}(x,y) + S_{ee}(-x,y) + C_{ee}(x,y) \\
M_{2,ee}(x,y) &= A_{ee}(-x,y) + B_{ee}(x,y) \\
M_{3,ee}(x,y) &= A_{ee}(-x,y) + B(r) \\
M_{4,ee}(x,y) &= A_{ee}(-x,y) + C_{ee}(x,y)\,,
\end{aligned}
\tag{5}
$$

which has one variable too many and is therefore not solvable; nor can we pair the flats differently to generate more equations. This problem is of a fundamental nature: even-even parts do not respond to mirroring or rotation operations; they are always “plus” themselves, never “minus”, and can therefore not be subtracted out. In other words, we must assume $S_{ee}(-x,y) = 0$.

In light of the radially symmetric index distribution in Fig., this is probably a very good approximation; nonetheless it shows that the sag map must be determined very carefully, because even-even errors entering the calibration while flipping the B flat cannot be recognised and will eventually appear as part of the actual flats in the calibration data [11]. In the absence of an even-even system error,

$$
\begin{aligned}
M_{1,ee}(x,y) &= B_{ee}(x,y) + C_{ee}(x,y) \\
M_{2,ee}(x,y) &= A_{ee}(-x,y) + B_{ee}(x,y) \\
M_{4,ee}(x,y) &= A_{ee}(-x,y) + C_{ee}(x,y)
\end{aligned}
\tag{6}
$$

gives sufficient information, since for the even-even part the symmetry problem depicted in Fig. does not exist. There are numerous other combinations of measurements to create a solution, but we have shown here that four measurements (involving a rotational average) are sufficient and even leave enough room to deal with some instrument errors. Since we have used a full 360º average and no flips of the y co-ordinate (as generated by e.g. a 180º rotation of a flat: $B(x,y) \rightarrow B(-x,-y)$), we could have used simple mirror symmetry [9] to solve Eq. 1. Unfortunately this would not capture $S_{eo}(-x,y)$, as we would have had to ignore it together with $S_{ee}(-x,y)$.

After these steps, it is generally useful to record a fine-structure average as well [12] and replace the fine structure in the calibration file with it, since displacements at the sub-pixel level occur during measurement and also during computer generation of the symmetry components. Also, the procedure can undo the effect of bad pixels quadrupling during the symmetry operations. Fig. shows results from a recent three-flat calibration.

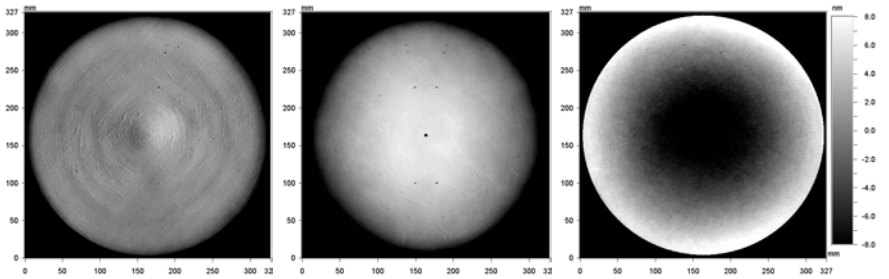

Fig. 6. Left to right: Calibration file for flat A in reference position (with clearly visible shear term); flat B in test position (supported); flat C in test position (suspended). Scale is –8 to +8 nm in all images.

4 Conclusion

We have shown one straightforward way to carry out a three-flat test and have emphasised the salient points when solving the equation system:

(i) reduce the number of variables by using symmetry properties;

(ii) use a true rotational average to allow very simple solutions;

(iii) eliminate even-even system errors as they cannot be detected.

For simplicity, this discussion has neglected the more subtle issue of statistical robustness.

The power and limits of solution strategies are by now so well understood that new solutions can be generated very quickly to suit the practical measurement set-up and sequence, and as such the last word on three-flat calibration is probably not far away.

5 Acknowledgements

Many thanks to Ulf Griesmann, who shared Ref. [14] with us, and with whom we had a friendly competition for the most elegant solution during the preparation of this paper. This has greatly helped to clarify some very important points.

6 References

1. Schulz, G, Schwider, J (1967) Precise Measurement of Planeness. Applied Optics 6:1077-1084
2. Schulz, G (1967) Ein Interferenzverfahren zur absoluten Ebenheitsprüfungs längs beliebiger Zentralschnitte. Opt. Act. 14:375-388
3. Grzanna, J, Schulz, G (1990) Absolute testing of flatness standards at square-grid points. Opt. Comm. 77:107-112
4. Oreb, B, Farrant, D, Walsh, C, Forbes, G, Fairman, P (2000) Calibration of a 300-mm-aperture phase-shifting interferometer. Appl. Opt. 39:5161-5171
5. Parks, R (1978) Removal of test optics errors. Proc. SPIE 153:56-63
6. Freischlad, K (2001) Absolute interferometric testing based on reconstruction of rotational shear. Appl. Opt. 40:1637-1648
7. Ai, C, Wyant, J (1993) Absolute testing of flats by using even and odd functions. Appl. Opt. 32:4698-4705
8. Küchel, M (2001) A new approach to solve the three flat problem. Optik 112:381-391
9. Griesmann, U (2006) Three-flat test solutions based on simple mirror symmetry. Appl. Opt. 45:5856-5865
10. Griesmann, U, Wang, Q, Soons, J (2007) Three-flat tests including mounting-induced deformations. Opt. Eng. 46:093601
11. Burke, J , Oreb, B, Netterfield, R (2005) Customized three-flat calibration method for a 320 mm aperture Fizeau interferometer with vertical optical axis. Proc. ASPE 2005:31
12. Hariharan, P (1996) Optical flat surfaces: direct interferometric measurements of small-scale irregularities. Opt. Eng. 35:3265-3266
13. Parks, R, Shao, L, Evans, C (1998) Pixel-based absolute topography test for three flats. Appl. Opt. 37:5951-5956
14. Griesmann, U (2008) Three-flat calibration (unpublished booklet).

A New Flatness Reference Measurement System Based on Deflectometry and Difference Deflectometry

Gerd Ehret*, Michael Schulz*, Manuel Stavridis**, Clemens Elster**
* Physikalisch-Technische Bundesanstalt
Bundesallee 100, 38116 Braunschweig, Germany
** Physikalisch-Technische Bundesanstalt
Abbestr. 2-12, 10587 Berlin. Germany

1 Introduction

A new optical flatness reference system for specimens with diameters of up to 700 mm is being set up at the Physikalisch-Technische Bundesanstalt (PTB). The system is designed for absolute optical flatness measurements with uncertainties in the sub-nanometre range. It is based on deflectometry as well as difference deflectometry procedures. Both principles use the straight propagation of light as a straightness reference, and thus no external reference surface with known topography is required.

In the deflectometric procedure, the specimen is scanned by a penta-prism or double mirror. The angle of the reflected beam of the surface is measured with a high-resolution calibrated autocollimator. In contrast, the procedure of difference deflectometry measures angle differences between two points on the sample separated by a constant lateral shear chosen between some millimetres to centimetres. This has the advantage that the measurement will not be influenced by height shifts or tilts of the sample. Due to the extended shear, this procedure was named ESAD (Extended Shear Angle Difference measurement).

With the existing ESAD set-up, initially built up almost a decade ago and improved by upgrades over the years, uncertainties in the range of 1 nm and below for specimens with a diameter of 150 mm have been reached [1]. The specimen dimensions are rather limited. The most severe restrictions of this system are the weight of the samples and the restriction to horizontally oriented samples. The set-up of the new system will be different from the existing system. It is designed with the highest accurate mechanical stages and improved optics. In this way, the uncertainty of the measurements will be even more reduced. Additionally, it will be more

flexible than the existing ESAD system, allowing horizontal or vertical samples to be measured.

We present the principle, the mechanical and the optical properties of the new optical flatness reference system. Since both procedures (direct deflectometry and difference deflectometry) will be implemented in the new flatness reference system, we will compare these procedures. The influence of the mechanical guide errors of the stages on the measurement results will be discussed. For this purpose, a realistic mathematical simulation environment has been developed. We present quantitative results obtained by this simulation tool which allows for the estimation of accuracies that can be reached by the new DFR (deflectometric flatness reference) system.

2 Traceable Measurements of Flatness using direct or difference Deflectometry

Apart from the three-flat test [2], interferometric procedures rely on an external reference surface of known topography. In contrast to this, deflectometric procedures use the straight propagation of light as flatness reference, and the measured topography can be traced back to the SI unit metre by traceable angle and traceable length measurements.

With the new DFR system, two different deflectometric procedures are realised: the direct and difference deflectometry. It is common to both procedures that by means of highly precise and accurate angular measurements with an autocollimator, the topography of the specimen can be reconstructed. The principle of the direct deflectometric procedure is shown in Fig. 1 left; there, the autocollimator is firmly connected with the granite base and measures the slopes $\sigma(x_k)$ of the surface, while the "double mirror" scans the specimen. Afterwards, the topography $h(x_k)$ will be calculated by "direct" integration of the measured slopes, in simple cases, by the trapezoidal rule:

$$h(x_k) = h(x_0) + \sum_{m=1}^{k} \frac{\Delta x}{2} \cdot \left[\sigma(x_m) + \sigma(x_{m-1})\right] \tag{1}$$

If the measurement data are noisy, improved integration algorithms such as spline interpolation integration can be applied [3]. The direct deflectometric procedure has the advantage of a short measurement time and the disadvantage that the optical path of the autocollimator changes during the measurement. Thus the calibration of the autocollimator

becomes more extensive and demanding. The direct deflectometric procedure is, e.g., realised in the "The Nanometer Optical component measuring Machine – NOM" of Bessy in Berlin, Germany [4].

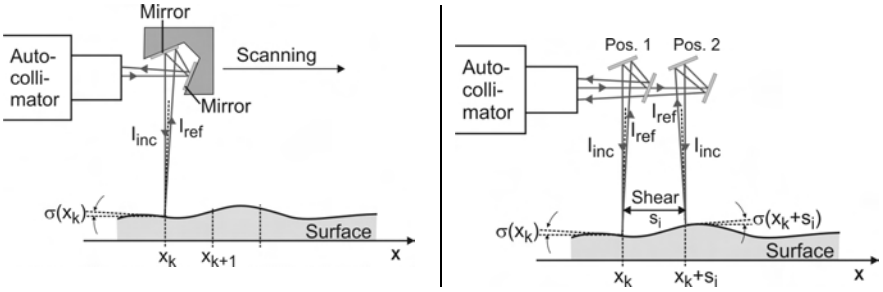

Fig. 1. Principle of direct deflectometry (left) and difference deflectometry (right). Surface height is drawn strongly exaggerated.

With the difference deflectometric procedure, angle differences between positions with fixed distances – the so-called shears s_i – are measured (see Fig. 1 right). The positions are launched by moving the pentaprism with a linear stage. This procedure is called the "Extended Shear Angle Difference" (ESAD), because large lateral shears from mm to cm are used. ESAD was invented at the PTB ten years ago and implemented in the ESAD measurement system [5, 6]. In order to receive a unique solution, usually two shears $s_1 = \nu_1 \cdot \Delta x$ and $s_2 = \nu_2 \cdot \Delta x$ are required, where ν_1 and ν_2 are natural numbers which are relatively prime. The number of reconstructed points are $N = \nu_1 \cdot \nu_2$ [7]. An optimum shear combination exists, which is most robust with respect to both random and systematic residual error influences on the difference data [1]. The measurement yields the following angle of differences:

$$\Delta\sigma(x_k, s_i) = \sigma(x_k + s_i) - \sigma(x_k) \text{ with } i = 1,2 \text{ for } k = 1,2,...n_i \qquad (2)$$

From these difference angles the slopes $\sigma(x_k)$ can be computed using natural extension and shearing transfer functions [7]. Afterwards, the topography can be calculated by the integration of these slopes according to Eq. 1 or improved algorithms [3]. The difference deflectometry can be accomplished with the autocollimator fixed at a global position as well as following the pentaprism and being fixed only during the difference measurement. By the latter, the optical path of the autocollimator is almost constant.

3 Design of the New Deflectometric Flatness Reference

The new deflectometric flatness reference system (DFR) consists of two separate systems. System I is designed for the measurement of horizontal specimens by direct and difference deflectometry as well as vertical specimens by direct deflectometric measurements. System II is designed for measuring vertical probes by difference deflectometry. Fig. 2 shows a design drawing of system I. The system is composed of a granite base with a granite bridge, where an air bearing stage is mounted. Carriage 1 of this air bearing stage is used for the autocollimator and carriage 2 for the pentaprism or double mirror. A straightness and flatness reproducibility of less than 0.5 µm and an angle reproducibility of less than 0.5 arcsec over a travel range of 1 m is aimed at. The specimen lies on a tilting table which is equipped with two piezoelectric actuators for fine adjustment of the specimen. In order to scan the specimen at different locations – also off-axial – the rotation stage and the linear stage mounted on the granite base can be used.

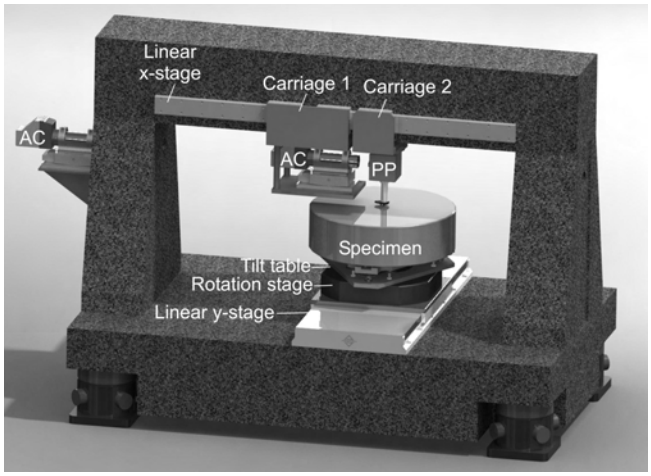

Fig. 2. Scheme of deflectometric flatness reference (system I) for horizontal specimens (AC: autocollimator, PP: pentaprism or double mirror) .

The DFR system allows round samples with a diameter of up to 700 mm and elongated samples of up to 1000 mm with a weight of up to 120 kg to be measured. For the topography, a standard uncertainty in the sub-nanometre range is aimed at.

4 Modelling of the New Flatness Reference System

To estimate the influence of the input quantities (e.g. guiding errors, optical errors, environmental influences) on the derived topography, a realistic model of the DFR system has been developed. The model is implemented in a universal simulation environment developed at PTB. Fig. 3 shows the guidance errors of the x-stage assumed for the simulations.

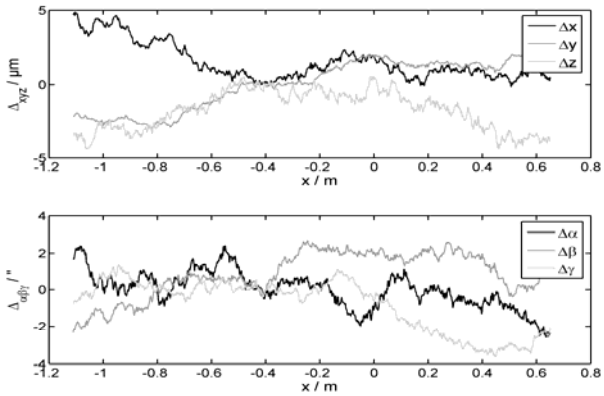

Fig. 3. Assumed guiding errors of the air bearing x-stage with systematic errors of 5 µm for $\Delta x, \Delta y, \Delta z$ and 5 arcsec for $\Delta\alpha, \Delta\beta, \Delta\gamma$.

As test surface, a parabolic surface of 800 mm in diameter with a height of 200 nm is used. As an example, the influences of the guiding errors of the x-stage on the errors of the derived topography for the different modes of operation are listed in Table 1, where the root mean square errors err_{rms} are shown.

Table 1. Example of one input parameter: Influence of the guiding errors of the x-stage on the resulting topography errors for different modes of operation.

Guiding error of the x-stage	Direct deflectometry	Difference deflectometry (AC is fixed)	Difference deflectometry (AC is moving)
$\Delta x, \Delta y, \Delta z$ = 5 µm $\Delta\alpha, \Delta\beta, \Delta\gamma$ = 5 arcsec	err_{rms} = 0.001 nm	err_{rms} = 0.001 nm	err_{rms} = 0.004 nm
$\Delta x, \Delta y, \Delta z$ = 5 µm $\Delta\alpha, \Delta\beta, \Delta\gamma$ = 25 arcsec	err_{rms} = 0.027 nm	err_{rms} = 0.027 nm	err_{rms} = 0.107 nm

Further input quantities such as the alignment of the pentaprism, the autocollimator calibration, the air influences to the autocollimator beam, different optical path lengths or temperature effects will be included in the model in the next steps. With the existing ESAD measurement system, a standard uncertainty of less than 1 nm for specimens with diameters of 150 mm has already been reached [1]. It is expected that a standard measurement uncertainty of the new DFR system in the sub-nanometre range should be possible.

5 Conclusion

The set-up and the different modes of operation of the new DFR systems have been presented. In addition, first results of modelling the system, which was implemented in the simulation environment, are shown.

With the new optical flatness reference measurement system, we will be able to provide industry and other customers with highly accurate flatness calibrations for horizontal and vertical specimens, even of large size.

6 References

1. Geckeler, R D, Weingärtner, I (2002) Sub-nm Topography Measurement by Deflectometry: Flatness Standard and Wafer Nanotopography, in Proc. of SPIE 4779:1-12
2. Griesmann, U, Wang, Q, Soons, J (2007) Three-flat tests including mounting-induced deformations, Opt. Eng. 46:093601-1-15
3. Elster, C, Weingärtner, I (2002) High-accuracy reconstruction of a function f(x) when only d/dx f(x) or d^2/dx^2 is known at discrete measurement points, in Proc. of SPIE 4782:12-20
4. Siewert, F, Lammert, H, Zeschke, T (2008) The Nanometer Optical component measuring Machine – NOM, Modern Developments in X-Ray and Neutron Optics, Springer Series in Optical Sciences 137, Springer-Verlag, Berlin / Heidelberg
5. Weingärtner, I, Schulz, M, Elster, C (1999) Novel scanning technique for ultra-precise measurement of topography, in Proc. of SPIE 3782:306-317
6. Geckeler, R, Weingärtner, I, Just, A, Probst, R (2001) Use and traceable calibration of autocollimators for ultra-precise measurement of slope and topography, in Proc. of SPIE 4401:184-195
7. Elster, C, Weingärtner, I (1999), Solution to the Shearing problem, Applied Optics 38 (23):5024-5031

Quasi absolute Test for Aspherics via dual Wavefront Holograms and a radial Shear Position

Klaus Mantel, Irina Harder
Max Planck Institute for the Science of Light
Günther-Scharowsky-Str. 1/Bau 24, 91058 Erlangen
Germany
Eduard Geist, Norbert Lindlein
Institute of Optics, Information, and Photonics
University of Erlangen-Nürnberg
Staudtstr. 7/B2, 91058 Erlangen
Germany

1 Introduction

Calibration methods – “absolute tests” – in interferometric testing of surfaces are usually carried out in a null test configuration. Examples for spherical surfaces are the three position test [1], as well as the shift-rotation procedure [2]. A calibration method for aspherics [3] that is currently under investigation consists of an adaptation of the three position test for spheres. Since aspheric waves in general have no focus, a dual wavefront hologram [4] has to be used to obtain the cat´s eye position.

However, absolute testing procedures involving a cat´s eye position suffer from several disadvantages. The object wave is inverted so that the use of spatial partially coherent illumination to reduce coherent noise requires special means [5]. An additional optical path length of twice the radius of curvature of the specimen is introduced, causing wave aberrations and impairing the calibration results. Furthermore, the adjustment of the cat´s eye position is hindered because lateral shifts of the specimen do not lead to misalignment aberrations and, therefore, have to be detected by other means. It seems to be for these reasons that the shift-rotation procedure, which does not rely on a cat´s eye position, achieves highest accuracies [6]. However, this method needs a specimen with a spherical symmetry and cannot be directly applied to aspherics.

In this work, we propose to avoid the cat´s eye position by using a dual wavefront hologram to obtain a second null test position, where the surface deviations of the aspheric are radially sheared with respect to the interferometer frame (see Fig. 1). Together with rotational movements of

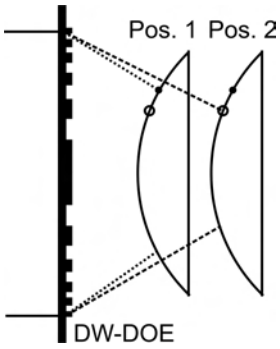

Fig. 1. The radial shear movement used. The dual wavefront hologram (DW-DOE) provides two null test wavefronts which can be switched on and off via a wavefront selective mask (not shown). In Pos. 2, a radial shear has taken place with respect to Pos. 1, marked by the black dot and the circle

the specimen around the optical axis it is then possible to test aspherics in an absolute manner without the disadvantages associated with the cat´s eye position.

2 Measurement Principle

With the help of the radial shear movement shown in Fig. 1, two different absolute testing methods for aspherics are possible. The first method combines the radial shear with rotational averaging [7] (Fig. 2). With this method, the non-rotational symmetric parts of the surface deviations can be obtained by taking the difference between a single measurement in what may be called the basic position (Fig. 2, left, corresponds to Pos. 1 in Fig. 1) and the rotationally averaged data for the same position (Fig. 2, middle). The systematic aberrations of the interferometer cancel. By using rotational averaging in the radial shear position (Fig. 2, right, corresponds to Pos. 2 in Fig. 1), it is now possible to reconstruct the rotational symmetric part as well. The difference of the rotationally averaged data in both the basic and the radial shear position gives a phase distribution proportional to an r-dependent difference quotient of the surface deviations. These data can be integrated to give the rotational symmetric part of the surface deviations.

A second method (Fig. 3) uses measurements of data proportional to the difference quotients in both φ- and r-direction (difference of measurement data of Fig.3 left and middle, and right and middle, respectively) and a two dimensional integration to retrieve the surface deviations of the aspheric.

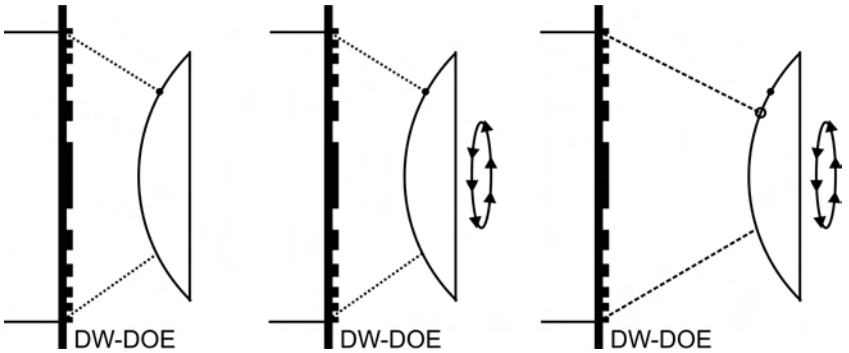

Fig. 2. The radial shear movement combined with rotational averaging. Subtracting the first two positions gives the non-rotational symmetric parts of the surface deviations of the aspheric, while subtracting the last two positions gives an *r*-dependent difference quotient which can be integrated

A prerequisite for the validity of absolute methods involving a radial shear movement is that the systematic aberrations of both wavefronts used are of the same order. Since the difference of the wavefront aberrations is of the order $\Delta\varphi \sim 2\pi\Delta p(1/p_1 - 1/p_2)$, where Δp is the structuring error of the lithography machine and p_1, p_2 are the local periods of the two DW-DOE structures, it is necessary that either the structuring error of the lithography device is small, or that the local periods of the two DW-DOE structures are similar. Since this condition can only be fulfilled approximately, we use the term “quasi absolute” procedure for both methods.

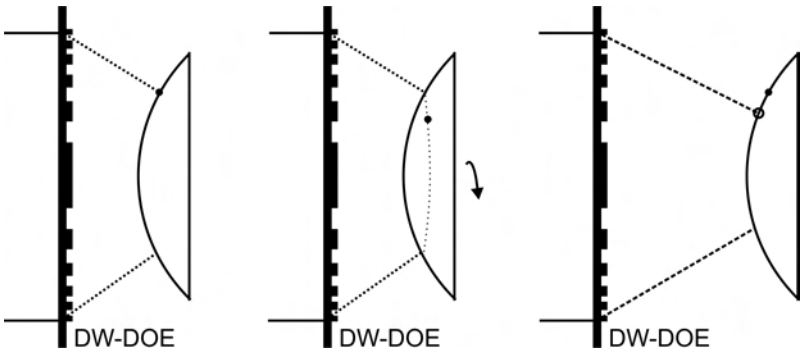

Fig. 3. The measurement results in the radial shear position (right) and in a rotated position around the optical axis (middle) are subtracted from the result of a standard null test position (left), respectively, to give the difference quotients of the surface deviations along the *r* and φ-directions

As is common for shearing techniques, there are parts of the surface deviations that cannot be determined in one run, namely those parts which are invariant under the shear chosen. Such missing parts can be reconstructed by a second measurement with a different shear.

It should be noted that, in contrast to commonly applied shearing techniques, the radial shear depends on the radial coordinate r in a way determined by the ideal shape of the aspheric. Consequently, the sensitivity of the procedure varies over the surface of the specimen. In particular, at the center of the aspheric – or, generally speaking, at any points with horizontal tangent – the shear and the sensitivity are zero. Information about the surface deviations in these regions can only be obtained in the sense of interpolation. However, since measurements of such regions in reflected light are usually troubled with parasitic reflections, this restriction can be tolerated.

For the reconstruction of the surface deviations, a polynomial based approach is used. An appropriately sheared polynomial system, in our case Zernike polynomials, is matched to the measurement data in the least squares sense, giving the surface deviations represented by the coefficient vector of the system.

3 Limitations of absolute Tests using a radial Shear Position

The use of the radial shear position leads to potential limitations for the overall accuracy with which the surface deviations can be recovered. Such limitations arise when measurement results from two different null test geometries are combined, as is the general idea of the proposed measurement procedures.

A limitation which is especially prominent has its roots in the misalignment elimination, a step performed during the software evaluation of the measurement data [8]. Systematic wave aberrations associated with a misalignment of the specimen with respect to the interferometer frame are removed from the measurement results in the least squares sense. In particular, this removal also affects the parts of the surface deviations which are of the same form as the misalignment aberrations. Since the measured aperture of the specimen is different in the two different null test positions, the misalignment elimination can introduce errors in the data leading to a large residual error in the reconstructed surface deviations. Fig. 4 shows measurement data for a surface with deviations in the form of spherical aberration in the basic (left) and the radial shear position (right).

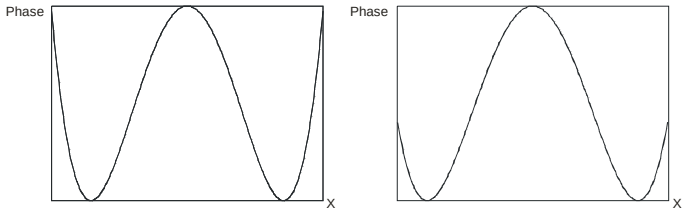

Fig. 4. A specimen showing spherical aberration, measured in the basic (left) and radial shear position (right). In the radial shear position, a defocus term is present, in contrast to the basic position

A misalignment elimination, however, will remove a defocus term from the radial shear position, changing the difference quotient and thereby impairing the integration result.

It is possible, though, to eliminate the resulting residual aberration ex post. It turns out that the residual errors, stemming from the integration of misalignment terms, contain aberrations proportional to the misalignment terms themselves, and characteristic for the respective degrees of freedom. Since misalignment terms are, by definition, not a part of the surface deviations, a misalignment elimination can determine the amount of errors present in the data before integration. In this way, the residual error can altogether be avoided.

4 First Measurement Results on Spheres

To have a comparison with other, established methods, a spherical specimen has been chosen. Fig. 5 shows the absolute surface deviations of

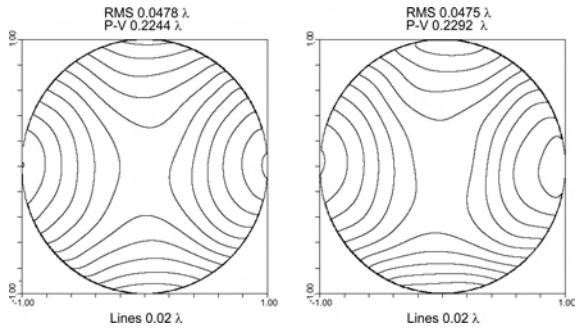

Fig. 5. Absolute testing results of a concave sphere, obtained by the three position test (left, after polynomial fit of degree 12) and the radial shear method via difference quotients (right, represented by Zernike polynomials of degree 12)

a concave sphere, obtained by the radial shear procedure via difference quotients as well as by the three position test. The system of Zernike polynomials used for integration was of degree 12.

5 Conclusion

The introduction of a radial shear position allows the absolute testing of aspherics without a cat´s eye position and its associated disadvantages. Despite possible limitations, we think this is a promising way for calibrating aspherics; it may even be transferred to other, non rotational symmetric lens systems, like acylindrical lenses.

6 Acknowledgments

This project is supported by the Deutsche Forschungsgemeinschaft under the contract LI 1612/1-1.

7 References

1. A. E. Jensen, “Absolute calibration method for laser Twyman-Green wave front testing interferometers”, J. Opt. Soc. Am. 63, 1313A (1973)
2. B. Dörband, G. Seitz, “Interferometric testing of optical surfaces at its current limit”, Optik 112, No. 9 (2001)
3. J. Schwider, “Absolutprüfung von asphärischen Flächen unter Zuhilfenahme von diffraktiven Normalelementen und planen sowie sphärischen Referenzflächen”, German patent 19822453.2 (20. June 1998)
4. A. F. Fercher, “Computer-generated holograms for testing optical elements: error analysis and error compensation”, Opt. Acta 23 (1976)
5. M. Küchl, “Apparatus and method(s) for reducing the effects of coherent artifacts in an interferometer”, Patent-No. 6,804,011 (2004)
6. G. Seitz, “Hochaufgelöste interferometrische Absolutmessung rotationssymmetrischer Oberflächenfehler”, DgaO Proceedings, ISSN 1614-8436 (2006)
7. C. J. Evans, R. N. Kestner, "Test optics error removal", Appl. Opt. 35, (1996)
8. E. W. Young, “Optimal removal of all mislocation effects in interferometric tests”, Proc. SPIE 661 (1986)

Rapid and flexible measurement of precision aspheres

Eugenio Garbusi, Goran Baer, Christof Pruss and Wolfgang Osten
Universität Stuttgart, Institut für Technische Optik
D-70569 Stuttgart
Germany

1 Introduction

In the last years aspherical surfaces have grown to become a key element in the design of optical systems [1,2] mainly because of the increasing demand for compact optical systems with high imaging quality and the introduction of new fabrication techniques like ion-beam figuring and magnetorheological finishing (MRF). Although a major breakthrough has been accomplished in the processing and shaping of surfaces by these (and other) technologies, there still remains the problem on how to achieve an accurate and efficient surface characterization. The aspheric production chain lacks, even today, of a proper measurement system that combines accuracy, flexibility and small measurement time.

Two different modalities in the measurement of aspherics can be distinguished: so called null-test and non null-test configurations. The first ones are based on the use of some sort of compensation element (null-optic) that shapes a planar or spherical test wavefront into one that impinges normally to the aspherical surface [3]. A disadvantage of this method is that every new asphere shape requires a matching compensation element so they do not really fulfill the flexibility requirement. Design and fabrication of the null-optic becomes costly and time consuming.
In contrast, non-null test configurations offer the required flexibility at the cost of dealing with problems like vignetting, high fringe density and so-called retrace errors [4,5]. Since the incidence of the test beam to the test surface is no longer normal, we have to deal with aberrations introduced by the test optics itself (interferometer). This requires the development of special algorithms to tackle with the massive amount of errors introduced (mostly) by the transmission sphere and the imaging optics of the interferometer.

In the last years several solutions to the aspheric metrology problem based on stitching [6] or scanning Fizeau interferometers [7] have been

proposed. Although they posses the required flexibility, a repositioning of the test object is usually required during the measurement process (in space for stitching procedures and along the optical axis of the interferometer for the scanning Fizeau). Clearly a disadvantage, since a dedicated mechanic is necessary and the overall measurement time increases rapidly.

In this work a new interferometer [8-10] operating in a non-null test configuration is presented. The system makes use of a two-dimensional array of point sources to generate a set of test waves with increasing tilts. These allow the compensation of local gradients on the test surface, thus avoiding classical problems like subsampling and vignetting artifacts.
In the next section the basic interferometer setup will be described and in section 3 a brief outline of the evaluation algorithms is presented. Finally results for a test asphere are presented.

2 Interferometer description

The interferometer setup is depicted in Fig. 1. A stabilized HeNe laser source L (λ = 632.8 nm) is spatially filtered, collimated and split into the reference (upper path) and test beam (lower path) of the interferometer by the beamsplitter BS_1. A diffractive optical element (PSA- Point Source Array) consisting of a microlens array (MA) on the front side and a matching pinhole array (PA) on the backside is placed in the test path. This element generates a two-dimensional matrix of point sources that after collimation by lens L_2 result in a set of test wavefronts with different tilts. Afterwards the transmission sphere O focuses them again to test the surface T. After reflection on the test surface, lens L_3 images the test wavefront onto the camera interfering then with the plane reference wave from the upper branch of the interferometer.

At the Fourier plane of L_3, the interferometer aperture B limits for each source of the array the fringe density on the detector. Since a given source compensates the surface gradients only in a small neighborhood (see Fig. 2), aperture B introduces a spatial limitation for the extension of the interferogram produced by each source. This allows the parallel evaluation of each interferogram without the need of individual activation of the sources.

Still, some overlap between contiguous sources takes place leading to an incorrect calculation of the corresponding interferogram. The solution is the sequential activation of the source array by means of a blocking mask (M in Fig. 1), where every fourth source is selected to perform a

measurement. The complete measurement of the test surface requires thus four steps (as shown in Fig. 2) and can be completed in about 40-50 seconds.

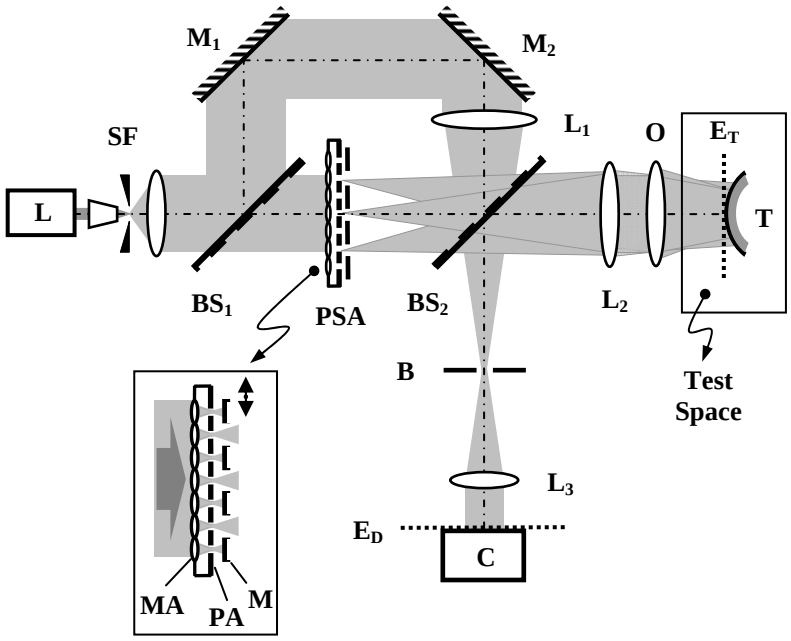

Fig. 1. Interferometer setup. L, HeNe laser; SF, spatial filter and beam expander; M_1 and M_2, fold mirrors; L_1, focusing lens; BS_1 and BS_2, beamsplitters; PSA, point source-array; MA, Microlens Array; PA, Pinhole Array; M, source selection mask; L_2, collimation lens; O, transmission sphere; T, test object; B, interferometer aperture; L_3, imaging lens; C, camera

3 Outline of the algorithms

Since the measurement of the aspherical surface is based on a non-null test configuration, it becomes essential to characterize the contribution of the interferometer (induced system aberrations) to the measurement of the test object in order to obtain meaningful results. In the next a brief outline of the system calibration and measurement procedure will be given [11].

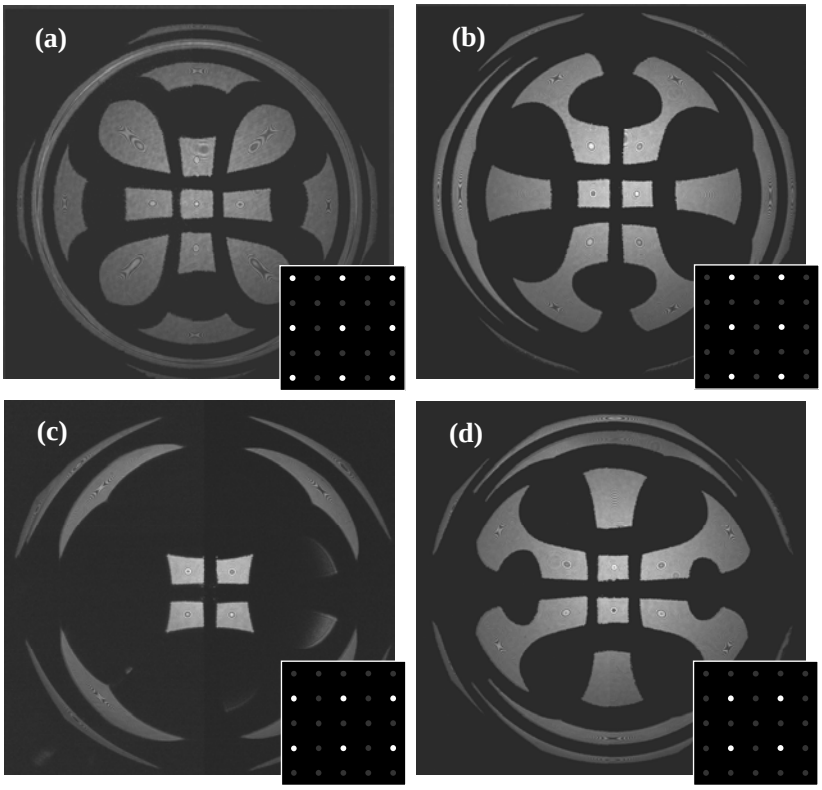

Fig. 2. Measurement sequence. Figures (a)-(d) show the activation sequence of the source array (bottom right of each picture) and the corresponding interferogram as seen on the camera

3.1 System calibration

We will define the test space as the space after the transmission sphere where the test object is physically located for the measurement (see Fig. 1). The aberrations between source and test space, as well as from test space to detector must be fully characterized.

As a natural extension of a single source interferometer, each test beam (source) is characterized with the help of a reference sphere at different locations in the test space. Each position is taken to minimize the number of fringes on the detector for its corresponding source.

The measured aberrations (for each sphere position) combined with the reference sphere position and the nominal design of the interferometer are fed to an optimization process to finally obtain a polynomial-based description of the wavefronts propagating to- and from the test space of the

interferometer. This allows a mathematical model of the interferometer that contains the necessary information to estimate retrace errors given a test surface located somewhere in the test space of the interferometer [11], and therefore making possible the calibration of the system.

3.2 Measurement

Once we have determined the calibration function of the system we are in position to identify in the measurement, the aberrations due to the test surface from those that belong to the interferometer itself.
To determine the figure error of the asphere we take a parametrization of the surface using a suitable basis of functions e.g. Zernike polynomials. Then, with every coefficient a perturbation analysis of the surface is performed [11] where the design data of the asphere is used as the nominal state of the surface. Analyzing the optical path changes at the detector due to coefficient perturbations, we can build a perturbation matrix that establishes the phase changes on the detector due to a set of coefficient perturbations of the test surface. Using the measured phase we then solve for the perturbations to finally obtain the figure error.
The process relies upon the concept that changes in the parameters that describe the asphere result in characteristic optical path variations at the output of the interferometer. In this way we can unambiguously relate phase changes at the detector with the figure error of the asphere.

As shown in Fig. 3, the complete description of the surface is composed of the measured figure error plus the mid-frequency components of the surface. High frequency errors determine the amount of scattered light by the surface (transmission losses in the optical system) and therefore it is not possible to measure them with the described system.
Obtaining the correct representation of the mid-frequency surface errors on the test surface requires the back-propagation of the residual error from the camera plane to the test surface. This is possible since the system calibration establishes a complete description of the path between test space and camera and therefore the aberrations along this path are known.

4 Results

A rotationally symmetric convex test surface with 650 μm deviation (PV) from its best-fit sphere and 8° maximal slope deviation in 50 mm (diameter) clear aperture was measured with the system described in Section 2.

The sources are generated by 30μm pinholes with a numerical aperture of 0.24 and a separation of 2.5 mm between them. The transmission sphere consists of a JENFizar 4'' f # 0.75 (NA = 0.67).
The maximal slope deviation of the test surface from its best-fit sphere that we can measure with this system is in principle, determined by the largest tilt generated by the source array.

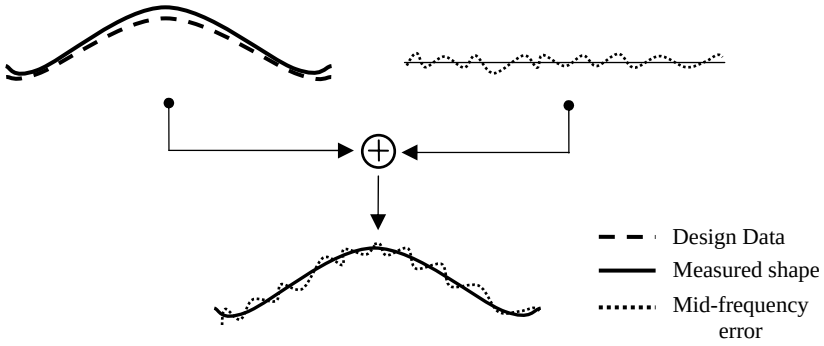

Fig. 3. Figure and mid-frequency surface errors. The residual (mid-frequency) error is projected onto the test surface to obtain the complete measurement the asphere

But, due to the limited aperture of the transmission sphere the vignetting will increase as we tilt the test beam so a reduction of the effective test volume results given a fixed slope deviation. This effect can be appreciated in Fig. 4 where the slope deviation for each tilted test beam from the best-fit sphere was calculated taking into account the limitation imposed by the JENFizar transmission sphere. The reduction of the maximum test diameter D_{MAX} is clearly visible as we move along the axis considering a constant slope deviation.

4.1 Positioning of the test surface

Since all the positioning errors traduce themselves in false surface figure errors a systematic and accurate positioning of the test object is desired. With the calibrated system, and the nominal shape of the aspheric surface an iterative process is implemented to automatically position the surface for the measurement. The positioning is performed with the help of an air-bearing stage reaching a final positioning accuracy of approximately 1 μm in space.

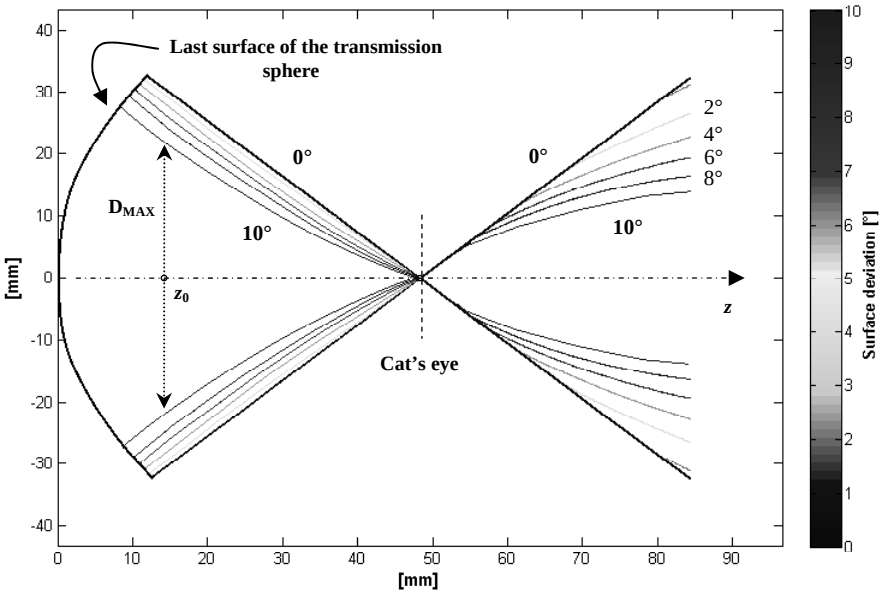

Fig. 4. Interferometer dynamic. Each one of the curves indicates lines of constant slope deviation of the test surface from the best-fit sphere (iso-angle curves). The reduction of the maximum test diameter (D_{max}) for a constant slope deviation is mainly given by vignetting at the transmission sphere

4.2 Figure and mid-frequency surface errors

After calculating the figure error as explained in section 3.2 we obtain mainly spherical and higher order aberrations with approximately 3 µm deviation (PV) from the design shape of the asphere. With the figure error we can then calculate the residual error due the mid-frequency spatial components of the surface and back-propagate them to the test surface.
Figure 5 shows a section of the surface of the asphere with polishing marks due to a magnetorheological finishing process. The detail of the MRF polishing spot is shown in Fig. 5 (b). The depth of the footprint amounts to approximately 180 nm (PV).

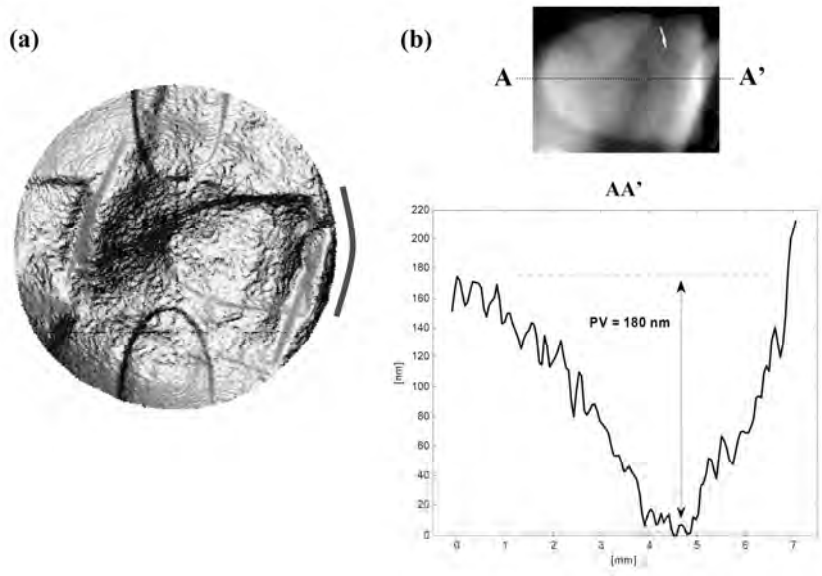

Fig. 5. Measurement result after back-propagation of the residual surface error. (a) Residual surface error showing marks of the MRF polishing spot. (b) Detail on the MRF footprint highlighted in (a)

5 Conclusions

A flexible interferometer for the rapid measurement of steep aspherical surfaces was presented. Full-field measurements of aspherical surfaces in short time are possible due to the use of an extended array of sources. Inherent problems in aspheric metrology like vignetting and subsampling artifacts are avoided by a local compensation of the surface gradients.
Since no repositioning of the test object is necessary to reduce the fringe density the measurement takes place in a short time interval (40-50 sec) making the system suitable for industrial integration.

6 Acknowledgments

Financial support from the Bundesministerium für Bildung, Forschung und Technologie (BMBF) FKZ 13N8742, as well as from our industrial partner Jenoptik L.O.S. is gratefully acknowledged.

7 References

1. Schulz, G. (1988) Aspheric Surfaces. Progress in Optics, Vol. XXV, Ed. Wolf, E., North-Holland, Amsterdam
2. Braunecker, B., Hentschel, R., Tiziani, H. J. (2008) Advanced Optics Using Aspherical Elements. SPIE Press Monograph PM173
3. Malacara, D. (1992) Optical Shop Testing: Null tests using compensators. 2nd Ed. (Wiley Interscience)
4. Evans, C. J. and Bryan, J.B. (1993) Compensation for errors introduced by nonzero fringe densities in phase-measuring interferometers. CIRP Annals Manufacturing Technology 42(1):577-580
5. Lowman, A. E. and Greivenkamp, J. E. (1996) Interferometer errors due to the presence of fringes. Appl. Opt. 35:6826-6828
6. Tricard, M. (2008) Subapertur-Stitching-Interferometrie: Messtechnik für die Asphären-Präzisionsfertigung. Photonik 6:38-41
7. Kuechel, M. F. (2007) Interferometric measurement of rotationally symmetric aspheric surfaces. Optatec TDO4-25
8. Liesener, J., Garbusi, E., Pruss, C., and Osten, W. (2006) Verfahren und Messvorrichtung zur Vermessung einer optisch glatten Oberfläche. Deutsches Patent und Markenamt: 10 2006 057 606.3
9. Liesener, J. (2006) Zum Einsatz räumlicher Lichtmodulatoren in der interferometrischen Wellenfrontmesstechnik," Dissertation, Universität Stuttgart
10. Garbusi, E., Pruss, C., Osten, W. (2008) Interferometer for precise and flexible asphere testing. Opt. Lett. 33:2973-2975
11. Garbusi, E. and Osten, W. (2009) Perturbation methods in optics: application to the interferometric measurement of surfaces. Submitted for publication to JOSA A

Measurement of the shape of objects by the interferometry with two wavelengths

Pavel Pavlicek
Joint Laboratory of Optics of Palacky University and Institute of Physics of the Academy of Sciences of the Czech Republic
Tr. 17. listopadu 50a, 772 07 Olomouc
Czech Republic
Gerd Häusler
Institute of Optics, Information and Photonics, Max Planck Research Group, University of Erlangen-Nuremberg
Staudtstrasse 7, D-91 058 Erlangen
Germany

1 Introduction

White-light interferometry is an established method for the measurement of geometrical shape of object with smooth or rough surface [1]. One of the disadvantages of white-light interferometry is that the required broadband light sources suffer from a low luminance. This shows up when the shape of object with a weakly reflecting surface is measured or when the measured area is large. One way to overcome this disadvantage is to replace the broadband light source by two (or more) lasers with various wavelengths.

If the broadband light source is replaced by two lasers with various wavelengths, a typical beat pattern arises at the output of the interferometer instead of white-light interferogram. The beat pattern can be used for the determination of the position of the object's surface in a similar way as white-light interferogram. Unlike to white-light interferogram, the beat pattern is periodic and therefore the unambiguity range is limited.

2 Theory

If a Michelson interferometer is illuminated by a laser with wavelength λ_1, the output intensity as the function of the object's position z is given by

$$I_1(z) = I_0\left[1 + V\cos\left(2k_1 z\right)\right], \tag{1}$$

where I_0 is the mean intensity, V is the visibility a $k_1 = 2\pi/\lambda_1$ is wave number. A similar expression results for a laser with wavelength λ_2. If the interferometer is illuminated by two lasers with equal intensities and wavelengths λ_1 and λ_2, the output intensity as the function of z is given by

$$I(z) = 2I_0\left\{1 + V\cos\left[\left(k_1 - k_2\right)z\right]\cos\left[\left(k_1 + k_2\right)z\right]\right\}, \tag{2}$$

which is the known expression describing the beat pattern. The envelope of the beat pattern is equal to

$$E(z) = V\cos\left[\left(k_1 - k_2\right)z\right] = V\cos\left(\frac{2\pi}{\Lambda}z\right), \tag{3}$$

where

$$\Lambda = \frac{2\pi}{\left|k_1 - k_2\right|} = \frac{\lambda_1\lambda_2}{\left|\lambda_1 - \lambda_2\right|} \tag{4}$$

is synthetic wavelength. It follows from Eq. 3 that the unambiguity range of two-wavelengths interferometry is given by $\pm\Lambda/4$ [2].

The expression for the output intensity as the function of z given by Eq. 1 is valid only for objects with smooth surface. If the surface of the measured object is rough, the reflected light wave results from superpositions of large numbers of scattered waves with random phases and random amplitudes [3]. Consequently an additional phase shift φ_1 arises in the argument of cosinus in the expression in Eq. 1

$$I_1(z) = I_0\left[1 + V\cos\left(2k_1 z + \varphi_1\right)\right]. \tag{5}$$

If we take into account phase shift φ_2 for the light with wavelength λ_2, the envelope of the beat pattern takes the form

$$E(z) = V\cos\left[\frac{2\pi}{\Lambda}z + \frac{1}{2}\left(\varphi_1 - \varphi_2\right)\right]. \tag{6}$$

It follows from Eq. 6 that the phase shift gives rise to error Δz, which is equal to

$$\Delta z = \frac{1}{4\pi}\Lambda\left(\varphi_1 - \varphi_2\right). \tag{7}$$

The corresponding measurement uncertainty is expressed as the standard deviation of error Δz

$$\delta z = \frac{1}{4\pi}\Lambda\sigma_{\varphi}, \tag{8}$$

where σ_φ denotes the standard deviation of phase shift difference (φ_1 - φ_2).

Numerical simulations show that the standard deviation σ_φ depends on the local intensity I_{obj} of the speckle pattern (the subscript obj means the intensity at the output of the interferometer with shut reference arm), synthetic wavelength Λ, and rms surface roughness σ_h. If the amplitudes of light with λ_1 and λ_2 are large (large intensity I_{obj}) and the two wavelengths are close (large synthetic wavelength Λ), the standard devitation σ_φ of phase shift will be small [3]. Finally the numerical solution provide following expression for measurement uncertainty

$$\delta z = \frac{1}{\sqrt{2}}\sqrt{\frac{\langle I_{obj}\rangle}{I_{obj}}}\sigma_h, \tag{9}$$

where $\langle I_{obj}\rangle$ denotes the mean value of I_{obj}.The expression in Eq. 9 has the same form as that derived by Dresel for white-light interferometry in quasi-monochromatic approximation [4, 5]. Thus the measurement uncertainty is directly proportional to rms roughness and inversely proportional to the squared root of the local intensity in speckle pattern.

3 Measurement

The schematic of experimental setup is shown in Fig. 1. Michelson interferometer is illuminated by two laser diodes with wavelengths $\lambda 1$ and $\lambda 2$. The temperature and operating current of the laser diodes are controlled to minimize intensity fluctuations and maintain wavelength stability.

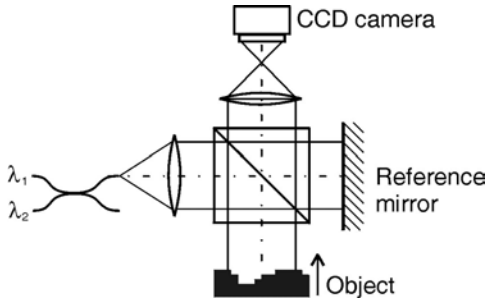

Fig. 1. Schematic of the interferometer with two wavelengths

The light from the lasers is transmitted by optical fiber, which ensures that the light beams of both wavelengths are parallel. The measured object is shifted in the longitudinal direction as indicated by the arrow. During the shifting, the intensity at the output of the interferometer is captured by a CCD camera. From the recorded interferograms for each pixel of the camera, the shape of the measured object is determined.

First, a flat stainless steel plate with rough surface is used as the measured object. Rms roughness of the plate is $\sigma h = 0.45$ μm. The measurement is performed with wavelengths $\lambda 1 = 830$ nm and $\lambda 2 = 839$ nm and the results are depicted in Fig. 2.

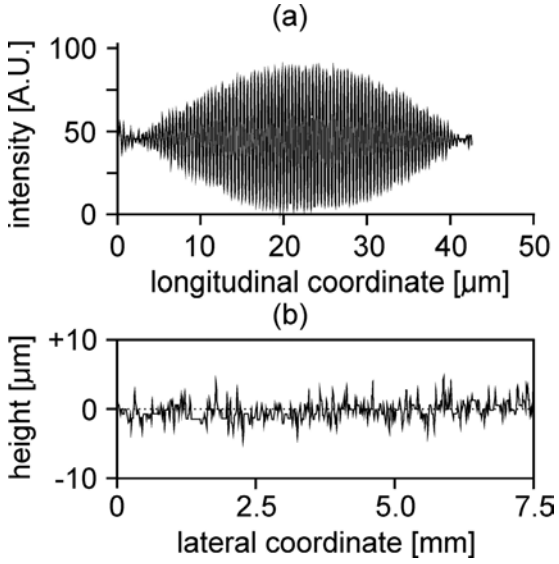

Fig. 2. (a) Measured interferogram, (b) measured height profile

Figure 2(a) shows the recorded interferogram, which has the typical form of the beat pattern. According to Eq. 4, the synthetic wavelength for given λ_1 and λ_2 is Λ = 78 μm. In Fig. 2(b), the measured height profile is plotted.

A disadvantage of the described method is that the measurement range is limited to $\pm\Lambda/4$. Therefore the synthetic wavelength must be chosen long enough. On the other hand a wide interferogram is difficult to evaluate. This disadvantage can be overcome by overlay measurement. Figure 3(a) shows the measured grey-scale coded height profile of the earthball on the 1 euro cent coin. The height profile was measured with wavelengths λ_1 = 830 nm and λ_2 = 836 nm (Λ = 116 μm). After this measurement, the height profile was measured with wavelengths λ_1 = 830 nm and λ_2 = 785 nm (Λ = 14.4 μm). The task of the second measurement is to improve the results obtained from the first measurement. The cross section of the height profile along the vertical line is depicted in Fig. 3(b).

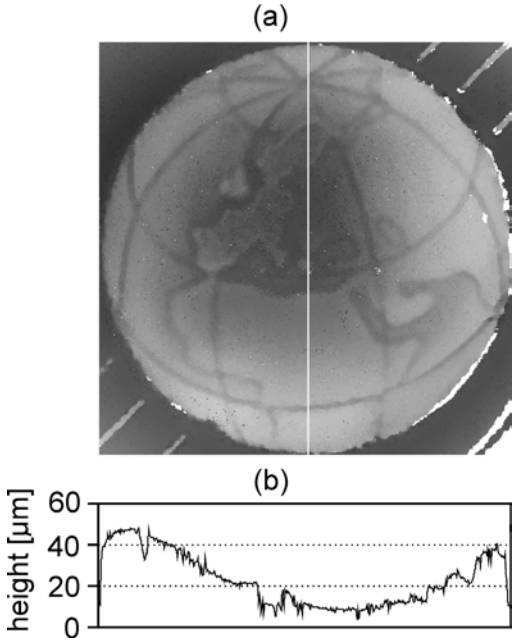

Fig. 3. (a) Grey-scale coded height profile of the part of 1 euro cent coin, (b) cross section of the height profile along the vertical line (from up to down)

4 Conclusions

The numerical calculations have shown that measurement uncertainty of two-wavelength interferometry depends on the surface roughness and the local intensity in the speckle pattern. The measurement uncertainty obeys the same equation as the measurement uncertainty of white-light interferometry.

Interferometry with two wavelengths can be used for the measurement shape of objects. However the measurement range is limited by the used synthetic wavelength. The results of the measurement can be improved by overlay measurement when three or more wavelengths are used.

5 Acknowledgements

This research was supported financially by the projects MSM 6198959213 and 1M06002 of Ministry of Education, Youth and Sports of the Czech Republic.

6 References

1. Dresel, T, Häusler, G, Venzke, H (1992) Three-dimensional sensing of rough surfaces by coherence radar. Appl. Opt. 31: 919–925
2. de Groot, P, Kishner, S (1991) Synthetic wavelength stabilization for two-color laser-diode interferometry. Appl. Opt. 30: 4026-4033
3. Fercher, A, Hu, H, Vry, U (1985) Rough surface interferometry with a two-wavelength heterodyne speckle interferometer. Appl. Opt. 24: 2181-2188
4. Dresel, T (1991) Grundlagen und Grenzen der 3D-Datengewinnung mit dem Kohärenzradar. Master's thesis, University Erlangen-Nuremberg
5. Pavlicek, P, Hybl, O (2008) White-light interferometry on rough surfaces - measurement uncertainty caused by surface roughness. Appl. Opt. 47: 2941-2949

Recording-plane division multiplexing (RDM) in pulsed digital holography for optical metrology

Xiaolei Wang, Caojin Yuan and Hongchen Zhai
Institute of Modern Optics, Nankai University
Key Lab of Optoelectronics Information Science and Technology
Ministry of Education of China
Weijin Road No. 94, Tianjin 300071, China

1 Introduction

Multiplexing techniques, such as angular division multiplexing[1-3], wavelength division multiplexing[4], and etc[5], have been widely applied to different optical information processes. In this report, we introduce RDM(recording-plane division multiplexing) approach developed in pulsed digital holography to record multiple sub-holograms on a single recording plane, which can be employed in optical metrology for measurements of high temporal or spatial resolution. The principle of the RDM will be analyzed in section2, and some of the experiment results of that will be detailed in section 3 and 4, respectively.

2 Principle of RDM recording

Fig.1 shows the principle of RDM recording in pulsed holography on a single frame of CCD, where reference beams composed of a series of sub-pulses with different incident spatial angles and object beams composed of a series of sub-pulses with the same incident spatial angle are employed to record a series of sub-holograms overlapped on a single frame of CCD, as shown in Fig. 2.In the reconstruction, the holograms will be Fourier-transformed into its Fourier plane as shown in Fig.3, which can be filtered and reconstructed digitally respectively, by inverse Fourier transformation and be displayed as a series of independent images.

This approach can be applied to measure the phase distribution in ultra-fast processes with a temporal resolution as high as femto-seconds in temporal domain, depending on the pulse duration and the repeat frequency of the sub-pulses, or to implement aperture-synthesis for high transverse resolution in spatial domain.

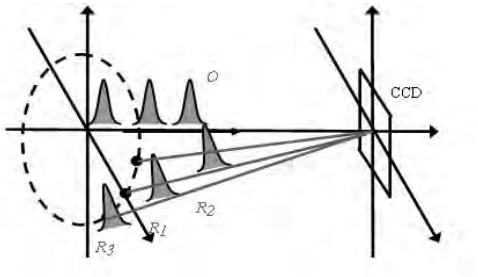

Fig. 1. RDM recording in digital holography

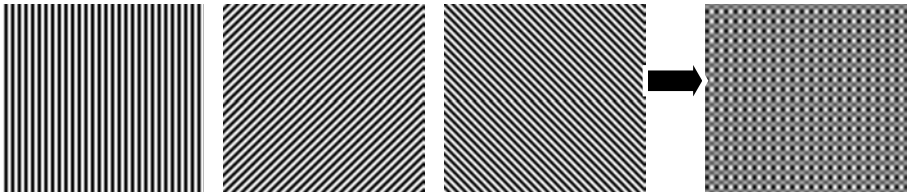

Fig. 2. Sub-holograms recorded by RDM and their overlapped result

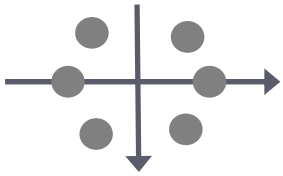

Fig. 3. Fourier Transformation of the RDM recording

3 RDM recording for phase measurement in ultra-fast processes

The pulsed holographic experimental system of RDM is shown in Fig. 4, where the laser pulse output from a Ti: sapphire laser amplifier system combined with a half-wave plate is divided by a polarizing beam splitter into two parts, the test beam and the recording beam. The former can be focused by lens L to induce an ultra-fast event, and the latter will be further divided by the beam splitter BS_1 into two parts, for SPG_1 to generate the sub-pulse-train of object beam and for SPG_2 to generate that of reference beam, respectively. Beam splitter BS_2 is used to couple the object beam and the reference beam optically into the recording plane of the CCD. Each of the SPGs are composed of a set of mirrors and beam

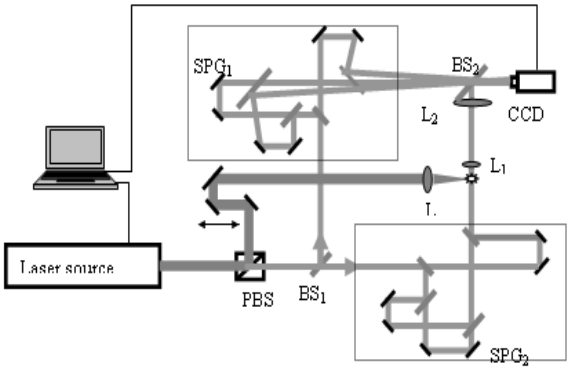

Fig. 4. Pulsed holographic recording system with RDM recording for phase measurement in ultra-fast processes

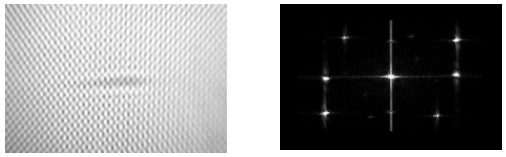

Fig. 5. Overlapped sub-holograms and their Fourier frequency spectra

Fig. 6. Contour maps of phase difference digitally reconstructed from the sub-hologram

splitters, which can be adjusted with different spatial incident angle for reference beams and the same for object, as shown in Fig.4. This can ensure a successful RDM recording object at the same viewing angle. Furthermore, by tuning the mechanical stage over a range of μm to mm, the time delay between the sub-pulses can be adjusted from femto-second to pico-second order, unless there is no overlap between them within their coherence time. The 4f system composed of L_1 and L_2 is used to record amplified image holograms at the recording plane of a single frame of the CCD.

The overlapped sub-holograms and their Fourier frequency spectra are shown in Fig. 5. It is noticed that, by employing the RDM recording, three Fourier frequency spectra of the sub-holograms along different orientations are well spatially separated in the Fourier plane.Their digitally reconstructed intensity images and their corresponding contour maps of

phase difference are shown in Fig. 6, of which the exposure time is 50 fs and the frame intervals are 300 fs demonstrating clearly the gradient increase of electron density within the plasma of the femto-second order.

4 RDM recording for aperture-synthesis

Fig. 7 shows a pulsed digital holographic system with RDM recording for aperture-synthesis. It is noticed that in the path of the object beams of the recording system, a laser pulse is amplitude divided into three sub-pulses with a given time delay and different incident angles to offer off-axis object illumination in a time sequence, marked as O_1, O_2, O_3, respectively, which ensures that more angular spectrum of object can be incident to the recording plane of CCD. Three sub-pulsed reference beams with the same time delay marked as R_1, R_2, R_3, of different spatial angles, will interfere with the object diffraction fields at the recording plane of the CCD successively, which ensures their Fourier spectra will separate from each other on the spectrum plane and can be reconstructed independently through a filtering process to obtain different portions of the object spatial frequency.

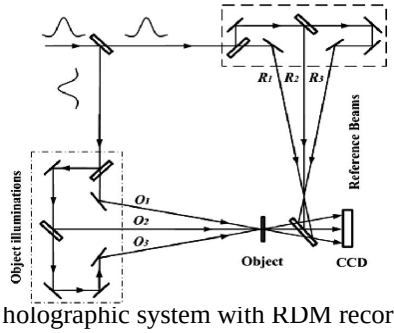

Fig.7. Pulsed digital holographic system with RDM recording for aperture-synthesis

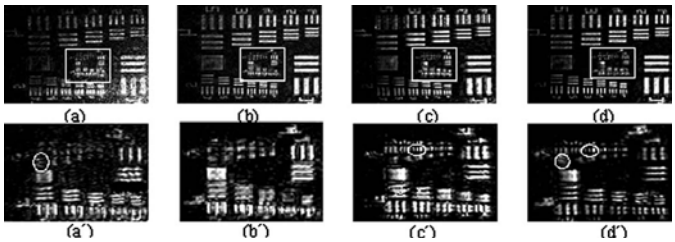

Fig. 8. a) to c): Intensity distribution of the reconstructed images of different object illuminations; d): Their aperture-synthesized image, a') to d'): Central part enclosed in the rectangle of fig.a) to d), respectively

The same time delay between the three pairs of recording beams is adjusted longer than the pulsed width of the laser source to ensure an incoherent overlapping of the three sub-holograms, during the three successive recordings. This takes the advantage of the ultra-short pulsed laser to make the three pairs of recording beams incoherent in the time domain and ensures consequently the successively recorded three sub-holograms can be incoherently overlapped within a single frame of CCD.
In the experiment, the object to be recorded is a USAF-1951 test target. The reconstructed images of the object and their magnified parts with different illumination conditions are shown in Fig. 8, where Figs. a) to c) are the results obtained by a single object illumination of O_1, O_2, O_3 object illumination, respectively, while d) are obtained by synthesizing the three complex amplitudes above. Fig a') to d') is the central part enclosed in the rectangle of Fig a) to d), respectively. By comparing Fig. 2d' with the conventionally reconstructed image of on-axis illumination in Figs. 4b and 4b', it is found that, while keeping the resolution of the low-frequency portion of the reconstructed image unchanged, the maximum resolution of the high-frequency portion has been improved from 71.84 Lp/mm to 128.00 Lp/mm in the vertical direction and from 90.51 Lp/mm to 161.30 Lp/mm in the horizontal direction, respectively.

5 References

1. Zhiwen Liu, Martin Centurion, George Panotopoulos, John Hong, Demetri Psaltis, (2002) Holographic recording of fast events on a CCD camera. Optics Letters 27(1): 22-24
2. Xiaolei Wang, Hongchen Zhai, Guoguang Mu, (2006) Pulsed digital holography system recording ultrafast process of the femtosecond order. Optics Letters 31: 1636-1638
3. Caojin Yuan, Hongchen Zhai, Haitao Liu, (2008) Angular multiplexing in pulsed digital holography for aperture synthesis. Optics Letters 33(20): 2356-2358
4. Xiaolei Wang, Hongchen Zhai, (2007) Pulsed digital micro-holography of femto-second order by wavelength division multiplexing, Optics Communications 275 (1): 42-45
5. Martin Centurion, Ye Pu, Zhiwen Liu, Demetr Psaltis, (2004) Holographic recording of laser-induced plasma. Optics Letters 29(7): 772-774

Identification of deformation components in TV holography and digital holography

János Kornis, Richárd Séfel
Department of Physics
Budapest University of Technology and Economics
Budafoki 8. Budapest, Hungary, H-1111

1 Introduction

Digital holography and TV holography is the most promising tool for industrial applications. The usual output of these measurements is a fringe pattern (phase map) or a 3D plot of the deformation.
For a successful industrial measuring system automated evaluation is necessary. Also this intelligent measuring system can help us to understand what happened with the object due to the load. As the result of this ”understanding”, the fringe system or the deformation map as the usual result of the investigation can be transformed into a more simpler information set: ”what happened with the object”.
To develop this kind of measuring system the fringe compensation principle was used. Because both digital holography and TV-holography operate with images recorded with a digital camera, several computer based compensation methods can be applied. In our investigations automated compensation techniques were investigated to develop industrial measuring systems.
The analog reconstruction of a wave front and its application in comparative measurement is well known from comparative holography.[1.] Thanks to the rapid development of high quality spatial light modulators, different methods applying the analog reconstruction of digital holograms has been developed in digital holography too. The SLM is also capable to generate computer calculated wave fronts (not belonging to an existing object), and multiple such projections can be performed during the measurement time [2.].
In digital holography the compensation method can be easier, using digital compensation, performing the compensation process in the computer using the recorded complex amplitude of the scattered light from the investigated object. In this case the compensation is based on the phase manipulation of the reconstructed waves.

The digital compensation method was chosen for our investigation in TV holography too. Our previously developed fringe synthesizing method was applied in Tv holographic measurements. In this method a set of phase shifted fringe patterns of the investigated object is recorded. Using the recorded fringe systems new contour fringe pattern can be generated. It means that every point of the resultant image is chosen from the corresponding points of the set of the fringe patterns using a selection algorithm. This new contour fringe pattern acts as a result of a virtual measurement featuring with modified sensitivity or with the elimination of additional unwanted effects (e.g. without the effect of the misalignment of the investigated object in the setup for shape measurement or reduced fringe density for deformation measurement).
Based on the above mentioned methods automated compensation methods were developed for digital holography and TV holography. The evaluation program can set the sensitivity of the measurement, can separate different deformation components (e.g. rotation, local deformation) after the measurement was performed. Measuring the separated deformation components we can generate a new alternative output of the measurement: a list of the deformation components with its features.

2 Automatic compensation of deformation components in TV holography

To producing automatically compensated measurements by the fringe synthesizing method, the evaluation program must find the features of the original fringe system. One possible solution is the identification of different fringe components [3] (e.g. parallel fringes from rotation or circular fringes from local deformation). In this article identification of parallel and circular fringes were investigated only.

A typical fringe system which has circular fringe systems with fringes due to rigid body rotation can be seen in Fig. 1.a. In the investigations a denser variant of the previous fringe system was used (see Fig.1.b).

The evaluation program was able to find the center of the circular fringes and also gives information about the rotation. These tasks ere done by a Kohonen type neural network

In this case the rotation component was compensated by the fringe synthesizing method. The result can be seen in Fig. 2.a. As can be seen the compensation is not perfect. Using a second run a more efficient compensation can be done (see Fig.2.b.).

At the identification of the circular fringe system not only the center point position is determined, but the shape (size) of this component.

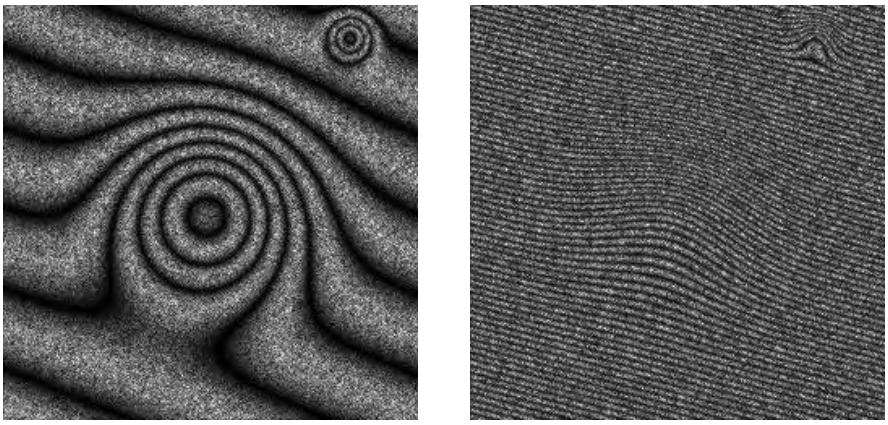

a, b.

Fig. 1. Fringe pattern due to rigid body rotation and two local deformations (a.). The same case but rotation value increased (b.). In this case the evaluation of the fringe system not possible and the large rotation covers up the local deformations.

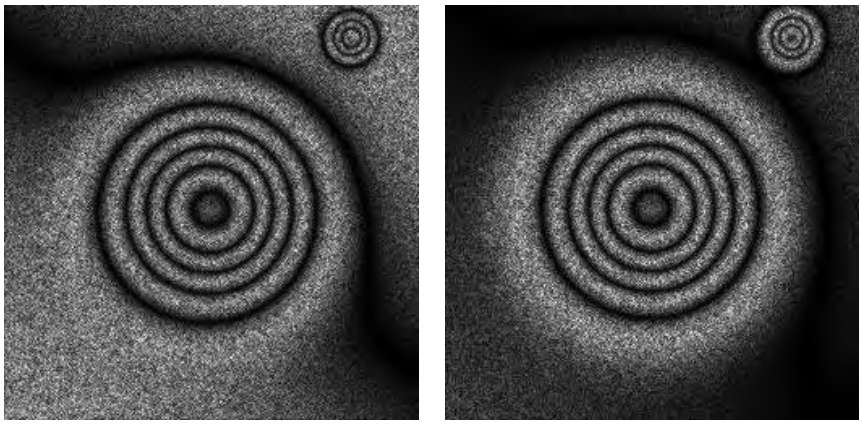

a. b.

Fig. 2. Fringe pattern after the automatic compensation of the rigid body rotation. Result after the first run (a.). Affter the second run the rotation is fully compensated (b.).

3 Compensation by combination of digital holography and desensitized TV holography

A desensitized dual-beam TV holography with phase shifting allows us to calculate a deformation map on a large scale with which the digital hologram can be compensated to make its otherwise indistinguishable interference fringes processable. This is a much more precise displacement map, compared to its range, than it would be possible using any of the two measurement techniques on its own. Interferometric digital holography provides complex values, their argument corresponding to the deformation and magnitude having speckle nature, without taking phase-shifted captures. Therefore deformation compensation can be carried out right away in the form of multiplication by a complex number of unit absolute value [4.].

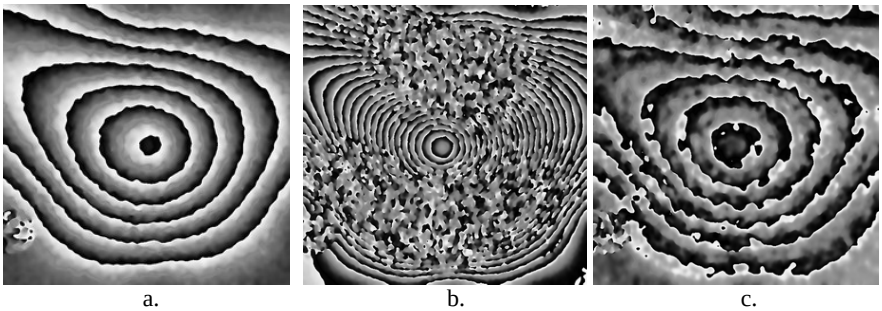

a. b. c.

Fig. 3. Desensitized TV holographic deformation phasemap (a.). Interferometric hologram phasemap without compensation (b.) and with compensation (c).

4 References

1. Rastogi P. K., (1995) Interferometric comparison of diffuse objects using comparative holography. Optical Engineering 34, 1923-1929
2. Osten W., Baumbach T., Jüptner W. (2002) Comparative digital holography. Optics Letters 27(20), 1764-1766
3. Kornis J., Németh A. (1999) Fringe compensation displacement measurement using synthesized reference beam TV holography. Optics Communications 167, 203-210.
4. Gombkötő B., Kornis J., Füzessy Z., (2002) Difference displacement measurement using digital holography. Optics Communications 214, 115-121

Extending the capabilities of the sphere interferometer of PTB by a stitching procedure

Guido Bartl, Arnold Nicolaus
Physikalisch-Technische Bundesanstalt (PTB)
Bundesallee 100, D-38116 Braunschweig
Germany

1 Introduction

The kilogram, SI base unit of mass, is still defined in relation to an artifact. Since this artifact is being suspected to change its mass, a new definition of the kilogram based on a natural constant has been taken into consideration. One option is a precise redetermination of Avogadro's constant [1]. In the scope of the International Avogadro Project – among other quantities – the volume of a single-crystalline silicon sphere has to be measured. The sphere has a mass of 1 kg and a surface of optical quality with a roundness error of only some ten nanometers.

The volume is determined at PTB by measuring the absolute diameter of the sphere with a specially developed Fizeau interferometer with spherical reference faces. The intended measurement uncertainty is below 1 nm. As in principle the sphere interferometer allows only the diameters to be measured, the result is a diameter topography. This means that the measured diameters are located point-symmetric to a mathematical centre of the sphere due to the lack of knowledge of its real position. To determine the real form of the sphere and, therefore, to obtain the radius topography, which is most likely not point-symmetric, it is desirable to evaluate the measured data in a way, that regards the topographic information of both sides of the sphere separately. Stitching approaches for concatenating segments of a topography are known in the field of optics fabrication and wavefront testing [2,3]. The stitching technique can also be used in the case of the topography of a sphere in order to yield its radius topography or rather its form error if the absolute diameter is unknown. Griesmann et al. [4] combined form and radius-of-curvature measurements to obtain the real form of the sphere under test.

Pursuing this idea the stitching algorithm specially developed for the sphere interferometer of PTB makes use of the absolute diameter results combined with the two-sided measurement principle.

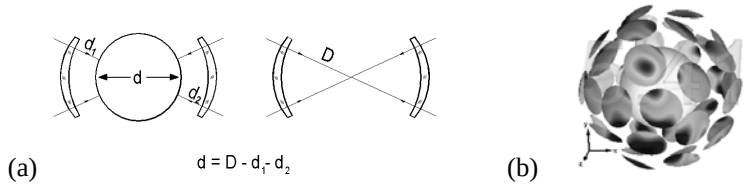

Fig. 1. Principle of the diameter measurements

2 Diameter measurements with the sphere interferometer

The interferometer for spheres of PTB [5] basically consists of two spherical reference faces (Fig. 1a) whose aperture ratio of 1 allows topography segments of 60° of the surface to be measured at once. Each segment consists of almost 10,000 single diameter values. With a set of about 40 segments – depending on the amount of overlap – the sphere can be covered completely with measuring points. Since D, d_1 and d_2 are only the fractional parts of an order of interference, an offset d_0 (known from mass and density measurements), that corresponds to the integral part of orders of interference, has to be added to get the actual diameter d.

During the measurement procedure for getting the whole topography the sphere is handled by a lifting and positioning mechanism. In the upper position, the sphere can be rotated around two axes. A sequence of measurements with the sphere in different orientations (Fig. 1b) yields an amount of values d_1 and d_2 distributed all over the sphere and covering the topography thoroughly.

3 The stitching algorithm

The basis of the algorithm is given by a system of equations that treats the topographic information $d_1(\vartheta, \varphi, n_{px}, B)$ and $d_2(\bar{\vartheta}, \bar{\varphi}, n_{px}, \bar{B})$ from both sides of the sphere separately. n_{px} is the pixel position in the image, B and $\bar{B}$ are the image numbers of one two-sided measurement and (ϑ, φ) are the coordinates of the position on the sphere with the opposite position $\bar{\vartheta} = \pi - \vartheta$ and $\bar{\varphi} = (\varphi + \pi) \bmod 2\pi$. The system of equations is:

$$
\begin{aligned}
-d_1(\vartheta,\varphi,n_{px},B) &= \sum_{l=0}^{N_l}\sum_{m=-l}^{l} k_{lm}Y_{lm}(\vartheta,\varphi) - \sum_{i=0}^{3} {}^{B}z_i Z_i(n_{px}) - \sum_{i=4}^{N_Z} {}^{1}o_i Z_i(n_{px}) \\
-d_2(\bar{\vartheta},\bar{\varphi},n_{px},\bar{B}) &= \sum_{l=0}^{N_l}\sum_{m=-l}^{l} k_{lm}Y_{lm}(\bar{\vartheta},\bar{\varphi}) - \sum_{i=0}^{3} {}^{\bar{B}}z_i Z_i(n_{px}) - \sum_{i=4}^{N_Z} {}^{2}o_i Z_i(n_{px}) \,.
\end{aligned}
\tag{1}
$$

$Y_{lm}(\vartheta,\varphi)$ are a number of real spherical harmonics limited to the order of N_l that parameterize the surface of the sphere with the coefficients k_{lm}. $Z_i(n_{px})$ are Zernike polynomials that parameterize the topographies of the reference faces each defined by the set of coefficients ${}^{1}o_i$ and ${}^{2}o_i$, respectively, and limited to the maximum order N_Z. And the coefficients ${}^{B}z_i$ and ${}^{\bar{B}}z_i$ specify the Zernike parameterization of the appearance of offset, tip, tilt and defocus in each single measurement. Setting up this overdetermined system of equations results in a matrix of the size $m \times n$ with m in the order of 10^5-10^6 and n in the order of 10^3-10^4. The main objective is the first term of Eq. 1 describing the properties of the sphere.

4 Results

Using the solution for the set of coefficients k_{lm} one can reconstruct a representation of the surface of the sphere that is not point symmetric contrary to the diameter topographies. Since the previous knowledge of the offset d_0 is not yet included, one can use the mean of the absolute diameter topography as additional information and replace the mean of the relative radius topography by half the mean of the diameter topography.

In Fig. 2 the diameter topography (left) and the radius topography (right) of the ^{28}Si sphere S8 are displayed in Mollweide projection for comparison. The grey scale corresponds to approximately 70 nm and 50 nm peak-to-valley for the left and right image, respectively. Note that

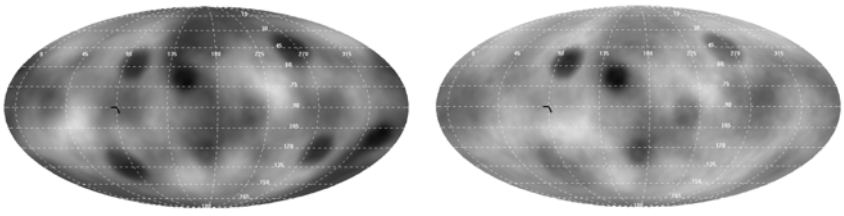

Fig. 2. Resulting diameter (left) and radius (right) topographies in Mollweide projection

each feature of the surface appears twice in the diameter topography. A hole on one side of the sphere seems to be accompanied by an identical hole on the opposite side. In contrast to that the distinctive features are located only on one side of the sphere in the radius topography. Shifting the sum of all opposite radii symmetrically to the center reveals the diameter topography.

5 Conclusions

As the conventional method of evaluating the measurement results of the sphere interferometer only yields diameter topographies, the real form of the sphere under test could only be examined by sphericity measurements. With the approach described here the field of application of the sphere interferometer can be extended to measurements of absolute radius topographies in the nm range. An improvement of the presented procedure to yield absolute radius topographies by including the diameter information in the system of equations is in progress.

6 Acknowledgements

We are grateful to Dr. Michael Krystek for providing the solver routine and mathematical expertise. Sincere thanks are extended to Axel Wiegmann for helpful discussions. Financial support of the Braunschweig International Graduate School of Metrology (IGSM) is gratefully acknowledged.

7 References

1. Becker, P, et al. (2007) Considerations on future redefinitions of the kilogram, the mole and of other units. Metrologia 44:1-14
2. Otsubo, M, Okada, K, Tsujiuchi, J (1994) Measurement of large plane surface shapes by connecting small-aperture interferograms. Optical Engineering 33:608-613
3. Murphy, P, et al. (2003) Stitching Interferometry: A Flexible Solution for Surface Metrology. Optics & Photonics News 14:38-43
4. Griesmann, U, Soons, J, Wang, Q (2004) Measuring Form and Radius of Spheres with Interferometry. Annals of the CIRP 53:451-554
5. Nicolaus, R A, Bönsch, G (2005) Absolute volume determination of a silicon sphere with the spherical interferometer of PTB. Metrologia 42:24-31

Fringe contrast improving in low coherence interferometry by white light emitting diodes spectrum shaping

Anna Pakula, Leszek Salbut
Institute of Micromechanics and Photonics,
Warsaw University of technology
8 Sw. A. Boboli, 02-525 Warsaw
Poland

1 Introduction

Low coherence interferometry (LCI) is a powerful tool for microstructures identification. Nowadays, when new light sources as Light emitting diodes (LEDs) and organic light emitting diodes (OLEDs) are on hand it is possible to enhance its potential.

LCI is based on the zero order fringe detection or the maximum of the coherence envelope of the fringes detection. The envelope detection is mostly time and numerical resources consuming because of complicated computation of a lot of data required. On the other side detection of zero order fringe is difficult because of the low differences in intensity of the detecting fringe and the adjacent ones ,however, it is very simple from computation point of view.

The issue of insufficient intensity modulation in fringe distribution is possible to overcome by applying two specially matched incoherent light sources [1] or even three, which is the subject of this paper.

2 LED as a subject of new LCI source

LEDs are very promising light sources because of their properties like small features, broad variety of light spectrum, efficiency and low power consuming. The materials used for their manufacturing allow to cover all visible spectrum and part of infrared region. Also the packaging in case of white LEDs is very useful, as in those which are assembled from three separated light sources (red, green and blue) under one plastic lens.

Moreover, the change in operating current of an LED leads to significant changes of its spectral characteristics while maintaining the quasi Gaussian spectrum. Changes of the most important features of emitting spectrum of white light LED consisting of three sources are listed in the table 1.

Table 1. Changes in emitting spectrum of an LED

Light source colour	I [mA]	U [V]	λ_{max} [nm]	$\Delta\lambda$ [nm]
Red	20.1	2.3	630	15.1
	30.3	2.6	634	13.4
Green	20.1	3.2	515	33.6
	34.9	3.6	514	34.2
Blue	20.0	3.2	476	20.3
	30.	3.6	569	17.2

I operating current, U power voltage, λ_{max} wavelength with the highest intensity, $\Delta\lambda$ half intensity width

Those changes may be very useful while shaping spectrum for LCI.

3 Application of two and more LEDs

It was proved that usage of two low coherent sources improves the intensity difference between the zero order fringe and those adjacent [1, 2].

For one light source, described as follows I_1 – light intensity, λ_1 – mean wavelength and L_{C1} – coherence length of the source, there is possible to find one matching light source ($\lambda_2 = \lambda_1 + \Delta\lambda$) fulfilling criterion described in [1]. The authors prove that not necessarily only one source within the visible spectra and more in ultraviolet and infrared region fulfils the criterion

3.1 Matching source criterion

Using at least two light sources involves changes in intensity of fringe distribution. In some cases the second groups of fringes appear like it is shown in Fig. 1. The criterion, which authors cite after [1], requires the intensity of zero order fringe adjacent fringes (I_{01}) to be equal to those of the maximum intensity fringe of the second group (I_{10}) (see Eq. 1).

$$I_{01} = I_{10} \tag{1}$$

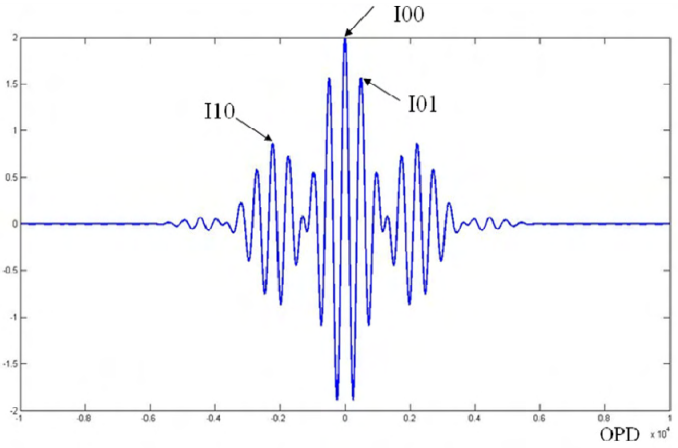

Fig. 1. Localization of maxima in fringe distribution for two light sources in respect to optical path difference (OPD): zero order fringe (I_{00}), adjacent fringe (I_{01}), second group maximum (I_{10})

3.2 Two matching sources

Using criterion described in previous section for a source described as: λ_1 = 500nm and L_{C1} = 5μm, simulations shows that there are four matching sources (L_{C2} = L_{C1}) in the range of 15μm. The matching light sources are as follow: UV region λ = 29nm, visible region λ = 384nm and λ = 684nm, IR region λ = 2070nm. In Fig. 2., the distribution of intensity differences $|I_{10} - I_{01}|$ is shown. The best matching sources are found in places where the function reaches zero.

The region of wavelengths near the λ = 500nm described in Fig.2. (called by the authors forbidden region)indicates the case where the second group of fringes does not exist, and the $I_{01} = I_{10}$ never occurs. This region is getting narrower while the half intensity width is decreasing (coherence length of the sources is increasing). Following this track we are leaded to the issue of equivalent wavelength used in laser interferometry: the biggest equivalent wavelength for two coherent sources occurs for the smallest wavelength difference [3, 4].

The changes in matching wavelengths and forbidden region width for light sources with main wavelengths from the visible range

for different half intensity widths: 50nm, 70nm, 90nm, 110nm and 130nm, are shorn in Fig.3.

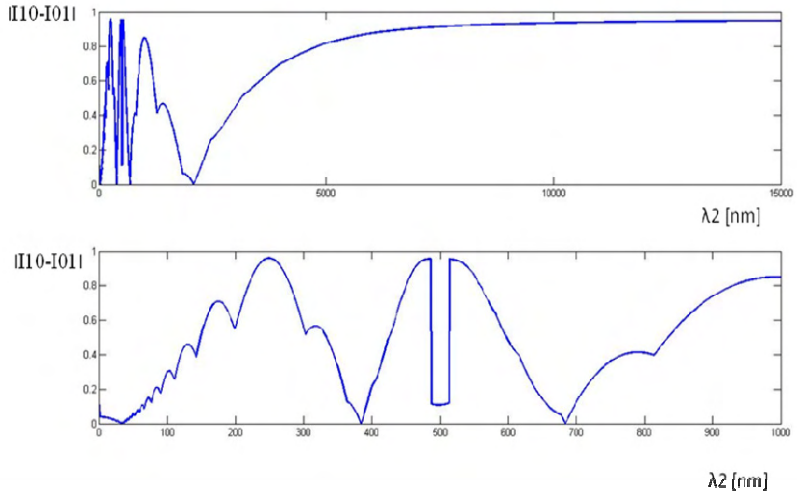

Fig. 2. Finding the matching source location for the λ = 500nm and L_C = 5μm

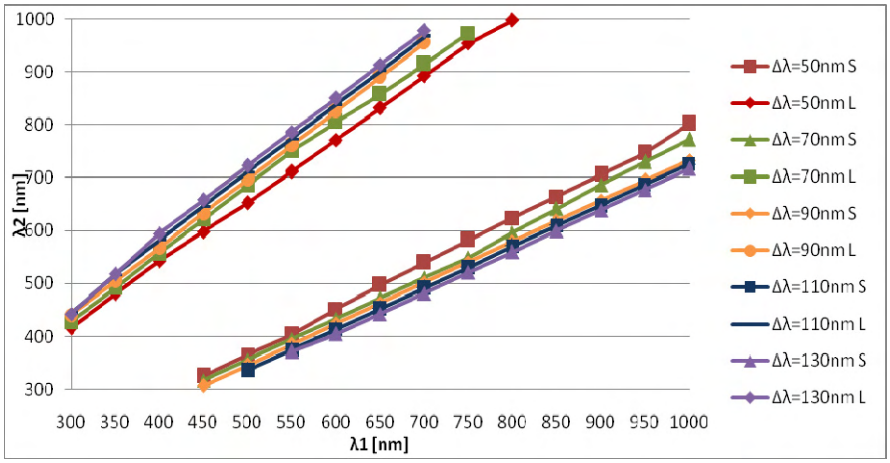

Fig. 3. Matching wavelengths in visible range for sources with different half intensity width. Matching sources with the main wavelength from S – shorter, L – longer wavelengths region.

3.3 Third matching source

Adding the third light source to the two that are already matching improves the intensity distribution in low coherence interferogram

significantly. For simulations taken for two matching light sources: λ_1 = 550nm and λ_2 = 393nm of the coherence length L_{C1} = L_{C2} =3µm, two matching sources ware found: λ_3 = 316nm and λ_3 = 546nm (L_{C3} = L_{C1}). The intensity differences between zero order fringe and those adjacent for sources described above are shown in the table 2. The visualization of the fringe distribution for described three sources is shown in the Fig.4.

Table 2. Intensity difference between zero order fringe and adjacent fringe for using third matching source to two existing: λ_1 = 393nm, λ_2 = 550nm, $L_{C1,2,3}$ = 3µ

λ_3 [nm]	I_{00} - I_{10}
316	0.71
546	0.52

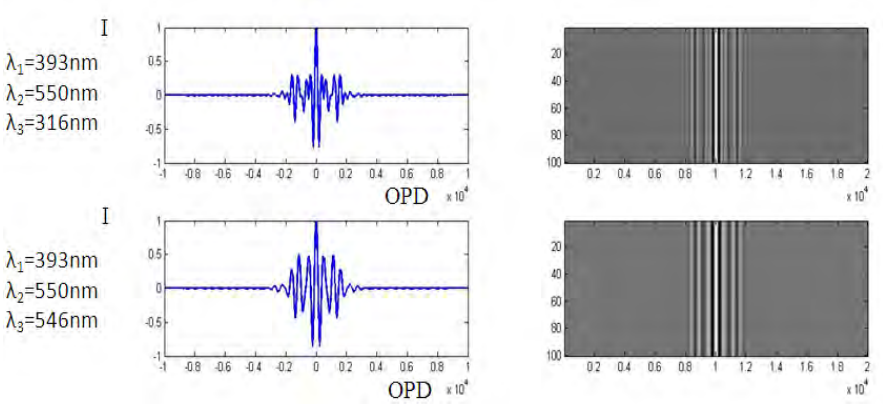

Fig. 4. Intensity distribution for three matching light sources

Surprisingly, the third matching light source lies in close range to one of the two first sources. If the main wavelength difference in the range of few nanometres it is possible to use two the same sources and change the operating current in order to get the characteristics that are looked for.

4 Conclusions

Carried simulations of using three low coherence light sources for fringe distribution shaping shows very promising results. The exaggeration of zero order fringe, which reaches even over 70%, is significant. This method, while used in low coherence interferometry, may improve this

technique. With such intensity difference the noise influence in the interferogram drops, and allows the use of fast computation, which may be carried on by the hardware such as CMOS detectors. Application of fast mathematical algorithms and decreasing of time needed for the measurement to the quasi real time would allow this technique to be used for in-situ measurements. Such kind of measurements is required in fabrication technology of microoptics and MEMS/MOEMS structures [5].

Moreover, extending the interest for new light sources on Organic Light Emitting Diodes (OLED) gives the possibility to minimize the influence of spatial coherence by imagining homogeneous planar light source on the object under test in the full field of view.

5 Acknowledgments

Authors acknowledge the financial support through grant of Ministry of Science and Higher Education n. R01 013 02 and grant of Dean of Mechatronics Department Warsaw University of Technology.

6 References

1. Pluciński, J, Hypszer, R, Wierzba, P, Strąkowski, M, Jędrzejewska-Szczerska, M, Maciejewski, M, Kosmowski, B (2008) Optical low-coherence interferometry for selected technical applications. Bulletin of the Polish Academy of Sciences vol. 56, 2: 155-172
2. Maciejewski, M, Pluciński, J, Strąkowski, M, Jędrzejewska-Szczerska, M (2006) Modeling of broadband light source to use with optical coherent tomography system. Proc. of SPIE 6159: 870–875
3. van Brug, H, Klaver, R. G (1998) On the effective wavelength in two-wavelength interferometry. Applied Optics 7: 1465–1471
4. Decker, J. E, Miles, J. R, Madej, A. A, Siemsen, R. F, Siemsen, K. J, de Bonth, S, Bustraan, K, Temple, S, Pekelsky, J. R (2003) Increasing the range of unambiguity in step – height measurement with multiple – wavelength interferometry – application to absolute long gauge block measurement, Applied Optics 28: 5670 – 5678
5. Pakula, A, Lukaszewski,D, Tomczewski, S, Salbut, L, Van Erps, J, Gomez, V, Thienpont, H (2008) Interferometric method for in-situ monitoring of fiber insertion in 2D fiber connectors fabricated through Deep Proton Writing, Proc. of SPIE, vol. 7064: 7064 -26

Absolute testing of aspherics in transmitted light using an amplitude DOE

Andreas Berger[1], Klaus Mantel[2], Irina Harder[2], Norbert Lindlein[1]
[1]Institute of Optics, Information and Photonics, University of Erlangen
Staudtstrasse 7/B2, 91058 Erlangen
[2]Max Planck Institute for the Science of Light
Günther-Scharowsky-Str.1/Bau24, 91058 Erlangen
Germany

1 Introduction

Aspheric testing is commonly carried out by using null elements [1]. The necessary degree of freedom for designing the null element is achieved by using diffractive optical elements (DOE). Due to light passing the DOE twice, common null tests using reflected light setups suffer from a whole set of disturbing waves. Furthermore, this well introduced technique requires more and more calibration methods to reach high accuracies [2], [3]. Here, a calibration procedure for aspheric lenses [4] is presented using transmitted light to provide single pass geometry and therefore the advantage of reduced spurious diffraction orders, reduced spatial frequency demand for the DOE, and reduced impact of parasitic reflections. Moreover the whole optical power of the aspheric element is measured.

2 Systematic aberrations

The measured phase of a DOE null test comprises the aspheric lens aberration Φ_{asph} and additional systematic aberrations (Fig. 1). The wave front error Φ_{dejust} is caused by the misalignment of the aspheric lens against the DOE null. The aberration of the interferometer Φ_{setup} is caused by the other optical elements of the setup. The aberrations Φ_{subst} depend on optical thickness variations or surface deformations of the DOE substrate. The structural aberration Φ_{struct} of the DOE is caused by the limited accuracy of the lithographic devices used for producing this null element.

3 Interferometric test setup

The basic setup is a Mach-Zehnder interferometer (Fig. 2). The intended calibration method requires a high degree of freedom for the movement of the test arm components. To enable these necessary movements a fibre base solution is realized. Using polarizing maintaining mono mode fibres together with a polarising beam splitter group allows external tuning of the mean intensity and the splitting ratio for the two beams of the interferometer. Optical isolation from feedback into the laser is done with a Faraday isolator. The test arm provides sufficient space for a range of aspherics having different focal lengths and high apertures. Phase shifting of the reference wave is realized by moving the second beam splitter in the direction marked in Fig. 2.

4 Calibration procedure

Absolute interferometric lens testing requires freedom from aberrations of the setup. Therefore, it is necessary to eliminate intrinsic deviations of the interferometer and also of the null element. To achieve this, a multi-step procedure is proposed (Fig. 3). The systematic aberrations Φ_{posA} are measured in pos. A (Eq. 1).

$$\phi_{posA} = \phi_{subst} + \phi_{setup} + \phi_{dejust} + \phi_{struct} + \phi_{asph} \tag{1}$$

$$\phi_{posB} = \phi_{subst} + \phi_{setup} \tag{2}$$

Φ_{dejust} can be determined by fitting a suitable functional. If an amplitude DOE is used the aberrations Φ_{subst} and Φ_{setup} can be measured using the zeroth order of the DOE null element shown in pos. B. The difference (Eq. 1, Eq. 2) now contains the structural aberrations of the DOE and the aberration of the testing specimen. To determine the structural aberration of the DOE, the basic idea of absolute testing of spherical surfaces is used. Since aspheric lenses in general have no sharp focus, a spherical wave front matching the aspheric wave front in a least squares best fit sense is additionally encoded in the DOE null element. This so called COMBO-DOE (CDOE) consists of alternating stripes of structures generating aspherical and spherical wave fronts. These structures can be described by local periods p_a and p_s (Fig. 4). This spherical wave front is measured against an adapted blazed DOE (BDOE). The diverging (pos. C) and

converging (pos. D) spherical wave front of the CDOE can be used to separate the aberrations of the BDOE (Φ_{sph}) and the substrate aberrations (Φ_{subst},) from the structural aberration (Φ_{struct}^{sph}) of the CDOE (Eq. 3, Eq. 4, Φ_{setup}, Φ_{dejust} are already subtracted).

$$\phi_{posC} = \phi_{subst} + \phi_{sph} - \phi_{struct}^{sph} \tag{3}$$

$$\phi_{posD} = \phi_{subst} + \phi_{sph} + \phi_{struct}^{sph} \tag{4}$$

$$\phi_{asph} = \phi_{posA} - \phi_{posB} + \frac{1}{2}(\phi_{posC} - \phi_{posD})\frac{p_s}{p_a} \tag{5}$$

Taking the matching condition for CDOEs into account, it is possible to calculate in a good approximation the correction function for the aspheric wave front (Eq. 5).

5 First results

The positions C and D in fig. 3 for eliminating the structural aberrations have not been realized yet. We can show first preliminary results of the elimination of $\Phi_{dejust}+\Phi_{subst}+\Phi_{setup}$ and a first attempt to make the structural aberration visible (Fig. 5). Using rotation averaging methods through rotating the aspheric lens and keeping the CDOE constant the approximated aberration of the aspheric lens can be separated from the remaining aberrations.

6 Conclusion

We have presented a calibration procedure for an absolute test of aspheric lenses in transmitted light using an amplitude DOE and have shown first results for the elimination of systematic aberrations.

7 Acknowledgement

This project is supported by the DFG (Deutsche Forschungsgemeinschaft).

8 References

1. Schwider, J (1999) Interferometric tests for aspherics. OSA TOPS Fabrication and Testing of Aspheres 24:103-114
2. Simon, F, Khan, G, Mantel, K, Lindlein, N, Schwider, J (2006) Quasi-absolute measurement of aspheres with a combined diffractive optical element as reference. Appl. Opt. 45:8606-8612
3. Beyerlein, M, Lindlein, N, Schwider, J (2002) Dual-wave-front computer-generated holograms for quasi-absolute testing of aspherics. Appl. Opt. 41:2440
4. Schwider, J, Lindlein, N, Mantel, K,. Harder, I (2007) On the calibration of diffractive nulls for transmission test of aspheric components. Opt. Comm. 279:262-272

9 Figures

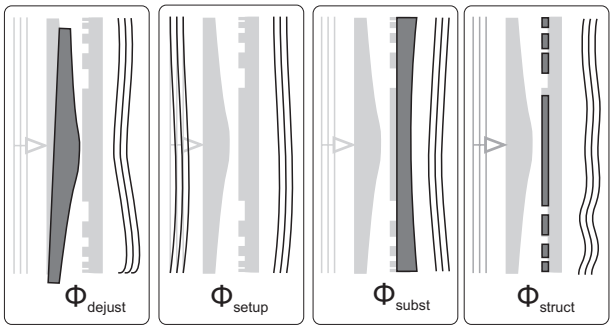

Fig.1. Systematic aberrations that must be eliminated

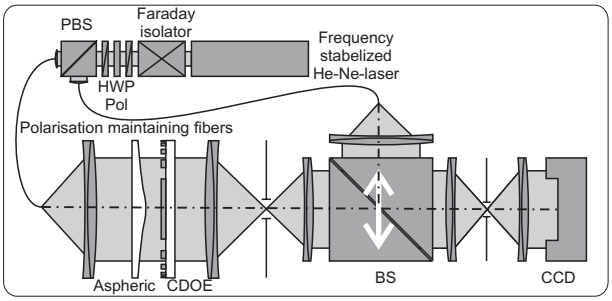

Fig. 2. Interferometric setup

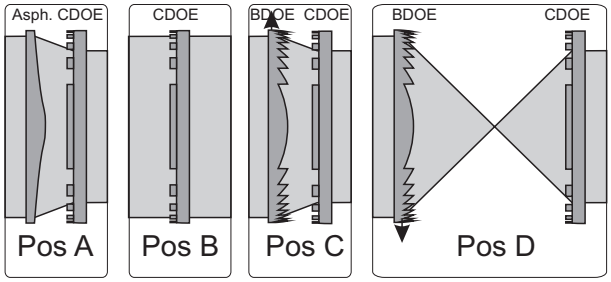

Fig. 3. Measurement Positions

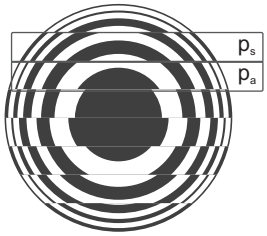

Fig. 4. CDOE with wave fronts and local periods

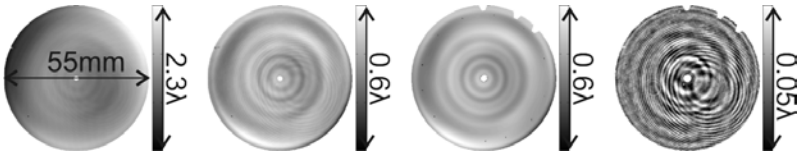

Fig. 5. (1) measured phase, (2) after substracting Φdejust+Φsubst+Φsetup, (3) approximate aberration of the aspherical lens, (4) remaining error

MEMS Calibration Standards for the Optical Measurement of Displacements

J. Gaspar[1], M. E. Schmidt[1], G. Pedrini[2], W. Osten[2], and O. Paul[1]
[1]Dept. Microsystems Eng. (IMTEK), Univ. Freiburg, Germany
[2]Institut für Technische Optik, Univ. Stuttgart, Germany

Abstract

The goal of this work is to develop miniaturized reference standards for the optical measurement of in-plane displacements serving for the calibration of optical systems used in the production and characterization of MEMS. The proposed devices consist of SOI-based in-plane micro-actuators. The displacements resulting from both mechanical and electro-static actuations are measured using optical techniques such as stroboscopic illumination, laser-deflection and digital speckle interferometry.

1 Introduction

The trend towards miniaturization of microelectromechanical systems (MEMS) and micro-opto-electromechanical systems (MOEMS) continues to lead to more and more compact devices. Advantages lie in the integration with control electronics, lower power dissipation, higher sensitivity and better performance. Applications cover a wide range of fields, from optical telecommunications to medicine [1]. Part of the functionality and reliability of MEMS devices is based on the displacement and deformation of micromechanical parts under mechanical, thermal, magnetic or electrostatic loads. The measurement of the deformation of such systems is thus of great importance for confirming analytical and finite element models, accessing material and device properties, detecting potential defects and determining performance. These data can then be used in further device optimization. Since typical structures exhibit dimensions in the order of some micrometers, it is necessary to measure their deformation with accuracies down to the lower nanometer range. Standardized approaches and calibrated setups are therefore essential for the measurement of shape, displacement and deformation fields in the static and dynamic cases.

Several non-contact measuring procedures, suitable for the measurement of shape, deformation and strain of small objects, have been previously reported [2]. Even though these techniques have been successfully tested in laboratory, their implementation in industrial micro-manufacturing environments has only taken place in few cases. A deficit is that calibration procedures are not available yet, or more precisely, have only been developed for macroscopic components in projects such as the standardization project for optical measurement of strain (SPOTS) [3], [4].

The work presented here aims at narrowing this gap by developing standards or norms for the use of different full-field optical techniques in the measurement of in-plane displacements of microsystems. The process involves (i) the development of micromechanical reference components designed to deform in a reproducible and precise way when submitted to known loads, (ii) their calibration by means of optical techniques, and (iii) uncertainties determination according to the guide of expression of uncertainty in measurement (GUM [5]) and certification of the optical calibration setups by official bodies, allowing for traceability of the observed quantities to the SI standards. After development and calibration, the reference devices may then be used for the general calibration of optical measurement systems used in the MEMS industry.

This paper presents the fabrication and characterization of such micromechanical reference structures. The processing technology is based on the micromachining of silicon-on-insulator (SOI) substrates. The design tries to cover a broad variety of specifications found in micromechanical devices by including (a) several predefined displacement ranges tuned through mechanical demultiplication mechanisms, (b) surfaces with different optical characteristics (in terms of reflectivity, roughness and geometry patterns) and (c) several actuation mechanisms on the same chip.

2 Micromechanical Reference

The developed reference test structure is schematically shown in Fig. 1. It consists of a movable large body connected to anchors through parallel springs and mechanically coupled by a bending element to a smaller displacement structure, which is also stabilized by parallel elements. The bending element is responsible for demultiplying the displacement between the two movable bodies. The structural elements are made of crystalline silicon (c-Si) from the active layer of SOI substrates with a

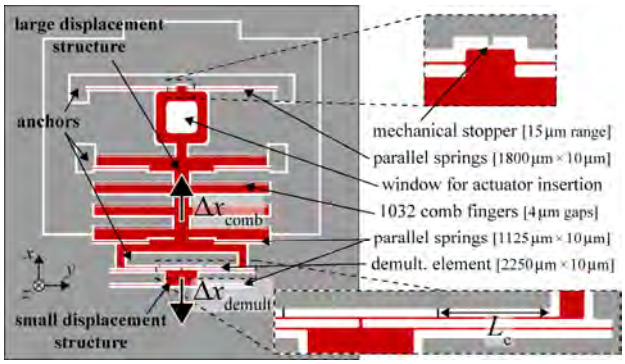

Fig. 1. Schematics of micromechanical reference object with in-plane movable structures connected to anchors by parallel springs. The dis-placement demultiplication $\Delta x_{demult}/\Delta x_{comb}$ is set by the clamping length L_c.

thickness t of 25 µm, whose fabrication process is explained in detailed elsewhere [6]. Scanning electron microscope (SEM) graphs of a fabricated microdevice are shown in Fig. 2

As a consequence of the arrangement and dimensions of the parallel springs, the test structure is relatively resilient in the x-direction and strongly constrained in the y- and z-directions, which allows for the in-plane displacement of the inner frame along the x-axis when a force is applied to it.

The test structure can be actuated by mechanical and/or electrostatic means. In the case of mechanical excitation, the design includes a window, connected to the large displacement structure, allowing for the insertion of the pin of an external actuator. Electrostatic actuation is achieved by applying a voltage between the electrodes of a comb drive.

Mechanical stoppers are implemented, limiting the displacement of the

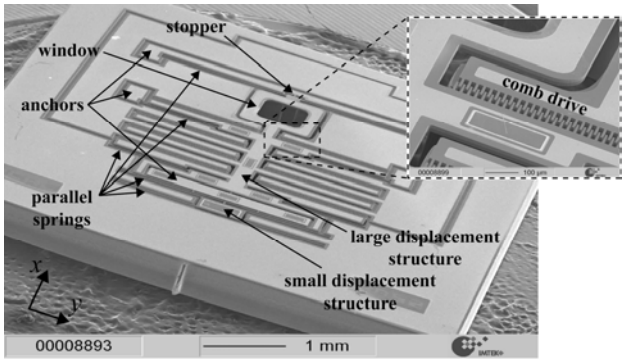

Fig. 2. SEM micrograph of a fabricated reference test structure.

comb structure to target values of 15 μm. By construction, the displacements imposed to this body, Δx_{comb}, are demultiplied to amplitudes Δx_{demul} with opposite direction of the small displacement structure. Two different ranges are thus available on the same device, enabling its use in optical calibration systems with different characteristics. The demultiplication factor $\Delta x_{demul}/\Delta x_{comb}$ is tuned by varying the clamping length L_c.

3 Characterization

The different optical arrangements used to characterize the micromechanical reference are shown in Fig. 3. The mechanical actuation is provided by a commercial PZT actuator with a pin mounted on its tip, which is inserted into the window of the mechanical structure and enables its displacement along the *x*-direction. The electrostatic excitation is made possible by applying a voltage to the comb actuator via electrical connections to the socket into which the chip carrier with wirebonded device is mounted. The sample is placed inside a vacuum chamber with window, enabling optical measurements at pressures from 760 Torr down to 10^{-6} Torr.

Both laser-deflection method and stroboscopic video microscopy techniques are shown in Fig. 3 (a). In the case of the laser-deflection technique, a laser diode is partially focused on the microdevice, whose movement modulates the intensity of the reflected beam, which is monitored with an avalanche photo diode (APD) detector [7]. The stroboscopic apparatus is a commercial system that combines acquisition of pictures synchronized with the object motion and digital analysis.

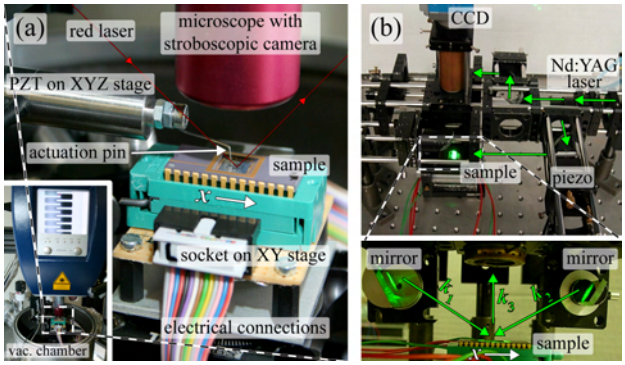

Fig. 3. (a) Laser-deflection test setup and stroboscopic microscope for measurements in vacuum, and (b) digital speckle interferometer developed to characterize the displacements of the micromechanical references in air.

The speckle interferometer is shown in Fig. 3 (b): the pattern of the speckle fields, recorded with a CCD camera, is produced by illuminating the sample with a Nd:YAG laser from two directions [8], [9].

Figure 4 shows typical measurement results. In Fig. 4 (a), the displacement of the comb Δx_{comb} of a device with $L_c = 536.5$ µm clearly shows a well-defined range, 15.84 µm, as the displacement of the external PZT actuator is increased via the voltage applied to it, V_{PZT}. This value is close to the design value of 15 µm, limited by the contact point between the PZT and test structure and by the implemented mechanical stopper. The resulting demultiplied motion amplitude Δx_{demul} shown in Fig. 4 (b) is limited in this case to 948 nm, linear with V_{PZT} but, as expected, with negative slope. The resulting demultiplying characteristic, i.e. Δx_{demul} plotted as a function of Δx_{comb}, is shown in Fig. 4 (c), from which a factor of ~ –60 nm/µm is extracted. The measured electrostatic characteristics of a device with $L_c = 687.5$ µm are summarized in Figs. 4 (d) to (f), where a voltage with DC and AC components is applied to the comb drive. A demultiplication factor of ~ –37 nm/µm is obtained in this case, consistent with finite element simulations.

4 Conclusions

A micromechanical in-plane reference device for the calibration of MEMS optical measurement systems is proposed, fabricated and characterized. Both mechanical and electrostatic actuations are possible. Different coatings processed on the movable parts make it possible to characterize

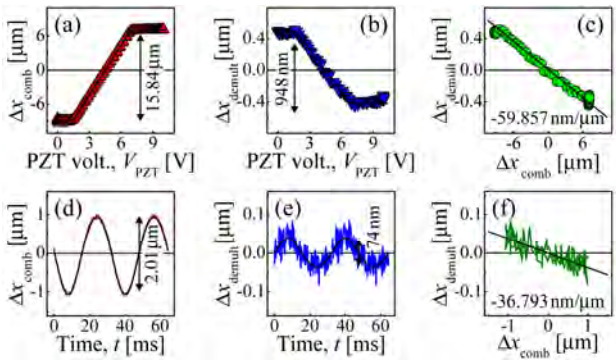

Fig. 4. Displacements (a) Δx_{comb} and (b) Δx_{demult} as a function of the external PZT voltage and (c) demultiplication curve. (d)–(f) Data obtained from applied electrostatic comb loads [$V_{DC} = 4V_{AC} = 40$ V, f = 31 Hz].

optical setups based on different principles using the same device. Moreover, a simple demultiplication mechanism extends the working range of the reference standard, thus covering a larger spectrum of displacements of MEMS devices.

5 Acknowledgements

The authors gratefully acknowledge A. Baur (IMTEK RSC) for assistance in clean room processing, M. Pappalardo (IMTEK MML) for development of the laser-deflection setup in vacuum and T. Wu (ITO) for development of the speckle interferometer. This work was supported by the German Research Foundation (DGF) under grants PA792/4-1 and OS111/22-1.

6 References

1. Korvink, J, Paul, O, *MEMS – A Practical Guide to Design, Analysis and Applications*, William Andrew Publishing, Norwich, 2006.
2. Osten, W, ed Optical Inspection of Microsystems, CRC Press, Boca Raton, FL, 2006.
3. http://www.opticalstrain.org.
4. Kujawinska, M, et al. (2006) Calibration and Assessement of Full-Field Optical Strain Measurement Procedures and Instrumentation. Proc. SPIE 6341: 63410Q.
5. International Standardization Organization (ISO), Guide to the Expression of Uncertainty in Measurement (GUM), Geneva, 1995.
6. Gaspar, J, Held, J, Pedrini, G, Osten, W, Paul, O (2009) Development of Calibration Standards for the Optical Measurement of In-Plane Displacements of Micromechanical Components. Proc. IEEE MEMS 2009 Conf.: 7-10.
7. Gaspar, J, Chu, V, Conde, J P (2005) Electrostatic microresonators from doped hydrogenated amorphous and nanocrystalline silicon thin films. J. Microelectromech. Syst. 14: 1082-1088.
8. Pedrini, G, Gaspar, J, Wu, T, Osten, W, Paul, O (2009) Calibration of optical systems for the measurement of microcomponents. Optics and Lasers in Engineering 47:203-210.
9. R. Jones, C. Wykes, Holographic and Speckle Interferometry, Cambridge University, NY, 1989.

About the feasibility of nearfield-farfield transformers based on optical metamaterials

Steffen Maisch, Philipp Schau, Karsten Frenner, and Wolfgang Osten
University of Stuttgart, Institute of Technical Optics (ITO)
Pfaffenwaldring 9, D-70569 Stuttgart
Germany

1 Introduction

1.1 About Metamaterials

After the theoretical prediction of *V. Veselago*[1] in 1976, materials with simultaneous negative magnetic permeability $\mu < 0$ and electric permittivity $\varepsilon < 0$ being able to transmit electromagnetic waves without exponential damping, *J. Pendry*[2] showed these systems bending light in the "wrong direction", namely showing a negative index of refraction $n < 0$.

The famous Abbe limit requires at least two diffraction orders to form an image in a microscope objective lens. The distance d, below which two points cannot be resolved, is in the order of magnitude given by (1).

$$d \approx \frac{\lambda}{2 N_A} \tag{1}$$

Lowering the wavelength λ, and increasing the numerical aperture N_A of the lens used improves the resolving power. For practical reasons, wavelengths are usually in the visible or near UV range. The numerical aperture $N_A < 1$ with air as the ambient medium limits the resolution, and can be increased to the value of the refractive index of an immersion medium. As most transparent liquids have refractive indices $n < 2$, this method only gives a moderate improvement in lens resolution, while complicating the sample preparation especially in automated processes.

Since the time around 1873, when these facts were systematically examined by *E. Abbe*, it is often believed, that theses limits are universally valid, and no optical image forming system can overcome them. However, this is not true. It is a question of how the optical system is manipulating the electromagnetic wave in the near field.

It took until 1991, when *E. Betzig* constructed an optical near field microscope, the SNOM (scanning near field optical microscope).[3] It scans a surface by using an optical fibre with a sub-λ aperture opening on its end, which is both the illuminator and the analysing tool simultaneously. It allows for resolutions far below the Abbe limit. Betzig was able to resolve 12 nm with visible wavelengths; but the scanning mode of operation is very slow and prone to artefacts. Nevertheless, it is a method for imaging the optical near field.

Pendry predicted, that a slab of a transparent material with a real part of the index of refraction $\mathrm{Re}(n) = -1$ performs as an image forming device both in the limit of geometric ray optics, and for the electromagnetic near field. Under the additional constraint of a vanishing imaginary part of the index of refraction of the material used (i. e. it is perfectly transparent with no ohmic losses in the material), it produces a perfect non-magnified image. This system is often referred to as "Pendry's superlens".[2]

Because of this, metamaterials showing a negative real part of the index of refraction gained much attention as they can be used for the construction of sub-λ resolution imaging devices and applications like invisibility cloaking.

Generally, metamaterials contain internal 'features' which are smaller than the wavelength used, but for use in the visible optical range much larger than typical interatomic distances, molecule sizes, and lattice constants of a crystal. Therefore, it is technically much easier to develop a metamaterial in the microwave range, where the structures are in the millimetre range. *R. Shelby* constructed a microwave metamaterial from an assembly of resonant copper structures etched on printed circuit boards and showed it to refract an incident microwave beam in the negative direction.[4] The fabrication of metamaterials for visible wavelengths involve the use of advanced nano fabrication tools and require a careful design and simulation of the optical properties before the manufacturing process is started. The aim of this work is to provide optimized structures and geometries for the nanofabrication of optical metamaterials and the design of optical elements used for super-resolution imaging.

1.2 Super-resolution Imaging

Super-resolution imaging in terms of a "super microscope" requires both a nearfield-farfield transformer made of the metamaterial, and a conventional objective lens with high N_A. It is indispensable that the nearfield-farfield transforming element simultaneously magnifies the image, which a simple slab of negative index material does not. Otherwise,

the resolution is still limited by the microscope objective. Therefore, a geometric shape function must be superimposed on the metamaterial device.

In one of the easiest cases (Fig. 1a), this could be a slanted cut edge, forming a wedge of the metamaterial that gives a magnified image perpendicular to the plane of incidence, assuming the angles being chosen accordingly.[20 - 22]

A hemispherical shape (Fig 1b) works by the same principle.[23, 24]

Additionally, and due to its relatively easy manufacturing process highly desirable, is a Fresnel lens like structure placed on top of the metamaterial slab (Fig 1c).

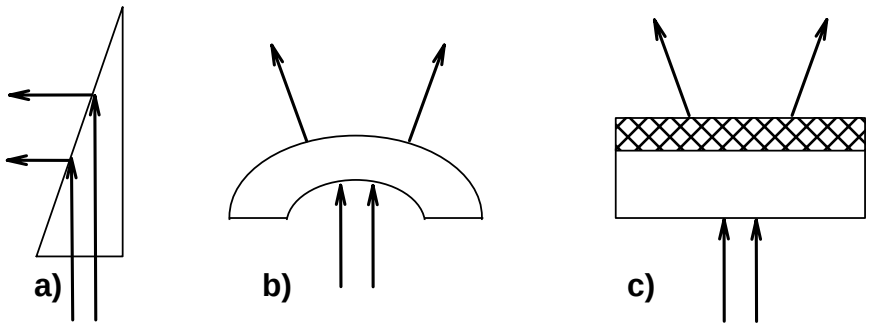

Fig. 1. Geometric shape functions for magnifying superlenses.

2 Optical Metamaterials

2.1 Simulation Tools

While many different possibilities for the realisation of an optical metamaterial do exist, we have chosen the split ring resonators (SRR)[5, 6] and meander structures[6] as our main goals for numerical simulation and optimization.

The simulation may be performed by equivalent circuit techniques[7, 8] and extracting *S*-Parameters, finite element methods for the numerical solution of the Maxwell equations[9], discrete dipole approximation[10-12] or RCWA (rigorous coupled wave analysis). RCWA uses a Fourier modal algorithm for the numerical solution of the differential equations by transforming them into linear matrix algebra.[13-17] We use a Matlab implementation of this algorithm,[16, 17] which is capable of simulating both 1D (translational invariant in one direction of the *xy*-plane) and 2D

problems. The output of the RCWA algorithm is the diffraction efficiencies and phases of the diffraction orders. They can be used to calculate transmission and reflection spectra. As the periods of metamaterials should be smaller than the wavelength used, usually only the zeroth diffraction order needs to be considered therefore. Given the absorbance, the Kramers-Kronig relation, which relates the imaginary to the real part of any analytic response function, may be used to calculate the real part of the refractive index. On the other hand, *A. Nicolson* and *D. Smith* give a method for retrieving refractive indices from the RCWA data in [18] and [19], which was the mainly used method in this work.

2.2 Geometric description

Fig. 2a shows the geometry of the SRRs. The five geometric parameters defined in this figure plus the period of translation invariance *a*, and the complex dispersion $n(\omega)$ of all materials involved in the system provide enough data to perform a rigorous analysis of its optical properties.

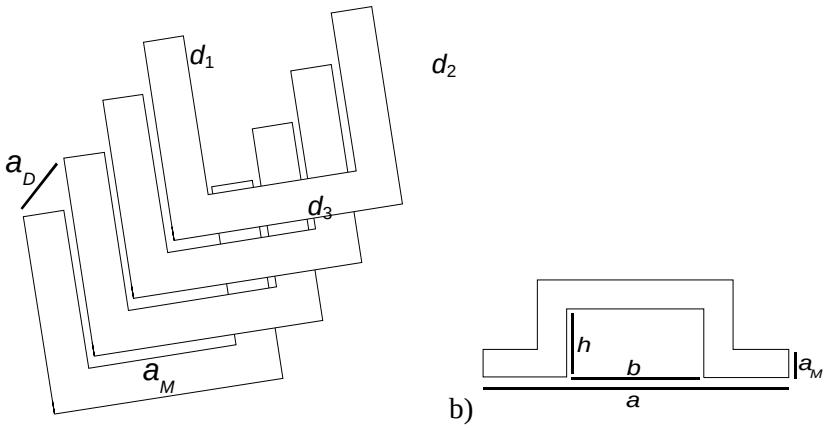

Fig. 2. Geometric definition of the SRR structures. a) Example of a four layer SRR structure. aM is the thickness of the metal layer, and aD of the separating dielectric. The horseshoe shape of a single SRR is defined by three parameters d1 – d3. b) Geometric parameters of the meander structure.

The meander structures (fig. 2b) are described by their period *a*, the height of the meander loops ('modulation') *h*, the thickness of the metal layer *d*, and the duty cycle *p* as measure of the ratio of the peaks to the whole period. In case of meander double layers, the distance d_2 of the two layers, which are separated by a dielectric, and the phase φ of the

geometric placement of the lower layer against the upper one, also need to be considered.

3 Results

Fig. 3 shows RCWA simulated transmission and reflection spectra of the four layer SRR structure. The resonance in **p** polarization is clearly seen. The SRRs give very valuable information for comparison of experimental data with the theory. However, single SRRs do probably not exhibit electric and magnetic resonance simultaneously, thus showing negative permeability, but no negative index of refraction.

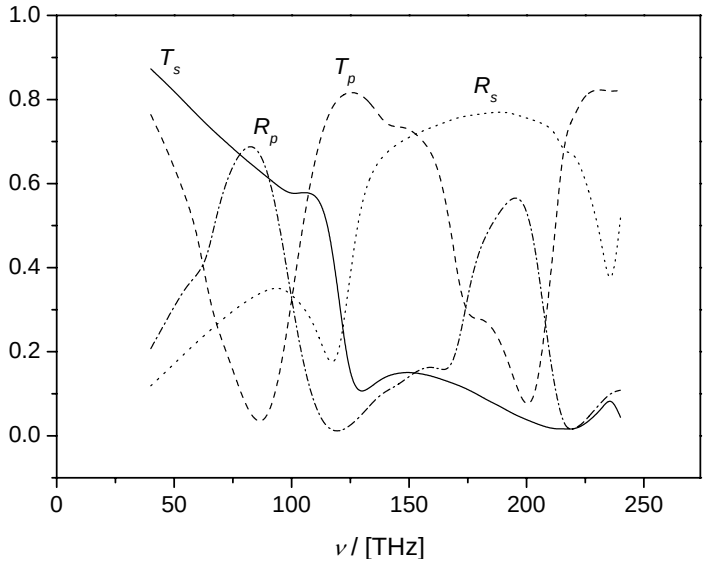

Fig. 3. Transmission (T) and reflection (R) spectra of the four-layer SRR structure defined in fig. 1a; both in s and p polarisation (a = 700 nm; aM = 20 nm; aD = 50 nm; d1 = 80 nm; d2 = 340 nm; d3 = 350 nm; metal is gold, and the dielectric is assumed to have a constant refractive index nD = 1.55 + 0.00 i).

The meander structures, however, are capable of performing a resonance that leads to negative refraction. Fig. 4 shows transmission spectra of a closed meander surface with varying loop height *h*, which is shown as an example of one set of similar spectra yielded by varying one parameter. From these simulations, optimized structures for negative refraction are obtained by retrieving the refractive index from each spectrum by the methods mentioned above.

Fig. 5 shows the retrieved real and imaginary part of the index of refraction of an optimized meander structure. The negative real part is accompanied by a jump in the imaginary part characteristic for the resonant absorption due to ohmic losses. In this thin layer system, the loss is still acceptable, but poses a problem for the route to “bulk” metamaterials.

In fig. 6, a dispersion plot of the meander structure is shown. This is an example of a very versatile method for examining the physical properties of metamaterials, as the symmetry properties of the plasmons involved can be deduced. Plotting the absorbance as a function of frequency and transversal linear momentum shows the dispersion curves. The momentum is varied in the RCWA simulation by applying different angles of incidence.

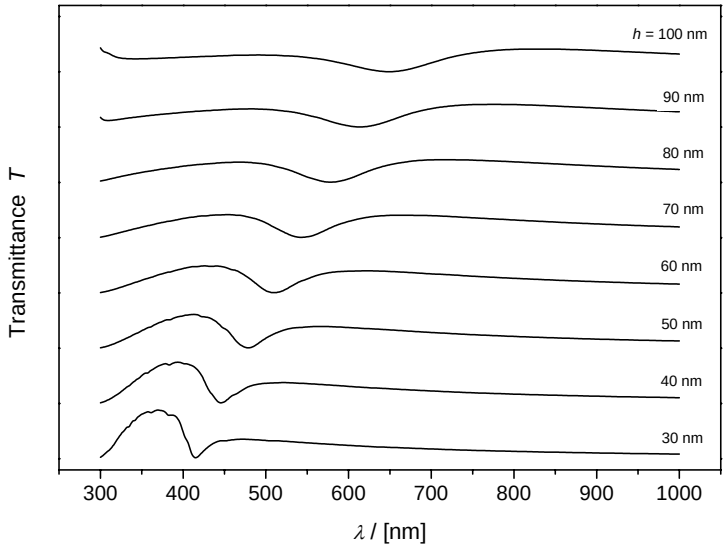

Fig. 4. RCWA simulated transmission spectra of meanders with varying loop height h. The other parameters are as follows: a = 200 nm, b = 80 nm, aM = 20 nm.

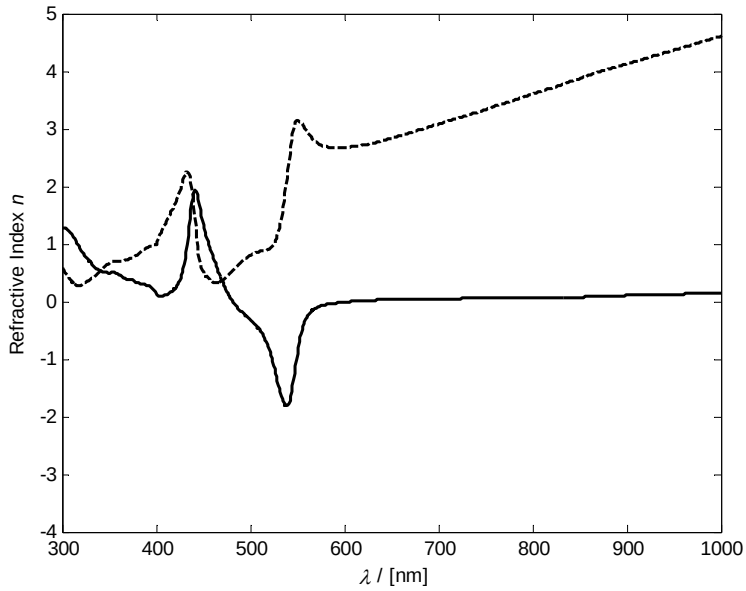

Fig. 5. Retrieved real (solid line) and imaginary (dashed line) part of the refractive index of an optimized meander structure (a = 400 nm, b = 170 nm, h = 30 nm, aM = 30 nm).

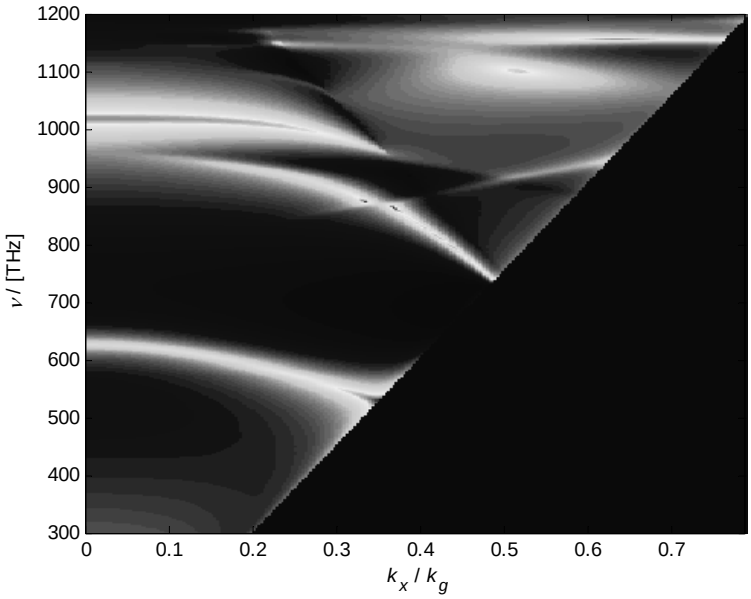

Fig. 6. Dispersion plot of a meander (a = 200 nm, b = 80 nm, h = 50 nm, aM = 20 nm). Shown is the absorbance as a function of frequency and the transversal momentum.

4 Conclusions

We were able to perform a RCWA simulation of very different metamaterial structures with varying geometries and consisting of different materials. It is seen that the noble metals silver and gold are suitable for the visible, and also partly for the near UV energy range. These metals are chemically inert, which makes the thin layers oxidation insensitive and very stable. Our simulation only considered structures being able to get fabricated with acceptable technical effort, as they are the basis for future metamaterial applications. It was possible to simulate structures exhibiting a negative real part of the index of refraction, which is always linked to a resonance and thus limited to a small bandwidth. Furthermore, the use of passive materials shows strong absorption bands due to ohmic losses. These losses are still low for very thin layers, making them suitable for flat imaging elements. These materials can be used as nearfield-farfield-transformers, e. g. for the construction of superlenses.

5 Acknowledgement

We like to thank “Landesstiftung Baden-Württemberg” for funding the project OPTIM.

6 References

1. Veselago, V (1968) *Sov. Phys. Usp.* **10**: 509
2. Pendry, J (2000) *Phys. Rev. Lett.* **85**: 3966
3. Betzig, E, Trautman, J K, Harris, T D, Weiner, J S, Kostelak, R L (1991) *Science* **251**: 1468
4. Shelby, R, Smith, D R, Schultz, S (2001) *Science* **292**: 77
5. Liu, N, Guo, H, Fu, L, Kaisre, S, Schweizer, H, Giessen, H (2008) *Nature Mat.* **7**: 31
6. Schweizer, H, Fu, L, Gräbeldinger, H, Guo, H, Liu, N, Kaiser, S, Giessen, H (2007) *Phys. Stat. Sol. A* **204**: 3886
7. Fu, L, Schweizer, H, Guo, H, Liu, N, Giessen, H (2007) *Appl. Phys. B* **86**: 425
8. Schweizer, H, Fu, L, Gräbeldinger, H, Guo, H, Liu, N, Kaiser, S, Giessen, H (2007) *Phys. Stat. Sol. B* **204**: 1243
9. O’Leary, D P (2005) Computing in Science and Engineering **7**: 72
10. Draine, B T (1988) *Astrophys. J.* **333**: 848

11. Flatau, P J (2004) *Optics Express* **12**: 3149
12. Shimura, K, Milster, T D (2001) *J. Opt. Soc. Am A* **18**: 2895
13. Moharam, M G, Gaylord, J (1982) *J. Opt. Soc. Am.* **72**: 1385
14. Moharam, M G, Grann, E B, Pommet D A (1995) *J. Opt. Soc. Am A* **12**: 1068
15. Moharam, M G, Pommet, D A, Grann, E B (1995) *J. Opt. Soc. Am A* **12**: 1077
16. Totzek, M (2001) *Optik* **112**: 381
17. Schuster, T, Ruoff, J, Kerwien, N Rafler, S, Osten, W (2007) *J. Opt. Soc. Am A* **24**: 2880
18. Nicolson, A M, Ross, G F (1970) *IEEE Trans. Inst. Meas.* **IM-19**: 377
19. Smith, D R, Schultz, S, Markoš, P, Soukoulis, C M (2002) *Phys. Rev. B* **65**: DOI 10.1103/PhysRevB.65.195104
20. Salandrino, A, Enghata, N (2006) *Phys. Rev. B* **74**: 075103
21. Jacob, Z, Alekseyev, L V, Narimanov, E (2006) *Opt. Express* **14**: 8247
22. Narimanov, E, Alekseyev, L V (2006) *Opt. Express* **14**: 11184
23. Liu, Z, Lee, H, Xiong, Y, Sun, C, Zhang, X Nicolson (2007) *Science* **315**: 1686
24. Smolyaniov, I, Hung, Y J, Davis, C (2007) *Science* **315**: 1699

Analogy of white-light interferometry and pulse shaping

Reinhard Berger, Wolfgang Osten
Institut für Technische Optik, Universität Stuttgart
Pfaffenwaldring 9, 70569 Stuttgart
Germany

1 Introduction

The comparison of two known optical issues must have a reason: In our case the measurement principle of a vertical scanning white-light interferometer can be abstracted when considering the field of pulse shaping. In this context it is possible to obtain a new perception of white-light interferometry. The introduced analogy helps further to start numerical simulations of such an optical system. This will especially be demonstrated for non ideal white-light interference signals for example when transparent layers, steps and/or roughness exist on the measured object. Even the investigation of a white-light interferometer with chromatic aberrations in combination with local tilts on the object can be transferred to the field of pulse shaping.

Vertical scanning white-light interferometry is a 3D-measurement technique resulting in absolute height values for the topography of the test object. During a measurement the object is moved relatively to the objective in the object arm of the white-light interferometer. If a camera with a two-dimensional chip is used, it is possible to measure the height values parallel of all object points in the field of view. A first automated three dimensional topography measurement using a white-light interferometer was first published by Balasubramanian in 1982 [1]. Vertical scanning white-light interferometers are today versatile tools for topography measurements of many different object types [2-4].

With pulse shaping it is possible to change the waveform of an available electromagnetic pulse. This technique is often used to generate ultrashort laser pulses especially in the femtosecond range for example for ultrafast spectroscopy, for pulse control in femtosecond amplifiers, in nonlinear fiber optics and in optical communication. The generation of pulses below 100 fs duration was first published in 1981 [5], nearly to the same time as the commercial implementation of white-light interferometry in metrology.

2 Equivalent optical setup

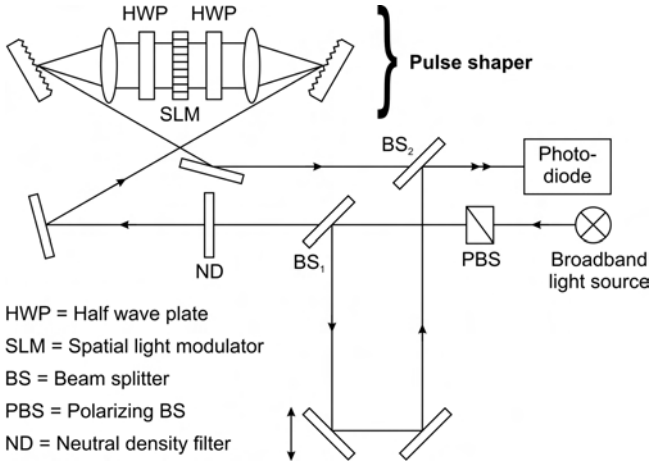

Fig. 1. Equivalent optical setup for a pointwise white-light interferometer using a pulse shaper [6] based on a spatial light modulator for spectral frequency dependent phase shifts

The frequently applied method for ultrafast pulse shaping is the spatial masking of the spatially dispersed optical frequency spectrum. Often a SLM is used to shift the phase for each spectral component [6]. In white-light interferometry the interaction of broadband light with some test objects and the interaction with an imperfect optical setup can cause a wave number dependent phase shift of the light passing the object arm [7]. In analogy the SLM of the equivalent optical setup also shifts the phase of each spectral component in the object path arbitrarily (Fig. 1).

3 Signal generation in white-light interferometry

The measurement principle of a two-beam interferometer is the comparison of two wavefronts after passing through the object and the reference arm, respectively. Normally a plane mirror is used for the optical reference element. Corresponding to the Wiener-Kinchin-theorem and in the theoretical case of a perfect optical setup and a “perfect object” such as a plane mirror, perpendicular to the optical axis, the white-light interference signal can be understood as an auto-correlation of incoherent light. Consequently, the following can be written referring to the Wiener-Kinchin-theorem (Eq. 1.):

$$\Gamma_{11}(\tau) = \int_0^\infty 4 \cdot S(\upsilon) \cdot \exp(-i2\pi\upsilon\tau) d\upsilon \quad (1)$$

S(υ) is the power spectral density of the incoherent light source and τ is a time coefficient for the auto-correlation Γ_{11}. Based on this relation the white-light interference signal is also called correlogram.

If the electromagnetic field in front of one pixel of the camera is considered, a harmonic interference signal for each wavelength is generated when the object is moved in z-direction by small steps. Vertical scanning white-light interferometry uses normally a monochromatic detector. Therefore the intensity values of all monochromatic interference signals are added. For each step of the z-scan the total electromagnetic field in the detector plane is integrated over a time period. Additionally the intensities of each of these interference signals are weighted corresponding to the intensity spectrum of the incoherent light source (see also Eq. 1.). The real part of exp(-i2πυτ) in Eq. 1. relates to the described monochromatic interference signals in the detector plane during the vertical scan.

During the z-scan every object point achieves the zero z-position of the white-light interferometer after a different amount of steps of the piezo scanner. Eq. 1. can also be extended to a Fourier transform by changing the lower integration limit. Therefore an arbitrary object height h causes an additional phase ramp in the Fourier domain of the correlogram corresponding to the Fourier shift theorem.

Chromatic aberrations in the optical system combined with local tilts on the test object [7,8] or transparent layers on the test object produce normally a more complex phase shift of each spectral component of the reflected light in the object arm dependent on the wave number. One or more height steps within an optical resolution cell of the white-light interferometer can also cause a wave number dependent phase shift of the reflected light in the object arm. This will cause an impact to each monochromatic interference signal in the detector plane. For example when a single height step within the optical resolution cell is considered, a three beam interference model given in [9] can be used for explanation. The light reflected from the bottom and from the top of this height step superpose to one interference signal of the object arm, which will later interfere with the light of the reference arm. Since the wave number for each spectral component is different but the step size is constant, the totally reflected light in the object arm has a different phase shift for the different spectral components compared to the light of the reference arm.

In these cases the generation of the white-light interference signal is a cross-correlation of the light from the object and the reference arm. This normally results in a difference of the height value obtained from the coherence information and the phase information of the correlogram [7,8].

4 Conclusions

3D-measuerments of real test objects with a real optical setup based on white-light interferometry often result in non ideal correlograms. The presented equivalent optical setup should help to understand the generation of such signals and to start numerical simulations.

5 References

1. Balasubramanian, N (1982) Optical system for surface topography measurement. US Patent No. 4340306
2. Dresel, T, Häusler, G, Venzke, H (1992) Three-dimensional sensing of rough surfaces by coherence radar. Applied Optics, Vol. 31: 919-925
3. Kim, S-W, Kim, G-H (1999) Thickness-profile measurement of transparent thin-film layers by white-light scanning interferometry. Applied Optics, Vol. 38: 5968-5973
4. de Groot, P, de Lega, X C, Liesener, J, Darwin, M (2008) Metrology of optically-unresolved features using interferometric surface profiling and RCWA modelling. Optics Express, Vol. 16: 3970-3975
5. Weiner, A M, (2000) Femtosecond pulse shaping using spatial light modulators. Review of Scientific Instruments, Vol. 71: 1929-1960
6. Wang, L , Weiner, A M (1999) Programmable spectral phase coding of an amplified spontaneous emission light source. Optics Communications 167: 211–224
7. Berger, R, Sure, T, Osten, W (2007) Measurement errors of mirrorlike, tilted objects in white-light interferometry. Proceedings of SPIE, Vol. 6616: 66162E-1
8. Berger, R, Körner, K, Osten, W (2008) Chromatische Aberrationen in der Weißlichtinterferometrie. DGaO-Proceedings: A30
9. Rahlves, M, Seifert, M, Fahlbusch, T, Frühauf, J, Reithmeier, E (2007) Bewertung von Weißlichtinterferometermessungen mit einer Kantenteststruktur. DGaO-Proceedings: P54

TOPIC 3

4D Optical Metrology over a Large Scale Range

Chairs:

Christophe Gorecki
Besançon
(France**)**

Anand Asundi
Singapore
(Singapore)

Invited Paper

Nanomeasuring and Nanopositioning Engineering

Gerd Jäger, Eberhard Manske, Tino Hausotte, Hans-Joachim Büchner
Ilmenau University of Technology
Faculty of Mechnical Engineering
Institute of Process Measurement and Sensor Technology
P.O. Box 100 565, 98684 Ilmenau
Germany

1 Abstract

The paper describes traceable nanometrology based on a nanopositioning machine with integrated nanoprobes. The operation of the high-precision nanomeasuring machine having a resolution of 0,1 nm over the range of 25 mm x 25 mm x 5 mm is explained. Single beam-, double beam- and triple beam interferometer arranged with an Abbe offset-free design are installed into the nanomeasuring machine in order to measure and control the six degrees of freedom. The high performance of the machine is described with a metrological analysis. This analysis shows some today´s limits of nanopositioning and nanomeasuring engineering.

2 Introduction

Micro- and nanotechnology has experienced enormous progress in the last few years. Moore's law is still valid to this day. According to the International Technology Roadmap for Semiconductors structure widths of 22 nm (DRAM ½ pitch) must be measureable on wafers of 450 mm. Therefore, the semiconductor industry is one of the biggest drivers of nanometrology and of nanopositioning and nanomeasuring technology.

The development of appropriate physical standards for structure widths, step heights and surfaces carries great importance for the mastery of high technologies. Determining the form deviations, waviness and roughness of objects on the micro- and nano-scales is a current and ongoing task. A further challenge facing nanometrology is the measurement of optical and mechanical precision components with nanometre accuracy. Some prominent examples include the measurement of aspherical and free-form

surfaces as well as the characterisation of microoptics, precision moulds, ring gauges, microgears, small holes etc.

The measurement of samples can be subdivided into different scanning modes.

In sample scanning mode the sample being measured is moved three-dimensionally and remains in contact with the fixed probe system, which acts as a zero indicator. Some scanning probe microscopes utilise this mode. [1, 4].

Conversely, scanning probe mode uses the movement of a 3-D contact probe to measure a fixed sample. This principle is mainly implemented in 3-D coordinate measuring machines.

Finally, a measurement in mixed scanning mode involves moving the sample in the x-y-plane and having the measuring system able to perform movement in the z-axis [2, 3].

The successful solution to all of the aforementioned challenges calls for effective long-range nanopositioning and nanomeasuring machines with integrated nanoprobes. Such a nanopositioning and nanomeasuring machine has been developed by the Institute of Process Measurement and Sensor Technology of the Technical University of Ilmenau, Germany [4]. The device implements sample scanning mode over a range of 25 mm x 25 mm x 5 mm with a resolution of 0.1 nm. The measurement uncertainty is about 5 nm. After a short explanation of the nanomeasuring machine's set-up, the next few sections describe its high performance through a metrological analysis. This analysis will show some of today's limits within nanopositioning and nanomeasurement engineering. The various applications of the nanomeasuring machine are based on the installation of optical and tactile nanoprobes above the nanopositioning 3-D stage.

3 Metrological basis and analysis

3.1. The set-up of the nanomeasuring machine

Figure 1 illustrates the set-up of a nanomeasuring machine. The nanomeasuring machine consist of following main components:

- traceable linear and angular measurement instruments
- 3D-nanopositioning stage
- Optical and tactile nanoprobes
- Control equipment

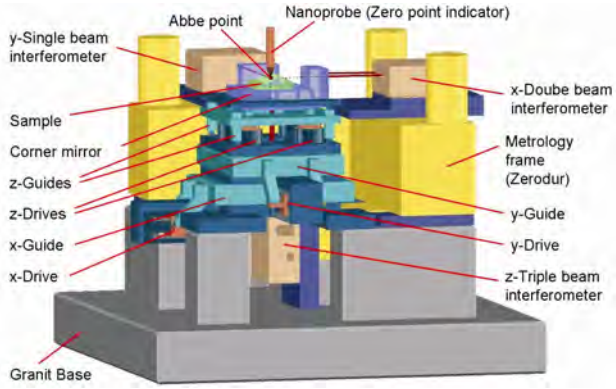

Fig. 1: Set-up of a nanomeasuring machine

Both the metrology frame, which carries the measuring systems (interferometers and angular sensors), and the 3-D stage are arranged on a granite base. The upper Zerodur® plate (not shown in fig. 1) of the metrological frame is constructed such that different nanoprobes can be easily installed and removed. A corner mirror is moved by the 3-D stage, which is built in a stacked arrangement. The separate stages consist of ball-bearing guides and voice coil drives [4]. The positions of the corner mirror are measured by three plane-mirror interferometers [7].

3.2. Basis and limits of interferometric length measurements

If two planar, monochromatic, linear-polarised waves with the frequency ω interfere, the intensity distribution can be described by equation (1).

$$I = I_1 + I_2 + 2\sqrt{I_1 I_2}\,\cos\left(\gamma + \frac{2\pi}{\lambda_0}\cdot n \cdot i \cdot s\right) \tag{1}$$

where

- γ - the phase before the reflector displacement
- λ_0 - the wavelength of light in a vacuum
- n - refractive index of air
- i - interferometer factor
- s - reflector displacement

From equation (1) it follows for the displacement s:

$$s = \frac{k \cdot \lambda_0}{i \cdot n} = \frac{k \cdot c_0}{i \cdot n \cdot f_{HeNe}} \tag{2}$$

with

k -	the change of the interference order from a displacement s of the reflector
$f_{HeNestab}$ -	the frequency of a stabilised HeNe laser
c_0 -	the speed of light in vacuum

The smallest resolvable displacement s_q can be determined, if an interference order (k = 1) is divided into e electronic increments. It follows from equation (2) that:

$$s_q = \frac{\lambda_0}{e \cdot i \cdot n} \tag{3}$$

Some parameters affecting the uncertainty of the measurement of s can be derived from equation (2):

- Nonlinearities of the interpolation electronics must be considered when determining k
- c_0 is fixed at a value of 299792458 m/s
- n depends on air pressure, humidity, temperature and on the composition of the air
- $f_{HeNestab}$ must be known as indicated in equation (2). For this, the difference is determined between $f_{HeNestab}$ and the frequency of an iodine-stabilised HeNe laser [5, 6], the frequency of which is coupled to the caesium frequency standard f_{cs133}. The wavelength of the iodine-stabilised HeNe laser resulting from the traceable connection is $\lambda_{HeNeiodine}$ = 632.99139822 nm with a relative standard uncertainty of $2.5 \cdot 10^{-11}$ [6].

Further influences affecting the measurement uncertainty of interferometric measurements must also be considered. Such influences can be caused for example by not following the Abbe comparator principle or as a result of the instability of the metrological frame.

3.3. The performance of the nanomeasuring machine

The excellent performance of the nanomeasuring machine is based on three important characteristics: (1) the Abbe error-free arrangement of the laser interferometers, (2) the application of an effective concept for compensating the stage errors and (3) the nanoprobes' acting as zero-point indicators only.

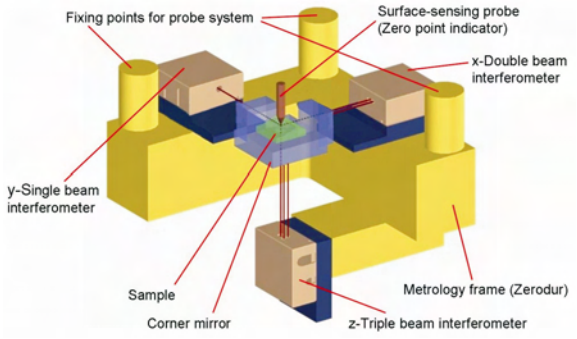

Fig. 2: Abbe offset-free design of the nanomeasuring machine

The three laser interferometer measuring beams are reflected off the outer surfaces of the corner mirror, whereby the virtual extension of the reflected beams intersect at the point of contact between the specimen and the sensor (see fig. 2). Because sample scanning mode is implemented in the nanomeasuring machine, the Abbe comparator principle is realised over the entire measuring range. In this mode the probes only have the function of a zero-point indicator, which can be realised with very high precision.
Angular deviations of the guide systems are detected at the corner mirror by means of a single beam-, a double beam- and a triple beam interferometer. The detected angular deviations are compensated by a close-loop control system.

4 Zero-point nanoprobes suitable for use in the nanomeasuring machine

The optical and tactile nanoprobes each have different advantages and disadvantages. It is therefore necessary to be able to use both types of nanoprobes in the nanomeasuring machine, each probe type for appropriate tasks. The following section describes the set-up, function and measurement results of some zero-point nanoprobes in combination with the nanomeasuring machine.

4.1 Focus sensor

The focus sensor was developed in cooperation with Prof. Fan Kuang-Chao of National Taiwan University [8]. The main part of the focus sensor is the so-called hologram laser unit (Fig. 3).

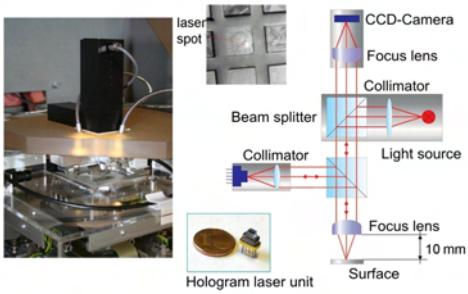

Fig. 3: Set-up of the focus-sensor

The optical system has been dimensioned such that a measuring range of ±3 µm with a resolution of < 1 nm can be achieved [9]. With a new sensor design the working distance was increased to 10 mm. In combination with the nanomeasuring machine, the focus sensor allows the measurement of step height standards of samples with heights up to 5 mm. For example, a 2 mm step height standard was measured with an expanded uncertainty of only 2.7 nm for k = 2 (Fig. 4).

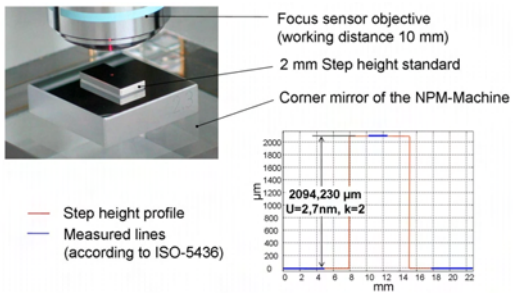

Fig. 4: Results of the measurement of a 2 mm step height standard

4.2 White light sensor

A white light interferometric sensor (Mirau interferometer) was also installed into the nanomeasuring machine. The Mirau objective is firmly attached to the nanomeasuring machine's Zerodur® mounting plate (Fig. 5). The sample to be measured can now be positioned in the z-direction in 1 nm steps over a range of 5 mm with the help of the machine's 3-D stage in order to localise the zeroth order white light interferences within an x-y-area of 600 x 800 µm^2. In addition to the large measuring range of 5 mm in the z-direction, there exists an additional advantage in that many 600 x

800 µm^2 large sample areas can be combined together without stitching over a range of 25 x 25 mm^2.

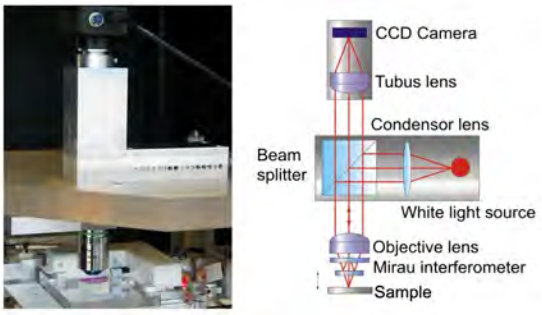

Fig. 5: White light interferometric sensor integrated into the NPM machine

4.3 Tactile nanoprobe

Focus and white light sensors fail to perform when used for form and contour measurements of sample surfaces with large slopes. However, tactile sensors lend themselves well to these types of analyses.
The 3-D stage of the nanomeasuring machine in combination with additional opto-mechanical components presents an ideal method of measuring the material properties of nanocoatings on substrates as well as the precise form and contour of samples. For that a force-calibrated quartz glass parallel spring can be deflected in the z-direction with great sensitivity at a resolution of 0.1 nm using the 3-D positioning stage of the machine (Fig. 6).

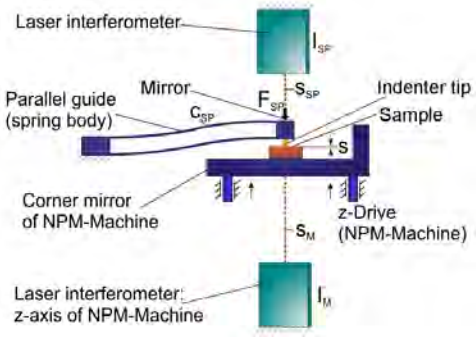

Fig. 6: Nanoindenter (s – indentation, s_{SP} – spring deflection, s_M – display of I_M, c_{SP} – spring constant, F_{SP} – indentation force)

The measurement of this deflection is carried out with an external plane-mirror interferometer, also with a resolution of 0.1 nm. Therefore, the contact forces exerted on the sample can be determined exactly in cases where an appropriate stylus is fitted to the free end of the parallel spring. Measurements with variable contact forces are significant in determining the interaction between the probe and the sample.

5 References

1. H.-J. Büchner et al: Laserinterferometrically assisted 3D-nanometrology on the atomic force microscope type VERITEKT; Proceedings of the euspen-Conference, 1999
2. P. Lehmann: Measurement of microgeometry using white-light interferometry and confocal microoptical sensors; VDI-Berichte Nr. 1950; Messtechnik für Mikro- und Nano-Engineering, pp. 119 – 128, 2006
3. Fan, K.C. et al: Development of a low cost micro-CMM for 3D micro/nano measurements; Meas. Sci. Technol. 17, pp. 524 – 532, 2006
4. G. Jäger et al: A nanopositioning and nanomeasuring machine, Operation, Measured Results, Nanotechnology and Precision Engineering; Vol. 2, pp. 81 – 84, 2004
5. Documents concerning the new definition of the meter; Metrologia 19, pp. 163 – 177, 1984
6. T.J. Quin: Practical realization of the definition of the meter; Metrologia 36 (3), pp. 211 – 244, 1997
7. H.-J. Büchner; G. Jäger: Plan mirror interferometers for precision length measurements; Proceedings of the euspen-Conference, Montpellier, France, pp. 45 – 48, 2005
8. Kuang-Chao Fan et al: A displacement spindle in a micro/nano level; Meas. Sci. Technol., 18, pp. 1710 – 1717, 2007
9. R. Mastylo et al: A focus sensor for an application in a nanopositioning and nanomeasuring machine; SPIE, Optical Measurement Systems for Industrial Inspection IV, München, Proceedings of SPIE, Vo. 5856, pp. 238 – 244, 2005

Reconstruction of Shape using Gradient Measuring Optical Systems

Jörg Seewig, Tobias Damm, Janick Frasch, David Kauven, Sebastian Rau, Johannes Schnebele
University of Kaiserslautern
Gottlieb Daimler Straße, 67663 Kaiserslautern
Germany

1 Introduction

This paper deals with the problem of reconstructing a surface topography for a special type of surface sensor that measures the surface slope instead of the height. As an example, a scattered light sensor with an incoherent light source is considered. In contrast to many other applications, the scattered light sensor is used to measure form deviation in the nanometer range of mirror like surfaces. The concept is as simple as possible: A linear detector positioned in the focal plane of the lens measures the angle distribution of the back scattered light. The center of mass of the angle distribution is proportional to the gradient of the surface. The reconstruction of the shape is done by integration.

For a better understanding, the reconstruction process is described in the frequency domain in a generic way. The instrument transfer function will play a central role in the reconstruction process. This is the basis to decide whether a reconstruction process is suitable and what are the expected errors. Because of the generic approach the given results can be easily adapted to other sensors like deflectometry systems.

2 Problem statement in the frequency domain

For simplicity, we consider the 2D case (profile traces). The whole transfer chain of the measuring system is shown in Fig. 1. It is assumed that all transfer elements are linear and shift invariant. Furthermore it is assumed that any given profile trace on the surface can be expressed by its Fourier transform $P(\omega)$. All inner and outer noise components are described by the Fourier transform $D(\omega)$. We start with the case $D(\omega) = 0$. Following

Fig. 1, the first transfer element is a derivative operator and its output the slope of the profile trace. The second element is the transfer function $H_s(\omega)$ of the given sensor. The sampling of the profile slope with a sampling distance of Δx is expressed by a delta impuls modulator (a multiplication with a sequence of shifted delta impulses in the spatial domain) [1]. The operator "$*$" denotes the convolution in the frequency domain. The next step is essential for the reconstruction of the profile. An interpolation filter with the transfer function $H_i(\omega)$ converts the sampled values to a continuous function in the spatial domain. After that, the reconstructed slope is integrated and results in the reconstructed shape $P_r(\omega)$.

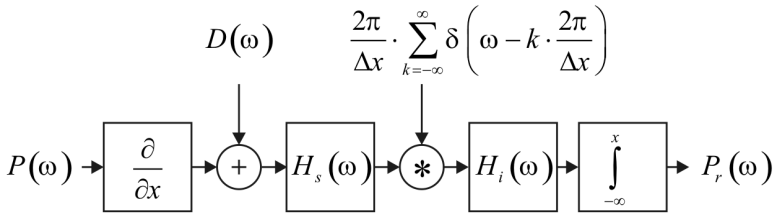

Fig. 1. Transfer chain of the measurement procedure consisting of the sensor transfer function followed by an impulse modulator and the reconstruction filter

The overall transfer function can be expressed according to the given transfer chain by the equation

$$P_r(\omega) = \frac{H_i(\omega)}{i \cdot \omega} \cdot \frac{1}{\Delta x} \sum_{k=-\infty}^{\infty} M\left(\omega - k \cdot \frac{2\pi}{\Delta x}\right) + C \cdot 2\pi \cdot \delta(\omega), \tag{1}$$

where $M(\omega) = i \cdot \omega \cdot P(\omega) \cdot H_s(\omega)$ is the Fourier transform of the continuous output signal of the measuring system. The second term is a constant which takes a possible offset into account. In spatial domain equation (1) can be rewritten to

$$p_r(x) = \int_{-\infty}^{x} \sum_{n=-\infty}^{\infty} m(n \cdot \Delta x) \cdot h_i(\xi - n \cdot \Delta x) \cdot d\xi, \tag{2}$$

where $m(n \cdot \Delta x)$ are the sampled values at position $x = n \cdot \Delta x$ and $h_i(x)$ is the weighting function of the interpolation filter. In the following it is assumed that the sensor transfer function $H_s(\omega)$ is a low pass filter with a cut-off frequency ω_c. Cut-off means, that the signal is damped to a

desirable level e. g. 50% (a standard value in geometrical measurement techniques). Following Nyquist's sampling theorem we must choose the sampling distance to $\Delta x \leq \pi/\omega_c$. Otherwise we get unwanted aliasing effects due to overlapping of the spectra. Hence, the choice of the sampling distance strongly depends on the instrument transfer function due to its low pass characteristic. Fig. 2 shows the sampling situation without aliasing.

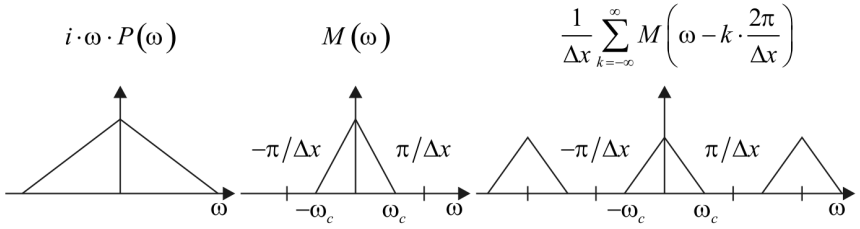

Fig. 2. The sampling theorem visualised by a triangular spectrum which is sampled with a sampling distance $\Delta x \leq \pi/\omega_c$

The main task of the interpolation filter is to extract the spectrum within the range $-\pi/\Delta x < \omega < \pi/\Delta x$. For this reason, the best choice is the ideal low pass filter with the following transfer function and corresponding weighting function

$$H_{i,ideal}(\omega) = \begin{cases} \Delta x & -\pi/\Delta x < \omega < \pi/\Delta x \\ 0 & otherwise \end{cases}, \quad h_{i,ideal}(x) = \frac{\sin(\pi/\Delta x \cdot x)}{\pi/\Delta x \cdot x}. \qquad (3)$$

Consequently, the best possible approximation of the original shape is $P_{r,ideal}(\omega) = P(\omega) \cdot H_s(\omega)$, the multiplication of the profile spectrum and the instrument transfer function. Unfortunately, the ideal interpolation process leads to a weighting function which is unbounded in x. Windowing is one possibility to overcome this problem. But after windowing, the interpolation function cannot be integrated analytically. Hence, two popular interpolation functions are used in practice: the piecewise constant interpolation and the linear interpolation which are defined by

$$h_{i,0}(x)=\begin{cases}1 & -\Delta x/2<x<\Delta x/2\\ 0 & \textit{otherwise}\end{cases},\quad H_{i,0}(\omega)=\Delta x\cdot\frac{\sin(\omega\cdot\Delta x/2)}{\omega\cdot\Delta x/2}$$
$$h_{i,1}(x)=\begin{cases}1-\frac{|x|}{\Delta x} & -\Delta x<x<\Delta x\\ 0 & \textit{otherwise}\end{cases},\quad H_{i,1}(\omega)=\Delta x\cdot\left(\frac{\sin(\omega\cdot\Delta x/2)}{\omega\cdot\Delta x/2}\right)^2 \tag{4}$$

Both functions can be easily integrated but have poor approximation properties. A better choice is a cardinal cubic spline interpolation with the transfer function [2]

$$H_{i,spline}(\omega)=\Delta x\cdot\frac{3}{2+\cos(\omega\cdot\Delta x)}\cdot\left(\frac{\sin(\omega\cdot\Delta x/2)}{\omega\cdot\Delta x/2}\right)^4. \tag{5}$$

The cardinal cubic spline interpolation is numerical efficient and smooth (continuously differentiable up to the second derivative). A detailed description of the approximation properties is given in [3]. Fig. 3 shows the spectra of the four interpolation functions. A good approximation of the ideal interpolator is truly the cardinal cubic spline filter.

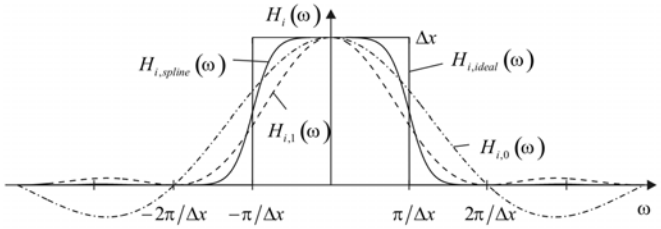

Fig. 3. Transfer functions of four interpolation methods: ideal low pass $H_{i,ideal}(\omega)$, piecewise constant $H_{i,0}(\omega)$, triangular $H_{i,1}(\omega)$ and cardinal cubic spline $H_{i,spline}(\omega)$

Next, we consider an additional error term, e. g. the roughness of the surface, and set $D(\omega)\neq 0$. According to equation (1) and depending on the error term we get a virtual or let's say a "ghost" shape caused by the integrating process

$$\Delta P(\omega)=\frac{H_i(\omega)}{i\cdot\omega}\cdot\frac{1}{\Delta x}\sum_{k=-\infty}^{\infty}H_s\left(\omega-k\cdot\frac{2\pi}{\Delta x}\right)\cdot D\left(\omega-k\cdot\frac{2\pi}{\Delta x}\right). \tag{6}$$

Due to the transfer characteristic of the integrator, long wave components in $D(\omega)$ superimpose the reconstructed shape with an unwanted signal and give undesirable results (an example is given in the next chapter). The only way to suppress such components is a high pass filter which is applied to $P(\omega)$. Consequently, reliable results are only given in a defined frequency band which depends on the instrument transfer function and the estimated spectrum $D(\omega)$.

3 The scattered light sensor

As an example, Fig. 4 shows the optical setup of the considered scattered light sensor. On the left side, the luminous area of an LED is imaged onto the surface of the workpiece by a collimator and measurement objective. The spot diameter is D'. On the right side, the reflected light is collected by the measuring lens and projected onto an intensity detector, a small array of diodes. The intensity detector lies in the focal plane of the measurement objective. Because the measurement objective is an F-Theta lens, the tangent of the surface gradient is proportional to the center of mass of the intensity curve.

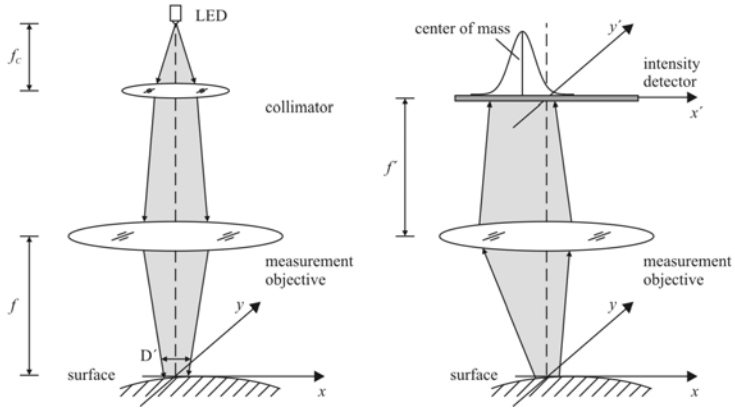

Fig. 4. Left: illumination path with the light source, collimator and the measurement objective. Right: measuring path with the measurement objective and the intensity detector

The instrument transfer function $H_s(\omega)$ is derived in detail in [4]. For the considered scattered light sensor it is given by $H_s(\omega) = 2 \cdot J_1(0.45mm \cdot \omega)/(0.45mm \cdot \omega)$, where J_1 is the Bessel function

of the first kind and the first order (spot diameter $D' = 0.9mm$). The 50% cut off is $\omega_c \cong 2\pi \cdot 0.7/0.9$. Fig 5 shows the instrument transfer function after sampling with a distance of $\Delta x = \pi/(5 \cdot \omega_c)$. Also shown are the piecewise constant interpolator and the cardinal spline interpolator. It is clear, that an increasing of the sampling distance leads to an undesirable result due to overlapping of the instrument transfer function. Therefore, it is absolutely important to choose the right sampling distance Δx.

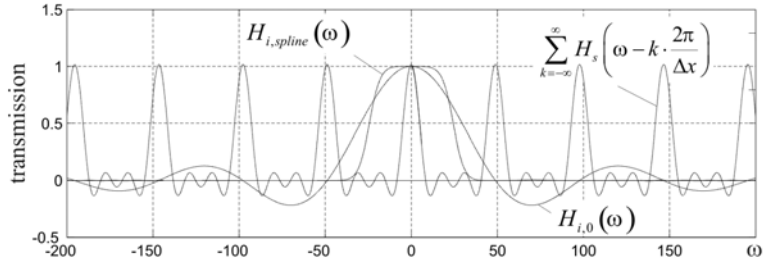

Fig. 5. Instrument transfer function of the scattered light sensor with a sampling distance $\Delta x = \pi/(5 \cdot \omega_c)$. Also shown are the transmission function of the constant piecewise interpolator and cardinal cubic spline interpolator

To illustrate a "ghost" shape, a stochastic slope distribution is considered and integrated using a piecewise constant interpolator (Fig. 6). For simplicity, the stochastic slope is a white gaussian noise with a standard deviation of $\sigma = 0.001$. The sampling distance is $\Delta x = 100\mu m$. The 95% confidence interval is given by $\varepsilon = 2 \cdot n^{1/2} \cdot \sigma \cdot \Delta x$ where $n \cdot \Delta x$ is the sampling position.

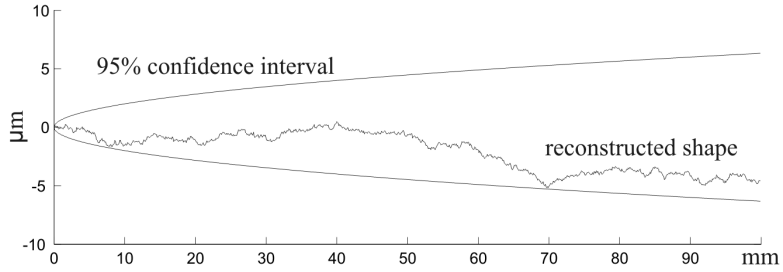

Fig. 6. Numerical integration (piecewise constant) of a white noise slope with $\sigma = 0.001$

4 References

1. Openheim, A. V.; Schafer R. W.: Discrete-time signal processing, Prentice Hall signal processing series, ISBN 0-13-754920-2
2. D. Petrinovic: Continuous time domain properties of causal cubic splines, Signal Processing 89 (2009) 1941–1958, Springer
3. De Boor, C.: A practical guide to splines, Applied mathematical sciences 27, Springer, ISBN 0-387-95366-3
4. Seewig, J.; Beichert, G.; Brodmann, R.; Bodschwinna, H.; Wendel, M.: Extraction of Shape and Roughness using Scattering Light, Spie, 2009

Metrological SPM with positioning controlled by green light interferometry

Josef Lazar[a], Petr Klapetek[b], Ondřej Číp[a], Martin Čížek[a], Jan Hrabina[a] and Mojmír Šerý[a]
[a] Institute of Scientific Instruments, Academy of Sciences of the Czech Republic, Královopolská 147, 612 64 Brno, Czech Republic
[b]Czech Metrology Institute, Okružní 31, 638 00 Brno, Czech Republic

1 Introduction

Dimensional metrology dealing with objects in the micro- and nanoworld relies predominantly on AFM (Atomic Force Microscope) and related local probe microscopy techniques where the object topology, dimensions and other properties are examined by scanning the sample. Positioning of the probe in AFM microscopes through piezoelectric (PZT) transducers offers sub-nm resolution but small range over several tens of micrometers. More, PZT transducers suffer errors of repeatability, non-linearity and hysteresis. Metrological AFM can be calibrated using etalon gratings or samples of height staircase type in the scale of hundreds or thousands of nanometers.

The problem of traceability [1] is a complex one where a system independent on an etalon samples should be linked directly to the primary etalon of length. This means employment of laser interferometry techniques for measurement of the probe position and taking care for all other sources of error starting with the uncertainty of the laser optical frequency [2]. Systems designed to follow this demand represent a setup mostly consisting of an AFM head, positioning stage and displacement measuring arrangement where a multiaxis laser interferometers dominate [3,4,5] but other approaches based on optical methods may represent suitable solution [6]. Measurement of the sample position in three orthogonal axes is sufficient when the guides of the stage can ensure negligible angle errors. Full control of the stage position should engage evaluation of tilting of the stage where non-contact optical methods a preferred [7]. A more complex interferometric measuring system needs also a complex approach to all sources of errors caused by angle deviations from orthogonality of the measuring beams, angle errors of reflecting surfaces, etc. [8]. Interferometric measuring techniques in dimensional

metrology are well established and represent a link between the fundamental etalon of length and mechanical measuring systems. Significant effort has been invested into improvement of their performance in the nanoscale through linearization of the fringe interpolation [9].

Transforming the local probe microscope from an imaging tool into a measuring system for metrological purposes means replacement of the often small scale positioning of the probe with an external stage moving the sample and interferometric monitoring or even control.

Laser interferometry seems to be a solution not only due to its direct traceability to the fundamental etalon of length but also the incremental interferometer in its fringe counting mode gives an excellent dynamic range limited only by the fluctuations of the refractive index of air and offers nanometer or even subnanometer resolution over large range. We concentrated onto a small range flexture three-axis nanopositioning stage equipped with closed-loop motion control with capacitive sensors embedded in a frame with six-axes interferometric system supplied from a stabilized single-frequency frequency doubled 532 nm Nd:YAG laser.

2 Positioning design

In the design presented here we concentrated on a commercial positioning stage with 200 x 200 x 10 μm travel and its enclosure into a frame containing interferometric displacement monitoring system. Full control of the stage and evaluation of all its positioning errors needs six-axis measurement. In our arrangement we equipped the stage with a top plate – a sample holder and a set of flat mirrors. It overlaps the stage and makes possible the measurement of the vertical displacement around the stage by three interferometers pointing upwards. Together with the mount of the local probe microscope the side view is in Figure 1. Thus the vertical position in the z-axis together with pitch and roll angles can be evaluated.

Horizontal measurement of x- and y- axes is ensured by three interferometers which allow also evaluation of the yaw. Interferometers are with flat-mirror reflector and a fixed corner-cube reflector in both reference arm and measuring arm. Double-pass arrangement enhances resolution in simple fringe-counting regime to $\lambda/4$ (Figure 2).

The resolution of the interferometric detection and data processing system here is 10 bit with 1 LSB being the 1/1024 of one cycle of the interferometric signal. Together with the double beam pass it results in $\lambda/4096$ which means for the 532 nm wavelength resolution 130 pm.

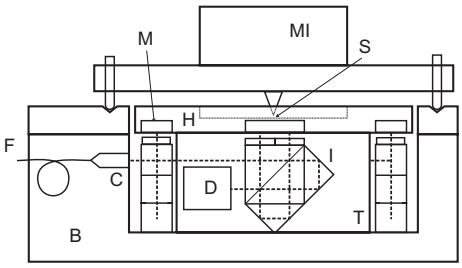

Fig.1. Side view of the stage with vertical interferometers, B: baseplate, MI: microscope, S: sample, F: fiber light delivery, C: collimator, H: sample holder, T: stage, I: interferometer, D: homodyne detection unit, M: mirror

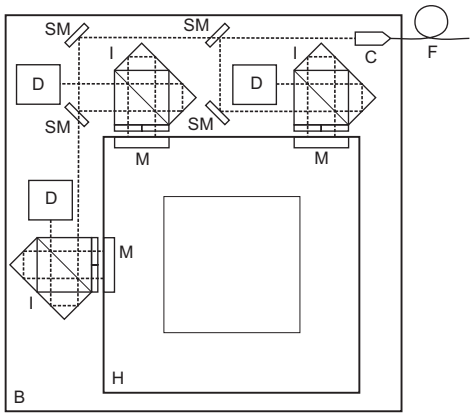

Fig. 2. Top view of the interferometric configuration with measurement in the x- and y-axes, SM: beam steering mirror, others see Figure 1

Compensation for the fluctuations of the refractive index in interferometric systems is traditionally ensured through the evaluation of the Edlen formula and under laboratory conditions results in relative uncertainty between 10^{-6} and 10^{-7}. Here when due to small dead length (0.1 mm) and travel range the maximum length of the measuring arm is 0.3 mm. The influence of the refractive index of air may prove significant only at the 0.3 nm level.

The small range of positioning ranging within 200 μm in the horizontal plane and only 10 μm in the vertical axis enhances the importance of the linearity of the scale. Linearity of the fringe division is further improved by software linearization algorithm embedded directly into the signal processing of the interferometer signal [10, 11]. With the shorter wavelength of the green laser (compared with the traditional 633 nm red He-Ne laser of commercial interferometers) another small resolution improvement was achieved.

The laser source is a 50 mW intracavity frequency doubled Nd:YAG laser operating in a single-frequency regime. The laser is stabilized through a linear spectroscopy in molecular iodine by locking to a Doppler broadened absorption transition R(56) 32-0. This follows the recommendations of CIPM [2] and ensures the traceability to fundamental etalon. Laser frequency locking is based on traditional derivative spectroscopy detection technique resulting in stability at the 10^{-8} level. The light delivery is here fibre-optic (Figure 3).

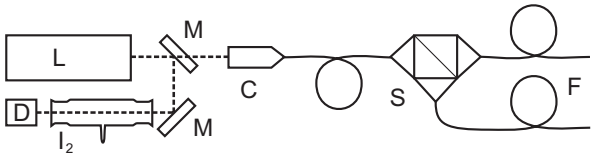

Fig. 3. Configuration of the laser with iodine cell for stabilization and fiber-optics, L: laser, M: mirrors, C: collimator, D: photodetector, I_2: iodine cell, S: beamsplitter, F: fibers

3 Evaluation and testing

The system performance was tested through calibration grating at the Czech Metrology Institute in Brno. A two-dimensional grating with 2 μm steps was selected. The evaluation of overall uncertainty included verification of the laser wavelength by a calibrated wavemeter and comparison of the grating dimensions derived from measurement via the metrological AFM and through laser diffraction technique. The image of a fraction of the grating is in Figure 4 together with a typical profile in the x-axis.

Evaluation of the grating spacing was done by comparing of the position derived from built-in capacitive sensors and position measured through the interferometric frame. Laser based diffraction technique allowed measurement of the overall value of the groove spacing with small uncertainty compared to statistical evaluation of average value from AFM measurement. Results are summarized in table 1.

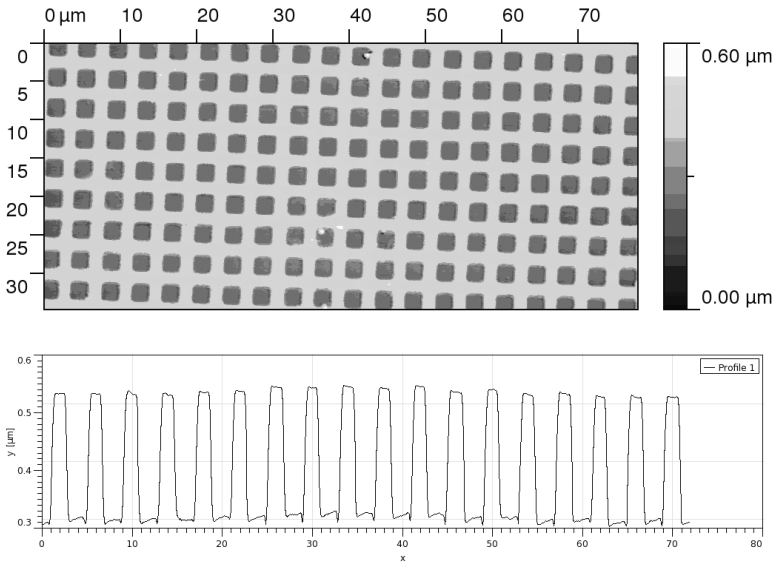

Fig. 4. Image of the grating under test together with a cross-section of the profile

Table 1. Spacing of the measured grating with estimated statistical uncertainty

	capacitive sensors	interferometer	diffraction
x-direction	3995 ± 6 nm	4001 ± 6 nm	3996.7 ± 1.8 nm
y-direction	4002 ± 10 nm	4001 ± 10 nm	3994.2 ± 1.1 nm

Statistical uncertainty associated with the AFM measurement either through capacitive sensors or interferometers includes angle errors caused by non-linear motion of the stage. Together with uncertainty of the coincidence of the measuring tip and measuring axes of the interferometers this introduces additional errors. Further improvement towards closed-loop operation derived from the interferometers will help significantly. Especially the correction of angle deviations which needs introduction of small-range PZT transducers controlling pith, roll and yaw angles.

4 Acknowledgements

The authors wish to express thanks for support to the grant projects from Ministry of Education, Youth and Sports of CR, projects No.: LC06007, 2C06012, the AS CR, projects No.: AV0 Z20650511, Ministry of Industry

and Commerce, projects No: 2A-1TP1/127, FT-TA3/133, 2A-3TP1/113 and GA CR, projects: GA102/09/1276, GA102/07/1179.

5 References

1. Korpelainen V and Lassila A (2006) Calibration of a commercial AFM: traceability for a coordinate system, Meas. Sci. Technol., 18: 395-403
2. Quinn T J (1992) Mise en pratique of the definition of the metre, Metrologia 1993/94, 30: 523-541
3. Jäger G, Gruenwald R, Manske E, Hausotte T and Fuessl R (2004) A nanopositioning and nanomeasuring machine: operation—measured results Nanotechnology and Precision Engineering 2: 81-4
4. Weckenmann A, Hoffmann J and Schuler A (2008) Development of a tunnelling current sensor for a long-range nano-positioning device, Meas. Sci. Technol. 19: 064002, 7pp
5. Dai G, Pohlenz F, Min Xu, Koenders L, Danzebrink H U and Wilkening G (2006) Accurate and traceable measurement of nano- and microstructures, Meas. Sci. Technol., 17: 545–552
6. Otsuka J, Ichikawa S, Masuda T, et al. (2005) Development of a small ultraprecision positioning device with 5 nm resolution, Meas. Sci. Technol., 16: 2186-2192
7. Kim J W, Kang C S, Kim J A, et al. (2007) A compact system for simultaneous measurement of linear and angular displacements of nano-stages Optics Express, 15: 15759-15766
8. Koops K R, van Veghel M G A, Kotte G J W L and Moolman M C (2007) Calibration strategies for scanning probe metrology, Meas. Sci. Technol., 18: 390–394
9. Hou W and Wilkening G (1992) Investigation and compensation of the nonlinearity of heterodyne interferometers, Prec. Eng, 14: 91-98
10. Číp O and Petrů F (2000) A scale-linearization method for precise laser interferometry. Meas. Sci. Technol., 11: 133-141
11. Petrů F and Číp O (1999) Problems regarding linearity of data of a laser interferometer with a single frequency laser. Precision Engineering, 23: 39-50

Measuring Shape and Surfaces down to the Nanometer and Nanosecond scales by Digital Holographic Microscopy

Christian Depeursinge[1], Isabelle Bergoënd[1], Nicolas Pavillon[1], Jonas Kühn[1], Tristan Colomb[2], Frédéric Montfort[2], Etienne Cuche[2], Yves Emery[2],
[1]Ecole Polytechnique Fédérale de Lausanne (EPFL), Advanced Photonics Laboratory, CH-1015 Lausanne, Switzerland
[2]Lyncée Tec, SA, PSE A, CH-1015 Lausanne, Switzerland

1 Introduction

Digital Holographic Microscopy (DHM) is an imaging technique that allows measuring quantitatively the wavefront transmitted through or reflected by a microscopic specimen. A hologram, composed by the interference of the wave scattered by the object with a generated reference wave, is recorded with a digital camera and then numerically processed to extract both the amplitude and the phase the wavefront with a very high accuracy. When evaluated in the spatial and / or in the time domain, the phase of the reflected wavefront yields the topography of the specimen with an accuracy around one nanometre. This ultra-high accuracy can be preserved in the measurement of dynamic phenomena by exploiting the capability to acquire a single hologram in a very short period of time defined either by the acquisition time of the camera which can be as low as a few microseconds and / or by the recourse to a pulsed source which can be as short as a few nanoseconds or even less with femtosecond lasers. Indeed, a single hologram taken in the off-axis configuration permits to reconstruct the complex wavefront and therefore to measure the phase, perfectly resolved in time. The applicability of DHM to metrology is also facilitated by the remarkably high measurement stability and robustness of DHM.

2 Measuring technique

In order to demonstrate the ultrahigh accuracy of time and space dependence of the specimen topography, measurements were made on a cantilever with a reflection DHM set-up, based on a modified Michelson

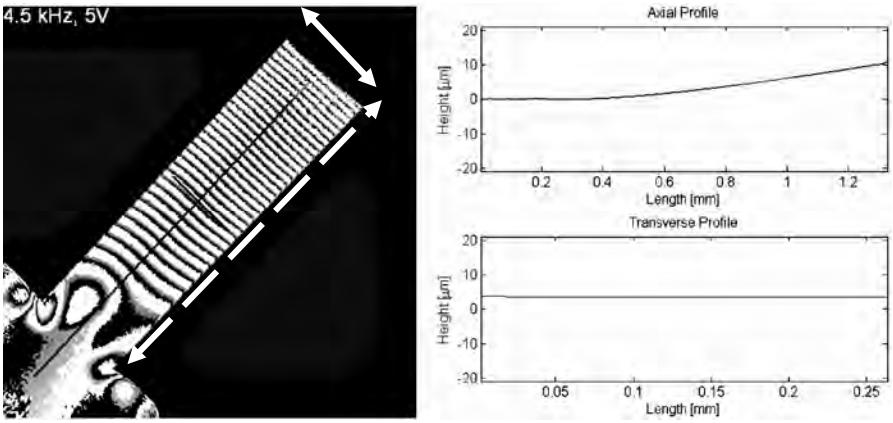

Fig. 1. Wrapped phase image of a cantilever excited at 4.5 kHz. The diagrams of the right part of the figure show the axial and transverse profile of the cantilever displacement after phase unwrapping

interferometer. As a bright field technique, DHM permits a high acquisition rate only limited by the performance of the camera, which can reach several tens of thousand holograms per second, and therefore permits fast, non-repetitive dynamics to be measured: transients can be measured with a few tens of microseconds resolution. In the case of a repetitive process, such as a vibration or an oscillation, stroboscopic mode can be used to image deformations for up to several tens of MHz excitation frequencies: 25 MHz in our case, by synchronizing the camera acquisition and / or the illuminating source with the micro-device driving signal.

The optical topography can be captured along the whole movement cycle of the micro-device. The retrieval of the full three-dimensional information with a nanometre vertical resolution is therefore possible with very high temporal resolution, ranging down to the nanosecond scale.

3 Experimental results

The example of a cantilever is given, illuminated with a laser diode (λ = 682 nm), the image being recorded in the Fresnel zone with a charge-coupled device (CCD) camera with 20x magnification,. The hologram was reconstructed with spatial filtering method. The complex wavefront was digitally propagated into focus with a numerical implementation of the Fresnel integral [1, 2].

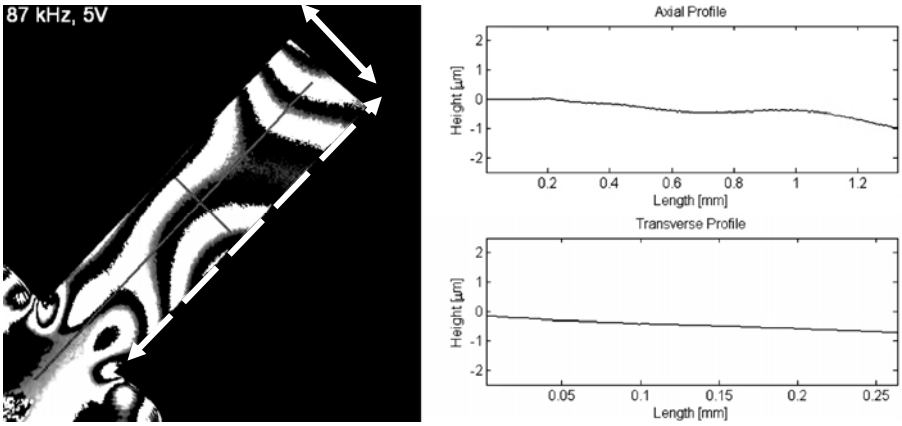

Fig. 2. Wrapped phase image of a cantilever excited at 87 kHz. The diagrams of the right part of the figure show, after phase unwrapping, the axial and transverse profiles of the cantilever displacement

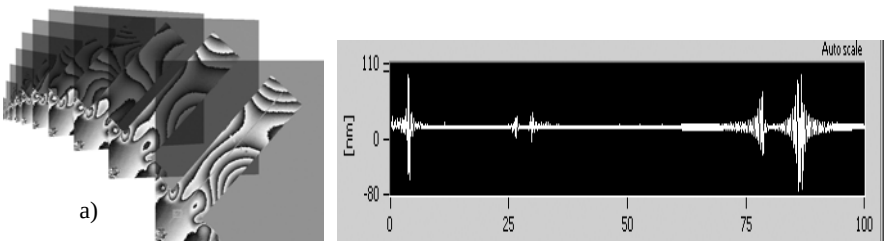

a)

b) Frequency (kHz)

Fig. 3. a) Synthetic phase images of the cantilever at various excitation frequencies. b) Amplitude response as a function of excitation frequency

The topography of the cantilever at the time of maximum extension is illustrated on Fig. 1: the axial and transversal profile show the monomodal character of the vibration. Fig. 2. shows the same axial and transversal

profile of the cantilever vibrating at 87 kHz: the complex shape reveals a complex multimodal regime.

The analysis of the resonant frequencies and modal decomposition of the cantilever deformation can be achieved by a frequency scan of the exciting signal. This is illustrated on Fig. 3: the different resonances appear on the amplitude signal as a function of the frequency.

The particularities of the cantilever topography at 87 kHz are presented in Fig. 4. The coupling between different modes is visible from the quantitative measurement of the topography.

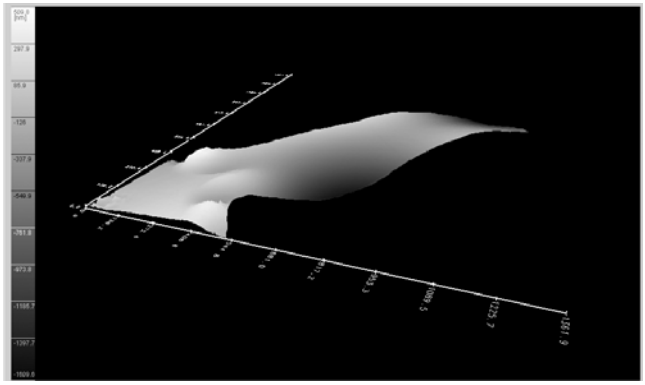

Fig.4. 3D representation of the topography of the cantilever at 87 kHz

4 Conclusion

By the analysis of the resonant frequencies of micro-structures like cantilevers, flexure joints, micro-bridges or membranes, one can evaluate the geometrical factor effects, the Young's modulus, the mean residual stresses, and some particular effects such as the effect of air damping, or the study of micro-systems ageing. The calibration of displacement is simple: vertical calibration only depends on the wavelength, which ensures an accuracy that is intrinsically not limited by the precision of the mechanical control of moving parts. When developing MEMS and MOEMS, there is a constant need to efficiently compare numerical simulations to the real micro-device movements and to adapt the production process by modifying geometric characteristics. The method can be applied to the observation of the movement of a micromechanical system: MEMS, MOEMS: oscillating micro-mirrors for example. The method can be also applied to the observation of the mechanical wave propagation in a medium.

5 Acknowledgements

Part of this work has been supported by the European Project Real 3D. The authors would like to thank their colleagues in the MVD Group and in Lyncee Tec SA (www.lynceetec.com) for their cooperation and several fruitful discussions.

6 References

1. Depeursinge, C (2006) Digital Holography applied to Microscopy, in Digital Holography and Three-Dimensional Display: Principles and Applications. S.S.B. Media, TC Poon Editor., Springer Science+Business Media: New York.
2. Cuche, E, Marquet, P, Depeursinge, C (1999) Simultaneous amplitude-contrast and quantitative phase-contrast microscopy by numerical reconstruction of Fresnel off-axis holograms. Applied Optics 38:6994-7001

Deflectometry: 3D-Metrology from Nanometer to Meter

G. Häusler[1,2], M. C. Knauer[1], C. Faber[1], C. Richter[1], S. Peterhänsel[1], C. Kranitzky[1], K. Veit[2]
[1]Institute of Optics, Information and Photonics, University of Erlangen-Nuremberg, Staudtstr. 7/B2, 91058 Erlangen, Germany
[2]3D-Shape GmbH, Henkestr. 91, 91052 Erlangen, Germany
Author e-mail address: haeusler@physik.uni-erlangen.de

1 Introduction

Deflectometry offers a wide spectrum of applications. The intrinsic features of deflectometry made this technique popular over the last years [1, 2, 3]. Deflectometry enables to measures the local slope of specularly reflecting objects with high information efficiency. It is possible to measure structures quantitatively in the nanometer regime. Due to incoherent illumination the data display no coherent noise.

The standard setup is suited for measurements in reflection. Applications have been the measurement of the surfaces of eyeglass lenses, mirrors or reflectors. As well, the measurement of the reflection-optics of car windshields had been an interesting application.

Recently we adapted deflectometry for measurements in transmission at macroscopic and microscopic scale to expand the possible range of applications.

2 Sensor Principle

“Phase-measuring Deflectometry” (PMD) meanwhile is well established to measure specular surfaces in reflection [4]. Hereby a sinusoidal fringe pattern at a remote distance from the object is observed using the object under test as a mirror. Depending on the local slope of the object the observed pattern is disturbed (see Fig. 1). With this setup local surface details in the nanometer regime can be measured quantitatively. With the local slope as the primary data we can determine the height of the object by numerical integration [5] and the local curvature of the object by differentiation. Some major applications are the measurement of

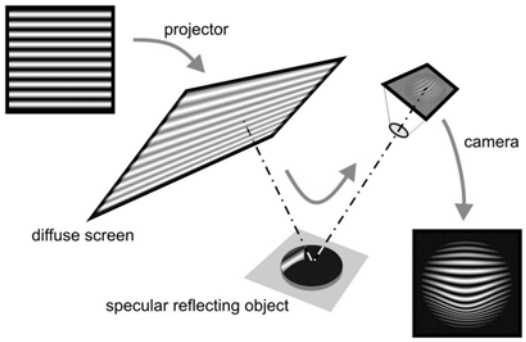

Fig. 1: Principle of Phase-measuring Deflectometry in reflection

progressive eye glasses or the “reflection-optics” of car glass windows. Beside this aesthetic-relevant aspect of the “reflection-optics” it is also necessary to measure the security-relevant refractive power of car windows. This has to be done in transmission. The question was if it is possible to setup PMD in transmission to provide a more accurate and traceable method in addition to the existing one [6]. The basic principle (see Fig.2) is very similar to that in reflection. It again consists of a sinusoidal pattern which is observed by the camera through the transparent object. The distortion of the pattern depends on the local prismatic action of the object under test. To test this setup we measured a whole set of lenses from -250 to 250 mD. The lenses were calibrated by the National Physical Laboratory (UK). The values measured by our PMD correspond to the nominal values with an error better than 1 mD. With this setup suspicious areas of a windshield were measured. In Fig. 3 you can see an example measurement with a defect in the windshield. Having the whole curvature tensor it is possible to distinguish the so called float drawlines (visible in the x-direction) from other details.

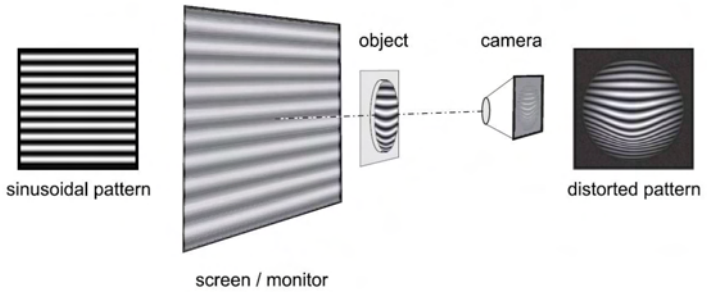

Fig. 2: Principle of Phase-measuring Deflectometry in transmission

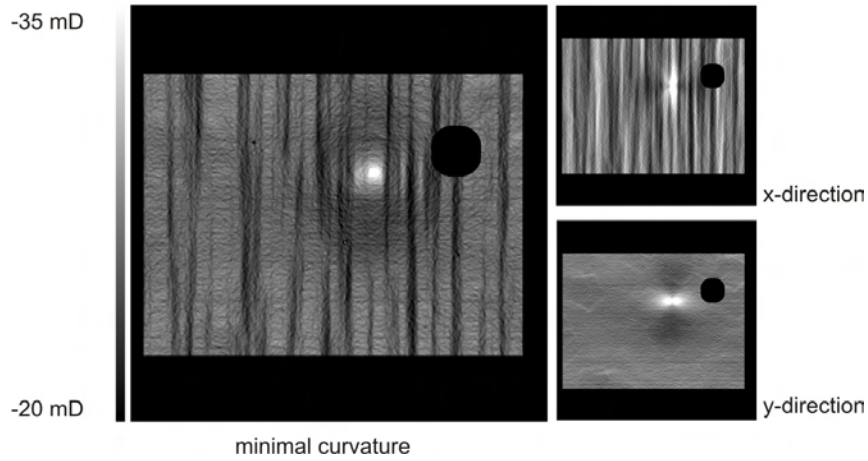

Fig. 3: Defect on a windshield. Different types of artefacts are encoded in the local refractive power.

3 Microscopic Setup

Adapting the principle to measure fields down to 100 µm opens the benefits of PMD to new applications. These are, for example, the measurement of cutting tools, MEMS, wafers and biological samples. Using objectives with high numerical aperture and high lateral resolution many surfaces which are matt in the macroscopic regime display specular reflection. For the realization of microdeflectometry we had to change the whole setup. Because of the small working distances of the microobjectives we can no longer use a diffuse remote screen for fringe projection. Instead we project an aerial image of a fringe pattern at a remote distance to the object.

3.1 Microdeflectometry in reflection

In the setup for measurements in reflection we use the same micro objective for projection as for observation [7].Figure 4 depicts a schematic setup for measuring in reflection. The fringe pattern is generated by an electronically controllable light modulator. The setup enables an incoherent and coaxial illumination with low optical noise and no shadowing. Using objectives with high numerical aperture enables measurements with high lateral resolution and big angular range up to ±60°. For a PMD measurement it is necessary that the measured phase in

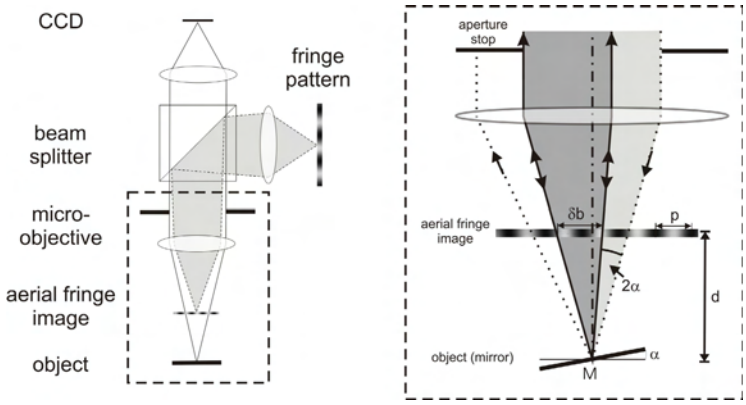

Fig. 4: Schematic setup of microdeflectometry in reflection

an object point M depends on the local slope of the object. This is true for microdeflectometry as well. The schematic imaging of one object point M is as follows. The cone of imaging rays is represented by the dark gray area. The observed image intensity is given by the intensity within this cone, averaged over the distance δb. The tilted object causes vignetting and the rays within the light gray cone do not contribute to imaging. The cone of imaging rays depends on the slope α. Hence the observed phase φ depends on the slope, with $\varphi = 2\pi d\alpha/p$. Due to the vignetting, microdeflectometry is only half as sensitive as macroscopic deflectometry.

Regarding the physical limitations an uncertainty relation was derived [4]. Equation (1) reveals that the measuring uncertainty δa is connected with the lateral resolution δx. With smaller δx (with higher numerical aperture)

$$\delta\alpha \cdot \delta x = \frac{\lambda}{Q} \tag{1}$$

the measuring uncertainty $\delta\alpha$ will increase. Q is a quality factor and depends on the camera noise and is approximately 1000 in our setup. If we put this in Eq. (1) we get roughly:

$$\delta\alpha \cdot \delta x \approx 1nm \tag{2}$$

Equation (2) reveals that the minimum height variation δz that can be detected within the diffraction-limited resolution distance of the microscope is constant and in the range of only 1 nm. This equation is not only valid for microdeflectometry but also for the macroscopic setup as

well (There are systems for slow pointwise macroscopic measurement [8] with $Q > 10^6$ and, hence, with a much smaller δz). Also the measuring uncertainty is independent from the distance of the fringe pattern to the object. This as well is valid for both setups.

3.2 Microdeflectometry in transmission

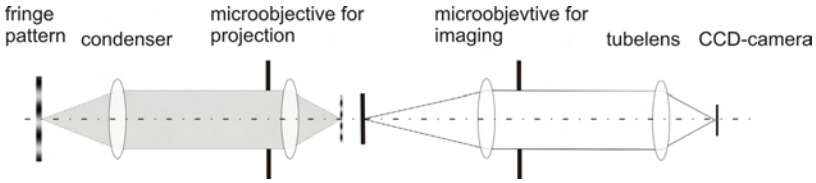

Fig. 5: Schematic principle of microdeflectometry in transmission

For the transmissive setup we need two micro objectives, one for projecting the fringe pattern and one for observing the object. In Figure 5 a scheme of the setup is depicted. The signal generation is quite similar to the setup in reflection and exploits the vignetting caused by the local prismatic action of the object. This can be induced by local structures on the surface of the object or by changes of the refractive index of the transparent material. The appearance of the results can be compared with differential interference contrast, phase contrast and some new microscopic techniques [9]. In Figure 6 you can see an example measurement of a biological sample. On the left image an intensity image of a hookworm is depicted. On the right side the deflectometric measurement is shown. You can see an intensity-encoded gradient image in x-direction. The visible structures are caused by a jump in the refraction index at the membranes of the cells. The advantage of microdeflectometry in transmission is that histological specimen can be measured without staining and that it is possible to obtain quantitative data.

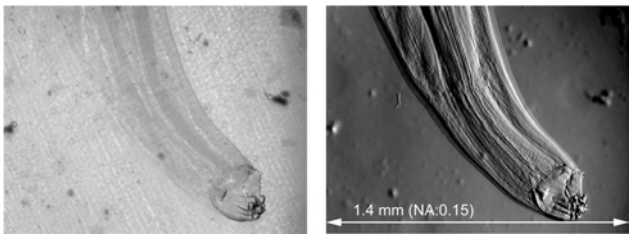

Fig. 6: Left: Light microscope image of a hookworm. Right: Intensity-encoded gradient in x-direction.

4 Conclusion

The principle of deflectometry is simple and offers interesting, maybe unique, features. We demonstrated that deflectometry can be scaled to measure the local slope of specularly reflecting surfaces from µm-size to meter-size. The minimal detectable height variation within the lateral resolution is less than 1 nm for all systems. The sensor can also be set up to measure in transmission. Here it can be used to measure the local refractive power with an accuracy of less than 1 mD. It can also measure the local changes of the refraction index in the range of 0.05 within the lateral resolution cell.

5 References

1. R. Ritter, R. Hahn: Contribution to analysis of the reflection grating method. Optics and Lasers in Engineering 4(1): 13-24 (1983)
2. G. Häusler: Verfahren und Vorrichtung zur Ermittlung der Form oder der Abbildungseigenschaften von spiegelnden oder transparenten Objekten, Patent: DE19944354 (1999)
3. T. Bothe, W. Li, C. Kopylow, W. Jüptner: High Resolution 3D Shape Measurement on Specular Surfaces by Fringe Reflection. Proc. Spie 5457: 411-422 (2004)
4. M. Knauer, J. Kaminski, G. Häusler: Phase Measuring Deflectometry: a new approach to measure specular free-form surfaces. Proc. SPIE 5457: 366-376 (2004)
5. S. Ettl, J. Kaminski, M. C. Knauer, G. Häusler: Shape reconstruction from gradient data. Applied Optics 47(21): 2091-2097 (2008)
6. C. G. Masi: Moiré interferometry spots windshield defects. Vision Systems Design 7(10) (2002)
7. G. Häusler, C. Richter, K.-H. Leitz, M. C. Knauer: Microdeflectometry – a novel tool to acquire 3D microtopology with nanometer height resolution. Opt. Lett. Vol. 33: 396-398 (2008)
8. R. D. Geckeler, I. Weingärtner: Sub-nm topography measurement by deflectometry: flatness standard and wafer nanotopography. Proc. SPIE 1779, 1-12 (2002)
9. S. B. Mehta, C. J. R. Sheppard: Asymmetric illumination based differential phase contrast (AI-DPC) for full field transmission imaging of phase information in biological specimens. Focus on Microscopy 2008 (Awaji, Japan)

3-D Sensing for Microstructures Using Dynamic DOEs

Shihao Dong, Xiang Peng*, Yingjian Guan, Ameng Li, Yongkai Yin, and Jindong Tian
College of Optoelectronics Engineering
Key Laboratory of Optoelectronic Devices and Systems, Education Ministry of China, Shenzhen University, 518060 Shenzhen, China
Corresponding author: xpeng@szu.edu.cn

1 Introduction

Optical 3-D shape measurement technique based on fringe projection profilometry (FFP) has become one of the most popular methods in many application areas such as industrial inspection, robot vision, reverse engineering, to name just a few [1]. In particular, a suitably designed FPP sensing technique is also applicable for the automatic inspection of microstructures. With FPP optical sensing technique, one is possibly able to achieve high throughput and high accuracy inspection with respect to 3-D shape microstructures as used in microelectronics industry.

There are several possibilities to generate desired fringe pattern(s) for structured illumination in the FPP scheme. For example, a laser interferometer or a digital light processing (DLP) projector can be applied for this purpose. However, in the case of using laser interferometer as a structure light generator, the stability to vibration and other turbulences caused by the working environment are critical issues to be addressed whereas using digital projectors to generate structural light illumination, the depth of field (DOF) is limited during practical measurement and the optical engine design is relatively complex although digital projector is flexible to deliver required patterns for the illumination.

Recently, several fringe generating techniques have been studied to overcome above drawbacks. Su et al[2] reported a novel fringe projection approach based on holographic strategy for large-scale object measurement, in which a hologram was used to record the sinusoidal pattern and the desired fringe pattern was then generated by launching a conjugate beam into the hologram. This holography-based fringe projection technique could achieve large DOF, however, the recording and reconstruction of desired fringe pattern were sensitive to the turbulences

and system configuration. Lubeley[3] proposed another useful method using a liquid crystal spatial light modulator LC-SLM as a dynamic phase grating to generate points array by employing an iterative Fourier transform approach. In this work, an optimization algorithm for modifying points array to eliminate ambiguities was further introduced.

In this paper, we present a method to generate a series of desired fringe patterns using dynamic diffractive optical elements (DDOE) designed with help of phase retrieval technique under a platform of phase-only SLM (PO-SLM). The PO-SLM can be viewed as a dynamic optical device that allows for the generation of any arbitrary structural light illumination by appropriate design. Combined fringe projection with stereo vision arrangement, the DDOE concept can realize multi-sensing mechanism for 3D measurement.

The rest of paper is organized as follows: Section 2 investigates the phase retrieval method for DDOE design. Section 3 introduces the system configuration using PO-SLM as a dynamic fringe generator. Section 4 presents a set of experimental results to show the effectiveness of proposed method. Section 5 concludes the paper.

2 DDOE Design Using Modified Gerchberg-Saxton (GS) Algorithm

The GS [4] algorithm has been widely used to design DOE. GS algorithm aimed at calculating the phase distribution $\phi(x,y)$ from intensity measurement(s), $I(u,v)=\left|f(u,v)\right|^2$. The GS algorithm is an iterative scheme and its implementation can be summarized and illustrated in Fig. 1.

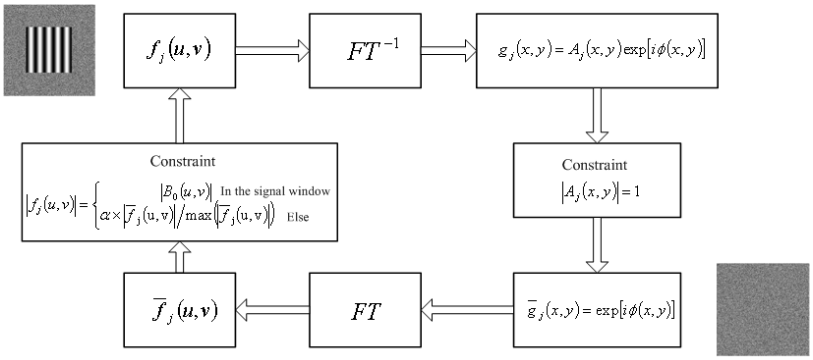

Fig. 1. Flowchart of GS algorithm

The GS algorithm involves Fourier transforms back and forth between the object and Fourier domain, satisfying the constraints in each domain. In our approach, PO-SLM is used as phase-only modulation element. The convergence of the algorithm can be monitored by computing the mean square error or restricting the iteration times. It is found that an appropriate support strategy could achieve an optimized solution with consideration of the balance between the image quality and diffraction efficiency.

In order to evaluate this algorithm, a sinusoidal pattern with size 200×200 pixel is taken as target image. We calculate the phase distribution of DOE from this target image. The DOE size is set to 256×256 pixel. Fig.2 (a) and Fig.2 (b) show the calculated phase distribution and its diffraction pattern, respectively. Fig.2(c) shows the cross section of desired fringe pattern. It is worthy noting that this method allows for generating arbitrary desired patterns with help of phase retrieval technique.

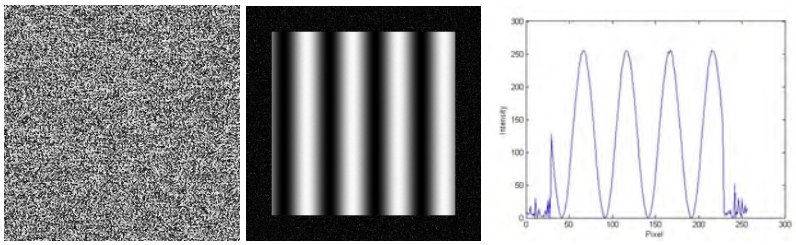

Fig. 2. Computed results using modified GS (a) phase distribution (b) diffraction pattern of DOE (c) cross section data of (b)

3 Fringe Projection Using PO-SLM as DDOE

PO-SLM has already shown the importance in optical information processing. An optimization phase-only modulation can be achieved with special care to adjust the rotation angles of the polarizer and analyzer [5]. In our approach, the PO-SLM serves as a DDOE that is used to generate desired fringe patterns. As shown in Fig.3, a PO-SLM was employed in conjunction with two cameras, leading to a special FPP system. This setup was mainly composed of (1) A laser source (2) Polarizer (3) PO-SLM (4) Analyzer (5) Imaging Lens (6) Cameras and PC. In this setup, the phase distribution computed for DDOE was pre-stored in the memory and addressed on the SLM. The desired diffraction pattern that can be used for structured light illumination was generated at the back of focal plane of the

lens. The size and position of diffraction pattern can be adjusted according to the focus length and position of imaging lens.

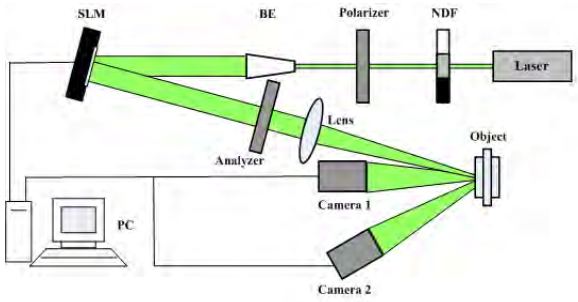

Fig. 3. Setup of Modified diffraction based fringe projection system

Compared with other FPP scheme, the proposed scheme is simple since no complex optical engine is needed, providing a compact fringe generator. Moreover, because the desired pattern is formed based on the diffraction theory, the presented system can be stable against turbulence caused by working environment. With aid of phase retrieval technique, arbitrary light pattern can be generated for realizing multi-sensing applications.

4 Experimental Results and Discussion

To verify the proposed 3D sensing system, we carried out some experiments with the configuration illustrated in Fig.3 where LC-R 2500 reflective SLM from HOLOEYE was used for generating dynamic DOEs. The SLM is controlled by a PC with 2.00 GHZ CPU and 1 GB of main memory. The generated fringe patterns are captured by two DH-1303UM industrial cameras with resolution of 1024×1280 pixels.

A calibration procedure is firstly needed in order to obtain accurate measurement results from DDOE-FPP scheme [6]. With aid of MATLAB Calibration Toolbox provided by Bouguet [7], the binocular system was easily and accurately calibrated with a planar calibration target. Then, we carried out a real inspection for Ball Grid Array (BGA) on a printed circuit board (PCB) where a few solder pastes were missing and the shapes of those solder pastes could be identified not being uniform. The experiment result was shown in Fig.4 (a) and Fig. 4 (b) show the performance of proposed approach. In order to reduce the effect of speckle noise on the phase calculation of captured fringe patterns, filtering techniques were

employed to preprocess the degraded fringe pattern. The 3D coordinates of BGA were calculated using triangulation procedure with calibrated system parameters and absolute phase maps on the retinal plane of two cameras.

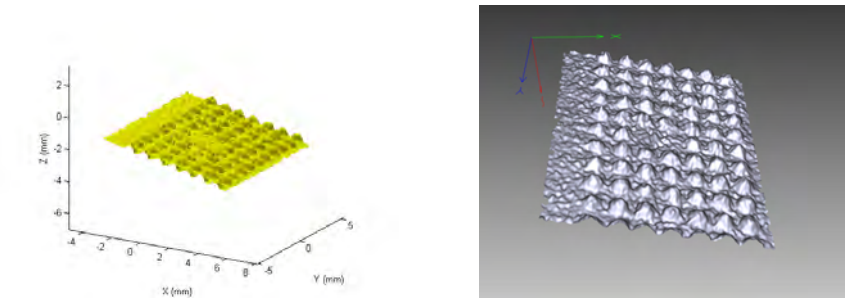

(a) (b)

Fig. 4. Inspection results of BGA (a) 3D coordinates (b) 3D plot

5 Conclusion

In this paper, we have presented a 3D sensing scheme that combines binocular vision and fringe projection. A phase-only modulation SLM serves as a dynamic DOE to form a fringe pattern generator. The homologous points on both cameras can be accurately figured out with help of absolute phase encoding. Experiment results for the inspection of BGA on a PCB show the effectiveness of presented approach.

6 Acknowledgements

This work is supported by the National Natural Science Foundation of China (grant 60775021), the Science & Technology Bureau of Shenzhen (grant 200734) and the Nanshan Scientific and Technology Project. The authors would like to thank Professor Wolfgang Osten, Professor Hans Tiziani, Dr. Tobias Haist, Dr. Klaus Körner and other colleagues at Institute of Applied Optics (ITO) of Stuttgart University for their helpful comments, suggestions and discussions.

7 References

1. Carsten Reich, Reinhold Ritter, Jan Thesing (2000) 3-D shape measurement of complex objects by combining photogrammetry and fringe projection. Optical Engineering 39: 224-231
2. Wei-Hung Su, Wei-Jen Chen, Jun-Shan Huang, Cho-Yo Kuo (2006) Projected fringe profilometry using a hologram for the objects with large depth discontinuities. Proc. of SPIE 6314: 1-12
3. Dominik Lubeley (2007) Unambiguous Dynamic Diffraction Patterns for 3D Depth Profile Measurement. DAGM 4713: 42-51
4. R. W. Gerchberg, W. O. Saxton (1971) Phase determination from image and diffraction plane pictures in the electron microscope. Optik 34: 275-284
5. Christian Kohler, Tobias Haist, Wolfgang Osten (2009) Model-free method for measuring the full Jones matrix of reflective liquid-crystal display, Optical Engineering, 46: 044002.
6. Zhengyou Zhang (1998) A Flexible New Technique for Camera Calibration, Technical Report, MSR-TR-98-71, Microsoft Research
7. Jean-Yves Bouguet, Camera Calibration Toolbox for Matlab http://www.vision.caltech.edu/bouguetj/calib_doc/

Doppler phase-shift fringe analysis and digital holography using high-speed digital camera

Toyohiko Yatagai and Daisuke Barada
Center for Optical Research and Education,
Utsunomiya University
Yoto 7-1-2, Utsunomiya, Tochigi 321-8585, Japan

1 Introduction

Interference fringe analysis is one of the most powerful tools in shape measurement, deformation and vibration analysis in many engineering fields. Digital holography has been anticipated as three-dimensional imaging and shape measurement techniques. In both methods, high speed interference fringe analysis is strongly desired. Many techniques have been developed, including instantaneous phase-shifting, pixelated mask spatial carrier phase shifting and so on.

In this paper, a new technique is proposed, in which a phase-shifting algorithm utilizing the optical Doppler effect and a high-speed CMOS camera are employed. In many phase-shifting algorithms, the phase distribution of the object is calculated by using a few reference phases with equal phase difference. In our proposed method, the arbitrary shift, including linear continuous and random phase, is introduced. The resultant phase difference between the object and the reference beams by vibrating an optical system can also be regarded as the phase-shifting introduced by the optical Doppler effect. The phase distribution of the object is calculated by Fourier transforming the time-depending interference fringe data. If the reference phase shift is equally introduced to all the data points in the interference fringe image, the phase distribution at the peak frequency component in the Fourier spectrum gives the phase distribution of the object[1]. Since a few hundred or more images were required in this method, a CMOS camera with a high frame rate of 500fps was used.

2 Doppler phase analysis

Figure 1 shows the optical system for our method. Complex amplitudes of an object beam U_O on a reference beam U_R on a CMOS camera are expressed by

$$U_U(x,y,t) = A_o(x,y)\exp\{i[\phi_o(x,y,t) - \omega_o(t)t]\} \quad (1)$$

$$U_R(x,y,t) = A_R(x,y)\exp\{i[\phi_R(t) - \omega_R(t)t]\} \quad (2)$$

where A_o, A_R, ϕ_o, ϕ_R, ω_o and ω_R are amplitudes, phases, and angular frequencies of object and reference beams, respectively. Each phase is shifted by moving a reference mirror or vibrating the optical system. The angular frequencies are difference between the object and reference beams because of optical Doppler effect as

$$\omega_o(t) = \omega_0\sqrt{\frac{1+v_0(t)/c}{1-v_0(t)/c}}, \quad (3)$$

$$\omega_R(t) = \omega_0\sqrt{\frac{1+v_R(t)/c}{1-v_R(t)/c}} \quad (4)$$

where ω_o, c, v_o, v_R and ω_R are the frequency of incident beam, the speed of light, and the velocities of the target object and reference mirror, respectively. The intensity recorded by the CMOS camera is expressed by

$$I(x,y,t) \propto |U_O(x,y,t) + U_R(x,y,t)|^2$$

$$\propto A_C^2(x,y) + A_R^2 + 2A_oA_R\cos[\Delta\phi(x,y) - \Delta\omega(t)t]\} \quad (5)$$

$$\Delta\phi(x,y) = \phi_o(x,y) - \phi_R(x,y) \quad (6)$$

$$\Delta\omega(t) = \omega_0(t) - \omega_R(t) \quad (7)$$

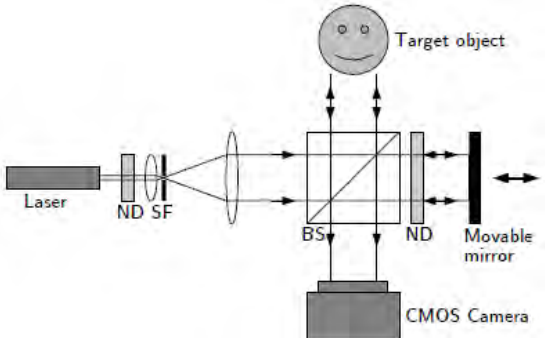

Fig. 1. Optical system for Doppler phase shift interferometer.

The time-domain Fourier transform $F[..]$ of Eq. (5) is expressed by

$$F[I](x,y,\omega) = [A_C^2(x,y) + A_R^2]\delta(\omega) + A_O A_R a_1(\omega)\exp\{i[\Delta\phi(x,y) - b_1(\omega)]\} + A_O A_R a_r(\omega)\exp\{i[\Delta\phi(x,y) - b_r(\omega)]\} \quad (8)$$

where a_1, a_r, b_1, and r are arbitrary functions of frequency. When $\omega = \omega_1$ at $a_1(\omega_1) \neq 0$ and $a_r(\omega_r) = 0$, only the wavefront of the object beam can be extracted as

$$F[I](x,y,\omega) \propto A_O(x,y)\exp\{i[\Delta\phi(x,y) + C(\omega_1)]\} \quad (9)$$

Therefore, the wavefront of the object beam on the target object can be obtained by diffraction calculation as

$$U'_O(x',y') = \frac{i}{\lambda}\iint_{-\infty}^{\infty} F[I](x,y,\omega_1)\frac{\exp(-i\sqrt{(x-x')^2+(y-y')^2+d^2})}{\sqrt{(x-x')^2+(y-y')^2+d^2}}dxdy \quad (10)$$

where λ and d are the wavelength of object beam and diffraction length, respectively. The intensity I' and phase ϕ'_O images of the target object are obtained by

$$I'(x',y') = |U'_O(x',y')|^2 \quad (11)$$

$$\phi'_O(x',y') = \arg[U'_O(x',y')] \quad (12)$$

3 Experimental results

In experiment, a Japanese one-yen coin was used as a target object. A He-Ne laser (632.8 nm) was used for recording. The frame rate of the CMOS camera is 500 fps. Figure 2 and 3 show the experimental results. In the experiment of Fig. 2, only the reference mirror on a motor stage was moved in the constant velocity. Figure 2 (a) shows the velocity spectrum. The velocity difference between the target object and reference mirror were changed from frequency [Eq. (7)]. The wavefront of the target object on the CMOS camera is calculated by discrete Fourier transform (DFT) at the velocity difference of 10.3 μm/s using 216 images. The intensity pattern of the diffracted beam from the wavefront on the CMOS camera is shown in Fig. 2 (b). A zeroth order spot and a conjugate image was removed using our method.

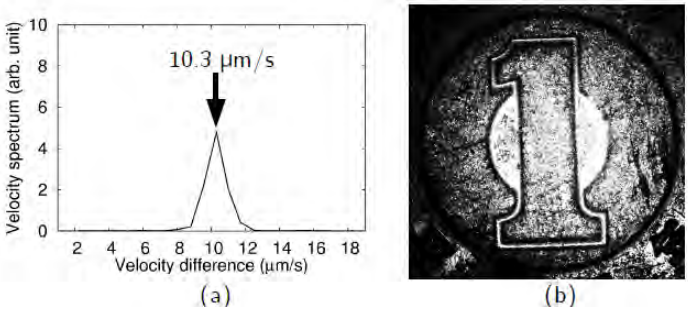

Fig. 2. Experimental result in the case of only shifting the reference mirror. (a) is the velocity spectrum versus the velocity difference between the target object and reference mirror. (b) is the intensity pattern of the diffracted beam where the zeroth order spot and conjugate image are removed.

In the experiment of Fig. 3, the optical system was vibrated knocking the optical table. The velocity spectrum is shown in Fig. 3 (a). The wavefront of the target object on the CMOS camera is calculated by DFT at the velocity difference of 46.5 μm/s using 500 images. Although the phase difference between a object and reference beams were shifted by only the vibration, the object image could be observed as shown in Fig. 43(b). The shift amount of 0.59π can be estimated from the velocity difference, the frame rate, and the wavelength. Since the shift amount is larger than π, some errors was not removed.

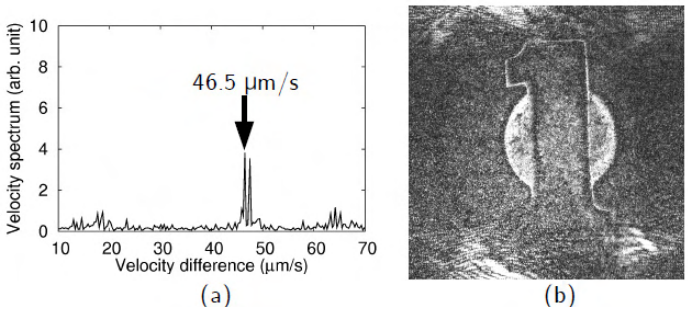

Fig. 3. Experimental result in the case of only vibrating the optical system. (a) is the velocity spectrum versus the velocity difference between the target object and reference mirror. (b) is the intensity pattern of the diffracted beam where the zeroth order spot and conjugate image are removed.

4 Conclusion

In this paper, a novel phase-shifting digital holography utilizing Doppler effect was proposed. The digital holograms were recorded with moving a reference mirror or vibrating the optical system. The holographic image could be reconstructed with removing the zeroth order spot and the conjugate image. This technique is applicable to obtain a holographic image of a moving object.

5 Reference

1. G. Lai and T. Yatagai, Use of the fast Fourier transform method for analyzing linear and equispaced Fizeau fringes, Appl. Opt., **33**: 5935-5940(1994).

Shape and Deformation Measurement of Moving Object by Sampling Moiré Method

Yoshiharu MORIMOTO*, Motoharu FUJIGAKI*, Akihiro MASAYA*, and Kousuke SHIMO**
*Department of Opto-Mechatronics, Faculty of Systems Engineering, Wakayama University
**Graduate School of Systems Engineering, Wakayama University
Wakayama, Japan, 640-8510, morimoto@sys.wakayama-u.ac.jp

1 Introduction

It is important to analyze the shape and the strain distributions of a moving object such as a rotating tire. Moiré method is used to measure the shape and the strain distributions of an object. Conventional moiré method uses a specimen grating and a reference grating. The superposition of the two gratings shows a fringe pattern which provides the information of the deformation of a specimen grating. In order to analyze the moiré fringe pattern, phase analysis method is useful to obtain accurate result. It requires more than three images which have different phase-shifted fringe patterns. However, it is difficult for the moving object to obtain the phase-shifted images with the same condition.

Recently sampling moiré method or scanning moiré method is used [1-3]. It does not use a reference grating. A specimen grating pattern on an object is recorded by a digital camera. Though the digitized image shows only the grating, a moiré fringe pattern appears by thinning-out the pixels, i.e., by sampling the image with a constant pixel pitch. If the sampling pitch is changed, the moiré pattern is changed. If the phase of the sampling i.e., the start point of the sampling is changed, the phase of the moiré pattern is changed [4-6]. The method can analyze phase values from one image of a grating pattern. The analyzed phase is very accurate because several phase-shifted moiré fringe patterns are obtained by changing the sampling phase.

By using this sampling moiré method, the deformation of the shape and the strain distribution of the surface of a rotating tire running at 80 km/h speed are analyzed.

2 Principle of sampling moiré method

Figure 1 illustrates the appearance of moiré fringe patterns by sampling moiré method. In this figure, only three horizontal lines are shown. In actual case, the sampling line is corresponding to the number of the camera resolution such as 640, 1280 pixels, etc. Figure 1(a) shows the deformed grating pattern attached on the specimen. The pitch of grating in this figure is 1.125 times larger than that of the sampling points. Then, the recorded image by the camera is shown in Fig. 1(b), in which no moiré fringe pattern can be discerned. Figure 1(c) shows the moiré fringe patterns when the sampling points of a camera are changed. That is, every N-pixel (in the figure, $N = 4$) from the first, second, third and fourth pixels are picked up from Fig. 1(b) as the sampling start points, respectively. This process corresponds to the phase-shifting of the moiré fringe pattern. These sampled images shown in Figs. 1(c) are interpolated using neighbouring data. Figures 1(d) show the linear interpolated images from Figs. 1(c), respectively. Then, multiple phase-shifted moiré images are obtained from single picture.

The k-th phase-shifted images can be expressed approximately as follows:

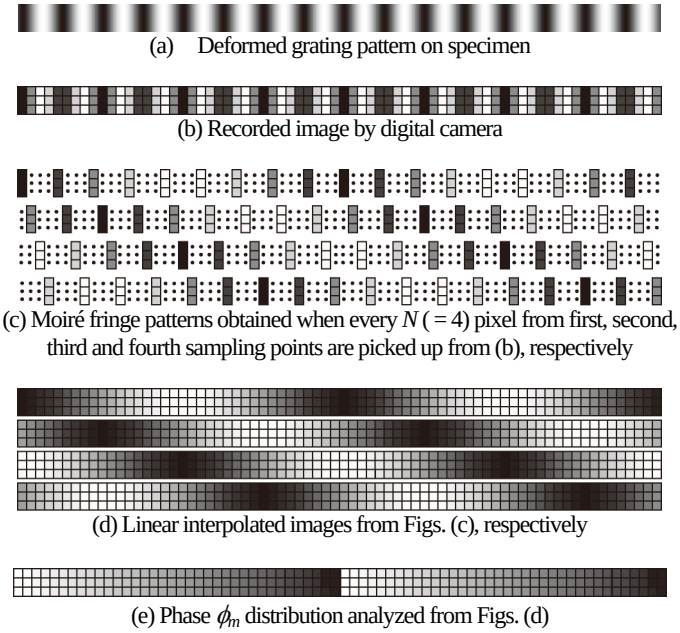

(a) Deformed grating pattern on specimen

(b) Recorded image by digital camera

(c) Moiré fringe patterns obtained when every N (= 4) pixel from first, second, third and fourth sampling points are picked up from (b), respectively

(d) Linear interpolated images from Figs. (c), respectively

(e) Phase ϕ_m distribution analyzed from Figs. (d)

Fig. 1. Schematic explanation of principle of phase-shifting moiré method

$$I_k(i,j) = I_a(i,j)\cos[\phi(i,j) + k\frac{2\pi}{N}] + I_b(i,j) \quad (k = 0,1,...,N-1) \tag{1}$$

where $I_b(i,j)$ represents background intensity in the image, which are insensitive to the change in phase; $I_a(i,j)$ represents the amplitude of the grating intensity and $\phi(i,j)$ is the initial phase value. The phase distribution of the moire pattern can be obtained by Discrete Fourier transform (DFT) algorithm using Eq. (2) or phase-shifting method using Fourier transform (PSM/FT) [6,7].

$$\phi(i,j) = -\tan^{-1}\frac{\sum_{k=0}^{N-1} I_k(i,j)\sin(k\frac{2\pi}{N})}{\sum_{k=0}^{N-1} I_k(i,j)\cos(k\frac{2\pi}{N})} \tag{2}$$

The phase ϕ_m of the moire pattern is the difference between the grating phase ϕ_s and the phase ϕ_r of reference grating (the sampling phase) as follows:

$$\phi_s = \phi_r - \phi_m \tag{3}$$

The phase ϕ_r of the reference grating is a constant. Therefore, the phase ϕ_s of the grating pattern can be calculated from the phase ϕ_m of the moiré pattern.

3 Experiments

3.1 Experimental setup for shape and strain measurement

By using this sampling moiré method, the deformation of the shape and the strain distributions of the surface of a rotating tire running at 80 km/h speed are analyzed. As the analysis method for the shape of the object, a calibration method for an accurate and high-speed shape measurement using two-reference planes with a 2-D grating fixed on the surface [8,9]. The analysis method is used in this paper.

Figure 2 illustrates an experimental setup with a projector, a camera, a reference plane and an object. A rubber sheet with a two-dimensional grating is pasted on the surface of the tire. The grating is recorded by two cameras from different positions. The phase distributions of the two deformed grating images are analyzed by sampling moiré method. The correspondence of a position on the object recorded by the two cameras is

determined from the same phase position of the two grating images. The three-dimensional position is analyzed by stereoscopic analysis with two cameras. From the surface positions of the grating, the shape, the deformation and the strain distributions are analyzed.

3.2 Experimental results

In this experiment, the grating pitch on the rubber sheet is 2.0 mm. The three-dimensional position at each pixel point is calculated using a linear interpolation between the phases of the two-reference planes. The grating image recorded by the left camera is shown in Fig. 3(a). The phase distribution of the moiré fringe pattern analyzed by sampling moiré method is shown in Fig. 3(b). The phase distribution of the grating is obtained by using Eq. (3). By unwrapping the phase distribution, the phase distribution is obtained as shown in Fig. 3(d). The image recorded by the right camera is analyzed in the same process.

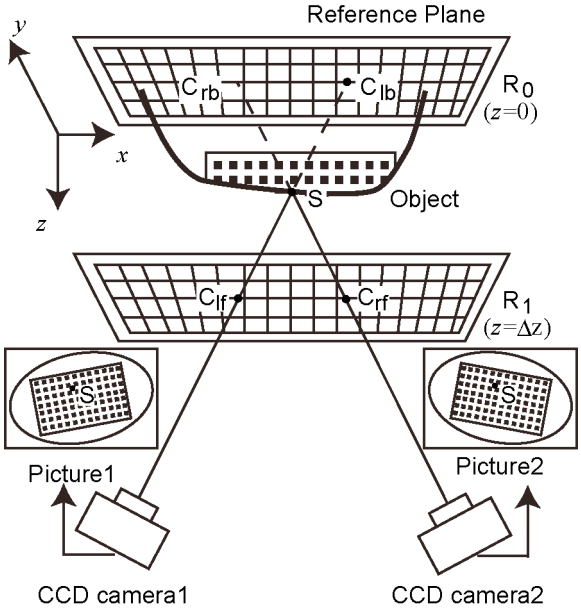

Fig. 2. Shape measurement

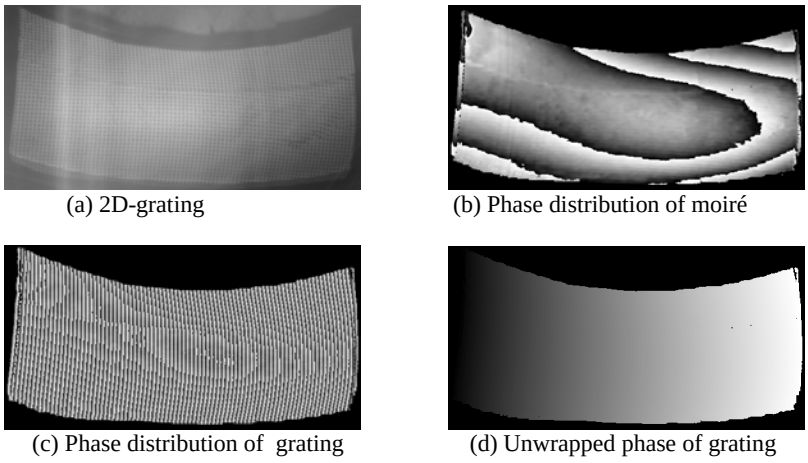

(a) 2D-grating (b) Phase distribution of moiré

(c) Phase distribution of grating (d) Unwrapped phase of grating

Fig. 3. Phase analysis (in x-direction)

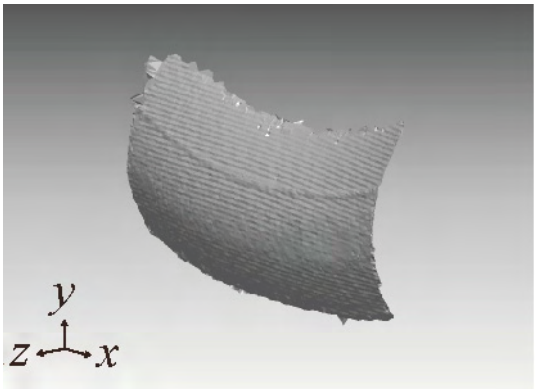

Fig. 4. Measurement results of shape

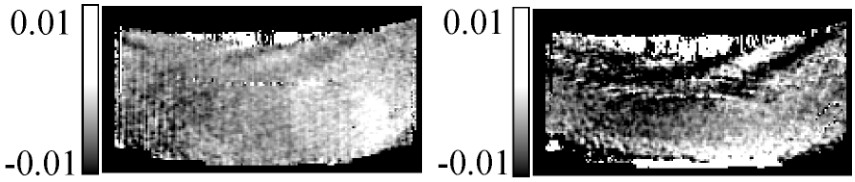

(a) *x*-directional strain (b) *y*-directional strain

Fig. 5. Measurement results of strain distributions

The correspondence is obtained easily by checking the positions with the same phase value on the two unwrapped phase distributions obtained by two cameras. From the correspondence, the three-dimensional position

is obtained as shown in Fig. 4. The three-dimensional positions before and after deformation, the *x*- and *y*-directional strain distributions on the surface of the object are analyzed as shown in Figs. 5(a) and (b).

4 Conclusions

Shape and strain distribution measurement method by sampling moiré method were proposed. The method applied to a rotating tire running at 80km/h.

5 References

1. Morimoto, Y. and Hayashi. T. (1984) Deformation Measurement During Power Compaction by a Scanning-moiré Method. Experimental Mechanics. 24 (2): 112-116.
2. Arai, Y. and Kurata, T. (1986) High Speed- and High Resolutive-Moiré Topography by the Method of Fringe Scanning Interferometry, Japanese Journal of Optics (in Japanese), **15**(5): 402-406
3. Morimoto, Y., Yang, I.-H. and Gu, C.-G. (1996) Scanning Moire Method for Obtaining Smooth Fringe Patterns, Optics and Lasers in Engineering, 24: 3-17
4. Arai, Y., Yokozeki, S, Shiraki, K and, Yamada, T. (1997) High Precision Two-Dimensional Spatial Fringe Analysis Method, Journal of Modern Optics, 44(4): 739-751
5. Ri, S., Fujigaki, M., Matui, T. and Morimoto, Y. (2006) Accurate pixel-to-pixel correspondence adjustment in a digital micromirror device camera by using the phase-shifting moiré method, Appl. Opt. **45**(27): 6940-6946
6. Ri, S., Fujigaki, M. and Morimoto, Y. (2008) Sampling Moiré Method for Accurate Small Deformation Distribution Measurement," Exp. Mech., DOI 10.1007/s11340-009-9239-4x, in press.
7. Morimoto, Y. and Fujisawa, M. (1994) Fringe Pattern Analysis by a Phase-shifting Method Using Fourier Transform, Optical Engineering, 33(11): 3709-3714.
8. Morimoto, Y. and Fujigaki, M. (1993) Automated Analysis of 3-D Shape and Surface Strain Distributions of a Moving Object Using Stereo Vision, Optics and Lasers in Engineering, 18: 195-212
9. Fujigaki, M., Yang, I. H., Morimoto, Y., and Han, E. K. (1996) Strain Analysis of Moving Object Using Fourier Transform Grid Method, NDT & E International, 29(4): 197-203.

New Interferometry Tools for AeroOptics

James Trolinger and Vladimir Markov
MetroLaser Incorporated
8 Chrysler, Irvine, CA 92618
USA

1 Introduction

When an optical wavefront passes through an aerodynamic flow, its phase and amplitude are modulated, resulting in distortion and loss of optical information and energy. Its phase is modulated by diffraction and spatial and temporal variations in refractive index. These effects deteriorate the ability to transmit and focus a beam onto a target. Refractive effects cause 1) image shift, also known as boresight error, 2) wavefront distortion (image blur) and 3) beam jitter (a kind of time varying boresight error). The ability to store and compare wavefronts directly provided by holography led to quantum leaps in understanding how turbulence affects optical imaging, and holographic interferometry provided one of the very first direct quantitative and visual observations of aero optical effects. MetroLaser has moved this powerful tool to a new level, incorporating digital techniques and producing unique diagnostics methods that enhance tests designed to study and correct aero-optical effects on imaging and energy projection. The fundamental concept is built around a wavefront sensor/recorder that records and reconstructs optical wavefronts known as the PhaseCam™. The PhaseCam is a digital phase shifting holographic interferometer that produces four simultaneous phase shifted interferograms that are solved to produce an instantaneous phase map of the wavefront. As a part of the diagnostics capability we developed supporting software and procedures to collect and analyze PhaseCam™ data and extract aero-optical parameters (e.g. Strehl ratio, point spread function, wavefront error) as well as software for simulating, modeling and interpreting such data. This paper describes the concepts and methods including applications in wind tunnel turret tests of optical systems.

A wavefront is projected from the PhaseCam™ through a flow field to a mirror, which returns the beam double passed through the same flow field. The PhaseCam™ then records the aero optically modulated wavefront and

analyzes it to deduce all of the data required to fully characterize the aero-optical nature of an optical system.

Examining a single wavefront provides the required input for an adaptive optical system to correct aero-optical effects. Recording two wavefronts and subtracting one from the other and varying the time separation, provides the temporal response required of the adaptive optics. Examining the detailed nature of the wavefront and its changes in time quantifies the flow structure.

Aero optics tests of flow control and flow field effects must provide:

- Strehl ratio or RMS wavefront distortion (i.e., wavefront quality) and Bore site error (BSE), (the tilt of the wavefront).
- Structural changes in the flow and/or wavefront, i.e., coherence, size, and regularity of structures.
- Temporal characteristics of the flow structure, i.e., decorrelation time.

2 Aero Optical Measurements

Parameters of merit that are commonly employed to describe the deterioration of a propagating wavefront are:

- σ, RMS wavefront variance;
- S, Strehl Ratio (peak intensity loss) which can be computed from σ;
- Image size at the focus of an ideal lens (also known as blur circle, encircled energy, diffraction limited spot size, point spread function, far field pattern, energy in the bucket), which also can be computed from σ.

When the aperture is large compared to the extent of spatial variation in refractive index (mean turbulence structure size) these are approximately related by

$$S = I/I_o = \exp(-k^2\sigma^2),$$

where S - Strehl Ratio, I - beam intensity, I_0 - beam intensity on the axis, $k = 2\pi/\lambda$, σ - RMS deviance of the wavefront.

The far field intensity, I_f, can be estimated as

$$I_f = S(\pi PD^2/4\lambda^2R^2)$$

where P - power, R - distance to the target, D - aperture diameter.

Therefore, possibly the most useful and important fundamental measurement is that of σ, which characterizes the wavefront statistically.

Therefore the required wavefront sensor captures wavefronts and determines σ. Some wavefront sensors are capable of capturing pieces of

wavefronts and inferring σ. Only one of these, interferometry, is capable of capturing the whole wavefront with high spatial resolution. Conventional interferometry is too sensitive to vibration to be employed in aero optics experiments. However, the "PhaseCam™" solves the usual problem with robustness and enables interferometry to be employed in harsh, high vibration environments. Still, the job is not without problems related to high vibration in the measurement.

The makeup and technical details of the PhaseCam, itself, are discussed elsewhere and are not repeated here. The system has the capability to capture and reconstruct an entire wavefront (phase and amplitude) in the instant during which it enters the instrument, including the following data required to fully characterize the aero optical nature of an optical system.

- Examining a single wavefront provides the required instantaneous input into an adaptive optical system for correction for aero optical effects. This determines the spatial requirements of adaptive optics required to correct the wavefront.
- Recording two wavefronts and subtracting one from the other and varying the time separation provides the exact settings and temporal response required of an adaptive optical system to correct for aero optical effects. This tells how fast the adaptive optics must be.
- Measuring wavefront quality reveals how much you have improved or degraded the wavefront. This reveals the aero optical effect of flow control.
- Examining the detailed nature of the wavefront and its changes in time quantifies the aero optical flow structure effects. This shows what the flow control is doing, aero optically, to the flow.
- When we subtract one wavefront from another that passes through the flow at a later time, the extremes are 1) that the time difference is large so that the wavefronts are uncorrelated, and 2) the time difference is small so the wavefronts are similar and correlated.
- By varying the time difference of the two compared waves from zero to a larger value we can determine the correlation distance or turbulence scales. By keeping the time separations small, we can subtract out all steady flow effects and slower time varying effects such as room air currents.

To get good statistics, since we are dealing with turbulence and random flow states, ten or more data sets per test condition is adequate. Upon receipt, manuscripts and illustrations become the property of ITO and will not be returned to the author. With the submission of the manuscript authors assign to ITO and Springer copyright ownership in their paper including all used artwork, drawings and photographs.

3 Experimental Data Examples

We have applied these methods in a variety of aeroptical tests including flows over cavities and optical turrets. The following provides a sample of some of the data for flow over a hemispherical turret. The most obvious flow feature observed at the 90 degree angle was the normal shock. It is best seen in Figure 1. This is most easily seen from a wrapped phasemap. Two of these are shown in Figure 1. Several conclusions can be drawn from these figures. The shock is dynamic. In 180 microseconds it moves from right to left. In some recordings it cannot be seen at all. The wavefront itself is much smoother at 90 degree look angle. However, a considerable boresight error still exists. This may be due to both mirror vibrations as well as the flow.

Interferograms for a wide range of conditions were examined to demonstrate the usefulness in aero optical assessment. We demonstrated the ability to measure boresight error, Strehl ratio, turbulence scale, and the temperal characteristics of these parameters. Figure 2 illustrates how the system can quantify the temporal characteristics of a wavefront and also quantify the turbulence structure and scale. Two wavefronts with a 180 µsec time spacing differ only in tilt (beam jitter) whereas two wavefronts spaced in time by 440 µsec show a significant difference caused by turbulence.

Examining more data, turbulence effects were seen to come and go as expected and without considering the statistics, general conclusions about turbulence may be premature. The quantity of available data will allow us to do the statistics that can lead to more general conclusions.

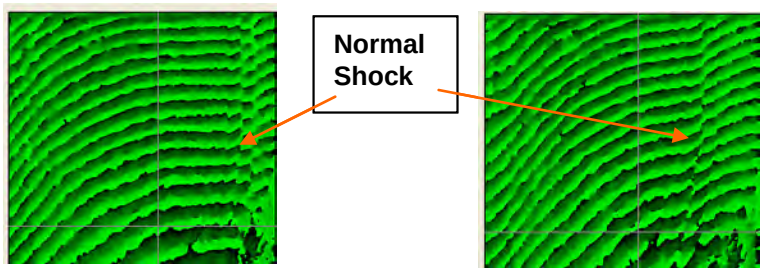

(a) Wrapped phase map (b) 180 µsec later.

Fig. 1. Wavefront aero optics at 90 degree look angle

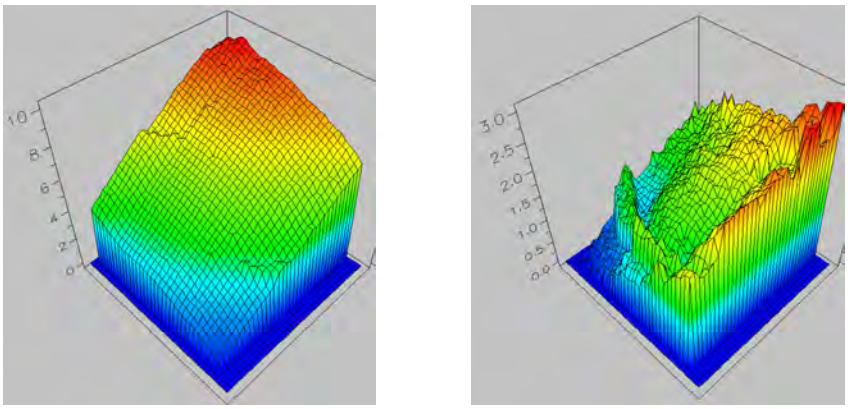

a) $\Delta t = 180$ µsec b) $\Delta t = 440$ µsec

Fig. 2. Phase difference map showing very low, small-scale turbulence effects on aero optics at (a) the 180 µsec rates but increasing the time difference to 440 µsec (b) brings in the effects of turbulence thus defining the speed at which adaptive optics must operate

4 Conclusions

In the foregoing we have described the application of digital holographic interferometry in aero optical testing. A digital holocamera based on instantaneous phase shifting interferometry provides all of the information needed to aero optically characterize and optical system including and defines the requirements of an adaptive optical system that would be required to correct the problems caused by deleterious aero optical effects.

5 Acknowledgments

The work reported in this paper was supported by an SBIR program from Wright Patterson Air Force Base, Wright Laboratories. The project officer was Don Saunders.

6 References

1. Trolinger, J.D., “Aero-Optical Characterization of Aircraft Optical Turrets by Holography, Interferometry, and Shadowgraph,” Aero-

Optical Phenomena, Editors: Keith G. Gilbert and Leonard J. Otten, American Institute of Aeronautics and Astronautics, Inc., 1982, p. 200.

2. Trolinger, J.D., Craig, J.E. & Rose, W.C. *"Propagation Diagnostic Technique for Turbulent Transonic Flow,"* AIAA No. 84-0104, AIAA 22nd Aerospace Sciences Meeting, Reno, Nevada, 9-12 January 1984.
3. Anderson, C. and Trolinger, J.D., "New Developments in Digitial Electronic Flow Diagnostics Methods," *SPIE Proceedings*, International Conference, San Diego, CA (July 2001).
4. Trolinger, J.D., "Interferometric Flow Measurement," Chapter 3 in Optical Diagnostics in Fluid and Thermal Flows, edited by Carolyn Mercer, Kluewer Press International (May 2003).
5. Brock, N.J., Millerd, J.E., and Trolinger, J.D. "A Simple and Versatile, Real-Time Interferometer for Quantitative Flow Visualization," AIAA99-0770; 37th Aerospace Sciences Meeting and Exhibit, Reno, NV (January 1999).
6. Smythe and Moore, "Instantaneous Phase Measuring Interferometry," *Opt. Eng*. vol. 23, p. 361 (1984).
7. Trolinger, J., "A Digital Wavefront Sensor for Aero-Optics and Flow Diagnostics," ICIASF Congress on Laser Flow Diagnostics, 2003.

Dynamic Fizeau Interferometers

Brad Kimbrough, Brian Medower, James Millerd
4D Technology Corporation
3280 E. Hemisphere Loop, Ste. 146
Tucson, Arizona 85706

1 Introduction

4D Technologies pixelated polarization mask phase sensor allows single frame, quantitative phase aquisition for vibration insensitive measurements of optical surfaces and has been sucessfully used on a variety of interferometer types [1,2,3,4]. Application of the pixelated mask phase sensor requires the test and reference beams of the interferometer to be orthogonally polarized. This requirement poses a significant challenge to the utilization of the pixelated mask sensor with a Fizeau interferometer.

One of the primary advantages of the Fizeau interferomter is its common path arrangement, which allows for very high uncalibrated accuracy on-axis measurements. However, this common path arrangement makes it diffucult to orthogonally polarize the test and reference beams. One solution to this problem is to introduce an angle between reference and test beams. The angle can be used to generate a spatial carrier pattern directly on the sensor [5], or filtered for polarization using a polarizing prism and then recombined [6]. The major drawback with this technique is that with the tilted reference surface, the returning test and reference beams no longer follow a common path, resulting in so-called retrace errors in the measurement, which negates the common-path advantage of the Fizeau. For planar reference and test optics it is possible to design the interferometer to have reasonably low retrace errors; however, the use of transmission spheres introduces substantial retrace errors. In addition, there is a direct tradeoff between the spatial resolution of the measurement and the retrace errors, Fig. 1. The use of small tilts, on the order of a few dozen fringes produces a small retrace error (<1/10th wave) but the data must be filtered to avoid harmonics (either optically or in software) leaving only very low spatial frequencies. The use of higher angles allows the filter bandwidth to be increased but the retrace error increases dramatically. Calibration at large tilts is difficult because of the need to produce the

exact amount of tilt between measurements and the attendant error introduced from subtracting large aberrations to calculate small values.

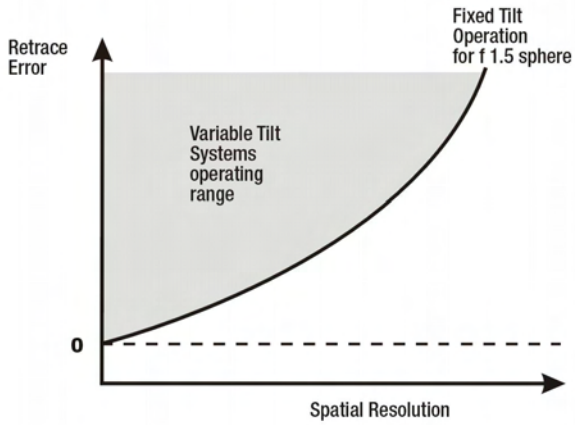

Fig. 1. Retrace error vs. Resolution for an f1.5 sphere. As tilt is increased to provide better spatial resolution, retrace error also increases, limiting performance for tilted beam systems.

In this paper we demonstrate two methods of incorporating the pixelated phase mask sensor with a Fizeau interferometer that preserves the on-axis advantages of the Fizeau configuration. The first method involves the use of a low coherence source along with a mechanism to introduce an optical path delay between the orthogonally polarized test and reference beams. This particular implementation also allows for the measurement of absolute optical thickness over a range of hundreds of millimeters with micron accuracy. The second implementation utilizes a high coherence source in conjuction with a polarization frequency shifting device. In this paper the design and implementation of the low coherence and the high coherence Fizeau interferometers will be described. This will be followed by a discussion of some unigue measurement capabilities with some example measurement results.

2 Short coherence vibration insensitive Fizeau Interferometer

An implementation of a polarization based Fizeau was proposed by Kuchel [9] that uses a low temporal coherence source and an optical delay-line that splits the source beam into two orthogonally polarized components

and allows a controllable phase difference between the two beams. This idea was combined with the 4DTechnology pixelated polarization mask sensor in order to produce a short coherence vibration insensitive Fizeau interferometer.

The basic layout of the short coherence vibration insensitive Fizeau interferometer is shown in figure 2. The illumination system is composed of a short coherence laser source and an optical delaying device that splits the source beam into two orthogonally polarized components and applies a controllable optical path difference between the two beams. This output is used as the illumination source for a standard Fizeau interferometer arrangement. The output of the Fizeau is imaged onto the pixelated mask sensor.

The optical delaying device is essentially a polarization Twyman-Green interferometer. It is convenient to think of the illumination as being composed of two separate but overlapping beams, the *s*-polarized beam and the *p*-polarized beam. The half wave plate just in front of the laser source is used to adjust the intensity ratio between the two beams. Upon exiting the optical delaying device, there is an optical path delay between the s-polarized and the p-polarized beams. Mirror M1 is mounted to a stage and allows the optical path length of the exiting p-polarized beam to be adjusted relative to that of the s-polarized beam which originates from M2.

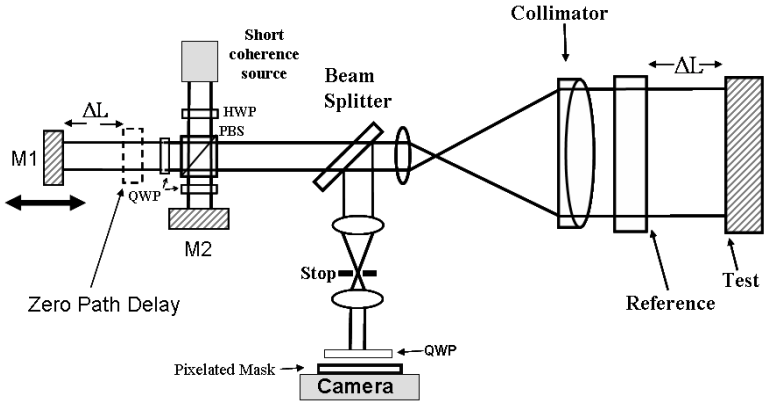

Fig. 2. Short coherence vibration insensitive Fizeau interferometer

Both the *s* and *p*-polarized beams illuminate and are reflected by the test and reference surfaces. The returning beams undergo reflection at the non polarizing beam splitter and are imaged via an afocal imaging system onto the pixelated mask sensor. The quarter wave plate, QWP, just prior to the pixelated mask is used to convert the linearly polarized test and reference

beams into right and left circular polarizations as is necessary for the operation of the pixelated mask sensor.

Ignoring multiple Fizeau cavity reflections, there are essentially 4 beams incident upon the pixelated mask sensor; *s* and *p*-polarized test surface reflected beams, and *s* and *p*-polarized reference surface reflected beams. For the pixelated mask sensor we would like interference to occur between either the s-polarized reference beam and the p-polarized test beam, or between the p-polarized reference beam and the s-polarized test beam. Since the source has a very short coherence length, approximately 250 um, only those beams whose optical paths, from the source to the camera, have been matched will interfere. No interference will occur between the other beam pair and there intensities will simply add to the background.

The benefits of this instrument are three fold. First, the systems permits high spatial resolution instantaneous phase measurement in a single camera frame. Secondly, the two orthogonally polarized beams are collinear – allowing true on-axis operation so that transmission flats and spheres can be used without calibration. Finally, the delay line allows matching of the reference and test beam optical paths, facilitating the measurement of specific surfaces within an optical cavity and for measuring absolute optical thicknesses over several hundred millimeters with micron accuracy. Additionally, the use of very low temporal coherence sources reduces coherent system noise due to spurious reflections. An in depth analysis of the theory and operation of this interferometer can be found in [3].

3 Long coherence vibration insensitive Fizeau Interferometer

While the short-coherence method works well for many applications, it is less well suited for test set-ups with very long cavity lengths, for example large telescopes or beam trains, or in situations where multiple surface reflections are not present. Additionally, measurement cavity lengths are restricted by the maximum OPD obtainable with the interferometer's internal path matching mechanism.

In order to provide a high quality, general lab instrument that can easily be configured and used over very long path lengths, we have developed a long coherence vibration insensitive Fizeau Interferometer. This instrument has the advantages of an on-axis Fizeau design together with vibration insensitive measurement capability and long temporal coherence. The Fizeau interferometer is realized through the use of a pixelated

polarization mask spatial carrier phase shifting technique, in conjunction with a polarization frequency shifting device. In this arrangement, differential motion between the test and reference surfaces, in conjunction with the polarization frequency shift device, is used to effectively separate out the orthogonally polarized test and reference beam components for interference. With both the test and the reference beams on-axis, the common path cancellation advantages of the Fizeau interferometer are maintained. Additionally, the use of a high coherence source eliminates the need to path match the test and reference arms of the interferometer.

The basic layout of the synchronous frequency shifting Fizeau interferometer is shown in figure 3. This system is composed of three major sections: (1) A high coherence source, (2) A polarization frequency shifting device; and (3) A Fizeau interferometer with a pixelated mask sensor.

The source used in our experiments was a 1mW stabilized HeNe laser. However, the only requirement is that the laser source coherence length be at least as large as the Fizeau cavity being measured.

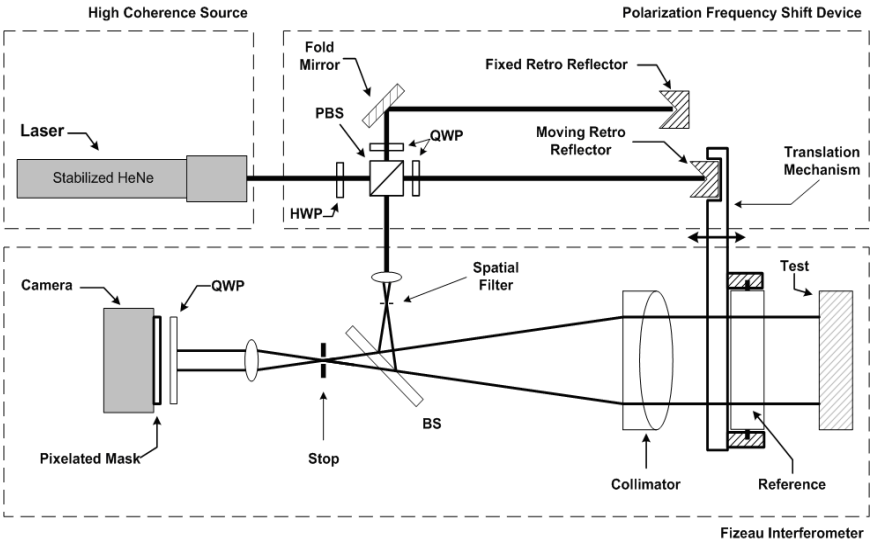

Fig. 3. Long coherence vibration insensitive Fizeau interferometer

The polarization frequency shift device is essentially a polarization Twyman-Green interferometer. It consists of a half wave plate, HWP, a polarizing beam splitter, PBS, two quarter wave plates, QWP, a fixed retro reflector, and moving retro reflector. The polarization frequency shifting device splits the source beam into two orthogonally polarized components

and applies a controllable frequency shift to one polarization component of the beam relative to the other orthogonally polarized component. This frequency shift is obtained by rapidly translating the moving retro reflector in a direction parallel to the beam. The two beams are then recombined and spatially filtered.

The combined beam is then launched into a standard Fizeau cavity consisting of a reference and a test optic. It is convenient to think of this input beam as being composed of two separate but overlapping beams, the *s*-polarized beam and the *p*-polarized beam. The half wave plate just in front of the laser source is used to adjust the intensity ratio between the two beams.

Both the *s* and *p*-polarized beams illuminate and are reflected by the test and reference surfaces. The reference surface is translated in a direction substantially parallel to the incident optical beam, such that the reflected beams are imparted with a frequency shift equal in magnitude with the polarization frequency shift device. The returning beams are imaged onto the pixelated mask sensor. The quarter wave plate, QWP, just prior to the pixelated mask is used to convert the linearly polarized test and reference beams into right and left circular polarizations as is necessary for the operation of the pixelated mask sensor. Alternatively, the quarter wave plate can be introduced just prior to the spatial filter to produce orthogonal circularly polarization between the two beams.

There are essentially 4 beams incident upon the pixelated mask sensor: *s* and *p*-polarized test surface reflected beams, and *s* and *p*-polarized reference surface reflected beams. For the pixelated mask sensor, the test and reference beams must be orthogonally polarized.

In this case, each of the 6 possible beam combinations produces an interference pattern at the camera. However, there is a relative frequency shift between the beams making up each pair in all but one of the beam combinations. In other words, the fringes from all but one of the beam combinations are moving. The stationary beam combination is composed of the *s*-polarized beam from the test surface and the *p*-polarized beam from the reference surface. The frequency shift imparted by the moving retro reflector and the reference surface is selected to produce at least one full cycle of phase shift during the integration time of the camera. Therefore, the moving fringe combinations will be highly attenuated, and the contrast of the stationary fringe combination will remain high. Thus, the system functions as a single shot, polarization phase-shift interferometer with both the reference and test beam remaining on axis. An in depth analysis of the theory and operation of this interferometer can be found in [4].

4 Measurement Results

4.1 Short coherence system measurements

The short coherence Fizeau has several novel measurement capabilites, including direct solid cavity measurements, thickness or absolute distance measurements, and homogeneity measurements of polished parallel sided glass blanks.

Consider the case of a parallel sided glass substrate. When measuring a parallel sided part with a long coherence interferometer, some means of eliminating the interference of the solid cavity must be employed. With the short coherence Fizeau system, we can pathmatch to the cavity formed by the front and back surfaces of an uncoated part and make a direct measurement of the optical thickness variation across the part. Figure 4 shows just such an measurement on a 166 um thick glass wafer. Note that a transmission flat is not required for this measurement. This same technique allows for direct measurement of uncoated window wedge in glass substrates with a small wedge angle.

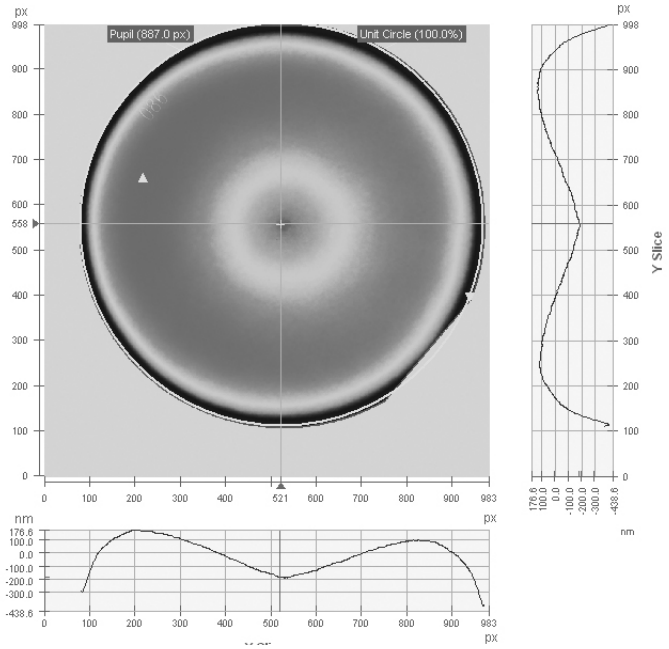

Fig. 4. Optical thickness variation measurement on a thin glass plate using the short coherence Fizeau interferometer.

The pathmatching capability of the system provides a means of measuring optical thickness of a part. Measuring modulation vs. pathmatch stage position provides a direct measurement of absolute optical thickness. With knowledge of the optical index we can calculate the physical thickness of a cavity. Figure 5 shows the repeatability of a typical physical thickness measurement for a 166µm thick glass wafer of index n=1.5. By using a Gaussian peak fitting algorithm, we were able to demonstrate submicron repeatability with this technique over a 400mm measurement range. This same technique can be applied to multi-cavity systems or to radius of curvature measurements for spherical parts.

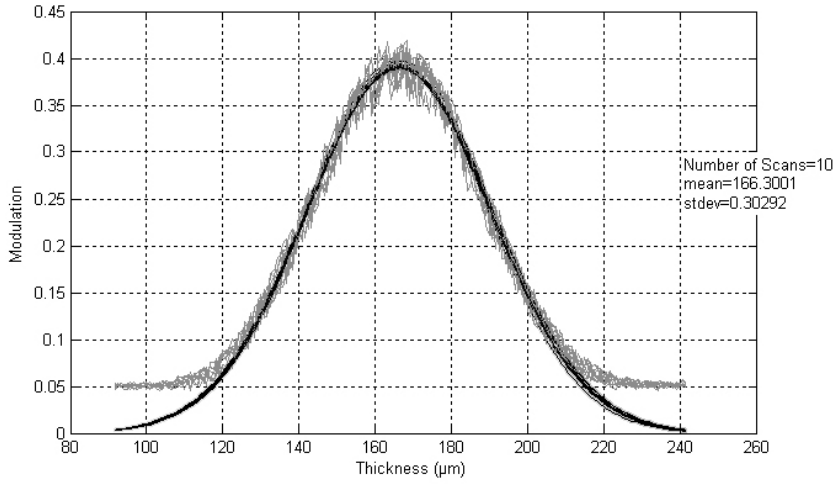

Fig. 5. Absolute thickness measurement of a thin glass plate using the short coherence Fizeau interferometer.

4.2 Long coherence system measurements

The long coherence Fizeau interferometer that was built can be operated in both dynamic mode as discussed above, and in standard temporal phase shifting mode. Since temporal mode requires the acquisition of at least four frames of data at the standard video rate of 30 fps, total acquisition time is at least 120 ms. By comparison; the dynamic measurements were taken with an integration time of about 250 usec. Due to the relatively long acquisition time, the temporal measurements must be conducted on a vibration isolated surface. One of the primary advantages of an on-axis dynamic Fizeau interferometer over dynamic systems that utilize a tilted beam arrangement is that a transmission sphere can be used without

introducing several waves of retrace error. Measurements of the convex surface of a plano-convex lens using an f/3.5 reference sphere were conducted. The reference sphere was specified at 1/10 wave. The lens had a diameter of 50.4mm, a focal length of 200 mm, and was uncoated. Measurement results are shown in figure 6. The noise peak in the center is due to a stray reflection off of the back planar surface of the lens. The temporal measurement has a peak-to-valley and RMS of 0.1294 and 0.0263 waves respectively. For the dynamic measurement, the peak-to-valley and RMS were 0.1303 and 0.0260 waves respectively.

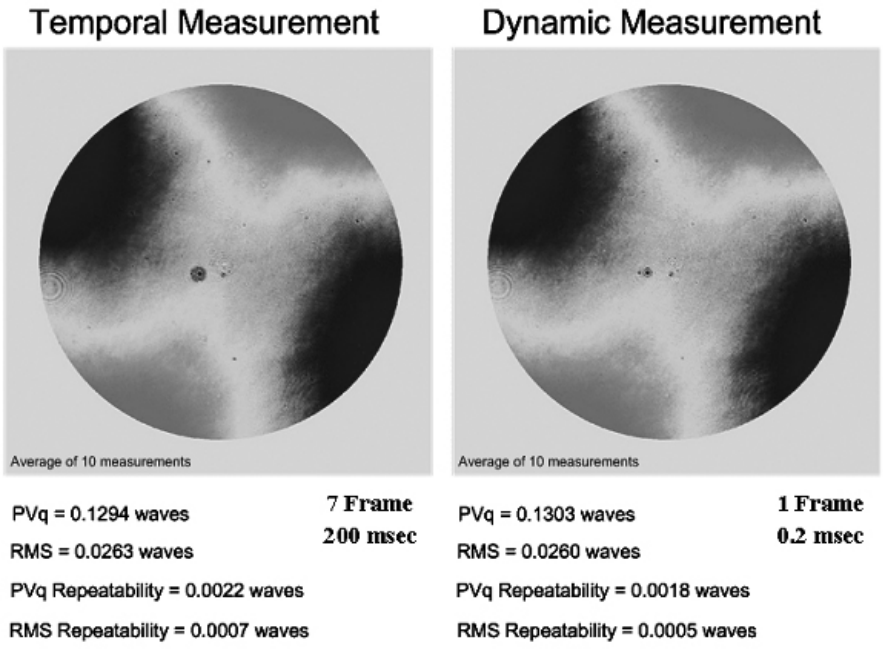

Fig. 6. Spherical surface measurements made with the long coherence vibration insensitive Fizeau interferometer. Measurements were made in both temporal and dynamic mode for comparison.

5 Summary

We have demonstrated two methods of incorporating the pixelated phase mask sensor with a Fizeau interferometer that preserves the on-axis advantages of the Fizeau configuration. Both systems overcome the retrace limitations of tilted beam style polarization Fizeau interferometers. Both instruments produce high quality measurements, comparable with standard

Fizeau arrangements while operating in a non vibration controled enviroments. Some additional advantages of the low coherence Fizeau are its ability to measure objects with multiple parallel surfaces, and to provide absolute optical thickness measurements over several hundred milimeters.

6 References

1. Millerd, J. E, Brock, N. J, Hayes, J. B, North-Morris, M. B, Novak, M, and Wyant, J. C, (2004) Pixelated phase-mask dynamic interferometer. Proc. SPIE 5531:304-314.
2. North-Morris, M., Millerd, J., Brock, N., Hayes, J., and Saif, B. (2000) Dynamic Phase-Shifting Electronic Speckle Pattern Interferometer. Proc. SPIE 5869:50
3. Kimbrough, B., Millerd, J., Wyant, J., Hayes, J., (2006) Low Coherence Vibration Insensitive Fizeau Interferometer, Proc. SPIE 6292:15
4. Kimbrough, B., Frey, E., Millerd, J., (2008) Instantaneous phase-shift Fizeau interferometer utilizing a synchronous frequency shift mechanism. Proc. SPIE 7063:pg
5. Rabinovich, E., Carr, B., (2006) Fizeau Interferometers Evaluated Using FlashPhase and Phase-Shift Fringe Analysis. Photonics Spectra Magazine, August
6. Millerd, J. E., (2005) Pixelated Phase-Mask Dynamic Interferometer. in “Fringe 2005,” edited by W. Osten, (Springer, New York), pg 640.
7. Crane, R., Polster, H. D., et al. (1969) New developments in interferometry. Applied Optics 8(3):521-556
8. Kimbrough, B. T., Pixelated mask spatial carrier phase shifting interferometry algorithms and associated errors, Applied Optics 45(19):4554-4562
9. Küchel, M., (1989) Interferometer for measuring optical phase difference. U. S. Patent 4,872,755

Surface contouring of vibrating objects using quadrature transform

Ricardo Legarda-Saenz[a], Ramon Rodriguez-Vera[b], Juan Antonio Rayas[b]
[a]Facultad de Matematicas, Universidad Autonoma de Yucatan. Apdo. Postal 172. 97110. Merida, Yucatan. Mexico.
[b]Centro de Investigaciones en Optica. 97110 Leon, Guajanuato. Mexico.

1 Introduction

Non-contacting measurement of three-dimensional shape or object profile is important in many areas, including medicine, on-line inspection, computer-aided design-manufacturing and reverse engineering. With recent advances in computing technology, some of these techniques have become automated, easier to use in applications and more efficient in data reduction, which has resulted in the development of full-field optical techniques that are being used for real-time profile measurements in a wide range of settings.

One important task of real time measurement is the dynamic evaluation. Several optical measurement techniques are used such as fringe projection, holography, moiré interferometry and shearography. In the particular case of fringe projection, early set-ups were used to observe time-averaged contours; however, these were not suitable to measure the transient deformation of a vibrating object [1]. With the availability of high-speed digital recording, it is possible to acquire a large sequence of images with the fluctuations of the projected fringe due to the object deformations. Several approaches are founded in literature concerning with the automatic processing of this fringe sequence, where the displacement of the fringe patterns is analyzed pixel by pixel as a function of time.

In this work, a combination of temporal phase unwrapping technique [2] and Fourier-based quadrature transform [3,4] are used to obtain the surface displacement from a vibrating object. The quadrature transform has the property of demodulate correctly a fringe pattern despite some errors in the estimation of fringe orientation [3]. This property results an important feature that is used to implement the processing of a sequence of fringe patterns.

A large sequence of the projected fringe pattern on the vibrating object is acquired and each is demodulated using the quadrature transform, where

a rough knowledge of the spatial-carrier orientation is used. Then, the difference between a consecutive phases are computed using the well-known temporal phase unwrapping technique, and the resultant unwrapped phase can be related directly to the surface contour of the vibrating object. The performance of the proposed method is shown on examples of experimental measurements of the surface displacement of a fixed end homogeneous cantilever using vibrational excitation.

2 Processing of the fringe patterns

The fringe pattern projected over the object under analysis is defined as

$$I(r,t) = a(r) + b(r)\cos\left(\frac{2\pi}{p} r \cdot n_0 + \varphi(r,t)\right) \tag{1}$$

where r = (x,y), $a(r)$ and $b(r)$ are the background and the modulation, respectively. The vector n_0 is the normal direction of the pattern projected over the vibrating object, p is the fringe period, and φ is related with the deformed surface of the object at the time t.

The first step of the procedure is to extract the phase term from the fringe pattern, Equation (1). A sequence of N-frames are taking from the dynamical movement of the object in such way that

$$\{I(r,t_0), I(r,t_0 + \Delta t), I(r,t_0 + 2\Delta t), \ldots, I(r,t_0 + [N-1]\Delta t)\}$$

where Δt is the temporal period of the captured frame and is smaller than the temporal period of the vibration cycle. Under this conditions, every frame can be seen as

$$I_k(r) = a(r) + b(r)\cos\left(\frac{2\pi}{p} r \cdot n_0 + \varphi_k(r)\right) \tag{2}$$

where $I_k(r) = I(r,t_0 + k\Delta t)$ for k = 0,1,...,N-1.

The demodulation of a single fringe pattern defined by equation (2) consists of estimate the quadrature term of the fringe pattern [3,4]. First, it is assumed that the background illumination $a(r)$ is filtered from the fringe pattern defined in Eq. (2), that is

$$g(r) = b(r)\cos(\psi(r)) \tag{3}$$

where

$$\psi(r) = \frac{2\pi}{p} r \cdot n_0 + \varphi_k(r)$$

The quadrature estimation consists of transforming the fringe pattern shown in Equation (3) into its quadrature term defined by

$$\hat{g}(r) = b(r)\sin(\psi(r))$$

and obtaining the following fringe complex pattern

$$g(r) - i\hat{g}(r) = b(r)\exp(i\psi(r)) \tag{4}$$

The bi-dimensional quadrature transform is defined as [3,4]

$$Q_2(g) = n_\psi(r)FT^{-1}\left\{-i\frac{q}{(q)}FT\{g\}\right\} = -b(r)\sin(\psi(r)) \tag{5}$$

where $FT\{.\}$ indicates the Fourier transform, $q = (u_1, u_2)$ is the vectorial position on the frequency domain, and $n_\psi(r)$ is the unit vector to the isophase contours; usually this is related to the orientation of the fringe pattern [3,4].

The quadrature transform used to demodulate the fringe patterns has several computation advantages, such that fast algorithms to compute the discrete Fourier transform [5], and the second-order error contribution to the demodulated phase due to the errors in the orientation estimation [3]. This property results an important feature that is used to implement the proposed processing of a sequence of fringe patterns: every frame acquired in the experiment is demodulated using Equation (5) where the carrier-frequency orientation is assigned to the term $n_\psi(r)$ of the quadrature transform. This assignation allows to automatically processing every fringe pattern of the sequence, given only the orientation is known from the experimental setup.

Once every fringe pattern was demodulated, two consecutive frames, for instance *k* and *k*-1, are used to calculate the *k*th phase map using temporal phase unwrapping [2]. This resultant phase map is related with the setup parameter to obtain the displacement of the object.

3 Experiments and results discussion

The performance of the proposed method was proved by reconstructing the surface of a vibrating a fixed end homogeneous cantilever excited by a loudspeaker and signal equals to 59.7 Hz. A high-speed camera captured a sequence of frames at rate of 1/400 of second. The acquired frames are demodulated using Eq. (5) where the orientation of the carrier frequency is assigned to the term $n_\psi(r)$ which allows processing the sequence automatically. Examples of the captured frames and the resultant demodulated fringe patterns using the quadrature transform are shown in

Figure 1. As it can be observed in Fig. 1, an accurate demodulation is obtained despite the variations on the fringe orientation.

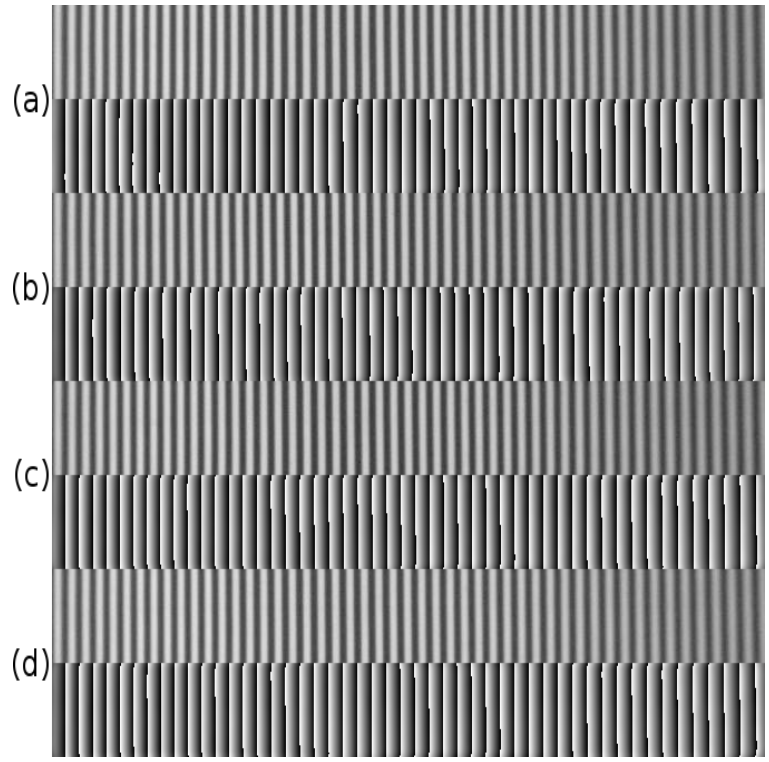

Fig. 1. Captured fringe patterns from object under vibrating and the resultant demodulation: (a) k = 6, (b) k = 104, (c) k = 236, and (d) k = 381.

The phase map is estimated from two consecutive frames using the temporal phase unwrapping [2]. The resultant reconstructions from the fringe pattern of Fig. 1 are shown in Figure 2.

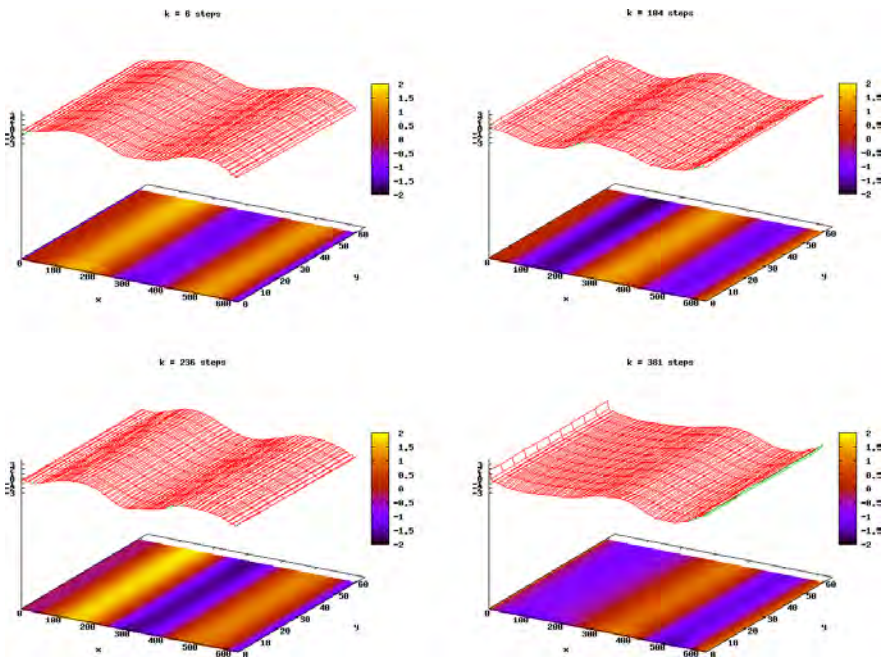

Fig. 2. Resultant 3D reconstruction using fringe patterns of Fig. 1.

4 Concluding remarks

In this work, it is presented a combination of temporal phase unwrapping technique and Fourier-based quadrature transform to obtain the surface displacement from a vibrating object. The proposed combination allows an accurate and versatile 3D reconstruction of the object under analysis, and it is based on simple and computational efficient techniques. An extra advantage of the proposed method is its feasibility to be implemented on a dedicated hardware for processing in real-time, which is the aim of future research.

5 Acknowledgements

R. Legarda-Saenz was supported by Consejo Nacional de Ciencia y Tecnología (Mexico) under grant 25793-CB-2005-01-49753.

6 References

1. K. J. Gäsvik, *Optical Metrology. Third Edition.* (John Wiley & Sons Ltd., 2002).
2. J. M. Huntley, H. Saldner, *Applied Optics* 32, 3047 - 3052 (1993).
3. K. G. Larkin, D. J. Bone, M. A. Oldfield, *Journal of The Optical Society of America A* 18, 1862 - 1870 (2001).
4. M. Servin, J. A. Quiroga, J. L. Marroquin, *Journal of The Optical Society of America A* 20, 925 - 934 (2003).

Development and Application of a 10 Hz Nd:YAG Double Pulse Laser for Vibration Measurements with Double Pulse ESPI

Ernst Heinrich Nösekabel
Steinbichler Optotechnik GmbH
Georg-Wiesböck-Ring 12, D-83115 Neubeuern
Wolfram Honsberg
BMW AG, Forschungs- und Innovationszentrum
D-80788 München
Reinhard Kelnberger
InnoLas GmbH
Justus-von-Liebig-Ring 8
D-82152 Krailling

1 Introduction

Since many years, double pulse lasers combined with pulse ESPI sensors are applied in the development laboratories of many industrial branches. Most of these systems are stationary installations, which are used for the investigation of the vibration behaviour of components and sub-systems under either sinusoidal excitation or under operational conditions. Other typical applications are reliability tests of components or the investigation of transient events.

The existing installations mainly use double pulse ruby lasers as light sources. These lasers provide between 1J and 10J light energy per double pulse and can be fired in intervals of 10s to 20s. The rugged design of these lasers allows applications outside the laboratory, e.g. at engine or brake test benches, but the weight and size of the laser head, its supporting structure carrying also the optical setup and its power supply and controller unit require significant efforts for system transportation. Hence, application engineers demanded a smaller, portable system, suitable for transportation with a station wagon and to be loaded and set up by two men without requirement of additional equipment like fork lifts or similar. In addition, a higher shot repetition rate was requested to reduce measurement time at test benches.

2 The Laser

As the above mentioned demands could not be fulfilled with available ruby lasers (neither with respect to the size of the laser and its controller nor regarding a significantly increased pulse repetition rate), a frequency doubled Nd:YAG laser with an additional seed laser (InnoLas SpitLight 600) has been selected as light source, as shown in Fig. 1. The design of this laser is modular and hence allows for flexible configuration and adaptation to various requirements. The main module of the laser includes the oscillator and an additional amplifier. Both laser rods are located within one common pumping chamber. The simultaneous pumping of both crystals is done with one flash lamp, thermal stability of the laser rods and cooling of the flash lamp is achieved with a temperature controlled water flow through the pumping chamber. A Pockels cell within the oscillator allows Q-switched operation either in single pulse or in double pulse mode for each flash lamp pulse, with a user selectable pulse separation time between 1µs and 200µs. At the laser amplifier output, a 45° quartz rotator and a type II KTP crystal are fitted as Second Harmonic Generator. Two dichroitic mirrors at the laser output are used to separate the infrared and the green laser light.

To reduce the build up time of the laser in Q-switched mode, a 1µm fibre seeding laser with its control unit is used. Cavity length matching is done by a piezo-electric actuator mounted to the oscillator rear mirror.

The control unit of the laser comprises the power supply for the flash lamp, the controllers for all laser components and the cooling unit for the internal cooling loop. The laser head and the control unit are connected by a flexible conduit for the pipes of the internal cooling loop and the high voltage flash lamp supply and an additional signal cable.

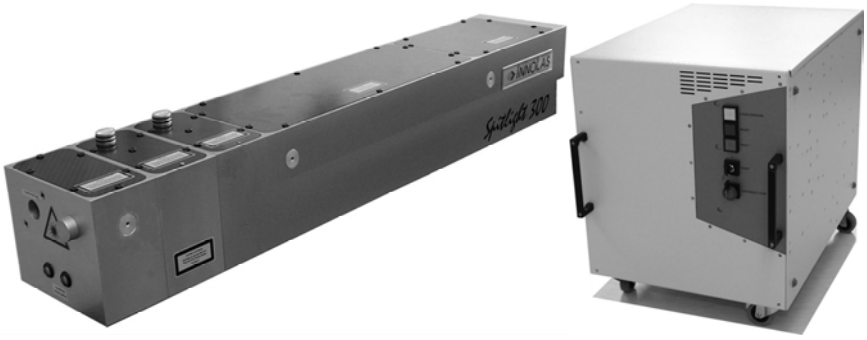

Fig. 1. The SpitLight 600 laser head (left) and the laser control unit with power supply and integrated cooler (right).

A fibre optic link is used to connect a PC with the control software to the control unit.

For the desired high shot repetition rate of the laser, a water / water cooling system is necessary. The external cooling of the heat exchanger is done with an external secondary chiller, so that the system remains independent from tap water sources.

Other than ruby lasers which are typically designed for single shot operation, the SpitLight 600 laser is designed to operate with a constant flash lamp repetition rate to keep the pumping chamber thermally balanced and to provide excellent beam quality, mode stability and a sufficient coherence length for ESPI measurements. Therefore, the control unit of the laser provides a built-in, stabilized signal generator for flash lamp triggering.

The main characteristics of the laser system are as follows:

- Weight: Laser head approx. 17 kg, control unit approx. 50 kg, secondary chiller approx. 25 kg.
- Pulse energy: Max. 400 mJ@532 nm
- Pulse length: Approx. 7 ns
- Double pulse separation: 1 µs to 200 µs
- Coherence length: Approx. 0.4 m

3 The first System Tests

The first pulse ESPI measurements with the laser have been carried out in its single pulse mode to assess its mode stability for independent pulses. For this purpose, the laser, the pulse ESPI camera and an aluminium plate vibrating with a low frequency have been mounted on a vibration insulated table. An external optical set up with a beam splitter was used to separate the reference beam from the illumination beam. With two consecutive pulses, the reference state and the deformed state of the object have been acquired using spatial phase shifting. Fig. 2 (left) shows a phase image of the vibrating plate from the first test series.

The following tests where carried out using the laser in double pulse mode with varying pulse separation times. During these tests, the internal flash lamp trigger generator of the laser was used, so that the laser shots where not synchronized to the object vibration. Although many of the measurements showed good fringe pattern quality, some of the measurements, especially those recorded shortly after switching the flash lamp cycle on, showed only poor fringe quality. It turned out that the seeking procedure of the piezo controlled rear mirror of the oscillator

cavity played an important role for the quality of the obtained fringes: Good measurements were obtained, if the laser was thermally stable and if the cavity length was settled. Fig. 2 (right) shows the vibrating plate recorded in double pulse mode.

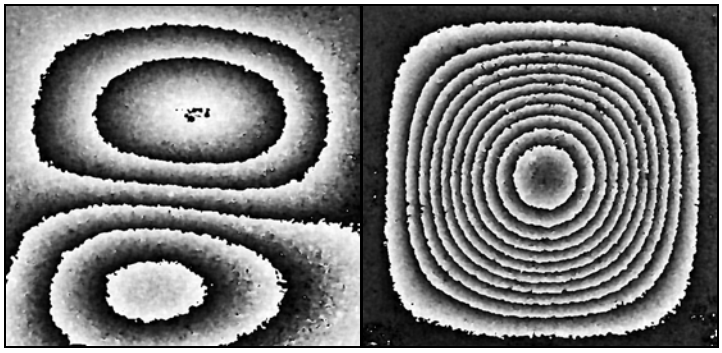

Fig. 2. A vibrating aluminium plate recorded with two independent single pulses (left), and a phase image of the same plate vibrating at a lower frequency, recorded in double pulse mode (right).

4 The Triggering System

In its standard configuration, the laser operates with a fixed, internally generated 10 Hz sequence of double pulses to keep it thermally balanced. For most measurement applications, such an internal automatic triggering is not suited, as it does not permit the synchronization of the laser pulses to independent external events like e.g. the vibration of the sample object to be measured.

As a modification of the internal laser triggering circuit would be very complex, and as the flash lamp of the laser can be triggered from an external source, it became obvious that an external laser triggering system had to be developed. This triggering system should allow a maximum of flexibility for the triggering of double pulses to external events, at the same time the thermal balance of the laser should be kept as stable as possible. This means that the nominal 10 Hz flash lamp repetition rate of the laser had to be maintained.

The first system tests have shown that the laser requires some time after the start of its flash lamp cycle before thermal stability has been reached and interferograms with good fringe quality can be recorded. Therefore it is not possible to synchronize the complete 10 Hz double pulse sequence to the external event. It was hence decided to operate the laser with a 10

Hz double pulse sequence generated by the triggering system and to synchronize an additional double pulse to the external event. At the same time, the external event should initialize the synchronization of the pulse ESPI camera to the double pulse, so that data is only recorded for the externally triggered double pulses. This is necessary to avoid the overwriting of the acquired measurement data with the next nominal laser pulse. The synchronization of the camera itself is done in the same way as in conventional set ups with ruby lasers, where a Pockels cell sync signal is used.

In order to keep the average energy within the laser constant, the nominal double pulse following the externally triggered one is omitted. This procedure keeps the average energy within the laser almost constant. It is obvious that this concept does not allow completely free laser synchronization to external events: Such an event can not trigger the laser immediately after a nominal double pulse, since the laser controller must restore sufficient energy for the flash lamp pumping. In addition, two shots following each other too quick lead to significantly decreased beam quality. In practice, however, this limited freedom of triggering is acceptable for most measurements of repetitive events.

Another issue to be integrated into the triggering system was the exploitation of the build up time of the laser pulses. To avoid the recording of speckle interferograms with poor fringe quality, the trigger controller and the camera synchronization unit do not forward external trigger events to the laser while the piezo controlled rear mirror of the oscillator cavity is seeking.

The laboratory tests of the laser combined with the triggering system showed that consecutive measurements with a very good repeatability could be carried out.

5 Other System Components

Another issue during the development was the layout of the external optical components for the pulse ESPI camera. The emitted laser pulses are with only 7 ns very short, so that all optical components have to withstand extremely high power during the shots. Appropriate coating of all mirrors and lenses is hence mandatory. Of course, the optical fibre used to guide the reference light to the pulse ESPI camera must match the wavelength of the laser.

The pulse ESPI camera and the data acquisition and evaluation PC with its software are standard products and did not require modification.

6 Industrial Applications

The here shown measurements have been carried out at the Forschungs- und Innovationszentrum of BMW AG in Munich. For vibration investigation of components and assemblies under operational conditions, the triggering signal for the pulse ESPI system is usually extracted from the signals of accelerometers connected to the test object. Depending on the measuring task, additional signals coming from the test bench may be necessary to synchronize the laser triggering to the desired vibration event.

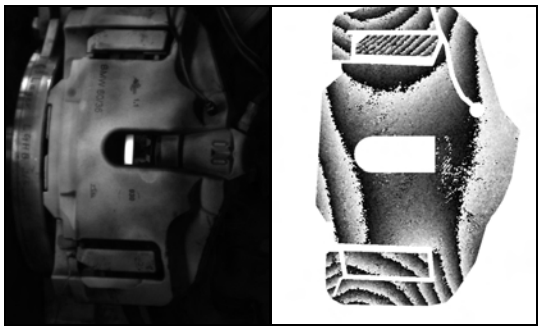

Fig. 3. A brake assembly investigated under operational conditions. The orientation and density of the fringes indicate independent vibration of the brake bracket and the calliper carriers.

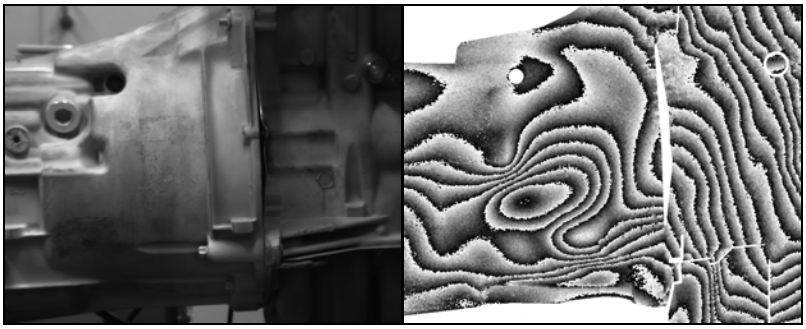

Fig. 4. An engine - gearbox assembly, measured under operational conditions. The fringe pattern indicates independent vibration of the two components.

7 Acknowledgments

Fig. 1 courtesy of InnoLas GmbH, Krailling
Fig. 3, Fig. 4 courtesy of BMW AG, München

Combining novel fringe analysis and photogrammetry for industrial shape measurement

Y. R. Huddart, J. D. R. Valera, A. J. Moore
Heriot-Watt University
Edinburgh EH14 4AS
U.K.N. J. Weston
Renishaw Plc.
Edinburgh EH14 4AP
U.K.

1 Introduction

High-precision measurement of manufactured parts commonly uses contact measurement methods. A probe attached to a coordinate measuring machine (CMM) touches the surface of the part at multiple points, and the probe tip position is sensed and recorded for each touch. Recently, devices have been developed that enable the probe tip to be scanned in a continuous path across the surface, providing for a shorter measurement time. Contact measurement is highly accurate and fast for shapes that are easily parameterized such as a sphere or a plane, but it requires considerable user input for less easily described objects, such as those with free-form surfaces. There is an increasing need within industry for measurement of complex manufactured parts with free-form surfaces.[1]

Non-contact measurement can be achieved by a fringe projection probe consisting of a camera and a fringe projector. The methods usually used to provide a phase step for automated measurement of surface shape from the projected fringe pattern require either an accurately calibrated translation stage to move a grating or the light source, or a programmable projector, which are currently impractical for mounting on a CMM due to weight limits or the delicate parts required.

Alternatively, a phase step may be produced by moving the probe relative to the object, thus eliminating the need for a complex projector or moving parts within the probe itself [2,3]. Herein we present a method for phase calculation based on this new approach.

2 Theory

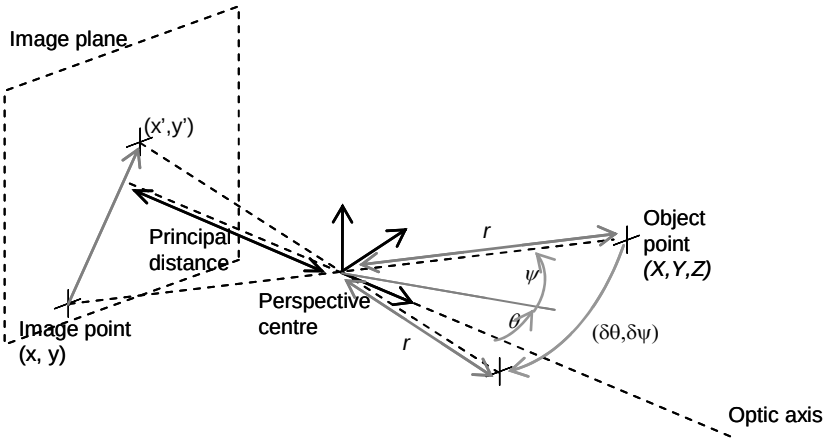

Fig. 1. Pinhole or central perspective projection model

The camera is modelled by the pinhole or central perspective projection camera model used in photogrammetry [4], Fig. 1. It consists of an array of pixels normal to the optic axis, and a pinhole or perspective centre through which light rays scattered from an object are considered to pass in a straight line. The distance from the perspective centre to the pixel array is the principal distance. Lens distortions and other internal parameters are taken into account through subsequent calibration.

A point on the object's surface $\underline{X}$ may be expressed relative to the perspective centre as

$$\underline{X} = \begin{pmatrix} X \\ Y \\ Z \end{pmatrix} = \begin{pmatrix} r\sin\theta\cos\psi \\ r\sin\psi \\ r\cos\theta\cos\psi \end{pmatrix} \tag{1}$$

where θ and ψ are azimuth and zenith angles and r is the distance from the origin as indicated in Fig. 1. According to the pinhole camera model, this point is imaged, in camera coordinates, at $\underline{x} = (x, y, -z_c)$ where

$$\frac{x}{z_c} = \frac{X}{Z} = \tan\theta\,,\ \frac{y}{z_c} = \frac{Y}{Z} = \frac{\tan\psi}{\tan\theta} \tag{2}$$

and z_c is the camera principal distance. It can be shown [5] that if pixel (x, y) images a point $\underline{X}$ on an object, the same point on the object is

imaged by pixel (x', y') after the object is moved through angles $(\delta\theta, \delta\psi)$, where

$$x' = z_c \tan(\theta + \delta\theta) = z_c \frac{x + z_c \tan\delta\theta}{z_c - x\tan\delta\theta} \tag{3}$$

and

$$y' = z_c \frac{\tan(\psi + \delta\psi)}{\cos(\theta + \delta\theta)} = z_c \frac{y + \sqrt{x^2 + {z_c}^2}\tan\delta\psi}{\left(x\sin\delta\theta - z_c\cos\delta\theta\right)\left(\frac{y}{\sqrt{x^2 + {z_c}^2}}\tan\delta\psi - 1\right)} \tag{4}$$

Because the object has moved relative to the projector, repeating the rotation and compensating for the motion in the camera image each time produces a set of phase stepped images which may be used to calculate the phase and therefore the object height.

3 Experimental setup and results

The experimental setup to validate the theory outlined above consisted of a digital video projector and a camera that were fixed within the measuring volume of a five-axis CMM, attached to which was a test object. Traditional temporal phase steps were produced by the projector; phase-stepped images due to probe motion relative to the object were produced by rotating the CMM-mounted object in an arc about the camera perspective centre and compensating the images for the motion using equations 3 and 4. Wrapped phase maps were calculated from the two sets of images using the synchronous phase shift algorithm [6] and Carre's algorithm respectively and then unwrapped using a standard "flood-fill" algorithm [7]. The zero order fringe from which to start the unwrapping was identified in an image of a single projected line. A phase-to-height calibration was used to calculate 3D coordinates [8].

Fig. 2 shows a sample image of projected fringes distorted by the object and the resulting wrapped phase map from rotation about the perspective centre. Fig. 3(a) shows a plot of the calculated height along a single line across the image. The inset shows the height in more detail, and a close match between the two methods can be seen. Fig. 3(b) plots the difference in the two results along the same line. The mean difference between the two is less than 30μm, and the RMS difference is 170μm. The periodic nature of the error is indicative of non-sinusoidal projected fringes and has

been reduced to a mean error of 10μm and an RMS error of 60μm by using an extra phase step [5]. Other potential sources of error, including non-constant phase shift between frames, and change in reflectance with viewing and illumination angles, are shown to have only a small effect under the small angular motion required to produce a satisfactory phase step [5].

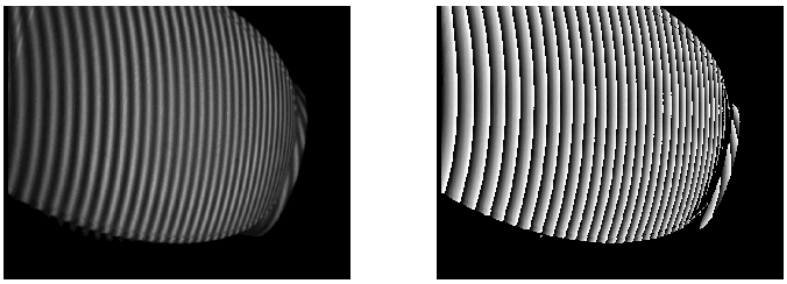

Fig. 2. (a) Sample fringe image and (b) unwrapped phase map from a set of phase-stepped images produced by rotation about the camera perspective centre

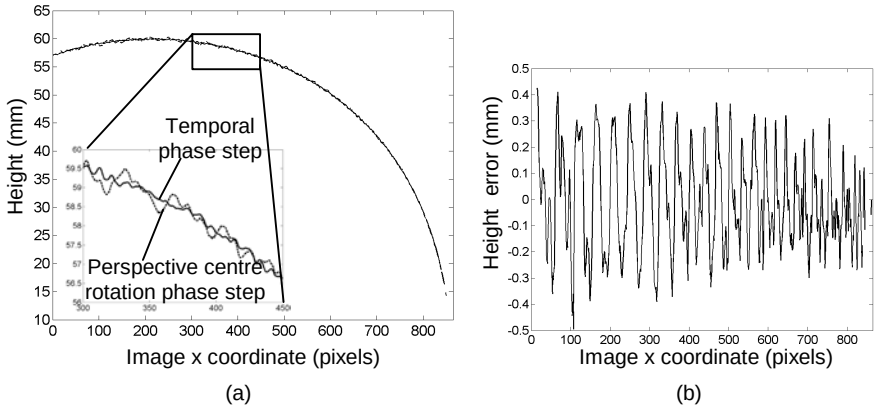

Fig. 3. (a) Calibrated height of object measured using traditional and perspective centre rotation, phase-step approaches; (b) difference in height between the two measurements

4 Conclusions

A novel method has been proposed to create phase-stepped images by rotating a CMM-mounted probe comprising a fringe projector and a camera (with a fixed spatial relationship) about the camera's perspective

centre. The recorded images can then be compensated for the relative motion of the camera independently of the distance to the object. The method enables shape measurement using only a single projected pattern, desirable when a light and robust probe without moving parts is required for CMM-mounted applications.

5 Acknowledgment

This work was partly funded by the Engineering and Physical Sciences Research Council [grant numbers GR/T11289/01, EP/F02553X/1]. Andrew Moore acknowledges the support of AWE through its William Penney Fellowship Scheme.

6 References

1. Harding, K (2008) Engineering precision. Nature Photonics 2:667-669.
2. Weston, N J, Huddart, Y R, Moore, A, J, Featherstone, T C (2009) Phase analysis measurement apparatus and method. International Patent Application, Publication Number WO 2009/024757.
3. Weston, N J, Huddart, Y R (2009) Non-contact probe. International Patent Application, Publication Number WO 2009/024758.
4. Cooper, M A R, Robson, S (2001) Theory of close-range photogrammetry. In Atkinson, K B (ed.) Close range photogrammetry and machine vision. Whittles Publishing.
5. Huddart, Y R, Valera, J D R, Weston, N J, Featherstone, T, Moore, A J (2009) Phase-stepping fringe analysis using a single projected pattern. In preparation for submission to Optics Express.
6. Bruning, J H, Herriott, D R, Gallagher, J E, Rosenfeld, D P, White, Brangaccio, D J (1974) Digital wavefront measuring interferometer for testing optical surfaces and lenses. Applied Optics 13(11):2693-2703.
7. Carre, P (1966) Installation et utilisation du comparateur photoelectrique et interferential du Bureau International des Poids et Mesures. Metrologia 2:13-23.
8. Reeves, M, Moore, A J, Hand, D P, Jones, J D C (2003) Dynamic shape measurement system for laser materials processing. Optical Engineering 42(10):2923-2929.

Digital holographic interferometry for deformation measurement by means of an acoustical device

Dipl.-Ing. Hendrik Fischer, Prof. Dr.-Ing. Rainer Tutsch,
Institut für Produktionsmesstechnik, TU Braunschweig

1 Introduction

In holographic interferometry, two or more wave fields, of which at least one was recorded and reconstructed via holography, are compared interferometrically. In digital holography the process of reconstructing the original wave field along with the interferometric superposition in digital holographic interferometry, is carried out numerically via PC.

In the special case of acoustical digital holography the recording of the hologram is done by means of a microphone array or a microphone scanned in a plane. A major difference between optical and acoustical recording of a hologram is that a real reference wave field in acoustics is not needed. This is caused by the fact, that in acoustics it is possible to have direct access to the phase information of a wave field. The recording of the acoustical hologram can be done using an electronic reference, which simplifies the measurement setup.

In this contribution the experimental setup for recording acoustical holograms in the low-frequency ultrasonic range, the process of recording and reconstructing acoustical wave fields, and the results of a deformation measurement realized via this setup is presented. The results of the acoustical deformation measurement are compared with the results of an optical deformation measurement carried out using a fringe projection system.

2 Experimental setup

The experimental setup consists of an ultrasonic transducer, a reflector of simple geometry (a thin metal sheet), and a standard microphone that is scanned in a plane using an x-y stage. The metal sheet is insonified with an ultrasound beam (a sine wave with constant frequency of 50 kHz) and the

reflected wavefield is measured by the microphone in the hologram plane. Simultaneously to the signal of the microphone, the driving voltage of the ultrasound transducer, which acts as reference, is acquired. The actual hologram results as superposition of both signals. The metal sheet is fastened to a carrier framework in a way that by means of a micrometer screw it is possible to impose a defined deformation on the sheet.

The metal sheet acts upon ultrasound as a mirror as the roughness compared to the wavelength of the ultrasound is negligible. Therefore, by recording the hologram of the reflected wavefield, not the hologram of the object (the metal sheet) itself can be acquired, but in effect the hologram of the originally emitting source (distorted by the reflecting surface).

3 Reconstruction and holographic interferometry

Both in optical and acoustical digital holography the reconstruction is carried out numerically via algorithms based on scalar diffraction theory [1]. Most frequently the integral forms of the monofrequent wave equation are applied [2]. These mean that with knowledge of the complex field function in one plane, the field function in any point in space can be computed by a surface integration. Thereby before the integration takes place, the field function is multiplied by the normal derivative of the Greens function disappearing on the plane. Especially used in this contribution is the Fresnel Kirchhoff diffraction formula [3]:

$$A_{re}(x_0, y_0, z_0) = \frac{i}{\lambda} * \int_{-\infty}^{\infty}\int_{-\infty}^{\infty} A_h(x_h, y_h) R(x_h, y_h) \frac{e^{-ikd}}{d} \left(\frac{1}{2} + \frac{1}{2}\cos\Theta\right) dx_h dy_h \qquad (1)$$

In (1) A_{re} represents the complex soundpressure, λ the wavelength, A_h and R the complex soundpressure of the hologram and the reference wave, respectively, k the wave number, d the distance between a point in the hologram and a point in the reconstruction plane and Θ the obliquity factor.

In principle this diffraction formula can be easily interpreted considering Huygens principle of spherical wave propagation. Thereby the reconstruction consists of spherical waves emanating from the measured points in the measurement plane (amplitude and phase of the spherical waves are the same as recorded in theses points). Additionally the superposition of the spherical waves is scaled by the inverse wavelength and multiplied by a phase factor and a geometry-dependant obliquity factor, as well.

The direct application of the Fresnel Kirchhoff diffraction formula has the advantage that the plane for calculating the reconstructed wavefield can be choosen freely in space and is not linked to the orientation of the measurement plane as would be the case with algorithms based on one or more fourier transforms. As the number of total elements sampled in the acoustical measurement is insignificant compared to pixel elements in digital cameras used in optical digital holography, the calculation time is no drawback. Since the insonification of the metal sheet is done under an angle of about 17 degrees the unrestricted possibility to choose the plane for reconstruction is of essential importance.

In digital holographic interferometry two holograms of the same object in different deformation states are recorded. For each of the two holograms a numerical reconstruction of the phase distribution in a reconstruction plane is carried out. The reconstruction plane is defined in such a way that it corresponds to the original position of the metal sheet. The information about the deformation of the object can be derived from unwrapping the calculated phase difference of the phase distributions won by the reconstructions.

4 Results

Two holograms of the metal sheet in different deformation states were recorded (once undeformed and once deformed at 1mm by the micrometer screw). The results are shown in figures 1 and 2. Figure 1 shows the amplitude distribution, figure 2 the phase distribution in the hologram plane. The special sampling of the x-y stage in both directions was 5 mm, giving a total of 1024 sampled positions.

The reconstructed deformation from these holograms is given in figure 3 a). The deformation is coded in grayscales by phase difference in radian. Figure 3 b) shows the results of an optical measurement carried out via a fringe projection system. The grayscales define deformations directly in mm. It can be seen that the acoustical measurement delivers accurate results concerning the biggest deformation in the middle of the sheet. The surrounding area has perceptible deviations in the range of up to 0.1 mm. The cause of these deviations is the subject of further work.

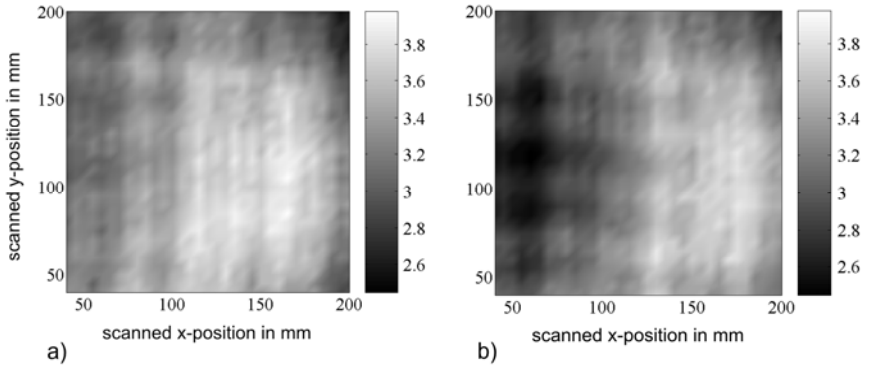

Fig. 1. Amplitude (greyscaled; microphone output voltage in V) of the reflected soundfield in the hologram plane; a) before deformation and b) after deformation

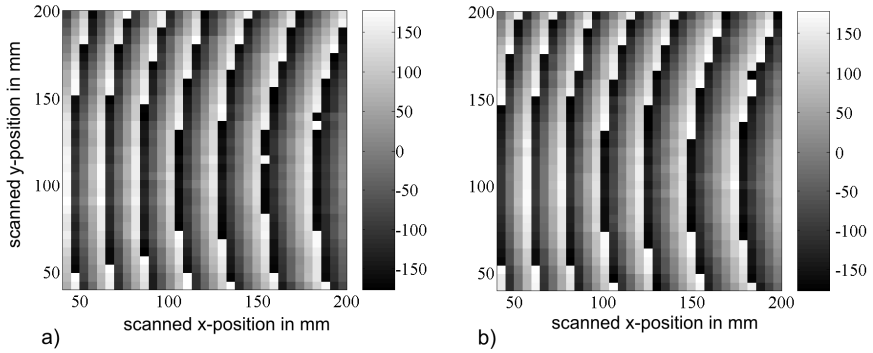

Fig. 2. Phase distribution of the reflected wavefield (in degree); a) before deformation and b) after deformation

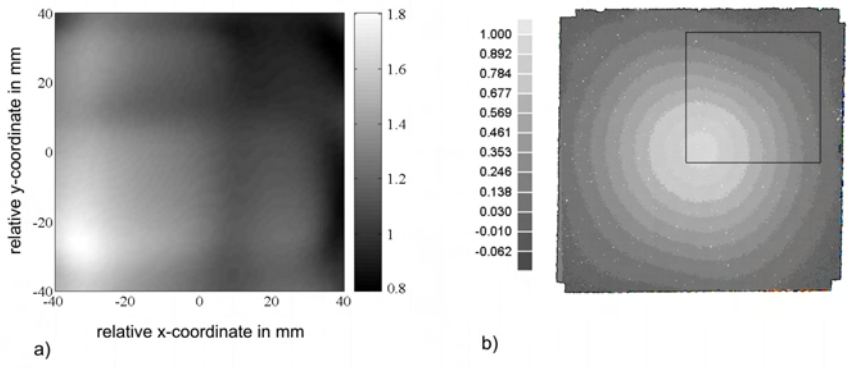

Fig. 3. Reconstructed deformation of the object a) acoustical, b) optical

5 References

1. Goodman, J W (1986) Introduction to Fourier Optics, San Francisco, McGraw-Hill
2. Nagai, K (1988) Synthetic aperture ultrasonic imagery; Advances In Electronics And Electron Physics, Volume 70, S. 215-314
3. Schnars, U, Jüptner, W P O (2002) Digital recording and numerical reconstruction of holograms, Measurement Science and Technology, Volume 13, R85-R101, IOP Publishing

Pump-probe interference microscope observation for femtosecond-laser induced phenomena

Yoshio Hayasaki, Akihiro Takita, and Mitsuhiro Isaka
Center for Optical Research and Education (CORE)
Utsunomiya University
7-1-2 Yoto, Utsunomiya, 321-8585, Japan

1 Introduction

An ultra-fast time-resolve imaging of laser-induced spatiotemporal phenomena including nonlinear light absorption and propagation, microplasma, shockwaves, and cavitation bubbles is very important to know an appropriate irradiation condition in femtosecond laser processing. The pump-probe shadowgraphy was firstly applied to observe a temporal evolution of the femtosecond-laser-induced phenomena [1-4]. Some types of pump-probe observations using interferometry [4-6], digital holography [7], and modified shadowgraphy [8] have been developed to obtain a phase change of the probe pulse for quantitative evaluations of the laser-induced phenomena. The quantitative evaluations, however, don't have been studied so much in a laser processing system having an objective lens with a high numerical aperture, which is important to fabricate nanostructures. Furthermore, in holographic femtosecond laser processing technique developed for improving the laser irradiation throughput and light-use efficiency [9,10], the laser-induced phenomena doesn't have studied yet. In this paper, we demonstrate a spatial and temporal evolution of phenomena induced in glass with femtosecond laser pulse irradiations with measurements using a pump-probe interference microscope.

2 Experimental setup

In an optical setup for a pump-probe interference microscope, the pump pulse was an amplified femtosecond laser pulse with a center wavelength of 800 nm. The pump pulses spatially divided by a beam splitter were focused inside a sample with a 100× objective with a numerical aperture

(NA) of 1.25. The sample was a cover slip. A probe pulse was a second-harmonic femtosecond laser pulse with the center wavelength of 400nm generated by a Barium Borate (BBO) crystal. The probe pulse was irradiated to the sample with a delay time Δt from the arrival of the pump pulse and introduced to the interferometer after transmitting the sample. Δt was controlled with an optical delay line. An interference fringe was taken with a cooled charge-coupled device (CCD) image sensor. A phase change $\Delta\phi$ was obtained by analyzing the fringes with the Fourier-transform method [11].

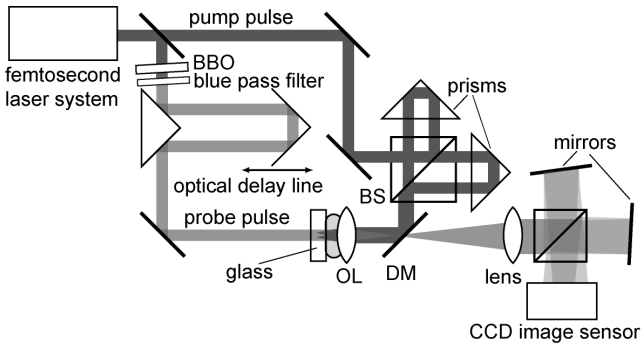

Fig. 1. Experimental setup.

3 Experimental results

The experiments were performed with changes of an irradition pulse energy to 150 nJ, a delay time to 6 ns, and an irradition pattern of pulses. Figure 2 shows phase distributions at the delay time of Δt = 10ps after a single pump-pulse with the irradition energies of (a) 0, (b) 27, (c) 32, (d) 70, and (e) 100 nJ was irradiated inside the glass sample. A positive phase change corresponding to a negative refractive index change caused by microplasma generated by a multi-photon absorption at the laser-focused point was apperaed from the threshold enegy of 25nJ. The phase change at the center of the circular area increased with an increase of the irradition energy and its size also increased. The phase change rapidly increased at the energy from 25 to 36 nJ because of an increase of the plasma diameter. The phase changes in the energy more than 40nJ were small because the plasma diameter didn't increase.

Figure 3 shows phase distributions at Δt = 500 ps for the irradition energies. The positive phase change at the center was almost same as those

at Δt = 10ps under the energy of less than 35 nJ. When the energy was more than 35 nJ, the positive phase changes decresed from those at Δt = 10ps. The circular negative phase changes corresponding to positive refractive changes appeared. This negative phase changes was generated by shockwaves whose speed was 5400 m/s. The speed agreed to the sound speed in glass of 5440 m/s. The shockwaves was formed by a compression of glass around the microplasma given by its expansion and propageted outward. The negative phase change increased with an increase of the energy. The negative phase changes was caused by an increase of compression and an increase of the axial length of shockwaves with the energy increase.

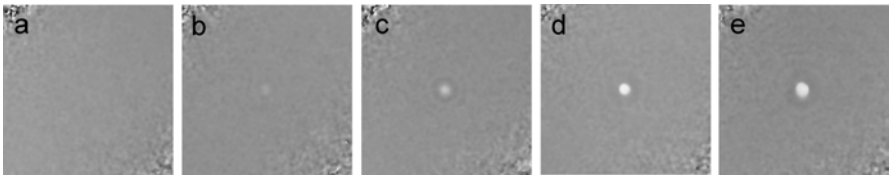

Fig. 2. Phase changes at the delay time of Δt = 10ps formed by a single laser pulse with the energies of (a) 0, (b) 27, (c) 32, (d) 70, and (e) 100 nJ. Side length of these pictures was 10 μm.

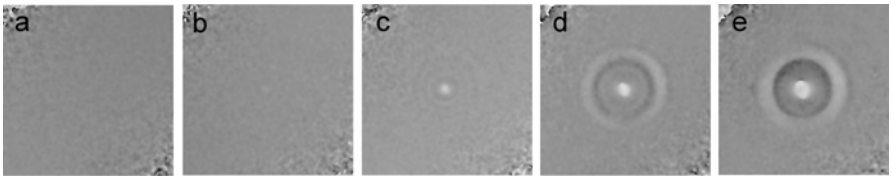

Fig. 3. Phase changes at the delay time of Δt = 500ps formed by a single laser pulse with the energies of (a) 0, (b) 27, (c) 32, (d) 70, and (e) 100 nJ.

4 Conclusions

Positive phase changes generated by a laser-induced microplasma were measured with a pump-probe interference microscope. The postive phase changes increased with an increase of the irradiation energy of the pump-pulse. Expecially, an increase of the plasma diameter gave a rapid increase of the phase change at the energy from 25 to 36 nJ. The subsequent shock waves generated negative phase changes with a ring structure. The experiments were performed with changes of an irradition pulse energy, a delay time, and an irradition pattern of pulses. We will discuss the

diffrence between phenomena induced by a single pulse irradiation and parallel laser pulse irradiations.

5 References

1. Emmony, D C, Siegrist, M, Kneubühl, F K (1976) Laser-induced shock waves in liquids, Appl. Phys. Lett. 29: 547-549
2. Vogel, A, Busch, S, Parlitz, U (1996) Shock wave emission and cavitation bubble generation by picosecond and nanosecond optical breakdown in water, J. Acoust. Soc. Am. 100: 148-165
3. Schaffer, C B, Nishimura, N, Glezer, E N, Kim, A M-T, Mazur, E (2002) Dynamics of femtosecond laser-induced breakdown in water from femtoseconds to microseconds, Opt. Express. 10: 196-203
4. Abraham, E, Minoshima, K, Matsumoto, H (2000) Femtosecond laser-induced breakdown in water: time-resolved shadow imaging and two-color interferometric imaging, Opt. Commun. 176: 441-452
5. Sun, Q, Jiang, H, Liu, Y, Wu, Z, Yang, H, Gong, Q (2005) Measurement of the collision time of dense electric plasma induced by a femtosecond laser in fused silica, Opt. Lett. 30: 320-322
6. Centurion, M, Pu, Y, Liu, Z, Psaltis, D, Hänsch, T W (2004) Holographic recording of laser-induced plasma, Opt. Lett. 29: 772-774
7. Balciunas, T, Melninkaitis, A, Tamosauskas, G, Sirutkaitis, V (2008) Time-resolved off-axis digital holography for characterization of ultrafast phenomena in water, Opt. Lett. 33: 58-60
8. Minardi, S, Gopal, A, Tatarakis, M, Couairon, A, Tamošauskas, G, Piskarskas, R, Dubietis, A, Trapani, P D (2008) Time-resolved refractive index and absorption mapping of light-plasma filaments in water, Opt. Lett. 33: 86-88
9. Hayasaki, Y, Sugimoto, T, Takita, A, Nishida, N (2005) Variable holographic femtosecond laser processing by use of spatial light modulator, Appl. Phys. Lett. 87: 031101
10. Hasegawa, S, Hayasaki, Y, Nishida, N (2006) Holographic femtosecond laser processing with multiplexed phase Fresnel lenses, Opt. Lett. 31: 1705-1707
11. Takeda, M, Ina, H, Kobayashi, S (1982) Fourier-transform method of fringe-pattern analysis for computer-based tomography and interferometry, J. Opt. Soc. Am. 72: 156-160

Three-dimensional shape measurement of dynamic objects with spatially isolated surfaces

Qican Zhang, Xianyu Su, Liqun Xiang
Department of Opto-electronics, Sichuan University, Chengdu 610064, China.

1 Introduce

In past twenty years, many researches have been done on Fourier Transform Profilometry (FTP) [1,2] to enlarge its measure range, improve its precision and extend its application [2-6]. Due to the high frequency component abandoning by the bandwidth-pass filter in fringe analysis process, the reconstructed object looks smoother than the natural one. In addition, an accurate 3D reconstruction can not be completed by FTP if the tested object has discontinuous height steps or surface spatially isolated. Meanwhile, lots of work has been done to make full use of the temporal infromation of a seriers of fringe patterns in measuring a complicated objects. Temporal phase unwrapping [7-10] is a successful and popular method for this aim. It independently unwrap the phase of each pixel along the temporal axis, so the errors propagate in spatial domain can be avoided. With this outstanding advantage and a series of projected grating, this method can be used to measure static object which has discontinuous height steps or surface spatially isolated, overcoming the shadows caused by slits and holes or the difficult of spatial phase unwrapping.
In this paper, a new method is proposed to 3D shape measurement of a dynaimc object. The 3D shape of a tested dynamic object, including the high frequency component in its spatial domian, is modulated into the temporal domian by a multi-period phase shifting grating. Then, the 3D phase distribution is extracted by a 1D Fourier transform along the temporal axis. So the high frequency component in the spatial domian can be preserved without any damnification and reduction.

2 Temporal Fourier Transform Profilometry (TFTP)

The optical geometry of a TFTP system is similar to that of FTP, expect a multi-period phase shifting projector, which can be acted by a digital

projector. The CCD camera should work synchronously with the fringe projector, so its external synchronizing trigger function is needed. When a multi-period shifting sinusoidal grating is projected on a diffused dynaimc object's surface, a sequence of deformed fringes which modulated by the height of the tested object will be recorded by the camera. At time *t*, the deformed fringe on the object surface is:

$$g(x,y,t) = a(x,y) + b(x,y)\cos(2\pi x/p_0 + \phi(x,y,t) + 2\pi f_t t) \tag{1}$$

p_0 is the spatial period of the projected grating. $\phi(x,y,t)$ is the phase distribution modulated by the height information of the tested object and is a function of time. $2\pi f_t t$ is the phase modulation at time *t* casued by the multi-period phase shifting. In the temporal domain, the signal distribution of each pixel is periodic with f_t, the temporal period of the phase shifting. For each signal at one fixed point (*x*,*y*), the $\phi(x,y,t)$ is a slowly changing signal comparing with f_t. If 1D Fourier transform along the temporal axis *t* is carried out for each pixel's signal and the frequency components of its Fourier spectrum $G(x,y,f)$ will be separated:

$$G(x,y,f) = a(x,y)\cdot\delta(f) + \frac{c(x,y)}{2}\psi(x,y,f-f_t) + \frac{c'(x,y)}{2}\psi^*(x,y,-(f+f_t)) \tag{2}$$

Filtering out one of the fundamental frequencies with a proper 1D filter window along *t* axis and doing 1D inverse Fourier transform F^{-1}. The result of its complex distribution is:

$$\hat{g}(x,y,t) = F^{-1}\left\{\frac{C(x,y)}{2}\psi(x,y,f-f_t)\right\} = \frac{C(x,y)}{2}e^{i\phi(x,y,T)}e^{i2\pi f_t T} = \frac{C(x,y)}{2}e^{i[\phi(x,y,t)+2\pi f_t t]} \tag{3}$$

Then, $\phi(x,y,t)$ can be extracted from this complex distribution. By unwrapping processing, the 3D continuous phase distribution $\Phi(x,y,t)$ can be obtained:

$$\Phi(x,y,t) = unwrap\{\phi(x,y,t)\} = unwrap\{\arctan\frac{\mathrm{Im}[\hat{g}(x,y,t)]}{\mathrm{Re}[\hat{g}(x,y,t)]}\} - 2\pi f_t t \tag{4}$$

where, *unwrap*{#} is an unwrapping operator. In order to get the natural phase of the tested object, the time modulated factor $2\pi f_t t$ should be removed. Finally, the 3D shape distribution $h(x,y,t)$ will be calculated by the same process in FTP.

3 Experimental results

In order to verify this method, an experiment is carried on a cracking thin plate which impacted by a flying hammer. The spatial period of the projected grating is 11 pixels. A camera (Lumenera Lu050M, 200 fps) has been employed to record 100 frames fringe patterns at 156×156 pixels

during 20 periods phase shifting with the increment of $2\pi/5$. Four frames of the deformed fringes are shown in Fig.1.

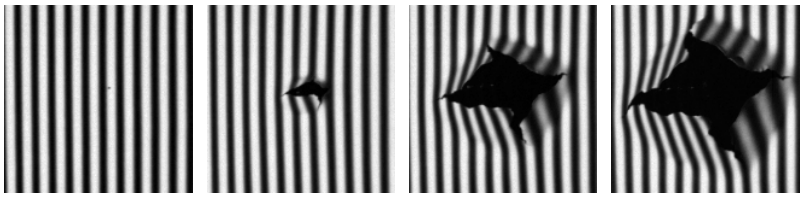

Fig. 1. Four deformed fringe patterns of the cracking thin plate

The temporal signals and their corresponding 1D Fourier spectrum distributions at (1,1), (40,40), (79,79), (118,118) and (156,156) pixels are shown in Fig.2 (a) and (b) respectively.

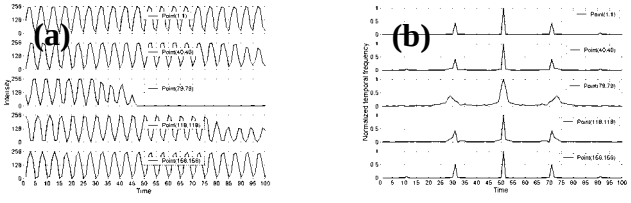

Fig. 2. The temporal signals and Fourier spectrum distributions of 5 pixels.(a) Temporal signals; (b) Fourier spectrum of the signal in (a)

Figure 3 show the reconstructed phase distributions of four corresponding sampling moment shown in Fig. 1.

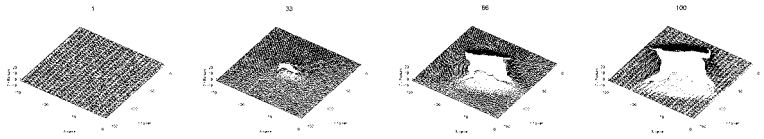

Fig. 3. The reconstructed 3D shape of the corresponding sampling moment shown in Fig. 1

4 Conclusion

The most difference between this new method and FTP is how the 3D wrapped phase is obtained. There are three advantages of the new method: (1) There is no spatial filtering in TFTP, so the spatial spectrum will not be damaged and the high frequency components will be preserved carefully. (2) If one of the 2D spatial wrapped phase in the whole 3D field can be

unwrapped, the whole 3D wrapped phase will be successfully unwrapped along the temporal axis. (3) The most important is that all the TFTP process has little relevancy with f_0, the modulated spatial frequency of the structured illumination, and the lower spatial frequency can be used for easier 2D spatial unwrapping. So the discontinuous object can be correctly measured, even the dynamic one.

5 Acknowledgment

This work was support by National Natural Science Foundation of China (60807006).

6 References

1. Takeda M, Mutoh K. (1983) Fourier Transform Profilometry for the auto measurement of 3-D object shapes. Applied Optics 22:3977-3982
2. Su Xianyu, Chen Wenjing. (2001) Fourier transform profilometry: a review. Optics and Lasers in Engineering 35:263-284
3. Lin Jin-Feng, Su Xian-Yu. (1995) Two-dimensional Fourier transform profilometry for the automatic measurement of three-dimensional object shapes. Optical Engineering 34:3297-3302
4. Ge Zongtao F, Kobayashi S, Matsuda, et al. (2001) Coordinate-transform technique for closed-fringe analysis by the Fourier-transform method. Applied Optics 40:1649-1657
5. Chen Wenjing, Yang Hu, Su Xianyu, et al. (1999) Error caused by sampling in Fourier transform profilometry. Optical Engineering 38:1029-1034
6. Zhang Qican, Su Xianyu. (2005) High-speed optical measurement for the drumhead vibration. Optics Express 13:3310-3316
7. Huntley J, Saldner H. (1993) Temporal phase-unwrapping algorithm for automated interferogram analysis. Applied Optics 32:3047-3052
8. Salder H, Huntley J. (1997) Temporal phase unwrapping: application to surface profiling of discontinuous objects. Applied Optics 36:2770-2775.
9. Huntley J, Salder H. (1997) Shape measurement by temporal phase unwrapping: comparison of unwrapping algorithms. Measurement Science Technology 8:986-992
10. Tian Ailing, Makihata T, Takeda M, Jiang Zhuangde. (2004) Three-dimensional profile measurement of objects with spatially isolated surfaces by modified temporal phase unwrapping. Journal of xi'an jiaotong university 38:1196-1198 (in Chinese)

Optical design of a DOE-based laser interferometer for inspection of MEMS/MOEMS

M. Józwik[1], M. Kujawińska[1], U.D. Zeitner[2], K.H. Haugholt[3]
[1] Warsaw University of Technology, Institute of Micromechanics and Photonics, 02-525 Warsaw, 8 Sw. A. Boboli St., Poland
[2] Fraunhofer Institute for Applied Optics and Precision Engineering IOF, Albert-Einstein-Str. 707745 Jena, Germany
[3] SINTEF 7465 Trondheim, Strindveien 4, Norway

1 Introduction

The passive and active characterization of microsystems is a strongly growing field of science [1]. Industry uses most often interferometry implemented by means of commercial instruments applied sequentially to the elements at a wafer. This is a bottle-neck in Micro-(Opto)-Electro-Mechanical Systems (M(O)EMS) production today limiting their high volume throughput. Below we present the new approach towards microsystems characterization at wafer level developed under EU project „SMART InspEction system for High Speed and multifunctional testing of MEMS and MOEMS" (SMARTIEHS) [1],[2]. The goal of the project is to provide fast, cost effective and flexible optical inspection system. Two different interferometer approaches are pursued in the project's development process: a refractive optics based Mirau type low coherence interferometer and a diffractive optics based Twyman-Green laser interferometer. Below we present the basic concept and design of the Twyman-Green interferometer in an array arrangement.

2 Design of the laser interferometer

The design of the laser interferometer is based on a Twyman-Green (TGI) configuration. Such interferometers are frequently used for non-contact, full-field measurements of MEMS/MOEMS with reflective surfaces and they have been proven to be very efficient setups for active MEMS testing [3],[4]. The multifunctional approach of the laser interferometer measurement concept allows within one instrument to inspect MEMS shape and deformation as well as to characterize a spatial distribution of

out-of-plain amplitude of vibration at a resonance frequency. However its application is restricted to objects with a continuous surface and relatively small surface gradients.

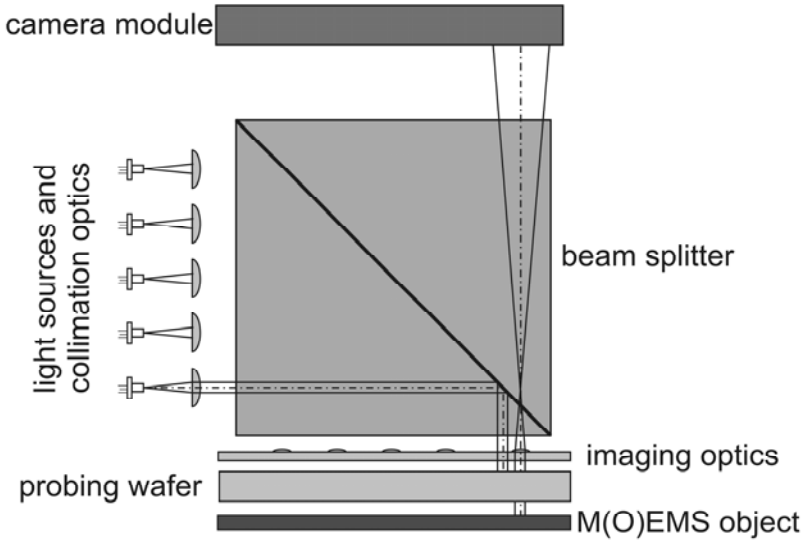

Fig. 1. The scheme of an array of Twyman-Green interferometers for parallel M(O)EMS testing

In the project the array of TGIs at probing wafer is integrated with illumination module, light guiding beam splitter, imaging optics and camera (Fig.1). 5x5 laser diodes with aspheric collimation optics provide input plane beams for 5x5 interferometer channels. The probing wafer incorporating the DOE structures is illuminated via a beam splitter cube, playing here an auxiliary role. The beam is separated into two beams illuminating the reference surface (flat surface) and the object (investigated M(O)EMS). After reflection, the beams are recombined along a common path of the imaging optical system. Finally, the detector captures the interference pattern, which can be processed by chosen fringe analysis method. The full image of the camera consist of the matrix of sub-images given by the interferometer matrix.

2.1 Architectures of the probing wafer

Two different architectures of probing wafer have been investigated:
- fabricated from a single glass substrate (Fig.2a),

- fabricated from two glass substrates supported by additional alignment and bonding processes (Fig.2b).

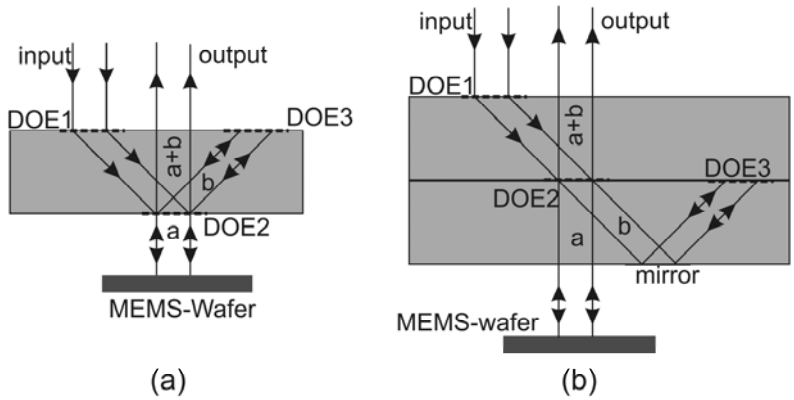

Fig. 2. The scheme of DOE-based architecture: a) single wafer, b) on two wafers setups.

Both architectures require custom designed diffractive optical elements. The top surface of the substrate includes etched diffractive optical element DOE1. It allows changing a direction of the incident, collimated beam in order to illuminate DOE2 fabricated on the bottom side. DOE2 in both architectures serves as a beamsplitting and beams recombining element. The light transmitted by DOE2 forms an object beam which is reflected by an investigated MEMS structure. In the first architecture, DOE2 reflects part of light and directs it to DOE3, which acts as a reference mirror. In the second version, DOE2 transmits light to a mirror which direct the beam to DOE3. Both beams after reflections are recombined by DOE2 and imaged through an imaging optics at a camera. After detailed analysis the two wafers configuration was selected due to less demanding design of DOE2, mostly connected with work of this element only in transmission mode.

2.2 DOE requirements

In order to optimize the system design, the analysis of optical components is crucial, especially in case of DOE's. The elements are designed for an illumination wavelength of λ=650nm. The DOE's used in the laser interferometer having different functionality: incoupling DOE1, beamsplitting DOE2 and reflecting DOE3. The grating period of DOE1 and DOE2 will be 1µm while the period of the retro-reflecting grating DOE3 will be 500nm. The fabrication all grating structures will be done by electron-beam lithography and reactive ion etching. As the lateral feature

size is demanding it is foreseen to realize all three gratings with a binary surface profile only. In order to achieve high diffraction efficiency especially for the asymmetrically used incoupling DOE1 the structure within one grating period is realized as an effective refractive index modulation with sub-wavelength feature sizes. By this technique it is possible to achieve a theoretical efficiency for the deflection into the +1 diffraction order of nearly 70% while the surface profile remains binary only.

3 Conclusions

This paper focus on the optical design of DOE based Twyman-Green laser interferometer. Two different architectures of probing wafer have been presented. The advantage of the structure fabricated on single glass substrate is its monolithic construction. However, for technological reasons, structure based on two substrates has bigger chances to be implemented. Before the final integration, the each of the DOE structure will be fabricated individually and characterized. The single channel interferometer built-up from those elements will be used to characterize the performance of the system.

4 Acknowledgment

SMARTIEHS is a collaborative project funded under the Grant Agreement 223935 to the 7th Framework Program Objective 2007-3.6.

5 References

1. www.ict-smartiehs.eu
2. Gastinger K, Kujawinska M, Løvhaugen O, Beer S, Gorecki C, Zeitner U (2008) SMARTIEHS – Smart inspection system for high-speed and multifunctional testing of MEMS and MOEMS. 14th Micro Optics Conference 2008 (MOC'08) Brussels, Belgium
3. Osten W (2006) Optical inspection of Microsystems, Taylor and Francis, New York
4. Gorecki C, Józwik M, Sałbut L (2005) Multifunctional interferometric platform for on-chip testing the micromechanical properties of MEMS/MOEMS. Journal of Microlithography, Microfabrication, Microsystems 4(4): 1-10

Time Resolved High Resolution Shape and Colour Measurement using Fringe Projection

Zonghua Zhang[1,2], David P. Towers[1], Catherine E. Towers[1],
[1]School of Mechanical Engineering, University of Leeds, Leeds, UK
[2]School of Mechanical Engineering, HeBei University of Technology, Tianjin, China. 300130

1 Introduction

The use of projected fringe techniques for shape measurement is now well established in a number of market sectors, e.g. engineering, art preservation, validation of design [1]. However, there are increasing demands from the media sector, medical imaging and security industries for single snapshot real time 3D shape and color texture acquisition. For the measurement of generic artefacts containing discontinuities or discrete objects absolute fringe order information is needed which is most routinely obtained through multi-wavelength methods [2,3]. Ideally, wrapped phase information at the multiple wavelengths needed will be obtained from a single image, thereby removing any requirements for high speed image recording devices [4]. Similarly, in applications where colour texture data is needed it would be convenient to use a colour camera to acquire both the shape and texture information such that they are pixel locked to each other.

In this paper we present a strategy to satisfy these requirements by projecting a custom static pattern from a DLP projector onto the test object and imaging the scattered light onto a 3-chip colour camera. The different fringe patterns are multiplexed in the three primary colour channels [5] (rather than limit the bandwidth and hence range of surface slopes that can be analysed using frequency multiplexing [6]) and The Fourier transform approach is used to obtain phase information from the fringe image in each colour channel [7]. The effects of chromatic crosstalk [5] and chromatic aberration [8] can be removed using software techniques.

2 Multi-Wavelength Wrapped Phase Measurement

A different number of fringes is encoded into the red, green and blue channels of a DLP projector and imaged off-axis by a colour CCD. The

spectra of the colour channels in commercial off-the-shelf projectors and cameras tend to overlap in order to avoid any colour blind areas, hence crosstalk between the channels is unavoidable. The amount of crosstalk can be determined in advance as a coefficient representing the amount of light in a particular illumination channel being detected in a different channel at the detector. Given that the crosstalk coefficients are known, a set of corrected intensities can be determined. The Fourier transform algorithm can then be used to extract the wrapped phase and the background intensity information (denoting the colour texture) from the corrected intensities in each colour channel.

3 Absolute Fringe Order Calculation

The optimum multi-frequency selection process defines the numbers of fringes to project as $N_{fi} = N_{f0} - \left(N_{f0}\right)^{(i-1)/(n-1)}$ [3], where N_{f0} and N_{fi} are the maximum number of fringes and the number of fringes in the *i*th fringe set, respectively, n is the number of fringe sets used and $i = 1, ..., n-1$. When three fringe sets are used, it is usually referred to as the optimum three-frequency method. For example, if $N_{f0} = 49$ and $n = 3$, the other two fringe sets have fringe numbers of $N_{f1} = 48$ and $N_{f2} = 42$. This method resolves fringe order ambiguity as the beat obtained between N_{f0} and N_{f1} is a single fringe over the full field of view. All the wrapped phase data are obtained with relatively high numbers of projected fringes and hence averaging can be used to further improve the sub-fringe phase resolution. With 49 projected fringes the fringe order calculation is reliable to 6σ providing the phase noise to one standard deviation is better than $1/59^{th}$ of a fringe [3]. Lateral chromatic aberration generates a small distortion in the number of projected fringes between colour channels which can be compensated in software [8]. The fringe order is determined at each pixel independently, so the method can measure objects with discontinuities and/or isolated surfaces by using three fringe sets.

4 Results

The images presented were captured using a Benq data projector and Hitachi 3-chip colour CCD camera. Fig. 1 shows the crosstalk corrected intensities in the R, G and B channels (parts a-c), and the calculated shape (part d) and texture rendered shape (part e). The scene consists of two flat

surfaces separated in height. Without the multi-wavelength phase data the relative position of the surfaces could not be assigned correctly. Further evaluation of the process was performed by varying the height difference between the two surfaces and in all cases the correct position was obtained.

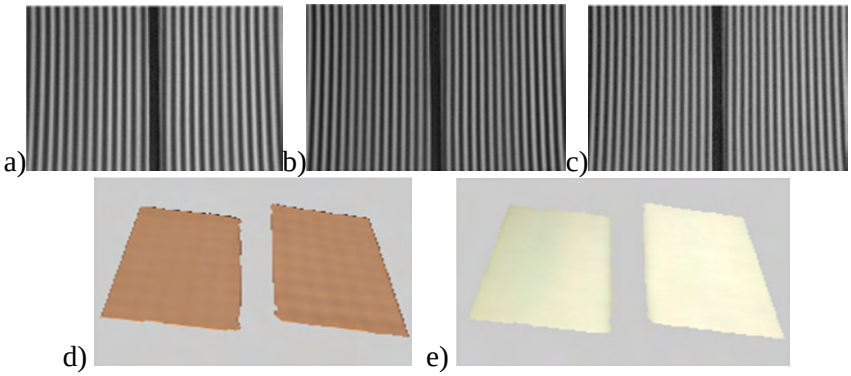

Fig. 1. Projected fringe data on two separated flat surfaces. a)-c) the intensities after correcting for crosstalk and showing the different numbers of fringes projected in the R, G and B colour channels, d) the reconstructed surfaces, e) texture rendered surfaces

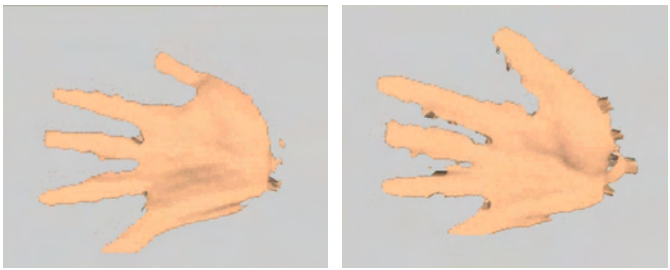

Fig. 2. Rendering of a moving human hand at two instants from a video stream using optimum 3-wavelength phase analysis and recording with a colour camera.

The process has also been evaluated on a moving human hand. Two 3D renderings of the hand are given in Fig. 2 after applying the same process. The images were captured at 7.5 frames/s and each rendering is derived from a single image. There are some noisy data around the edges as these areas have large slope and the windowing involved in Fourier phase analysis limits the range of surface slopes that can be determined correctly. These images demonstrate that the proposed method can measure 3D shape and colour information of a moving object.

5 Summary

In this paper it has been shown that 3-wavelength absolute fringe data can be obtained reliably of generic artefacts with all the data processed from a single image. A colour camera has been used to multiplex the multi-wavelength information with Fourier phase analysis used to derive the wrapped phase at each frequency of projected fringes. It has been shown that chromatic aberrations and crosstalk can be effectively compensated.

6 Acknowledgments

The authors acknowledge support through grant EPSRC EP/C540042.

7 References

1. Chen, F, Brown, GM, Song, M (2000) Overview of three-dimensional shape measurement using optical methods. Opt. Eng. 39:10-22
2. Burke, J, Bothe, T, Osten, W, Hess, C (2002) Reverse engineering by fringe projection. SPIE 4778:312-324
3. Towers, CE, Towers, DP, Jones, JDC (2005) Absolute fringe order calculation using optimised multi-frequency selection in full-field porfilometry. Opt. Lasers Eng. 43:788-800
4. Zhang, S, Yan, ST (2006) High-resolution, real-time 3D absolute coordinate measurement based on a phase-shifting method. Optics Express 14:2644-2649
5. Zhang, ZH, Towers, CE, Towers, DP (2006) Time efficient color fringe projection system for 3D shape and color using optimum 3-frequency selection. Optics Express 14:6444-6455
6. Takeda, M, Gu, Q, Kinoshita, M, Takai, H, Takahashi, Y (1997) Frequency-multiplex Fourier-transform profilometry: a single-shot three-dimensional shape measurement of objects with large height discontinuities and/or surface isolations. Applied Optics 36:5347-5354
7. Takeda, M, Mutoh, K (1983) Fourier transform profilometry for the automatic measurement of 3D object shapes. Appl. Opt. 22:3977-3982
8. Zhang, ZH, Towers, CE, Towers, DP (2009) Compensating lateral chromatic aberration of a colour fringe projection system for shape metrology. Optics and Lasers in Engineering, accepted for publication

Dynamic 3-D shape measurement techniques with marked fringes tracking

Xianyu Su[1], Qican Zhang[1], Yansan Xiao[2], Liqun Xiang[1]
1 Opto-Electronics Department, Sichuan Univ., 610064 Chengdu, China
2 China Three Gorges University

1 Introduction

Dynamic 3-D shape measurement techniques, based on grating projected and fringe analysis, have been researched widely. Fourier transform profilometry (FTP) requires only one frame of the deformed fringe pattern, which makes real-time data acquiring and processing of dynamic process possible[1,2]. Dynamic 3-D shape measurement has important application in some fields such as high-speed rotation, hydromechanics, stress analysis, impact and detonation process, and so on[3,4]. When the measured dynamic object is spatially isolated or breaking into several isolated parts (e.g. an impact process), it will bring some difficulties for phase unwrapping. When CCD's time sampling frequency does not satisfy the sampling theorem in time domain, it will bring same difficulties for phase unwrapping. In this paper we proposed a new method marking fringe order, in which a special mark was embedded into some projected sinusoidal gratings to identify the fringe order. These phase values at marked strip keep the relation of same fringe order, even the fringe was broken when dynamic process in which object is spatially isolated or breaking into several isolated parts. The phase unwrapping process of each broken parts will be done from the local marked strip respectively.

The experiment of dynamic 3-D shape measurement is to test a breaking ceramic tile. In projection fringe pattern we design three marked fringes. In the experiment the ceramic tile was broken into four spatial-isolated blocks after being impacted. With marked fringes tracking the phase unwrapping was done correctly in four spatial-isolated blocks. Experiment proves the feasibility of this method. The dynamic 3-D shape of a measured object, which was divided into several parts in impact, was reconstructed correctly.

2 Measurement system for dynamic 3-D shape

The optical geometry of the measurement system for dynamic object is similar to traditional FTP, as shown in Fig.1.

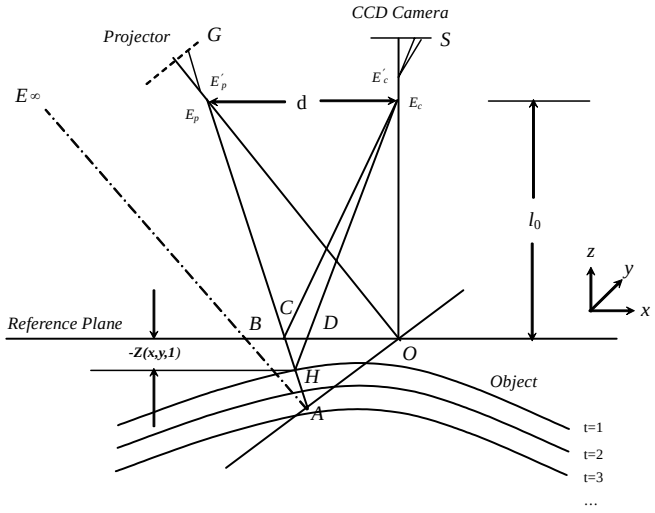

Fig. 1. Optical geometry of a dynamic 3-D shape measurement system

A sequence of the deformed fringe patterns can be grabbed by CCD camera and stored into a computer rapidly. The intensity distributions of these fringe patterns in difference time can be expressed as:

$$g(x,y,z(t))=\sum_{n=-\infty}^{+\infty}A_n r(x,y,t)\exp\{i[2n\pi f_0 x+n\phi(x,y,t)]\} \qquad (t=1,2,...,m)$$

where $\phi(x,y,t)$ represents the phase modulation caused by the object height variation in the different time, m is the number of all fringe images grabbed by CCD camera. Fourier transform, filtering only the first order term (n=1) of the Fourier spectra, and inverse Fourier transform are carried out to deal with each fringe pattern grabbed by CCD camera at the different time. Complex signals at different time can be calculated:

$$\hat{g}(x,y,z(t))=A_1 r(x,y,t)\exp\{i[2\pi f_0 x+\phi(x,y,t)]\}$$

Then the phase calculation and 3D phase unwrapping should be done. When the measured dynamic object is spatially isolated or breaking into several isolated parts, it will bring some difficulties for phase unwrapping.

3 Marked fringe pattern for phase unwrapping

We embedded a special mark into the projected sinusoidal gratings to identify the fringe order. It is shown in Fig.2. The orientation of the Fourier spectra of the mark is perpendicular to that of the fringe, therefore the mark will not affect the Fourier spectra of the deformed fringe and could be extracted easily with a proper band-pass filter in the other direction.

The phase value on the same marked strip is equivalent and known, so these phase values at marked strip keep the relation of those separated fringes. The phase unwrapping process of each broken parts will be done from the local marked strip respectively.

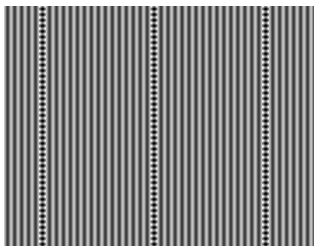

Fig.2 Marked fringes image

4 Dynamic 3-D shape measurement for breaking object

The experiment of dynamic 3-D shape measurement is to test a breaking ceramic tile. The experimental results are given in Fig. 3 and Fig.4. Obviously the tile is divided into 4 spatial-isolated blocks and the fringe discontinuity is followed. The introduced marked fringe has been used to ensure the phase unwrapping process error free. The whole breaking process contains 47 frames and lasts 235 ms. Six of them are shown in Fig.3. Fig. 4 shows the reconstructed 3-D shape of the breaking tile at the corresponding sampling instants in Fig.3

The experimental results show the validity of the proposed method. The dynamic 3-D shape of a measured object, which was divided into several parts in impact, was reconstructed correctly. Even when CCD's time sampling frequency does not satisfy the sampling theorem in time domain, the method still works well.

5 Acknowledgements

This project was supported by the National Natural Science Foundation of China (No. 10876021 and 60838002).

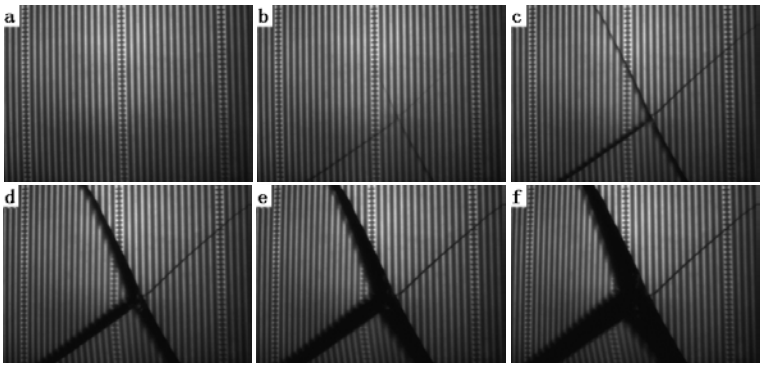

Fig. 3. Six frame deformed fringes images.

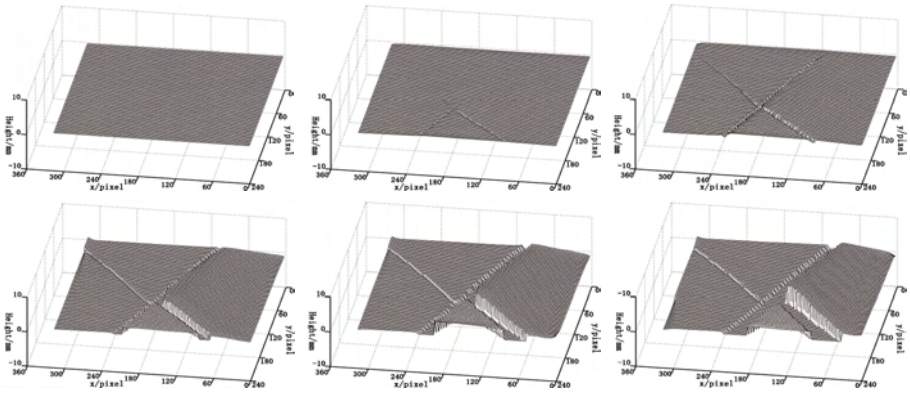

Fig. 4. Six grid charts of restored shape of breaking tile.

6 References

1. Takeda M, Motoh K. Fourier transform profilometry for the automatic measurement of 3-D object shapes. Appl Opt 1983;22(24):3977–82.
2. Su XY, Chen WJ. Fourier transform profilomitry: a review. Opt Laser Eng 2001;35(5): 263-84.
3. Su XY, Chen WJ, Zhang QC. Dynamic 3-D shape measurement method based on FTP. Opt. Lasers Eng, 2001; 36[1]:49-64.
4. Zhang QC, Su XY, Cao YP. An optical 3-D shape and deformation measurement for rotating blades using stroboscopic structured illumination. Opt Eng 2005; 44(11):113601-1~7.

Optical measurement and color map projection system to highlight geometrical features on free form surfaces

T. L. Pinto, A. V. Fantin, C. A. Carvalho, A. Albertazzi
Federal University of Santa Catarina
Caixa Postal 5053, Florianopolis, SC, 88040-970
Brasil

1 Introduction

Fringe projection is frequently used in several engineering applications for 3D geometry measurement. These systems are basically composed by cameras and a fringe projector. In many situations, it is difficult to locate the measured points or irregularities in the real surface, mainly on free form surfaces that do not have notable reference points like holes or edges. In this work the multimedia projector is used to perform two tasks: (1) to project the fringe patterns on the surface for measurement; (2) to project the measurement result using color maps to highlight areas directly on the evaluated surface. The color maps projection can be used to assist in-place inspection, the evaluation of the surface deviation and its reshape. This work presents the methods to measure 3D regular meshes, to project color maps considering the geometry and the relative position of the system. The developed measurement principle allows different combination between cameras and projector resulting in a regular mesh that minimizes occlusion problems.

2 The regular grid measurement

Several industrial and medical applications demands the measurement of complex and free-form surfaces, and fringe projection have become an important tool for these applications [1,2].
The developed system use two cameras and one multimedia projector to project sequences of sine fringes and gray-code patterns only in one direction (e.g. vertical) onto the object. These patterns are observed by the cameras and the phase maps are calculated as described in [3]. Besides of

it, a theoretical phase map is produced by the projector and these data are combined to produce clouds of points in regular meshes. It starts by mathematically defining a regular mesh in the measurement volume. The mesh can be defined in rectangular, cylindrical, spherical or any other coordinate system. The process starts with a node on the structured grid, defined by two independent coordinate. The third coordinate is defined by virtually scanning the measurement volume along this coordinate until the correspondent projected points in the cameras maps or projector map have the same phase value. It's possible to look for the minimal phase difference for a pair (Fig.1) or the minimum variance for three or more cameras and projector [4]. These combinations between cameras and projector can result in a cloud of points with less occlusions problems and a larger area measured. This approach produces naturally structured data with relatively small computational effort. The projected point is calculated by the well know projection matrix and distortion coefficients determined by previous calibration for cameras and projector. The calibration method is described in [5], but we used a calibration pattern composed by rings instead of color checkerboard.

A pipe measurement example is show in Fig.1, where a cloud of points was measured by both cameras.

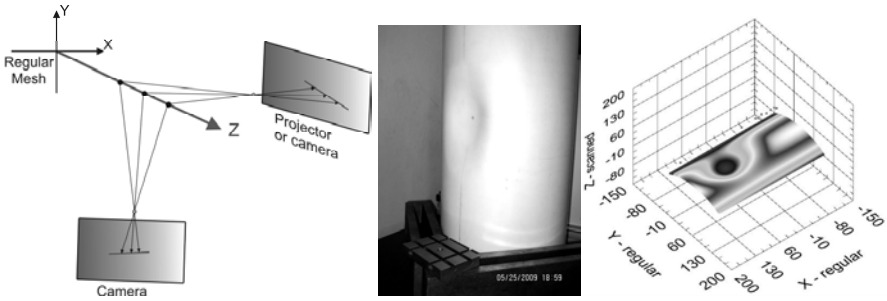

Fig. 1. Measure principle of Z scan [4] and a pipe measurement.

2.1 Color map projection

In some free-form surfaces, without notable points like holes or edges, is very difficult to locate the measured points or irregularities in the real surface. This association can be useful to aid inspections and reshape tasks. To solve this problem, a color map (Fig.2) can be calculated using the 3D measured points and the projector calibration data. The cloud of points are mathematically projected in the projector image plane and then displayed onto the object surface. Each point color can be associated to its Z

coordinate, the difference from a reference surface or another attribute of interest.

The difference between two surfaces can be easily calculated if the regular grid is the same or can be transformed to be the same, like described in our early work [6].

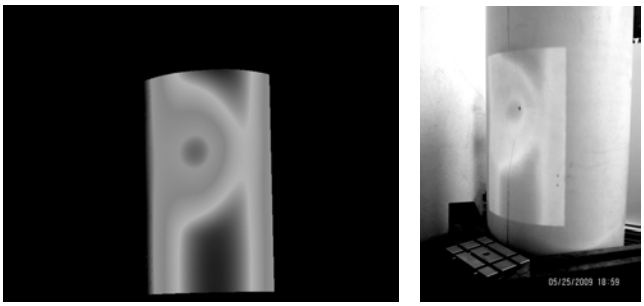

Fig. 2. The 2D calculated color map and its projection on the measured surface.

3 Measured surfaces

Different types of surfaces were measured to test the system and algorithms. A reference surface was measured and a moldable surface was compared and reshaped, guided by the color map projections (Fig.3). The color map was created based on the difference between the actual surface and the reference one. In places that has less material then the reference blue was associated and red for excesses. Green was associated with differences less than a defined tolerance, in this case +- 2 mm.

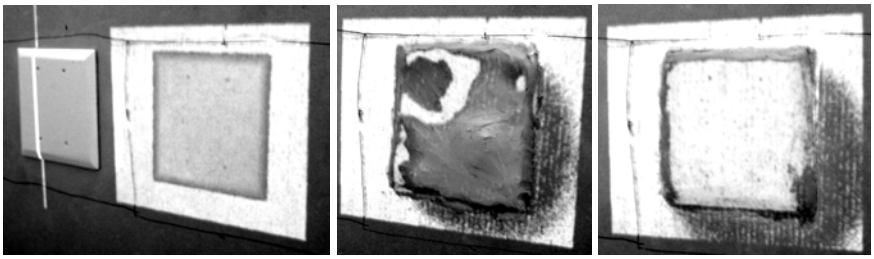

(a) (b) (c)

Fig. 3. .Color map projection to guide reshape: (a) measured part and indication to add material, (b) excess, in tolerance and lack indications and (c) inside tolerance.

This type of projection showed to be very helpful in reshape task, but more work to treat the outliers and smooth the color map has to be done.

4 Conclusion

In this work we show that is possible to assist technicians to evaluate and reshape free-form surfaces using color map projections calculated from 3D measurements and the calibration data for the projector.

The 3D point calculation algorithm results in regular grid of points, making easy to calculate the difference between surfaces, used to guide the reconstruction of a reference measured surface.

Future work include treat the outliers, smooth the color maps and the calculation of the color map based on the relative position of the system within big cloud of points in real time to dynamically project these color maps while movement the system.

5 Acknowledgments

The authors would like to thanks the financial support of CNPq and FAPESC and the valuable help of Dr. Christian Kohler.

6 References

1. Breitbarth M., Burchardt C. *et al* (2008) Measurement of optical free-form surfaces with fringe projection. Proc. of SPIE Vol. 7066, 706605.
2. Chen F., Brown G. *et al* (2000) Overview of three-dimensional shape measurement using optical methods, Opt. Eng. 39(1) 10-22.
3. Proll, P. K. (2004) Optische Topometrie mit räumlichen Lichtmodulatoren, Doctoral Tesis, Institut für Technische Optik der Universität Stuttgart.
4. Fantin, A Albertazzi, A *et al* (2007) An Efficient Mesh Oriented Algorithm for 3D Measurement in Multiple Camera Fringe Projection, Proceedings of the SPIE, Vol. 6616.
5. Zhang S. Huang P. (2006) Novel method for structured light system calibration. Optical Engineering Vol. 45(8), 083601.
6. A. V. Fantin, T. L. Pinto *et al* (2008) Measurement and Stitching of Regular Cloud of Points, Proceedings of the SPIE, Vol. 7066.

Digital holographic recording of large scale objects for metrology and display

Thomas Meeser, Silke Huferath-von Lüpke, Thomas Kreis
Bremer Institut für angewandte Strahltechnik GmbH
Klagenfurter Straße 2, 28359 Bremen
Germany

1 Introduction

Holography [1] is a method to record and display the whole optical wavefields including intensity and phase. It is used in numerous applications, e.g. in metrology for interferometric measurement of shape, deformation, or refractive index distributions, as well as particle detection and analysis [2]. Another application is holographic 3D-displays, e.g. in arts or security issues. Holographic 3D-television is a topic of actual research and development [3].

The photographic emulsion of the early holography has been replaced by recording on CCD- or CMOS-targets. The captured digital holograms are stored in a computer, where the complex wavefields can be reconstructed numerically [4,5], or the hologram data are inscribed into a spatial light modulator, whereby the wavefield is reconstructed optically [6,7].

The main difference between holographic film and CCD-targets is the resolution. While silver halide holofilm can resolve up to 7000 line pairs/mm, common CCD-cams have a pixel pitch of e.g. $\Delta\xi$ = 3,45µm, which equates to a resolution of 144 line pairs/mm. The sampling theorem states, that a reliable reconstruction of the recorded hologram is possible, if the fringe period p in the hologram is sampled by more than two pixels.

$$p > 2\Delta\xi \tag{1}$$

The fringe period p at any point in the hologram is given by:

$$p = \frac{\lambda}{2 \cdot \sin(\theta/2)}, \tag{2}$$

where λ is the wavelength and θ the angle between reference and object wave at the hologram point under consideration. In order to fulfil Eq. (1) for all points in the hologram and all points of the object, the angle θ must

remain small. This can be obtained by recording objects of small size, but sometimes one needs to measure large objects. Another way for the detection of large objects is to place the object far from the recording target, but optical arrangements with distances of several meters are bulky and prone to amplify small vibrations.

A solution of these problems is the optical reduction of the angle θ. This is done by bringing the object wave from a small virtual image of the object to the target instead of the original reflected or scattered wave [8].

In the following we will describe optical systems which perform this reduction and we will present results produced by these systems.

2 Optical reduction

Without an optical reduction the optical arrangement for capturing a hologram will have the length d_{nolens} from the object to the CCD-Chip [2]:

$$d_{nolens}(h) > \frac{(h + N\Delta\xi)\cdot\Delta\xi}{\lambda}, \tag{3}$$

where h is the height of the object and N the pixel number in one direction.

Using a single lens to decrease the optical field reduces the total length from object to CCD-Chip to $d_{onelens}$, based on Eq. (3) and imaging equations:

$$d_{onelens}(h) > \left(-\frac{f_1\cdot h}{g_1 - f_1} + N\Delta\xi\right)\cdot\frac{\Delta\xi}{\lambda} + g_1 + \frac{f_1\cdot g_1}{g_1 - f_1}, \tag{4}$$

where g_1 is the object distance to lens L_1 and f_1 is its focal length.

The reduction of the angle can be further increased by repeating the imaging of the object. That means that the first virtual image I_1 (Fig. 1) is displayed by a second lens L_2. The distance from object to CCD-Chip now is $d_{twolenses}$.

$$d_{twolenses}(h) > \left(\frac{f_1 f_2 h}{\Delta L(g_1 - f_1) - f_1 g_1 - f_2(g_1 - f_1)} + N\Delta\xi\right)\frac{\Delta\xi}{\lambda} + \Delta L - \frac{f_1 g_1}{g_1 - f_1} + \frac{f_2(\Delta L(g_1 - f_1) - f_1 g_1)}{\Delta L(g_1 - f_1) - f_1 g_1 - f_2(g_1 - f_1)}, \tag{5}$$

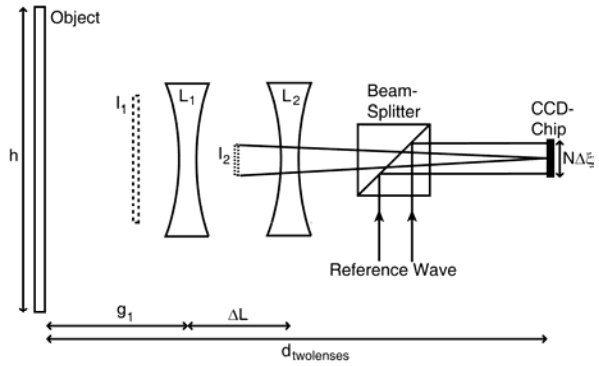

Fig. 1. Arrangement of the two lenses L_1 and L_2 considering the sampling theorem

with f_2 the focal length of lens L_2 and ΔL the distance between L_1 and L_2. This system can be enlarged to three or more lenses but the obtained reduction is small compared to that of the first two lenses.

Generally convex lenses do the same job [2], but the reduction is less than that of concave lenses.

3 Experimental results

A setup with two concave lenses has been successfully applied to an object of height 18cm (the Bremen Town Musicians). The capturing has been done by Fresnel holography as well as by lensless Fourier transform holography. With the two lens setup we obtained an object-CCD-Chip distance of about 18cm (f_1 = 75mm, f_2 = 50mm, N = 2452, λ = 532nm), see Fig. 2, while for a setup without lenses more than 1.2m would be necessary.

The resulting reconstructed intensity images shown in Fig. 3 demonstrate the feasibility of the presented method.

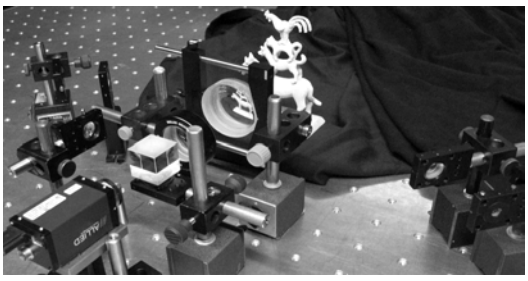

Fig. 2. Setup for capturing using two concave lenses for reducing the angle θ

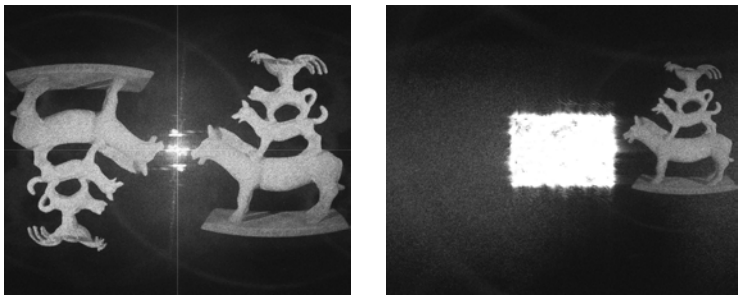

Fig. 3. Numerical reconstruction of an off-axis lensless Fourier transform hologram (left) and of an off-axis Fresnel hologram (right)

4 Acknowledgements

The authors thank J. Mundt for his support in the experiments. The research leading to these results has received funding from the European Community's Seventh Framework Programme FP7/2007-2013 under grant agreement n° 216105. This support is gratefully acknowledged.

5 References

1. Gabor, D, (1948) A New Microscopic Principle. Nature 161:777-778
2. Kreis, T, (2004) Handbook of Holographic Interferometry. WILEY-VCH Verlag GmbH & Co. KGaA
3. Onural, L, Gotchev, A, Ozaktas, H M, Stoykova, E, (2007) A Survey of Signal Processing Problems and Tools in Holographic Three-Dimensional Television. IEEE Transactions on Circuits and Systems for Video Technology 17:1631-1646
4. Yaroslavskii, L P, Merzlyakov, N S, (1980) Methods of Digital Holography. Consultants Bureau, New York
5. Schnars, U, (1994) Direct phase determination in hologram interferometry with use of digitally recorded holograms. Journal of the Optical Society of America A 11:2011-2015
6. Kreis, T, Aswendt, P, Höfling, R, (2001) Hologram reconstruction using a digital micromirror device. Optical Engineering 40:926-933
7. Agour, M, Kreis, T, (2009) Experimental Investigation of Holographic 3D-TV Approach. IEEE 3DTV Conference
8. Schnars, U, Kreis, T, Jüptner, W, (1996) Digital recording and numerical reconstruction of holograms: reduction of the spatial frequency spectrum. Optical Engineering 35:977-982

Multiwavelength laser interferometry

Bretislav Mikel, Martin Cizek, Zdenek Buchta, Josef Lazar and Ondrej Cip
Institute of Scientific Instruments, Academy of Sciences of the Czech Republic, Kralovopolská 147, 612 64 Brno, Czech Republic, Fax: +420 541 514 402, Tel: +420 541 514 252, e-mail: mikel@isibrno.cz

1 Introduction

Highly precise industrial distance measurements use mostly conventional laser interferometry techniques with He-Ne lasers as standard optical sources. There are two types of the most perspective semiconductor lasers to replace He-ne lasers.

First type is VCSEL laser diode 1. The enhancement of mode-hop free tuning range up to several nanometers becomes also possible. Spectroscopic VCSEL lasers at 760 nm with mode-hop free tuning range about 1 nm are affordable now. Their small size, narrow linewidth bellow 5 MHz, small threshold and operating injection current, and Gaussian output beam (TEM00) allow their application as a laser source for techniques of laser interferometry. We developed laser head based on this 760 nm spectroscopic VCSEL diode 1.

Second type of perspective semiconductor lasers is DFB laser diode. Now are affordable DFB laser diodes with 760 nm wavelength. In comparison with VCSEL diodes, the DFB diodes don't have Gaussian output beam due to different construction of the chip. On the other side they have linewidth bellow 1 MHz and they are available in butterfly package where are directly collimated to the optical fiber. They have mode-hop free tuning range above 1 nm and the output power is up to several tens miliwatts. Among VCSEL, 1 nm tuning range can be achieved by change of the temperature of the chip.

With respect to the characteristics of these laser diodes we can improve interferometry techniques. In contrast to conventional laser interferometry, the other one based on a tunable laser source allows to detect distances in a static way without moving the reflector. Then the synthetic wavelength, which is limited by a continuous tuning range of the laser, determines the scale resolution of the absolute distance interferometer.

2 Laser sources

For the laser sources we developed current sources and the temperature controller.

2.1 VCSEL laser source

We designed the laser head and supporting electronics of the VCSEL laser diode with respect to using such a laser source in the absolute laser interferometer techniques. Therefore, we oriented to spectral characterization and analysis of the laser output from the VCSEL laser diode involved in the laser head setup 2.

We arranged the measurement of wavelength tuning characteristic by a highly precise lambdameter with 0.1 pm resolution. We measured the tuning range of the VCSEL diode with respect to full input range of the temperature controller. We could observe about 0.7 nm wavelength mode-hop free tuning range for 7000 mK temperature sweeping. We studied also the mode-hop free tuning range by means of the injection current controller tuning. The wavelength tuning interval up to 1.4 nm has been traced for 2.9 mA continuous sweeping of the injection current repeatedly.

We measured of the spectrum of the VCSEL laser diode by Fabry-Perot resonator with injection current of the VCSEL diode 6.4 mA and modulation frequency 1 kHz. The linewidth was measured 100 MHz.

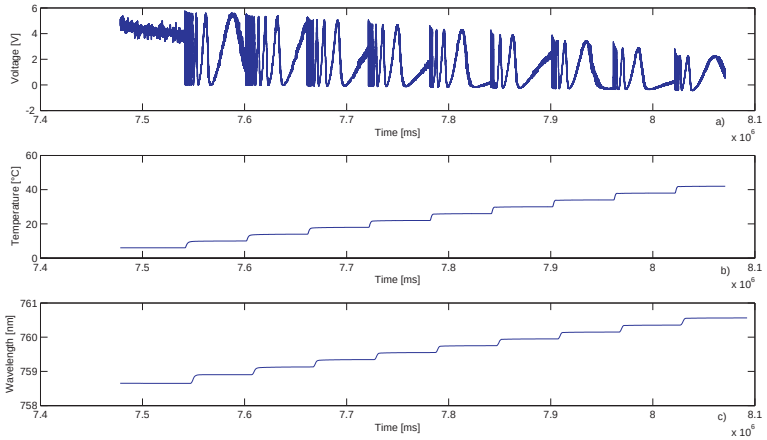

Fig. 1. The tunable range of the wavelength of the DFB diode by change of the temperature; a) The record from the F-P resonator - The number of passed resonance periods of a stable F-P resonator is 40 for each temperature step. b) The temperature of the chip. c) The wavelength of the DFB laser diode measured by lambdameter.

2.2 DFB laser source

We prepare electronics for this type of laser diode to connect our standard current controller and the temperature controller 3. The temperature stability under ±1 mK was achieved due to construction of the butterfly package and the calculation techniques of the temperature stabilization of the temperature controller.

We arranged the measurement of wavelength tuning characteristic by a highly precise lambdameter with 0.1 pm resolution with our laser interferometer from the fig. 2. to control of measurement of the tunable range of the wavelength of the DFB laser diode by change of the temperature of the chip. The F-P resonator in the laser interferometer was used to measure the wavelength tunable range of the DFB diode. Counting of the number of passed resonance periods of a stable F-P resonator during the tuning process identified the range of the tuning of the VCSEL laser diode. The temperature of the DFB diode has been changed from 6°C to 42°C for 4°C temperature steps and the injection current equate to 80 mA. The record from the F-P resonator is in the Fig. 1a. The number of passed resonance periods of a stable F-P resonator is 40 for each 4°C temperature step. It corresponds to measurement of the wavelength tunable range by lambdameter, Fig. 1c. The temperature of the chip is in the Fig. 1b.

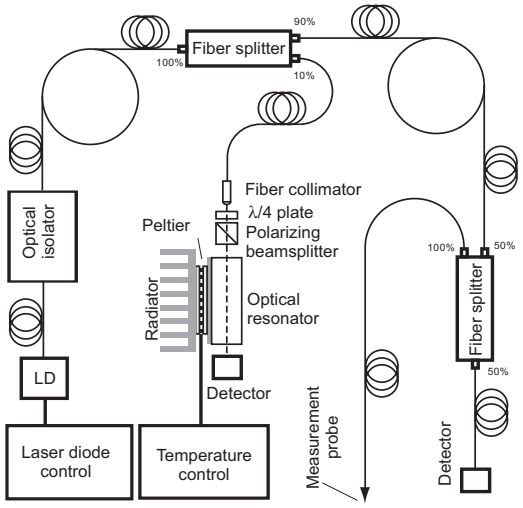

Fig. 2. Set up of the fiber laser interferometer for 760 nm wavelength VCSEL and DFB laser sources.

3 Fiber laser interferometer

The design of an absolute laser interferometer which was intended to operate in applications oriented to precision manufacturing and testing where the ability to measure distance directly is needed and where the measured distances are relatively small ranging over no more than few cm, see fig. 2.

4 Conclusion

We developed two laser sources based on 760 nm semiconductor diodes (VCSEL and DFB) for laser interferometry to replace standard He-Ne lasers. VCSEL lasers has been primary developed for using in absolute laser interferometry with tuning of the wavelength of the laser source. On the other side the newest DFB laser is primary developed to single frequency regime. In this regime we plan to use methods of frequency stabilization to F-P resonator and to absorption spectrum of rubidium and cesium vapor to increase wavelength stability.

5 Acknowledgement

The authors thanks for support to the Ministry of Education, Youth and Sports of the Czech Republic, projects no.: LC06007, 2C06012, ASCR, project no.: KAN311610701, Ministry of Industry and Commerce, projects no: 2A-1TP1/127, FT-TA3/133, 2A-3TP1/113 and GACR, projects no.: GA102/07/1179, GP102/09/P293, GP102/09/P630, GA102/09/1276.

6 References

1. Zappe, H P, di Sopra, F M, Gauggel, H P, Gulden, K H, Hovel, R, and Moser, M (2000) High spectral-purity VCSELs for spectroscopy and sensors. Book High spectral-purity VCSELs for spectroscopy and sensors: 106-116.
2. Mikel, B, and Cip, O (2002) Stabilization of VCSEL laser source for absolute laser interferometry. Seventh International Symposium on Laser Metrology Applied to Science, Industry, and Everyday Life, Pts 1 and 2 4900: 918-923.
3. Lazar, J, Jedlicka, P, Cip, O, Ruzicka, B (2003) Laser diode current controller with a high level of protection against electromagnetic interference. Review of Scientific Instruments 74: 3816-3819.

Accurate and fast three-dimensional imaging with use of fringe projection profilometry

Ameng Li, Xiang Peng*, Yongkai Yin, Yinjian Guan, Xiaoli Liu
College of Optoelectronics Engineering
Key Laboratory of Optoelectronic Devices and Systems
Education Ministry of China, Shenzhen University, 518060 Shenzhen, China
Corresponding author: xpeng@szu.edu.cn

1 Introduction

Three dimensional imaging and modelling (3DIM) technology has been widely used in the fields of industrial inspection, reverse engineering, digital archive generation, virtual museum, and heritage conservation [1]. Among optical 3-D digitizing techniques, the fringe projection profilometry (FPP) is becoming more popular due to its inherent natures of non-contact and non-invasive, full-field scanning, simple layout, and automatic range image processing.

In general, the FPP system utilizes one projector and one camera setup. The projector projects a series of known fringe patterns onto test object surface. The patterns deformed by surface height and observed by the camera. Then use temporal phase unwrapping (TPU) technique to recover the absolute phase map [2]. The phase is the connection of the projector and the camera. A calibration procedure is required to determine the system parameters of the FPP in order to achieve accurately 3-D imaging [3]-[4].

In this paper, we propose an approach for fast imaging of 3-D objects using FPP system. This approach is based on a fast 3-D reconstruction technique that relies on a special phase-coordinate mapping established in a virtual space, leading to a highly efficient and accurate reconstruction for the range images.

2 Fast reconstruction algorithm

We use vectors $\theta^c = \left[f_u^c, f_v^c, u_0^c, v_0^c, \gamma^c, k_1^c, k_2^c, k_3^c, p_1^c, p_2^c\right]$ and $\theta^p = \left[f_u^p, f_v^p, u_0^p, v_0^p, \gamma^p, k_1^p, k_2^p, k_3^p, p_1^p, p_2^p\right]$ to denote the intrinsic parameters of camera and the projector, and specify the extrinsic relationship between camera and projector with a rotation matrix R_s and a translation vector t_s [5]. These parameters can be calculated by the stereo calibration method, such as Zhang's algorithm [5].

Once the FPP system is calibrated, the 3-D reconstruction can then be carried out. We propose a fast algorithm for the reconstruction of range images, which is explained as follows: For every given 3-D world coordinates there is image pixel coordinates $p_c^i = [x_c^i, y_c^i, z_c^i]^T$ $m_c = [u_c, v_c]^T$ and an equivalent image point at projector retinal plane $m_p^i = [u_p^i, v_p^i]^T$ corresponding to this 3-D point, they are homologous points. Hence there exists a mapping $f : u_p^i \rightarrow p_c^i = \left[x_c^i, y_c^i, z_c^i\right]^T$, where f is a mapping function defined by camera projective transformations. In the process of 3-D reconstruction using the FPP system, the absolute phase of fringe pattern generated and projected by the projector can be written as

$$\varphi_c = \varphi_p = (u_p - x_0)/t \cdot (2 \cdot \pi) \tag{1}$$

where *t* is the spatial period of fringe pattern counted in pixels, x_0 is a position regarding to zero phase at projector plane so that an equivalent relation $f : \varphi_c^i \rightarrow p_c^i = \left[x_c^i, y_c^i, z_c^i\right]^T$ is also valid to represent the mapping between absolute phase values and the coordinates of 3-D points. On the other hand, any continuous function within a closed interval can be expressed as a polynomial with *n* orders according to functional analysis [4] such that following equations are valid to represent the mapping relationship mentioned above:

$$\begin{aligned} x_c(\varphi_c) &= a_0 + a_1\varphi_c + a_2\varphi_c^2 + \cdots + a_n\varphi_c^n \\ y_c(\varphi_c) &= b_0 + b_1\varphi_c + b_2\varphi_c^2 + \cdots + b_n\varphi_c^n \\ z_c(\varphi_c) &= c_0 + c_1\varphi_c + c_2\varphi_c^2 + \cdots + c_n\varphi_c^n \end{aligned} \tag{2}$$

Where $a_0, a_1, \cdots, a_n, b_0, b_1, \cdots, b_n, c_0, c_1, \cdots, c_n$ denote the coefficients of the polynomials. As long as these coefficients can be determined, we can

directly make use of Eq. (2) to calculate the coordinates of 3-D points from detected absolute phase map obtained from the TPU technique. Actually, the coefficients of the polynomials can be determined by epipolar geometry. For a given image point $m'_c = [u'_c, v'_c]^T$, there exists an epipolar line at retina plane of the projector, which can be described as [3]

$$I_p = (A_p^{-T}[t]_\times R_s A_c^{-1}) \cdot m'_c = F \cdot m'_c \tag{3}$$

where $[t]_\times$ is defined as an inversely symmetric matrix formed from translation vector $t_s = [t_x, t_y, t_z]^T$, F is referred as a fundamental matrix that has already been determined by the calibration procedure described above. Therefore, the coefficients in Eq. (2) can be achieved by following steps:

(I) for every image point $m'_c = [u'_c, v'_c]^T$ at camera plane, calculate its epipolar line I_p at projector plane using Eq. (3);

(II) select a set of sampling points $m'^i_p = [u'^i_p, v'^i_p]^T$ on the I_p and calculate the corresponding phase values $\varphi^i_c (= \varphi^i_p)$ with Eq. (1);

(III) combine $m'_c = [u'_c, v'_c]^T$ and $m'^i_p = [u'^i_p, v'^i_p]^T$ homologous point-pairs and calculate the 3-D point $p^i_c = [x^i_c, y^i_c, z^i_c]^T$.

These three steps result in a set of measurement values $\{\varphi^i_c, x^i_c, y^i_c, z^i_c\}_{i=1,\cdots,n}$, which can be utilized to determine the coefficients of the polynomials in Eq. (3) through a procedure of least-square-fitting. Once those coefficients determined, we can establish a lookup table (LUT) by the mapping relationship described by Eq. (2). With the LUT, the computational efficiency of 3-D reconstruction is greatly increased.

3 Experiment verification

To verify the efficiency of our proposed calibration method and fast of 3-D reconstruction, we carried out the experiments on a prototype of a FPP system, which included a camera device (DH-HV1303UM) with a resolution of 1280x1024 pixels coupled with a 16mm imaging lens (Computar M1614), and a projector device (PLUS PX-200 DLP) with 1024x768 pixels. We measured a metal plate as a test object with a size of

60mm x 60mm. Then we constructed a plane by fitting all measured points as shown in Fig.1(a). The discrepancy of each measured point from the fitting-plane can be calculated and shown in Fig. 1(b). The standard deviation of measurement errors was proved to be 0.0059mm. Furthermore, we measured an object with free-form surface, shown in Fig. 1 (c).

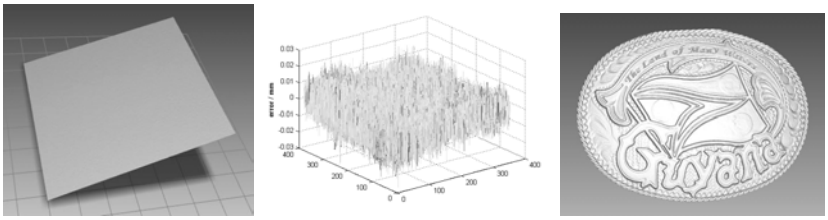

Fig. 1. Experimental results: (a left) fitted plane, (b middle) measurement error, (c right) A reconstructed of a free-form surface

4 Acknowledgements

This work is supported by the National Natural Science Foundation of China (grant 60775021), Science & Technology Bureau of Shenzhen (grant 200734), the Nanshan Scientific and Technology Project, and the Natural Science Foundation of Shenzhen University (grant 000018).

5 References

1. Chen F, Brown G M, Song M. Overview of three-dimensional shape measurement using optical methods. Opt Eng, 2000, 29(1): 10-22
2. H. Saldner and J. M. Huntley, Temporal phase-unwrapping: application to surface profiling of discontinuous object, Applied Optics, 36(13): 2770-2775, 1993
3. Reich C, Ritter R, Thesing J. 3-D shape measurement of complex objects by combining photogrammetry and fringe projection. Opt Eng, 2000,39(1): 224-31
4. R. Legarda-Sáenz, T. Bothe, W. P. Jüptner, Accurate procedure for the calibration of a structured light system. Opt Eng, 2004, 43(2): 464-71
5. Z. Y. Zhang, A Flexible New Technique for Camera Calibration. Technical Report, MSR-TR-98-71, Microsoft Research, December 1998
6. Peter D. Lax., Functional analysis, Higher Education Press, 2007

3D vibration analysis of granular materials with two-color digital Fresnel holography

Patrice TANKAM1, Pascal PICART1,3, Denis MOUNIER2,3, Jean-Pierre BOILEAU3, Vincent TOURNAT1, Vitali GUSEV2,3
1LAUM CNRS, Université du Maine, Avenue Olivier Messiaen, 72085 LE MANS Cedex 9, France
2LPEC CNRS, Université du Maine, Avenue Olivier Messiaen, 72085 LE MANS Cedex 9, France
3ENSIM, rue Aristote, 72085 LE MANS Cedex 9, France

1 Introduction

Digital holography became properly available since its confirmation was established in 1994 [1]. In few years, a lot of spectacular applications have been demonstrated such as microscopic imaging and phase-contrast digital holographic microscopy [2], three-dimensional object recognition and securing information [3], vibrations analysis with pulsed lasers and time averaging, also multidimensional dynamic investigations [4] and digital color holography [5]. The perspective of measurement of 3D vibration motions using digital Fresnel holography could be very important for getting insight in the fundamental dynamics of disordered granular materials. It is established that continuum elasticity, applied to grain assembly, actually decreases significantly below a length scale of typically 30 to 50 grain sizes [6,7]. At shorter scales the response of an unconsolidated granular material even to normal compression loading is nonaffine, i.e. contains additional component of the displacement field of predominantly rotational nature, which is rather controlled not by the symmetry of loading but by the characteristic of the disorder. Consequently 3D monitoring of the dynamics of disordered granular media could provide opportunity to study 3D nonaffine motion, to characterize its spatial scale and statistic (correlation) properties, and to attack the fundamental question [6,7]: “What modes of vibration contribute to vibration anomaly (Boson peak) in disordered materials?”. In this paper, as a preliminary study, we present an experimental investigation of the 3D motion of granular medium by using a two-color digital holographic interferometer.

2 Theoretical bascis

Classically, numerical reconstruction of digitally encoded holograms is performed by use of a discrete version of the Fresnel transform associated with a zero-padding. However, a simultaneous multi-dimensional measurement will be possible only if it is possible to perfectly separate the contribution of each component of a 3D vibration. For this, the size of each hologram along each wavelength must be quite similar during the reconstruction process in order to get a perfect pixel to pixel superimposition. Several algorithms have been developed in this sense [3,5]. In this paper we discuss about a modified version of the wavelength dependant zero-padding algorithm presented in [5].

Consider the case of a two-color set-up with a HeNe laser (λ_R=632.8nm) and a 2ωNdYAG (λ_G=532nm). Along each wavelength the sampling pitches are given by $\Delta\eta_R=\lambda_R d_0/K_R p_x$ and $\Delta\eta_G=\lambda_G d_0/K_G p_x$ where K_R and K_G are the number of data point in the Fresnel transform. In order to get $\Delta\eta_j$=const for each color j, it must be $K_R/K_G=\lambda_R/\lambda_G$=1,189473. Since K_R and K_G must be integer, one can chose $1000K_R/K_G$=integer with integer=1189. Furthermore, in order to get exactly $\Delta\eta_G=\Delta\eta_R$ one can chose $d_G=d_0$ and d_R to be proportional to d_G, such that d_R=1189/1000×λ_G/λ_R×d_0 at a given precision. Here d_R and d_G are respectively the reconstruction distance for the red and green holograms.

In the case of this paper, the set of granular material is placed at d_0=1400mm from the sensor. According to what precede, the perfect superposition of the red and green holograms will be achieved for the green hologram with $\{K_G;L_G\}$={2000;2000}, $d_G=d_0$=−1400mm, λ_G=532nm, then the red hologram will be reconstructed with $\{K_R;L_R\}$={2378;2378}, d_R=−1399.442mm and λ_R=632.8nm. This ensure a sampling pitch equality at a precision of 10^{-3}mm.

3 Experimental set-up and results

The optical set-up is described in Fig. 1. It uses a continuous green laser and a continuous red laser. It is composed of a twin wavelength Mach-Zehnder interferometer and a monochrome CCD camera (PCO Pixel Fly). The sensor is a 12-bit digital CCD with (M,N)=(1024,1360) pixels with pitches $p_x=p_y$=4.65μm. Each laser beam is split into an illuminating beam and a reference beam which are co-polarized for each wavelength. The two laser beams illuminate the object under interest with symmetric

illuminating angles θ_{xy} and θ_z. The smooth and plane reference waves are produced through the two spatial filters (SF1 and SF2). Since the monochrome sensor is not able to record the two colors simultaneously at each pixel, the spatial frequencies of the reference waves (*R* and *G*) are adjusted so that the two-color holograms are spatially multiplexed in the field of view. Thus, the off-line holographic recording is carried out using the two spatial filters in which each collimating lens is displaced out of the afocal axis by means of two micrometric transducers (not represented in Fig. 1). Thus, the amount of the translation of each lens fixes the spatial frequency along each color, i.e. $\{u_0^R, v_0^R\}$ and $\{u_0^G, v_0^G\}$ [4]. Considering the illuminating geometry, the phase changes along each color are given by Eq 1:

$$\begin{aligned}\Delta\varphi_R &= \frac{2\pi}{\lambda_R}\left[\sin\theta_{xy}u_x - \cos\theta_{xy}u_y + (1+\cos\theta_z)u_z\right]\\ \Delta\varphi_G &= \frac{2\pi}{\lambda_G}\left[-\sin\theta_{xy}u_x - \cos\theta_{xy}u_y + (1+\cos\theta_z)u_z\right]\end{aligned} \tag{1}$$

with $\mathbf{U}(t)=u_x\sin(\omega_0 t+\varphi_x)\mathbf{i}+u_y\sin(\omega_0 t+\varphi_y)\mathbf{j}+u_z\sin(\omega_0 t+\varphi_z)\mathbf{k}$ is the 3D vibrating displacement vector of the object, $\{u_x,u_y,u_z\}$ are the maximum amplitudes at pulsation $\omega_0=2\pi f_0$, $\{\varphi_x, \varphi_y, \varphi_z\}$ are the mechanical vibrating phase along $\{x,y,z\}$. Designing by $u_{yz} = -\cos\theta_{xy}u_y + (1+\cos\theta_z)u_z$ the mixing of *y* and *z* components, then

$$\begin{aligned}u_x &= \frac{\lambda_R\Delta\varphi_R - \lambda_G\Delta\varphi_G}{4\pi\sin\theta_{xy}}\\ u_{yz} &= \frac{\lambda_R\Delta\varphi_R + \lambda_G\Delta\varphi_G}{4\pi}\end{aligned} \tag{2}$$

The sum and difference of the phase changes, multiplied by their respective wavelength allows extraction of the *x* component and a mixing between *y* and *z* components. Since the *z* component represents the global mode of the vibration, we can compute an approximation $\tilde{u}_{yz}$ of u_{yz} by *n* smooth Zernike polynomials. Thus $\tilde{u}_{yz} = \sum_{i=1}^{n}\langle P_i, u_{yz}\rangle P_i$ with P_i the Zernike polynomial of rank *i* and $\langle P_i, u_{yz}\rangle$ the scalar product between P_i and u_{yz}. So u_y and u_z can be extracted with Eq. 3:

$$u_z = \frac{\tilde{u}_{yz}}{1+\cos\theta_z} \qquad u_y = -\frac{u_{yz}-\tilde{u}_{yz}}{\cos\theta_z} \tag{3}$$

Granular under interest are excited in the frequency range 400Hz-3kHz by using a mechanical shaker. The studied field is a circular wobble plate that is 30mm in height and 53mm in diameter, and filled with granular materials made of glass with 0.15mm in diameter and placed at d_0=1400mm from the CCD.
Light pulses are produced simultaneously using a four sector mechanical shopper. An electronics system is used to synchronize the shopper and the excitation signal. Since the size of the reconstructed holograms are controlled along each wavelength, the two-color holograms can be pixel to pixel superimposed thus allowing the 3D motion computation according to Eq. 1-3. For the estimation of the 3D motion at a given frequency, it is necessary to compute phase differences between stroboscopic recordings and to estimate amplitude and phase of the vibration using a dedicated algorithm. The measurement principle leads to a 3-frame phase shifting algorithms, described in [4], which allows the determination of 3D amplitude and phase of the movement. Fig. 2 shows the mean quadratic velocity of the media. Fig. 3 shows 3D results at 2760Hz proving that the determination of individual vibration amplitudes and phases are made possible by using the Zernike polynomial fitting. Fig. 4 shows the 2D in-plane displacement vector at 2760Hz which emphasizes the existence of in-plane swirling modes.

4 Conclusion

The paper has presented a first investigation of 3D vibration of granular media using a two-color digital holographic interferometer. To the best of our knowledge, results presented in this paper constitute a first attempt to visualize in plane vibration modes in granular medium.

5 References

1. Schnars, U, Jüptner, W (1994) Direct recording of holograms by a CCD target and numerical reconstruction. Applied Optics 33:179-181
2. Zhang, T, Yamaguchi, I (1998) Three-dimensional microscopy with phase shifting digital holography. Optics Letters 23:1221-1223
3. Javidi, B, Tajahuerce, E (2000) Three-dimensional object recognition by use of digital holography. Optics Letters 25:610-612

4. Picart, P, Leval, J, Grill, M, Boileau, J-P, Pascal, J-C, Breteau, J-M, Gautier, B, Gillet, S (2005) 2D full field vibration analysis with multiplexed digital holograms. Optics Express 13:8882-8892
5. Ferraro, P, De Nicola, S, Coppola, G, Finizio, A, Alfieri, D, Pierattini, G (2004) Controlling image size as a function of distance and wavelength in Fresnel-transform reconstruction of digital holograms. Optics Letters 29:854-856
6. Wittmer, JP, Tanguy, A, Barrat, J-L, Lewis, L (2002) Vibrations of amorphous, nanometric structures: When does continuum theory apply?. Europhysics Letters 57:423-429
7. Léonforte, F, Tunguy, A, Wittmer, JP, Barrat, J-L (2006) Inhomogeneous elastic response of silica glass. Physical Review Letters 97:055501

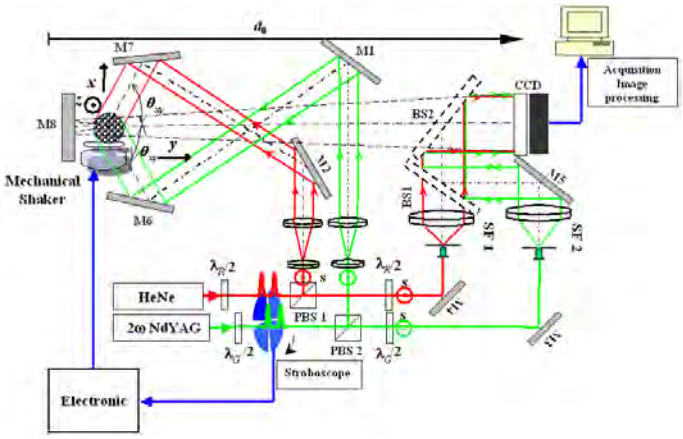

Fig. 1. Holographic set-up: M: Mirrors, BS: beam splitter; SF: spatial filter; PV: mechanical shaker

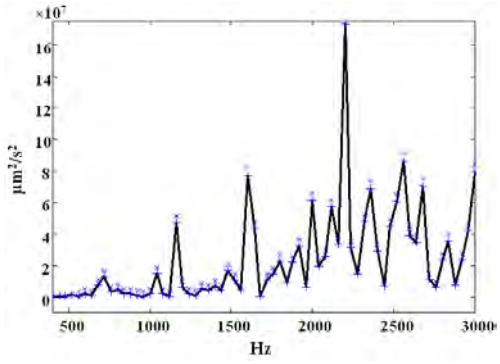

Fig. 2. Mean quadratic velocity in the range 400Hz-3000Hz ($\mu m^2/s^2$)

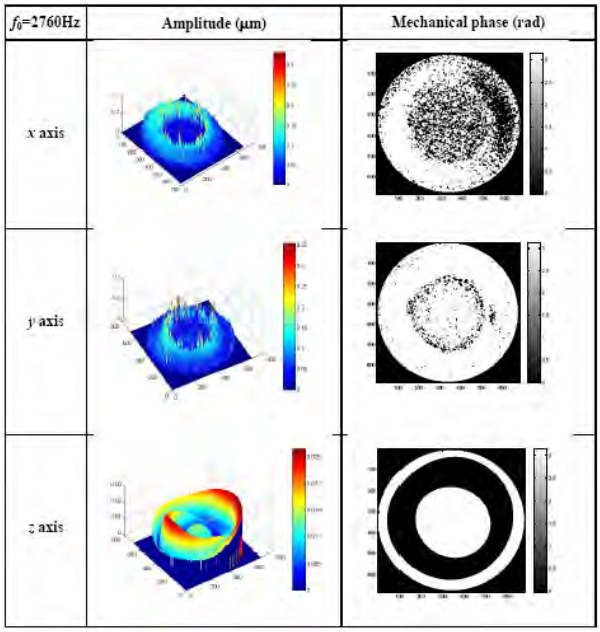

Fig. 2. Vibration amplitude and phase in the 3 dimensions at 2760Hz

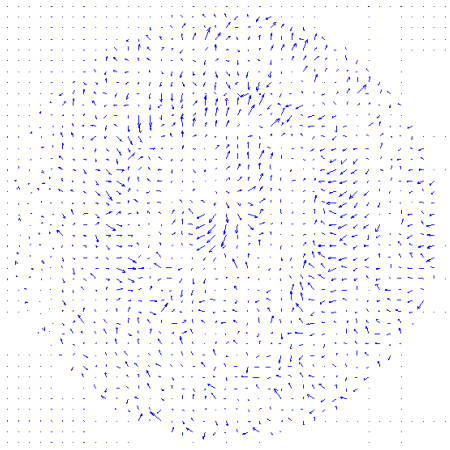

Fig. 3. 2D in plane displacement vector at 2760Hz

System for transient spatio-temporal (4D) vibration imaging and non-destructive inspection

James M Kilpatrick, Adela Apostol and Vladimir Markov
MetroLaser Incorporated
8 Chrysler, Irvine, CA 92624, USA

1 Introduction

Electronic speckle pattern interferometry (ESPI) provides unique capabilities in vibration and deformation study, non-destructive inspection and defect detection. However, the space-bandwidth limitations of existing CCD/CMOS detectors limit application of this technique to static or time-averaged capture of full-field deformations. Unlike the ESPI technique, the LDV, and its more advanced scanning implementation (SLDV), enables detection, measurement and evaluation of high-frequency vibration modes with wide range of surface displacements (from sub-nm to mm), and fits well to the needs and requirements of structural testing. This approach however requires a large number of sequential measurements, making the evaluation process slow and thus suited to steady-state or well characterized vibrations, generated under controlled conditions.

This presentation discusses development, performance and applications of a multi-beam (matrix) laser vibrometer (MLV). Based on a 2D sensor array comprising $n \times m$ illumination and detection channels the MLV demonstrates a simple conceptually design and robust implementation. It enables fast 2D measurements of arbitrary (steady state, non-steady state, transient) solid body vibrations without scanning the laser beam.

The principal advantages of the MLV approach are due to: (A) *data integrity* - parallel data acquiring grants the immunity to variations of the external factors and measuring conditions, and (B) *high inspection speed* – concurrent and rapid acquisition of 2D data with no scanning or image synthesis. These two key factors make MLV system applicable to study the (1) *non-linear, transient or non-repeatable vibrations* encountered in failure or fatigue testing of components, in acoustic emission studies, or in mechanical systems subject to unknown and variable forcing functions; (2) *energy flow diagnostics*, where the vibration phase information reveals energy flow between sources and sinks in mechanical systems, highlighting the predominant forces responsible for structural vibration

and a potential indicator for gaining insights into noise generation and control.

2 MLV System Design

The conceptual design of the MLV integrates its two units – the probe head and the electronics/controller module.. Effective use of the telecom fiber-optics components enabled the MLV design with the active electronics (laser source, detectors and digitizers) to be separated from the measurement (probe) head, making the latter largely passive and of sufficiently low-weight and size to facilitate its deployment in inaccessible areas or around large structures. The system architecture, illustrated in Figure 1(a), shows the MLV measurement probe, linked by a bi-directional fiber-optic umbilical, to a remote electronics unit which houses a narrow linewidth Er-Yb fiber laser operating at 1550 nm, a multi-channel fiber-coupled InGaAs receiver array, and a multi-channel A-to-D digitizer/processor array capable of 0.625 MS/s/channel conversion rates.

Laser light conveyed to the probe, is split by a polarization maintaining fiber coupler/splitter (A) between the reference and signal arms of the interferometer, as shown in Figure 1(b). The reference channel is fiber guided via a waveguide phase modulator (B) into the beam conditioning module (C) where it is launched toward the focal plane array (F). The signal beam is similarly fiber guided to the conditioning module where a diffractive optical element is employed to generate a 16×16 beam array which is transmitted by an adjustable zoom objective lens and brought to a focus on the measurement surface. The current configuration supports a (x 4) zoom range to achieve working distances from 0.5 m up to 2.0 m with beam coverage from 75 x 75 mm up to 300 x 300 mm (beam spacing 4.3 mm through 20 mm). The mixed optical signals collected by each fiber in the back focal plane of the probe are conveyed by a fiber ribbon array to a remote detector. The fiber ribbons, which comprise the bundle, are protected by a lightweight stainless steel umbilical casing and terminate into a bank of fiber connectors which mate via bulkhead connectors to 4 detector modules. Each module houses a 64-channel InGaAs pin diode receiver. The analog outputs from the detector array are supplied to an array of PCI 16-channel 0.625 MS/s/channel A-to-D converters with 8 MB/channel on board RAM and a 400 MHz on-board processor. Each processor executes an identical digital phase demodulation sequence locally and hands off the processed base-band data in 16-channel blocks to

a central processor where the signals are collated and displayed as full-field displacement or velocity images.

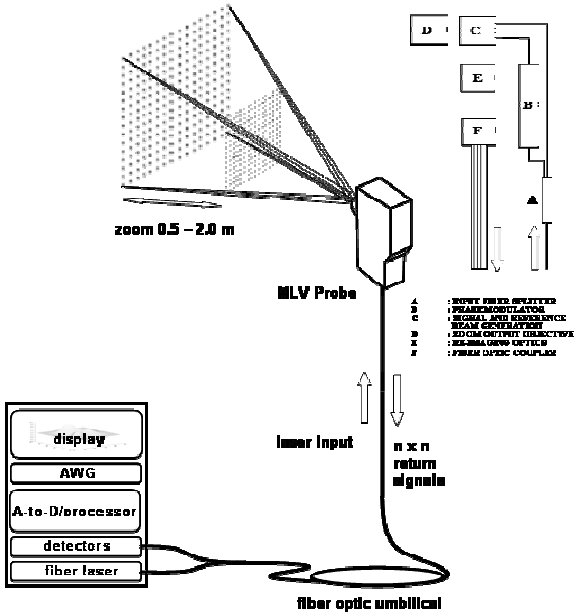

Fig. 1. (a) Schematic of MLV system, showing compact measurement probe linked by the fiber-optic umbilical to the remote electronics unit. (b) Internal schematic of probe unit

3 Experimental Data Examples

Experimental tests of the MLV system were conducted with the 12×12 prototype module by studying the dynamic behavior of a center pinned aluminum plate as a convenient test subject. The data obtained are thus sufficient to illustrate the principal strength of the MLV, namely (i) its capacity for rapid 2D capture of steady-state vibrations, in principle capturing only several cycles of the motion or (ii) continuous full-field capture of transient (non-steady state) vibrations. For these tests the MLV zoom was set to 0.5 meter such that the beam array illuminated the central portion of a high-stiffness circular disk of diameter 90 mm and thickness 6.0 mm. A small piezo-element glued to the rear face of the plate was for its mechanical excitation.

This test simulates the burst mode capture of a transient vibration, for which the piezo was driven with a sinusoidal frequency chirp from 1.0 through 50 kHz of duration 109 ms, while the plate response was measured

with the MLV. The data of Fig. 2 show the time domain velocity profile (Channel No. 67 of 144) from 0 to 109 ms comprising 65536 data points. The recorded data represent a complete record showing the temporal evolution of the plate operational modes driven by the piezo from 1 through 30 kHz and the evolution of the operational deflection profile as the excitation approaches and passes through the various resonant modes of the plate. The data of Figure 2 also show the 2D velocity profile of the plate selected at several most prominent velocity peaks corresponding to the $m_{i,j}$ vibration modes.

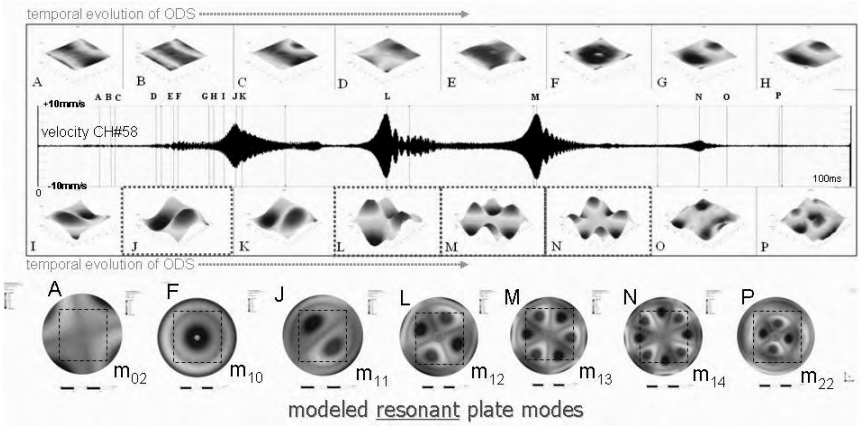

Fig. 2. Temporal velocity profile of the MLV channel #58 response to vibration of the center-pinned aluminum plate excited by a 109ms long 1-50 kHz frequency chirp. This figure shows also the subset of 2D velocity images and corresponding modeled mode patterns selected at principal resonant peaks.

4 Conclusions

This presentation discusses development and initial test results of the prototype MLV system. The obtained data illustrate the unique potential of the MLV concept for variety of applications, including the study of whole field transient vibration phenomena, NDT, and defect detection in composite structures.

5 Acknowledgments

The work reported in this report paper was supported by the SBIR contracts No. F09650-03-C-0027 and N072-118-0012.

Microelements vibration measurement using quasi-heterodyning method and smart-pixel camera

A. Styk[1], M. Kujawińska[1], P. Lambelet[2], A. Røyset[3], S. Beer[4]
[1] Warsaw University of Technology, Institute of Micromechanics and Photonics, 8 Sw. A. Boboli St., 02-525 Warsaw, Poland
[2] Heliotis AG, D4 Busines Center Luzern, Platz 4, 6039 Längenbold, Switzerland
[3] SINTEF, Strindveien 4, 7465 Trondheim, , Norway
[4] CSEM, Technoparkstrasse 1, 8005 Zürich, Switzerland

1 Introduction

Rapid increase of M(O)EMSs production with the focus on highly responsible elements requires 100% quality control of the products and therefore also development of the suitable measurement methods with high accuracy and high speed. Vibration measurements play an important role in the micromechanical object characterization especially during reliability testing, objects functionality testing, material properties derivation and also defect detection. Optical characterization methods suits well this requirements. Among different optical measurement methods interferometric techniques are of the main interest due to their noncontact and non contaminating character as well as high measurement precision. Laser Doppler Vibrometry (LDV) [1] is considered to be the most accurate method for determination of resonance frequencies as well as determination of vibration amplitude distribution over an object under test. However as a point method, for the second task it requires a 2D scanning, which elongates the measurement time considerably. For fast measurement full field optical methods are preferable. The most widely used are the time-averaging and stroboscopic interferometry [2]. Unfortunately both methods require the vibration amplitude of at least 0.19λ to be able to detect resonant frequency of an object. That limitation puts strong constrain on the excitation method and a type of an element to be tested.

An interesting method allowing measurement of small vibration amplitudes with high accuracy is so called heterodyning time-averaging interferometry [3]. It requires, however, more complex measurement

system with electro-optic modulator in one arm of the interferometer. This setup puts constrain on separation of both system arms.

To maintain high speed measurement time and extend the range of amplitudes to be measured (especially below 0.19λ) we propose a new vibration measurement technique which uses sinusoidal modulation of a light source and specially designed smart-pixel camera. This technique encodes an useful information on the vibration amplitude in the modulation distribution (analogically as in the time averaging interferometry) and is capable to measure the amplitudes of the magnitude of 0.02λ. The proposed measurement technique is developed under SMARTIEHS EU project [5] which main goal is to speed up the measurement time of M(O)EMS on the wafer level. The decrease of inspection time is achieved by means of innovative measurement concept which bases on a specially designed probing wafer consisting of a micro-optical interferometer array adapted and aligned with the wafer under test and novel Smart-Pixel Camera.

2 Smart-Pixel camera working principle

In the project the specially designed Smart-Pixel Camera is used. It allows for the demodulation of the time dependent interferometric signal at the detection level with demodulation frequencies (ω_D) up to 100 kHz [5]. The working principle lies in direct demodulation implemented within every pixel creating two main signals: **I** (in-phase) and **Q** (quadrature-phase), see Fig. 1.

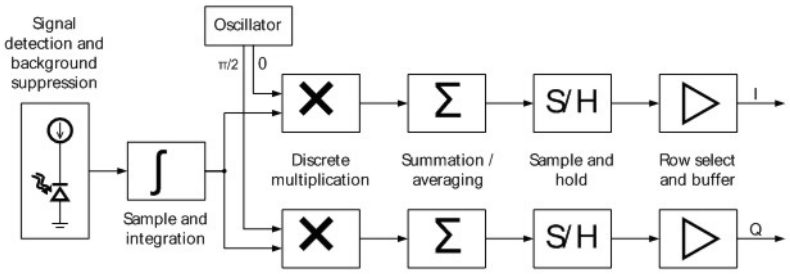

Fig. 1. Smart-pixel camera working principle

The optical signal collected and converted into an electrical signal is integrated and sampled in every pixel. Each pixel have background suppression circuit to avoid saturation and small input signal contrast, The

signal samples are consecutively multiplied by a signal of the same frequency and averaged on two paths, phase shifted by π/2 with respect to each other. A sample and hold stage in both circuit branches allows simultaneous demodulation and read-out, which means that while the stored values are read out of the imager pixel field, the input signal is demodulated to already generate the next values. The outputs of the two paths are read out of the imager to the PC allowing for direct calculation of amplitude and phase of sampled optical signal.

3 Mathematical description of measurement technique

In order to use all capabilities of Smart-Pixel Camera and fulfil the requirement on fast and accurate measurement of small amplitude vibrations a novel measurement technique has been proposed. Let as assume that the object is vibrating with the amplitude A_V and frequency ω_V respectively. The time dependent intensity changes in selected pixel of the resulting interferogram can be described as:

$$I(t) = I_0\left(1+\gamma\cos\left(\left(\frac{4\pi}{\lambda}A_V\cos(\omega_V t+\varphi_V)\right)+\varphi_{obj}\right)\right), \tag{1}$$

where I_0 is the interferogram average intensity, γ is the fringe pattern contrast and φ_{obj} is the interferogram phase encoding objects' initial shape.

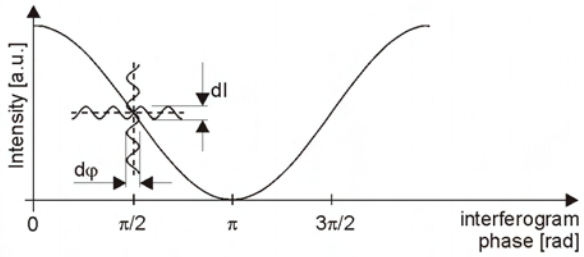

Fig. 2. Localization of the working point in vibration measurement

If the interferometer phase is adjusted to an operating point in the middle (linear) part of the interference pattern (φ_{obj} = π/2 or –π/2), see Fig.2 the detector signal changes into:

$$I(t) = I_0\left(1+\gamma\sin(\frac{4\pi A_V\cos(\omega_V t+\varphi_V)}{\lambda}\right). \quad (2)$$

To sample every pixel at this point of the interference pattern, 4 successive measurements separated by $\Delta\varphi_{obj} = \pi/8$ will be taken.
If, instead of continuous, we use the illumination modulated cosinusoidally at high frequency ω_L, slightly shifted comparing to the sample frequency $\omega_L = \omega_V - \omega_D$, where ω_D is chosen to be the reference (low) frequency of the smart-pixel camera demodulation, the measured signal becomes:

$$I(t) = I_0[1+\cos(\omega_L t)+\gamma\sin(\frac{4\pi A_V\cos(\omega_V t+\varphi_V)}{\lambda}) + \gamma\cos(\omega_L t)\sin(\frac{4\pi A_V\cos(\omega_V t+\varphi_V)}{\lambda}] \quad (3)$$

If the amplitude of the measured vibration is small $A_V << \lambda$ (we consider the amplitudes of measured objects less than 80 nm), than we may approximate sin(x) ~ x. Moreover, the detector integration time for each sample is $T_D/4$ (T_D is a period of camera demodulation signal) therefore each cosinusoidal term oscillating with frequency > ω_D will be averaged to zero. Hence, the resulting signal detected by the camera is:

$$I(t) = I_0\left(1+\left(\frac{2\pi\gamma A_V}{\lambda}\right)\cos(\omega_D t+\varphi_V)\right). \quad (4)$$

The above described signal is oscillating at the lock-in frequency and will be measured directly by the camera. This signal is now linear with respect to the objects amplitude A_V. Moreover the phase of vibration φ_V can be measured and used for accurate resonance frequency determination, as φ_V changes abruptly when passing from the low to the high frequency side of the resonance peak.

4 Measurement process

As the main goal of the project is to speed up the measurement process, the vibration measurement using described technique is conducted by the processing path presented on Fig.3. After setting the measurement conditions such as the range of the measured frequencies, frequency sampling interval and object load the search for resonant frequencies is performed. For this purpose the camera demodulation mode with limited

area of interest is used. As a result the function of an amplitude and phase change with respect to the frequency change is obtained. By analyzing the function the resonant frequencies may be distinguished. The set of measured resonant frequencies can be straightforwardly compared to the theoretical data supplied by the objects' manufacturer.

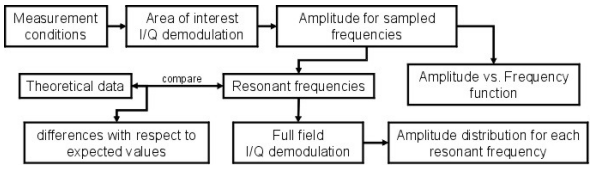

Fig. 3. Scheme of the data processing for vibration measurements

After having the set of resonant frequencies the amplitude distribution during the resonance is measured. For this purpose the full field camera demodulation mode is used. The variance of the measured parameters with respect to the expected ones gives the basis for the positive or negative classification of the measured objects.

5 Acknowledgments

SMARTIEHS is a collaborative project funded under the Grant Agreement 223935 to the 7th Framework Program Objective 2007-3.6.

6 References

1. Kilpatrick, J.M, Markov, V (2008) Matrix laser vibrometer for transient modal imaging and rapid nondestructive testing. Proc. SPIE 7098
2. Osten W (2006) Optical inspection of Microsystems. Taylor and Francis, New York
3. Ellinsgrud S, Løkberg O.J, Pedersen H.M (1990) Recording and analysis of (high frequency) sinusoidal vibrations using computerized TV-holography. Proc. SPIE 1399: 30-41
4. Beer S (2006) Real-time photon-noise limited optical coherence tomography based on pixel-level analog signal processing. PhD dissertation, University of Neuchâtel
5. Gastinger K, Kujawinska M, Løvhaugen O, Beer S, Gorecki C, Zeitner U (2008) SMARTIEHS – Smart inspection system for high-speed and multifunctional testing of MEMS and MOEMS. 14th Micro Optics Conference 2008 (MOC'08) Brussels, Belgium

Dynamic multipoint vibrometry using spatial light modulators

F. Schaal[1], M. Warber[1], C. Rembe[2], T. Haist[1], W. Osten[1]
[1] Universität Stuttgart, Institut für Technische Optik, D-70569 Stuttgart, Germany
[2] Polytec GmbH, D-76337 Waldbronn, Germany

1 Introduction

Laser-Doppler vibrometry is a non-contact vibration measurement technique. It is widely used in industry and enables measurements with high-frequency bandwidth and resolution. The measurement principle is based on the Doppler frequency shift of a laser beam, due to the vibration of the measured surface [1]. The frequency shift between measurement beam and reference beam is usually measured with an interferometer and meters the vibration in the focus of a laser.
For many applications the spatial resolved measurement of vibration is important. The state of the art technique for this purpose is scanning a measurement spot over the surface. The drawback of this method is the time offset between each measurement point. Therefore, it is in general not possible to measure non-repeatable transient vibrations.
To overcome this limitation it is necessary to measure the vibration in all measurement points simultaneously (multipoint vibrometry). First setups based on diffractive optical elements have been already realized [2-5]. The drawback of these setups is the fixed measurement point pattern. Due to the complex fast demodulation electronic, the number of measurement points is typically limited. For the optimal usage of these measurement points on arbitrary measurement objects, a user defined measurement point distribution would be useful. This can be achieved by the use of digital holograms written into a spatial light modulator (SLM).
In the following we present first results for a dynamic multipoint vibrometer using spatial light modulators.

2 System Design

The system uses a digital hologram written into a spatial light modulator for the dynamic generation of the measurement spots.
Due to the fact that, the position of the measurement points are flexible and the sensor positions are fixed it is necessary to image the measurement points with a second digital hologram to the sensor positions.
The major problem for the system design is the generation of spurious diffraction orders due to the structure of the light modulator.
We considered different techniques for the suppression of the diffraction orders, based on aperture plates, focal plane, polarisation optics, and hologram optimization.
First test showed that it's possible to reach a sufficient contrast of up to 1750:1 between the intensity of measurement spots and spurious diffraction orders by the use of optimized holograms.
The optimized hologram calculation algorithm is based on a modified Gerchberg Saxton algorithm [6]. To achieve more degrees of freedom for the hologram not only the phase in the reconstruction plane, but also the intensity outside the optimization window, is used during iteration.
The ratio of spurious diffraction orders inside and outside the window is controlled by multiplying the region outside the window in the object plane of the Gerchberg Saxton algorithm with a coupling factor.
A larger coupling factor shifts the spurious diffraction orders from the window to the outside of the window, but on the other hand reduces the diffraction efficiency.

3 Experimental setup

For a first test of the approach we used an experimental setup (Fig. 1) based on the commercial fiber coupled Laser-Doppler vibrometer Polytec CLV 3000. The fiber coupling of the vibrometer leads to the restriction that only measurements on reflecting surfaces are possible. One half of the SLM (Holoeye SLM LC-R 1080P, 1920x1080 Pixel, 8 µm pixel pitch, planar nematic) is used for the generation of 16 measurement points, the second half of the SLM is used for steering the reflected measurement points in the pinhole plane. One measurement point is selected by a pinhole for the vibration measurement with the vibrometer.

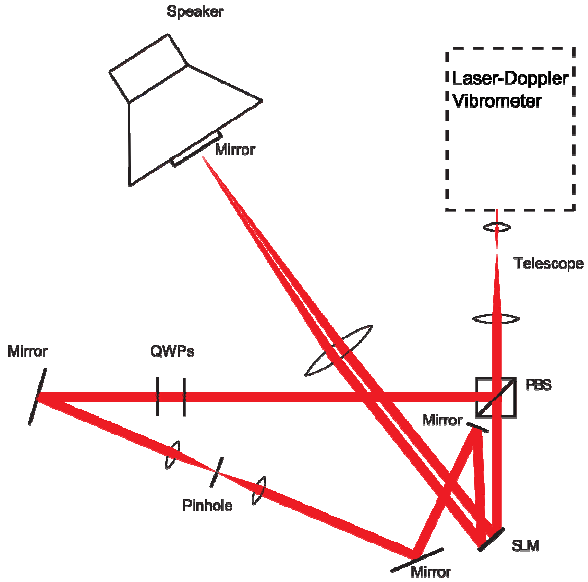

Fig. 1. Dynamic multipoint vibrometer setup based on a commercial Laser-Doppler vibrometer

4 First experimental results

Measurements were performed on a mirror attached to a speaker membrane. The analogue speed signal of the vibrometer was digitalized with a data acquisition board (NI PCI-6229). In Fig. 2 measurement results with an excitation frequency of 900 Hz are shown in the frequency domain. The excitation frequency and its higher harmonics are clearly visible.

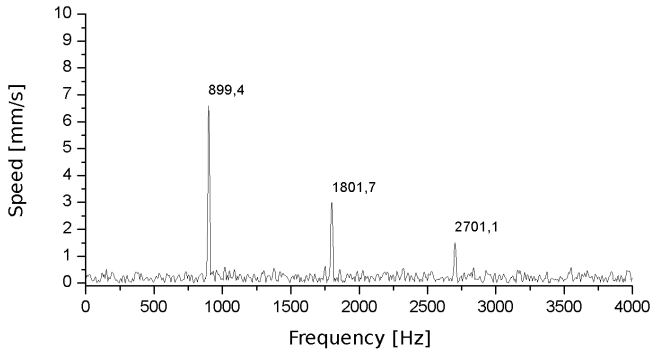

Fig. 2. Measurements on a vibrating mirror (900 Hz excite frequency)

5 Conclusion

We realized a first prototype of a dynamic multipoint vibrometer based on a spatial light modulator. The suppression of spurious diffraction orders has been achieved by optimized holograms. A first experimental setup for generating multiple measurement spots and measuring one spot has been realized and measurements on a vibrating mirror have been performed.
Further work will be done on the system setup, to allow measurements on scattering surfaces, simultaneous measurements off multiple points and to optimize the signal quality.
We thank the German Ministry for Education and Research for financial support under the grant 13N9339.

6 References

1. Rembe, C., Boedecker, S., Dräbenstedt, A., Pudewills, F., Siegmund, G. (2008) Heterodyne laser-Doppler vibrometer with a slow-shear-mode Bragg cell for vibration measurements up to 1.2 GHz. Proc. SPIE, Vol. 7098, 70980A
2. Zeng, W., Kruzelecky, R.V., Changkakoti, R. (1998) Multi-channel laser vibrometer and its applications. Proc. SPIE, Vol. 3411, 376
3. Cupido, E., Morel, S., Smith, D. (2003) Multipoint laser Doppler vibrometer for transient analysis, Proceedings of IMAC XXI, Orlando, USA.
4. Aranchuk, V., Lal, A., Sabatier, J. (2006) Multi-beam laser Doppler vibrometer for landmine detection. Optical Engineering 45(10):104302
5. Connelly, M. J., Szecówka, P. M., Jallapuram, R., Martin, S.; Toal, V., Whelan M. P. (2008) Multipoint laser Doppler vibrometry using holographic optical elements and a CMOS digital camera. Optics letters 33(4):330-2.
6. Gerchberg, B.W., Saxton, W.O. (1972) A Practical Algorithm for the Determination of Phase from Image and Diffraction Plane Pictures. Optik 35, 227–246

TOPIC 4

Hybrid Measurement Techniques

Chairs:

Pietro Ferraro
Pizzuoli
(Italy**)**

Invited Paper

Optoelectronic method for device characterization and experimental validation of operational performance

Ryszard J. Pryputniewicz
CHSLT – Center for Holographic Studies and Laser micro-mechaTronics
NEST – NonoEngineering, Science, and Technology
Department of Mechanical Engineering
Worcester Polytechnic Institute, 100 Institute Rd.,
Worcester, MA 01609 USA
Telephone: (508) 831-5536, Fax: (508) 831-5713, Email: rjp@wpi.edu

Abstract

This paper presents recent advances in the optoelectronic methodology for characterization of microelectromechanical systems (MEMS) and experimental determination of their functional behavior, by making high spatial resolution measurements with nanometer accuracy, which is especially needed in order to perform studies of long-term effects.

Although there has been significant research addressing MEMS errors, there is a lack of work regarding long-term reliability of packaged systems. Residual thermomechanical stresses may relax over time which may change physical distances within a package, ultimately affecting performance of a device. One reason that there has not been sufficient work performed on the long-term effects on microstructures may be a lack of a tool capable of characterizing the pertinent effects. Commercially available systems are able to make high resolution measurements, however they require significant user interface. To study aging effects on components a test may need to run continuously for many days or even weeks, with systematic operations performed during the process. Such a process is conducive to an automated data acquisition system operated by a custom software suit.

In this paper, performance impact of thermal deformations and relaxation are characterized by testing gyroscopes using an automated optoelectronic system with custom thermal loading fixture. The devices used are represented by their type known as Tuning Fork Gyroscope (TFG).

One source of errors for the TFGs is thermal loading which adversely affects the bias and scale factor of the sensors. Based on bias and scale factor for a TFG, characterized by functions of temperature, adverse effects due to temperature changes during normal operation of a gyroscope may be mitigated.

Although preliminary results shown herein are for a particular design of a TFG, the optoelectronic system can be used to measure other MEMS devices to enable verification of their operation as well as refinement and optimization of specific designs. In fact, the methodology offers a considerable promise for effective development of various designs. Also the methodology facilitates characterization of dynamic and thermomechanical behavior of the individual devices, their packages, and other complex material structures.

1 Introduction

A TFG functions by sensing a Coriolis acceleration. Proof masses are excited in plane, such that the motion is sinusoidal. A rotation, normal to the excitation direction, results in a Coriolis acceleration based on the cross product of the input rotation and the proof mass in-plane velocity. The Coriolis force displaces the proof mass, normal to a chip by an amount related to input rotation. The in-plane (drive) and out-of-plane (sense) motions of the proof masses are offset by 90º, placing these positions in quadrature. Quadrature error is present when the proof masses do not oscillate in plane, but rather have a small degree of out-of-plane motion. This error may cause a zero rate output (ZRO) in the sensor, also known as a bias error.

For applications involving inertial sensing TFGs are often implemented [1]. The sensor detects rotational rates about a central axis by tracking a Coriolis induced displacements. Key components of a TFG are shown in Fig. 1. The proof masses, supported by spring flexures resonate in the *x* direction. The actuation is achieved by electrostatic comb drives located on the outer edges of the proof masses. A drive mode is achieved where masses oscillate in opposite directions (coming to the center together).

Any rotation about the *y* axis, coupled with the velocity of the proof mass, $\boldsymbol{v}$, results in a Coriolis acceleration as

$$\boldsymbol{a}_c = 2\boldsymbol{\Omega}_I \times \boldsymbol{v} \tag{1}$$

where $\boldsymbol{\Omega}_I$ is the rotation about the *y* axis and $\boldsymbol{a}_c$ is the Coriolis acceleration. Due to the cross product between the drive direction (*x*) and the sense axis (*y*), the Coriolis acceleration is normal to both, acting in the *z*-direction.

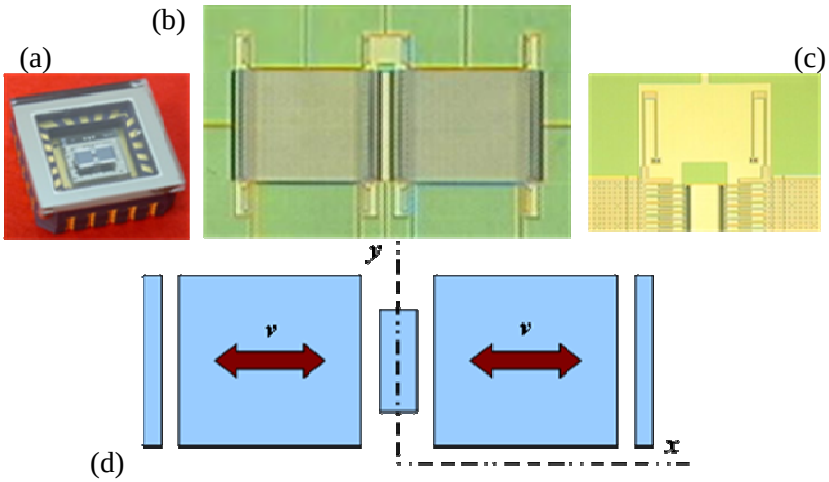

Fig. 1. TFG used in this study: (a) typical package, (b) dual proof mass configuration, (c) detail of the support spring flexures in the middle of the configuration, (d) schematic corresponding to part (b)

The velocity, ***v,*** is the time derivative of the position of the proof masses, which follows a sinusoidal motion of the form

$$x(t) = \Delta x \sin(\omega_d t) \tag{2}$$

where Δx is the proof mass stroke distance, ω_d is the frequency, and t is time. The Coriolis acceleration is obtained by solving for $\dot{x}(t)$ and substitution into Eq. 1, that is

$$a_c(t, \Omega_i) = 2\omega_d \Delta x \Omega_i \cos(\omega_d t)\,. \tag{3}$$

The out-of-plane motion, $\Delta d(t, \Omega_i)$, is determined by following Newton's second law to find the force acting on the proof mass, m, and then multiplying by the spring constant, k, of the support flexures in the z direction, giving

$$\Delta d(t, \Omega_i) = 2\omega_d m \Delta x \Omega_i k \cos(\omega_d t)\,. \tag{4}$$

The out-of-plane motion of a proof mass is also time dependant, with a cyclical behavior. The sensed signal, which is a capacitance measured between the proof mass(es) and the substrate, is therefore modulated by the drive frequency. The motions in the *x* and *z* directions are out of phase by 90º, resulting in the motion cycle shown in Fig. 2.

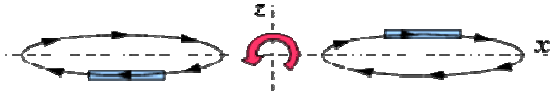

Fig. 2. Motion of proof masses while subjected to a rotation

This case of a 90º phase difference between position in *x* and *z* is referred to the signals being in quadrature [2].

In non-ideal operation the proof masses may not oscillate solely in the *x*-*z* plane, but have some out-of plane motion with no input rotation. This quadrature error is caused by several factors, including mass imbalances, flexure geometry error (where the minimum bending axis is not in the drive direction), or a distorted substrate due to die bonding in a package [3]. Quadrature error may result in a ZRO, where an erroneous output from a TFG indicates false rotations. The motion cycles of the TFG proof masses without rotation and with input rotation, are shown in Fig. 3.

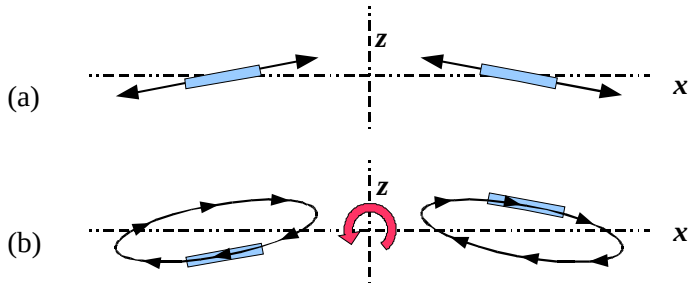

Fig. 3. Quadrature error in a TFG: (a) without rotation, (b) with input rotation

In general, quadrature error is measured by monitoring of the electrical signals from a microgyro. However, determination of the cause of the out-of-plane movement with no input rotation may be difficult.

The non-contact, non-invasive optoelectronic methodology discussed herein is used to directly measure the out-of-plane motion of a functional gyroscope. Due to non-planar surfaces of both the proof mass, and the substrate, second order polynomial surfaces model the measured regions. Integration over the overlapping area of the proof masses and the substrate is performed after applying a nominal offset between the surfaces, to determine the change in the sense gap distance throughout the drive cycle.

A LED illumination is modulated at the operating frequency of a TFG to effectively freeze motion of the proof masses, while measurements are being made. The phase of the light modulation signal, relative to the drive cycle, is adjusted such that quantitative measurements are made throughout the entire drive cycle.

2 Optoelectronic laser interferometric microscope system

Optoelectronic laser interferometric microscope (OELIM) system is a non-contact, non-invasive, tool that allows for full field of view, three-dimensional measurement [4,5]. The in-plane resolution is governed by the diffraction limit of light; however the out-of-plane measurements are accurate to sub-nanometer resolutions. The interference phenomenon produces fringes (superimposed over the imaged object), which modulate based on the relative position of a reference mirror to a beam splitter. The fringes represent out-of-plane shape, similar to a topographical map.

For measurements made on MEMS components, a Michelson OELIM configuration is utilized with phase shifting interferometry (PSI) techniques [5]. A schematic of the system emplyed is shown in Fig. 4.

Five phase stepped images are recorded, with verification of the phase step quality performed prior to storage of the images. If the phase step is not ideal (90º) the process is repeated until an acceptable step has been obtained. The threshold for an acceptable phase step, generally set at ±1º, is a user defined value. The iterative phase stepping has been automated within a software suite developed at WPI [2].

During analysis the phase is solved for as a part of an arctangent function, generating a discontinuous surface ranging from 0-2π [6]. The PSI measurements require an unwrapping procedure to extract quantitative information, which is then scaled based on the wavelength of illumination and the interferometer geometry. Phase unwrapping limits the measurements to a continuous surface which reflects sufficient light for fringe modulation. Separate measurements are required for each surface of interest, such as the MEMS proof masses and the substrate below the structure.

3 Measurement procedure

The TFG test articles used in this work resonate at approximately 10 kHz. These devices have been fabricated specifically for this process, with a glass lid brazed on, Fig. 1a, to allow optical inspection while maintaining a vacuum environment [7]. The device has an output voltage signal corresponding to the in-plane position of the proof masses, which is used as a trigger signal for the strobe illumination. A phase variable function generator allows for complete definition of multiple signals, including relative phase, while sharing the master frequency.

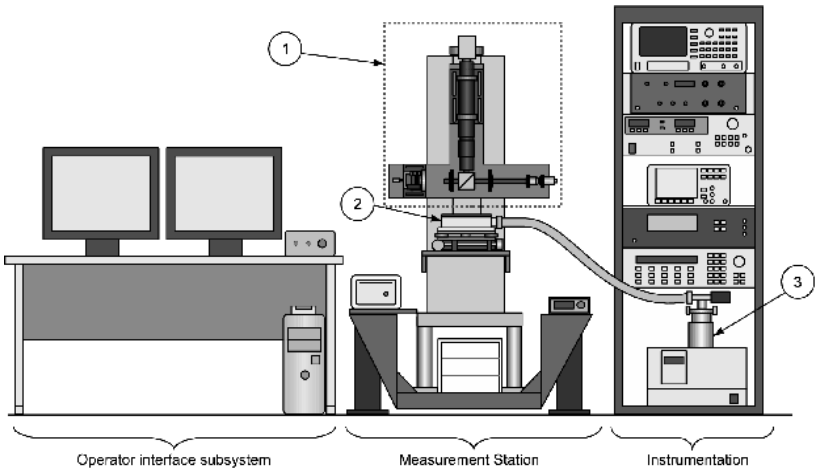

Fig. 4. Schematic of a modular optoelectronic station for characterization of MEMS: (1) interchangeable interferometer modules, (2) thermal/vacuum chamber, (3) turbomolecular vacuum pump

A square wave with a duty cycle of 8.5% is defined to trigger the illumination. Once a measurement is made the phase is adjusted to the next position in the cycle and the measurement is repeated. The entire procedure is scripted for automated data acquisition of 19 phase positions, from 0-360º, in 20º increments. After all 19 phase positions have been recorded the reference mirror is linearly adjusted such that a measurement may be made on the substrate. By not adjusting tilt of either the test article, or the reference mirror, the analyzed results of the proof masses and the substrate may be compared with a nominal, constant, offset set between them.

Second order surfaces are fit to both of the proof masses, as well as the substrate, via the least squares method. Once analytical models of the surface are obtained integration over the proof mass area is performed to determine the volume between surfaces. The pseudo gap distance is approximated by dividing the volume by the total area of the proof mass. This gap distance is not representative of the actual gap distance, sine the offset between surfaces is not known for this procedure. Changes in the pseudo gap, however, are identical to changes in the actual gap distance, allowing for determination of the amount of out-of-plane movement in the proof mass during normal operating conditions with no input rotation. The changes in the gap distance are a direct measurement of the amount of non-planar motion during a drive cycle, thus estimating a quadrature error.

4 Results

A total of five cycles of a TFG are recorded, with a measurement of the substrate made after each cycle, resulting in 100 measurements per device. The in-plane position of a proof mass is normalized for visualization purposes, showing the left proof mass traveling from -1.5 to -0.5, and the right proof mass traveling from 0.5 to 1.5. This presents an intuitive plot of the in-plane position. The pseudo gap distance is plotted relative to the first measurement (inner most position of the proof masses). These changes in the pseudo gap distance are identical to changes in the gap distance. The results of all five cycles are shown in Fig. 5a.

The five cycles may be compared, providing 38 points which are the average of the five cycles (the 19 positions for each of the left and right proof masses). The maximum standard deviation between the five cycles for the 38 points is 2.05 nm, showing about 2% variation for values upwards of 100 nm of gap distance change.

The percent changes in principal curvatures are plotted as a function of in-plane position, as displayed in Fig. 5b. The average of the five cycles is plotted in Fig. 5b with error bars representing the standard deviation for the five measurements.

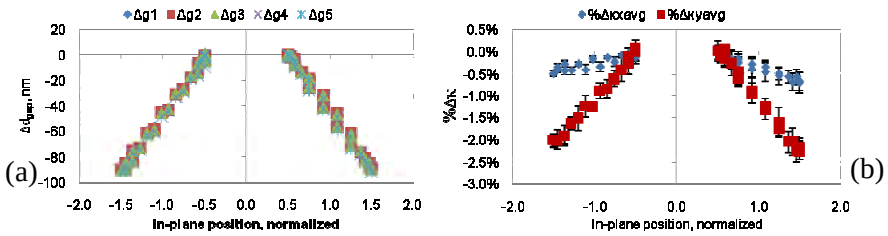

(a) (b)

Fig. 5. Changes during drive cycle in (a) gap distance and (b) principal curvature

5 Discussion

A methodology has been presented for monitoring of the gap distance in a TFG device during a drive cycle. Surfaces are measured by PSI, with an analytical model of the surfaces calculated by the least squares. Integrating between surfaces of the proof masses and the substrate allows for tracking of changes in a pseudo gap distance at finite positions of the drive cycle. This integration considers the distorted shape of the substrate in analysis, which is due to thermo-mechanical residual stresses from die packaging [3]. Changes in the gap distance represent direct measurement

of the quadrature error, or changes in the gap distance with no input rotation.

The preliminary results suggest that the optoelectronic methodology, as presented herein, may be valuable in design optimization to mitigate the zero rate output and to improve operational performance of microsystems.

6 Acknowledgments

Assistance by members of ME/CHSLT is very appreciated. This work was supported by the NEST Program at WPI-ME/CHSLT.

7 References

1. Barbour, N., and Schmidt, G., "Inertial sensor technology trends", *The Draper Technology Digest*, Draper Laboratory, Cambridge, MA, 1999, Vol. 3, pp. 5-13.
2. Marinis, R. T., *Development and implementation of automated interferometric microscope for study of MEMS inertial sensors*, PhD Dissertation, Worcester Polytechnic Institute, Worcester, MA, 2009.
3. Hanson, D., Marinis, T. F., Furlong, C., and Pryputniewicz, R. J., "Advances in optimization of MEMS inertial sensor packaging," *Proc. Internat. Congress on Experimental and Applied Mechanics for Emerging Technologies*," SEM, Bethel, CT, 2001, pp. 821-825.
4. Brown, G. C., and Pryputniewicz, R. J., "New test methodology for static and dynamic shape measurements of microelectromechanical systems," *Opt. Eng.*, 2000, Vol. 39, pp. 127-136.
5. Klempner, A. R., Hefti, P., Marinis, and Pryputniewicz, R. J., "Development of a high stability optoelectronic laser interferometric microscope for characterization and optimization of MEMS," *Proc. 15th Internat. Invitational UACEM Symp.*, Springfield, MA, 2004, pp. 275-285.
6. Pryputniewicz, R. J., "Quantitative determination of displacements and strains from holograms," Ch. 3 in *Holographic interferometry*, Vol. 68 in Springer series in sciences, Springer-Verlag, Berlin, 1995, pp. 33-72.
7. Marinis, T. F., Soucy, J. W., Lawrence, J. G., Marinis, R. T., and Pryputniewicz, R. J., "Vacuum sealed MEMS package with an optical window," *Proc. of IEEE Electronics Components and Technology Conference (ECTC)*, Orlando, FL, 2008, pp. 804-810.

Computational inverse holographic imaging: toward perfect reconstruction of wavefield distributions

Vladimir Katkovnik, Artem Migukin, Jaakko Astola
Signal Processing Institute, Tampere University of Technology,
P. O. Box 553, Tampere, Finland.
E-mails: {vladimir.katkov, artem.migukin, jaakko.astola}@tut.fi.

Introduction

Let $u_d(x,y)$ be a complex-valued 2D wavefield defined in the sensor plane $z=d$ as a function of the lateral coordinates x and y. According to the scalar diffraction theory there is a linear diffraction operator D_z linking the sensor wavefield distribution with the object wavefield $u_0(x,y)$ in the object plane $z=0$ as $u_d(x,y)=\mathsf{D}_d\{u_0\}$. The inverse of this operator defines the estimate of u_0 from u_d as $\hat{u}_0(x,y)=\mathsf{D}_{-d}\{u_d\}$. This estimate is perfect (precise for any u_0), $\hat{u}_0=u_0$, only provided that $u_d(x,y)$ is given for all (x,y), i.e. the sensor is of the infinite size [1].

Starting from the early days of the digital holography (70-80th of the 20th century) the algorithms developed and in conventional use for coherent imaging (at least in most planar optical setups) are based on digital approximations of the inverse operator D_{-z}. These algorithms can be given in the form $\hat{u}_0(x,y)=\hat{\mathsf{D}}_{-z}\{u_z\}$, where the hat stands for a discrete approximation of D_{-z}. All of these discrete algorithms (convolutional methods, the Fourier and Fresnel transforms, etc.) inherit the principal limitation of the integral inverse operator D_{-z} and are not able to give a perfect reconstruction of the object wavefield just because of the finite size of the sensor.

Contrary to it the *inverse imaging* paradigm is based on a numerical inverse of the *forward* propagation operator D_z. The finite size of the sensor may result in the ill-conditioning of this inverse problem. This limitation being of a mathematical nature to some extend can be overcome or at least attenuated in the imaging using special computational methods.

The starting point of the inverse technique considered in this paper is a matrix digital approximation $\hat{\mathsf{D}}_z$ of D_z for the finite size sensor output proposed in [2] and used for calculation and analysis of the forward and backward operators. This matrix model is precise and aliasing free for pixel-wise invariant object distributions exactly as it is for the frequency domain model developed in [3].

The results and discussion in this paper are focused on phase-object distributions. It is shown that the rank of the matrices in the matrix forward propagation model can be used as good indicators of the accuracy of the object distribution reconstruction. In this way this paper is an essential complement to [2], where all experiments concern amplitude-object distributions only.

1 Matrix Discrete Diffraction Transform (M-DDT)

Let the pixels in the object and sensor planes can be rectangular of the different sizes ($\Delta_{y,0} \times \Delta_{x,0}$) and ($\Delta_{y,z} \times \Delta_{x,z}$), respectively. Assuming the Fresnel approximation of the kernel in the diffraction operator D_z the discrete forward propagation model can be presented in the form [2]:

$$\mathbf{u}_z = \mu \cdot \mathbf{A}_y \cdot \mathbf{u}_o \cdot \mathbf{A}_x^T, \ \mu = -j \exp(j2\pi \cdot z/\lambda)/(\lambda \cdot z) \tag{1}$$

where $\mathbf{u}_z = (\mathbf{u}_z[s,t])_{N_{y,z} \times N_{x,z}}$ and $\mathbf{u}_0 = (\mathbf{u}_0[k,l])_{N_{y,0} \times N_{x,0}}$ are matrices of complex-valued wavefield distributions in the sensor and object planes, respectively. Elements of the "*averaged*" transfer matrices $\mathbf{A}_y = (\mathbf{A}_y[s,k])_{N_{y,z} \times N_{y,0}}$, $\mathbf{A}_x = (\mathbf{A}_x[t,l])_{N_{x,z} \times N_{x,0}}$ are calculated as

$$\mathbf{A}_y[s,k] = \frac{1}{\Delta_{y,z}} \int_{-\Delta_{y,z}/2}^{\Delta_{y,z}/2} \int_{-\Delta_{y,0}/2}^{\Delta_{y,0}/2} \exp[\frac{j\pi}{\lambda z}(k\Delta_{y,0} - s\Delta_{y,z} + \xi + \xi')^2] d\xi d\xi' \tag{2}$$

$$\mathbf{A}_x[t,l] = \frac{1}{\Delta_{x,z}} \int_{-\Delta_{x,z}/2}^{\Delta_{x,z}/2} \int_{-\Delta_{x,0}/2}^{\Delta_{x,0}/2} \exp[\frac{j\pi}{\lambda z}(l\Delta_{x,0} - t\Delta_{x,z} + \eta + \eta')^2] d\eta d\eta' \tag{3}$$

The matrices $\mathbf{A}_y$ and $\mathbf{A}_x$ manipulate by rows and columns of the object matrix $\mathbf{u}_0$, respectively. The formula (1) defines what we call *Matrix Discrete Diffraction Transform* (*M-DDT*). It is shown in [2] that calculations of the double integrals in Eq. (2) and (3) can be reduced to integration on single variables. By definition, the *M-DDT* defines the propagation model which is precise for any pixel-wise invariant (pixelated) object distribution. Being precise, this is an aliasing free model.

2 Inverse reconstruction of object distribution

When the accurate discrete forward propagation model is built, then, in principal, the accurate reconstruction of the object distribution $\mathbf{u}_0$ from $\mathbf{u}_z$ is possible. Formally, it can be done as a solution of Eq. (1). This solution gives the inverse of the forward propagation and defines what can be called *inverse backward propagation modeling*. If the accurate inverse can be found the perfect reconstruction of the pixelated object distribution can be achieved. Thus, due to the proposed matrix model the problems of the perfect reconstruction are reduced to the corresponding algebraic ones.

For rectangular object and sensor planes the perfect reconstruction can be achieved provided the following assumptions:

1. The support of the sensor plane distribution is equal or larger than the support of the object plane distribution ($N_{x,z} \geq N_{x,0}$ and $N_{y,z} \geq N_{y,0}$);
2. The $\mathbf{A}_y$ and $\mathbf{A}_x$ are full rank matrices, $rank(\mathbf{A}_y) = N_{y,0}$, $rank(\mathbf{A}_x) = N_{x,0}$.

If the conditions 1 and 2 are satisfied then the perfect reconstruction $\hat{\mathbf{u}}_0 = \mathbf{u}_0$ is given with the following formula:

$$\hat{\mathbf{u}}_o = (1/\mu) \cdot (\mathbf{A}_y^H \mathbf{A}_y)^{-1} \mathbf{A}_y^H \mathbf{u}_z \mathbf{A}_x^* (\mathbf{A}_x^T \mathbf{A}_x^*)^{-1} \tag{4}$$

where $(\cdot^{\mathrm{H}})$ stands for the Hermitian conjugate, $\mathbf{A}_y^H = (\mathbf{A}_y^*)^T$.

The numerical study shows that depending on the parameters, in particular, on the distance *d*, pixel's sizes, and object and sensor sizes the matrices $\mathbf{A}_y^H \mathbf{A}_y$ and $\mathbf{A}_x^H \mathbf{A}_x$ can be extremely ill-conditioned. This ill-conditioning means that these matrices are *numerically singular* and the formula (4) being formally correct practically is useless. The corresponding calculations cannot be fulfilled and gives unstable results highly sensitive with respect to the parameter variations, round off errors of calculations and observation noise. The regularization, for instance the standard Tikhonov`s one, is a conventional technique for various ill-conditioned problems. Instead of the solution (4) we are looking for the regularized estimate of $\mathbf{u}_0$ defined by minimization of the quadratic criterion:

$$\hat{\mathbf{u}}_0 = \arg\min_{\mathbf{u}_0}\{L\},\ L = \| \mathbf{u}_z - \mu \cdot \mathbf{A}_y \cdot \mathbf{u}_0 \cdot \mathbf{A}_x^T \|_F^2 + \alpha \| \mathbf{u}_0 \|_F^2 \tag{5}$$

where the Frobenius norm $\| \mathbf{u}_0 \|_F^2$ is the Tikhonov`s regularization penalty. The regularization parameter $\alpha \geq 0$ controls the level of

regularization or smoothness of $\hat{\mathbf{u}}_0$. It is shown in [2] that this regularized inverse can be given in the form

$$\hat{\mathbf{u}}_0 = (1/\mu)\cdot(\mathbf{A}_y^H\mathbf{A}_y + (\alpha/\mu)\mathbf{I})^{-1}\mathbf{A}_y^H\mathbf{u}_z\mathbf{A}_x^*(\mathbf{A}_x^T\mathbf{A}_x^* + (\alpha/\mu)\mathbf{I})^{-1} \quad (6)$$

The inverse wavefield reconstruction is a general and flexible approach applicable for different optical setups. However, we wish to emphasize that practically the accuracy of the reconstruction (6) depends seriously on the rank of the matrices $\mathbf{A}_y^H\mathbf{A}_y$ and $\mathbf{A}_x^H\mathbf{A}_x$ as it is illustrated in [2] and in the next section. It is confirmed by multiple simulation experiments that the rank of these matrices give a clear indication of the accuracy of reconstruction.

3 Simulations

We consider the discrete wavefield propagation of a phase-only object distribution $\mathbf{u}_0 = \exp(j\boldsymbol{\varphi}_0)$ and try to reconstruct this distribution from a given complex-valued observation in the sensor plane $\mathbf{u}_z = \mathbf{M}\circ\exp(j\boldsymbol{\varphi}_z)$, where $\circ$ stays for the Hadamard (elementwise) product, $\boldsymbol{\varphi}_0$ and $\boldsymbol{\varphi}_z$ are matrices of the phase distribution in the object and sensor planes, and $\mathbf{M}$ is an intensity (module) distribution in the sensor plane. We assume that $\boldsymbol{\varphi}_0 = \pi(\mathbf{u} - 1/2)$, where the matrix $0 \le \mathbf{u} \le 1$ is the square test-image (Baboon in our experiments) of the size $N_{y,0} = N_{x,0} = N_0 = 512$. The image in the sensor plane is square of the size $N_{y,z} = N_{x,z} = N_z = qN_0$, where the parameter $q \ge 1$ defines a redundancy of the sensor with respect to the object distribution. The pixels are square of the equal size in the sensor and object planes, $\Delta_{y,0} = \Delta_{x,0} = \Delta_0$, $\Delta_{y,z} = \Delta_{x,z} = \Delta_z$, $\Delta_z = \Delta_0 = 5\,\mu\text{m}$. The accuracy criterion is the root mean square error (*RMSE*) calculated for the difference of the phase (angle) of the object distribution and its reconstruction (estimate).

3.1. Matrix ranks and reconstruction accuracy

Note, that while the matrices $\mathbf{A}_y$ and $\mathbf{A}_x$ are rectangular, $N_z \times N_0$, the matrices $\mathbf{A}_y^H\mathbf{A}_y$ and $\mathbf{A}_x^H\mathbf{A}_x$ are square, $N_0 \times N_0$, for any $N_z = qN_0$.

The ranks of the matrices $\mathbf{A}_y^H\mathbf{A}_y$ and $\mathbf{A}_x^H\mathbf{A}_x$ depend on the sensor and pixel sizes, distance between the sensor and object planes and on the parameter *q*. It is shown in [2] that the distance corresponding to the sampling conditions which appear in the discrete Fresnel transform enables the maximum value of the ranks of $\mathbf{A}_y^H\mathbf{A}_y$ and $\mathbf{A}_x^H\mathbf{A}_x$ and the object distribution reconstruction to be perfect or nearly perfect. We call this distance as the *"in-focus"* distance with notation $d_f|_q$. It is calculated as

$$d_f|_q = N_z \cdot \Delta_z \cdot \Delta_0 / \lambda = q \cdot N_0 \cdot \Delta_z \cdot \Delta_0 / \lambda \,. \tag{7}$$

In our experiments we assume that the pixels have a fixed size, while the distance *d* and the sensor redundancy parameter *q* are varying.

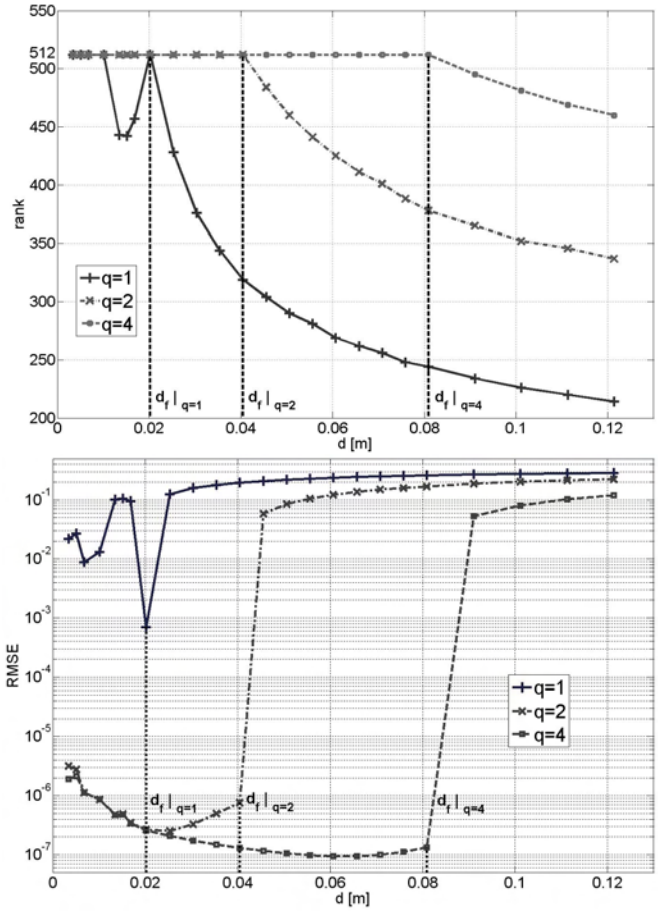

Fig. 1. The rank of $\mathbf{A}_y^H\mathbf{A}_y$ (top) and *RMSE* (bottom) versus the distance *d* for *q= {1, 2, 4}*

The numerical rank of the matrix $\mathbf{A}_y^H \mathbf{A}_y$ and the corresponding *RMSE* accuracy (in radian) of the phase-object distribution reconstruction are shown in Fig. 1 (top) and Fig. 1 (bottom) respectively for three different values of *q={1, 2, 4}*. These are complementary images allowing to track the dependence of the accuracy on the distance and to link this accuracy with the rank of the matrix. It is clear that the rank value close to the maximum value 512 results in a very high accuracy. For the redundant sensors of the size larger than the size of the object with *q=2* and *q=4* the ranks are decreasing functions for $d > d_f|_{q=2}$ and $d > d_f|_{q=4}$, respectively. These rank values are much higher than it is for *q=1*. We can see that if *q=2* or *q=4* we obtain the maximum values of the rank and practically perfect reconstruction for all $d \le d_f|_{q=2}$ or $d \le d_f|_{q=4}$, respectively. As soon as $d > d_f|_q$ the numerical ranks decreases and the accuracy of reconstruction is going down. For *q=1* the accuracy is uniformly worse than that is for *q={2, 4}*. Referring to the results shown in [2], we note that a very similar behavior is observed for the reconstruction accuracy of amplitude-object distributions.

3.2. Comparative accuracy analysis

The comparative accuracy analysis of the different algorithms for various distances *d* can be produced from the results shown in Fig. 2.

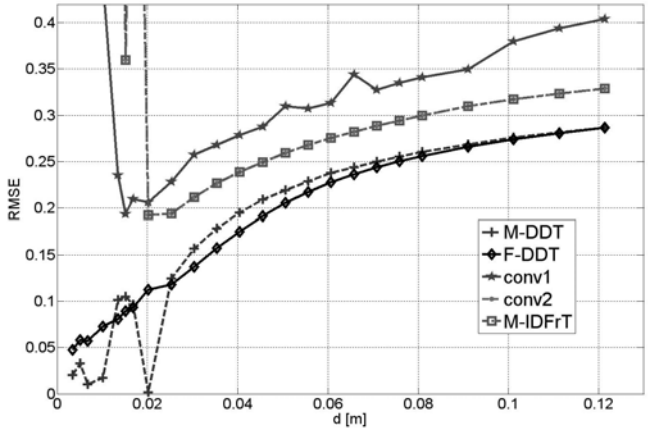

Fig. 2. The accuracy of the image restoration (*RMSE*) versus the distance *d* for the following algorithms: *M-DDT*, the recursive regularized inverse *F-DDT* [3], the convolutional inverse *conv1* and *conv2*, and *M-IDFrT* [2], $d_f|_{q=1}$ = 0.02 m

The regularized inverse *M-DDT* algorithm (see Eq. (6)) demonstrates the high-accuracy performance for nearly all distances. A quite close performance with sometimes slightly better results is shown by the recursive (10 iterations) regularized inverse frequency domain *F-DDT* [3]. It is emphasized that *M-DDT* enables the perfect reconstruction for $z = d_f|_q$. If the square pixels are of the equal size in the object and sensor planes and the corresponding images are of the equal size the standard double-size zero-padding convolutional algorithm (*conv2*) and matrix inverse discrete Fresnel transform (*M-IDFrT*) give practically identical results within the calculation accuracy. The curves corresponding to these algorithms are overlapping in Fig. 2. The accuracy of these algorithms is much better than it can be obtained by the ordinary convolutional algorithm (*conv1*).

Let the pixels be rectangular ($\Delta_{y,0} = \Delta_{y,z} = 8$ μm, $\Delta_{x,0} = \Delta_{x,z} = 5$ μm) and the same in the object and sensor planes. According to Eq. 2 and Eq. 3 the matrices $\mathbf{A}_y$ and $\mathbf{A}_x$ are different. In this case the calculation of the averaged matrices $\mathbf{A}_y$ and $\mathbf{A}_x$ and the choice of the in-focus distance become much more complex. The in-focus distance for *M-DDT* is calculated according to the following formulas [2]: $d = \min(d|_{f,y}, d|_{f,x})$, $d|_{f,y} = q \cdot N_{y,0} \cdot \Delta_{y,z} \cdot \Delta_{y,0} / \lambda = 0.05$ m, $d|_{f,x} = q \cdot N_{x,0} \cdot \Delta_{x,z} \cdot \Delta_{x,0} / \lambda = 0.02$ m.

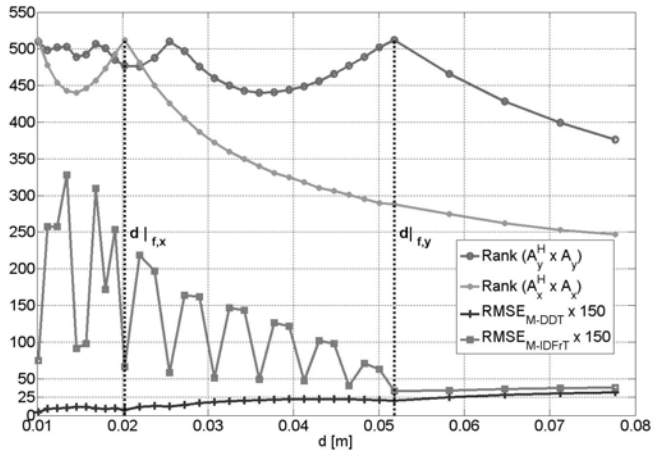

Fig. 3. The ranks of the matrices $\mathbf{A}_y^H \mathbf{A}_y$ and $\mathbf{A}_x^H \mathbf{A}_x$ for the rectangular pixels and *RMSE* for the wavefield reconstruction with the *M-DDT* and *M-IDFrT* algorithms versus the distance *d*

The numerical ranks of matrices $\mathbf{A}_y^H \mathbf{A}_y$ and $\mathbf{A}_x^H \mathbf{A}_x$ and the corresponding RMSE values versus the distance *d* are shown in Fig. 3. The best accuracy is obtained when the ranks of $\mathbf{A}_y^H \mathbf{A}_y$ and $\mathbf{A}_x^H \mathbf{A}_x$ are simultaneously close to their maximum values. For the considered parameters it happens at the in-focus distance equal to $d|_{f,x}$.

4 Conclusion

This paper concerns a novel discrete modeling for forward and backward propagation. The regularized inverse of the M-DDT is used for reconstruction of the object wavefield distribution. It is shown that the ranks of the used matrices serve as quite accurate predictors for the reconstruction accuracy. These sort of results have been demonstrated in [2] for the amplitude-modulation of the object distribution. It is done for the phase-modulation in this paper. Together these two papers prove that the ranks of the matrices of M-DDT can be used for design and optimization of experiments involving the wavefield reconstruction.

5 Acknowledgments

This research is supported by the Academy of Finland, project No. 213462 (Finnish Centre of Excellence program 2006 - 2011), and the work of Artem Migukin is funded by the Tampere Graduate School in Information Science and Engineering (TISE).

6 References

1. Kreis, Th. (2005) Handbook of Holographic Interferometry (Optical and Digital Methods). Wiley-VCH Gmbh&Co.KGaA, Weinheim.
2. Katkovnik, V, Migukin, A, Astola, J (2009) Backward discrete wavefield propagation modeling as an inverse problem: toward perfect reconstruction of wavefield distributions. Appl. Opt, 2009, http://www.cs.tut.fi/~lasip.
3. Katkovnik, V, Astola, J, Egiazarian, K (2008) Discrete diffraction transform for propagation, reconstruction, and design of wavefield distributions. Appl. Opt. 47, 3481-3493.

Cooperative Sensor Approach for holistic geometrical Measurement Tasks on Cutting Tools

Albert Weckenmann, Laura Shaw
Chair Quality Management and Manufacturing Metrology (QFM)
University Erlangen-Nuremberg
Naegelsbachstrasse 25, 91052 Erlangen
Germany

1 Introduction

Increasing requirements on the complexity and accuracy of dimensional metrology demand the application of multisensor data acquisition and fusion techniques to achieve holistic geometrical measurement results. Those cannot be determined on the basis of data from an individual sensor only. If the most suitable sensors are chosen for measurements of particular features of workpieces, and if the gained information is combined, the results will be improved e.g. due to the increased spatial and temporal coverage or a better resolution in important areas [1] [2].

Examples of such requirements can be pointed out in the metal cutting industry where the stability under load of tools to survive certain cutting processes depends on the shape, edge geometry, material, coating etc., characteristics which cannot be captured with a single-sensor system.

Focusing on the geometrical measurement tasks, complex cutting tools with improved dimensional- and shape-accuracy, needed for the production of workpieces with increasingly smaller dimensions and tolerances, have to be monitored. Precision cutting tool inserts (tolerance ± 0.025 mm), as used in turning machines, achieve workpiece tolerances of about 0.1 mm without additional adjustment. Figure 1 illustrates relevant dimensions on the example of a cutting tool insert: For a repeatable positioning in the tool holder especially the diameter of the clamping hole and the test size m are of importance. Corner angel ε_r, cutting edge radius r_β and nose radius r_ε are important to monitor to control the cutting behavior and the surface quality [3].

Next to the shape of the cutting tool, the profile of the cutting edge and the effective cutting geometry, the quality of the produced workpiece is especially influenced by wear and the micro structure of the cutting edge,

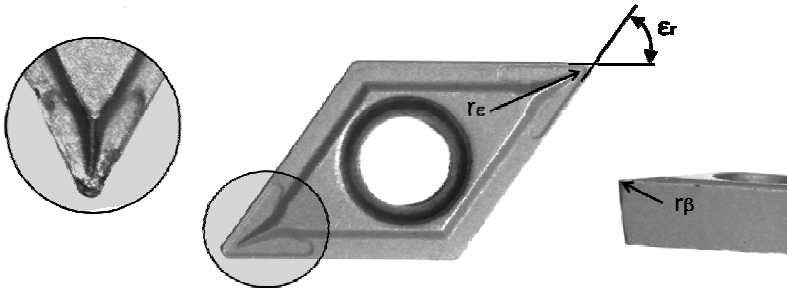

Fig. 1. Geometrical measurement tasks on a rombical cutting tool insert requiring data acquisition with different sensor principles: Macro shape with corner angel ε_r and nose radius r_ε (center); Micro shape with cutting edge radius r_β (right); Wear (left)

which influence the cutting force, the surface quality and the chip shape during production. Therefore it is important to measure and use wear characteristics, as shown in figure 1, as limiting values for unwanted changes in cutting tools. Their analysis gives information about quality indices such as cutting properties and life time and ensures the quality of surface and form of the produced workpieces.

2 Cooperative sensor approach

A multisensor measurement strategy, based on cooperative sensor configuration, can combine the advantages of different sensor concepts to achieve function oriented and holistic measurement data for such cutting tools. In comparison to single-sensor systems the information about the macro shape for the holistic testing of cutting tools as well as the micro shape in the areas of the cutting edges, e.g. to evaluate and characterize wear, becomes available in one three-dimensional data set. Inhomogeneous sensors with different resolutions are required to obtain the measurements: For the measurement of the macro shape a fringe projection system in combination with a positioning system is applied. With a light microscope working after the principle of focus variation the micro shape of cutting edges is measured. These optical distance sensors are classified as areal-sensors. Their surface data sets represent points on the surface of a workpiece or a feature and therefore are also often named “point clouds”.

The measurement area of the applied fringe projection system (41.1 mm × 31.3 mm × 10 mm) enables measurement of cutting tools of all standard sizes. The resolution of the sensor with 25 µm lateral and 3 µm vertical is

appropriate for typical tolerances of cutting tools (e.g. control size m ± 0.38 mm). The light microscope with focus variation is chosen based on its higher lateral resolution (2.2 µm) which is necessary to measure the structure of the cutting edges as well as its ability to measure high slope angles (up to 45°) compared to other optical areal sensors such as white light interferometers or confocal microscopes. For the measurement of cutting edges the lens applied has a measurement range of 2.9 mm × 2.2 mm.

Table 1. Resolution and measurement ranges for cooperative sensors

Sensor	Lateral measurement range in mm	Vertical measurement range in mm	Lateral resolution in µm	Vertical resolution in µm
Fringe Projection Sensor	41.1 × 31.3	10	25	3
Light microscope with focus variation	2.9 × 2.2	1.4	2.2	2

With these sensors the same attributes are measured over a number of different ranges and scales to capture and evaluate geometrical deviations, functional shapes and form defects.

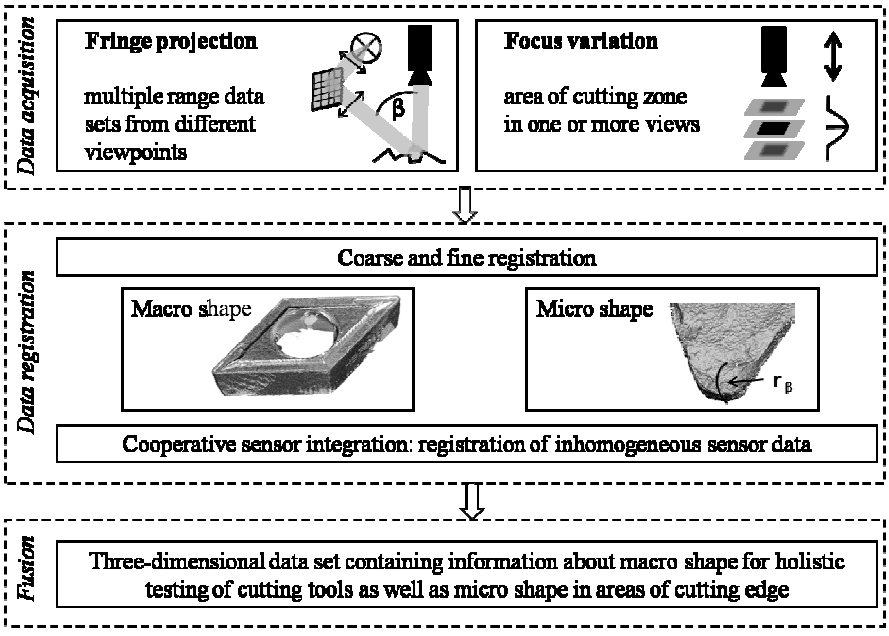

Fig. 2. Cooperative sensor approach for holistic testing of cutting tools

In at least three measurements the cutting tools are captured from different viewpoints with the fringe projection system. After filtering the data from outliers and noise the point clouds are combined into a single coordinate system applying the commercially available software SLIM3D [4]. During this process deviations appear which are caused e.g. by the imperfection of the measuring devices or the measuring conditions in the overlapping point clouds. During the registration process these deviations are minimized and the 3D transformation and rotation that transforms corresponding areas or points into each other are determined. Similarly the area of the cutting zone is measured in one or more views forming a data set wich contains information about the micro shape, see figure 2.

In the following step, the cooperative integration of inhomogeneous data sets (different resolutions) from fringe projection system and light microscope with focus variation is performed. The final result is a three-dimensional data set with an increased amount of information such as macro shape for holistic testing of cutting tools as well as micro shape in areas of cutting edges, presented with appropriate resolution.

3 Holistic geometrical measurements of Cutting Tools

For the registration of the data from fringe projection system and light microscope with focus variation their inhomogeneous data sets (different resolution) have to be correlated.

Figure 3 shows the registration process and results: The point clouds are roughly aligned calculating the transformation approximately by applying a feature based strategy. This process is still carried out interactively, by manually marking corresponding points with the advantage, that the most critical part of the registration process, the definition of features, is carried out as precise as possible and the danger that the algorithm will convert into a local minimum is reduced. The result of the coarse registration is a rotation matrix R and a translation vector t.

The remaining deviations are minimized, taking the whole data sets into account by using the iterative closest point algorithm. This numerical method needs no feature extraction and applies the mean square deviation as optimization function. In every iteration point correspondences between the data sets are established. The data set of the fringe projection system is not moved during the whole registration process. It serves as reference model for the data set of the light microscope with focus variation. Then the distances between the corresponding points are minimized realizing the

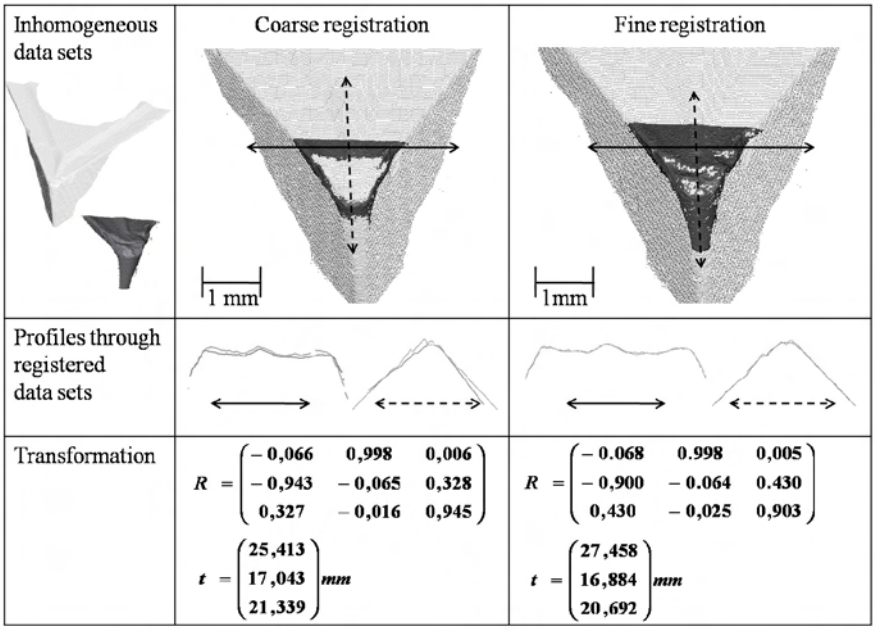

Fig. 3. Registration of inhomogeneous sensor data

optimization routine with an evaluation of the registration by the remaining deviation and a defined abort criterion.

The resulting three dimensional data set enables the required testing of the above mentioned measurement tasks in the macro and micro scale with sufficient resolution. Further monitoring of wear by comparing data sets before and during the application of tools becomes possible.

4 Outlook

Especially the coarse registration is an important step to realize the preferably low operator influence. As interactively carried out methods contain a high uncertainty, automatic methods have been developed for different application tasks:

The in [5] presented method is based on automatically finding points that are outstanding or salient, compared to other surface points. Such salient points can be robustly located on general free-form surfaces, even if there are no corners or edges as they are often used in feature based strategies. It is to be tested, whether surface data sets of cutting tool inserts show a sufficient number of features to apply this method.

Maier [6] proposes a method which uses planar surface parts to find the transfromation of the data sets. Three planes per surface data set have to be identified to perform the registration. This method proved to be rather robust against partial data loss, which can e.g. occur due to shadowing effects in optical metrology. Whereas the surface data sets of the fringe projection system representing the macro shape of the cutting tool inserts show plane elements, it has to be tested especially for the data sets of the light microscope, whether this method can be applied.

After the introduction of the cooperative sensor approach for holistic testing of cutting tools, which results in a three dimensional data set containing information about macro shape for holistic testing of cutting tools as well as micro shape in areas of cutting edge, future investigations will include the testing of the above mentioned methods for automatic coarse registration of point clouds of cutting tool inserts.

5 Acknowledgements

The underlying research is gratefully funded by the German Research Foundation (DFG) as part of the program of emphasis 1159 “New strategies for measurement and test techniques for production of microsystems and nanostructures”, project WE 918/28-2.

6 References

1. Weckenmann, A., Jiang, X., Sommer, K.-D., Neuschaefer-Rube, U., Seewig, J., Shaw, L., Estler, T., Multisensor data fusion in dimensional metrology, Annals of the CIRP 58/2/2009
2. Weckenmann, A., Nalbantic, K., Precision Measurement of Cutting Tools with two Matched Optical 3D-Sensors, Annals of the CIRP 52/1/2003: 443-446
3. Standard DIN ISO 1832:2005-11, Indexable inserts for cutting tools
4. http://www.3d-shape.com/home/home_d.php
5. Schön, N., Häusler, G., Automatic Coarse Registration of 3D-Surfaces by Information Theoretic Selection of Salient Points, Applied Optics, Vol. 45, pp. 6539-6550, 2006
6. Maier, T., Häusler, G., Segmentation Based Fast Registration of Free Form Surfaces in the Euclidean Space, Proceedings of VMV, Ed.: L. Kobbelt, T. Kuhlen, T. Aach, R. Westermann, Aachen, pp. 17-24, 2006

View Planning for 3D Reconstruction using Time-of-Flight Camera Data as a-priori Information

Christoph Munkelt[1], Michael Trummer[2], Peter Kuehmstedt[1], Joachim Denzler[2], Gunther Notni[1]
[1)] Fraunhofer Institute for Applied Optics and Precision Engineering, Albert-Einstein-Str. 7, 07745 Jena, Germany
[2)] Friedrich Schiller University of Jena, Chair for Computer Vision, Ernst-Abbe-Platz 2, 07743 Jena, Germany

1 Introduction

Automated multi view fringe projection systems are increasingly used for 3D surface reconstruction in industrial quality inspection, modelling, and reverse engineering. Unknown complex measurement objects require a great number of views in order to capture the complete object. View planning systems are used to efficiently acquire multiple views. They calculate the next sensor position from where the best possible results are expected. This is also called the Next Best View (NBV) problem.

We present a novel approach for active pattern projection (e.g. fringe projection) based 3D scanners, which improves scanning results with limited number of views. Fewer scans necessary translates into reduced scanning cost in terms of time and storage capacity. A time-of-flight (TOF) camera can provide preliminary surface topography during sensor movement, which considerably improves planning effectiveness. Without object information in the startup phase of the 3D scan, any planning system performs inferior to experienced human operators. They have a-priori a similar overview over the macro topography of the object.

Our mixed sensor (see Fig. 1 (b)) is composed of an optical high resolution fringe projection 3D sensor [1] and a TOF camera [2], which provides fast, but low resolution, low precision 3D measurements. Yet the swiftness of measurement enables data acquisition even during periods unsuitable for traditional 3D scanners, especially during sensor movement. Our goal therefore is to use this “free” TOF 3D data gathered during sensor positioning periods to acquire a rough 3D scan of the object. Thereby the view planner has preliminary object information in parts of the measurement volume yet unscanned by the high resolution scanner.

The proposed view planning system then iteratively fuses the scans into a volumetric data structure [3], thereby combining multiple quality criteria. Examined criteria include, for instance, the degree of orthogonality of the scan with respect to the surface angle, and the target point density. The overall scanning strategy performs a minimization of *not yet / poorly / TOF only measured* volume, while maximizing the aforementioned quality criteria. For that purpose, a generate-and-test approach, using a calibrated sensor model, optimizes the next view to be taken. Scanning and planning alternate, until the termination criterion is reached.

For further detail regarding our volumetric planning approach and a comprehensive literature review please confer to [4]. Distinguishing from there, this paper emphasizes more on TOF data usage motivation for view planning, TOF integration in both 3D sensor and planning system. Furthermore, improved TOF fusion and registration results are presented.

Experimental 3D reconstruction results are obtained by a robot mounted, fringe projection based stereo 3D sensor (see Fig. 1 (a)). The proposed planning approach exhibits advantages over other placement methods, especially in case of complex object geometries / limited number of views.

2 TOF Camera Data Integration for View Planning

The systems maximum measurement volume is modelled using a volumetric data structure. Therein, each volume element (voxel) aggregates available visibility [5], depth and quality information (like confidence, point density, fringe visibility [6] etc.) of the corresponding space region. Every new TOF or fringe 3D scan is evaluated and integrated into this planning volume (multi view fusion according to [3]). That way it represents the systems current knowledge about the object to be measured.

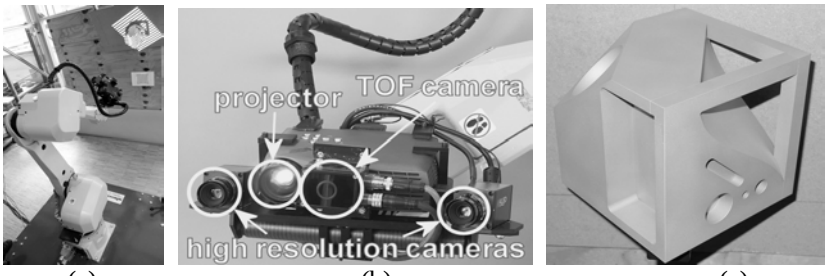

(a) (b) (c)

Fig. 1. (a) Utilized measurement system. (b) Sensor head combining stereo cameras, digital projector and TOF camera. (c) Photo of NBV test object [8]

In order to determine the NBV one must *evaluate* the result of previous scans (current partial object model) using a suitable sensor configuration (furthermore called sensor pose). The 3D sensor model includes intrinsic and extrinsic parameters, and the positioning systems parameters (hand-eye transformation). We utilize a generate-and-test approach and evaluate synthesized scans from (yet unseen) sensor poses (further on denoted as *estimation*). The goal of such an evaluation of a particular pose is a measure of its information gain respective to relevant quality criteria.

By ranking the view scores obtained by an objective function combining each potential next poses individual gains, the planning algorithm chooses consecutively sensor poses. The chosen next pose decreases at the same time uncertainty throughout the volume (by confidence gains for scanning unknown volume) and improves reconstruction quality of already scanned surfaces. This greedy-type approach implies, that scanning from this pose reveals enough new information about so far unseen volume.

Bearing an earlier approach [7] in mind, we used 3D data from a TOF camera to initialize the planning volume. The resulting quality criteria are weighted according to the TOF's increased uncertainty. The fusion of the TOF camera's 3D data is otherwise equal to the high resolution sensor data fusion. That way, TOF 3D data is used for view planning, but gets overwritten by subsequent fringe projection 3D data. Since capture and fusion of TOF 3D data can happen upon planning startup, during sensor movement, and during view planning computation, the necessary TOF scans should actually be regarded as "*free*" (contrary to additional views). Nevertheless they allow the planner to take the macro topography of the object into account and determine better next views.

Our data driven planning process consists of the following steps:

1. TOF 3D data capture before initial / during sensor positioning
2. *coarse sampling* of possible sensor parameter space over partial object model
3. repeat *iterative optimization*, while significant improvement:
   (a) *estimation* of sensor poses and *evaluation*; ranking of view score
   (b) locally *refine the sampling* of sensor's parameter space in the vicinity of the objective function's local maxima
4. termination test: continue data acquisition?
5. sensor pose change to best view from step 3; continue from step 1

During sensor movement, TOF camera 3D data capture is performed. In the second step, a number of uniformly distributed sensor poses is chosen from the accessible sensor parameter space (e.g. sensor position, focal length, or shutter speed). After *estimation* and *evaluation* of that poses,

those initial ones are replaced by a refined sampling of possible sensor parameters around local maxima of the objective function. This repeated refinement converges when no significant improvements over the last iteration can be achieved. The fourth step compares the current planning volume's *evaluation* against the effective termination criteria, like number of allowed views, object completeness, or significance of contribution compared to the last planned view. If planning continues, the optimal sensor position from step 3 is chosen as the NBV.

3 Experimental Results

The sensor head consists of two cameras, a TOF camera, and a digital projector. The reconstruction method employed is phase correlation based fringe projection [1] for the high resolution 3D scanner and TOF 3D scanning ("PMD O3" camera [2]). The used measurement object (NBV test object, see Fig. 1 (c) and [8]) was optimally aligned and wall-mounted, with sensor positions restricted to positions on a half sphere around it.

The TOF 3D sensor was placed between the two sensor cameras. Its field of view is substantial larger compared to the high resolution cameras, allowing better overview of the measurement volume (see Fig. 2 (a)). However, the low pixel count (64 x 48), combined with a specified repeatability of ±80 mm for the used measurement distance leads to noisy preliminary object information. Even after using robot position information and capturing TOF 3D data without sensor motion, reliable automatic registration of its 3D data with the partial 3D data of the high resolution sensor proved difficult.

The TOF 3D sensors considerably reduced resolution in object space is sufficient to represent the test objects macro topography. However, smaller

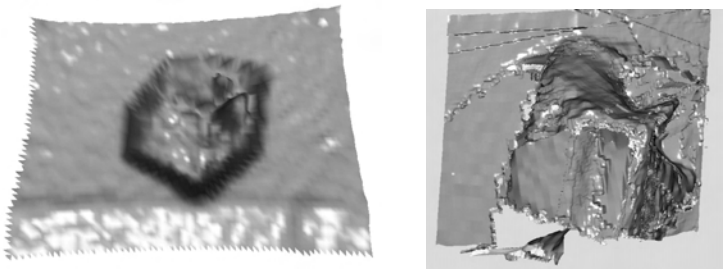

(a) (b)

Fig. 2. (a) Single frontal low resolution TOF 3D scan of NBV test object. (b) Multiple TOF 3D scans fusioned and registered into view planning framework

(a) (b)

Fig. 3. High resolution fringe projection 3D scanning results after 4 views. (a) Random sensor placement (b) View planning using ancillary TOF 3D data

object details, like the tripod structure, can hardly be scanned (see Fig. 2 (b)). The automatically planned first view is a frontal view, capturing all the three accessible faces of the test object at once. The next three views enable overall completeness of approx. 45% (human experts achieve in the same situation 49% on average). Figures 3 (a) and 3 (b) provide visual comparison of reconstruction results of two different sensor positioning strategies after four views. However, some smaller individual object details, like the tripod structure, are only partially scanned. Apparently false volume updates during the TOF data fusion due to erroneous depth measurements occur for a greater numbers of still unscanned volume elements.

4 Conclusions

We examined the application of TOF camera 3D data to improve view planning for 3D reconstruction. To our knowledge this has not been studied by others before. Only combinations of high resolution cameras with TOF 3D cameras for other purposes (e.g. robot navigation [9]) have previously been examined. By modeling the TOF camera as a conventional 3D sensor, easy integration into volumetric view planning approaches is possible. If TOF 3D data is gathered during up to now unused periods of time (e.g. before measurement start, during sensor movement, during prolonged planning calculation periods), the additional information can improve view planning without causing additional costs.

First experiments were successfully performed and confirm the general usability of TOF 3D data for view planning purposes. The reduced spatial resolution and increased measurement uncertainty of TOF cameras are not limiting the intended purpose for capturing the objects macro topography. Complete scans of delicate object details still need to be planned based on

the partial 3D model yielded by higher resolution sensors. Further advancements in TOF camera technology will also address this issue.

It also became evident, that the employed greedy-type ranking of potential new sensor poses is not the optimal strategy when planning multiple views. Highest ranked poses favor views, which improve the majority of the partial model. If, as is the case using TOF 3D data, more information about object structure is available beforehand, clustering of similar adjacent faces (see [10]) promises to improve on detail completeness.

5 References

1. Kühmstedt, P., Munkelt, C., Heinze, M., Bräuer-Burchardt, C., Notni, G. (2007) 3D shape measurement with phase correlation based fringe projection. In: Optical Measurement Syst. for Industrial Inspection V. Vol. 6616:66160B
2. PMDTechnologies GmbH http://www.pmdtec.com/e_inhalt/documents /datasheet_O3_v0100.pdf: PMD [vision] O3 Datasheet
3. Curless, B., Levoy, M. (1996) A Volumetric Method for Building Complex Models from Range Images. In: Proceedings of SIGGRAPH '96, ACM Press, pp. 303–312
4. Munkelt, C., Trummer, M., Kuehmstedt, P., Notni, G., Denzler, J. (2009) View Planning for 3D Reconstruction Using Time-of-Flight Camera Data. To appear in: Proceedings of 31th DAGM-Symposium
5. Massios, N. A., Fisher, R. B.: A (1998) Best Next View selection algorithm incorporating a quality criterion. In: 9th BMVC, pp. 780–789
6. Creath, K. (1993) Temporal Phase Measurement Methods. In: Interferogram Analysis – Digital Fringe Pattern Measurement Techniques. Institute of Physics Publishing, pp. 94–140
7. Munkelt, C., Kuehmstedt, P., Denzler, J. (2006) Incorporation of a-priori information in planning the next best view. In: Vision, Modeling, and Visualization (VMV 2006), pp. 261-268
8. Munkelt, C., Trummer, M., Denzler, J., Wenhardt, S. (2007) Benchmarking 3D Reconstructions from Next Best View Planning. In: Proceedings of IAPR Conf. on Machine Vision Applications. pp. 552–555
9. Prusak, A., Melnychuk, O., Roth, H., Schiller, I., Koch, R. (2008) Pose estimation and map building with a Time-Of-Flight-camera for robot navigation. IJISTA 5(3/4):355–364
10. Low, K. L., Lastra, A. (2006) An Adaptive Hierarchical Next-Best-View Algorithm for 3D Reconstruction of Indoor Scenes. In: 14th Pacific Conference on Computer Graphics and Applications

Stereo vision based approach for extracting features from digital holograms

Tomi Pitkäaho [1] and Thomas J. Naughton [2,1]
[1] University of Oulu, RFMedia Laboratory, Oulu Southern Institute
Vierimaantie 5, 84100 Ylivieska
Finland
[2] Department of Computer Science, National University of Ireland
Maynooth, County Kildare
Ireland

1 Introduction

With digital holography one can record and reconstruct real world three-dimensional (3D) objects [1,2]. The recorded interference pattern includes information about both amplitude and phase of a wavefront reflected from or transmitted through the object. However, some of the hologram capture setups pose a problem for the reliable reconstruction of quantitative phase information. This can be because the twin image or noise corrupts the reconstructed phase. In such cases it is usual that only amplitude is reconstructed and used as the basis for metrology. A focus criterion is often applied to this reconstructed amplitude to extract depth information from the sensed 3D scene [3,4]. In this paper we present an alternative technique based on applying conventional computer stereo vision algorithms to amplitude reconstructions. We show the effectiveness of our technique using digital holograms of both macroscopic and microscopic real-world 3D objects. We discuss sensitivity to the depth of field of reconstructions, and which hologram capture setups are, and which are not, suitable for the technique.

2 Method

From a single digital hologram of a 3D scene, we reconstruct two intensity perspectives [5] of the scene separated by a single known angle, and at a single known reconstruction depth. The angle is chosen so that the scene is approximately centred in each field of view. The stereo disparity [6] between these pairs is used to infer depth information for different regions

in the field of view. We calculate the disparity map as follows. For each pixel in the first perspective image (x, y) we estimate its corresponding pixel in the second perspective (x', y). In digital holography the epipolar geometry is known a priori, which simplifies the procedure and avoids the rectification stage. Because of this, for horizontally separated perspective positions, we need only look in the horizontal direction for correspondences. The disparity for pixel (x, y) is then difference in pixel locations ($x - x'$), and the set of disparity values corresponding to each pixel (x, y) is called the disparity space image (DSI).

If two different perspectives L and R are given, the disparity map D will be defined as

$$D(x,y) - \begin{cases} 0, & if \min\{argmax\ C_{xy}(u)\} \leq \tau \\ \min\{argmax\ C_{xy}(u)\}, & otherwise \end{cases} \quad (1)$$

where C is the correlation function used to estimate pixel location L(x, y) in R. Function argmax finds the disparity u that maximizes correlation. min{.} returns the minimum of a set. The minimum is used if there is more than one correlation peak. τ is a fixed threshold. For each pixel (x, y) in L, C is a one-dimensional normalized cross-correlation function defined as

$$C_{xy}(u) = \frac{\sum_{x'} t_x(x',y) f(x'-u,y)}{\sqrt{\sum_{x'} t_x(x',y)^2 \sum_{x'} f(x'-u,y)^2}} \quad (2)$$

where $t_x(x',y) = L_x(x',y) - \bar{L}_{xy}$, $f(x'-u,y) = R(x'-u,y) - \bar{R}_y$, and $\bar{L}_{xy} = \frac{1}{2t+1}\sum_{k=x-t}^{x+t} L(k,y)$. Expression $L_x(x',y) = rect(x-t,x+t)L(x',y)$ denotes a 2t + 1 sized region of pixels around pixel L(x, y), that is used to estimate the pixel's corresponding location in R. Finally, $\bar{R}_y = \frac{1}{N}\sum_{x'} R(x',y)$.

Middlebury College provides stereo pair of images that is used to test our algorithm [7]. Input images, ground truth [7], and output of our algorithm can be seen in Fig. 1. Our algorithm is capable of identifying each of the objects at their different relative depths by using the test image pair.

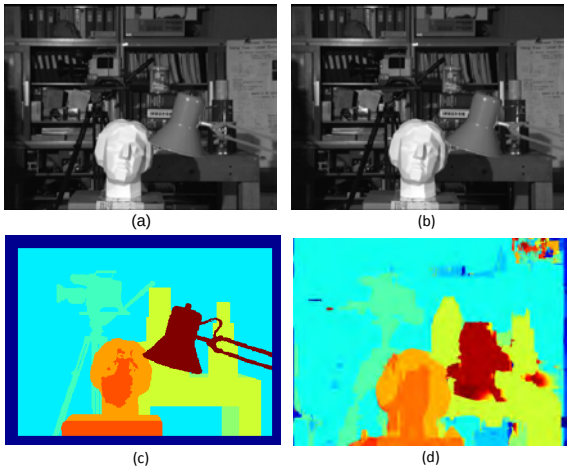

Fig. 1. Middlebury's test data. (a) left perspective, (b) right perspective, (c) ground truth, (d) output of our algorithm

3 Microscopic objects

The first setup used can be seen in Fig. 2. This simple Gabor-type setup consists of a laser, microscopic objective, pinhole, opaque microscopic sample, polarizer, and CCD (2208×3000 square pixels with side length 3.5 µm). Part of the light going through the sample is diffracted by the sample and creates the object beam, while part of the light goes around the sample undiffracted and creates the reference beam. The object in question is a set of human hairs, whose reconstruction from the whole hologram is shown in Fig. 3.

In Fig. 4 a region of interest from the left and right perspectives can be seen. Figure 4(c) shows the calculated DSI. One quarter of the hologram data was used for each reconstruction, and the depth chosen was the central depth of the scene (between the front and back hairs) In the DSI all three hairs are indentified as are their relative depths: two of the hairs being at the same depth and one of them at a different depth. Quantative measurements of distance were not taken at this stage, but the relative ordering of the objects was verified as being correct. In the colour coding, a whiter colour denotes an object closer to the camera, and a darker colour denotes an object further from the camera.

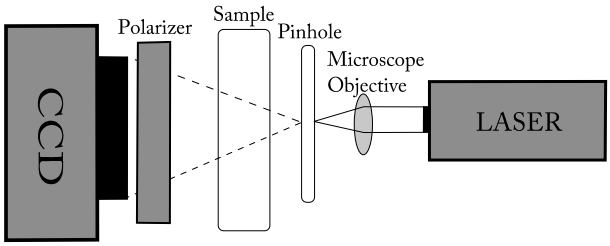

Fig. 2. Microscopic setup

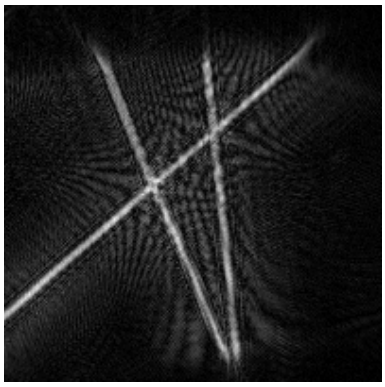

Fig. 3. Human hair reconstruction

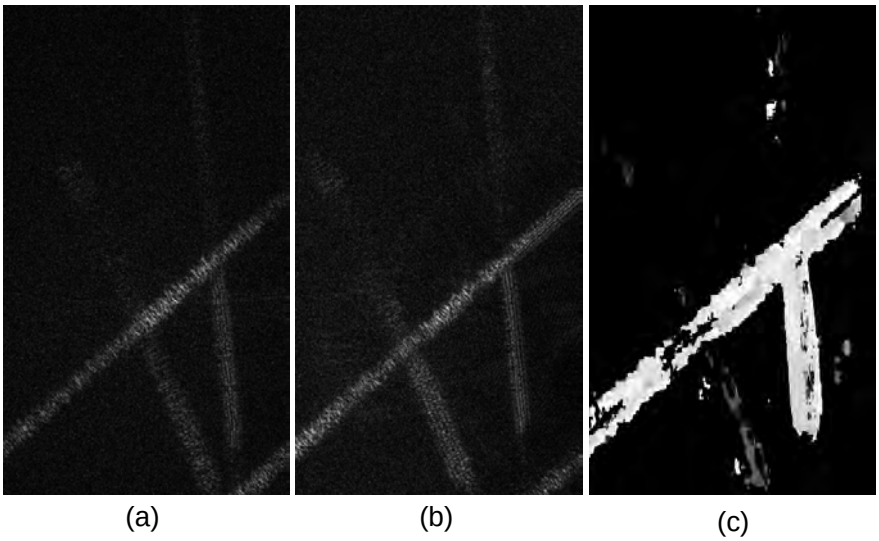

Fig. 4. Human hair. (a) cropped reconstruction intensity image from left perspective, (b) cropped reconstruction intensity image from right perspective, (c) calculated DSI

4 Macroscopic objects

DSI calculations are possible also when using macroscopic real world 3D objects. The setup used is a Mach-Zehnder interferometer architecture. In Fig. 5(a) the intensity of a reconstructed hologram of macroscopic object can be seen. Figure 5(b) shows the calculated DSI, where it can be easily seen which part of the object is located in the front and which is in the back (same colour coding as before). Figures 5(a) and 5(b) show the effect of using different amount of hologram data in each reconstruction. Using only a small part of the data gives bigger depth of field, at the expense of reconstruction quality. In DSI calculations a bigger depth of field is usually better because more of the scene is in focus in the reconstructions.

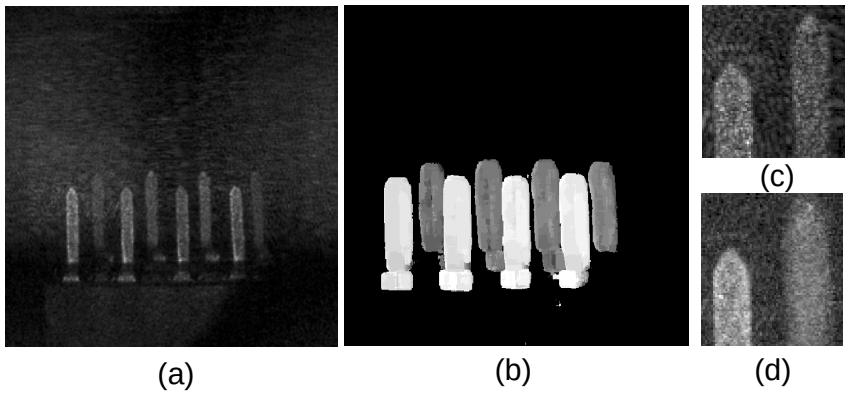

Fig. 5. Macroscopic object, (a) reconstructed intensity from left perspective using ¼ of the hologram data, (b) calculated DSI, (c) zoomed part of a, (d) zoomed part when using ½ of the hologram data

5 Conclusions

We have shown that a traditional computer stereo vision approach can be used in digital holography with different capture setups to obtain depth information of a 3D real-world object. The approach is particularly useful where phase information in the reconstructed domain cannot be readily used to infer depth. Our method uses amplitude reconstruction information only and works well with noisy images, particularly as a result of extending the depth of field, if they have sufficient contrast with their backgrounds.

Both macroscopic and microscopic object hologram capture setups have been show to provide suitable data for our technique. In the microscopic setup case, the applicable setups will be limited to those Gabor type setups where there is sufficient distance between the object and camera. Digital holographic microscope setups whose camera is very close to an image of the observed object are not appropriate for this technique, but they can use reconstructed phase directly for a very accurate quantitative measurement of depth. Our technique could provide clear advantages where one's optical setup does not allow reliable reconstructed phase.

6 Acknowledgments

We thank Emmanouil Darakis for capturing the digital holographic data. This project was supported by the Academy of Finland, Science Foundation Ireland, a European Commission Marie Curie Inter-European Fellowship, and the European Community's Seventh Framework Programme FP7/2007-2013 under grant agreement no. 216105.

7 References

1. Kreis, T (2005) Handbook of Holographic Interferometry. Wiley-VHC, Berlin.
2. Schnars, U, Jueptner, W, (2004) Digital Holography: Digital Hologram Recording, Numerical Reconstruction and Related Techniques, Springer.
3. Ma, L, Wang, H, Li, Y, Jin, H (2004) Numerical reconstruction of digital holograms for three-dimensional shape measurement. Journal of Optics A: Pure and Applied Optics, 6, 396-400.
4. McElhinney, C, Hennelly, B, Naughton T, (2008) Extended focused imaging for digital holograms of macroscopic three-dimensional objects. Applied Optics, 47, D71-D79.
5. Javidi, B, Tajahuerce, E (2000) Three-dimensional object recognition by use of digital holography. Optics Letters, 25, 610-612.
6. Barnard, S, T, Fischler, M, A, (1982) Computational stereo, ACM Computing Surveys, 14(4), 553-572.
7. Scharstein, D, Szelisk, R, (2002) A taxonomy and evaluation of dense two-frame stereo correspondence algorithms. International Journal of Computer Vision, 47, 7-42.

Flexible Combination of Optical Metrology Strategies for the Automated Assembly of Solid State Lasers

Robert Schmitt, Alberto Pavim*
Laboratory for Machine Tools and Production Engineering WZL at
RWTH Aachen University, Chair of Metrology and Quality Management
Steinbachstr. 19, 52074 Aachen
Germany
* Scholarship holder of the Brazilian CNPq

1 Introduction

The technological development of opto-mechanical products is driven by the dynamical change of the customer preferences/needs and by the trend of miniaturisation, which defines big challenges to the fields of precision manufacturing and assembly. Especially the field of precision assembly of optical components is still characterised by a significant amount of manual procedures, resulting in higher costs associated to the assembly tasks. These can reach up to 80% of the total manufacturing costs, which states a strong demand for automation in this sector.

Optical technology has become a key and cross-sectional technology in different technical fields: medical engineering, information technology, metrology, production engineering etc., growing in its economical relevance. Laser systems for labelling/marking materials are extensively used today and comprise a significant slice of the world market. But still, their assembly is determined by manual, and therefore expensive, processes. In this context, new solutions for the flexible and automated assembly of hybrid high-precision products are developed at the RWTH Aachen University. Currently, the assembly of a miniaturised diode-pumped solid-state (DPSS) laser for labelling/marking applications is under research [1,2] inside the scope of a major research initiative – the "Aachen House of Integrative Production" [3]. The project goal is the reduction of manual manufacturing processes for a cost-effective assembly through self-optimising [4] and automated assembly strategies. These strategies are achieved by the combination of flexible manufacturing, sensing and information technologies.

2 Laser design and automated assembly concept

The miniaturised laser system is designed and developed by the Fraunhofer ILT. It consists of a laser arranged in a compact and planar configuration (fig. 1 left) that facilitates the automated assembly. All the optical components can be positioned and assembled from above. They are soldered on a coated ceramic carrier plate without the possibility of readjustment after the assembly process.

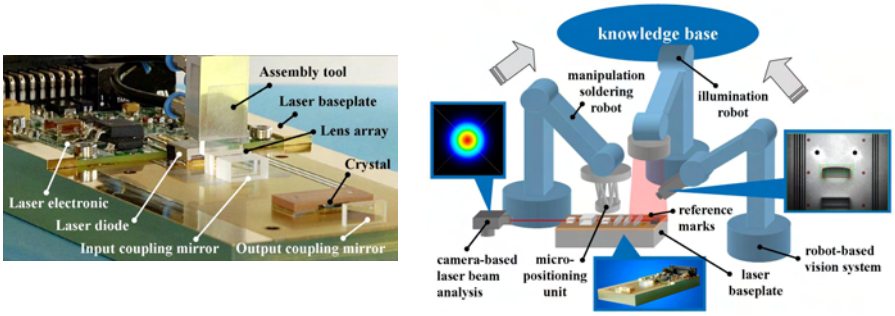

Fig.1. DPSS laser and its components (left). Combining multiple measurement information to the system knowledge base to enable the learning and optimisation processes (right)

The manual assembly of the laser system is performed in an empiric way, demanding high expertise for positioning the components and leading to increased time and cost efforts. In order to automate the process, the assembly must be divided into systematic steps where flexible metrology must be applied to follow the assembly state. The automation approach developed at the WZL, IPT and ILT research institutes is based on a flexible assembly module, which makes use of three robots (fig. 1 right): 1) a handling and soldering robot for picking, positioning and soldering the components on the laser plate, 2) a machine vision robot for different measurement purposes and 3) an illumination robot to support the image acquisition tasks. The entire system is continuously updated with multi-sensor information about the assembly process provided by a robot-based camera, a camera-based laser beam analysis and sensors for handling the electronic laser control. This information is stored into a knowledge base which enables the system to learn from its previous experiences.

A flexible assessment of the assembly state must be performed along the systematic assembly steps for retrieving multiple laser features, like: presence/absence and correct positioning from components and reference marks, assembly tolerances, characterisation and dynamic choice of optical components according to a tolerance matching strategy [2], in-process

active adjustment of critical optical components, characterisation of the laser beam power/quality, identification of assembly failure states as well as its interpretation and recovering to a desired state.

In order to flexibly control the complex and dynamical assembly process at any possible configuration, a sensor data fusion [5] strategy is required to handle the different kinds of information acquired and processed by the system. This process occurs in three distinct levels:

- **1st level (signal level):** images from the robot-based camera in different time intervals are combined in order to improve the signal-to-noise ratio and enhance the laser features
- **2nd level (features level):** the measurement tasks are performed in micrometer scale and therefore the camera's field of view is reduced. Multiple pictures of the laser have to be acquired and reference marks must be recognised and correlated to build up the whole system image
- **3rd level (decisions level):** the biggest challenge is to identify assembly failure states, as well as interpret their reasons and provide feedback to return to a normal assembly state. This procedure involves the acquisition of information from both camera systems and is supported by an expert system [6], which is the cognitive element needed for making decisions based on the interpretation of the sensor information

The expert system contains a model of the laser system and its desired quality indexes. At each laser assembly step, a series of questions is performed by the expert system, which must be automatically answered by the sensor systems. Combining the different measurements performed, the state of the assembly is assessed. If an assembly failure is detected, its reason is interpreted and retrieved by the expert system, which also links a probable solution for the problem. Figure 2 illustrates a failure state during the assembly in which the irradiated laser beam does not pass perfectly through the laser crystal. Instead, it falls partially upon the crystal housing and can be detected due to the strong reflection pattern. A possible solution is to choose an adequate optical component that brings the laser beam back to an ideal path through the laser crystal.

3 Conclusions and perspectives

The proposed solution for the automated assembly of a miniaturised laser system on the basis of flexible combination of optical measurement strategies helps to reduce manufacturing time and costs. Sensor data fusion allows to flexibly assess different and dynamical assembly states. An expert system provides cognitive reaction to changing conditions and

possible failure states, which guarantees the robustness of the solution. The sensor data fusion solution achieves the main self-optimisation premises strived for in the project. It constantly assesses the current state of the laser assembly, dynamically defines its new assembly goals according to the current state, as well as adapts itself to accomplish them.

In the next phases of the project, an autonomous control concept for the assembly is planned by modelling the whole system based on multi agent technology [7]. This will increase the flexibility and autonomy of the whole assembly cell, allowing hybrid hardware and software to cooperate, reducing assembly time and costs. The main aspects that will be handled by different agents are: the control of the three cooperative robots, the different assembly and sensor tools and the cognitive software elements.

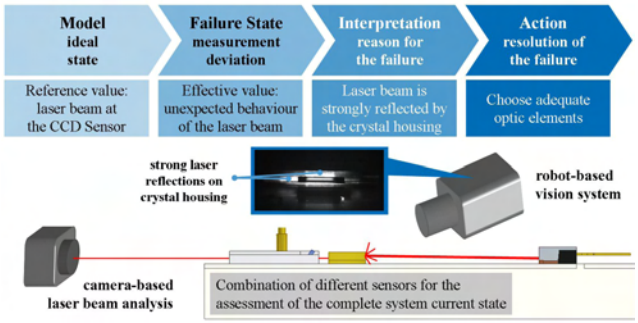

Fig. 2. Identification and resolution of a failure state during the first assembly step

4 References

1. Schmitt, R et al. (2008) Sensor fusion techniques for the self-optimised assembly of a micro-laser. 7th International Heinz Nixdorf Symposium 223:331-343
2. Schmitt, R et al. (2008) Flexibel automatisierte Montage von Festkörperlasern. wt Werkstattstechnik online 11/12:955-960
3. Schuh, G et al. (2007) Excellence in Production. Apprimus-Verlag
4. Gausemeier, J et al. (2004) Selbstoptimierende Systeme des Maschinenbaus. HNI-Verlagsschriftenreihe
5. Russer, H, León, F P (2007) Informationsfusion – Eine Übersicht, Technisches Messen 74(3):93-102
6. Beierle, C , Kern-Isberner, G (2006) Methoden wissensbasierter Systeme. Vieweg
7. Russel, S J, Norvig, P (2003) Artificial Intelligence: A Modern Approach. Prentice Hall

A Numerical Simulation Benchmark of Tilt Scanning Interferometry for 3D Metrology

Gustavo E. Galizzi
Instituto de Física Rosario
Bv. 27 de Febrero 210 bis, S2000EZP Rosario, Argentina
Pablo D. Ruiz
Wolfson School of Mechanical and Manufacturing Engineering
Loughborough University, LE11 3TU Loughborough, United Kingdom
Guillermo H. Kaufmann
Instituto de Física Rosario and Centro Internacional Franco Argentino de Ciencias de la Información y de Sistemas
Bv. 27 de Febrero 210 bis, S2000EZP Rosario, Argentina

1 Introduction

Tilt scanning interferometry (TSI) is a newly developed experimental technique used to determine multi-component displacement fields inside semitransparent scattering materials [1]. It can be considered as an extension of speckle interferometry in 3D, in which the illumination angle is tilted to provide depth information, or as an optical diffraction tomography technique with phase detection. In this paper, we present a numerical model to simulate the speckle fields recorded in TSI. The model is an extension of the one developed in Ref. [2], and allows the separation of all the different effects that affect the phase measurements, which may lead to spurious displacements.

2 Simulation of speckle fields on a TSI system

Assuming that an arrangement of scattering centres is placed across the input plane of an optical system and no depolarisation effects occur, the incident optical field amplitude u_i can be expressed as

$$u_i = \exp\left[j\left(\varphi_d + \varphi_s\right)\right] \tag{1}$$

where $j=(-1)^{1/2}$ is the imaginary unit, φ_s is a random phase value uniformly distributed in the interval $[-\pi, \pi)$, which represents the optical path fluctuations introduced by the scattering centres and due to the light

propagation through a semitransparent material, and φ_d is a deterministic phase value that depends on the optical path from the light source to the output plane of the system. Considering that the optical system operates under the paraxial approximation, the optical field amplitude u_o detected at the output plane can be easily computed in the Fourier domain as

$$U_o = \mathrm{FT}(u_o) = H\ \mathrm{FT}\{\exp[j(\varphi_d + \varphi_s)]\} \tag{2}$$

where FT stands for the Fourier transform operator, U_o is the Fourier transform of u_o and H is the optical transfer function of the system.

In a free space propagation configuration, the transfer function H_{fs} can be expressed as [2]

$$H_{fs} = \exp(jkn_r d_{fs})\exp[-j\pi\lambda n_r d_{fs}(f_x^2 + f_y^2)] \tag{3}$$

where d_{fs} is the distance separating the input and output planes, λ is the light wavelength, $k=2\pi/\lambda$ is the modulus of the wave vector, n_r is the refractive index of the medium, and (f_x,f_y) are the spatial frequencies in a plane perpendicular to the direction of propagation. In a 4*f* optical configuration, the transfer function H_{4f} is an ideal circular low-pass filter [2] with cut-off frequency Ω_c, which defines the speckle size.

Fig.1 depicts the simulated imaging system used to generate the speckle distributions. The origin of the coordinate system (x,y,z) is placed at point O. Two lenses L_i and L_o, each one with focal length *f*, and the aperture A compose a 4*f* optical configuration. A detector array D is located at the output plane of the system. The beam splitter BS is used to combine the scattered light collected from the object with a plane wave, which acts as the reference beam of the interferometer. Sample M is a semi-transparent

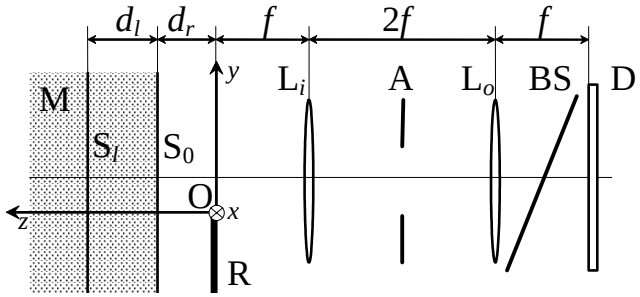

Fig. 1. Imaging system and sample geometry used to simulate the speckle fields used in TSI

object of uniform refractive index n_M positioned at $z = d_r$ and illuminated by a collimated beam of wavelength λ at an angle θ to the optical axis of the system. A rough opaque surface R, called reference surface, is placed

at the region $z = 0$ and $y \leq 0$ and blocks up part of the sample. R allows for carrier detection and error correction in the TSI system. It is supposed that the whole system is immersed in a transparent medium of refractive index $n_0 = 1$. The illumination beam is refracted at the object surface S_0, reaching an internal point with coordinates (x,y,z) at an angle θ_r to the optical axis. The phase difference between the light scattered at that point and the reference beam can be expressed as [1]

$$\phi(x, y, z) = \frac{2\pi}{\lambda}\left[n_0 x \sin\theta + n_0 d_r (1 + \cos\theta) + n_M (z - d_r)(1 + \cos\theta_r)\right] \quad (4)$$

The value of $\phi(x,y,z)$ represents the phase φ_d obtained when the optical field u_i is evaluated at the input plane of an internal layer located at a distance $z - d_r$ from the object front surface (see Eq. (2)).

The free space propagation configuration is identified by the distance from the scattering surface to the observation plane. In this paper, we model light propagation through the sample from each internal layer S_l to the sample surface S_0, and from S_0 up to the input plane of the 4*f* system using transfer functions H_{fsl} and H_{fs0} defined by Eq. (3) but associated to each free space propagation system. Similarly, the transfer function H_{4f} is related to the 4*f* system and is defined by an ideal circular low-pass filter.

The resulting optical field U_{oM} recorded at D can be evaluated by adding the contributions from every layer S_l and the surface S_0. Considering that U_{iS0} and U_{iSl} are the incident optical fields at S_0 and S_l, U_{oM} is expressed as

$$U_{oM} = H_{4f}\, H_{fs0}\left(U_{iS0} + \sum_l H_{fsl}\, U_{iSl}\right) \quad (5)$$

where l identifies each internal scattering layer.

Considering that U_{iR} is the incident optical field amplitude over R, the optical field U_{oR} generated by the light scattered at R is given by

$$U_{oR} = H_{4f}\, U_{iR} \quad (6)$$

Then, the total optical field U_{oT} recorded at D is equal to U_{oR} where R blocks up the view of M, and to U_{oM} elsewhere. Finally, a constant term must be added to U_{oT} to simulate the reference beam of the interferometer.

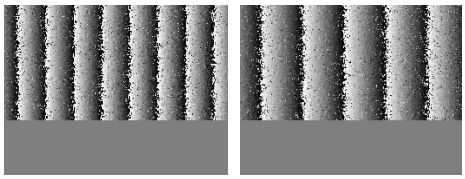

(a) (b)

Fig. 2. In-plane phase changes measured simultaneously at two different depths were used to validate a numerical model of a TSI system. The phase gradient decreases from the front surface (a) to an internal layer (b).

3 Results and conclusion

Two sequences of interferograms were generated whilst linearly increasing the illumination angle and an in-plane depth-dependent linear displacement was introduced between them For simplicity, it was considered that only two scattering layers existed in the sample, the object surface S_0 and the internal layer S_l. Figs. 2(a) and 2(b) depict the in-plane wrapped phase changes evaluated at S_0 and S_l, respectively. The bottom area showing a uniform phase map corresponds to the reference surface, which remains still. The evaluated phase change behaves as expected along the x direction for both layers and is larger at S_0 than at S_l.

This work presents a linear model to simulate the speckle field obtained when a semitransparent scattering material is illuminated with monochromatic light with the illumination strategy used in TSI. The ability of the model to simulate depth-resolved displacement measurements was illustrated with an example that included in-plane deformations. The advantage of being able to model the detected signal is the first step towards separating the effects of stress-optic coupling, refraction, scattering and absorption in the measured optical phase changes.

4 References

1. Ruiz P.D., Huntley J.M. and Maranon A. (2006) Tilt scanning interferometry: a novel technique for mapping structure and three-dimensional displacement fields within optically scattering media. Proceedings of the Royal Society A 462: 2481-2502.
2. Equis S. and Jacquot P. (2006) Simulation of speckle complex amplitude: advocating the linear model. Proc. SPIE 6341: 6341381.

A virtual telecentric fringe projection system

Haskamp, K.; Kästner, M.; Reithmeier, E.
Institute for measurement and automation control
Nienburger Street 17, 30167 Hannover
Germany

1 Introduction

Crank shafts are one of the most important components of a motor. Therefore the Collaborative Research Centre 489 “Process Chain for the Production of Precision Forged High Performance Components” (CRC 489), financed by the German Research Foundation (DFG), deals with the production of high precision forged crank shafts [2]. One topic of the subproject B5 “Geometry Analysis” is to build up a virtual multi sensor system, consisting of a fringe projection system, a shadow projection system and several linear axes. According to an estimation of statistical data such as the standard deviation it is useful to simulate the measuring procedure with a virtual multi sensor system [1]. In this paper the simulation model and the first simulation results will be presented.

2 Virtual fringe projection system

A fringe projection system consists of a beamer and one or more cameras. Common fringe projection systems use straight fringe patterns which are projected from the beamer onto an object [3]. Afterwards the deformed patterns on the surface of the measurement object are measured by the camera. In this simulation the general measurement process is inverted with the consequence that the camera pixels are projected onto the beamer stripes. To illustrate the virtual measurement process the characteristics of the simulation model and the optical way of the light rays should be pointed out at first. After that the simulation procedure and some results are explained.

2.1. Simulation model

A combination of a pinhole and an object-sided telecentric lens was used for the model of the camera objective and a simple pinhole for the beamer objective, as shown in Fig. 1. To decide if a pixel is illuminated the light intensity, emitted from the beamer, reflected from the measurement object and absorbed from the camera, is weighted in respect to the reflexion angle (Fig. 1).

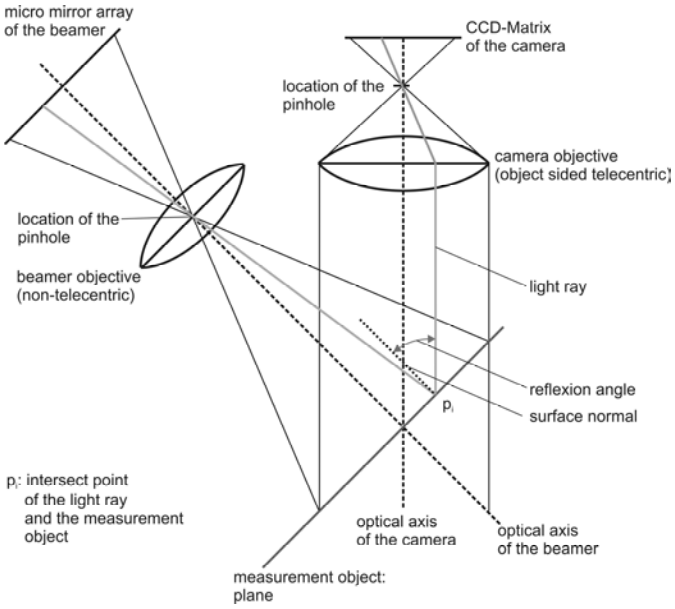

Fig. 1. Simulation model of the virtual fringe projection system

For the calculation of the reflexion angle it is necessary to acquire the surface normal of the measurement object at different points. Therefore a mathematical description of the object is required, which permits an easy calculation of the geometrical data. In this simulation the object is described by means of polygons so that a simple calculation of the normal is allowed. For the calculation of the surface normal the intersect point between the light rays and the measurement object is needed.

For this purpose the intersection points of the light rays and the camera objective is computed at first. After that the light rays run parallel to the optical axis of the camera and intersects the measurement object at point p_i. Therewith the surface normal at this point and the reflexion angle can be estimated.

2.2. Procedure of a simulation

The first step in the simulation is to calculate the intersect point for each light ray for all camera pixels with the measurement object, allegorised through polygons. Subsequently the beamer-stripe ϕ to the corresponding camera pixel, with regard to the weight of the reflexion angle, is estimated. Thereby a pair of values $\{i, j, \phi\}$ was generated, which can be used for the following simulation procedures, whereas i and j are the coordinates of the camera pixel and ϕ the phase of the beamer.

3 Comparison between simulation and real world system

To appreciate the quality of the virtual fringe projection system several fringe-sequences were generated using the real world system as well as the virtual system and detected by the real and the virtual camera. The differences between the measured and the calculated chart should constitute the accuracy of the simulation model, whereas the measurement object is allegorised by a plane which is orientated parallel to the beamer. After the measurement and the simulation the generated images were converted to binary images. Therefore a simple threshold was used.

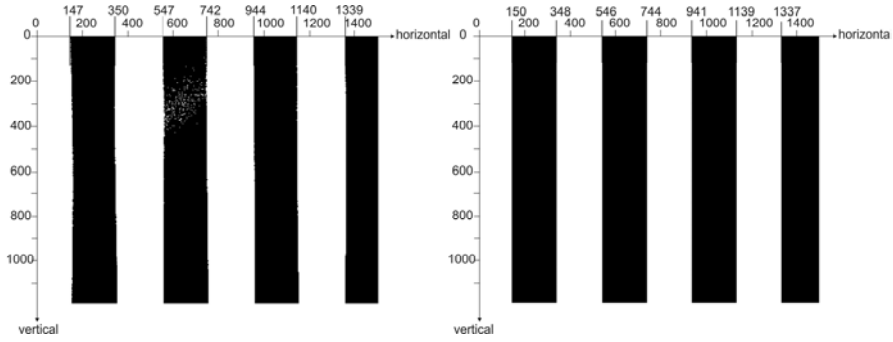

Fig. 2. Measured (left) and simulated (right) fringe sequenz

Fig. 2. shows the measurement and the simulation result. To compare the charts the position of the edges were established. As constituted in Fig. 2. the difference between the simulated and the measured result lies in the range of 3 pixels and is, relating to the great number of pixels (1188 x 1504), very small. The remaining deviation could be declared with the identified model parameters.

4 Conclusion and outlook

In this paper the simulation of the measurement process of a fringe projection system was described and a comparison between the virtual and the real world system was presented. The comparison from camera images of projected fringe sequences points out that there is a high accordance between the real and the simulation model.

In combination with monte carlo methods the model can be used to accomplish measurement uncertainties for several workpiece geometries. Furthermore it is possible to characterise the influence of the model parameters on the measurement accuracy. For example a relative motion between the measurement object and the fringe projection system can be simulated and the influence on the measurability can be examined.

To detect the geometry of a complex workpiece it is necessary to approach more than one position with the measurement object or with the measurement device. To fuse the measurement results to one global coordinate system the knowledge of the positions takes a significant influence on the accuracy of data fusion processes.

5 Acknowledgement

The authors would like to thank the German Research Foundation (DFG) for funding the project B5 "Geometric Analysis" within the CRC 489.

6 References

1. Böttner, T., (2009) Messunsicherheitsbetrachtungen an einem virtuellen Streifenprojektionssystem. Dissertation Leibniz University of Hannover
2. Kerber, K., Specker, A., (2006) Geschmiedete Präzision – Der Sonderforschungsbereich 489. phi Produktionstechnik Hannover Informiert, 7. Jahrgang, Ausgabe 1
3. Valkenburg, R. J., Mc Ivor, A. M., (1998) Accurate 3D Measurement using a structured light system. Image and Vision Computing :99-110

Inspection of an extended surface by an active 3D multiresolution technique

J. Vargas[1], R. Restrepo[1], J. A. Quiroga[2], T. Belenguer
[1]LINES, Instituto Nacional de Técnica Aerospacial (INTA),
Carretera de Ajalvir Km 4, 28850 Madrid, Spain
vargasbj@inta.es
[2]Optics Department, Universidad Complutense de Madrid,
Ciudad Universitaria s/n, 28040 Madrid, Spain

Abstract

Reliable inspection of large surfaces with low depth recovery error is needed in a wide variety of industrial applications, for example in deformation measurement or defect inspection of extended surfaces as communication antennas. Active triangulation measurement systems present a compromise between the depth recovery error and the measured area. For an optimized active three-dimensional measuring system the expected ratio between the depth resolution and the inspected area is in the rage of 10^{-4}. Therefore, if we want to scan a large object with a high level of detail we need multiresolution techniques.

In this work we demonstrate the application of an active triangulation multiresolution method for the inspection of communication antennas. The technique is based on a standard camera-projector system. The result is a global measurement formed by a set of superposed local measurement with high depth resolution.

1 Introduction

Sensor systems based on triangulation and structured light provide a non-contact, whole field and fast measurement compared to conventional coordinate measurement machines. The phase-shift method provides fast acquisition of dense point clouds. In general, systems with one camera and one projecting unit are used to acquire whole-field depth information on the inspected surface.

One characteristic of these systems is that the ratio between the depth recovery error and the lateral extension is a constant that depends on the

geometrical setup. Therefore standard active triangulation techniques are insufficient to measure the global shape of an extended object, as well as the low details of its surface. This problematic can be solved using multiresolution techniques [1-7].

In this work, we demonstrate the application of an active multiresolution method for the inspection of a satellite communication antenna.

2 Theoretical Foundations

In a 3D measuring setup, the most significant parameter is its depth recovery error. In a fringe projection system the depth recovery error depends on the measured area among other parameters [3].

Typical values of the area related resolution in an optimized fringe projection system are about 10^{-4} [3], that means that for a measurement of an area of 1 m^2 we can expect a depth resolution of about 0.1 mm. Therefore, if we have to inspect a satellite communication antenna with a depth recovery error of about 0.01 mm a solution is to divide the surface into smaller overlapping areas and perform a local measurement in each of them. This multiresolution method it is used to inspect a satellite antenna.

An active 3D measuring system with a rigid configuration is always observing the same small area of the antenna. To obtain a 3D measure of the whole surface, the antenna is mounted on a rotating step motor (see Figure 1). Finally, the different local measurements are combined in a unique global measurement.

For the registration of the different views, we have used a set of white markers sticked over the surface. In two consecutive measures (after and before activating the rotating motor), the corresponding mark's centroids in the camera image plane are obtained. Using the 3D measure of the two consecutive views and the different centroids position of corresponding marks the roto-translation matrix that relates the two 3D measures in a unique reference system it is obtained. Using this technique all the local 3D measures are related to the first 3D measure.

3 Experimental Results

The presented multiresolution technique has been applied using a rigid camera-projector triangulation system previously calibrated.

The explained multiresolution technique has been applied to inspect large satellite communication antennas. In Figure 1 it is shown an image of

the satellite communcation antenna we are interest in measuring. The antenna has a radius of 55 cm.

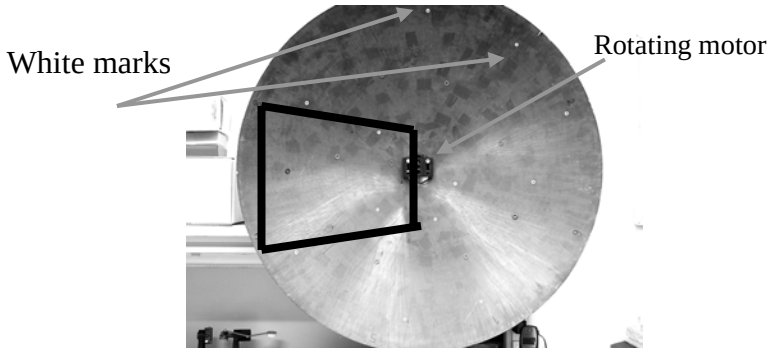

Fig. 1. Satellite communication antenna to inspect with a black rectangle that indicates the region where it is performed each local measurement, the rotating motor and the white marks used to register the different 3D measures

In Figure 1 it is shown with a black rectangle the area to inspect in each measurement and the white marks over the antenna to relate the different 3D measures to preserve a unique reference system.

In Figure 2 it is shown the whole 3D measure of the antenna depicting the different measurements by the explained registering process.

The number of inspected points over the antenna surface in Figure 2 is about of 1600000

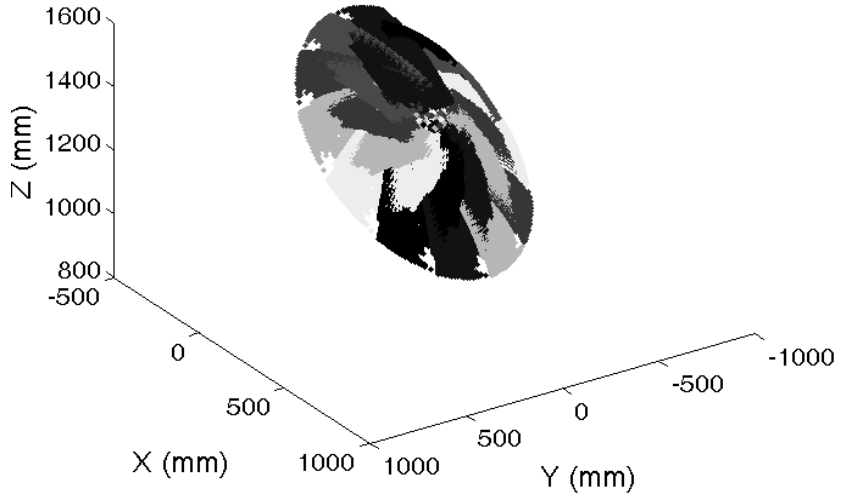

Fig. 2. Whole 3D measurement of the satellite communication antenna shown in Figure 1

In order to obtain the depth recovery error of the 3D measuring system we have measured a high quality plane. The computed root mean square (*r.m.s*) between the measured plane depth coordinate and the best fitted plane is of 7.8 μm. In Figure 3 it is shown a profile of the depth recovery error for the plane measure.

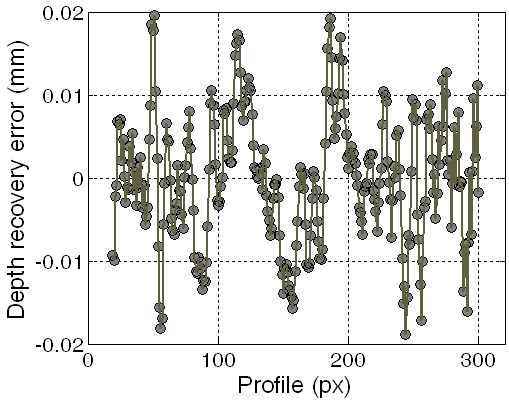

Fig. 3. Profile of the computed depth recovery error

4 References

1. H. Steinbichler, E. Heinrich Nösekabel, R. Rösch, "Optical inspection in the production line" in Fringe 2001, pp 311–323, (2001)
2. G. Notni, ''360-deg shape measurement with fringe projection—calibration and application'' in Fringe 2001, pp. 311–323, (2001)
3. G.Wiora, ''High resolution measurement of phase-shift amplitude and numeric object phase calculation,'' Proc. SPIE 4117, 289–299 (2000)
4. D. Kayser, T. Bothe, W. Osten, "Scaled topometry in a multisensor approach", Opt. Eng. 43, p. 2469-2477 (2004)
5. P. Andrä, E. Ivanov, and W. Osten, ''Scaled topometry—an active measurement approach for wide scale 3D surface inspection'' in Fringe 1997 pp. 179–189, (1997)
6. J. Vargas, J. A. Quiroga, "Novel multiresolution approach for an adaptable structured light system", Opt. Eng., 47(2), 023601-10 (2008)
7. J. Vargas, J. A. Quiroga, ''Multiresolution approach based on projection matrixes'' Applied Optics, 48(7), pp. 1295-1302 (2009)

Automated Multiscale Measurement System for micro optical elements

W. Lyda*, A. Burla*, T. Haist*, J. Zimmermann**, W. Osten*, O. Sawodny**
*Institut für Technische Optik,
** Institut für Systemdynamik,
Universität Stuttgart, Pfaffenwaldring 9, 70569, Stuttgart.

1 Introduction

Quality inspection of micro optical mechanical systems consisting of components from millimetres down to critical ones at sub-micron scales, require very high resolution measurements. Using a single sensor system at the prescribed resolution for such measurement tasks needs long time for a complete inspection of the target, which is not practical in most of the applications.

One solution is utilising a system with multiple sensors with predefined task specifications like measurement position, resolution etc. to reduce the measurement duration [1]. A known disadvantage is, a priori information about the possible defect positions and defect scales is often required for a complete inspection.

A multi sensor system which can adapt itself to the given measurement task and specimen automatically would resolve the restrictions mentioned above [2,3]. Different types of sensors (with different scales and capabilities) on the measurement system have to be connected with each other and a customisable positioning system should coordinate the whole inspection.

We present the concept of an Automated Multiscale Measuring System (AMMS) capable of the above mentioned properties. And show its potential and exemplary measurements with a prototype AMMS.

2 Measurement strategy

The AMMS pursues an active exploration approach by the interaction of the following three subcomponents: sensors and indicator functions, a positioning system and an information processing system.

Starting with an initial low resolution, an outline of the specimen is acquired using a coarse scale sensor and new regions of interest are identified by task specific indicator functions at this scale. Only these identified regions are explored using the next sensor, which is also selected based on the indicator evaluation results (fig. 1).

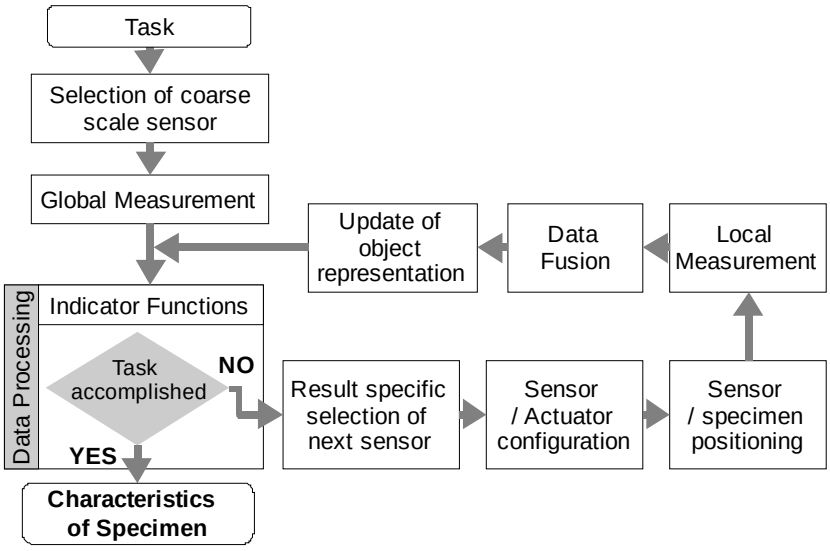

Fig. 1. Basic measurement strategy of the AMMS

The positioning system adapts to the selected sensor by a model based parameter calculation [4] and drives the sensor to the selected regions of interest for measurements.

The final subcomponent, the information processing system fuses different types of data from different sensors into a common coordinate system. Step by step the accuracy of the object representation is increased as more sensory and positioning data is acquired.

The objective of this AMMS is to run high resolution, time-consuming, measurements only at critical regions on the specimen, thus reducing the overall measurement time and increasing the throughput of the system.

To pursue this active exploration, the system has to be equipped with different sensor systems, covering different scales and representations of the specimen to collect multi scale and multi modal data.

Microlens arrays are one of the test specimens in our project. Accordingly three sensors are attached to the prototype AMMS.

In order to select task specific sensors and indicator functions, sensor models were developed. These models are used to adapt the sensor parameters according to the new task and estimate preliminarily uncertainty with respect to the measurement object and conditions. More details are presented in the following sections.

As mentioned before the positioning system is also a crucial part of the measurement strategy. The requirements to the positioning system depend on the measurement principle, sensor parameters and the measurement scale, which are taken from the task specification.

For example the confocal microscope needs a steady distance between the specimen and itself during the measurement. Hence the vibrations introduced by the confocal focusing system should be compensated by the positioning system [5].

3 Selection of Sensors and Indicator Functions

Depending on the task specification a planned assistant system selects the sensors to be used and the indicator detection functions. Indicator detection functions indicate the possibility of a defect at a particular scale. Finer scale measurements are needed to finally classify the defect.

As mentioned before for the task of measuring micro optical systems like microlens arrays, three sensors are chosen, a video microscope, a confocal microscope(for area related topography) and a confocal point sensor(for highly resolved topography scans). Two lighting systems are used at the coarse scale to measure the point spread function and scattered light from the microlens array.

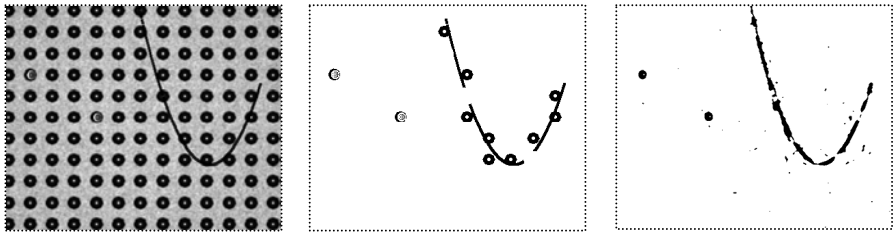

(a) (b) (c)

Fig. 2. (a)Point spread function of a microlens array with a scratch and defective lenses (simulated), (b) Results of evaluation with normalized cross correlation, (c) results of evaluation with Fourier self filtering.

Due to the periodic structure of the microlens array's point spread function, Fourier self filtering is a good indicator detection function at the

video microscopy level, normalized cross correlation can also be used effectively at this scale. Figure 2 shows results of these methods. Contrast based local thresholding is used to indicate scratches and particle pollution from the scattered light. Normalized cross correlation is used to identify good lenses at the confocal microscopy level and masking these out to find scratches or particle pollution at confocal microscopy level. Reference [6] provides more information about defects, indicators, and indicator function's reliability.

Fourier descriptor based methods can be used to finally classify the micro lenses from the topography data. Figure 3 shows lens analysis using two Fourier descriptor based methods isoring and spiral method (article due for publication).

A planned expert system takes as input the data from each sensor model and estimates the reliability of each indicator function for that particular sensor. This way the indicator functions and their parameters can be automatically generated for the given task. Further automatic optimization methods fine tune the indicator function's parameters.

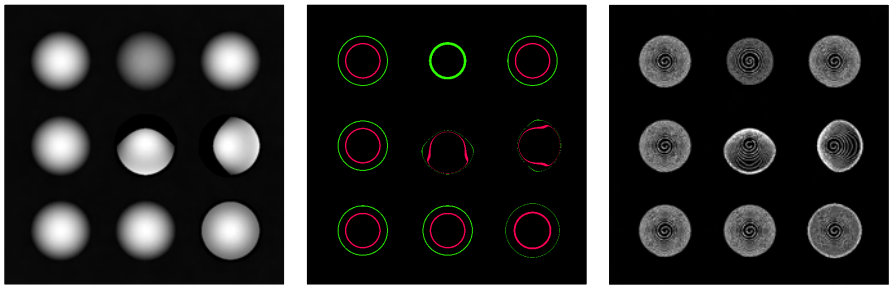

(a) (b) (c)

Fig. 3. (a) Confocal microscopy simulated data with four defective lenses, (b) lens analysis using Fourier descriptors isoring method, (c) lens analysis using Fourier descriptors spiral method.

4 Task Specific Sensor Parameter Tuning

Once the sensors are selected depending on the task specification, they have to be tuned according to the indicators, indicator detection functions and the task specification.

At every scale indicators are used to select the regions of interest for the next scale. Hence it is important to identify all the indications of a possible defect by the indicator functions. Since the input to the indicator functions

is taken from the sensor data, sensors should be tuned to correctly acquire all the indications.

Usually there are sensor parameters which can be controlled and those which can only be controlled with limitations. Table 1 below show these for the three sensors chosen for our task.

As an example we show how the confocal microscope's parameters depend on the concrete task specification. Also show how to estimate the measurement uncertainty of the microscope.

Table 1. Controllable parameters of the sensors

Video Microscope	• Choice of lighting systems • Camera Properties like exposure time, gain, etc. • Camera noise levels (limited) • Resolution of the system (limited)
Confocal Microscope	• Choice of the front lens • Sampling rate of the confocal signal • Over brightness tolerance • working distance between the system and the specimen (limited) • Numerical aperture (limited) • Resolution of the system (limited)
Confocal Point Sensor	• Variable actuator scan rate • Measurement field size and shape • Sampling rate (limited) • Measurement range (limited)

In the case of signal evaluation based on the centre of gravity of the confocal signal, the uncertainty (σ_C) depends on the uncertainty of the z-positioning system (σ_z) during a scan, and the intensity noise of the camera (σ_I).

$$\sigma_C{}^2 = k^2\sigma_z{}^2 + m^2\sigma_I{}^2$$

For a confocal signal taken from a plane mirror, given by $\mathrm{sinc}^2(z)$, the weighting factors k and m can be calculated by

$$k = \frac{1}{\sum_j \left(sinc(z_j)^2 - h\right)} \sqrt{\sum_j \left[2 \cdot \cos(z_j) \cdot sinc(z_j) - sinc(z_j)^2 - h\right]^2} \quad (1)$$

and $$m = \frac{1}{\sum_j \left(sinc(z_j)^2 - h\right)} \sqrt{\sum_j z_j^{\,2}} \qquad (2)$$

Both the factors depend on the signal evaluation threshold h, the FWHM and the sampling rate. In the case of optical surfaces the signal modulation depends on the surface characteristics. We have presented a model to calculate the surface influence on the signal modulation and the measurement uncertainty [5].

This model is used to calculate steps per FWHM for a given uncertainty for different front lenses. This helps choosing the front lens that fulfils the constraints for uncertainty, field, lateral resolution, axial resolution and measurement time. Figure 4 shows the uncertainty estimation for 20x and 10x over the sampling rate.

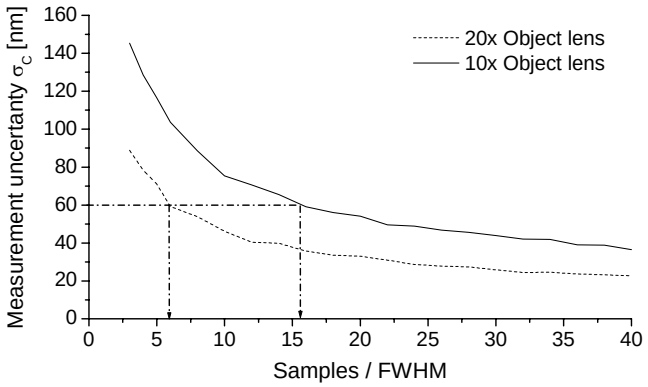

Fig. 4. Calculated uncertainty for optical surface plane surface, (line) 10x 0.3 object lens, (dashed) 20x object lens

5 Example Measurement

For the given task to detect all relevant defects like scratches starting with thickness of 10µm, particle pollution of 10µm and low frequency shape deviations of amplitude 250nm on a microlens array with 235µm lens diameter and 400µm pitch. Table 2 shows the sensor parameters that were considered for the specified task. Figure 5 shows the results of the measurement, a multi sensor multi model fusion is also shown in figure 5(c). From figure 5(c) we can clearly identify the difference between a scratch and an external fibre shaped particle at a finer scale (confocal

microscope). At the coarse global scale(video microscope) both are just indicators for a possible defect.

Table 2. The table shows parameters of the sensors suitable for measuring a microlens array.

Video Microscope	• 1.4 Mega Pixel camera (fovion chip) • A telecentric lens which has a measurement field of 17 x 12 mm². • 5 images with varying exposure times from 50-500µsec were stitched to get a homogeneous point spread function.
Confocal Microscope	• 10x front lens • Lateral resolution of 12 µm • Measurement field of 1.8 x 1.5 mm² • NA 0.3
Confocal Point Sensor (SiScan Sc 400 by Siemens)	• 8khz sampling rate • Axial range of 0.4 mm, • Axial resolution of 0.1 µm, • Lateral resolution of 0.6 µm

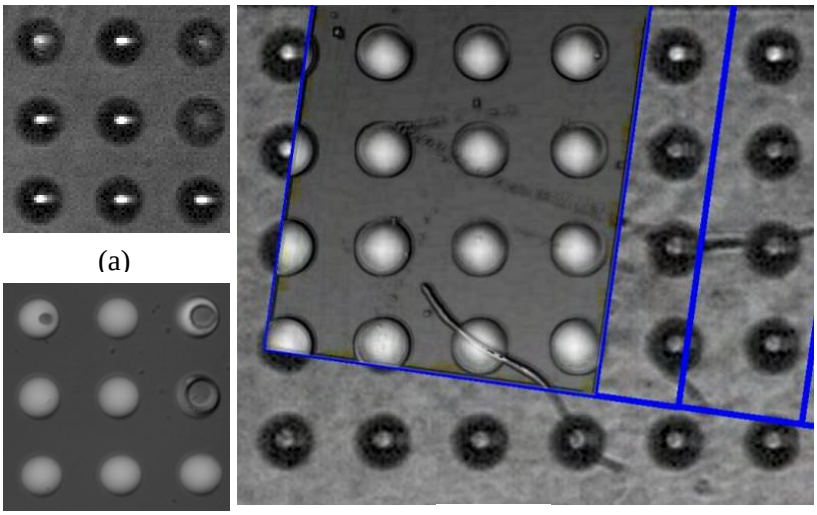

(a) (b) (c)

Fig. 5. (a, b) Lens defect indicators from video microscope's point spread function and confocal microscope. (c) An example of multi sensor and multi-model fusion.

6 Conclusions

Hence we have presented an Automated Multiscale Measurement System (AMMS) for the inspection of micro optical systems or micro mechanical systems. This AMMS only uses finer scale sensors where and when required making the whole inspection process fast and efficient.

We have shown that according to the task specifications sensors are tuned to reduce the measurement uncertainty. This is done with the help of sensor models. And depending on the type of sensor data and scale, indicator functions are selected. These functions provide regions of interest for the next scale, effectively reducing the area of measurement to critical regions saving measurement time.

Hence the AMMS can automatically measure the given specimen at different resolutions according to the task specification. The system also fuses the data from different types of sensors and provides a complete representation of the test specimen. An information processing system performs the data fusion with the help of Indicator detection functions.

This work was supported by the DFG under SPP-1159.

Thanks to IFF-Universität Stuttgart for Co-operation.

7 References

1. Weckenmann. A, Shaw. L, Krämer. P, Bookjans. M (2009) Trends in der Fertigungsmesstechnik: Multisensormesssysteme. Management und Qualität 1:2
2. Kayser. D, Bothe. Th, Osten. W (2004) Scaled topometry in a multisensor approach. Optical Engineering 43, 10:2469 – 2477
3. Wiesendanger. T, Osten. W, Pannekamp. J, Regin. R, Westkämper. E (2005) Neue multiskalige Mess- und Prüfstrategien für die Produktion von Mikrosystemen. Mikrosystemtechnik Kongress GMM, VDE, VDI, 677-680
4. Zimmermann. J, Sawodny. O (2007) Modeling for Simulation and Control of a X-Y High Precision Positioning Table. Proceesings of IEEE CASE 2007
5. Lyda. W, Zimmermann. J, Burla. A, Regin. J, Osten. W, Sawodny. O, Westkämper, E (2009) Sensor and actuator conditioning for multiscale measurement systems. Proceedings of SPIE 7389-02
6. Burla. A, Lyda. W, Regin. J, Zimmermann. J, Osten. W, Westkämper, E, Sawodny, O (2009) Relibility Analysis of Indicator Functions in an Automated Multiscale Measuring System. Proceedings of OPTO

Simulation based sensitivity analysis and optimization of Scatterometry measurements for future semiconductor technology nodes

Valeriano Ferreras Paz [a], Thomas Schuster [a], Karsten Frenner [a] ,
Wolfgang Osten [a], Laszlo Sziksai [b], Manfred Mört [b], Christoph Hohle [b] and Harald Bloess [b]
[a] Institut für technische Optik, Universität Stuttgart
[b] Qimonda Dresden, Center of Competence Metrology/Analytics

1 Introduction

The term scatterometry summarizes a rather great variety of techniques, all of which have in common that they investigate the diffraction spectrum from a periodic array of nanostructures.

During the past years optical scatterometry has proved to be a powerful technique for CD and profile metrology and has established itself as one of the mainly applied methods for CD metrology besides CD-SEM [1]. To reconstruct structure parameters, measured spectra are compared to simulated data obtained using software Maxwell-equations-solvers as for example the rigorous coupled wave analysis method (RCWA) [2] implemented in our software package MICROSIM [3]. Using this approach to solve the inverse problem allows us to reconstruct the real structure even if below the optical Abbe-limit. As the size of semiconductor structures keeps decreasing constantly, due to growing memory requirements and miniaturization, the demands on the scatterometry method keeps growing. Also the growing process complexity leads to a relative increase of phenomena such as line edge roughness. Using optimized measurement configurations can help to get and exploit maximum parameter sensitivity. These optimized configurations can be accessed with a simulation based approach, performing a sensitivity analysis for different structures, parameters and technology

2 Analysed structure types and simulation basis

We started our work with simple dense resist line gratings of different periods on silicon wafers. These line gratings were produced with e-beam lithography with pitches from 180 nm to 22 nm at Qimonda (Dresden). Later we repeated measurements and simulations with etched silicon line gratings with the same pitches and also with so called STI (shallow trench isolation) structures.

The scatterometry measurements on these structures were performed with an industrial scatterometry tool at a fixed incident angle with wavelengths from 200 to 900 nm.

The structures were modelled for simulation with our simulation package MICROSIM. Fig. 1 compares a cross section SEM image to the MICROSIM model we used for simulation of that structure.

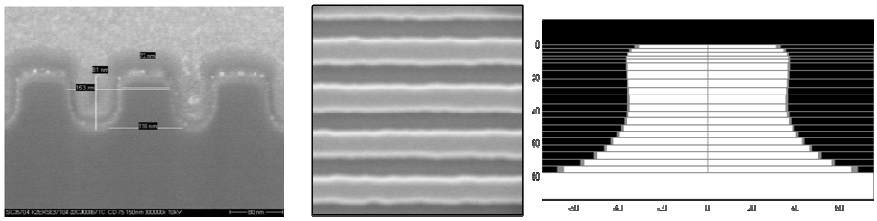

Fig. 1. From left to right: cross section SEM image of an etched silicon grating, top-down SEM with LER, MICROSIM model used for simulation

3 Verification of simulations

Before starting simulations for predicting sensitivity towards smaller nodes we performed several simulations to verify the agreement of our simulations with the measured spectra. All simulations have been made with our software package MICROSIM. For every structure a library was computed containing variations of CD, pitch, structure height, sidewall-angle, top- and bottom-rounding and depending on the structure type also SiO_2 layers and sidewall bowing. Performing a best mach search gives, as depicted in Fig. 2, very good agreement for structures down to 36 nm. Difficulties encountered for smaller nodes can be explained in structure quality issues and line edge roughness, which wasn't considered in these simulations but is subject of other investigations at our institute (see Ref. [4]).

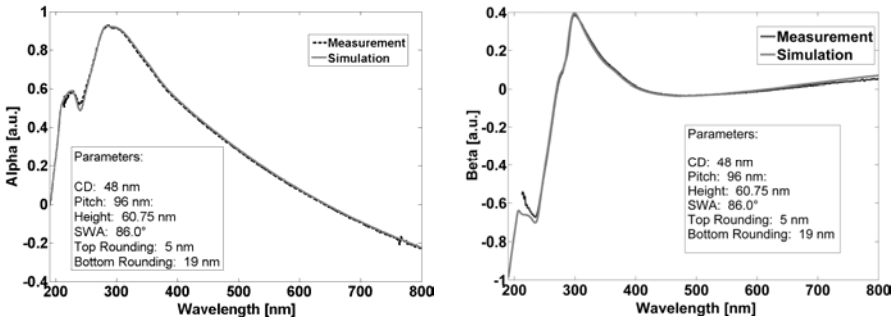

Fig. 2. Measured and simulated Alpha/Beta for resist structures (CD 48nm)

4 Sensitivity Analysis

To analyse the sensitivity towards a parameter of interest, we defined our sensitivity (see Eq. 1.) as the difference in signal ($\Delta Signal$) divided by the variation of the parameter (ΔVar) and normalised to the nominal parameter value (Var_0), so that a comparison between different technology nodes is possible.

$$S = \frac{\Delta Signal}{\Delta Var / Var_0} \tag{1}$$

From this definition the simulations can be performed for different parameters of interest (CD, pitch, SWA, height, roundings, etc), different structure types and in dependence of the measurement configuration (especially wavelength and incident angle).

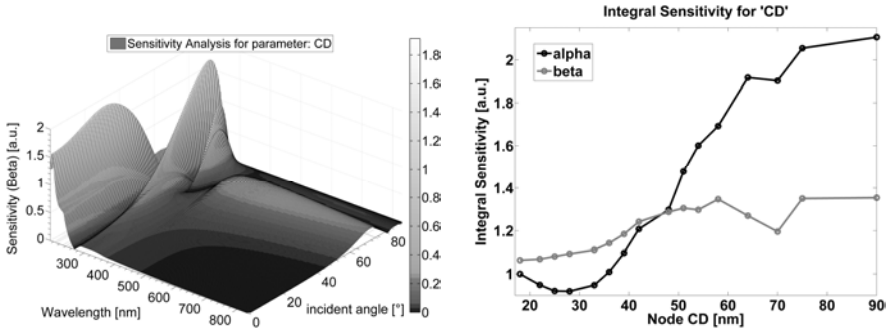

Fig. 3. a) Sensitivity for CD parameter depending on wavelength and incident angle for a dense-line resist structure with CD 36 nm **b)** Sensitivity trend for CD parameter of STI structures for different structure sizes.

The resulting images (see Fig. 3) give easy access to the most promising measurement configuration to get highest sensitivity towards the desired parameter. Furthermore it is possible to visualize sensitivity trends for smaller groundrules for each parameter and structure type (see Fig. 4).

The results show that sensitivity towards most parameters, as one would expect decreases for smaller structures, but they also show that there are configurations with highly increased sensitivity.

5 Summary and Outlook

We have shown that there are optimized measurement configurations for classical spectroscopic scatterometry depending on structure type, size and parameter of interest. Future industrial scatterometry tools will have to consider the available degrees of freedom to obtain maximum sensitivity. The method we show here gives access to the needed information and allows predicting optimized configurations [5], demands and extendability possibilities on future industrial scatterometry tools.

Investigations with more complex structures have been started. Also other possibilities to extend classical scatterometry as is Fourier-Scatterometry and Phi-Scan Scatterometry [6] have to be considered.

6 Acknowledgement

This work was financially supported by the Federal Ministry of Education and Research of the Federal Republic of Germany (Project No.: 13N9432).

7 References

1. C.J. Raymond, AIP Conference Proceedings 788 (2005) 394-402.
2. M. Moharam, E. Grann, D. Pommet and T. Gaylord, J. Opt. Soc. Am. A 12 (1995), pp. 1068–1076
3. M. Totzeck, Optik 112 (2001) 399–406.
4. T. Schuster, S. Rafler, V. Ferreras Paz, K. Frenner, W. Osten Microelectronic Engineering 86 (2009) 1029–1032.
5. V. Ferreras Paz, talk at 245. PTB Seminar on Scatterometry and Ellipsometry on Structured Surfaces, Braunschweig, March 2009
6. T. Schuster, S. Rafler, W. Osten, P. Reinig, T. Hingst, Proc. SPIE, Vol. 6617, 661715 (2007)

Electronic Speckle Pattern Interferometry at Long Infrared Wavelengths. Scattering Requirements

Jean-François Vandenrijt[1], Cédric Thizy[1], Igor Alexeenko[2], Iagoba Jorge[3], Ion López[3], Idurre Sáez de Ocáriz[3], Giancarlo Pedrini[2], Wolfgang Osten[2], Marc Georges[1]
[1]Centre Spatial de Liège – Université de Liège,
Liege Science Park, 4031 Angleur, Belgium;
[2] Institut für Technische Optik, Universität Stuttgart,
Pfaffenwaldring 9, 70569 Stuttgart, Germany
[3]Centro de Tecnologías Aeronáuticas,
Parque Tecnologico de Álava, Juan de la Cierva 1, 01515 Miñano, Spain

1 Introduction

Holographic interferometry (HI) and electronic speckle pattern interferometry (ESPI) metrology techniques [1] in visible light are not often well suited for field applications or for large displacement measurement due to the short wavelength used, which imposes high stability constraints. One way to decrease this sensitivity is to use a longer wavelength. Our purpose is to investigate holography in the Long Wave InfraRed (LWIR) range and more specifically at 10 µm with CO_2 lasers. This shall provide us a typical 20 factor of decrease of the stability requirements, meantime the range of measurement shall be also increased by the same factor.
In previous papers we showed the first experiments of ESPI at such wavelengths, considering an in-plane ESPI configuration [2]. This scheme was simple to set-up since no reference beam was required, which did not impose to dismantle the off-the-shelf thermal imager (FLIR Thermacam) which was available for the experiment.
We already discussed a specific feature of the LWIR spectral range which is the fact that using a longer wavelength decreases the scattering reflectivity of objects. In order to overcome this we used a white scattering removable powder but, although speckle was observed, a strong specular peak was still present. The large incidence angles of illumination beams which were formed in the in-plane ESPI scheme prevented us to have the specular peak entering the costly thermal imager and damaging it. In this paper we present more recent ESPI set-up and discuss the scattering

requirements. We show that for carbon and glass fibre structures, speckle can be observed in the LWIR range.

2 Out-of-plane ESPI set-up

After the first in-plane ESPI experiment we were allowed to use an infrared camera without imaging objective lens, giving easy access to the sensor plane through small modifications. This opened the possibility of out-of-plane ESPI which require the use a beam combiner placed in front of the imaging sensor. An out-of-plane ESPI set-up was developed and shown in Figure 1 (a) [3]. The phase-stepping can be produced by a moving mirror equipped with a piezoelectric translator. The set-up was used to observe the rotation of a metallic plate which was covered by the same white scattering powder that is used to increase scattering in visible holography. The phase map obtained is shown in Figure 1 (b). The lens placed in front of the sensor has such an aperture that speckle can be observed at the 10 μm wavelength.

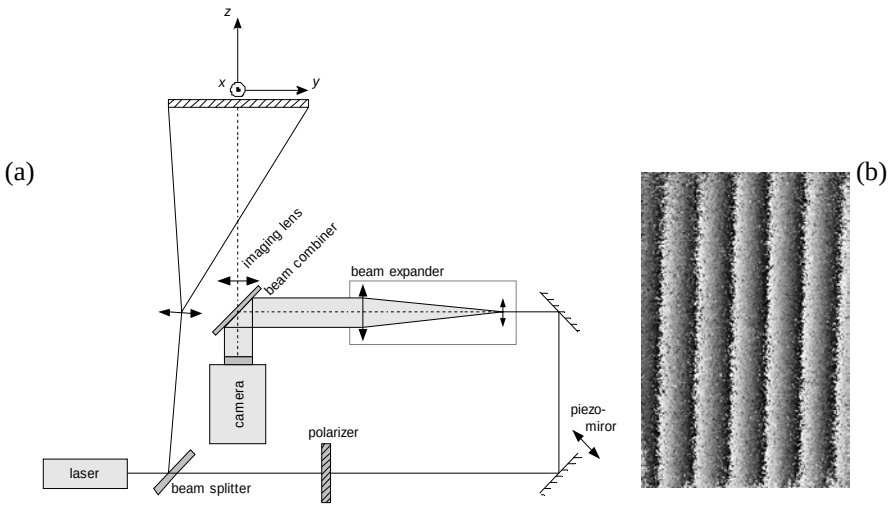

Fig. 1. (a) Scheme of the experimental set-up for out-of-plane LWIR ESPI. (b) Phase interferogram of a rotation after phase-stepping.

The object and reference beam intensities are equalized on the detector through a suitable beamsplitter. The camera is a Jade II LWIR from CEDIP Infrared Systems (now purchased by FLIR), with a 320 × 240 microbolometer array.

Compared to the in-plane set-up the specular reflection peak is a bigger problem for this out-of-plane set-up. Indeed the object is illuminated with a beam which is ideally coaligned with the optical axis of the camera. Here the object was slightly rotated for avoiding the specular peak entering the sensor. It is then not present in the images. However this constraint must be taken into account in the future development of the technique.

3 Scattering requirements

In order to obtain scattering surfaces in ESPI, Yamaguchi showed that the surface roughness R must be of the same order than the laser wavelength λ [4]. When $\lambda > R$, specular reflection is dominant. In intermediary situations, a specular peak is present, while some speckle can be observed outside of the peak direction, as was the case in our early LWIR experiments [2-3]. Recently a FP7 European project (FANTOM) started which aims at developing LWIR holography in the field of aeronautical Non Destructive Testing. In this case, the materials to be tested are made of carbon or glass fibres. Small samples representative of actual structures were manufactured and their roughness measured by white light interferometry (Zygo interferometer).

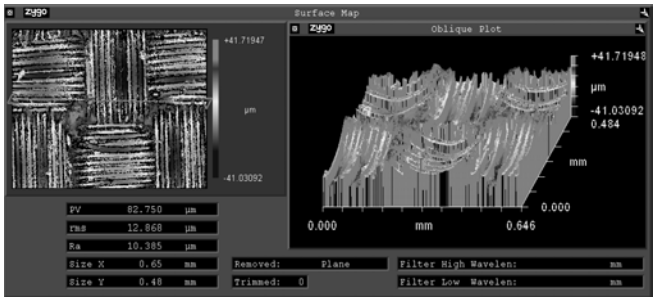

Fig. 2. Carbon fiber roughness measurement with white light interferometry.

Figure 2 shows an example of measurement obtained on carbon fiber. The grooves have different orientations and their amplitude is on the order of 13 µm, whereas it is ranged between 18 µm in the case of glass fibers. Illuminating such samples with a 10 µm CO_2 laser and observation with a thermographic camera (FLIR Thermacam) shows a good scattering (figures 3 (a) and (b)). In the case of glass fiber (figure 3(b)), the speckle is more easily resolved because of the higher roughness. In both cases, these

results indicate the possibility of performing ESPI and digital holography with laser illumination at normal incidence to the object.

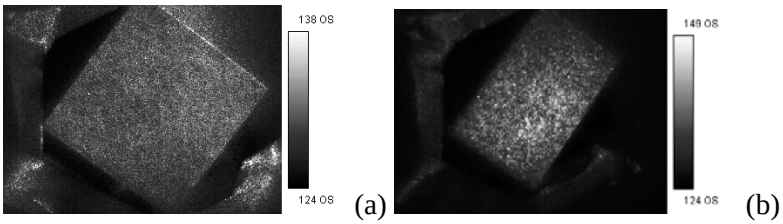

Fig. 3. LWIR images of carbon fiber (a) and glass fiber (b) illuminated with diverging CO2 laser beam, showing usable speckle.

4 Conclusion

ESPI and digital holography techniques are made possible in the LWIR spectral range due to the existence of suitable components. However a challenge is the possibility of observing scattering objects, and in particular resolve the speckle. We showed that in the case of aeronautical structures made of carbon and glass fibres, the roughness is sufficiently important to generate speckle grains which can be resolved by the imaging system.

5 Acknowledgements

The research is supported by the FANTOM project, funded by the European Union, under the contract ACP7-GA-2008-213457-FANTOM.

6 References

1. Kreis, T, (1996), Holographic Interferometry – Principles and Methods, Vol. 1, Akademie Verlag Series in optical metrology, Berlin.
2. Vandenrijt, J-F, Georges, M, (2007) Infrared Electronic Speckle Pattern Interferometry at 10 µm, SPIE 6616-72
3. Vandenrijt, J-F, Georges, M, (2008) Holographic techniques at long wave infrared wavelengths, Proc. of Int'l Symposium to Commemorate the 60th Anniversary of the Invention of Holography, 300-307
4. Yamaguchi, I (2003) Fundamentals and applications of speckle, SPIE 4933, 1-8

TOPIC 5

New Optical Sensors and Measurement Systems

Chairs:

Werner Jüptner
Bremen
(Germany**)**

Hans Tiziani
Stuttgart
(Germany)

Invited Paper

Novel interferometric measurement systems for the characterization of micro-optics

H. Ottevaere, H. Thienpont
Vrije Universiteit Brussel, Dept. of Applied Physics and Photonics
Pleinlaan 2, B-1050 Brussels
Belgium

1 Introduction and the importance of micro-optics characterization

Today the use of micro-optical components is very wide spread and they are becoming increasingly important components in many high-tech industrial applications such as image projection and display, optical tele- and data-communication, optical data storage, biophotonics and photonic sensing [1]. Making these photonics technologies faster and smaller requires at the same time the introduction of massive parallelism and aggressive micro-miniaturization. Over the last 20 years several research groups and industrial research labs have therefore been focusing their attention on the development of fabrication techniques for micro-optics. Some methods are relatively inexpensive and are based on existing technologies while others require dedicated processing tools and/or new materials with special properties. Most of these micro-optics fabrication methods yield micro-optical components that satisfy many of the optical quality requirements. They differ however in that some fabrication methods are more suitable either for rapid prototyping, for mass fabrication or for monolithic integration than others. More recently micro-optical components made out of semiconductor materials, such as silicon, germanium and gallium arsenide, are gaining importance in e.g. the automotive and space industry, thermal imaging, sensing and medical applications.
The next step in the micro-optics foodchain is the optical characterization. Although there exists today a variety of commercial and in-house developed measurement instruments for the characterization of micro-optical components in general and microlenses in particular, there is often a lack of a complete quantitative optical characterization of the latter components [2]. Besides a proper measurement, characterization and testing of micro-optical components is also essential for providing initial

data for modeling, for in-process product quality testing and for speeding up product development, … In this paper we will focus on the quantitative characterization of refractive microlenses. To investigate the geometrical and optical properties of discrete microlenses one of the most accurate and reliable techniques is interferometry [3]. It is well known that microlenses can be tested in transmitted light using instruments with a single pass geometry (e.g. Mach-Zehnder interferometer) as well as in reflected light interferometers using a double pass configuration (e.g. Twyman-Green interferometer). As the IR region of the electromagnetic spectrum is without doubt a key asset for the future potential of photonics we briefly discuss a Mach-Zehnder interferometer to characterize semiconductor microlenses in transmission, a unique measurement extension that to our knowledge was never demonstrated earlier. Up to now wavefront aberrations of microlenses fabricated in infrared materials are determined by raytracing, using the measured lens profile and calculating from these data the wavefront aberrations [4].

2 Overview of measurement tools for the characterization of microlenses

Today several standards (e.g. ISO 14880) describe and recommend test methods for microlenses and microlens arrays. The most important microlens parameters are the surface profile and optical properties. The microlens shape provides the necessary feedback for optimizing the fabrication process while the optical properties are more important for the application itself [2]. We have chosen to use the interferometric measurement concepts described in ISO 14880-3 [5].
This means in microlens testing it is essential to measure in a first step the shape or the surface profile of the microlenses or in case gradient-index lenses are concerned their refractive index distribution. In addition the paraxial parameters, such as the focal length, and the more complex properties like the wave aberrations and surface quality have to be characterized. As discussed in the introduction massive parallelism and miniaturization ask for the fabrication of microlenses and microlens arrays. The most critical features of these lenslet arrays are the uniformity of the microlenses and their mutual positioning accuracy. As a variation of these properties deteriorates the optical performance in most applications, dedicated test instrumentation is needed. In what follows we discuss different measurement instruments designed to characterize all the geometrical and optical parameters of microlenses. We want to remark

hereby that the measurements should preferably be done in a cleanroom environment as the smallest dust particle on the lens surface decreases the optical performance.

2.1 Surface profile measurements

A standard measurement method to determine the surface profile of microlenses and thus the diameter and the sag is an optical non-contact profiler or white light interferometer. In a non-contact profiler a white light beam passes through a beam splitter which reflects half of the incident beam to a reference surface and transmits the other half onto the sample. The light reflected from the sample and from the reference surface then recombine at the beam splitter to form interference fringes. The system measures the degree of the fringe modulation or the fringe contrast. Because white light has a short coherence length, interference fringes are present only over a very shallow depth for each focus position. The working principle of this white light interferometer is discussed in detail in [2]. In addition this interferometer allows to quantify the surface roughness on the top of the microlenses.

As a test case we show a measurement of a fused silica microlens performed with a WYKO non-contact profilometer. For each microlens we can derive from the contour plot (see Fig. 1a) the sag and the diameter of the microlenses along the x and the y direction. As an example we show in Fig. 1b the profile of the cross-section of a 200 µm fused silica microlens (NA =0.05; D=200 µm) along the x direction. The surface roughness on top of the microlens can also be derived from measurements with the non-contact profiler. As an example we show the fringes on the vertex area (65x61 µm²) of a 200 µm diameter lens as well as the average and root-mean square roughness on the vertex of the lens (see Fig. 2).

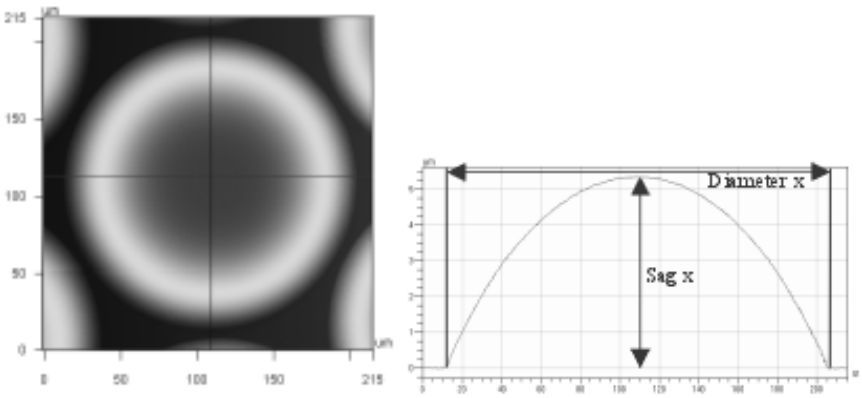

Fig. 1. (a) Contour plot of a 200 µm fused silica microlens as obtained with a non-contact profiler; (b) 2D lens profile of this microlens along the x direction

Roughness values	(nm)
Average roughness R_a	1.55
RMS roughness R_q	1.94

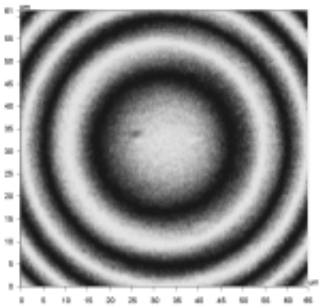

Fig. 2. Different roughness values on the vertex area of a 200 µm lens and fringes in this vertex area (65x61 µm²)

2.2 Measurements of the optical performance in the visible wavelength range

To investigate the optical properties of discrete microlenses one of the most accurate and reliable techniques is interferometry. With a transmission Mach-Zehnder interferometer the wave aberrations and the focal length of the microlenses can be measured, while a Twyman-Green interferometer can be used for the measurement of the surface deviations of a microlens from an ideal spherical shape and for the measurement of the radius of curvature of the surface [6].

2.2.1 Focal length and array uniformity through plane wave illumination

The Mach-Zehnder interferometer with planar wavefront illumination offers for slow lenses (NA<0.1) the opportunity to measure also the total phase lag introduced by the lenses as shown in Fig. 3a. This makes it possible to determine the focal length and hence the numerical aperture of the microlenses. For certain applications of arrays of microlenses it can also be important to know the uniformity of the lens array or at least of a part of the lens array. There are several different test methods (e.g. Smartt test, shearing test) which can provide a measure of the uniformity. One can even obtain the total phase retardation for a subsection of the microlens array (see Fig. 3b).

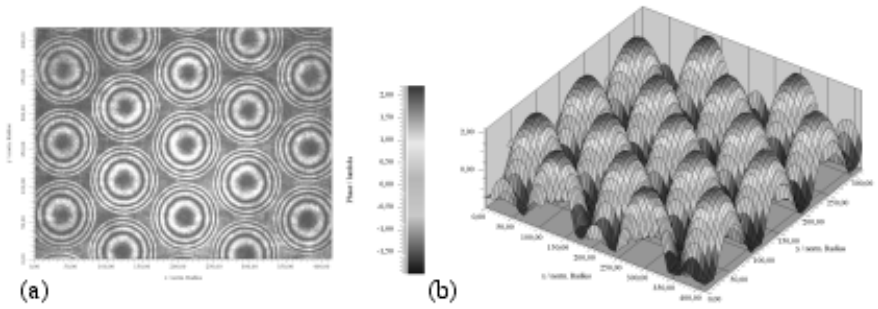

Fig. 3. Interferogram of an array of 200 µm diameter microlenses with an average NA of 0.05 and illuminated with a plane wavefront; (b) 3D representation of the phase lag (RMS 1.26 λ, PV 4.37 λ) for the same microlens array

2.2.2 Measuring the aberrations with spherical wave illumination

Wave aberrations of refractive microlenses can be determined with spherical wavefront illumination in the Mach-Zehnder interferometer (see Fig. 4).

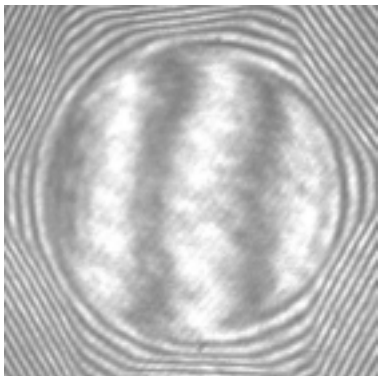

Fig. 4. Interferogram of a microlens under spherical wavefront illumination: the resulting plane wave is a measure for the wave aberrations

The measurement of the wave aberrations is carried out by using a phase shifting interferometry (PSI) algorithm. This requires a measurement of the intensity in each point of the aperture for 5 different reference phase values. The result of a PSI evaluation is the phase distribution $\Phi(x,y)$ in the exit pupil which is linearly dependent of the wave aberrations $\psi(x,y)$ of the lens under test.
From these data the software calculates the unwrapped phase distribution and by subtracting the tilt and defocus the deviation from an ideal wavefront (phase/lambda) can be found [7]. Fitting this deviation to a Zernike polynomial then gives the aberrations (phase/lambda). Besides the aberrations we also derive from the measured phase distribution other optical lens characteristics such as the modulation transfer function and the point spread function.

2.2.3 Measurement of the deviations from sphericity and the radius of curvature

To determine the surface deviation of a microlens from a perfect sphere one can make use of a Twyman-Green interferometer [8]. By using the latter interferometer it is also possible to determine the radius of curvature R of a microlens. An example of a 200 µm fused silica microlens with an NA of 0.05 is shown in Fig. 5. The deviation from an ideal sphere can be derived from the unwrapped phase after subtracting the tilt and defocus. Fitting the deviation to a Zernike polynomial then gives the surface deviation.

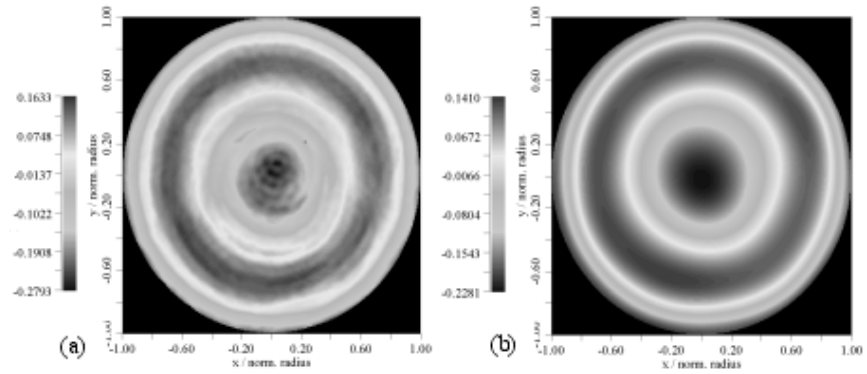

Fig. 5. (a) Measured deviation from an ideal sphere (phase/lambda) for a 200 µm lens with an NA of 0.05 as obtained with a Twyman-Green interferometer; (b) Polynomial fitted surface deviation (phase/lambda) of this microlens

2.3 Optical characterization of semiconductor micro-optics in the near-infrared region

In this section we will focus on the characterization of refractive microlenses fabricated in infrared materials. Wavefront aberrations of these microlenses are, up to now, determined by raytracing, using the measured lens profile and calculating from these data the wavefront aberrations [4]. For the characterization in transmission of refractive microlenses, the most suitable interferometer configuration, against other interferometers, is that of a Mach-Zehnder. It allows to measure and extrapolate geometrical and optical characteristics such as sag, focal length, and wavefront aberrations of microlenses. We started from the concept of such a MZ interferometer working at 632.8 nm [2] and adapted the design to the IR wavelength range. We opted to work at a wavelength of 1550nm, for which the most common IR materials (named ZnSe, ZnS, GaAs, AMTIR, Si and Sapphire) are transparent. The only exception is germanium, the transmission window of which starts at 1800nm wavelength. As explained before, we opted for the Mach-Zehnder configuration based on the design made by J. Schwider, Erlangen-Nürnberg University and adapted the optics and imaging detector to make the interferometer operational in the infrared region.

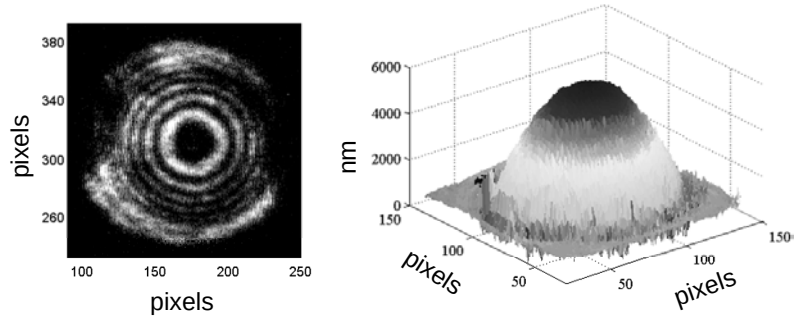

Fig. 6. a) Interferogram of the investigated silicon spherical microlens (diameter of 240 µm) acquired with the near-IR MZ. b) 3D surface profile of the silicon spherical microlens.

The first sample we measured with the IR MZ interferometer is a spherical silicon microlenses (diameter of 240µm and 4.6µm sag) were optically characterized in transmission (see Fig. 6). The measured average sag of the microlens with the IR MZ interferometer is 4.75 µm with a repeatability within 1.5 %. This gives a 3% deviation from the specified value. The average measured RMS wavefront aberration is 4.22nm with a standard deviation of 7 %.

3 Conclusion

We can conclude that micro-optics is a key technology with many applications in various areas of tomorrow's information society. It enables new functionalities and applications previously unachievable with conventional optics and improves product performance, stability and robustness while reducing cost, volume and weight. To realize the latter characteristics, high-quality micro-optical components are of crucial importance and thus making the choice of the most suitable fabrication technology and characterization method also very important.
In this paper we focused on novel interferometric measurement systems for the characterization of micro-optics and we introduced various instruments that one can use to quantitatively characterize refractive microlenses and microlens arrays: a non-contact profiler, a transmission Mach-Zehnder interferometer and a Twyman-Green interferometer. For the optical characterization of microlenses made out of infrared material we presented a novel transmission interferometer operational in the near-infrared region, more in particular a Mach-Zehnder interferometer working at 1550nm.

4 Acknowledgments

This research was supported by FWO-Vlaanderen, the IAP program 'Photonics@be', the OZR of the VUB, the EC 6th FP NoE 'NEMO', the EC 7th FP NoE 'P4L' and the EC 7th FP 'ICU' Project. Heidi Ottevaere is indebted to the FWO-Vlaanderen for her "Postdoctoraal onderzoekersmandaat".

5 References

1. Sinzinger, S, Jahns, J (1999) Microoptics. Wiley-VCH
2. Ottevaere, H, Thienpont, H (2004) Refractive Optical Microlenses: an Introduction to Nomenclature and Characterization Techniques. Encyclopedia of Modern Optics, Elsevier, Oxford, 4:21-43
3. Hecht, E (1987) Interference, chapter 9 in Optics. Addison-Wesley Publishing Company
4. Park, S-H, Jeon, H, Sung, Y-J, Yeom, G-Y (2001) Refractive Sapphire Microlenses Fabricated by Chlorine-Based Inductively Coupled Plasma Etching. Applied Optics 40, 22:3698-3702
5. Miyashita, T (2007) Standardization for microlenses and microlens arrays. Japan. J. Appl. Phys. 46:8B
6. Lindlein, N, Schwider, J (2001) Optical measurement methods for refractive microlenses and arrays. Micro- and Nano-optics for Optical Interconnection and Information Processing, Editors M.R. Taghizadeh, H. Thienpont, G.E. Jabbour, Proceedings of SPIE, 4455
7. Malacara, D, Servin, M, Malacara Z (1998) Phase unwrapping. Chapter 11 in Interferogram analysis for optical testing, Marcel Dekker Inc., New York
8. Schwider, J, Falkenstörfer, O (1995) Twyman-Green interferometer for testing microspheres. Opt. Eng. 34, 10:2972-2975

Design of a micro-optical low coherent interferometer array for the characterisation of MEMS and MOEMS

Kay Gastinger[(1)], Karl Henrik Haugholt[(1)], Arne Røyset[(1)], Jorge Albero[(2)], Uwe Zeitner[(3)], Christophe Gorecki[(2)]
(1) SINTEF, N-7465 Trondheim, Norway,
(2) CNRS FEMTO-ST, 16 Route de Gray, 25030 Besançon Cedex, France
(3) Fraunhofer IOF, A.-Einstein-Str. 7, 07745 Jena, Germany

1 Introduction

The EU-project SMARTIEHS (SMART InspEction system for High Speed and multi-functional testing of MEMS and MOEMS) develops a new inspection concept for MEMS and MOEMS (M(O)EMS) testing at the wafer level [1]. The inspection systems on the market today are based on a serial approach inspecting one M(O)EMS structure at the time. In SMARTIEHS a parallel wafer-to-wafer inspection concept is adopted from the electronic probing cards in the micro electronics industry. A micro-optical probing wafer is aligned with the M(O)EMS wafer under test.
The 4-inch probing wafer contains a 5x5 array of micro-optical low coherent interferometers, inspecting shape and deformations of 25 M(O)EMS structures within one measurement cycle. The measurement time can thus be reduced by a factor of 25, scaling with the no. of interferometers on the probing wafer. A 5x5 channel smart pixel camera array detects and demodulates the interference signals [2].
The design of the micro-optical low coherent interferometer array is presented. The configuration of the array elements is based on a Mirau interferometer. The main challenge is to use standard micro-fabrication processes to produce the micro optical interferometer array.

2 Optical design of the micro optical interferometer array

Fig.1a) shows the configuration of the optical unit of the instrument. The light from a 5x5 LED array is directed via a cube beam splitter towards the probing wafers positioned above the M(O)EMS wafer under test. The

M(O)EMS structure is imaged via the beam splitter and the interference signal is recorded by the smart pixel camera array. The whole unit is scanned in z-direction by an external scanning system [1].

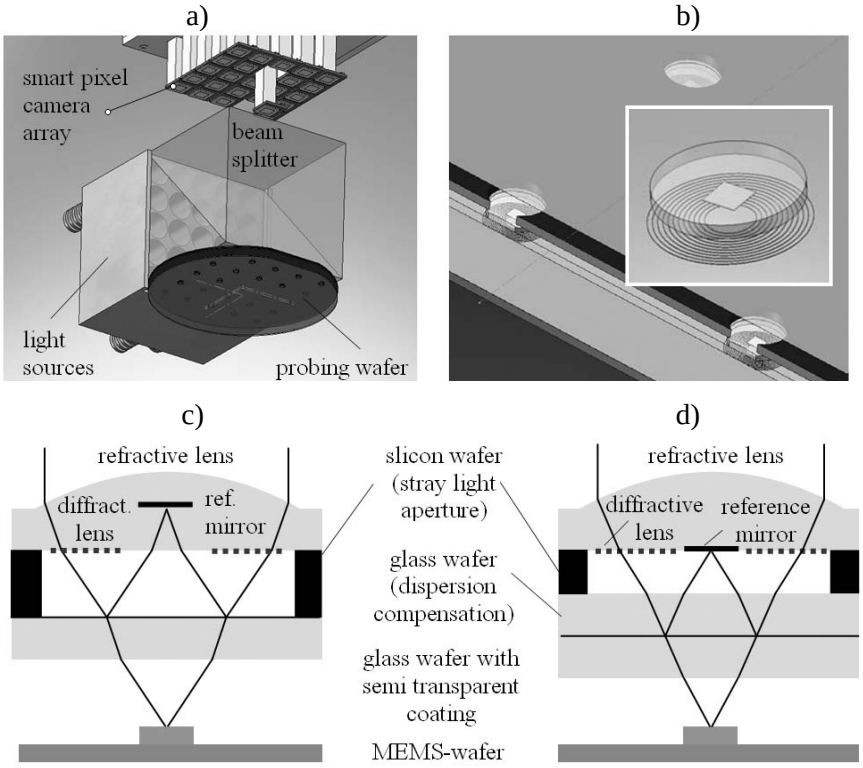

Fig. 1. Lay out of the optical unit: a) instrument configuration, b) close-up of the probing wafer with interferometer configuration (magnified interferometer inserted), c) and d) cross sections of two different configurations for the low coherence interferometer.

The interferometer array consists of a set of wafers that are bonded or glued together forming a wafer stack (fig. 1b). The essential parts are: a microlens array, a reference mirror array, and a beam splitter wafer.
Two different designs of micro-optical Mirau interferometers are developed (fig. 1c and 1d). In both configurations all micro optical components are produced on one single wafer to avoid additional alignment of the wafer stack. Configuration d) requires an additional glass wafer for dispersion compensation. Here the mirror can also be positioned on the topside of the compensation wafer, which however requires a wafer alignment step during bonding and additional spacers between beam splitter wafer and reference mirror wafer.

The optical requirements for the imaging lens of the Mirau-interferometer can barely be fulfilled by a single plano-convex micro-lens. Therefore, these lenses are combined with diffractive elements designed for compensating spherical- and, more important, chromatic aberrations. The design of both optical elements has been performed by using the optical design software ZEMAX [3].

The refractive lens has a circular surface shape with a diameter of 2,5mm and a sag of 162µm. The diffractive element has been considered in the system design as a radial symmetric phase function

$$\varphi(r) = a_1 r^2 + a_2 r^4, \quad (1)$$

which is realized as a diffractive surface profile. The design software then accounts for the special chromatic behaviour of this structure and the parameters a_1 and a_2 are optimised for the current system. By including the r^4 term in the design also the spherical aberrations of the imaging are reduced considerably [4].

The light intensity budget is the most critical challenge when using LED illumination in combination with a high speed smart pixel camera. The available light intensity limits the signal-to-noise ratio (SNR) and thus the demodulation frequency of the smart pixel camera. Less than 5% of the light passing through the illumination aperture is transmitted through the optical system towards the camera. To optimise the light efficiency all non-functional surfaces are anti-reflection coated.

Furthermore the size and shape of the reference mirror is optimised. Our micro optical design uses square mirrors instead of the circular mirrors in the conventional Mirau design, to increase the light efficiency. The size is slightly larger than the field of view to allow for some misalignment. If the light efficiency can be improved considerably even an unstructured semi transparent layer could be used, to minimise the alignment requirements.

The production variations of the focal length of the micro lenses can lead to defocused images in the array structure. As compensation the imager chips and the LED mounts can be moved individually along the optical axis to focus each channel separately. Unfortunately this will change the magnification.

Thickness variations of the glass wafers (typically 20µm) have minor influence. They can cause a depth variation in the focal plane in the interferometer channels and a mismatch between object and reference arm. As a result the position of the coherence region and the focal distance are separated. Furthermore dispersion effects occur reducing the contrast of the interference fringes slightly. Pre-selection of high quality planar wafers can help to avoid these effects.

Deformation of a wafer reduces the uniformity of the systems and will have a similar effect. The probing wafers must thus be mounted without introducing mechanical stresses and the system should be vibration isolated from the environment.
Stray light generates cross talk between the interferometer channels. To avoid this, a silicon aperture wafer is included in the design. It can be used as a spacer between the glass wafers or on top of the structure. Furthermore the backside of the reference mirror should be covered with a highly absorptive or diffusively reflective layer.

3 Micro fabrication process of the interferometer

The optical design of the interferometers requires large microlenses. The challenge is to fabricate these large lenses with high surface quality. As a first step, lens moulds are fabricated by chemical wet etching on a silicon wafer. The large size and sag implies a challenging multi-step etching process, combining anisotropic and isotropic wet etching of silicon [5,6].
Then the microlenses are replicated by a glass reflow process. The silicon wafer containing the moulds is anodic bonded to a borosilicate glass wafer in a vacuum environment. Heating the wafers melts the glass and fills the moulds. A first attempt can be seen in fig. 2. The back surface of the glass is polished to reach the needed thickness and optical quality of the glass substrate. Finally, the microlenses are released by etching away the silicon [6]. An alternative technique is the direct moulding of polymer.

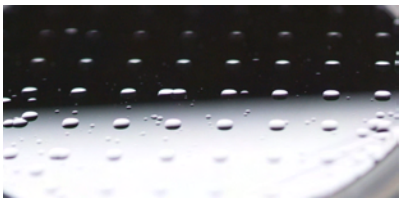
(a)


(b)

Fig. 2. a) First test of Si moulds. The diameter is successfully reached unless some surrounding defects appear. b) Glass lenses from the mould in before backside polishing

The fabrication of the diffractive structure will be done by laser lithography with the technique of continuous profile writing where a photo resist is exposed sequentially with an intensity modulated laser beam. A subsequent development process leads to a resist profile whose local height is proportional to the applied exposure dose at this position.

The resulting resist profile is then transferred into the final optical structure by UV reaction moulding onto the backside of the lens substrate. The latter process will be performed in a special mask aligner on the whole wafer at once [7]. This gives sufficient alignment accuracy between the refractive lens positions and the diffractive correction structure.
The reference mirror array and the beam-splitter are fabricated by standard micro-fabrication techniques on glass wafers. The reference mirrors are created by lift-off of a 100 nm thick aluminium layer deposited by evaporation. The beam splitter wafer can be realised with different splitting ratios using a multi-layer deposition by Low Pressure Chemical Vapour Deposition (LPCVD).

4 Scanning requirements

The demodulation scheme in the smart pixel camera requires that the frequency of Doppler shift of the interference signal generated by the scanning velocity, is matching the demodulation frequency generated in the synchronous in-phase and quadrature channels of the demodulator [2]. The Doppler shift is typically 1-50kHz and is given by a trade-off between short measurement time (fast scanning) and reduced data transfer requirement and SNR (slow scanning).
The demodulation frequency is set individually in each camera. This allows for variations in centre wavelength of the light sources in the array.
In order to obtain a stable translation of the entire probing wafer, three independent translation stages are needed on three sides of the optical unit. Each of them needs to fulfil the requirements on scanning speed accuracy set by the demodulator. It has been found that the requirement on the deviation for a slow scanning speed is 1%. The requirement on high frequency deviations is $\lambda/20$.

5 Experimental results

A 5-channel interferometer array based on micro-optical components is developed (fig. 3) to test the design principles. In difference to the described design five bulk imaging lenses (aspheric glass lenses, aperture Ø3mm) and a standard CMOS camera (Micron) are used.

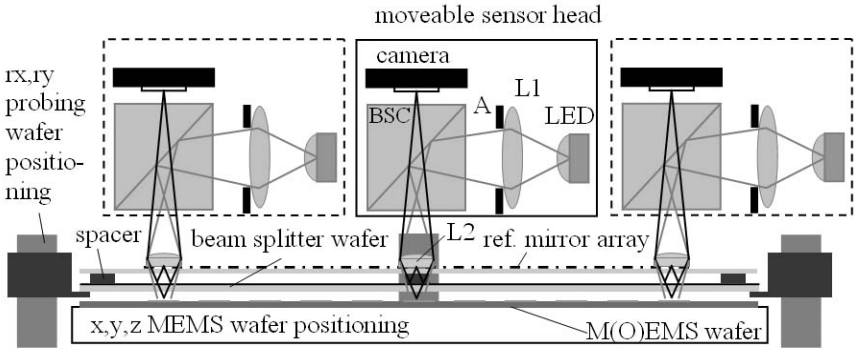

Fig. 3. Experimental setup, sensor head can be positioned at 5 different structures of the MEMS wafer (L1-bulk illumination lens, L2-bulk imaging lens, A-illumination aperture)

The demonstrator is applied to a commercially available MEMS object (Melexis IR sensor 81101BA). Five different structures on the wafer are measured (fig.4). The setup is optimised on the centre structure regarding focus and fringe contrast. Then the sensor head is moved to the corresponding corner of the wafer. The fringe pattern is found by adjusting the z-position of the MEMS wafer, simulating a z-scan. The interference fringes in the position of highest contrast are shown in fig. 4. The necessary adjustment is in the range between 5-20µm. It can be seen that the corner images are slightly defocused and contain fringes. However, the fringe contrast is sufficient over the whole wafer. This proves the feasibility of the interferometer design and the instrument concept.

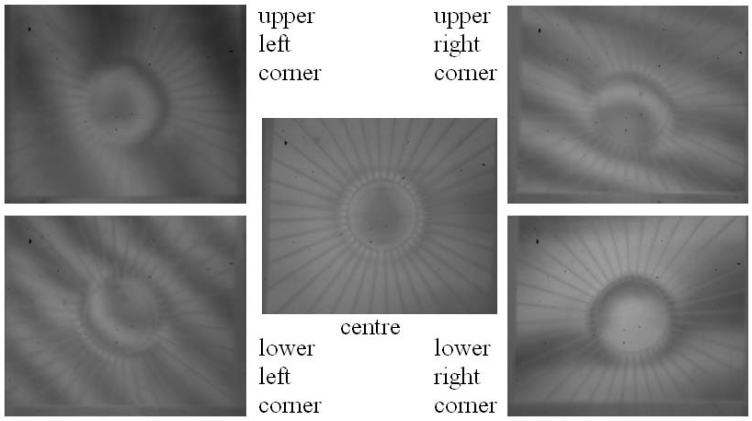

Fig. 4. Experimental results: interference fringes from 5 different MEMS structures on the corresponding position on the wafer when readjusting the z position in the range of 5-20µm

6 Conclusions

The novel design of a micro optical, low coherent interferometer array based on a Mirau configuration is presented. The design challenges imposed by the array approached are in particular: differences in focal lengths of the lenses, different centre wavelengths of the LED sources, the light budget, thickness variations of the glass wafers, stray light, and the accuracy of the scanning system. The refractive microlenses are corrected by a diffractive structure to improve the imaging quality. All micro optical components are produced by standard micro fabrication processes. A wafer based, five-channel setup is developed to proof the feasibility of the wafer based interferometer design. The preliminary experimental results, based on bulk lenses and one standard CMOS camera, show that interference fringes can be observed over the whole wafer area.

7 Acknowledgement

The authors want to thank Kari Anne Bakke (SINTEF) for contributing to the experimental investigations and Appo van der Wiel (Melexis) for providing the MEMS wafer. SMARTIEHS is a collaborative project funded under the Grant Agreement 223935 (7^{th} FP Objective 2007-3.6).

8 References

1. Gastinger, K., et al. (2009) Optical, mechanical and electro-optical design of an interferometric test station for massive parallel inspection of MEMS and MOEMS, Proc. SPIE 7389 (in print), 73891J
2. Beer, S., et al. (2004) Smart pixels for real-time optical coherence tomography, Proc. SPIE 5302: 21-32
3. Zemax Development Corp., www.zemax.com
4. Radtke, D. and Zeitner U.D. (2007) Laser-lithography on non-planar surfaces. Opt. Express 15: 1167-1174
5. Albero, J., et al. (2009) Fabrication of spherical microlenses by a combination of isotropic wet etching of silicon and molding techniques, Opt. Express 17: 6283-6292
6. Albero, J., et al. (2008) Si moulds for glass and polymer microlenses replication, Proc. SPIE 6992: 69920A
7. Dannberg, P., et al. (1999) Micro-optical elements and their integration to glass and optoelectronic wafers, Microsystems Technologies 6:41-47

Looking for a new generation of MEMS-type confocal microscopes

C.Gorecki[1], S. Bargiel[1], K. Laszczyk[1], J. Albero[1], J. Krezel[2], M. Kujawinska[2]
[1]Département MN2S, FEMTO-ST, Université de Franche-Comté
16 Route de Gray, 25030 Besançon cedex, France
[2]Warsaw University of Technology, 8 Boboli St., 02-525 Warszawa, Poland

1 Introduction

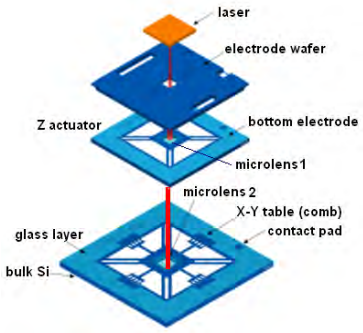

Fig. 1. Architecture of on-chip confocal microscope.

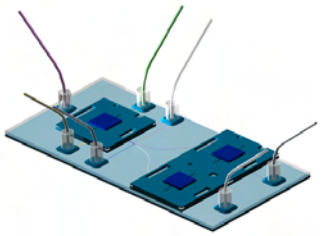

Fig. 2. Array of MEMS confocal microscopes on top of a microfluidic network.

In the field of optical scanning microscopy the micro-scale or nano-scale samples are observed and analysed via large macro-tools, too bulky and heavy for individual use in specialised key missions such as in situ or in vivo measuring. A need for compact, robust scanning devices for endoscopic applications has stimulated the development of MEMS scanning mirrors for confocal imaging and for optical coherence tomography.
The architecture of proposed on-chip confocal microscope is shown in Fig. 1 [1]. The individual microscope consists of two microlens scanner chips, a beamsplitter, a PIN detector and a pinhole aperture. The microlens scanner chips have microlens scanners as active components for focusing and scanning the light. The 3-D transmissive steering of the laser beam is

possible due to the combination of one vertical microactuator and an x-y translation table. With this architecture, the microscope (or several microscopes) can be mounted on top of a microfluidic network for lab-on-chip applications, as shown in Fig. 2.

2 Design, realisation and testing of 3-D MOEMS scanner

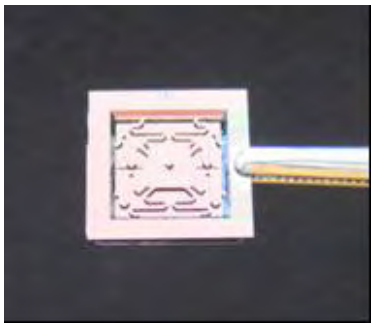

Fig. 3. View of parallel-plate z- scanner.

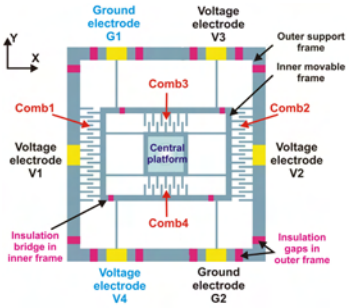

Fig. 4. The design of the silicon comb-drive x-y table.

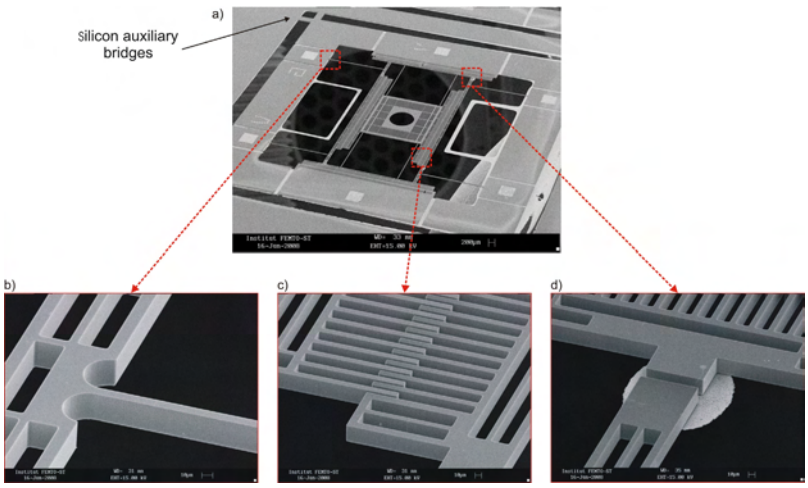

Fig. 5. The SEM images of x-y table: a) general view of the movable platform with 800-μm aperture; b) enlarged view of a Si spring; c) enlarged view of comb-drive fingers; d) top view of an insulation bridge.

The 3-D scanner consists of one parallel plate vertical actuator, shown in Fig. 3, and an x-y table with 4 comb-drive actuators included in a " frame-in-the-frame" architecture, where a system of spring suspensions is used to decouple two directions of motion [2]. Figure 4 shows the design of x-y table which is composed of two frames: an outer (not moveable) and an inner one (movable). The outer frame serves as the support of the chip, containing the electrical contacts and a first pair of the comb-drive actuators (Comb1 and Comb2). The inner frame, attached to the outer one by 4 springs, includes the second pair of the comb-drive actuators (Comb3 and Comb4) and the central platform suspended on additional 4 springs. To ensure the transmissive steering of the light by the microlens, the platform there has been fabricated with an aperture, to which the microlens will be aligned. Figure 5 represents a SEM image of the complete structure. The microstage is moving ± 28 µm along the x-axis, and ± 35 µm along y-axis, for a driving voltage of 100 V.

3 Fabrication of glass microlenses

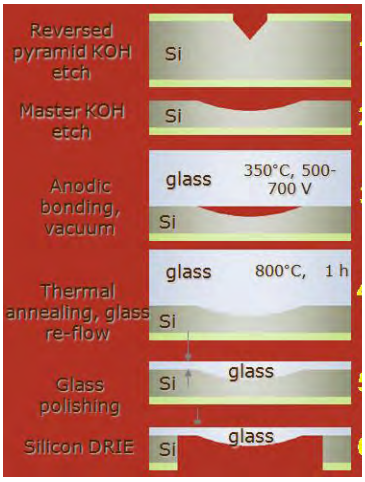

Fig. 6. Process flow of borosilicate glass microlenses

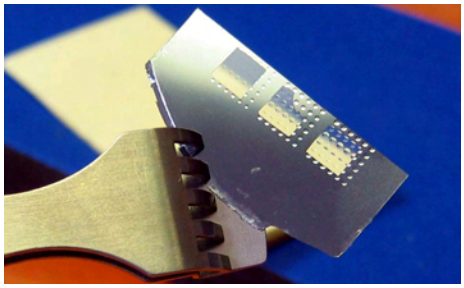

Fig. 7. Array of glass microlenses.

The fabrication process is shown in Fig. 6 [3]. This contains the formation of a microlens master by wet etching of silicon (steps 1-2), vacuum anodic bonding of a Borofloat glass substrate to the silicon master (step 3), the re-flow of the glass at elevated temperature to fulfill the master (step 4), the mechanical polishing of the glass (step 5), and releasing of the microlens

by back-side etch of the superfluous silicon (step 6). The method of formation of silicon master involves the double wet anisotropic etching of a (100)-oriented silicon substrate in alkaline solution. After the fabrication of silicon master, the anodic bonding under vacuum conditions has been performed, followed by thermal reflow of glass. The anodic bonding is carried out at 350° C. Once silicon and glass are bonded, they are annealed at temperature near the softening point of the glass (815° C). In this step the glass reflows and fills the etched cavities in silicon masters. The reflow parameters have to be adjusted to the dimensions of the microlenses cavities. After the reflow, the glass is mechanically thinned and polished to obtain 50 μm thick layer. Finally, the microlenses are released by selective back-side dry etching (DRIE). The resulting glass microlens array is shown in Fig. 7.

4 Conclusions

The demonstrated marriage of silicon micromachining with the microoptical technologies shows the feasibility and interest of on-chip confocal microscopes. This association permits to increase the compatibility of the fabrication method of micro-optical components with silicon MEMS, proposing easier integration of well-controlled refractive microlenses on top of movable parts of microactuators.

5 Acknowledgments

All acknowledgments for technical and financial supports from the programme Marie-Curie (Fellowship FP6-042123) and the European Network of Excellence on Micro-Optics (NEMO).

6 References

1. D. Heinis et al., Optics Express **14**, 3396, (2006).
2. C. Gorecki et al., Conference Transducers 2007, Lyon, June 2007.
3. J. Albero et al., EOS Topical Meeting on Diffractive Optics, Barcelone, November 2007.

Radial in-plane achromatic digital speckle pattern interferometer using an axis-symmetrical diffractive optical element

Armando Albertazzi G. Jr., Matias R. Viotti, Walter A. Kapp
Laboratório de Metrologia e Automatização
Universidade Federal de Santa Catarina,
88040-970, Florianópolis, SC, Brazil

1 Introduction

Electrical strain-gages are the most widely used devices by industrial and academic laboratories in order to monitor strain and stress fields in mechanical parts where their integrity has to be evaluated [1]. Even though portability, robustness, accuracy and range of measurement of strain gages have been firmly established, their installation is time-consuming and requires skills and aptitudes of a quite well trained technician.

Optical configurations for measuring in-plane displacements with DSPI are usually based on the two-beam arrangement first described by Leendertz in 1970 [2]. To simultaneously compute both in-plane components [2], DSPI systems based on polarization discrimination methods have been developed [3], however with some practical drawbacks [4].

Albertazzi et al. [5] have managed to deal with these limitations by means of the development of a novel double illumination DSPI system which measures radial in-plane displacement fields. In this work, the interferometer was combined with a pneumatic turbine drill to obtain a portable device for determining residual stresses by applying the hole-drilling technique. This device used a high quality conical mirror which makes it quite expensive, and requires a wavelength stabilized laser.

This paper reports on the application of a diffractive optical element (DOE) for generating double illumination and radial in-plane sensitivity. It is first demonstrated that the DOE has allowed development of an achromatic DSPI device, whose sensitivity is independent of the wavelength of the light source. It is sensitive only to the period of the grating of the DOE. Experimental results carried out in the laboratory by using an experimental setup with red and green light sources are presented. Furthermore, the paper briefly reports on results of residual stresses measurement in pipelines.

2 Radial in-plane interferometry with DOE

The most important element of the interferometer is an annular binary diffractive optical element. It has a circular shape formed by a set of concentric circular lines with a spacing of approximately 1.32 μm, and a clear central area. The first order of the light diffracted by the DOE is symmetrically directed to the centre forming a double illuminated central circular area. Fig. 1 (a) shows a cross section of the DOE displaying four particularly chosen light rays from a collimated illumination source. Symmetrical unitary vectors $\mathbf{k_1}$ and $\mathbf{k_2}$ and sensitivity vector $\mathbf{k}$ show how in plane sensitivity is reached in this section. This study can be extended to every point on the specimen surface and to all other cross sections. Thus, radial in-plane sensitivity is obtained for an illuminated circular region [6].

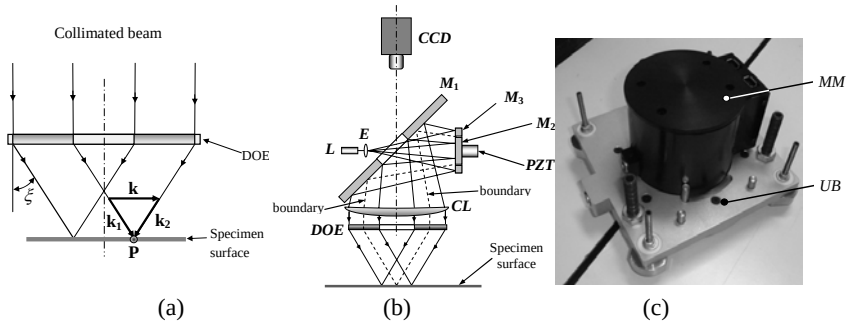

Fig. 1. (a) Cross section of the DOE showing radial in-plane sensitivity. (b) Sketch of the complete interferometer [6] and [8]. (c) Photograph of the portable device.

When monochromatic light illuminates a diffraction grating, it will generate an array of regularly spaced beams whose direction depend on the light wavelength and can be computed by the well known grating equation [7]. On the other hand, the sensitivity in a double illumination DSPI depends on the illumination angle as well as the wavelength of the laser source [6]. When both equations are combined, it can be verified that the resulting interferometer is not sensitive to the light wavelength at all, what makes the interferometer achromatic. Furthermore, in-plane sensitivity only depends on the grating period of DOE (see Eq. 1) which is very stable. A detailed explanation of this result can be found in Ref. 8.

$$u_r(r,\theta) = \frac{\phi(r,\theta)\, p_r}{4\pi} \quad (1)$$

where $u_r(r,\theta)$ is the radial component of the in-plane displacement field, $\phi(r,\theta)$ is the optical phase distribution and p_r is the period of the grating.

3 Experimental setup and testing procedure

The portable interferometer used to evaluate insensitivity to wavelength source was described in detail in Ref. 6. Mainly, it has a modular configuration namely, (a) an universal base (*UB*) to rigidly clamp it to the surface to be measured, (b) a measurement module (*MM*) to measure radial in-plane displacements fields, and (c) a hole drilling module (*HM*) for residual stress measurements by using the hole-drilling technique. Fig. 1 (b) shows a photograph of two modules of the portable device.
The original measurement module uses a 50 mW diode laser with a wavelength 658 nm as a light source. As the grating period of the DOE is about 1.32 μm, the diffraction angle is about 30° the interferometer's sensitivity will be 0.658 μm/fringe. In order to evaluate the effects of changes of the wavelength of the illumination source on the sensitivity of the interferometer, a diode-pumped solid-state laser (DPSS) was also used with a wavelength of 532 nm. According to Eq. 1, it can be verified that the sensitivity for green light remains about 0.658 μm/fringe. As an example, Figs. 2 (a) and (b) show respectively two wrapped phase distributions obtained with red and green laser sources and generated by the same amount of rigid body in-plane translations.

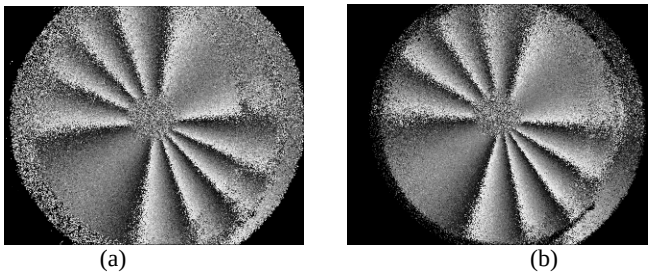

(a) (b)

Fig. 2. Rigid body wrapped phase maps obtained for a wavelength of the light source of: (a) 658 nm (b) 532 nm.

In order to generate highly repeatable rigid body displacements, an aluminum cantilever beam was loaded by means of a height gage block [8]. Mechanical systems such as screws or piezoelectric actuators were avoided to reduce hysteresis and to improve repetitiveness.
To measure in-plane displacement fields produced by the gage block, the loading device was rigidly fixed to an optical table. After that the radial in-plane interferometer was clamped on the optical table. Once the interferometer was positioned, a reference phase distribution was acquired and calculated by using a phase shifting algorithm. Afterwards, a gage

block was used to load the cantilever beam. After waiting some seconds, a new phase distribution was also calculated. Finally, the wrapped phase difference map was evaluated. This procedure was repeated 11 times with the red laser as light source. By following this procedure, another set of 11 measurements was performed with the green laser as light source. Fig. 2 shows the corresponding phase maps. Readers can find a detailed description of the loading device in Ref. 8.

4 Experimental result and application case

Table 1 lists both sets of 11 measured displacements with red and green lasers. According to this table, it can be seen that they had an average value of 2.3015 μm and 2.2968 μm respectively. Deviations between average translation values were about only 4.8 nm that is about 0.2%, what looks to be a good experimental indication that the interferometer is not sensitive to a wavelength change of almost 23%. A formal statistical hypothesis test shows very clearly that this difference is not significant since the standard deviation of the difference between both mean is 9.8 nm. By examining these results, and the phase maps showed in Figs. 2 (a) and (b), it is possible to conclude that wavelength changes do not affect significantly the interferometer sensitivity when a diffractive optical element is used to generate radial in-plane illumination.

Table 1. Radial in-plane displacements measured with the diffractive optical element.

	Measured rigid body translation [μm]	
Measurement	***Red laser***	***Green laser***
M_DOE1	2.304	2.308
M_DOE2	2.287	2.332
M_DOE3	2.300	2.314
M_DOE4	2.324	2.272
M_DOE5	2.274	2.319
M_DOE6	2.267	2.262
M_DOE7	2.313	2.271
M_DOE8	2.317	2.285
M_DOE9	2.332	2.331
M_DOE10	2.311	2.275
M_DOE11	2.288	2.296
Average value [μm]	2.3015	2.2968
Standard deviation [nm]	20.61	25.36

The portable interferometer was used outside of the laboratory to measure residual stresses in a risky area of a gas pipeline. This pipeline was place near to a river slope where soil moves constantly. In order to minimize soil movements and interactions between it and the pipeline, a contention structure was projected and built. Measurements with the interferometer were used to investigate the effectiveness of a repair.
Figure 4 shows two phase maps obtained in a laboratory environment on an optical table and in an in-field application. Even the second image was obtained outside the laboratory; fringe quality is comparable.

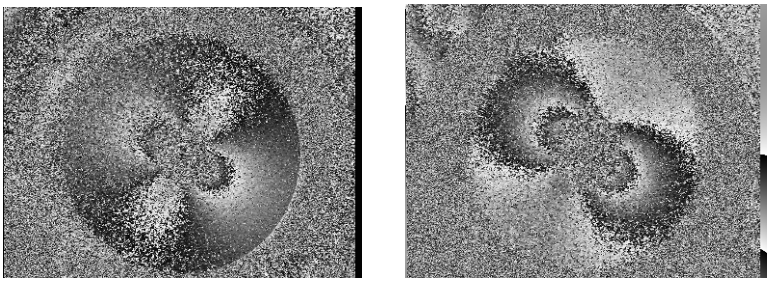

Fig. 4. Phase maps obtained: (left) on a laboratory and (right) on in-field environment (gas pipeline).

Figure 5 shows an application example of the developed interferometer to measure residual stresses in a gas pipeline. In this case a reference phase pattern was acquired. After, a small blind hole was drilled in the pipe wall. Finally, the final phase pattern was acquired. The phase diference map was used to compute the total amount of residual stresses. The resultes were used to evaluate the mechanical integrity of the pipeline in a critical area.

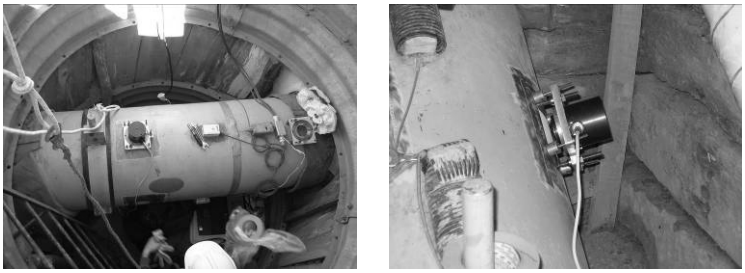

Fig. 5. Application of the developed interferometer to measure residual stresses in a gas pipeline.

5 Conclusions

The use of a binary diffractive optical element reported in this work enables the construction of a portable double illuminated achromatic digital speckle pattern interferometer with radial in-plane sensitivity. Moreover, DOE is responsible for generating radial in-plane sensitivity being only dependent on the period of the diffraction grating increasing considerably the robustness of the interferometer allowing its application outside laboratory environment. In field measurements demonstrated its successful use to measure residual stress fields in gas pipelines.

6 References

1. Dally, JW, Riley, WF (1991) Experimental Stress Analysis. 3rd edition. Mc Graw-Hill. Inc. New York.
2. Leendertz, JA (1970) Interferometric displacement measurement on scattering surfaces utilizing speckle effect. J. Phys. E. Sci. Instrum. 3: 214-218.
3. Moore, AJ, Tyrer, JR (1990) An electronic speckle pattern interferometer for complete in-plane measurement. Meas. Sci. Tech. 1: 1024-1030.
4. Viotti, MR, Albertazzi, AG Jr, Kaufmann, GH (2005) Measurement of residual stresses using local heating and a radial in-plane speckle interferometer. Opt. Eng. 44 (9) 093606.
5. Albertazzi, AG Jr, Borges, MR, Kanda, C (2000) A radial in-plane interferometer for residual stresses measurement using ESPI. In: Proc. of SEM, IX International Congress on Experimental Mechanics. SEM. 108-111.
6. Viotti, MR, Albertazzi, AG Jr, Kapp, WA (2008) Experimental comparison between a portable DSPI device with diffractive optical element and a hole drilling strain gage combined system. Opt. Lasers Eng. 46: 835-841.
7. O'Shea, DC, Suleski, TJ, Kathman, AD, Prather, DW (2003) Diffractive optics: Design Fabrication and Test. TT62. SPIE. Washington.
8. Viotti, MR, Kapp, WA, Albertazzi, AG Jr (2009) Achromatic digital speckle pattern interferometer with constant radial in-plane sensitivity by using a diffractive optical element. Appl. Opt. 48 (12): 2275-2281.

Wavefront Sensor Design based on a Micro-Mirror Array for a High Dynamic Range Measurement at a High Lateral Resolution

Robert Schmitt, Ingo Jakobs, Karl Vielhaber
Fraunhofer Institute for Production Technology IPT
Dept. Production Quality and Metrology
Steinbachstrasse 17, 52074 Aachen
Germany

1 Introduction

Optical testing is confronted with the challenge of a flexible testing of precision aspheres. This challenge can be faced by test equipment with a high measurement range at a high resolution, i.e. a high dynamic range. Compared to other sensor types for optical testing the Shack-Hartmann sensor (SHS) features a high dynamic range. In SHS the measurement range is limited due to the fact that all measurement points are detected simultaneously by an imaging device and the signals must be separable - thus the dynamic range is defined by the number of micro-lenses and the resolution of the imaging sensor. There are several approaches to enhance the dynamic range such as image processing approaches, e.g. spot tracking and unwrap algorithms [1] - or the use of additional optical elements, e.g. masks [2,3] or adaptive diffractive micro lenses as in the adaptive Shack-Hartman sensor [4]. But despite these approaches the contradiction between dynamic range and lateral resolution couldn't be resolved - a flexible wavefront testing of technically relevant aspheres is still restricted.
In this paper an approach of wavefront sensing is proposed in order to increase the dynamic range and the lateral resolution at the same time. The basic idea is to select and thereby encode single sub-apertures of the wavefront under test and to measure their propagation direction consecutively in a scanning procedure. In difference to the LCD based approach described in [3], here the selection of the sub-apertures is performed by a digital micro-mirror array (DMD). The use of the DMD promises a high reflectivity and lateral resolution as well as a very fast scanning ability. But there are specific challenges as the diffraction effects caused by the small dimensions of the array and the angular stability of the signal which will be addressed in this paper.

2 Set-up of the DMD-based wavefront sensor

The general set-up of the proposed sensor is depicted in Fig. 1. The wavefront to be measured is generated by a point light source - here realized by a fiber coupled laser diode (1, 2) - which is collimated by the lens under test (3). The wavefront to be measured (4) is imaged by a telescope in 4f-arrangement (5) onto a DMD (7). Form here on the evaluation of the wavefront differs from SHS. The micro-mirrors of the DMD can be addressed individually and can take two different tilt positions. By means of the DMD and its micro-mirrors any sub aperture can be selected and reflected towards the evaluation unit while the rest of the wavefront is reflected towards an absorber (6). The evaluation is performed by the same principle as in SHS, but with a single focusing lens (8). In the back focal plane of the lens the propagation direction of the selected sub aperture is transduced into a position which is detected by position sensor (9).

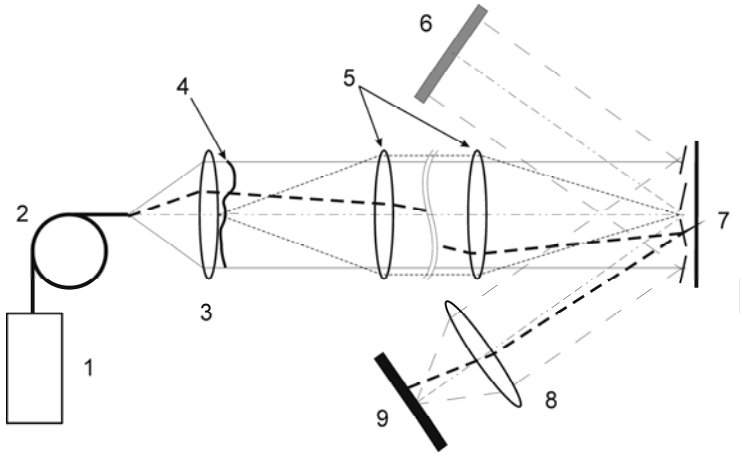

Fig. 1. Schematic sketch of the sensor set-up, 1: light source, 2: optical fiber, 3: lens under test, 4: aberrated wavefront, 5: imaging telescope, 6: absorber, 7: micro mirror array, 8: focusing optic, 9: position sensor

For the measurement of the whole wavefront all sub apertures are scanned consecutively. By this scanning procedure each measurement point can be evaluated with the whole dynamic range of the detector, whereas in SHS the dynamic range of the detector was used for the evaluation of all measurement points in parallel. Thus, the measurement range can be increased while accuracy is not reduced. Here a micro-mirror device SXGA+ Discovery™ 3000 by Texas Instruments is used which counts

more than thousand per thousand mirrors (see Table 1), determining the maximum number of scanned points to one over thousand of the lateral measurement range. Disadvantageous are the small dimensions of the single micro mirrors of the DMD that lead to diffraction effects.

Table 1. Technical data of the Texas Instruments DMD SXGA+ Discovery™ 3000 [5]

Number of micro mirrors	1400 x 1050
Tilt angle	±12°
Pitch (*a*) / mirror edge length (*b*)	13.68 µm / ~12.61 µm

3 Description of the diffraction effects

The microstructures of the TI DMD are associated with a Fresnel number of F ~ 3 10^{-3} while using light within the visible spectrum. Therefore diffraction in the Fraunhofer region can be expected.

The series of mirrors can be considered as a reflective blazed grating consisting of *N* tilted mirrors of the width *b* and the grating constant *a*. In case of the Texas Instruments SXGA+ DMD™ the blaze angle α is 12° and incident light will be reflected at $\beta = 2\ \alpha = 24°$.

To perform a measurement first all micro mirrors are tilted by $\alpha = +12°$ to direct the light onto the absorber. The centre of the diffraction pattern can be observed at $\beta = +24°$. The measurement signal is then generated by tilting a certain or more mirrors to $\alpha = -12°$, its centre will appear at $\beta = -24°$. A mathematic description to calculate the intensity profile $I(\theta)$ on the screen can be expressed as a product of two functions (see Eq. 1).

$$I(\theta) = I_{Grating} \cdot I_{Signal} \tag{1}$$

The first function $I_{Grating}$ considers the periodicity of the micro mirror array and defines the positions of the diffraction peaks (see Eq. 2).

$$I_{Grating}(u) = N^2 \cdot \frac{\sin^2\left(\frac{Nau}{2}\right)}{\sin^2\left(\frac{au}{2}\right)} \tag{2}$$

The second function I_{Signal} is the intensity distribution of a single mirror reflecting light onto the evaluation unit. Its intensity distribution is operating as an envelope of $I_{Grating}$ (see Eq. 3).

$$I_{Signal}(u) = b^2 \cdot \frac{\sin^2\left(\frac{b}{2}(u - k\sin\beta)\right)}{\left(\frac{b}{2}(u - k\sin\beta)\right)^2} \tag{3}$$

Finally, the variable u has to be substituted by the expression to find the Intensity $I(\theta)$ (see Eq. 4).

$$u(\theta) = k\sin(\theta) = \frac{2\pi}{\lambda}\sin(\theta) \tag{4}$$

For a plane monochromatic wave with a wavelength of λ = 712 nm incidenting perpendicular and the geometric specifications of the DMD as listed in Table 1, the intensity distribution can be calculated as displayed in Fig. 1.

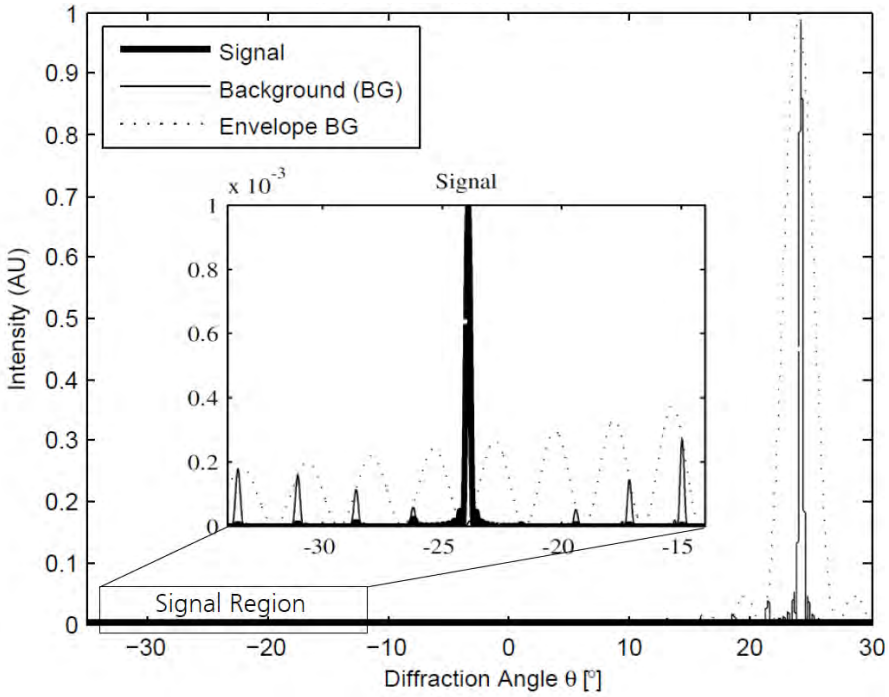

Fig. 1. Intensity profile of the reflected light for an illuminated DMD with an incident angle of 0° at a wavelength of λ = 712 nm and a signal generated by a super mirror of 3 x 3 mirrors

The wavelength is chosen in that way that the intensity of the grating $I_{Grating}$ reaches a minimum in the region of the signal since it represents an unwanted background signal. In Fig. 1 the intensity of the signal I_{Signal} was divided by 10,000 in order to take into account the smaller amount of light reflected by the mirrors contributing to the signal compared to the mirrors contributing to the background $I_{Grating}$.

4 Angular stability of the micro-mirror signal

Besides the consideration of the diffraction effects another important characteristic when using a DMD in the proposed set-up is the stability of the tilt angle of the mirrors. In order to determine the angular stability of the signal a high resolution measurement of a signal of 3 x 3 mirrors was conducted with a set-up similar to Fig. 1. The light of a fiber coupled laser diode with a wavelength of λ = 683.9 nm was collimated and directed on the DMD and reflected by the mirrors towards the evaluation unit. The focusing lens had a focal length of f = 60 mm and the position sensor was a 2D-position sensitive diode (PSD) with a sensitive area of 4 x 4 mm^2. The results are displayed in Fig. 4.

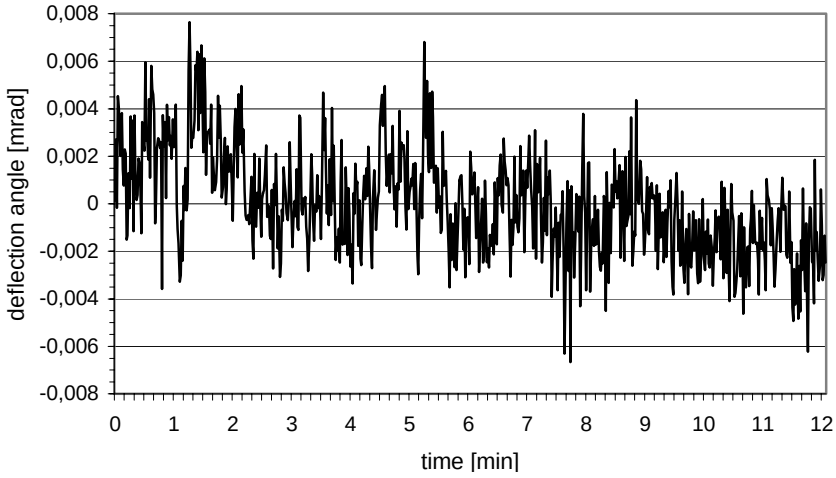

Fig. 2. Stability of the signal of 3 x 3 micro mirrors

The mirrors reflecting the signal were tilted with a frequency of 5 Hz and while tilting the position values were logged and the correspondent deflection angles were calculated. Each measurement point in Fig. 3 represents an average of 10 of values. The angle was logged over a period of more than 12 minutes in order to ensure that the drift of the system could be neglected during longer measurements. The stability of the signal had a reproducibility of s = 2.21 µrad.

5 Conclusion and outlook

The proposed wavefront sensor design based on a DMD promises to give a high lateral resolution at a high dynamic range. The diffraction effects that result from the small structures of the DMD can be reduced by the use of an appropriate wavelength. The angular stability of the signal showed to be applicable for a high resolution wavefront measurement.
Future work will mainly address the specific challenges that result from the possible high measurement range of up to 10°, such as errors that might be generated in the imaging telescope or in the focusing optic at higher field angles.

6 Acknowledgments

This work was part of the project “WaveSense” and was funded by the German Federal Ministry of Economics and Technology (BMWi). The project is supervised by the Arbeitsgemeinschaft industrieller Forschungsvereinigungen "Otto von Guericke" e.V. (AiF) and the Forschungsvereinigung Feinmechanik, Optik und Medizintechnik e.V. (F.O.M.). Their support is gratefully acknowledged. Furthermore the project is accompanied by the companies of Rodenstock, Trioptics, Möller-Wedel, Ingeneric and Aixtooling. Their contributions are also gratefully acknowledged.

7 References

1. Pfund, J et al. (1998) Dynamic range expansion of a Shack-Hartmann sensor by use of a modified unwrapping algorithm. Optics Letters 23 (13):995–997
2. Yoon G, Pantanelli S, Nagy L (2006) Large-dynamic-range Shack-Hartmann wavefront sensor for highly aberrated eyes. Journal of Biomedical Optics:030502-1 - 030502-3
3. Olivier, S et al. (2000) Liquid-crystal Hartmann wave front scanner. Applied Optics 39 (22):3838–3846
4. Seifert L et al., (2003) The adaptive Shack-Hartmann Sensor. Optics Communications 216 (4-6):313–319
5. http://www.vialux.de/chipset.pdf

Invited Paper

Intellectual property in industry and academia: where interests merge?

Nadya Reingand[1] and Wolfgang Osten[2]
[1]CeLight, Inc., USA, [2]Institut für Technische Optik, Universität Stuttgart, Germany

1 Abstract

Optical metrology presents a fusion of avant-garde science and industrial practicality. That's why business aspects are always of interest in this field. In this paper we analyze different types of intellectual property (IP) relevant to optical metrology, as well as peculiarities and limitations of IP protection in academia and industry. Traditionally, IP is considered being valuable assets for a company to achieve a commercial success. Alternatively, when 30+ years ago the right was given to academia to retain their inventions, the primary focus of this law was on dissemination of knowledge and stimulation of technological progress. This paper analyzes differences and common features in academic and industrial IP strategies and the ways to profit from those differences. We paid special attention to certain distinctions in IP laws in various countries, which is important due to the growth of international cooperation, outsourcing and multi-national character of companies.

2 Introduction

We are trying to implement a constructive approach in the discussion of academia-industry IP relationship aiming to facilitate the industrial technological progress by successful involvement of the academia IP. To academia we relate Universities, Universities of Applied Sciences and Research and Technology Organisations (RTO) such as National Laboratories. In the context we address some differences between filing a patent in U.S. and Europe and pay attention to current activities to improve the situation.

3 Types of intellectual property relevant to optical metrology

Optical metrology is connected to various aspects of IP: patents, trademarks and copyrights, which stimulate innovations by protecting creative work and investments. Besides the listed variety of IP, we should bear in mind territorial nature of intellectual property and consider a third dimension - a continuation of IP protection worldwide or in specific countries of interest.

3.1 Patents

Optical metrology products may be protected by patents of two types: utility and design. Generally speaking, utility patents address processes, devices and materials, while design patents protect ornamental appearance configuration, improved decorative appearance, or shape of an invention. Most of IP discussions are focused on utility patent analysis due to the importance of the technological aspects associated with utility patents. Examples of utility and design patents in Optical metrology are shown in Fig. 1 (a) and (b). Table 1 shows patent classes and subclasses relevant to optical metrology.

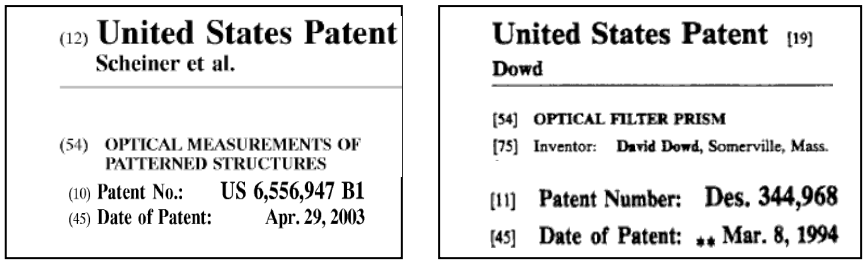
(12) **United States Patent**
Scheiner et al.

(54) OPTICAL MEASUREMENTS OF PATTERNED STRUCTURES

(10) Patent No.: US 6,556,947 B1
(45) Date of Patent: Apr. 29, 2003

United States Patent [19]
Dowd

[54] OPTICAL FILTER PRISM
[75] Inventor: David Dowd, Somerville, Mass.

[11] Patent Number: Des. 344,968
[45] Date of Patent: ** Mar. 8, 1994

Fig. 1. Examples of (a) utility patent, (b) design patent on optical metrology.

The complete procedure till granting the patent of your invention may take years (3-5 years on average). It is convenient to submit a provisional application (offered in U.S. since June 8, 1995, recommended in Europe by ProTon [1]) as soon as one has a patentable idea. The provisional application provides the opportunity to place an application on file (a) to obtain a filing date and to secure a priority date; and (b) to attach “patent pending” on your product and start the commerce. All of those advantages are achieved by submitting the invention description in informal manner

Table 1. Utility patent classes and subclasses relevant to Optical Metrology

USA Class	Sub class	Description
356		Optics: measuring and testing
	2	Contour plotting
	3	Range or remote distance finding
	27	Velocity or velocity/ height measuring
	32	Material strain analysis
	73	Plural test
	128	Refraction testing (e.g., refractometers)
	138	Angle measuring or angular axial alignment
	237.1	Inspection of flaws or impurities
	364	By polarized light examination
	450	By light interference (e.g., interferometer)
	600	Surface roughness
	601	Shape or surface configuration
	614	Position or displacement
	625	Dimension
	900	Interferometers

EU Class	Description
G01B011 and G01B009	Measuring length, thickness or similar linear dimensions; measuring angles; areas; irregularities of surfaces or contours: Measuring arrangements and instruments characterized by the use of optical means
GO2B026	Optical elements, systems or apparatus: optical devices or arrangements using movable or deformable elements for controlling the intensity, colour, phase, polarisation or dition of light, e.g. switching, gating, modulating

with minimal expenses (fee is ~ $100). If the commercial benefit of the idea patenting is obvious, after one year the inventor proceeds with filing non-provisional application. However, the provisional application does not provide rights against any infringement unless the following non-provisional application is filed.

Filing non-provisional application may result in a patent granting (~30% probability in US). Patents exclude others from making, selling and importing the kind of patented product on the territory of patent protection, for example, USA, Germany or a group of countries. As one can see from Fig. 2 more than a half of US patents are received by foreign residents. This clearly demonstrates international character of modern economy.

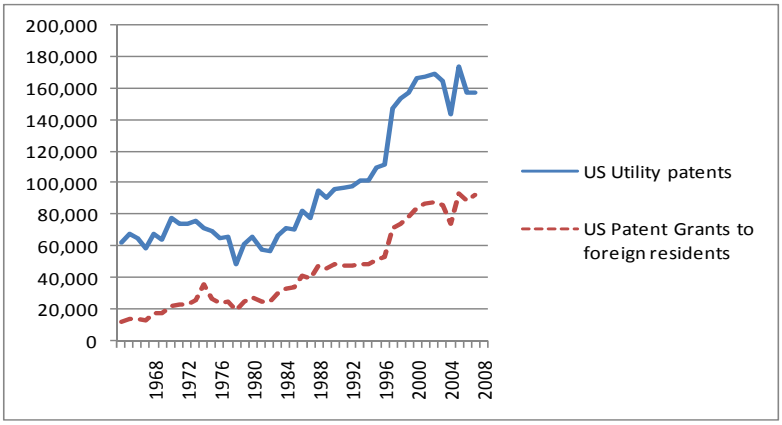

Fig. 2. Granted US Patents: solid line is the total number of patents and dashed line is the number of patents granted to foreign residents [2].

3.2 Trademark

A trademark and servicemark identified by the symbols ™ and ^{SM} (not yet registered) and ® (registered) is another type of IP relevant to Optical metrology. In industry and academia it is a distinctive sign used to discern that the products and/or services to consumers. Typical industrial trademark in optical metrology is shown in Fig. 3.

Word Mark	OMISTRAIN
Goods and Services	IC 009. US 021 023 026 036 038. G & S: Optical metrology apparatus and instrumentation, namely metrology tools for 2D and 3D visualization and measurement of the deformation motion and strain field in advanced electronic packages, system-on-chip and MEMS/MOEMS (micro-electro-mechanical systems I micro-opto-electromechanical systems) product engineering; computer software used for image acquisition, stressing control, image processing.

Fig. 3.. An example of trademark in Optical metrology.

University traditionally owns trademarks associated with the university name, for example, HARVARD SCHOOL OF ENGINEERING AND APPLIED SCIENCES®. However the whole trademark portfolio, which can be as large as Harvard's 103 trademarks, may include some specific types terms irrelevant to the name, see, for example, ASK WHAT YOU CAN DO^{TM}. The role of trademark is to promote education at this particular university, to protect university high standards from unauthorized use and to collect royalties through trademark licensing.

3.3 Copyright

Copyright identified by the symbol © protects the manner in which the ideas are expressed. The main traditional products of academia, books and any scientific papers are copyrighted, and any software code may be copyrighted too. If one created the work (for example, a software code) as an employee, acting within the scope of your employment, the work may be a "work made for hire", so the copyright owner is the employer. In the academic setting, the authors are frequently asked to transfer copyrights in the books and articles to publishers.

The use of copyrighted works can be via “fair use” or “with permission from the copyright owner”. Fair use is an important right to use copyrighted works at the university. Fair use can allow to clip, quote, scan, share, and make many other common uses of protected works in the classroom, in libraries, and for many other purposes.

In industry sponsored research (typically it is distinguished between contracted and collaborative research), typically IP rights on articles, dissertations, theses and books are not transferred to the sponsor, though research reports and partially software may be assigned to the sponsor. Academia intents to reserve the right to continue using data from the report in future research and to publish the results while accepting possible delay where the protection of intellectual property is envisaged, although this should be kept to a minimum [3]. Academia prefers to retain ownership on both object code and source code in the software developed for the sponsor; however, it may assign to the sponsor the object code specially developed in the frame of the project, keeping the right to use the source code for other research.

Academia often have special department to control fair use of copyrighted works in the academia education courses and the use of copyrighted material generated at the University in other institutions and organizations.

4 IP ownership at the university depends on a type of the project financing

Intellectual property ownership is regulated by research financing. We are limiting our discussion by listing the most important (from IP point of view) issues in the academia financing without detailed analysis of the university budget: (1) Government-funded research; (2) University non-profit status (tax exemption); (3) Industry sponsored research (contracted and collaborative research).

4.1 Government-funded research

In USA Bayh-Dole Act of 1980 allowed academia retaining their intellectual property. Prior to that patenting ocurred on case-to-case basis. Figure 4 shows rapid grows of granted patents since acceptance of Bayh-Dole Act: from less than 250 patents granted in 1975 to over 3,000 patents granted in 2000 [4]. Publicly funded biomedical research accounts for a major share of patents.

The advantages of the academic IP patenting include (1) monetary revenue through licensing to existing companies, (2) the rise of business activities through start-ups and (3) intangible values such as worldwide recognition and increased interest in admission.

The disadvantages of the academic IP patenting include negative effects on progress of research, especially in fields where advances are cumulative; tension between patenting and open science norms; potential biasing of academic research away from fundamental science.

The specific of academic patents is in (1) their greater generality and importance than industrial patents, and (2) they cover early-stage research that is far from ready for commercial use [5]. Despite of the essential growth, the percent of academic patents to total domestic patents in US is relatively very small; it grew from 0.16% in 1980 to 4% in 2000 (Fig.5).

4.2 Academia tax exempt status provides certain restrictions in IP

Currently, in unsteady market environment, universities report essential reduction of their endowment. For example, Harvard officials say the university's largest-in-the-nation endowment lost about 22 percent of its value, or $8 billion, in the four months since September 2008 [6]. Universities in US tend to raise operating capital through the issuance of tax-free bonds, which have a lot of federal regulations attached to them. To be considered qualified 501(c)(3) bonds (tax law provision grant exemption from the federal income tax to non-profit organizations), no more than 5% of the bond proceeds may be used for any private business use [7]. Use of bond proceeds or bond-financed facilities by university for the business other than education is considered private business use.

4.3 IP in industry-sponsored research

The types of US academia–industry agreements are the following:

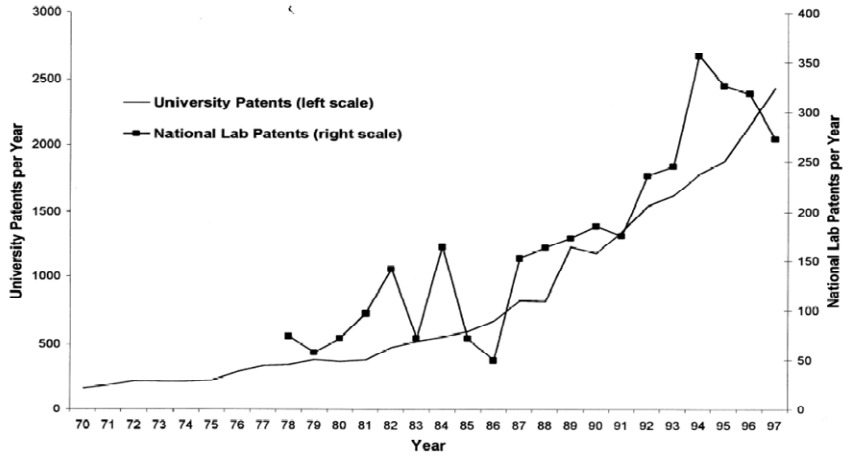

Fig. 4. A rapid growth of the University and National Lab's IP after Bahl-Dole Act of 1980

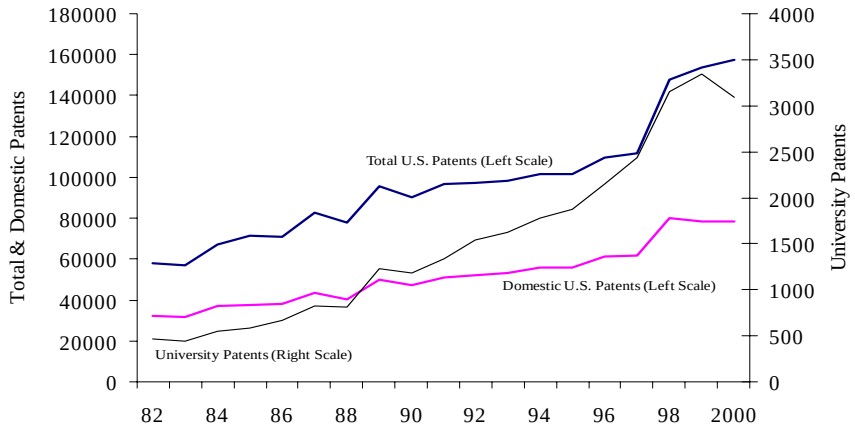

Fig. 5. The growth of the patenting in academia is faster than other patenting activity in the U.S.

a) ***Research Agreements.*** This is a project of mutual interest of the company-sponsor and university, which is in the frame of the university research program. It may be based on company or academia IP and may include development of new IP. There are three primary scenarios for the ownership of intellectual property rights: (1) the academia owns the

intellectual property; (2) the sponsor owns the intellectual property; and (3) the academia and sponsor jointly own the intellectual property.
b) ***"Fundamental" Research Agreements.*** This type of projects does not include any IP involvement, the research results in open publications and conference presentations.
c) ***Fee for Service Agreements.*** Academia can provide data or other information (without its processing or interpretation) for which university has unique capability to provide for the cost that cannot underbid for-profit providers of similar service, because of its tax exempt status. This agreement does not involve IP.
The European Commission published its Code-of-Practice [3] in April 2008 providing principles for the management of IP and knowledge transfer policies, principles for collaborative research and contract research and a set of good practice principles. The principles of the IP management are similar to the US ones. The major difference is that in contracted research industry may own all rights, provided they pay on a model that considers 100% of the costs including personal, equipment amortization and overheads.

4.3.1 Academia-owned IP

Academia may get profit from IP licensing and selling. License is a legal agreement granting someone permission to use a patent for certain purposes or under certain conditions. A license does not constitute a change in ownership of the patent. Exclusive license gives the licensee sole and entire rights to operate excluding all others, including the right to sublicense. Non-exclusive rights give the Licensee rights to make, use, import, offer to sell and/or sell the licensed technology.
Academia researchers must be able to publish and make presentations on the results of sponsored research. Sponsors usually obtain the right to review manuscripts prior to submission for publication or oral presentation. This is done to insure that no confidential information of the sponsor is released and to assess the patentability of any invention described in the material. Usually sponsors have about 40 days to review the material, and another 30 to 70 days to prepare and file a patent application. Periods of time are negotiable and depend on the type of the research.

4.3.2 Industry-owned IP

Industry is always interested in IP ownership, since it provides freedom to use various approaches to achieve competitive advantage. IP may be sold

or cross-licensed with the competitor, it also may be hold until the right moment in business. Licensing from academia, even exclusive licensing, limits the choice of business options.

4.3.3 Joint academia-industry IP

Joint patent ownership means that each owner has all rights to the IP. For example, the IP may be sold to someone without asking permission of another IP owner.

4.4 Some important differences between U.S. and Europe

In modern economy, the simplicity of communications, information exchange and transportation leads to increased number of company affiliations in different countries. The product development, production and sales may be performed in different parts of the world. Successful product sales in the country of origin may lead to the market expansion in other countries. Therefore it is important to understand some ***differences in patent systems of USA and Europe*** [8].

US patent law allows filing provisional application, which secures a priority date (see Section 3.1 of this paper). The following nonprovisional application needs to be filed within 12 months from filing the provisional. European patent system does not have provisional applications.

In US the patent application may be filed within 12 month from its public disclosure (so called grace period), for example, in published paper. European law does not have this provision, the patented materials needs to be undisclosed prior to the patent application filing.

Prior art definition is quite similar in both US and Europe. However, oral disclosure is qualified as prior art in Europe, and not qualified in USA. Secret prior art, such as secret sales or other, is considered being a prior art in USA, and not considered in Europe.

In USA the person who was the first to invent has a right for the patent on the invention. In Europe, the person who was the first to file the patent application has a right for the patent.

The US inventor submits to the US Patent Office an oath, stating that he/she truly believe that he is the one who invented the disclosed invention. There is no such oath in European patent system.

There is not one European patent, which is automatically valid in all 35 European countries. An EU patent is only valid in the states of EPC (European patent convention), which were indicated by the inventor, designation fees have been paid, and the specification translation has been

filed with respective national office. In contrast, the US patent is valid on all territory of the United States.

In US the inventor should disclose the most relevant prior art in "background" section of the specification and may submit IDS (information disclosure statement), which is the list of the most relevant references. There is such procedure in European law.

In USA the invention must describe the best mode to make the invented device (process, method, etc.). The requirement does not permit inventors to disclose only what they know to be their second-best embodiment, while retaining the best for themselves. There is no such requirement in European law.

There are certain differences in challenging the validity of a granted patent. Within nine months after the grant of a European patent, anyone can file an opposition with the EPO, stating why this patent should not have been granted. This is different from so called reexamination procedure in USA, which can be done at any time during the patent life.

The official fees for the US and EU patent filing and prosecution are quite different. A standard US fee paid by the academia for an invention, when the patent application is submitted, is $462 (filing + search + examination). The similar fee at EU office is €2650. The fee for each claim above 20 claims is $26 in USA. The same for each claim above 15 claims is €200. Besides, the EU inventor pays renewal patent fees for his patent application annually starting from the 3rd year of prosecution, this fee is from €400 (3rd year) to €1350 (10th year). There is no such renewal payment in US legislation.

In USA non-profit organization and small companies (i.e. with less than 500 employees) have 50% discount on major fees for the patent application. There is such fee reduction in Europe.

Organizational structure of the Offices of Technology Transfer is different in USA and Europe. In USA each University has such departments with a team of professionals, whose responsibility is to receive the disclosures of inventions, assist in the registration of copyrights and trademarks, help with the filing of patent applications (typically done by appointed law firm), determine who owns intellectual property, handle the commercialization/licensing of intellectual property and the allocation of net royalties received.

In Europe the organizational structure depends on the country. For example, Austria, Denmark, Germany and Norway have recently introduced new legislation to grant universities title to IP resulting from publicly funded research (which previously belonged to the individual inventor). In particular in Germany, as a consequence of this decision, the government supported financially the setting up of Patent Valorization

Agencies (Patentverwertungsagenturen/PVA). Each PVA commercializes research potential and results on behalf of a number of universities, university colleges and research institutes. Nearly all German Universities have bonds to one of the 20 PVAs.

ProTon Europe is the pan European association of knowledge transfer offices to public organizations. At the end of 2006, consolidated membership totalled 506 transfer offices providing services to 680 research organizations [1]. The goal of ProTon Europe is to provide changes in European legislation to facilitate efficiency of the technology transfer from academia to industry. Besides of the recent changes, EU public research organizations still file on average 5 times less patent applications than their US counterparts, although the total research budgets are comparable. In particular, ProTon suggested introducing a provisional application, a grace period, reducing the filing and maintenance fees for academia, waiving the translation requirement in national application, and others.

5 Patent licensing

Patent licensing is almost the only form of IP management at the university. Out of hundreds of invention disclosure forms (IDFs) that university receives annually, only 1/3 is chosen for patenting, and only ½ of those patents are licensed. On average, out of the hundreds of IDFs, only about 10% break even, 5% make some money and .01% generates a million dollars of revenue [9].

Academia licensing stimulates investment and promotes jobs even before sales of licensed products. According to [10], the economic impact of U.S. Academia licensing results in the investments in $20 billion per year range, thus creating over 150,000 jobs per year in the U.S. economy.

Academia licensing is performed through (1) start-up formation and through (2) licensing to existing companies. The proportion of those licenses is different for each academia in U.S., mostly depending on the academia specialization. An example of MIT [10] shows that although only 35 percent of the licenses were granted to start-ups, they accounted for 77 percent of the investment and 70 percent of the jobs.

The revenue from the patent licensing is split between the inventor(s), the university and the inventor's lab. In the case of more than one Inventor, each inventor shares equally in the inventors' earnings, unless all of the inventors agree in writing to a different distribution. Academia policy on the inventor compensation varies from one academia to another: the

inventors share varies from 25% to 70% of net earnings. Typically revenue generated from licensing is first applied to recovery of costs expended in seeking intellectual property protection for the technology. Then, some academia (for example, University of Iowa [11]) apply the earnings distribution policy, where the first $100,000 of net revenue is given to the inventors.

There are several forms of payment in patent licensing deals. For example, when academia is the licensor, a typical license will include a signing fee, reimbursement and ongoing payment of patent prosecution costs, milestone payments, minimum annual royalties and a percentage royalty on sales. Academia also might request that the licensee participate in sponsored research at the academia. The signing or licensing fee shows the level of commitment of the licensee to develop the technology. The milestone payments are related to certain stages in the technology development, and they may serve as compensation as the value of the licensed technology increases. The range for royalty rates is from ~2% for just discovered or engineered technologies to ~20% for a fully developed product approved for sale.

Licensing agreement for federally funded research may require U.S. manufacturing and retained Government rights.

Typically academia tries to retain rights in patents and copyright to materials produced as “work made for hire.”

Table 2 shows top patent revenue-generating universities in 2006 [12]. In many the cases the bulk of the university patent revenue is generated by one successful biotech patent. For example, NYU's serious return is in great part to medicine called Remicade, a rheumatoid arthritis drug developed along with Centacor and Johnson & Johnson. Ohio University came in fourth thanks to research on Somavert, a drug marketed by Pfizer to counteract the effect of the body's overproduction of growth hormones.

On average, the yield from patent licensing corresponds to about 2% of the university expenditures.

6 Conclusions

Among three types of Intellectual property (patents, trademarks and copyright) utility patents are considered being the most valuable assets. Various types of research financing (government-funding, academia bonds and industry-sponsored research) determine the type of IP ownership of the academic research results. In certain projects academia may not generate IP, because of their tax-exempt status.

Table 2. Top Patent revenue-generating Universities in 2006.

	University	Research Expendi-tures, M$	Research-Related Income, M$	Yield
1	New York University	210	157	75%
2	Wake Forest University	146.3	60.5	41%
3	Stevens Institute of Technology	28	4.56	16%
4	Ohio University	24	3.26	13%
5	Brigham Young University	26	3.07	11.7%
6	University of Rochester	355	38	11%
7	University of Minnesota	594	56	9.4%

The success of university-industry cooperation is usually estimated in revenue generated by patents through licensing to existing companies. The majority of million range revenues are generated by biotech patents. Among engineering patents, medical equipment patents bring the largest return of investments. So far we cannot provide an example of major financial returns in licensing IP in the field of optics and optoelectronics from universities.

Academia licensing through start-up formation is less than through existing companies, but they accounted for majority of the investment and jobs. In the field of optoelectronics this seems to be the major business opportunity for innovations. Academic patents typically more important than industrial patents, and they cover early-stage research that is far from commercial use. Start-ups provide a necessary step to prove the invented technology concept, and these start-ups may be later acquired by larger firms. There is no data on business transaction in this scenario, since the risk and return now assigned to start-ups.

The success of academic IP may also generate monetary and intangible assets other than through licensing. It may be increased interest in education at this particular academia, financial contributions from industry to continue basic research and others.

It is hard to underestimate to influence of academic IP on the society development. In the USA for example, 70% of all patents are based on discoveries made by public research organizations. From the 36 most successful European patents filed between 1990 and 2000, 50% came from public research institutions and the proof of principle of another 25% was made in partnership with public research institutions. Although the patent

applications filed by universities represent less than 3% of the total, they obviously have a much larger impact in terms of public benefits [1].

7 References

1. ProTon Europe: Improvements to the Patent System in Europe in order to facilitate Knowledge Transferfrom Public Research. http://www.protoneurope.org/Files/PatentPolicyStatement/attachment_download/file, 2007.
2. http://www.uspto.gov/web/offices/ac/ido/oeip/taf/h_counts.htm
3. European Commission Recommendation 2008, ISSN 1018-5593,
4. EC on the management of intellectual property in knowledge transfer activities and Code of Practice for universities and other public research organisations.
5. History of University IP Policies: Changing Objectives?, Yale AIDS Network, April 19, 2003
6. M. Jelinek and S. Markham Industry-University IP Relations: Integrating Perspectives and Policy Solutions, IEEE Trans. on eng. management, v.. 54, No. 2, May 2007.
7. Harvard endowment loses $8 billion, http://www.huffingtonpost.com/2008/12/03/harvards-endowment-tumble_n_148109.html.
8. K. Johnson, Industry – University Partnerships: The University Perspective, April 3, 2008, www.ccrhq.org/IP/Johnson_Johns%20Hopkins.ppt.
9. Patentanwälte Reinhard Skuhra, Weise und Partner: RSW News: Informations for Intellectual Property users. 2002
10. J. Rich, Who Owns My Invention? A Look at University Researchers and Technology Transfer , http://www.onlineethics.org/CMS/research/rescases/resethproblems/techtransfer.aspx.
11. Licensing of University Inventions Adds More than $20 Billion and 150,000 Jobs, MIT News Office, Oct. 27, 1995, http://web.mit.edu/newsoffice/1995/university-inventions.html
12. Inventor revenue distribution agreement, University of Iowa, research.uiowa.edu/uirf/downloads/forms/Revenue_Distribution_Agreement.doc.
13. P.Zura, 271 patent blog, http://271patent.blogspot.com/2008/09/forbes-top-patent-revenue-generating.html.

Moiré interferometer for surface mapping with liquid crystal grids

Jan A.N. Buytaert and Joris J.J. Dirckx
Laboratory of BioMedical Physics – University of Antwerp
Groenenborgerlaan 171, B-2020 Antwerp
Belgium

1 Introduction

Profilometry or the measurement of the height profile of surfaces offers many application fields, from manufacturing industry to medical research. Profilometers exist in many forms and use different techniques to obtain their topographic data. Using structured light projection techniques we can immediately obtain full-field height data, while many other techniques measure at a certain point and perform point-by-point scanning. The height resolution of structured light projection techniques is limited to the (sub)micrometer range. However, a useful advantage of these methods consequently is that the setup only requires micrometer stability. Laser interferometry or digital holography achieve higher resolution but require nanometer stability to measure with nano- as well as millimeter accuracy. Although structured light projection can be achieved in many ways, patterns of parallel lines or grids are widely used. Such line grids get projected onto the surface of an object and, when viewed under an angle, the projected line pattern gets deformed by the object geometry: the lines bend and shift in position and frequency. This deformation or modulation of the grid lines contains the height information. As can be seen from figure 1, there are many options to extract the encoded height information from deformed line grids. Initially one has two main options. Either one records the deformed grid lines directly, thus needing to resolve them individually. And their frequency will be high as only then it is possible to measure small height variations. The spatial resolution (and cost) of the recording device therefore needs to be high as well. Furthermore filtering is often involved, reducing the X-Y resolution. Either one projects the deformed grid lines on a second identical grid, generating geometrical interference called Moiré fringes (~ contours of equal height). In this case, we only need to resolve these much larger fringes and not necessarily the individual grid lines, thus making better use of the camera resolution.

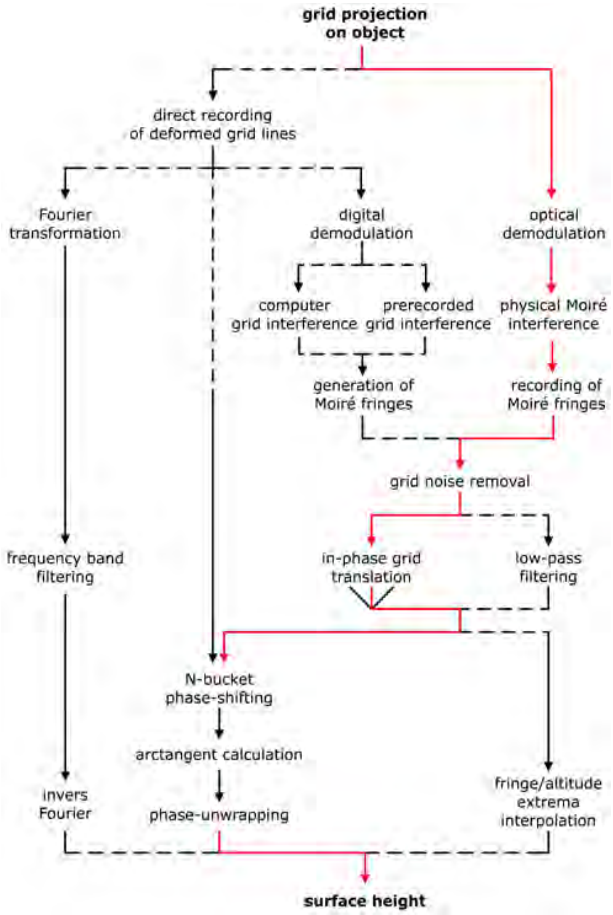

Fig. 1. Structured light projection techniques for profilometry: projection moiré profilometry with optical demodulation is the path/method/approach we prefer (*full gray line*)

The path or method which in our opinion delivers uncompromised resolution is shown in figure 1 with a full *gray* line. In short, we perform *optical* demodulation and record Moiré fringes with some remaining grid noise. After removal of the grid noise (without filtering) we use the phase-shifting and arctangent method to calculate the height accurately and independently for every pixel of the recording device from gray scale variations of several recorded phase-shifted fringe images.

Previously, grid projection often made use of fixed Ronchi grids and vapour lamps or slide projectors. Nowadays grid projection using liquid crystal display (LCD) projectors is popular because of its flexibility in adapting the grid pitch and thus the related sensitivity. The actual moiré

fringe generation or demodulation is however created *digitally* in the computer with a pre-recorded or virtually generated grid.
We developed a setup which not only projects the grid with liquid crystals, but also performs optical demodulation with a second grid on a liquid crystal panel. This offers us an even more flexible setup:

- The optical demodulation delivers uncompromised/optimal resolution
- No filtering or interpolation is needed: every *X*-*Y* pixel is independent
- We can easily project different grid shapes and different grid periods
- The grid noise removal and phase-shifting require the grids to be translated, which now can be done without mechanically moving components and very accurately on liquid crystal pixels

2 Device setup and theoretical description

Here we describe our setup, its performance and corresponding theory.

2.1 Optical setup

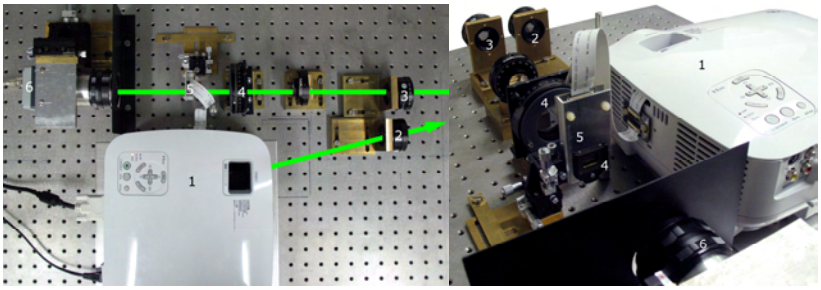

Fig. 2. View of our setup: a commercial LCD device projects the grid on the *green* liquid crystal panel (1) with lens L_1 (2). Lens L_2 (3) images the deformed lines on the *blue* liquid crystal panel (5) brought outside of the device. This panel contains a grid with the same pitch on it. Now a moiré interferogram is recorded behind the *blue* grid with a CCD (6).

We use a commercial LCD projector (NEC VT695) with 1024x768 p-Si TFT liquid crystal pixels for grid projection. Initially we introduced an extra separate liquid crystal panel which requires a lot of money, and extra hardware and software to control. We realised however that the commercial LCD device already possessed three of those panels. Only one is needed to perform the grid projection with. For instance, a grid created on the green liquid crystal panel is projected on the object. If we now bring the blue liquid crystal panel to the exterior of the projector (cf. figure 2)

and create a second identical demodulation grid on it, we do not need any extra hardware or software. To control the panels we just need to send an image with green or blue (or both) pixels to the projector. When we image the deformed projected grid lines on the surface onto the optical demodulation grid on the blue liquid crystal panel, a FOculus CCD camera (FO442 1392x1040 pixels) records the moiré interferogram (with some grid noise).

2.2 Theory

Sine functions are often used to describe the grid transmission function:

$$T(x) = \frac{1}{2} + \frac{1}{2}\sin\left(\frac{2\pi x}{p} + \phi\right) \tag{1}$$

The recorded intensity of the moiré interferogram is derived by taking into account the transmission function of the first and second grid, the magnification and intensity loses of the projection and observation lenses, and the reflection and deformation of the grid lines by the surface [1,2]. When both grids are translated together along *X*, the grid noise also shifts but the fringes remain stationary. This is used to remove and wash out the grid noise [3,4]. Previously both grids were continuously and mechanically translated together in one exposure time. Now we are working on discrete liquid crystal grids, so we need a discrete averaging theory. We derived that *N=4* or a multiple of 4 interferograms need to be recorded and averaged out [2]. Furthermore the grid period p_{pixels} should consist of a multiple of *N* (and 4). The expression for the intensity of the Moiré fringes on the surface after grid noise removal is:

$$I_k = A.\left[1 + \frac{1}{2}\cos\left(C.z + (k-1).\Delta\Phi\right)\right] + B \tag{2}$$

with *A* the modulation factor, *B* the background intensity and *C* a scaling factor between the height *z* and the fringe phase *C.z*.
We have only three unknowns so with 3 phase-shifted fringe images I_k ($k=1$ to 3) over $\Delta\Phi=\pi/2$, one can calculate the height *z*:

$$C.z = \arctan\left(\frac{I_3 - I_2}{I_1 - I_2}\right) \tag{3}$$

There are many other bucket phase-shifting algorithms with $k>3$ and other phase-shifts $\Delta\Phi$. However, the method using up till $k=4$ moiré fringe images I_k and $\Delta\Phi=\pi/2$ is most popular. An extra image $k=5$ is also often used as this method is more robust against phase-shift errors. The method $k=3$ is not so robust but needs the least amount of images I_k to be recorded.

3 Measurements and results

The theory of grid generation on two liquid crystal panels with grid noise removal and phase-shifting is easily implemented and controlled by a custom-made program in *Matlab* (Mathworks). We discuss our findings:

3.1 Grid noise removal

In theory, averaging of *N=4* or a multiple of 4 recorded moiré interferograms should remove all grid noise. In practise, *N* needs to be 8 or more (possibly caused by the limited fill factor of liquid crystal pixels) [1,2].
Combined with for instance *k=4* phase-shifted images this would mean at least 32 recordings and exposure times. This is too time-consuming. We developed a semi-continuous grid noise removal method [3], which first prepares and then loads all grid images to the memory of the graphics card and plays them as a fast movie with fixed framerate on the liquid crystal panels. In this way during *one* normal exposure time, all grid noise is immediately averaged out and a clear moiré fringe images is recorded.

3.2 Bucket phase-shifting

When one grid shifts relative to the other, the fringe location changes. We measured 3, 4 and 5 phase-shifted moiré fringes images (with grid noise removed). After calculation of the height with their respective algorithms, we found no difference in their height result, although the 5 image method was expected to perform better. The lack of difference between these measurements shows that we do not need a more robust 5 image method, because the grids are shifted so accurately on our discrete liquid crystal pixels. This also learns that with our liquid crystal setup the least amount (namely 3) recorded images (with semi-continuous grid noise removal) suffices to obtain a full-field accurate height map.

3.3 Sinusoidal grids

Although using sinusoidal transmission functions in the theory, one often uses square grids in practice as they are more readily available. Now we have the option, as we can just as easily generate square or (stepped) sine grids on our liquid crystal panels (cf. figure 3). We verified the light output of our LCD projector when a sine grid was put on the projection liquid crystal panel and concluded that a gamma-correction was needed.

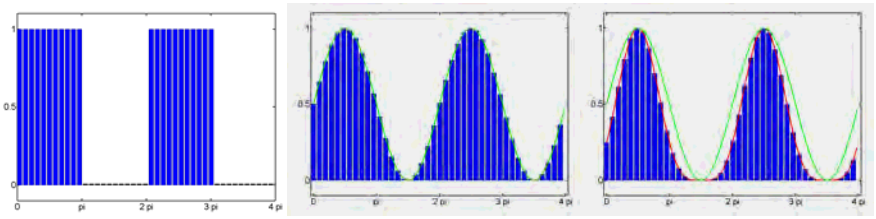

Fig. 3. Discrete grid profiles: Square, sinusoidal and gamma-corrected sinusoidal line pattern are created on our liquid crystal panels

Through function fitting of the measured light output with linearly increasing activation of the liquid crystal pixels, we derived the necessary gamma-correction. We can now choose between three grid line patterns to be projected (cf. figure 3), so we verified what the effect of their shape was on the moiré fringes and the eventual height measurement. Projection of square grids delivered more triangularly shaped moiré fringes; normal sinusoidal grids achieved more or less sinusoidal moiré fringes; but only gamma-corrected sinusoidal grids on the liquid crystal panels managed to achieve perfect moiré fringes (cf. figure 4).

Remember that our and most other theoretical descriptions use sinusoidal transmission functions so that sinusoidal moiré fringes will be obtained, as these can be easily used in the phase-shifting arctangent calculations. Therefore, any deviation from sinusoidal grids (and thus sinusoidal fringes) will deliver a systematic height error. This was confirmed in our actual measurements (cf. figure 4), where the square grids deliver a large systematic error, while the gamma-corrected sine grids only showed small height errors. Obviously, from now on we use sinusoidal line grids with gamma-correction for best height accuracy.

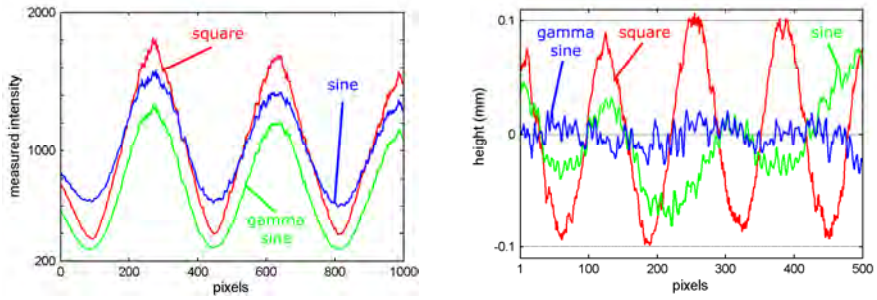

Fig. 4. *left:* Measured moiré fringe profiles of the three different projected grid shapes *right:* The corresponding error of these shapes on the actual height measurement

3.4 Calibration

The X-Y scaling factor (pixels to mm) varies at maximum 1% of its value over the depth of field, caused by the change in lens magnification. The Z scaling (arctangent result to mm) deviates even up to 2% near the edges of the depth of field. Most of this deviation is attributed to an approximation made in the used theory. We have already developed a first order correction which will improve this error [4], but it has not yet been implemented in our program.
For the moment we achieve a 15µm height resolution on objects of several tens of millimeters in dimension.

3.5 Demonstration objects

We measured the surface of a custom made pyramid. From the three-dimensional model, displayed in figure 5, it was shown that our setup is calibrated isometrically: The dimensions and angles are correct up till 2%, and the apex and edges are sharp and well resolved. We used a gamma-corrected sinusoidal grid with a period of 8 pixels, and semi-continuous grid noise averaging of N=8 images. This delivers 3.7 fringe pairs in the topogram mapped on the 3-D surface (fringe plane distance λ=4.5mm).

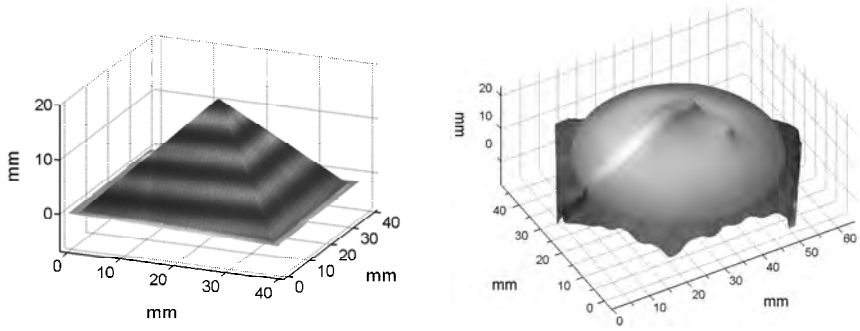

Fig. 5. *left:* Surface height of a small pyramid with apex *18mm* and *45°* side inclination
right: Measured height profile of a scaled latex eardrum model with point-indentation

Our profilometer is developed to measure eardrums of small animals. Figure 5 shows a 3-D representation of the measured surface of our scaled latex test model. The full-field deformation and effect of point-indentation on the membrane are measured. Through inverse modelling we want to obtain the elasticity of this and real eardrum membranes [5].

4 Conclusion

We developed a projection Moiré profilometer with resolution up to 15µm for objects of several centimeters in dimension. This can even be improved through first order corrections. The setup uses projection and performs optical demodulation with grids on liquid crystal panels

The optical demodulation, combined with phase-shifting and arctangent calculation, delivers an independent, uncompromised and accurate height resolution for every pixel. Thus, high X-Y and Z resolution is obtained. With our semi-continuous averaging method, moiré interferograms are immediately grid noise free in one recording, although working with discretely shifted grids. Only three of these moiré fringe interferogram recordings are needed to calculate the height, because of the accurate shifting on discrete liquid crystal pixels, without any mechanically moving components. Furthermore, sinusoidal grid projection is not only easily implemented with our device but the use of gamma-corrected sine grids is even a necessity for best resolution in projection moiré, even in general.

5 Acknowledgments

Financial support was given by the Research Foundation Flanders (FWO) and the Fondation belge de la Vocation.

6 References

1. Buytaert, J, Dirckx, J (2009 in press) Phase-shifting Moiré topography using optical demodulation on liquid crystal matrices. Optics and Lasers in Engineering
2. Buytaert, J, Dirckx, J (2008) Moiré profilometry using liquid crystals for projection and demodulation. Optics Express 16: 179-193
3. Dirckx, J, Buytaert, J (2009 in press) Implementation of phase-shifting moiré profilometry on a low-cost commercial beamer. Optics and Lasers in Engineering
4. Buytaert, J, Dirckx, J (2007) Design considerations in projection phase-shift moiré topography based on theoretical analysis of fringe formation. Journal of the Optical Society of America A 24: 2003-2013
5. Buytaert, J, Aernouts, J, Dirckx, J (2009) Indentation measurements on the eardrum with automated projection moiré profilometry, Optics and Lasers in Engineering 47: 301-309

High resolution tilt scanning interferometry system for full sensitivity depth-resolved displacement measurements in weakly scattering materials

Bona S. H. Burlison, P. D. Ruiz and J. M. Huntley
Loughborough University
Loughborough, Leics. LE11 3TU, UK

1 Introduction

Tilt-scanning interferometry (TSI) was recently proposed as a technique for measuring depth-resolved structure and 3D displacement fields within weakly scattering materials [1]. It is based on monochromatic illumination of a test sample with a temporal sequence of plane waves at different illumination angles. The scattered light for each illumination direction is recombined with a reference beam and all the resulting interferograms recorded as an image sequence. Depth information is encoded in the temporal frequency, and recovered through a Fourier transform of the recorded data along the time axis (or illumination angle axis). This approach differs from conventional optical coherence tomography [2] or wavelength scanning interferometry [3] in that only one wavelength is used throughout the measurement process. Angular spectrum scanning [4] and Lauer microscopy [5] are related techniques which found applications in profilometry and optical diffraction tomography for cell imaging. What all these technique have in common is that multiple interferograms are recorded whilst changing the angle of the illumination wave vector. The proof of principle setup developed in Ref. [1] was implemented with dual sensitivity (out-of-plane and one in-plane) and its axial resolution, determined by the tilting range of the illumination beam, was limited to ~1.1mm.

In this paper we present a novel TSI system which has several advantages over the previous one, including improved depth resolution, depth range, signal to noise ratio and repeatability. Moreover, it also provides full sensitivity to 3D displacements.

2 Depth-resolved microstructure and phase

In a TSI system in which the illumination angle lays on the x-z plane and tilts within the same plane, the modulation frequency produced by the interference between a reference wavefront and the backscattered light from a point (x, y, z) within a semitransparent scattering sample is given by [1]

$$f(x,y,z) = f(0,0,0) + \frac{n_0 \Delta\theta}{\lambda T}\left[x\cos\theta - z_1 \sin\theta - (z - z_1)\xi\right], \quad (1)$$

where n_0 is the refractive index of air, λ the wavelength, T the time it takes to scan the illumination angle from $\theta - \Delta\theta$ to $\theta + \Delta\theta$ and ξ is a refraction parameter that depends on the sample refractive index, θ and n_0. $f(0, 0, 0)$ is a carrier frequency due to the rigid body translation of the illuminating wavefront as it rotates around an axis parallel to the y-direction. The first term between the square brackets relates to a frequency that varies linearly with x, the second term to the frequencies accounting for the distance between a reference surface and the sample surface at z_1 and the last term to the frequencies accounting for the sample depth between the point at z and the sample surface at z_1.

A single illumination direction is required to get the scattering potential (internal microstructure represented by the magnitude of the Fourier transform) and the optical phase which is associated with the position of the scattering centres within the sample. The depth of a scatterer, $z(x, y)$, is obtained from the modulation frequency that it contributes to the interference signal in the time (illumination angle) axis:

$$z(x,y) = z_1 - \frac{\lambda T\left[f(x,y,z) - f(x,y,z_1)\right]}{\xi n_0 \Delta\theta}. \quad (2)$$

In order to measure in-plane and out-of-plane displacement components within the sample, image sequences from two symmetric coplanar illumination directions are required. The in-plane component is determined by subtracting the phase differences evaluated for each direction and the out-of-plane component is determined by the sum of those phase differences [1].

The depth resolution, δz, is defined as the minimum distance between points within the sample whose interference signals can be fully resolved in the frequency domain:

$$\delta z = \frac{\gamma\lambda}{n_0|\xi|\Delta\theta}, \tag{3}$$

where $\gamma = 4$ when a Hanning window is used to reduce spectral crosstalk.

3 TSI system with 3D displacement sensitivity

In order to obtain the three components of the displacement field, the new system was mounted on a rotation stage with a clear aperture (Newport RGV100), so that the illumination angle can be rotated around the optical axis (*z*-axis) of the imaging system, which remains fixed and looking through the aperture. Fig. 1 shows a schematic view of the illumination. The illumination angle lies on the plane formed by the illumination direction and the z-axis. It is scanned around $\theta = 45°$ with $\Delta\theta$ changing from −12.5 mrad to +12.5 mrad in steps of 0.015 mrad (1667 images are thus recorded). We use a PZT driven closed loop tilting stage (Physik Instrumente S-334-2SL) with a maximum achievable beam tilt of 100 mrad. However, as we use a 4× beam expander between the tilting mirror and the sample, the tilt angle is reduced by the same factor. To obtain the in-plane displacement component along the *x*-axis, for instance, it is necessary to record image sequences for illumination directions with azimuth angles α=0° and α=180°. Azimuth angles α=90° and α=270° are used for the in-plane component along the *y*-axis. In both cases it is possible to obtain the out-of-plane component.

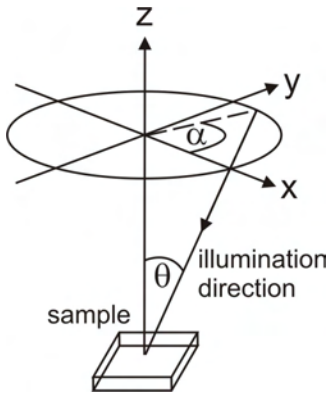

Fig. 1. The illumination beam can be directed to the sample with the same inclination and within the planes with different azimuth angle

4 Results

Figure 2 shows the interference intensity signal obtained from a pixel when an opaque surface is illuminated. We used a 12 bit, low noise CCD camera (Vosskühler CCD1300QLN). As in this case the signal originates from a single depth, only one frequency component should be present. A large number of modulation fringes is obtained for the whole tilting range but we only show the range (-5mrad, +5mrad) for clarity. The Fourier transform of the intensity modulation is shown in Fig. 3 (actually an average of the spectra for all pixels with the same *y* coordinate). The peak corresponds to the position of the surface observed relative to a reference plane and its width is related to the depth resolution. For λ = 532nm, ξ = 0.707, n_0 = 1 and $\Delta\theta$ = 22.5 mrad, the expected depth resolution, according to Eq. (3), is 134 μm. We used a linearization routine that interpolates and re-samples $I(x, y, t)$ along the temporal axis so that a constant phase change is introduced between successive frames. Small deviations from perfect collimation in the illumination beam can be a cause of non linearity of the frequency. Whilst the measured 'average' peak width in Fig. 3 is 910 μm, the width computed for the pixel used in the linearization routine is 470 μm, still 3.5 times wider than expected. This seems to be in part due to speckle decorrelation broadening and also due to an imperfect linearization. In [1] the phase noise was reduced by averaging neighbouring slices that lay within the depth resolution of the system. In the new system, the 12 bit camera resulted in superior modulation detection and higher signal to noise ratio, even without spatial averaging. Figure 4 shows a wrapped phase map due to in-plane displacements in a cross section of a semitransparent scattering sample.

5 Summary

A new system for Tilt Scanning Interferometry has been proposed. Multiple illumination directions can be easily set as the illumination optics is mounted on a rotation stage with a clear aperture through which the sample is viewed. The use of a closed loop tilting mirror with a wide tilting angle results in higher depth resolution. The signal to noise ratio is also considerably improved thanks to the use of a 12 bit low noise camera. The ability to rotate the illumination direction around the observation direction enables the measurement of 3D displacement components within semitransparent scattering materials. The measurement volume is approximately 1 cm^3.

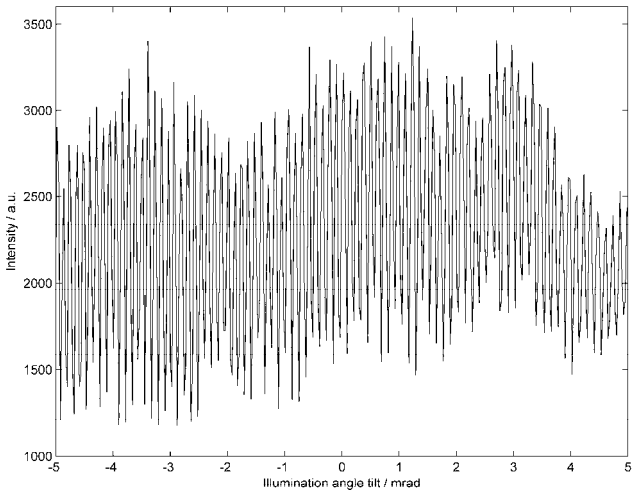

Fig. 2. Interference intensity signal obtained from a pixel when the illumination angle is scanned over an opaque surface

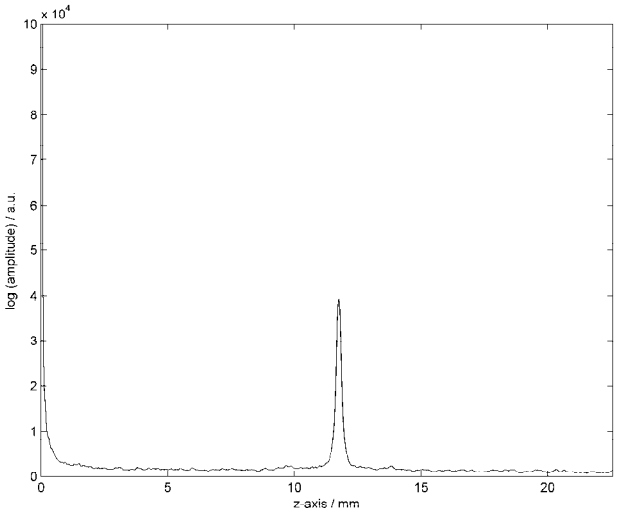

Fig. 3. Fourier transform of the signal shown partially in Fig.2. The peak corresponds to an opaque surface and its width defines the depth resolution of the system

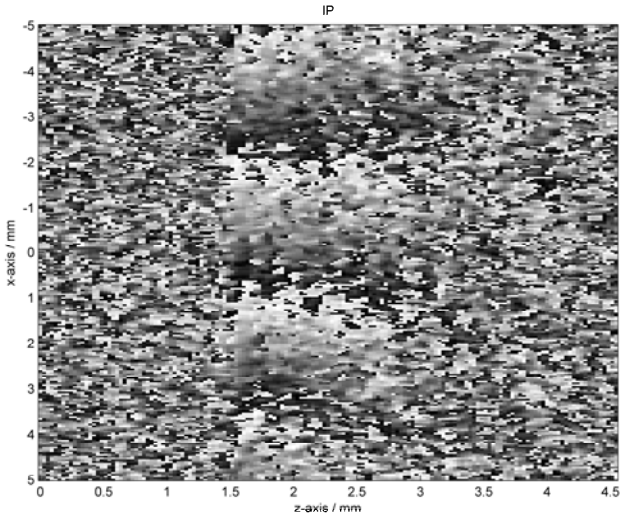

Fig. 4. Phase map corresponding to the in-plane displacement along the y-axis (normal to plane of the figure) in an x-z plane cross section of a semitransparent scattering sample. The object surface is at ~z = 1.5mm

6 References

1. Ruiz, P D, Huntley, J M and Maranon, A (2006) Tilt scanning interferometry: a novel technique for mapping structure and three-dimensional displacement fields within optically scattering media. Proc. Roy. Soc A 462:2481-2502.
2. Huang, D, et al, (1991) Optical Coherence Tomography. Science 254:1178-1181.
3. Ruiz, P D, Huntley, J M and Wildman, R D (2005) Depth-resolved whole-field displacement measurement by wavelength-scanning electronic speckle pattern interferometry. Appl. Opt. 44:3945-3953.
4. Duan, Z H , Miyamoto, Y and Takeda, M (2006) Dispersion-free optical coherence depth sensing with a spatial frequency comb generated by an angular spectrum modulator. Opt. Exp. 14:12109-12121.
5. Lauer, V(2002) New approach to optical diffraction tomography yielding a vector equation of diffraction tomography and a novel tomographic microscope. Journal of Microscopy 205:165-176.

Multifunctional phase-stepping interferometer for measurement in real time

Ventseslav Sainov, Elena Stoykova
Central Laboratory of Optical Storage and Processing of Information
Bulgarian Academy of Sciences
Acad.G.Bonchev Street 101, 1113 Sofia
Bulgaria

1 Introduction

Digital holography exhibits some exceptional features which makes it especially suitable for microscopy as quantitative phase-contrast imaging without multiple exposures or mechanical scanning [1-3], numerical focusing and 3D reconstruction, numerical manipulation of the optical field or multi-wavelength interferometry [4,5]. Digital holographic microscopy (DHM) can be used for marker-free observation of moving micro-objects, measurement of their optical parameters and 3D visualization [6]. Introduction of phase-shifting in digital holography enables using of in-line set-ups [7] but requires successive acquisition of at least three phase-shifted interference patterns. Different solutions have been recently proposed to get round this obstacle in order to achieve a real-time observation mode as Fourier decomposition of a low-coherence optical image field into two spatial components and introduction of controllable phase-shifts in one of them [8], or spatial segmentation of the reference wavefront using an array of cells in which each cell consists of several different phase retarders or polarizers in front of the image sensor [9,10]. The high rate of recording in the proposed solutions is achieved at the expense of a decreased number of pixels which contribute to image reconstruction, restrictions on the intensities of the reference/object waves or introduction of a carrier frequency, etc.
A multi-camera implementation of the in-line DHM is another potential solution for the real-time operation mode. In [11] we described a system with four Mach Zhender interferometers which, combined with four 2D sensors, yield four phase-shifted at $\pi/2$ fringe patterns. The requirement for all cameras to register images corresponding to the same spatial phase distribution caused by the object sets stringent restrictions on the optical transfer functions and optical paths in the four channels. One should take

into account the non-linear response of the CCD cameras, distortions due to slight differences in the point spread functions of the optical channels, non equal background intensity and contrast of the recorded interference patterns, misalignments between the fronts of the interfering waves, multiplicative and additive noises etc. A modified algorithm has been proposed in [11] for compensation of misalignments. The algorithm, however, relies on equal backgrounds and contrasts of the fringe patterns recorded in the four channels. Hence, the aim of the present work is to check efficiency of normalization and smoothing for processing patterns consisting of a large number of fringes with severe variations in the backgrounds and contrasts which are independent in the four channels.

2 Real-time multi-camera interferometric system

To realize a real time operation mode through simultaneous recording of four phase-shifted interference patterns, we built the set-up, shown in Figure 1. The presented system is based on parallel image plane holographic recording by four CCD cameras using four identical Mach Zhender interferometers with $\pi/2$ phase-shifted reference beams in one of their arms. The system in Figure 1 can be used both for digital holographic recording and image-plane interferometric phase determination.

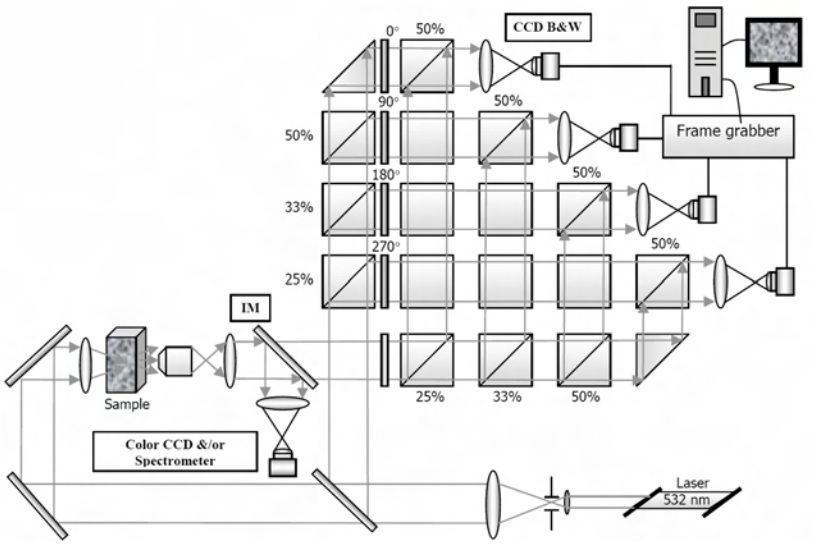

Fig. 1. Multi-camera system for parallel image plane holographic recording

To minimize the influence of errors, precise selection and adjustment of optical elements and CCD cameras is required to equalize the optical path changes and to set correct phase-steps in the four Mach Zhender interferometers. The optical paths in the interferometers are controlled by the incorporated in them beam-splitters, optical compensators and reflectors. The required phase steps are introduced by phase retarders. In addition a color CCD camera and a portable spectrometer OceanOptics HR-4000 are incorporated into the system for 2D color imaging in a non-coherent white light and for fluorescent analysis of the specimens in parallel with the 3D (holographic) imaging.

3 Phase retrieval

The CCD cameras in Fig.1 record the interference patterns in the image plane (l = 1,2,3,4):

$$I_l(x,y;\phi_l)=\left|U_O^l(x,y)+U_R^l(x,y)\right|^2=\left|U_R^l\right|^2+\left|U_O^l\right|^2+U_R^l U_O^{l*}+U_R^{l*}U_O^l, \qquad (1)$$

where $U_O^l(x,y)=A_O^l(x,y)\exp[i\varphi_0(x,y)]$ and $U_R^l(x,y)=A_R^l(x,y)\exp[i\phi_l]$ are the complex amplitudes of the object and reference beams in the channel "l" respectively, ϕ_l is the constant phase-step introduced between both beams, and $*$ denotes the complex conjugate. Registration of four interference patterns, $I_l(x,y)=I[x,y;(l-1)\pi/2]$, l = 1,2,3,4 makes possible calculation of the object complex amplitude [7] or the phase

$$\varphi_0(x,y)=\arctan\left[\frac{I_4(x,y)-I_2(x,y)}{I_1(x,y)-I_3(x,y)}\right]=\frac{2\pi}{\lambda}\int_0^{h(x,y)}[n_s(x,y,z)-n_m]dz \qquad (2)$$

where λ is the wavelength of the illuminating beam, n_s is the refraction index of the sample, n_m - that of the medium, and $h(x,y)$ is the height of the object. The recorded fringe patterns are given by

$$I_l(x,y)=I_l^0(x,y)+\gamma_l(x,y)\cos\Psi_l(x,y)+N_l(x,y), \qquad (3)$$

where the slow varying functions $I_l^0(x,y)$ and $\gamma_l(x,y)$ ($l=1,2,3,4$) correspond to the background and the contrast of the fringe pattern in the channel "l", $N_l(x,y)$ is the additive noise term, and the phase $\Psi_l(x,y)$ which contains the relevant information can be written as:

$$\Psi_l(x,y)=\varphi_0(x,y)+\psi_l(x,y)+\frac{\pi}{2}(l-1)+\delta_l, \qquad (4)$$

Let's take for the current modeling $\varphi_0(x,y)=2\pi\lambda^{-1}(n_s-n_m)h(x,y)$ where, without the lack of generality, we assume that the refraction index is constant throughout the sample. The error terms, δ_l and $\psi_l(x,y)$, describe the error in the phase step and the error induced by the misalignment of the wave fronts of the object and reference waves and/or by aberration of the optical system respectively for the channel "*l*". Obviously, for each channel in Figure 1 these terms are different thus creating a serious obstacle for correct object reconstruction. As we have shown in [11], the misalignment problem can be solved by preliminary calibration of the system. The phase errors $\psi_l(x,y)$ are systematic and can be evaluated beforehand in each of the channels through successive acquisition of four phased shifted at $\pi/2$ fringe patterns recorded without the object. Then, if we assume that the backgrounds and contrasts of fringes are adjusted to be very close in the four channels, we obtain the following corrected formula for the object phase:

$$tg\varphi_0=\frac{(I_4-I_2)(a_1+a_3)-(I_1-I_3)(b_2+b_4)}{(I_1-I_3)(a_2+a_4)+(I_4-I_2)(b_1+b_3)} \tag{5}$$

where we have $a_l(x,y)=\cos\psi_l(x,y)$, $b_l(x,y)=\sin\psi_l(x,y)$.

The algorithm was checked in [11] by modeling the system performance for zero order fringe patterns at misalignments up to half a minute. In the present work $\psi_l(x,y)$ is chosen to lead to a large number of fringes across the aperture of each CCD. Let's $\psi_l(x,y)$ is formed as a result of the interference of a plane object wavefront $U_0^l(\vec{r})=A_0^l\,exp(-j\vec{k}_0^l\vec{r})$ and a spherical reference wavefront in paraxial approximation with a radius *R* $U_R^l(\vec{r})=A_R^l\exp\{-jk[(x-x_l)^2+(y-y_l)^2]/2R\}$, where (x_l,y_l) are the coordinates of the wavefront apex with respect to the coordinate system attached to each camera. Actually, the specific forms of $\psi_l(x,y)$, *l*=1,2,3,4, are not important for the analysis; the fact that matters is that they i) do not coincide in the separate channels, and ii) introduce a large phase variation in the recorded patterns. If the plane wave vectors $\vec{k}_0^l$ subtend angles 90°- $\eta_{x,y,z}^l$ with X,Y and Z axes the phase term is given by

$$\psi_l(x,y)=\frac{2\pi}{\lambda}\left\{\left(x\sin\eta_x^l+y\sin\eta_y^l\right)-\frac{1}{2R}\left[(x-x_l)^2+(y-y_l)^2\right]\right\} \tag{6}$$

We modeled the contrast terms $\gamma_l(x,y)$ in Eq. 3 as

$$\gamma_l(x,y) = \gamma_0 \exp\left\{-\left[(x-x_{cl})^2 + (y-y_{cl})^2\right]/R_c^2\right\} \quad (7)$$

where x_{cl}, y_{cl} are different in the four channels. Figure 2 (top) depicts the grey scale maps of four phase-shifted at $\pi/2$ fringe patterns recorded by the four cameras in Figure 1 at misalignment of about 2' between the plane waves $U_0^l(\vec{r})$ and the planes of the CCD apertures. The patterns are simulated as 512×512 arrays of 8-bit encoded intensities at equal pitch along X and Y axes $\Delta_x = \Delta_y = \Delta =$ 0.24 μm and λ = 0.532 μm without phase step errors. We introduced an additive Gaussian noise $N(0,\sigma^2)$ with σ = 6. The object is a small flat top cylinder with height *h* = 2,4 μm and $n_s - n_m = 0.1$. We deliberately chose large differences in the backgrounds and contrasts in the four channels. The algorithm (5) fails to restore the object from the fringe patterns shown in Fig. 2 (top). To solve the problem, we normalized the fringe patterns using the Fourier transform filtering proposed in [12,13]. It is performed by rotation of a semiplane passband filter at steps of $2\pi/N$ in the frequency domain. The background removal and smoothing are accomplished through an annular passband filtering. We used *N* = 12 to decrease any possible distortions in the normalized patterns which are depicted in Fig.2 (bottom). The results from application of the modified algorithm to the normalized patterns for *h* = 2.4 μm are shown in Fig.3. The algorithm reconstructs well the vertical side walls of the cylinder whereas the flat surfaces are reconstructed with a rms error varying from 0.01 μm up to 0.05 μm. This rms error remains practically the same for larger cylinder heights; e.g. for *h* = 9.6 μm it reaches 0.07 μm which corresponds to less than 1% relative error in reconstruction of the 3D cylinder surface. The reconstruction can be improved by additional smoothing of the reconstructed image. The observed errors are partially due to small distortions introduced by the normalization procedure. Fig.4a depicts as an 8-bit encoded image the difference between the wrapped phase maps obtained for a reference plane from simulated normalized and non-normalized fringe patterns which correspond to successive recording in one of the channels in Fig.1. Accurate determination of the wrapped phase maps of the reference plane in the four channels is required for calculation of $a_l(x,y)$ and $b_l(x,y)$ in Eq.5.

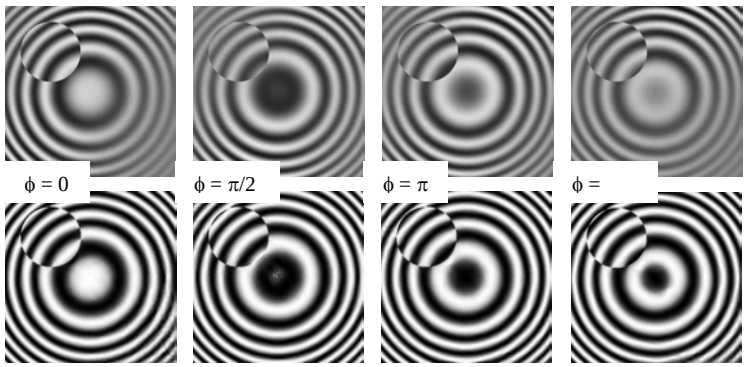

Fig. 2. Top: Grey scale 8-bit maps of four phase-shifted at π/2 fringe patterns with varying contrasts and backgrounds recorded in the four optical channels of the system in Fig.1 (simulation). Bottom: Normalized fringe patterns. The misalignment between the plane object beam and the plane of the CCD aperture in all figures is about 2' for each channel. In all figures we have $\gamma_0 = 100$, $x_{c1} = 200$, $x_{c2} = 240$, $x_{c3} = 280$, $x_{c4} = 320$, $y_{c1} = 160$, $y_{c2} = 320$, $y_{c3} = 240$, $y_{c4} = 80$, $R_C = 300$ and $I_1^0 = 150$, $I_2^0 = 128$, $I_3^0 = 112$, $I_4^0 = 102$.

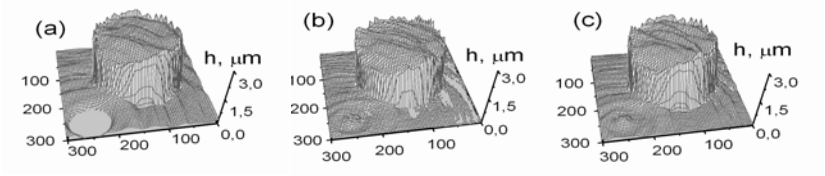

Fig. 3. 3D surface of a flat top cylinder with height 2.4 μm reconstructed from the normalized fringe patterns recorded in the four channels (simulation). (a) $R_c = 300$, $\sigma = 0$; (b) $R_c = 300$, $\sigma = 6$; (c) $R_c = 600$, $\sigma = 6$.

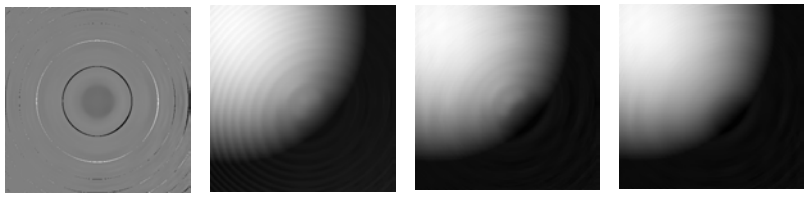

(a) (b) (c) (d)

Fig. 4. (a) – Difference between the wrapped phase maps of a reference plane obtained from simulated normalized and non-normalized fringe patterns. (b,c,d) - Unwrapped phase maps obtained with Eq.5 from a simultaneous measurement in the four channels of a dome with radius 800 m (simulation): (b) – non-normalized fringe patterns; (c) – normalized fringe patterns, a_l and b_l, are calculated from the normalized patterns; (d) – normalized fringe patterns, a_l and b_l, are calculated from the non-normalized patterns.

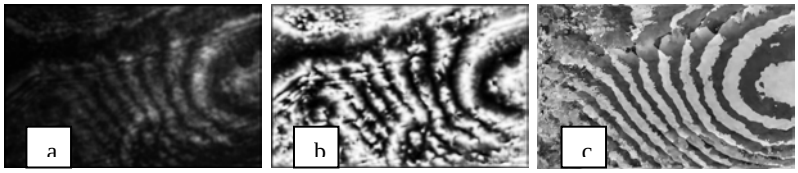

Fig. 5. Experimental observation of an epidermal onion cell at 200× magnification: (a) – non-normalized fringe pattern in one of the channels; (b) – normalized fringe pattern (a); (c) – wrapped phase map from simultaneous measurement with four cameras.

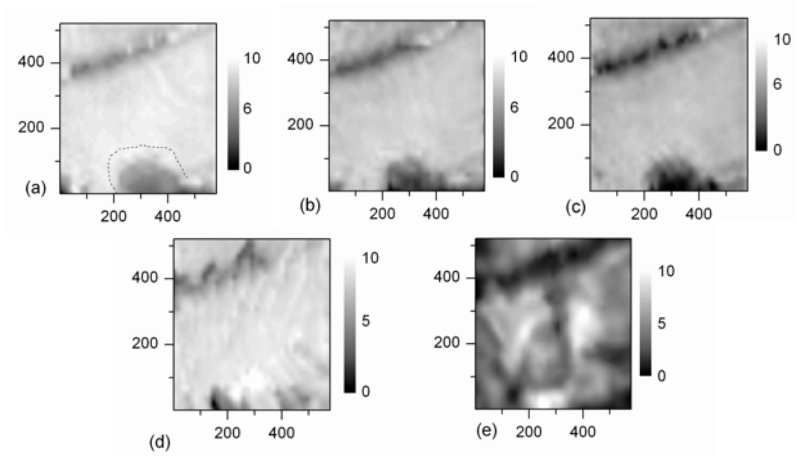

Fig. 6. Unwrapped phase maps of an epidermal onion cell at 200× magnification (experiment): (a),(b),(c),(d) – successive recording in the channels 1,2,3,4 in Fig.1; (e) - simultaneous recording with four cameras.

Figure 4 gives the unwrapped phase maps for a dome that have been calculated from i) non-normalized fringe patterns of the object (recorded simultaneously in the four channels) and the reference plane (recorded successively in each of the channels) - (b); ii) normalized fringe patterns of the object and the reference plane - (c) iii) normalized fringe patterns of the object, when a_l and b_l in Eq. 5 are calculated from non-normalized patterns of the reference plane. The best result is achieved in the last case.

Experimental verification (Fig.5 and Fig.6) of the system in Fig.1 was performed with epidermal onion cells observed at 200× magnification. A 1951 USAF resolution test chart was used to ensure that each camera captures the same object field. Normalization was applied only to object fringe patterns (Fig.5). The result from the simultaneous measurement differs from the results in separate channels due to the shift of the nucleus within the observed cell during successive acquisition of the phase-shifted patterns. This additionally shows the necessity of real time measurement.

4 References

1. Cuche, E, Bevilacqua, F, Depeursinge, C, (1999) Digital holography for quantitative phase-contrast imaging, Opt. Lett. 24: 291-293
2. Martínez-León, L, Pedrini, G, Osten, W (2005) Applications of short-coherence digital holography in microscopy, Appl. Opt. 44: 3977-3984
3. Mann, C, Yu, L Lo, C.-M, Kim, M (2005) High-resolution quantitative phase-contrast microscopy by digital holography, Opt. Express 13: 8693-8698
4. Dubois, F, Schockaert, C, Callens, N, Yourassowsky, C (2006) Focus plane detection criteria in digital holography microscopy by amplitude analysis, Opt. Express 13: 5895-5908
5. Gass, J, Dakoff, A, Kim, M (2003) Phase imaging without 2π ambiguity by multiple-wavelength digital holography, Opt. Lett. 28 (13): 1141-3
6. Kemper, B, Carl, D, Schnekenburger, J, Bredebusch, I, Schäfer, M, Domschke, W, von Bally, G (2006) Investigations on living pancreas tumor cells by digital holographic microscopy, J. Biomed. Opt. 11: 034005
7. Yamaguchi, I, Zhang, T (1997) Phase-shifting digital holography, Opt. Lett. 22 (16): 1268-1270
8. Popescu, G, Delflores, L, Vaughan, J, Badizadegan, K Iwai, H, Dasari, R, Feld, U (2004) Fourier phase microscopy for investigation of biological structures and dynamics, Opt. Lett. 29 (21): 2503-5
9. Awatsuji, Y Tahara, T Kaneko, A, Koyama, T , Nishio, K , Ura, S, Kubota, T, Matoba, O (2008) Parallel two-step phase-shifting digital holography, Appl.Opt. 47 (2): D183-D189
10. Novak, M, Millerd, J, Brock, N, North-Morris, M, Hayes, J, Wyant, J (2005) Analysis of a micropolarizer array-based simultaneous phase-shifting interferometer, Appl. Opt. 44: 6861-6868
11. Sainov, V Stoykova, E (2008) Multifunctional phase-stepping interferometer for measurement in real time, In: Intl. Symp. to commemorate the 60th anniversary of the invention of holography, 27-29 Oct. , Springfield, USA, R.J. Priputniewicz, ed., SEM, 2008, 53-60
12. Ochoa, N (2008) Normalization and smoothing algorithm for electronic speckle-pattern interferometry fringes, Opt.Eng. 47 (4), 045601
13. Kreis, T (1986) Digital holographic interference-phase measurement using the Fourier-transform method, J.Opt.Soc.Am. A 3(6): 847-855

Honorary Lecture

A Wonderful World of Holography, Interferometry, and Optical Testing

James C. Wyant
College of Optical Sciences
University of Arizona
Tucson, AZ 85749 USA
jcwyant@optics.arizona.edu
www.optics.arizona.edu/jcwyant

1 Introduction

This paper will briefly describe four projects I have especially enjoyed being involved with during my career. 1) Use of computer generated holograms for testing aspheric optics, 2) phase-shifting interferometry, 3) computerized interference microscope, and 4) dynamic (single-shot) interferometry.

2 Use of computer generated holograms for testing aspheric optics

It has been more than 40 years since Lohmann and Paris first described computer generated holograms (CGHs) [1]. The use of CGHs for testing aspheric optical elements was the first project I worked on after finishing college [2]. Computer generated holograms are now widely used in the testing of aspheric optical elements. While CGHs are most often used to test rotationally symmetric surfaces, a great advantage of CGHs is that they can be made for testing free form optics almost as simply as for testing rotationally symmetric optics. Crosshairs can be put on the CGH to aid in the alignment of the CGH and additional holograms can be placed on the CGH to aid in the alignment of the optics or to aid in calibration of the CGH. CGH interferometers work well with phase-shifting techniques.

2.1 Basic test setups

Figure 1 shows one setup for using a CGH to perform an optical test and Figure 2 shows a typical CGH.

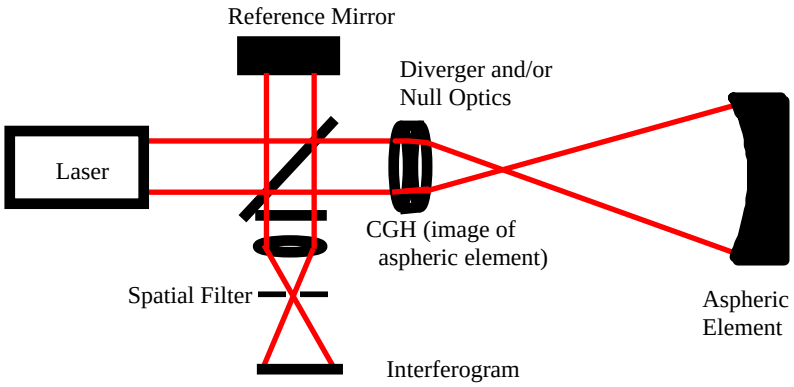

Fig. 1. Typical CGH Interferometric Setup.

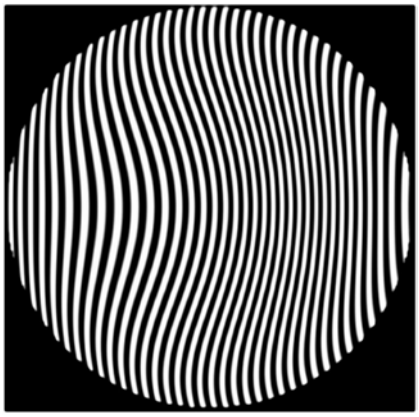

Fig. 2. Typical CGH.

The CGH can be thought of as a binary representation of the interferogram, or hologram, that would be recorded if we were to interfere the aspheric wavefront coming from a perfect aspheric surface with the reference beam. The procedure for making the CGH is to first raytrace the interferometer to determine the position of the fringes in the theoretical

interferogram that would be obtained if the mirror under test were perfect. A plotter, such as a laser beam recorder or an e-beam recorder, is then used to draw lines along the calculated fringe positions.

When the CGH is placed in the interferometer as shown in Fig. 1, the CGH and the interference fringes produced by the interference of the reference wavefront and the wavefront produced by the mirror under test produce a moiré pattern that gives the difference between the CGH and the interference fringes. If sufficient tilt is introduced into the CGH to separate the diffraction orders of interest, spatial filtering can be used to improve the contrast of the moiré pattern. Spatial filtering is accomplished by reimaging the hologram with an appropriately placed small aperture in the focal plane of the reimaging lens. This aperture is placed such that it passes only the wavefront from the mirror under test and the +1 order beam resulting from illuminating the hologram with a plane wavefront, or equivalently passing the reference beam and the -1 order produced by illuminating the hologram with the aspheric wavefront. In the first case we are interfering two aspheric wavefronts, one produced by the aspheric mirror and the second produced by the CGH. In the second case we are interfering two plane waves, one produced by the reference arm and the second produced by the CGH removing the asphericity in the test beam.

The largest source of error is in the drawing of the grating lines [3-8]. If $\varepsilon(x,y)$ is the error in the drawing a grating line and the localized line spacing is $s(x,y)$, the wavefront error $\Delta W(x,y)$ is given by

$$\Delta W(x,y) = \lambda \frac{\varepsilon(x,y)}{s(x,y)}$$

If we have an error in drawing a grating line of 0.1 microns and the localized line spacing is 20 microns, the wavefront error will be $\lambda/200$. Electron beam recorders currently have a positional error of less than 50 nm over a field of 150 mm.

Errors can also result from the hologram being in the wrong location. Lateral misalignment gives errors proportional to the slope of the wavefront [3]. Errors due to longitudinal misalignment are less sensitive if the hologram is placed in collimated light. Generally alignment marks, crosshairs, are placed on the CGH to aid in the alignment. Another good feature of a CGH test is that additional holographic structures can be placed on the CGH to produce alignment spots for the optical setup. Now that high quality plotters are available, CGHs are widely used in the testing of aspheric optics.

3 Phase-shifting interferometry

I started to work with phase-shifting interferometry in about 1970 for adaptive optics for classified defense systems and it has been part of most of my work since then. At that time, phase-shifting techniques were not very useful because the necessary detector arrays, computers, and electronics were not yet available. Fortunately, this has completely changed and now phase-shifting interferometry is commonly used and it is the best way of getting interferogram data into a computer.

In phase-shifting interferometry measurements are made of the irradiance of the interference pattern as the phase difference between the two interfering beams is changed. The phase difference can be made in discrete steps or it can be changed at a constant rate as the detector is read out three or more times. If the irradiance of the interference pattern is given by

$$I(x,y) = I_{dc} + I_{ac}Cos[\phi(x,y) + \alpha(t)]$$

and four frames of data are taken as the phase changes by 90^o between the readouts, the phase is given by

$$\phi(x,y) = ArcTan[\frac{I_4(x,y) - I_2(x,y)}{I_1(x,y) - I_3(x,y)}]$$

While this is a very simple equation, it is very powerful and an excellent way of getting interferogram data into a computer because the subtraction and division cancel out the effects of fixed pattern noise and gain variations across the detector, as long as the effects are not so large that the dynamic range of the detector becomes too small to be of use [9].

4 Computerized interference microscope

In about 1980 I became interested in the use of interference microscopes for the measuring of surface roughness. At about the same time solid state detector arrays and personal computers became available so it made sense to make a phase-shifting interference microscope and this led to the start of a company, WYKO Corporation, for the design, manufacture, and selling of phase-shifting interference microscopes. This section describes a computerized interferometric microscope system for the measurement of surface microstructure where a repeatability of the surface height measurements of less than 0.1 nm can be obtained for smooth surfaces and

by using vertical scanning techniques surfaces having height variations larger than 500 microns can be measured to within an accuracy of a few nanometers.

Figure 3 shows a simplified schematic of the instrument [10-12]. The configuration shown in the figure utilizes a two-beam Mirau interferometer at the microscope objective. A tungsten halogen lamp is used as the light source. In the phase shifting mode of operation, a spectral filter of 40 nm bandwidth centered at 650 nm is used to increase the coherence length. For the vertical scanning mode of operation described below the spectral filter is not used. Light reflected from the test surface interferes with light reflected from the reference. The resulting interference pattern is imaged onto the CCD array. The output of the CCD is digitized and read by the computer. The Mirau interferometer is mounted on either a piezoelectric transducer (PZT) or a motorized stage so that it can be moved. During this movement, the distance from the lens to the reference surface remains fixed. Thus, a phase shift is introduced into one arm of the interferometer. By introducing a phase shift into only one arm while recording the interference pattern that is produced, it is possible to perform either the phase-shifting technique described above or the vertical scanning coherence sensing technique also described below.

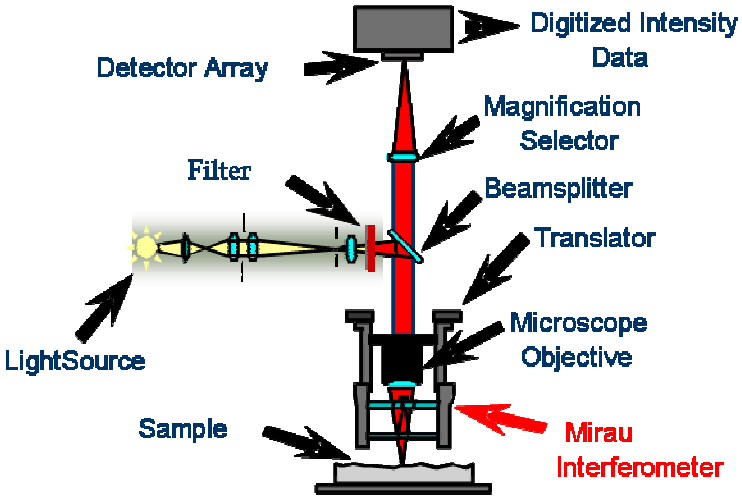

Fig. 3. Interference microscope

In the phase-shifting mode of operation the phase is obtained by calculating the arc tangent which gives the phase modulo 2π and hence there may be discontinuities present in the calculated phase. These 2π

discontinuities can be removed as long as the slopes on the sample being measured are limited so that the actual phase difference between adjacent pixels is less than π (surface height must change by less than a quarter-wavelength). The dynamic range can be increased by performing the measurement at two or more wavelengths [13], but a better way is to use vertical scanning [14-16].

In the vertical scanning coherence sensing mode of operation an unfiltered white light source is used. Due to the large spectral bandwidth of the source, the coherence length of the source is short, and good contrast fringes will be obtained only when the two paths of the interferometer are closely matched in length. Thus, if in the interference microscope the path length of the sample arm of the interferometer is varied, the height variations across the sample can be determined by looking at the sample position for which the fringe contrast is a maximum. In this measurement there are no height ambiguities and since in a properly adjusted interferometer the sample is in focus when the maximum fringe contrast is obtained, there are no focus errors in the measurement of surface microstructure. In the vertical scanning mode, nearly any type of surface can be measured as long as the reflected light gets back through the microscope objective.

5 Dynamic (single-shot) interferometry

Phase-shifting interferometry is extremely useful for the testing of optics, but in many situations, especially for the testing of large telescope optics, the measurement accuracy is limited by the environment and sometimes the environment is sufficiently bad that the measurement cannot be performed. This section describes some work I have recently been involved with in reducing effects of vibration by using dynamic (single-shot) interferometry techniques. The single-shot interferometer described is insensitive to vibration and many measurements can be averaged to reduce the effects of air turbulence enabling the precision measurement of large optical components.

In conventional phase-shifting interferometry 3 or more interferograms are obtained where the phase difference between the two interfering beams changes by 90-degrees between consecutive interferograms. Vibration effects can be reduced if all the phase-shifted frames are taken simultaneously. There are several ways of obtaining all the phase-shifted frames simultaneously. A technique that works well with multiple wavelengths or white light involves the use of a quarter waveplate followed by linear polarizers at different angles. For this technique the

phase shift between the two interfering beams is nearly independent of wavelength. The quarter waveplate is oriented to convert the test beam into left-handed circular polarization and the reference beam into right-handed circular polarization. It can be shown [17] that if these circularly polarized beams are transmitted through a linear polarizer a phase-shift between the two interfering beams proportional to twice the rotation angle of the polarizer results.

Thus, if a phase mask is made of an array of 4 linear polarizer elements having their transmission axes at 0, 45, 90, and -45 degrees as shown in Figure 4a, where a polarizer element is placed over each detector element, the mask will produce an array of four 0, $\pi/2$, π, and $-\pi/2$ degrees phase shifted interferograms. Figure 4b shows how the phase filter is made up of an array of 4 polarizer elements. The size of the polarizer elements must be equal to the size of the pixels making up the detector array. Below we will show how this polarizer array can be used with both Twyman-Green and Fizeau interferometers.

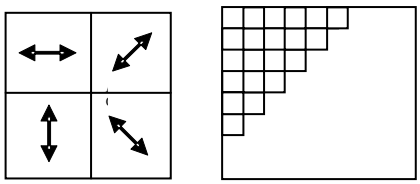

Fig. 4. Phase filter. (a) 4 polarizer elements giving 0, 90, 180, and -90^{o} phase shifts. (b) Phase filter made up of array of 4 polarizer elements.

5.1 Simultaneous (single-shot) Twyman-Green interferometer

Figure 5 shows a schematic of a Twyman-Green interferometer using the micropolarizer phase-shifting array. The essential characteristics of the two-beam interferometer is that the test and reference beams have orthogonal polarization and the size of the micropolarizer array matches the CCD array.

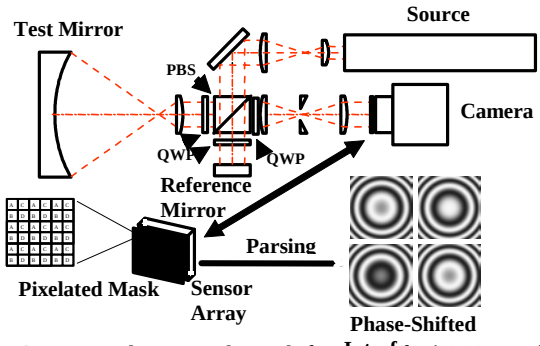

Fig. 5. Twyman-Green simultaneous phase-shifting interferometer configuration

Using this interferometer it is possible to have the optics under test and the interferometer on different tables without any vibration isolation. By averaging several frames of data the effects of air turbulence can be minimized. If a surface is vibrating it is possible to determine precisely how the surface is vibrating. Movies can be made showing how the shape of the vibrating surface is changing in time.

5.2 Single-shot laser-based Fizeau interferometer

A single-shot laser-based Fizeau interferometer is more difficult to construct than a Twyman-Green interferometer because the Fizeau is more common path and it is hard to obtain a reference and test beam having orthogonal polarization. In principle, a quarter-wave plate can be placed between the test and reference surfaces to rotate the direction of polarization of the test beam by 90 degrees, but in practice this does not work well, especially for the testing of spherical optics. Techniques where the reference and test beams are tilted with respect to each other have been described, but a better approach is the on-axis approach shown below [18].

In the interferometer shown in Figure 6 a short coherence light source is used. The source beam consists of two path delayed orthogonally polarized beams. The path difference between the two beams is set equal to the path difference in the Fizeau cavity. The desired interference results from the long path source beam reflected off the reference surface and the short path length source beam reflected off the test surface. All beams are on-axis so off-axis aberrations are not a problem. Since both source beams are reflected off both test and reference surfaces and only the two path-length matched beams give interference, the fringe contrast is reduced, but it is still more than adequate. Since a short coherence light source is used,

spurious fringes are greatly reduced. One source that works well is a modulated diode having a coherence length of approximately 300 microns.

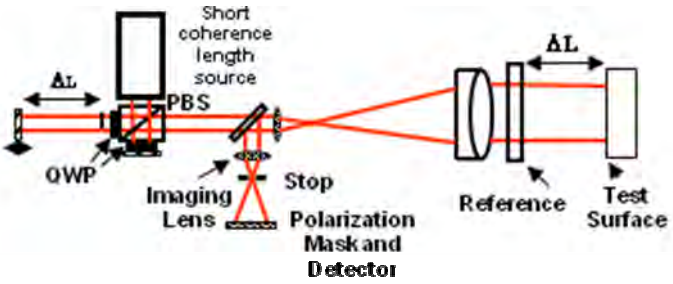

Fig. 6. Simultaneous phase-shifting Fizeau – short coherence length source.

This interferometer shown in Figure 6 can be used for testing windows having nearly parallel surfaces. If a long coherence source is used spurious fringes are obtained as shown in Figure 7, however with the short coherence source interferometer spurious fringes are eliminated and by selecting ΔL, it is possible to look at the fringes for reflection off the first surface or the second surface.

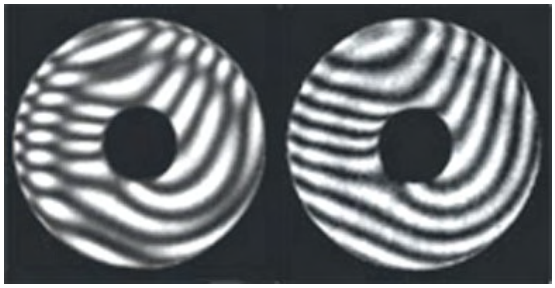

Fig. 7. Interference Fringes Obtain Testing a Thin Glass Plate. a) Long coherence length source. b) Short coherence length source.

A single-shot interferometer can go a long way in reducing the effects of what is often the largest source of error in phase-shifting interferometry, namely vibration. Errors due to air turbulence can be reduced by averaging many frames of data obtained using a single-shot interferometer. Averaging data frames in the presence of vibration will average out the double frequency errors common in phase-shifting interferometry and generally more accurate results can be obtained in the presence of vibration than can normally be obtained using conventional temporal phase-shifting interferometry in the absence of vibration. Also, it is

possible to measure a vibrating surface to determine precisely how the surface is vibrating and movies can be made showing how the vibrating surface shape changes. Once a person works with a simultaneous phase-shifting interferometer it is hard to go back to working with a temporal phase-shifting interferometer.

6 References

1. A. W. Lohmann and D. P. Paris, Appl. Opt. 6, 1739 (1967).
2. A. J. MacGovern and J. C. Wyant, Appl. Opt. 10, 619, (1971).
3. J. C. Wyant and V. P. Bennett, Appl. Opt. 11, 2833, (1972).
4. Y.-C. Chang and J. H. Burge, SPIE Proc. Vol. 3782, 358, (1999).
5. J. C. Wyant and P. K. O'Neill, Appl. Opt. 13, 2762, (1974).
6. Mathias Beyerlein, Norbert Lindlein, and Johannes Schwider, Appl. Opt. 41, 2440, (2002).
7. Stephan Reichelt, Christof Pruss, and Hans J. Tiziani, Appl. Opt. 42, 4468, (2003).
8. Steven M. Arnold and Robert Kestner, Proc. SPIE 2536, 117, (1995).
9. J. C. Wyant, "Use of an ac heterodyne lateral shear interferometer with real-time wavefront corrections systems," Appl. Opt. 14(11):2622-2626, Nov. 1975.
10. B. Bhushan, J.C. Wyant and C.L. Koliopoulos, "Measurement of surface topography of magnetic tapes by Mirau interferometry", Appl. Opt., 28:1489-1497, 1985.
11. J.C. Wyant, "Optical profilers for surface roughness", Proceedings of the Society of Photo-Optical Instrumentation Engineers, 525, 174-180, 1985.
12. J. C. Wyant and K. Creath, "Advances in Interferometric Optical Profiling," Int. J. Mach. Tools Manufact. Vol. 32, No.1/2, 5-10(1992).
13. U.S. Patent No. 4,832,489 "Two-wavelength phase-shifting interferometer and method," James C. Wyant and K. Creath, 1989.
14. M. Davidson, K. Kaufman, I. Mazor, and F. Cohen, "An Application of Interference Microscopy to Integrated Circuit Inspection and Metrology," Proc. SPIE, 775, 233-247 (1987).
15. T. Dresel, G. Hausler, and H. Venzke, "Three-dimensional sensing of rough surfaces by coherence radar," Appl. Opt. 31(7):919-3925, March 1992.
16. P. J. Caber, "An Interferometric Profiler for Rough Surfaces," Appl. Opt. 32(19):3438-3441, July 1993.
17. S. Suja Helen, M.P. Kothiyal, and R.S. Sirohi, "Achromatic phase-shifting by a rotating polarizer", Opt. Comm. 154, 249 (1998).
18. Neal Brock, John Hayes, Brad Kimbrough, James Millerd, Michael North-Morris, Matt Novak and James C. Wyant, "Dynamic Interferometry," Proc. SPIE 5875, 58750F-1, (2005).

Multifunctional Encoding System for Assessment of Movable Cultural Heritage

V Tornari[1], E. Bernikola[1], K. Hatziyannakis[1], W Osten[2], R, M, Grooves[2], M. Georges[3], T. Cedric[3], G. M. Hustinx[4], J. Rochet[4], E Kouloumpi[5], M. Doulgeridis[5], T. Green[6], S Hackney[6]
1. Foundation for Research and Technology-Hellas (FORTH), Institute of Electronic Structure and Laser (IESL), Vassilika Vouton-Voutes, 71110 Heraklion, Crete, Greece.
2. ITO Institut für Technische Optik, Universität Stuttgart, Pfaffenwaldring 9,70569 Stuttgart, Germany.
3. Centre Spatial de Liège, Liege Science Park, 4031, Angleur Liege, Belgium
4. OPTRION, Spatiopôle – Rue des Chasseurs Ardennais, B-4031 Liege, Belgium
5. Conservation Department, National Gallery – Alexandros Soutzos Museum,1 Michalacopoulou Street, 11601, Athens, Greece.
6. Conservation Department, Tate, Millbank, London SW1P 4RG, UK

Abstract

Implementation of non destructive and non contact holographic techniques is being exploited for providing responses of the artwork in the encoded form of fringe patterns. The parametrical usage of the fringe formation allows correlation to originality and impact versus time. Signatures of artwork are formed and if monitored over time provide impact and originality assessment. The paper refers to a European Commission funded research project during the 6th framework program with special task in impact assessment in movable cultural heritage.

1 Introduction

Art in transit is under threat from mishandling and fraud. The thermal and moisture related degradation processes, transportation and handling, various conservation and restoration actions, as well as the display and arrangement may systematically or rapidly influence the condition of the concerned artwork, monument or antique. A competitive tool to visualize

invisible defects, disintegration processes and interventions has been introduced through the principles of holographic interferometry [1-5].

Holography and related techniques involved in artwork structural diagnosis are classified as non-destructive, non-contact, and non-invasive since do not require any sample removal or surface preparation and are safe for use on varnishes and pigments. The methodology to visualize the defects of interest is based on differential displacement provoked in time by two slightly different positions of the artwork through external induced excitation. The displacement results in a relative optical path change of the reflected beam significantly modulated by the excited bulk defects influencing the surface. The procedure is repeatable and each phase map results in an “encoded” response of the examined artwork indicating its conservation state correlated to a distinct data collected over time.

2 Data collection and comparison

The comparison of data collected over time is based on standardised series of operations to collect, compare and update of *signatures* from time to time. Data is retrieved by hybrid combination of interferometry techniques that provide separate working modes such as a) "live mode", b) "high resolution mode", c) “vibration immune mode". Each mode is either used as a stand alone result corresponding to experimental constrains and preferences or as a cross-checking feed back to the results of the other modes.

In conditions similar to out-of-laboratory test the preferred choice is a geometry less sensitive to vibrations which allows for a fast overview of the condition [6]. Next usual step is the live mode to monitor dynamic reaction to change whereas the high resolution mode is preferred in normal laboratory conditions for detailed investigation of defects [7, 8]. The geometries of the three modes are seen in figure 1a-c accordingly.

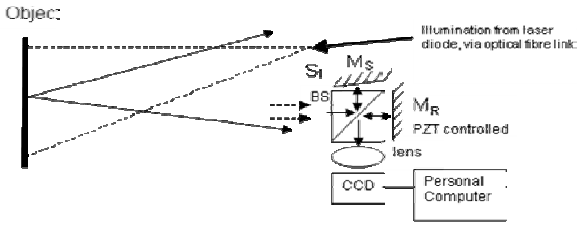

a) Out-of-plane sensitive sheared configuration for immune vibration mode. BS, beamsplitter; M_S, shearing mirror; M_R reference mirror

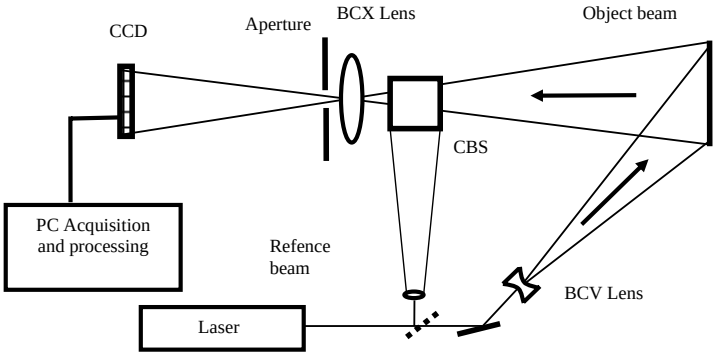

b) Out-of-plane sensitive digital holographic speckle pattern interferometry for live mode, CBS Combıning Beam Splitter, recombination at angle θ°

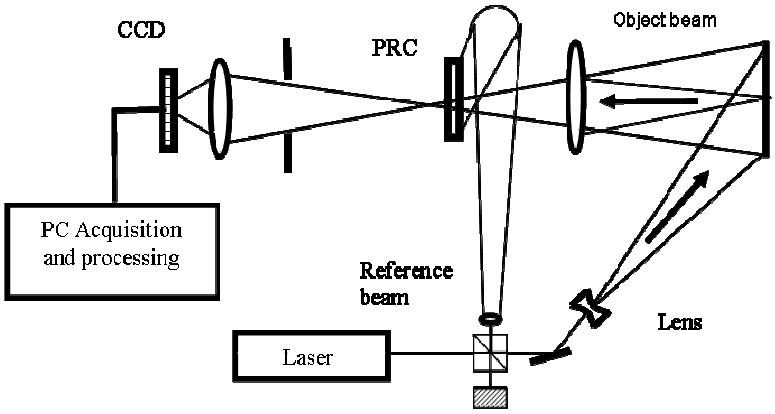

Fig.1(a-c). The geometries used to achieve the multifunctional investigation scheme to assess impact in artwork conservation

Figure 1 shows sketches of digital capturing holography geometries used for the investigation. Light from a laser (532 nm) serves to illuminate the object and enter into a shearing interferometer scheme as in a, or be divided for object and a reference beam as in b, c. The object beam illuminates the object and some of the light is scattered by the object in the observation direction towards the detector, where a positive lens forms an image of the object on a CCD sensor where the result of the interference between the reference beam and the object beam is gormed. The aperture serves to limit the spatial frequencies of the interference pattern. The

reference beam diverges toward the detector system from a biconcave lens or mirror located off-axis. The phase maps obtained show fringes sensitive to out-of-plane displacement.

The sample is recorded at an initial rest state and then is uniformly thermally excited to provoke an optical path difference among two or more sequential recordings. Thermal diffusion into the bulk excites the internal hidden defects which provide a differential to the rest of the body displacement. Each localised fringe pattern is stored and compared in future measurements for any changes with the amount and value of change being referred as impact.

Essential experimental parameters related to artwork and measurement protocol are stored in a dedicated database. The *signature* comparison over time required the development of specialised post-processing software and routines for measurement and signature selection. The comparison over time is secured through critical steps of co-registration and matching ratio algorithms described elsewhere in this volume [9].

3 Results

The experiments were carried out on samples simulating real artwork cases from paintings conservation either for canvas and panel paintings. As an example here an icon sample on wood support with known defects is seen in fig 2, examined with high resolution arrangement before and after ageing process. The sample was artificially aged by an aging protocol aiming to generate a natural aging of ≈60 years. The results confirm that even small impact which is a usual case in artwork conservation research can be detected and assessed. In the second result shown here in figure 4 a canvas painting was tested for accidental impact in transportation stimulated by a hammer hit.

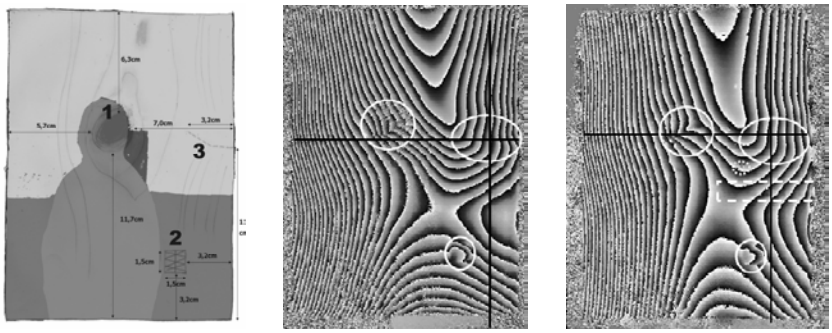

(a) (b)

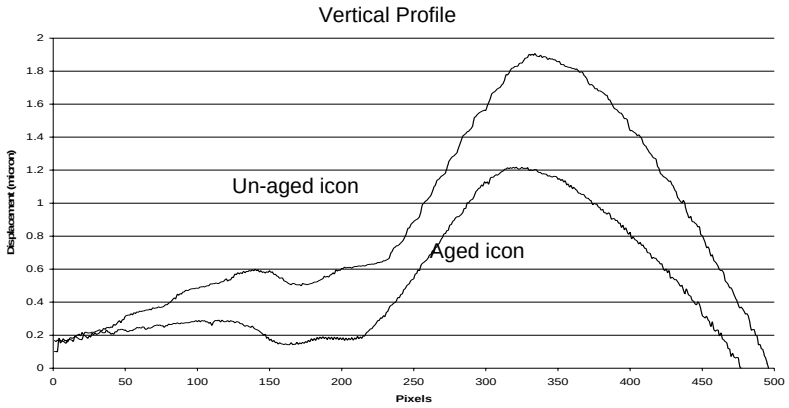

(c)

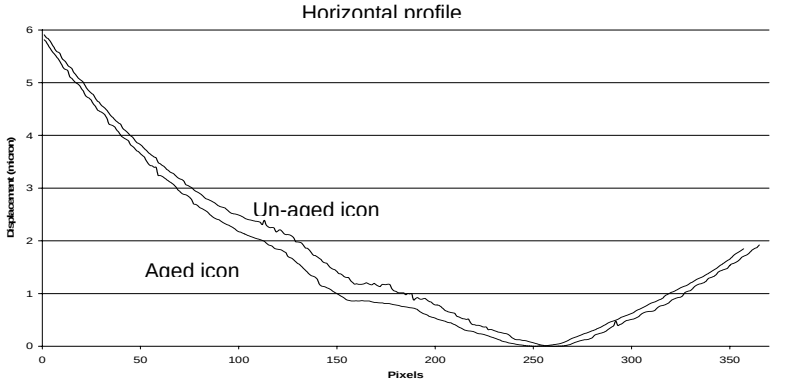

(d)

Fig. 2. Interferograms obtained before (a) and after (b) ageing, with (c-d) corresponding impact seen in displacement graphs drawn accordingly along the yellow lines, known defects are shown in red.

A naturally aged sample is expected to loose mechanical stability producing higher miscrostructure deformation and get higher displacement when compared under the same excitation and experimental boundary conditions. In the example of fig 2 is seen a decrease of displacement after aging proving that the initially tested un-aged sample was still fresh after construction and the artificial aging of 60 yrs just provided a better cohesion. The experimental aim was however reached since the change in either positive or negative impact concept is still small and non traceable by other techniques. In figure 3 is seen an example of icons before and after aging and conservation processes. The changes remain small but the probability of detection of change remains high >75% for all modes.

The thermal response is measured by a thermometer array from the surface of the sample. Although the cycles of impact do not alter the fringe pattern radically but steadily is worth noticing the change in the ΔT of the surface reaction at the same time after excitation indicating a slow degradation process as an effect of impact on mechanical integrity. In real aged artwork cases the mechanical decay allows high thermal diffusivity to be observed faster imposing narrow temporal windows for successful fringe formation.

Another interesting aspect of the techniques is the visulisation of instant impact without mechanical deterioration of the rest of the structure. In figure 4 is seen the canvas painting response to a hammer lasting for several days as it relaxes back to initial position.

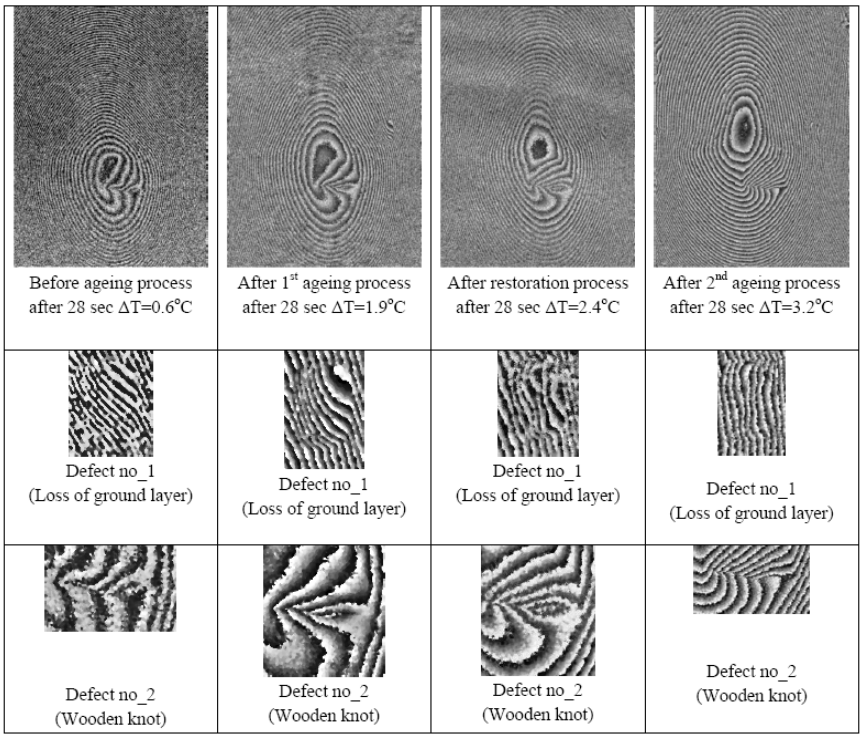

Fig. 3. Small changes in the same sample before and after cycles of impact are detected. In details known defects are repeatably present in the fringe formation acting as signatures

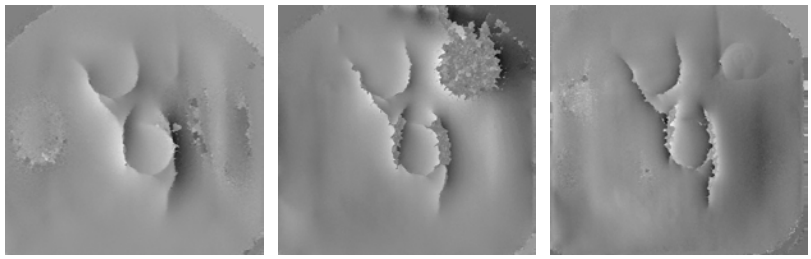

(a) (b) (c)

Fig. 4. The strain map (a) before impact, (b) 5 minutes after impact and (c) 1 week after impact. The field of view is the complete canvas 350x350 mm.

4 Conclusions

Coherent interferometry becomes a powerful method to assess impact on delicate objects such as works of art. Without any contact with precious surface and with non invasive and non destructive experimental procedure one can remotely assess fast and repeatable the whole surface or whole areas of interest from the artwork concerned. Aging, restoration, accidents can be revealed from the fringes of coherent interferometry as the artwork keeps the memory of the previous events in small scale of measurements which can only be revealed by the high spatial density content of coherent out-of-plane interferometry. The interferograms constitute rich sources of information in regards to multiple functions in art conservation applications and detection capability is not limited in defect detection but can be broadened in new fields of research such as impact detection and assessment.

5 Acknowledgments

The research project was funded by EC 6th FWP.

6 References

1. Vest, C. M. (1979) Holographic Interferometry. Wiley, New York
2. Amadesi, S, D'Altorio, A, Paoletti, D (1983) Real-time holography for microcrack detection in ancient golden paintings. Optical Engineering 22: 660-662

3. Tornari, V, Zafiropulos, V, Bonarou, A, Vainos, N. A, Fotakis, C (2000) Modern technology in artwork conservation: A laser based approach for process control and evaluation. J. Opt. Las. Eng., 34: 309-326.
4. Mieth, U, Osten, W, Juptner, W (2001) Investigation on the appearance of materials faults in holographic interferograms. Fringe 2001:163-173
5. Fotakis, C, Anglos, D, Zafiropulos, V, Georgiou, S, Tornari, V (2006) Lasers in the Preservation of Cultural Heritage; Principles and applications.Ed. R. G. W. Brown, E. R. Pike (Taylor and Francis, New York 2006).
6. Osten W, Kalms M, Juptner W, Tober G, Bisle D, Sherling D, (2000) A shearographic system for the testing of large scale aircraft components taking into account non cooperative surfaces. Proc SPIE 4101B:432–438
7. Thizy, C, Georges, M. P, Kouloumpi, E, Green, T, Hackney, S, Tornari, V (2007) Photorefractive Holographic Interferometry for Movable Artwork Assessment, in Controlling Light with Light: Photorefractive Effects, Photosensitivity, Fiber Gratings, Photonic Materials and More, OSA Technical Digest (CD) (Optical Society of America, 2007), paper MB49
8. Tornari, V (2007) Laser Interference-Based Techniques and Applications in Structural Inspection of Works of Art. Analytical and Bioanalytical Chemistry 387: 761-80
9. Groves, R.M, Derauw, D, Thizy, C, Alexeenko, I, Osten, W, Georges, M, Tornari, V Automated phase map referencing against historic phase map data (find elsewhere in same volume)

Investigation of electronic PCB component with two-color digital holographic interferometry

Patrice Tankam[1], D. Mounier[2], Eric Moisson[3], Pascal Picart[1],
[1]LAUM CNRS, Université du Maine, Avenue Olivier Messiaen, 72085 LE MANS Cedex 9, France
[2]LPEC CNRS, Université du Maine, Avenue Olivier Messiaen, 72085 LE MANS Cedex 9, France
[3]VALEO, 45 rue Charles de Coulomb, 14125 Mondeville Cedex, France

1 Introduction

Digital holography originated in the early 1970's and became properly available in the last decade [1,2] with high speed CCD cameras and the increasing power of computers. Recently, it has been demonstrated that digital Fresnel holography offers new opportunities for metrological applications: examples include object deformation [2], surface shape measurement [3] and twin-sensitivity measurements [4]. Recently we demonstrated some opportunities for simultaneous two-dimensional metrology by use of digital color holography and recording with a stack of photodiode sensor [4]. This paper presents an alternative method in which the recording is performed simultaneously along each wavelength by a two-color spatial multiplexing of the encoded object. In order to compensate the wavelength dependence of the pixel pitch in the Fresnel transform and to save the physical horizon of the object, we present a spectral scanning algorithm based on the Fresnel transfer function of the free space propagation.

2 Theoretical basics

At distance d_R, the diffracted field is related to the object field by a convolution relation between the initial field $U(x,y,z)$ and the convolution kernel, according to $U(x,y,z+d_R)=U(x,y,z)*h(x,y,d_R)$, in which the convolution kernel is the impulse response of free space propagation given by Eq. 1:

$$h(x, y, d_R) = \exp\left[\frac{i\pi}{\lambda d_R}\left(x^2 + y^2\right)\right] \quad (1)$$

With the computation of diffraction as a convolution formula, the pixel pitch in the reconstructed plane remains invariant and is equal to that of the detector, whatever the wavelength. Thus, this strategy is the more appropriate for digital color holography. In terms of spatial frequency bandwidth, it is necessary that the bandwidth of the kernel covers at least the full bandwidth of the object. If the object bandwidth is greater than that of the kernel, the numerical reconstruction must be implemented with a scanning of the spatial spectrum. In the x direction, if Δu_{object} is the bandwidth of the object and Δu_{kernel} that of the kernel, then the number of scanning is given by $n_x = \Delta A / Np_x$ (ratio between object size ΔA and detector size Np_x). A similar relation holds for the vertical direction y with number n_y. The size of the full reconstructed object will be $n_yM \times n_xN$. To reconstruct a region of the object centered at spatial coordinate $\{x_i,y_i\}$ with spatial extension of ($Np_x \times Mp_y$), the spectral filter must be centred at frequency $\{u_i,v_i\} = \{x_i/\lambda d_R, y_i/\lambda d_R\}$ in the hologram spectrum. The centering of the filter is performed by modulating the convolution kernel, according to $h_i(x, y, d_R) = h(x, y, d_R) \times \exp\left[+2j\pi(u_i x + v_i y)\right]$. The useful spatial frequencies of the filter bank are given in x and y directions by $\{u_i, v_i\} = \left\{u_0^\lambda + k_x Np_x / \lambda d_R, v_0^\lambda + k_y Mp_y / \lambda d_R\right\}$, with $k_x \in \left\{-(n_x - 1)/2, +(n_x - 1)/2\right\}$ and $k_y \in \left\{-(n_y - 1)/2, +(n_y - 1)/2\right\}$ and $\left\{u_0^\lambda, v_0^\lambda\right\}$ are the central spatial frequencies along each wavelength. This method allows a perfect pixel to pixel superposition between red and green reconstructed objects.

3 Experimental setup and results

Application of the proposed method is demonstrated through an investigation of mechanical causes of cracks inside a capacitance of an industrial PCB component. The component (capacitance) is cracked during the clamping of the PCB inside its electronics box. The investigation of the causes of this anomaly is made possible since digital holography is well adapted for contact less metrology and micro deformation measurements. Fig. 1 shows the component under interest and the region that is inspected by the two-color digital holographic set-up. The studied field is the circular blue zone which is 15mm in diameter, and containing the clamping zone

and the component of interest. The PCB is placed at 900mm from the sensor (monochrome CCD, 1024×1360 pixels with 4.65μm pitches). The mechanical simulation of the clamping is realized by use of a progressive loading of the rear panel of the PCB through the clamping region. This reproduces with a very good fidelity the real industrial situation. Fig. 1 shows a schematic of the optical set-up which includes two continuous lasers (green at 532nm and red at 632.8nm). The two object beams are collimated and illuminating the PCB with two symmetrical angles (θ_R=$-\theta_G$) thus giving a 2D sensitivity.

The proposed algorithm for the object reconstruction generates a set of 3×3 adjacent sub-images along each color. The optical phase changes between loadings of the PCB can be computed and since the physical object horizon is saved, differences between red and green phase changes can be computed in order to get the 2D measurement. The full procedure needs the recording of 90 two-color holograms. Fig. 2 shows the in plane and out of plane displacement field obtained after processing of the holograms. Note that the capacitance is localized in the region where the flexion is maximum. The After numerical processing of these results, Fig. 3,4 show the region of the component under interest which exhibit high non uniform deformations. These non uniform deformations are the cause of the cracking of the capacitance.

4 Conclusion

The paper has presented a two-color digital holographic setup and method for simultaneous two-dimensional metrology. Experimental results are presented in the case of the investigation of mechanical causes of cracks inside a capacitance of an industrial PCB component. The two-color holographic set-up gives then opportunities for a thorough understanding of causes of cracks inside the capacitance of this industrial PCB component.

5 References

1. Schnars, U, Jüptner, W (1994) Direct recording of holograms by a CCD target and numerical reconstruction. Applied Optics 33:179-181
2. Pedrini, G, Tiziani, HJ (1995) Digital double pulse holographic interferometry using Fresnel and image plane holograms. Measurement 18:251-260

3. Wagner, C, Seebacher, S, Osten, W, Juptner, W (1999) Digital recording and numerical reconstruction of lens less Fourier holograms in optical metrology. Applied Optics 28: 4812-4820
4. Picart, P, Mounier, D, Desse, JM (2008) High resolution digital two-color holographic metrology. Optics Letters 33:276-278

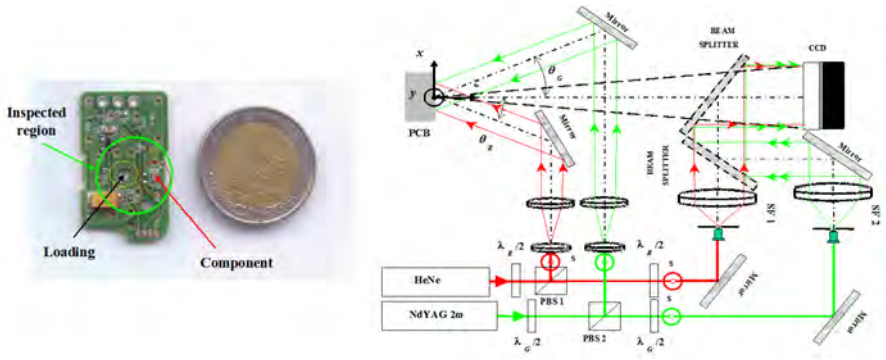

Fig. 1. PCD component under test and holographic set-up using two wavelengths: M: Mirrors, BS: beam splitter; SF: spatial filter

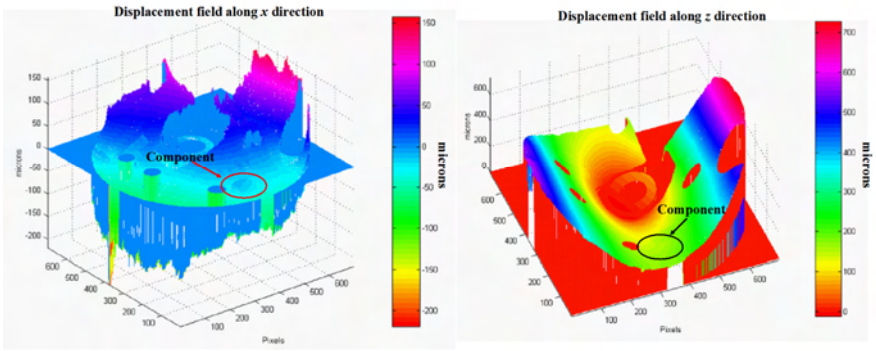

Fig. 2. In plane displacement field measured with 90 two-color holograms (left) and out of plane displacement field measured with 90 two-color holograms (right)

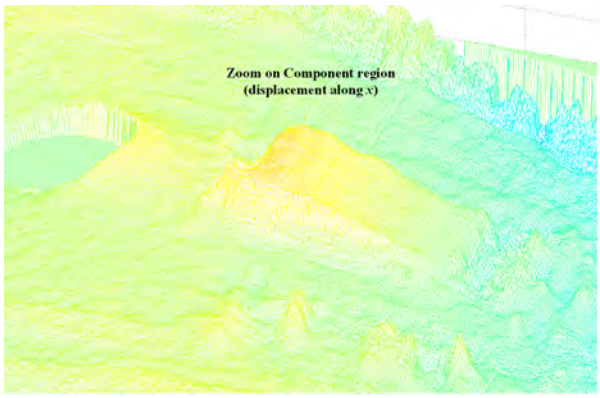

Fig. 3. In plane displacement field in the region of the capacitance after post processing

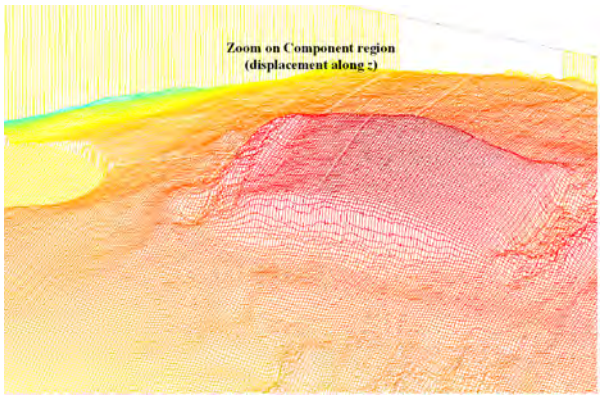

Fig. 4. Out of plane displacement field in the region of the capacitance after post processing

Integrated Microinterferometric Sensor

J. Krężel, M. Kujawińska
Warsaw University of Technology, Institute of Micromechanics and Photonics, 02-525 Warsaw, 8 Sw. A. Boboli St., Poland

1 Introduction

Continuous development of various technologies offers new possibilities for design and fabrication of novel non-contact measurement devices, whose scale is better fitted to the scale of a measured object/area. Application of replication microtechnologies enables mass production of low-cost or almost disposal sensors with the same properties as their bulk opto-mechanical equivalents. On the other hand there is a raising requirement of monitoring a variety of engineering structures with submicron resolution. Based on these facts we have developed the low-cost, full-field, optical sensor for measurement of in-plane displacement fields by means of grating interferometry (GI) (fig. 1a.).

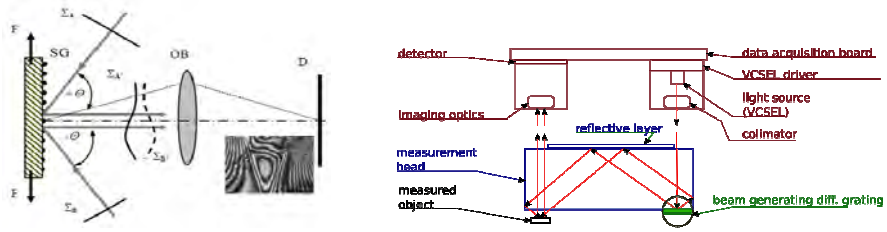

a) **b)**

Fig. 3. The principle of grating interferometry: a) the general scheme and b) the scheme of the miniaturized GI based sensor based on the Czarnek's configuration.

The technique requires a diffraction grating integrated with measured surface of an object and illuminated by two mutually coherent beams referring to +1 and -1 diffraction order. The idea of the measurement head providing the object illumination with lowered sensitivity for vibration and wavelength variations, had been proposed by R. Czarnek [1] and was implemented in the proposed below interferometric extensometer (fig. 1b). The extensometer consists of two modules: (i) illumination and detection module with VCSEL (λ= 665nm, linearly polarized light) as a light source,

collimator, imaging optics and CMOS matrix and (ii) measurement head – a beam guiding block providing proper illumination of an object. The measurement field of the system is 1.4 mm x 1.4 mm, magnification of imaging optics is -3.8x and the spatial frequency of the beams generating and object gratings – 1200 lines/mm. The measurement head is the novel, commercially not available module, so below we present its design and low cost fabrication concept.

2 Measurement head

The measurement head (fig. 2) is a passive module that generates object illumination beams and guides them in order to illuminate the specimen grating according to the GI principle (fig. 1a).

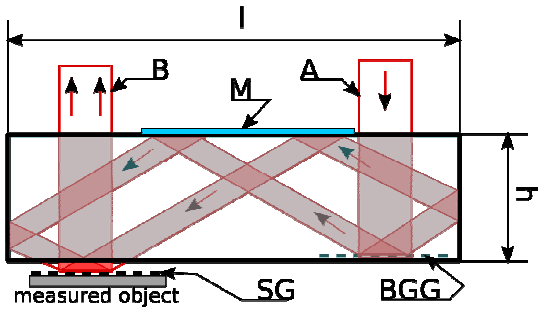

Fig. 2. The scheme of the measurement head. A – input plane beam, B – two output beam carrying conjugated information, M – reflective layer, l – length, h – height, SG – grating integrated on the object surface, BGG – grating integrated with the measurement head

Fabrication of a low-cost system can be achieved by lowering the unit price of the measurement head. The hot-embossing technology has been selected as the best suited replication process for measurement head. The developed technology chain is shown in fig. 3 [2] together with the main parameters of a fabricated structure which has to be optimized in corresponding steps. The hot-embossing process has been optimized to replicate measurement head with optical quality walls and a submicron diffraction grating integrated with part of the structure [2]. It had been partly performed within one of the ENoE NEMO projects and the optimization process is continued within Karlsruhe NANO MICRO Facility.

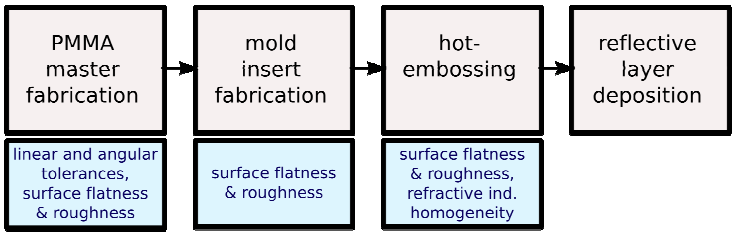

Fig. 3. The technology chain of the measurement head fabrication.

Ray tracing simulation revealed that linear and angular tolerances of measurement head's facets orientation can be up to 0.02 mm and 0.05^{o} respectively (separate influences). Cumulative influence of all tolerances depends on the combination of their influence on the geometry of the measurement head and may lead to unacceptable beam misguiding. Since linear and angular tolerances depend on the master fabrication process only, the replication technology by means of hot embossing should be optimised to fulfil the following requirements: local flatness – 0.12 μm over 4 mm^2, roughness – λ/10.

As the beams are travelling in the PMMA block the very important parameter is its refractive index distribution. It influences the propagation path and wavefront shape of object illumination beams and therefore it has to be investigated carefully. In simulations performed the beam was propagated in the measurement head with refraction index n distribution shown in fig. 4a. The model of this distribution was based on the experimental measurement of integrated refractive index ($\Delta n_{max}=4*10^{-4}$). The distribution of the ref. ind. corresponds to the distribution of stress arising during replica and mold cooling process, which was modeled with finite element method (FEM) and validated with qualitative tomographic measurements.

Simulation revealed that the replication technology is mastered in a sufficient way to replicate the structures with refractive index inhomogeneity low enough to affect the interference pattern in negligible manner (fig. 4b). At the moment the final optimization of the hot embossing technology is performed with the special focus on the flatness of the “working” walls of the structure and the quality of grating replication.

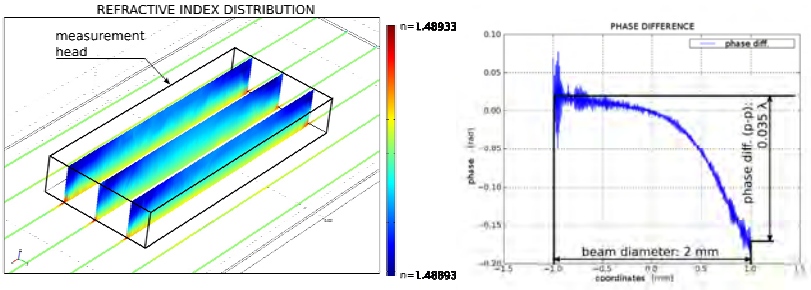

a) **b)**

Fig. 4. Investigation of the refractive index inhomogeneity influence on beam propagation. a) refractive index distribution slices, b) phase difference of two conjugated output beams.

3 Conclusions

The general idea of the miniaturized grating sensor has been verified numerically and is being examined experimentally as a laboratory setup. Applicability for outdoor measurement of the Czarnek's measurement head was proven with measurement on construction with exposure to vibrations and temperature variations. It was proven that it is possible to optimize of the hot embossing replication technology so that it fulfil the requirements of an interferometric system and allows to fabricate low-cost sensors in mass-production. Recently the works are performed within the project MONIT financed by European Funds of Regional Development.

4 References

1. Salbut L., (2002), “Waveguide grating (moire) interferometer for in plane displacement/strain fields investigation”, Opt. Eng. 2002 41, p. 626-631
2. Krajewski R. et al. (2008), “Characterization of the optical parameters of high aspect ratio polymer micro-optical components”, SPIE Proc., vol. 6992, p. 69921B

High Precision Measurement of plane-parallel Parts

Matthias Fleischer, Tobias Gnausch, Daniel Supp, Jonathan Becker
Robert Bosch GmbH
Robert-Bosch-Platz 1, 70839 Gerlingen-Schillerhöhe
Germany

1 Introduction

In the past time interferometry used to be a measurement method mainly used by optical and semiconductor industry. Nowadays we have an increasing amount of optical measurement systems used for applications in machine tools and automotive industry that used to be a domain of tactile measurement systems.

There are some reasons for this. With the ongoing development in e.g. automotive industry to improve energy efficiency as well as to achieve lower emission values there is a need for high precision parts. The measurement techniques follow this trend and in recent years tolerances which as for measurement systems with nanometer resolution have become commonplace.

With the invention of new optical measurement methods like e.g. white light interferometry high precision optical measurement systems developed for the versatility and stability needed for large-scale production under shop floor conditions. The large range of differently shaped parts needs some special applications of interferometric techniques, however.

In this paper we present a novel measurement system that fills a gap in the current range of products of optical measurement systems. It is dedicated to the fast measurent of plane-parallel parts - like sealing plates, gage blocks or casings - with interferometrical resolution. The interesting aspects are the flatness, thickness and parallelism of the parts.

The system is based on a conventional white light interferometer measurement head with a wavefront shaping optic to adjust the setup to the surface of parts with different dimensions. The images of the top and bottom surface of the object are overlayed on the camera and separated by coherence multiplexing. So the moving mass during the complete measurement cycle for both sides of the part is minimal.

Also there is no mechanical movement of the part itself. Therefore a high resolution and repeatability can be achieved.

2 Working principle

The system is based on a short coherent interferometer head with a Michelson setup. Similar setups are already described in the literature [1][2]. Fig. 1 shows the principle. Light from the light source is split into two beams by a beam splitter. One part is directed onto the reference mirror the other part is directed onto the object to be measured. Both the reference mirror and the object are imaged onto the camera.

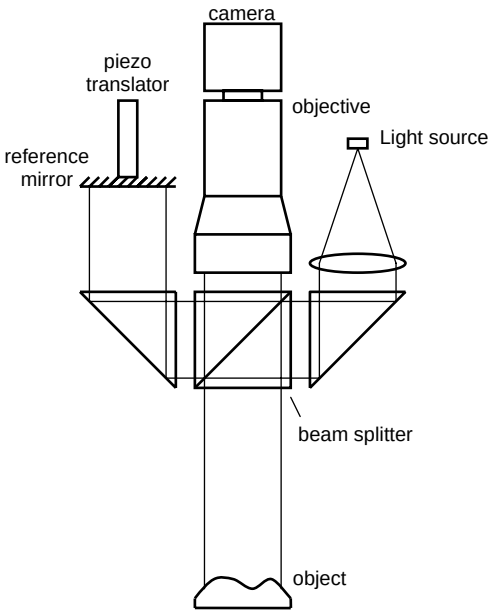

Fig. 1. Schematic of the interferometer head

During the measurement the reference mirror is scanned by means of a piezo translator. The camera acquires are series of images, one for each of the different positions of the piezo translator. The history of one camera pixel over time shows a correlogram which is the real part of the coherence function of the light source. The position of the correlogram in time is equivalent to the position of the object point along the optical axis. There are many methods to evaluate correlograms described in the literature [3]-[9]. All pixels together define a point cloud of the object surface.

This standard interferometer head is integrated into the measurement system as shown in Fig.2. The measurement head is mounted on a translation stage. The light of the object beam is split into two parts by means of a beam splitter. Each of the split beams is redirected with a mirror to one surface of the object. The translation stage allows to focus the system onto the surface of the object so objects of different thicknesses can be measured.

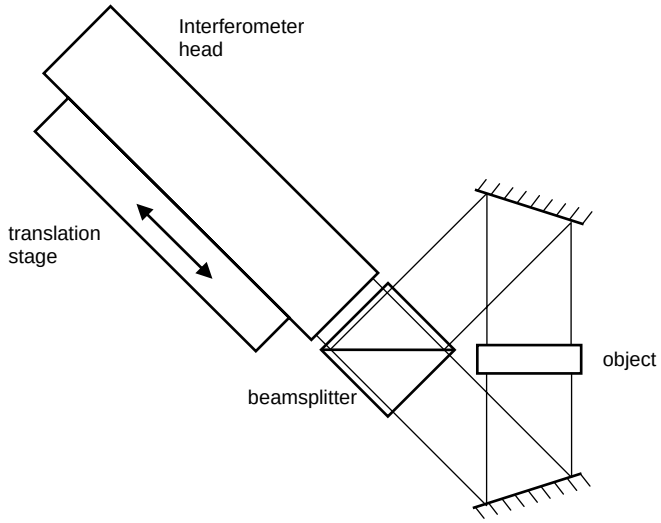

Fig. 2. Schematic of the measurement setup

Both sides of the object are imaged onto the camera simultaneously, so the full lateral resolution of camera and imaging lens can be achieved for both sides of the object.

3 Measurement Procedure

To assure that the pieces of different suppliers fit together, the measured features of production parts need to be traceable to common standards which are supplied by standardization institutes like PTB and NIST. The long-term stability of a system is one important issue when traceable results are required.

In the nanometer range the accuracy once achieved vanishes over time through drift effects introduced by temperature changes. In the longer term decalibration by mechanical shocks and deterioration of the components also add errors to the results. Therefore a system needs to be recalibrated

in regular intervals. This is done on calibrated standards, like e.g. gauge blocks.

4 References

1. Dresel T, Häusler G, Venzke H (1992). Three-dimensional sensing of rough surfaces by coherence radar. Applied optics 31:919-925.
2. Lee B S, Strand T C (1990). Profilometry with a coherence scanning microscope. Applied optics 29:3784-3788.
3. Caber P J (1993). Interferometric profiler for rough surfaces. Applied optics 32:3438-3441.
4. Deck L, de Groot P (1994). High-speed noncontact profiler based on scanning white-light interferometry. Applied optics 33:7334-7338.
5. Larkin K G (1996). Efficient nonlinear algorithm for envelope detection in white light interferometry. Journal of the optical society of America A 13:832-843.
6. Sandoz P, Devillers R, Plata A (1997). Unambiguous profilometry by fringe-order identification in white-light phase-shifting interferometry. Journal of modern optics 44:519-534.
7. Recknagel R J, Notni G (1998). Analysis of white light interferograms using wavelet methods. Optical Community 148:122-128.
8. Aziz D J (1998). Interferometric measurement of surface roughness in engine cylinder walls. Optical Engineering 37:1429-1434.
9. Fleischer M, Windecker R, Tiziani H J (2000). Fast algorithms fort he data reduction in modern optical 3-D profile measurement systems using MMX technology. Applied Optics 39:1290-1297.

Lateral Shearing Interferometry with Simultaneous Detection of both Gradient Fields on a Common Detector Grid

Vanusch Nercissian, Norbert Lindlein
Institute of Optics, Information and Photonics
University of Erlangen-Nürnberg
Staudtstr. 7/B2, 91058 Erlangen
Germany
Klaus Mantel, Irina Harder
Max Planck Institute for the Science of Light
Günther-Scharowski-Str. 1/Bau 24, 91058 Erlangen
Germany

1 Introduction

Planar wave fronts with small deviations from a constant phase can be tested using lateral shearing interferometry. The incoming wave front is split in to two identical copies which are laterally shifted with respect to each other. Their superposition gives, in a first approximation, the gradient component of the wave front under test along the direction of the shear. To reconstruct the original wave front, a second measurement with a shear along the orthogonal direction is necessary.

One possible measuring procedure to obtain the two orthogonal gradient components would be a rotation of the specimen or the shearing unit, respectively. But, this movement has to be carried out in such a manner that the coordinate systems keep in register.

Another approach could be to generate two laterally displaced copies of the wave front under test and then introduce simultaneously orthogonal shears in two orthogonal directions. Although the measurements are performed at the same time, the two interference patterns are now separated on the detector. However, this causes problems in the adjustment of the two gradient fields with respect to the coordinate system of the detector, especially in the presence of global distortions.
Hence, a method is desirable which enables a simultaneous recording of the interference patterns on the same spatial area of the detector.

2 Basic Measurement Principle

To be able to separate the interferograms for the orthogonal gradient components, a polarization signature is applied in the Fourier plane of a telescope, Fig. 1.

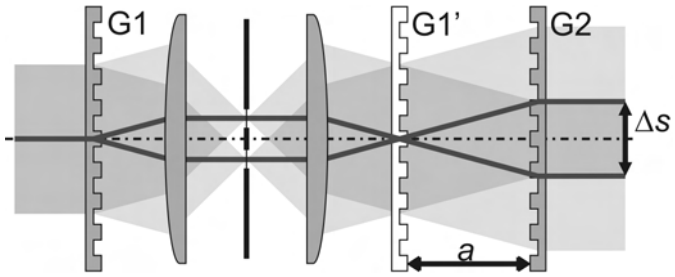

Fig. 1. Scheme of the shear unit consisting of two Ronchi phase gratings and a telescope to provide the possibility for manipulations in the focal plane

The shear is introduced by two Ronchi phase gratings arranged in series [1]. First, we consider the use of line gratings. The grating G1 generates several copies of the incident wave front. Only two diffraction orders can propagate due to a stop in the focal plane. Grating G2, which we assume to have the same period as G1, deflects those two wave fronts parallel to the optical axis. In addition, the two selected copies are laterally shifted with respect to each other in one dimension, providing the desired component of the gradient. The size of the shear Δs depends on the period of the gratings and the distance a between G1' (the image of G1) and G2.

Henceforth, the diffractive approach is expanded to a two dimensional shearing unit. For this purpose, checkerboard structured phase gratings with identical properties in both directions are used. Such a grating can be considered as a sequence of two line gratings rotated by 90 degree with respect to each other. Now, four diffraction orders are selected by the stop, creating two gradient-components in orthogonal directions if combined pairwise. In addition, the two gradients are each endowed with a polarization signature, which is allocated in the same focal plane by a "cross-patterned" polarizer. In this way, the desired components of the gradient of the wave front under test, which are recorded on the same spatial area of the detector, can be identified.

3 Phase Evaluation Methods

Two phase evaluation methods have been tested. If single shot measurements are intended the Takeda algorithm [2] can be used which applies a mathematical separation of the two gradient fields in the Fourier domain. The required carrier frequency interferogram can be produced by the use of gratings with different periods. To avoid the tilt of the wave fronts one can use instead the phase stepping method [3].

The phase shift is carried out by laterally shifting one of the gratings with respect to the other. The polarization signature enables the separation of the gradient fields by using a polarization sensitive detection. One possibility is to apply a pixelated polarization array in front of the camera, which allows to detect both desired fields in one measurement cycle, but reduces the lateral resolution. Another approach utilizing the whole detector grid for both wave fronts is to block one polarization at a time with a rotatable polarizer. Of course, this yields a time delay between the measurements.

4 First Measurement Results

To have a comparison between the different phase evaluation methods, Fig. 2 shows the results of measurements of a common test object. The reason for the discrepancy in the fine structure of the results is under investigation.

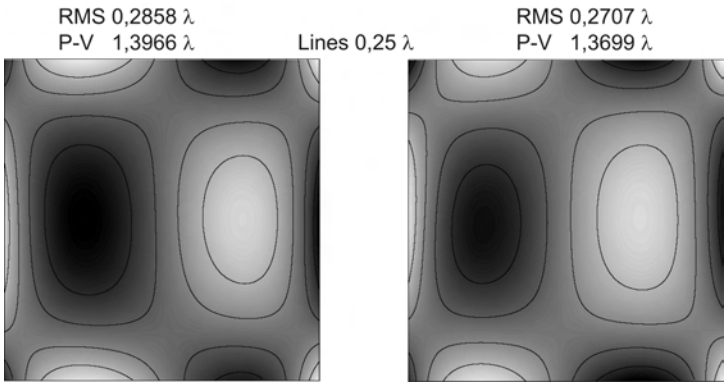

Fig. 2. Reconstructed wave front after numerical integration of the gradient. Left: using a 5 phase algorithm with a rotatable polarizer. Right: using the Takeda algorithm

5 Conclusion

A common path interferometer is presented with the ability of single shot phase evaluation or phase stepping evaluation, which avoids the disadvantage of laterally separated detector grids as well as it reduces the influence of global distortion. The application of lithographically fabricated phase gratings introduces only small errors and provides a simple adjustment of the setup. Nevertheless, the influence of the telescope has to be further investigated. In any case, the systematic aberrations of the setup can be substracted by performing a measurement without specimen.

6 Acknowledgments

This project is supported by the Deutsche Forschungsgemeinschaft.

7 References

1. Schreiber, H, Schwider, J (1997) Lateral shearing interferometer based on two Ronchi phase gratings in series. Applied Optics 36:5321-5324
2. Takeda, M, Ina, H, Kobayashi, S (1982) Fourier-transform method of fringe-pattern analysis for computer-based topography and interferometry. Journal of the Optical Society of America 72:156-160
3. Schwider, J, Burow, R, Elssner, K-E, Grzanna, J, Spolaczyk, R, Merkel, K (1983) Digital wave-front measuring interferometry: some systematic error sources. Applied Optics 22:3421-3432

Near infrared large aperture (24 inches) interferometer system development

Zhu Rihong*, Chen Lei, Gao Zhishan, He Yong, Wang Qing, Guo Renhui, Li Jianxin, Deng Shaogeng, Ma Jun
School of Electronic Engineering and Optoelectronic Techniques, Nanjing University of Science and Technology, Nanjing, 210094, *E-mail: zhurihong@mail.njust.edu.cn, fax: +8625-84315427

1 Introduction

In the past twenty years, our group has developed a series phase-shifting Twyman-Green or Fizeau interferometers. We also developed the simultaneous phase-shifting interferometrer system and the aspherical test system based on CGH, etc. One of our recent works presented in this paper is to develop a near infrared (1055nm) large aperture (24 inches) interferometer which is the first NIR large aperture interferometer in China. It can be used to test the optical element with large aperture, including surface flatness, refractive index homogeneity, etc. The difficulties existed are as follows. Firstly, as the apertures of the optical elements are large, the influence of the stress and temperature on the materials should be considered. Secondly, the alignment of the optical path is difficult as the light is invisible. Thirdly, the demand of the manufacture, test of the large aperture elements and the aligning of the overall system is very strict.

2 Design of the NIR Large Aperture Interferometer

The optical design ensures the quality of the output wavefront and the ability of frequency transfer. And the visible optical path is also designed to aid the aligning of the NIR optical path. The precise machinery ensures the surface quality of the large aperture elements, the test demand of the special angles, the stable movement and adjustment of the air flotation. The electronic part ensures the automation of the adjustment and sampling of the interferograms. The computer ensures the interferograms' adjusting, sampling, processing, wavefront analysis, etc.

2.1 Design of Optical System

Three basic aspects are illustrated below:
(1) The collimator with single aspherical lens is adopted, considering easily alignment and high accuracy output wavefront as well.
(2) In order to maintain the high value of MTF, telecentric system and image system with three levels magnification are adopted to generate proper defocus for the spatial filter. The rotating diffuse flat is cancelled in the formal system.
(3) Using the optical path compensation flat and combination of He-Ne optical path with near infrared optical path solve the alignment problem for near infrared optical path.

In Fig.1, laser from tuneable source (3) is expanded to be collimated light with 24 inches diameter after passing through beam expander, pin-hole and aspherical collimator (2). Then the light enters the interfermetric cavity consisting of fused silica transmission flat (TF) (1) and the ZERODUR reflective flat (RF). Wavefronts reflected by the two flats enter the beam-split after passing collimator, reflective mirror (10). The wavefront is split into two optical paths. One with higher power, reflected by the beam split, is aligned to the infrared CCD target to show the interferogram. The other one is aligned to the centre of crossing mark (14) that is imaged on to the CMOS.

2.2 Solution for supporting the key elements with large aperture

The supporting of key elements used in the system, such as collimator, transmission flat and reflective flat, need to be carefully designed. After

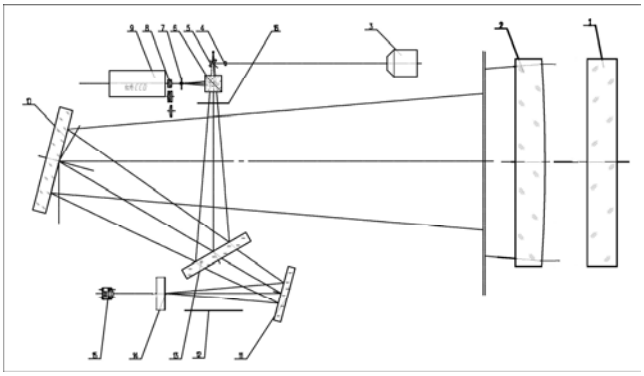

Fig.1. schematic diagram of NIR(1055nm) 24 inches optical system

Finite Element Method calculation with ANSYS, deformations of the elements supported by steel belts are obtained. In order to get the shape change of the surface, it is necessary to subtract the axial displacement of the whole element. The new surface equation is then fitted based on formal designed surface parameter. This data process is necessary for eliminating the elements' aberration. After calculation, side support solution used steel belt is finally proved to be feasible for the system. And experimental result shows that it is better to use chain structure, which is more stable and generates less stress compared with belt structural.

2.3 Algorithm of wavelength tuning interferometry

In our interferometer, the phase shift is induced by wavelength tuning. The phase-shifting value is related not only with the wavelength tuned value $\Delta\lambda$ but also with the cavity length h. To apply the phase-shifting algorithms with a certain step (usually is $\pi/2$), the phase-shifting value should be calibrated when testing at different cavity lengths. The phase calibration method based on the one-dimensional Fourier transform in time domain is developed as follows. The first step is phase calibration. The control voltages are calculated according to the approximate cavity length. Then the voltages are applied to the laser controller to change the output laser wavelength. M-frame interferograms are captured during the phase shifting. Fourier transform is calculated with M intensity values at every data point. After processing, we can get the relationship between the phase-shifting value and the voltages. According to this relationship, the voltages corresponding to $\pi/2$ phase-shifting value are obtained. Then the computer applies the calibrated voltages to the laser controller automatically. The interferograms are captured again. And the phase-shifting values are calculated using the method above. If the phase-shifting value corresponds to $\pi/2$, we can get the wavefront by the overlapping averaging 4-frame algorithms with a certain step. If it does not correspond to $\pi/2$, get the calibrated voltages with the deviation of the phase-shifting value and $\pi/2$. After capturing interferograms and calculating for some times, phase calibration and testing are realized.

3 Fabrication and Measurement for the Large Aperture Optical Elements and system assembly

The precision of the interferometer relies on the flatness of both the large aperture TF and RF. First, the ring polishing machine with diameter of 1 meter is used to polish TF and RF to make their surface flatness within λ/4. Then, the computer-control small grinding head polishing machine is used to revise the flats locally to make the precision of the surface distributions reach λ/10. Finally, the high frequency zonal errors induced by the second step are modified by manual polishing.

The inhomogeneity of TF is measured by the 24 inches Zygo GPI interferometer using four-step method and the result is $\Delta n = 5.74 \times 10^{-6}$ (pv). The absolute surface distributions of TF and RF are obtained by Three Flat Test. Because the test piece can not be rotated because of the deformations induced by mounting, only vertical profiles are obtained.

Due to the invisibility of the infrared light, the common path system is designed in particular both for the visible light and the infrared light. The compensator for the visible light is designed in order to compensate the chromatic aberration. By use of He-Ne laser source, every component of the interferometer is adjusted well enough. Then after changing to the near infrared source, and fine adjustment is achieved to accomplish the regulation. The collimation of the emitting light from the collimator of the interferometer is checked by the pentaprism scanning method which is also used to direct the alignments.

4 Summary

The main problems include in the NIR large aperture interferometer are that the laser source is invisible, the aperture of the optical elements is large, manufacture and test are difficult, aligning the system is hard, etc. The interferometer system will be finished in the near future.

5 Acknowledgments

It is a pleasure to acknowledge the technological contribution of Chengdou Fine Optical Engineering Research Center of China, Schott Company of Germany and NewFocus Company of USA, etc.

Interior Geometry Inspection Using Rerouted Fringe Projection

Omar Abo-Namous, Markus Kästner, Eduard Reithmeier
Institute of Measurement and Automatic Control, Leibniz Universität Hannover
Nienburger Str. 17, 30167 Hannover
Germany
Email: omar.abo-namous@imr.uni-hannover.de

1 Introduction

The transfer project T5 “geometry inspection of optically uncooperative surfaces” is a subproject of the collaborative research centre 489 “Process chain for the production of precision-forged high-performance parts” based at the Leibniz Universität Hannover. Its main goal is the transfer of measurement procedures and algorithms researched within the research centre into industrial application. The project aims at making surfaces of industrially machined parts compatible with fringe projection systems (FPS). For that purpose many surface treatment methods are being investigated in terms of their respective impact on the optical cooperativity of the object surfaces [1].

2 Measurement Problem

Many parts used in the drive technology consist of a revolved feature with a central bore. Though there are some methods to measure the bore quality, measuring more complex interior geometries like gearing is hard to achieve using conventional FPS. Particularly synchronization rings with inner gears of individual profiles that have to be finished precisely require more flexible measurement and inspection systems.

The inner surface of a synchronization ring consists of pikes at the front and back side and spherical cuts with very narrow tolerances. Due to the complexity of these features and their geometric interactions and tolerances the use of areal measuring systems as can be provided by FPS can be invaluable. Unfortunately typical FPS are too bulky to be fitted inside common bore diameters usually used in the drive industry.

3 Measurement Setup

3.1 Conventional Measurement Setup

Conventionally one would place the measurement object in a skewed angle, in order that the FPS looks 'inside' the cylindrical bore (Fig. 1), but this could result in strategic disadvantages in the measurement result:
By widening the measuring angle in respect to the axis perpendicular to the measurement surface (γ), more parts of complex surfaces become hidden for the measurement system. If the surface of the measurement object is taken in by more than one measurement, a data fitting process has to follow the measurement process and thus the quality of the measured data could be compromised and the measuring and processing time increases drastically.

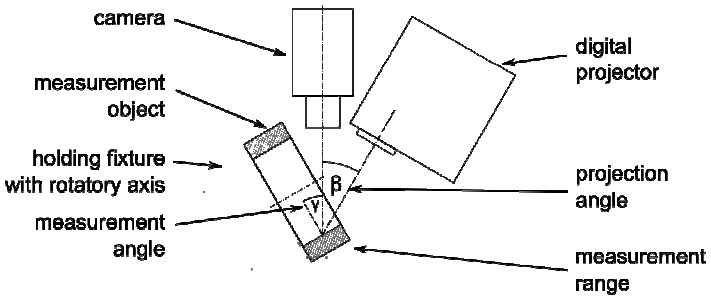

Fig. 1. Measurement setup using a conventional FPS

Furthermore, the measurement surface is positioned diagonally inside the measurement range, thus the imprecision of the measurement system is unevenly distributed which makes evaluating the results and considering the imprecisions of the measurement system more intricate.
Not having the flexibility of choosing the angle of approach to a given technical part with a typical glossy surface lowers the ability to avoid sensor over- and underexposure due to optical incooperativities.

3.2 Proposed Measurement Setup

Using a carefully placed mirror it is possible to measure the surface inside a cylindrical bore using fringe projection technology. Fig. 2 shows the general setup of the FPS using a mirror inside the bore. As in conventional

setups the projector is positioned as to draw its picture on the surface under a projection angle β past the flank of the measurement part. The camera is positioned parallel to the bore axis and views the mirror, that is positioned 45° to the relevant object surface inside the bore.

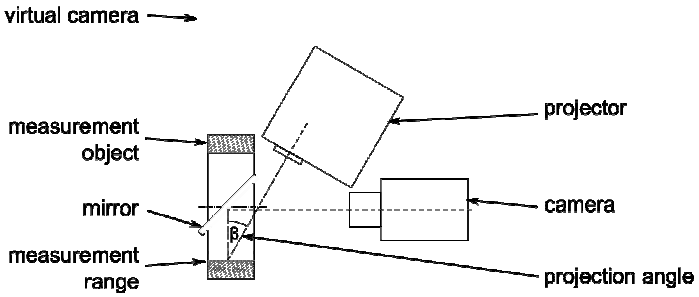

Fig. 2. Proposed configuration of the FPS

Using this setup the only limitation to the flexibility of the measurement system consists of the angle of the projection device which has to consider the dimensions of the measurement part.

4 Discussion

The proposed setup emulates a standard fringe projection setup that is represented by the virtual camera in Fig. 2. It is sufficient to use pinhole models for both the camera and the projector, since no telecentric objective is used. An analytical model for non-collimated fringe projection based on [2] can be used to describe the phase-to-height relationship (Eq. 1).

$$z_i = f(Y_i, \Phi) \tag{1}$$

Where z_i represents the height of the measurement point, Y_i the pixel coordinate perpendicular to the fringes and Φ the spatial phase at Y_i. Due to the mirror, attention should be given to the fact that Y_i has to be flipped along the X-axes of the pixel array inside the camera. The introduced mirror basically adds an additional degree of freedom to the system.

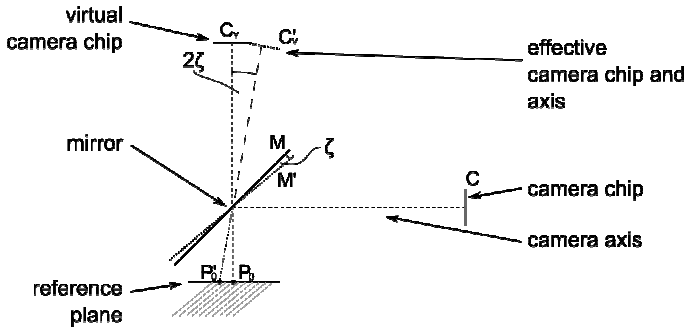

Fig. 3. Effect of the additional degree of freedom introduced by the mirror

As evident in Fig. 3**Fig.** a rotation of the mirror in the proposed setup by ζ causes a phase shift in the camera image equal to a disposition of the virtual camera by 2ζ which is proportional to the height of the mirror above the reference plane by sin(2ζ). For small ζ the tilt of the camera reference plane can be ignored thus leaving only a small and constant disposition in the measured topography.
The proposed FPS-setup may narrow the possible field of view since the projected light has to pass between the camera and the edge of the mirror. To avoid unnecessary measurement uncertainties one would draw the mirror as near to the objects surface as possible while allowing the projection to get by.

5 Acknowledgements

I would like to thank the German Research Foundation (DFG) for supporting and funding this research project.

6 References

1. Abo-Namous, O, Seewig, J, Kästner, M, Reithmeier, E (2008) Fast method to measure optical cooperativity. Proc. DGaO, p. A16
2. Rajoub, B A, Lalor, M J, Burton, D R, Karout, S A (2007) A new model for measuring object shape using non-collimated fringe-pattern projections, J. Opt. A: Pure Appl. Opt., 9, S66-S75

A Cellular Force Microscopic System for Cell Mechanics Investigation

Jing Fang, Jianyong Huang and Chunyang Xiong
Department of Biomedical Engineering,
Peking University, Beijing, 100871, PR China

1 Introduction

Understanding of mechanical behaviors of single cell requires an accurate and efficient method to estimate spatio-temporal dynamics of the cells as they interact with extracellular micro-environments, which has tremendous significance in tissue engineering, biomaterial design and pharmaceutical applications [1].With the help of flexible substrate such as polyacrylamide (PAA) gel [2], cell-substrate interaction can readily be characterized by monitoring elastic gel deformation and accordingly reconstructing cellular traction forces [3, 4].

The fundamental processes for assessing mechanical response of adherent cells onto substrate gel can be divided into steps of: preparation of soft elastic substrate with fluorescent bead embedding; fluoresce image recording and displacement evaluation of the substrate deformation caused by cell action; and cellular traction recovery from the substrate displacement data using theoretic model of elasticity. Based on the practical procedure, we present a microscopic system for cellular force investigation with *in vitro* surroundings. The available system integrates indispensable hardwares and softwares developed in our previous work into an applicable platform, which can easily carry out a precise and fast analysis of cell-substrate physical interaction.

2 Cellular Force Microscopic system

Polyacrylamide (PAA) gel is used as substrate material by modifying the concentration of acrylamide to change the Young's modulus of the gel [2]. Fluorescent polystyrene microbeads are randomly embedded to create fluorescent speckle maps. The gel surface is coated with type I collagen solution and cell suspension is plated to allow cells to adhere onto the substrate surface [5].

Fig. 1 gives the schematic representation depicting the cellular force microscopic system employed in our experiments. It is composed of an inverted fluorescent microscope (Olympus IX 71) with a high-resolution charge-coupled device (CCD) camera, (DVC-1312 cooled CCD, 1300(H)x1030(V)x12 bits, DVC Company), a perfusion chamber with temperature and humidity controller and a personal computer. The inverted fluorescent microscope is used to track the fluoresce images of substrate surface and the corresponding phase-contrast pictures of the adherent cells. To ensure the microscopic observation for a long time, a controller of temperature and humidity is introduced that consists of a thermometer, a heating rod, a feedback controller and a liquid pump. All the captured image data are stored for image processing.

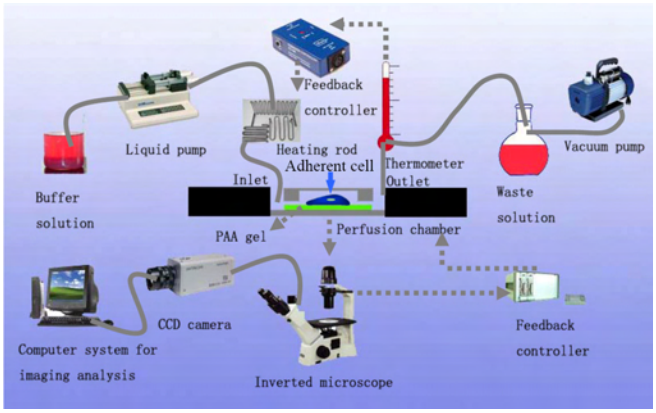

Fig. 1. A schematic of the cellular force microscopic system used in experiment

Digital image correlation (DIC) method is employed to acquire cell-generated substrate displacement fields. Typically, a rectangular subset of (2M+1)×(2M+1) pixels from the undeformed fluorescent image is selected to find its position in the corresponding deformed image by searching the peak value of the following cross-correlation coefficient [6]

$$C(u,v)=\frac{\sum_{x=-M}^{M}\sum_{y=-M}^{M}\left[f(x,y)-f_m\right]\left[g(x+u,y+v)-g_m\right]}{\sqrt{\sum_{x=-M}^{M}\sum_{y=-M}^{M}\left[f(x,y)-f_m\right]^2}\sqrt{\sum_{x=-M}^{M}\sum_{y=-M}^{M}\left[g(x+u,y+v)-g_m\right]^2}} \tag{1}$$

where, $f(x,y)$ and $g(x+u,y+v)$ denote the grey value of location (x,y) inside the chosen subste in the undeformed image, that of $(x+u,y+v)$ in the corresponding deformed image, respectively. By exploiting some sub-pixel registration algorithms, such as gradient-based sub-pixel registration

method [6], the measured accuracy of substrate displacement field can reach the sub-pixel scale (~0.1-0.2 pixel). To improve computational efficiency, the cross-correlation coefficient is calculated by employing the two-dimensional fast Fourier transform (FFT) algorithm.

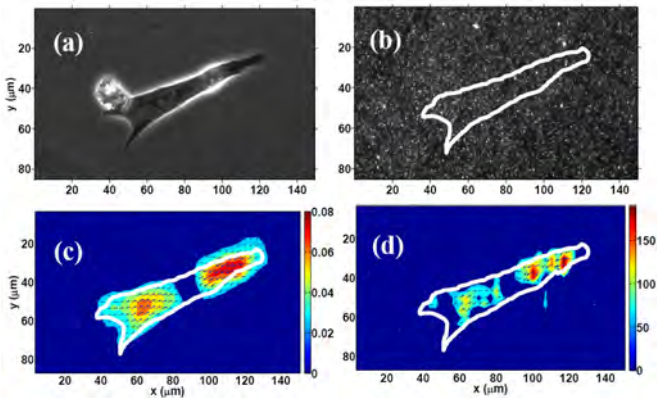

Fig. 2. (a) Phase contrast image of a single cardiac myocyte adhering onto PAA substrate; (b) Substrate fluorescent image; (c) Substrate displacement field (μm) and (d) cellular traction force distribution (kPa).

In the framework of elastic theory, the relation between tangential forces and elastic substrate deformation is governed by the Boussinesq solution [4]

$$u_i(r) = \int dr' G_{ij}(r - r') F_j(r') \tag{2}$$

where G_{ij} is the Green's kernel function, given by

$$G_{ij}(d) = \frac{1+\upsilon}{\pi E d}\left[\delta_{ij}(1-\upsilon) + \frac{(x_i - x_i')(x_j - x_j')}{d^2}\upsilon\right] \tag{3}$$

where E is the Young's modulus of the flexible substrate, υ is its Poisson's ratio; $d=|r-r'|$ the relative distance from the point-like force acting point r' to the distortion position r, and δ_{ij} is the Kronecker Delta with $i,j=1,2$. It is worth pointing out that the cellular traction calculation from the measured displacement data is a seriously ill-posed inverse problem in essence. In order to gain a stable and reliable solution, several approaches have been proposed to address the particular ill-posed feature[4]. In the microscopic system, we adopt a cellular traction recovery method based on an integral Boussinesq solution, which was published recently by us in [7]. The traction recovery method fully takes the true stress characteristic of focal adhesions into account and replaces the classic

Boussinesq solution founded upon a point-like force with an analytical expression obtained by integrating the classic Boussinesq solution over an rectangular element region, which can effectively restrict the ill-posed problem and accordingly stabilize force reconstruction. For more details, see Ref.[7]. Fig. 2 shows a cellular traction recovery based on the cellular force microscopic system we have developed.

3 Acknowledgments

The authors would like to gratefully thank Lei Qin and Jia Wu for their technical support. The project is supported by the National Basic Research Program of China (2007CB935602) and the NNSFC Grants (90607004 and 10672005).

4 References

1. Vogel, V, Sheetz, M (2006) Local Force and geometry sensing regulate cell functions. Nature Rev. Molecular Cell Biology 7:265-275
2. Pelham, RJ, Wang, YL (1997) Cell locomotion and focal adhesions are regulated by substrate flexibility. Proceedings of the National Academy of Sciences of the United States of America 94:13661-13665
3. Beningo, KA, Wang, YL (2002) Flexible substrata for the detection of cellular traction forces. Trends in Cell Biology 12:79-84
4. Sabass, B, Gardel, ML, Waterman, CM, Schwarz, US (2008) High resolution traction force microscopy based on experimental and computational advances. Biophysical Journal 94:207-220
5. Qin, L, Huang, JY, Xiong, CY, Zhang, YY, Fang, J (2007) Dynamical stress characterization and energy evaluation of single cardiac myocyte actuating on flexible substrate. Biochem. Biophy. Res Comm 360:352-356
6. Zhang, J, Jin, GC, Ma, SP, Meng, LB (2003) Application of an improved subpixel registration algorithm on digital speckle correlation measurement. Optics and Laser Technology 35:533-542
7. Huang, JY, Peng, XL, Qin, L, Zhu, T, Xiong, CY, Zhang, YY, Fang, J (2009) Determination of cellular tractions on elastic substrate based on an integral Boussinesq solution. J Biomech Engineering 131:06100

Candle flame analysis by digital three-wavelength holographic interferometry

Jean-Michel Desse
Office National d'Etudes et de Recherches Aérospatiales,
5, Boulevard Paul Painlevé, 59045, Lille, France
Pascal Picart
Laboratoire d'Acoustique de l'Université du Maine,
rue Aristote, 72085 Le Mans Cedex 9, France
Patrice Tankam
Ecole Nationale Supérieure d'Ingénieurs du Mans,
Université du Maine, rue Aristote,72085 Le Mans Cedex 9, France

1 Introduction

More and more, computational fluid dynamics needs to be validated by fine measurements in a smaller space or shorter time, or both at once. This is why ONERA has developed optical methods based on real-time true color holographic interferometry using transmission or reflection holographic plates [1]. This last technique combines the advantages of differential interferometry with those of monochromatic holographic interferometry. With this, not only small path differences but also large ones can be measured because the interference fringe diagram obtained is colored, very broad and well-contrasted. Also, color holographic interferometry generates the achromatic fringe and also provides absolute data throughout the entire field of observation. But, these methods are depending on holographic plates. In fact, plates are used as reference hologram and chemical treatment is a disadvantage because it produces variations in the gelatin thickness. A possibility to avoid chemical processing is related to digital three-color holographic interferometry.
Classically, digital holography was developed with a single wavelength. Optical metrology performed with color holography was described in references [1,2] in which color image holographic interferometry with panchromatic plates was presented. Recently, Yamaguchi et al proposed phase shifting digital color holography [3]. They recorded three color digital holograms with a 1636x1238 pixel matrix with pixel pitches of 3.9×3.9μm2. The sensor used a Bayer filter which consists in a spatial spectral filter. The authors showed the possibility for reconstructing a color

amplitude image. However, the resolution was degraded since the effective pixel number along each wavelength was 818x619. In 2003, Demoli et al developed a quasi-Fourier off-axis experimental setup using a monochrome CCD sensor with 1008x1018 square pixels, 9x9μm2 in size [4]. Strategy consisted in a sequential recording of the reference and measurement holograms along the three red-green-blue channels. Then, a movie was built using the three color results by applying the subtraction method to the digital holograms. It shows convective flows induced by the thermal dissipation in a tank filled with oil.

This paper presents the first digital three color holographic interferometer for flow visualization, allowing a simultaneous high resolution recording along each color (red, green and blue). For that, an optical setup has been designed to generate micro fringes in the observed field and the recording support (holographic plate) is replaced by a specific CMOS sensor constituted with three stacked photodiode layers. Then, interference micro fringes produced by the superimposition of three reference waves and three probe waves can be simultaneously recorded on the three spectral bands. Phase and amplitude images are computed using Fourier transform in delayed time. Spectral filtering is applied on each Fourier plane in order to eliminate the parasitic diffraction orders. Then, phase differences are obtained by subtracting the reference phase to the probe phase. Several optical setups were tested and the best configuration allows the visualization of field about 70mm and increases the sensitivity since the probe wave crosses twice the test section. Interferences induced by a flame candle have been recorded and intensities have been computed from the phase differences. Fringes obtained with this process are those found with real-time color holographic interferometry using classical holographic plates. The very good comparison between classical and digital holography allows the validation of the full processing, that is: recording, filtering and phase reconstructions along the three colors.

2 Digital three-color holographic interferometer

Fig. 1 presents the optical setup which uses three different wavelengths issued from two different lasers. A cw argon-krypton ionized laser delivers the red and green lines at λ_R = 647nm and λ_G = 514nm and a DPSS laser delivers the last one at λ_B = 457nm. The three lines are combined by dichroic mirror (2) and the acousto-optical cell (3) diffracts the other unwanted lines. The three reference waves and the three probe waves are divided by the beam splitter cube (6). An optical right angle prism formed

by the two small mirrors (1) is used to adjust the length of the reference and probe beams. The spatial filter (5), constituted by a microscope objective (x60) and a pinhole (25μm), expands and filters the beams. It is located just at the focal distance of the two achromatic lenses (7) in order to generate the reference and probe plane waves. The probe beam crosses the test section twice because the light is reflected by the flat mirror (11) located just behind the test section (8). Then, the beam splitter returns the probe beam into the sensor. The achromatic lens (9) forms an afocal beam expander system with lens (7). A polarizer (not shown) allows adjusting the beams in order to adjust the optical power in the recording plane. The displacement of one of the flat mirrors (1) is used to choose the fringe density and orientation in the detector plane. As the image size and fringe resolution depend on the achromatic lens (9), several different lenses were tested (focal length: 30mm, 50mm and 70mm) and the best results were obtained with the last one. The second beam splitter (6) allows interferences to be formed on the sensor.

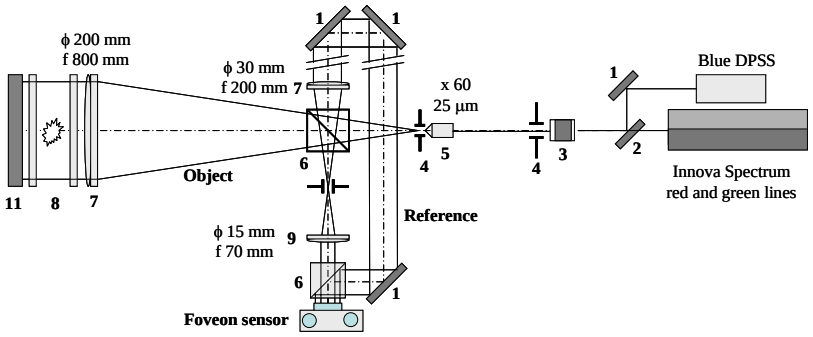

Fig. 1. Digital three-color holographic interferometer

3 Experimental results

The optical bench has been tested to determine the refractive index produced by a flame candle just placed in the front of the visualization windows. Two micro fringe images are recorded with and without the flame in order to constitute the RGB reference phase and the RGB probe phase. In the numerical processing, the spatial carriers were not removed. Phase difference was obtained by subtracting the reference to the probe phase for each color. Note that this operation leads to the automatic removal of the spatial carrier. Then, phase differences are unwrapped to

eliminate the 2π phase jumps and the optical path difference is deduced from the phase difference. Result is presented in Fig.2.

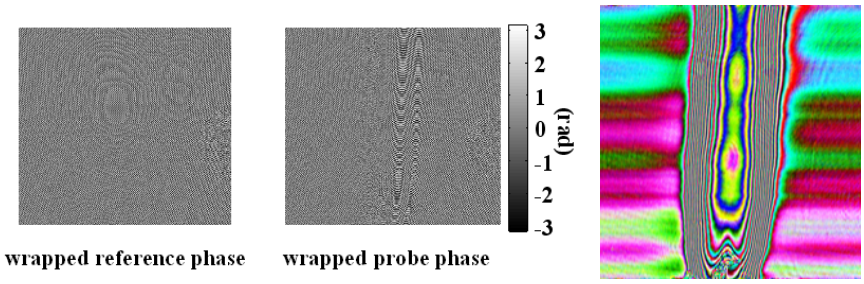

Fig. 2. Reference and probe phase (blue line) – Reconstruction of color fringes intensity

4 Conclusion

An optical setup based on digital three-color holographic interferometry has been designed for analyzing the unsteady wakes flows in future. Micro fringes images are recorded with a Foveon sensor which allows saving a very good resolution on the three planes.

Processing data performed by direct and inverse Fourier transform shows that the spatial carrier frequency has to be saved to reconstruct the phase difference maps. Currently, spatial filtering which is made manually could be improved using a quasi-automatic procedure.

Interest of using color has been demonstrated since the zero order fringe can be easily identified and variations in the background color due to disturbances can be quantified.

5 References

1. Desse, J M, Albe, F and Tribillon, J L, (2004) Real-time color holographic interferometry devoted to 2D unsteady wake flows. Journal of Visualization 7:217-224
2. Jeong, T H, Bjelkhagen, H I, Spoto, L M, (1997) Holographic interferometry with multiple wavelengths. Appl. Optics 36:3686-3688
3. Yamaguchi, I, Matsumura, T and Kato, J (2002) Phase-shifting color digital holography. Optics Letters 27:1108-1110.
4. Demoli, N, Vukicevic, D and Torzynski, H (2003) Dynamic digital holographic interferometry with three wavelengths. Optics Express 11:767-774.

Moiré fringe generation and phase shifting using a consumer product LCD projector

Joris J.J. Dirckx, Jan A.N. Buytaert, Sam A.M. Van der Jeught
Laboratory of Biomedical Physics – University of Antwerp
Groenenborgerlaan 171, B-2020 Antwerp
Belgium

1 Introduction

One of the most important uses of Moiré fringes is profilometry of 3-D surfaces. Grid lines are projected onto an object, and the deformed projection is imaged onto a second grid to obtain Moiré fringes [1]. Grid noise is removed by translating both grids simultaneously in their own plane. To obtain the surface height information the fringes can be traced, but much more detailed information is obtained by applying a phase shifting technique. The necessary phase-shifts of the Moiré fringes are obtained by changing the relative distance between the two grids. From at least three phase-shifted Moiré fringe patterns, object surface height is then calculated on all pixel points of the camera which records the Moiré fringe patterns. Classically, translation of the grids is performed mechanically. Recently we have introduced a method using two liquid crystal light modulators to perform high resolution phase-shifting Moiré topography without any mechanically moving parts [2]. We will now show how this new method can be implemented using a low-cost consumer product LCD projector.

2 Apparatus

2.1 Electro-optical measurement setup

In projection Moiré topography a CCD camera records three or more phase-shifted Moiré interferograms [1]. The phase shift is obtained by changing the relative distance between the projection and the demodulation grid. Apart from the Moiré fringes, the original grid lines are also seen in the images. To remove this so called grid noise, both grids

need to be translated simultaneously during the recording of each Moiré interferogram. We use one LCD to project grid lines onto the object. The deformed lines are projected onto a second LCD to generate Moiré fringes. An important advantage of this approach is that the CCD camera which records the Moiré topograms does not need to resolve the high frequency projected grid, and that no low-pass filtering is needed to remove the grid noise.
In a commercial LCD projector, the light of a high pressure gas discharge lamp is collimated, and divided into three spectral bands which are directed towards three liquid crystal light modulators. The light modulators themselves consist of a polarizer, a thin film transistor liquid crystal matrix (LCM), and a crossed polarizer. When a pixel on the liquid crystal modulator is activated, it rotates the polarization direction of the incoming light, so that this light now passes the second polarizer. To construct the phase-shifting Moiré profilometer, one liquid crystal device needs to be brought externally of the projector. In front and behind of the LCM, crossed polarizers are installed as well.
The standard lens of the LCD projector and a second similar lens can be used to measure objects with dimensions ranging from centimeters to several meters. In our own research, we wish to use the technique to study the shape and deformations of tiny objects such as the eardrum. In that case, the projection lens is removed from the LCD projector, and a set of lenses with longer focal distance (f=150mm) is used.

2.2 Control of the Moiré grids

To implement phase-stepping and grid averaging, the two LCM grids need to be controlled separately. In a commercial LCD projector, this can be easily realized since the images are controlled in RGB color space. If, for instance, a pixel on the projection LCM and on the demodulation LCM needs to be active, it suffices to send an image which contains the color cyan (or blue+green) to that pixel. The projector is connected as a second monitor on the graphics card. Grids of different pitches can easily be generated and translated, without any change to or moving components in the Moiré setup. This is another important advantage over mechanical setups, where Ronchi rulings of fixed pitch are used.

2.3 Semi-continuous grid averaging

The simplest way to remove the grid noise from the Moiré topograms is to record a number of interferograms each with the same relative phase

between the two grids, but with both grid line patterns shifted over a number of pixels for each interferogram.

When discrete grid averaging is used, a Moiré interferogram needs to be recorded at each grid position. The exposure time for the CCD camera depends on the intensity of the projector, but typically it will be in the range of some 200ms. When 16 images are needed for this discrete grid averaging [2], it amounts to a total recording time of 3.2s. The real bottleneck however, is the time needed to transfer and store the images coming from the camera, interleaved by uploading grid images on the display board. Using a commercial graphics board it is however possible to greatly speed up the averaging process. First, all colored grid images are prepared for all averaging positions in all four phases, and stored in bitmap file format. Next, a custom made program developed in C-Graphics (Cg Nvidia) is used to load all the images in four buffers in the memory of the graphics board (one for each Moiré phase). The graphics processing unit is programmed to continuously "play" the content of a certain buffer. For the first map or phase, this "movie" of 16 images is displayed at the highest frame rate the graphics board can deliver in combination with the projector (60 Hz), and the first Moiré topogram is recorded in one camera exposure time of about 267ms. Then the next "movie" is played, containing 16 images with a quarter grid period translation between the projection and the demodulation grid, and the next Moiré topogram is recorded. Finally, the same procedure is repeated for the third and forth topogram. In semi-continuous grid averaging the movie of grid positions needs to be rendered on the display exactly one time during the camera exposure. In practice, the fixed frame generation rate of the graphics board determines the minimal CCD exposure time to be used. On our system, for instance, exactly 266ms are needed to display one sequence of 16 images.

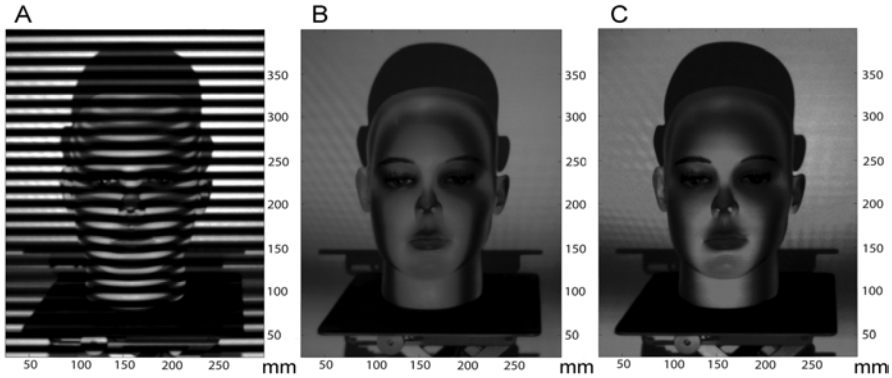

Fig.1. Moiré fringe on a mannequin head. A: without grid averaging. B: with discrete grid averaging. C: with semi-continuous grid averaging.

Figure 1 shows a Moiré interferogram obtained on a window display mannequin head without grid averaging (1A), using discrete averaging (1B) and semi-continuous averaging (1C). From the images one sees that both averaging methods remove grid noise equally well, but semi-continuous averaging requires only one recording and thus less time.

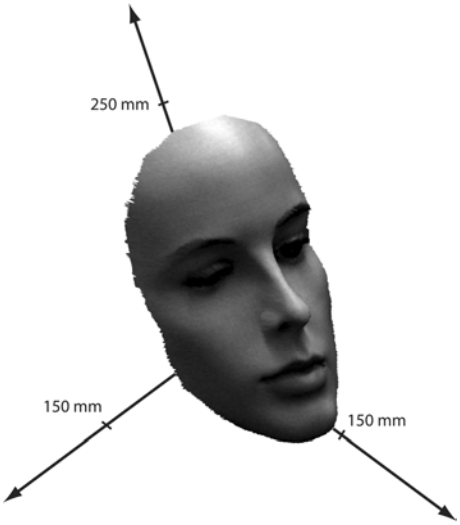

Fig.2. Shape measurement obtained on the mannequin head

3 Application examples and measurement resolution

For relatively large objects the original zoom objective of the LCD projector works well to adapt the measurement area to the object size. Figure 2 shows a 3-D representation of a shape measurement obtained on the life-sized mannequin head.

For high resolution measurements on small objects, the projector lens needs to be removed, and replaced by a lens of longer focal distance. The spatial resolution of the camera is not crucial: thanks to the optical demodulation and the phase-stepping method, the camera does not need to resolve the grid lines. The gray scale resolution of the camera, however, is important, since the number of gray scale steps is a determining factor for the height measuring resolution [3]. On objects of about a centimeter cube, we obtain a height measuring resolution of 15 micrometer. As an application example, figure 3 shows a shape measurement obtained on a rabbit eardrum during a point-indentation experiment. Such measurements are used to study the mechanics of the middle ear.

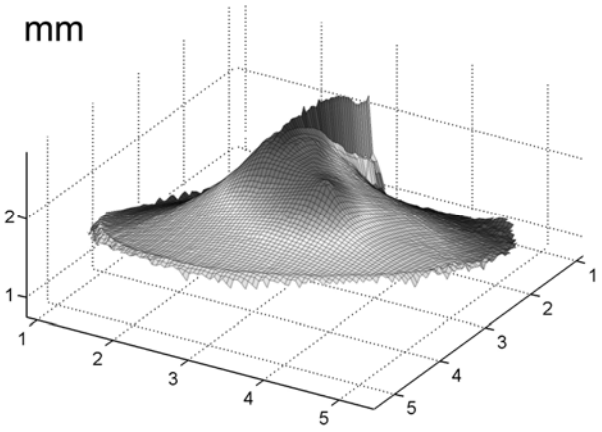

Fig.3. Shape measurement obtained on a rabbit eardrum with a point indentation

4 Acknowledgements

Financial support to this research was given by an aspirant fellowship of the Research Foundation – Flanders and a grant of the Rosa Blanckaert Foundation.

5 References

1. Takasaki, H (1970) Moiré topography. Appl. Opt. 9:1467-1472
2. Buytaert J, Dirckx J, (2008) Moiré profilometry using liquid crystals for projection and demodulation. Opt. Express 16: 179-193
3. Buytaert J, Dirckx J (2007) Design considerations in projection phase-shift Moiré topography, based on theoretical analysis of fringe formation, J. Opt. Soc. Am. A 24:2003-2013

Speckle velocimetry for high accuracy and multi-dimensional odometry

Tom O.H. Charrett and Ralph P. Tatam
Engineering Photonics Group, School of Engineering,
Cranfield University, United Kingdom

1 Introduction

The success of recent robotic vehicles for space exploration has led to a demand for a new generation of interplanetary rovers with increased capabilities. One area of particular interest concerns the navigation of the vehicle and in particular measuring a vehicle's movements. Odometry or 'dead reckoning' is commonly used to calculate a vehicle's position, and requires some measure of the distance travelled. The most commonly used method is wheel encoders which provide odometry information by measuring wheel rotations. These are very prone to errors due to wheel slippages, unequal wheel diameters, wheel misalignment, surface roughness and rounding errors due to the discrete sampling of wheel increments[1]. Typically these errors are around 3%, the accuracy of the NASA Spirit Mars rover was reported as[2] 3% after 3km. However on steep hillsides, in mixed sand/rock terrains and when crossing sanding ripples in other flat plains large slips occurred[2]. Speckle velocimetry, a non-contact, optical measurement technique, has the potential to provide a higher accuracy replacement for the wheel encoders. This paper describes our initial investigations into its application for high accuracy, multi-dimensional odometry for autonomous vehicles.

2 Speckle Velocimetry

A coherent light source is mounted on the rover and illuminates a small region of the surface over which the rover is travelling. A camera and associated imaging optics views the illuminated region and records the speckle pattern. This pattern will change if the illumination direction changes and/or the surface changes; for small movements, such as the motion of the rover between camera frames, the pattern will translate rigidly. A digital processing algorithm is used to extract the magnitude of

the translation and calculate the velocity of the rover from which the vehicles' odometry can be calculated.

3 Preliminary Studies

A preliminary study into the speckle velocimetry was conducted in collaboration with EADS Astrium for possible application on the EXOMARS rover[3]. In order to assess the different processing algorithms, hardware requirements and investigate the speckle patterns formed by Martian soil analogues a laboratory test system was constructed. It consisted of an illumination source, camera, pinhole and imaging lens mounted above a Petri dish containing the soil sample. The Petri dish was mounted on a linear translation stage to provide a controllable velocity and known translation.

3.1 Speckle formation from Martian soil analogues

A range of volcanic soil samples (provided by EADS-Astrium) and a Martian soil analogue (provided by the University of Aberystwyth, UK) were investigated at the two wavelengths to assess the signal level that could be expected. The volcanic soils ranged in particle sizes from fine sands, to large rocky chunks (~10-20mm in size). The Martian soil analogue was a fine white powder, which consisted of an olivine/quartz-sand mix that has been ground and sieved so that the particle distribution is analogous to the Martian regolith. Two illumination wavelengths, 633nm and 820nm, were used and speckle patterns were clearly visible at both (fig. 1) on all of the samples tested. However the corrected signal levels were found to be higher at 633nm than at 820nm.

3.2 Algorithms and Results

Several potential algorithms where then investigated using the laboratory system and computer modelling of speckle images. The performance of the algorithms was assessed for different image sizes, speckle sizes and different soils. Also the computational cost required and zero-velocity measurement performance was assessed. Table 1 summarises our findings. The typical error (Table 1) was measured using an A-B-A test; the stage was repeatability moved from one extreme to the other and back again. The calculated position was compared with the expected zero position.

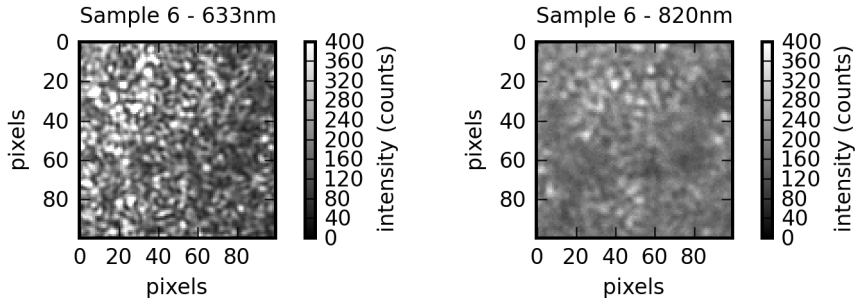

Fig. 1. Example speckle patterns recorded from the Martian soil analogue provided by the University of Aberystwyth. Illuminated at 633nm (left) and 810nm (right)

Table 1. Summary of speckle velocimetry algorithms investigated in the preliminary study

Method	Advantages	Disadvantages
Radon Transform [4]	(+) High resistance to noise.	(-) False measurements at zero velocity. (-) High computational cost.
Gradient based optical flow [5]	(+) Low computational cost. (+) Good zero velocity performance: calculated mean = $1.5x10^{-4}$ mm/s, standard deviation = $1.2x10^{-3}$ mm/s. *Typical error at 1mm/s = 1.9%*	(-)Calibration dependent upon surface material (-) Limited velocity range - 0 to 2.5 pixels shift between frames.
Cross correlation [7]	(+) Low/Moderate computational cost. (+) Ideal for hardware implementation. (+) Q-value as reliability measure. (+) Variable velocity range. (+) Good zero velocity performance: calculated mean = $1.3x10^{-3}$ mm/s, standard deviation = $2x10^{-3}$mm/s *Typical error at 1mm/s = 0.36%,* *Typical error at 50mm/s = 0.74%*	(-) Velocity range limited by condition that the shift must be smaller than the image size. (-) High frame rate camera required for higher velocities.

A Radon transform, previously reported for speckle velocimetry for an autonomous Antarctic vehicle4, was found to exhibit false measurements when stationary and was too computationally intensive.

Gradient based optical flow5 is the algorithm used in a simple form in optical computer mice, which operate in the same manner as speckle velocimetry, and in more complex forms in video motion compression. The typical measured error was ~1.9%, dependant upon the surface/soil

sample used, and a separate calibration was required for each surface, making the algorithm unsuitable for exploration rovers where the surface material is unknown in advance.
Improved performance was found using normalised cross-correlation[6] performed between consecutive image frames and the velocity found from the shift in the peak of the correlation and the known time interval between frames. The measurable velocity range can be varied by changing the inter-frame time. A further advantage is that the Q-value of the correlation (the ratio of the first and second peaks in the correlation) can be used as a reliability measure, to identify slippage events and possibly as a feedback mechanism to vary the measurement range. Typical measurement errors were around 0.36%. To assess the uncertainty at higher velocity, a piece of paper was moved beneath the camera in a closed path by hand with an approximate velocity of 50mm/s. The Q-value was used to determine that there were 6 bad results out of 999 correlations. The error was ~0.74% in position for a total path travelled of 375mm.

4 Conclusions and Outlook

The desired performance of <1% error has been found to be achievable at low speeds (~1mm/s to 50mm/s). The cross-correlation algorithm should scale well to higher velocities such that a similar uncertainty level should be achievable at typical rover velocities (~0 to 150mm/s) using a low resolution (~100x100 pixels) high frame rate (~300fps) image sensor. The algorithm is also ideal for implementation in hardware due to the large number of parallel computations required.

5 References

1. Borenstein, J., Feng, A., (1995), SPIE Conference on Mobile robots, Philadelphia, USA.
2. Maimone, M., Leger, P., Biesiadecki, J., (2007) IEEE International Conference on Robotics and Automation (ICRA) Space Robotics Workshop, Rome, Italy.
3. ESA, ExoMars webpage: http://www.esa.int/esaMI/Aurora/ SEM1NVZKQAD_0.html, Accessed May 2009.
4. Aliverdiev, A., Caponero, M., Moriconi, C., (2003), Tech. Phys.,**48** pp. 1460-1463.
5. Horn, B.K.P., Schunk, B.G., (1981), Artif Intell., **16**, pp 185-203.
6. Lewis, J., Accessed May 2009. http://www.idiom.com/~zilla/ Work/nvisionInterface/nip.html.

Determination of Refractive Index Changes in Biconical Optical Fiber Taper

Karol A. Stasiewicz[1], Rafał Krajewski[2], Małgorzata Kujawińska[2], Leszek R. Jaroszewicz[1]
[1]Institute of Applied Physic, Military University of Technology
Gen. Sylwestra Kaliskiego Street 2, 00-908 Warsaw
[2]Institute of Micromechanics and Photonics, Warsaw University of Technology, St. Andrzej Baboli Street 8, 02-525 Warsaw
Poland

1 Introduction

Development of optical fiber technology requires application the new elements with advanced properties built-in during technological process. Especially all elements which uses so-called optical transparent technology i.e. working without taking the light out form fiber structure a very promising because they protects small element sizes and low cost. The elements based on a optical fiber taper technology [1-4] are one of the most interested because they protect small insertion loss as well as geometrical size compare to optical fibers and allow to control light beam propagation in the fiber. From these reasons they are a basic for manufacturing advanced hybrid elements like polarization controller, optical switcher, white laser, and others [2, 5].
However the experimental investigation of the inside fiber structure changes, especially refractive index distribution, for different types of taper should be given for proper advanced elements manufacture. This aspect is the main area of this paper, where investigation of inside structure in taper region via interferometric tomography method is presented.

2 Biconical taper classification on the base of the fiber tapering process

The development set-up for biconical taper manufacturing (see Fig. 1a) is based on elongation fibre in low-pressure gas burner. The fiber heating up to it melting temperature is obtained by a propane-oxygen flame whereas

fiber elongation is realized by uniform fiber axial stretching in two points symmetrical located outside to the heating point.
The main advantages of this system is the different biconnical tapers manufacture possibility on all kind of telecommunication as well as photonic crystal fiber types. Speed of fiber elongation can be regulated by movement of flame. Through this move, the demanded length of taper waist can be obtained, too. In practice, the method of flame travelling under melting optical fiber is used for fabrication the three main types of biconical tapers: *punctonal* (Fig. 1b - punctual fiber heating by place immobile flame under fiber), *short waist* (Fig. 1c - flame brush oscillating moves along determined fibre distance with oscillation amplitude correlated with length of taper waist), and *long waist* (Fig. 1d - increased distance of flame brush travelling during tapering process with constant oscillation amplitude equal to the length of taper waist). For these types, the taper with length between 10 mm to 150 mm, and waist diameter to several micrometers can be produced.
The method of producing a different shape of biconical taper presented above can be theoretically described using Birks theory [3] which utylizes volume as well as distance laws, and gives good description of extrernal taper geometry. However for investigation refractive index changes inside maunfactured taper structure the nondestructive experimental method based on interferometric tomography should be used.

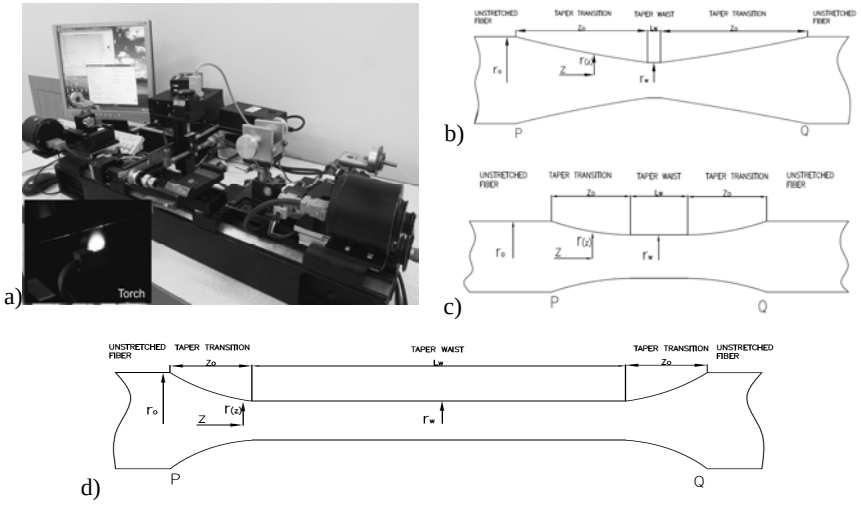

Fig. 1. Set-up for manufacturing biconical fiber taper a) and three main types of biconical taper: punctonal b), short waist c), and long waist d).

3 Tomography investigation of the optical fiber tapers

The interferometric tomography method [6] uses Mach-Zehnder interferometry (MZI) for detects phase distribution and spatial carrier phase shifting analyse [7] for final reconstruction of refractive index distribution along taper has been applied. Figure 2a shown MZI constructed by application two sinusoidal phase gratings beamsplitters (G1, G2) [8] which proper design minimizes the intensity in 0 diffraction order while maximizing it in +/-1. These beams operates as object and reference ones. Remaining 0 order beam is stopped by the shield (S). Object beam reflected from the side mirror (M1) passing through the inspected fiber taper (F) is recombined with reference beam by the second sinusoidal grating (G2) to form an interferogram captured by the CCD camera [9].

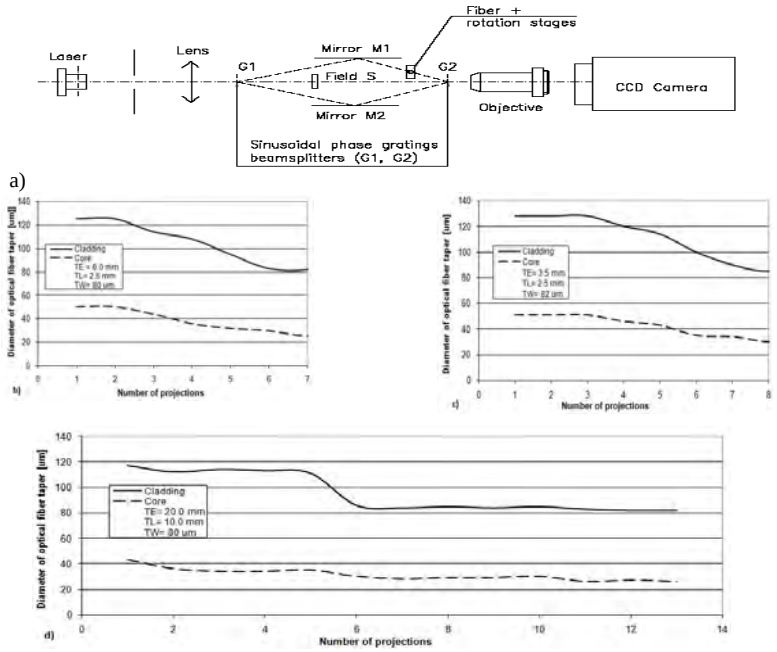

Fig. 2. Scheme of free-space MZI operates at 532 nm used for taper inspection [6] a) and refractive index distribution in cross section along the biconnical taper: *puctonal* b), *short wait* c), *long waist* d). Only half of total biconnical taper length is presented. Parameters: FE – fiber elongation length, TL – taper length, TW- taper waist diameter.

Figure 2b-d presesnts final reconstruction of the cross section refractive index changes along the fiber by tomography method.for three taper types manufactured according main technical parameters presented at pictures.

4 Conclusions

Obtained reconstruction of the refreactive index changes along taper region shows that punctonal and short waist taper protects core diameter reduction propotional to changes of outside diameter. For long taper the core/outside diameter ratio changes is nonlinear useful for SC generation.

5 Acknowledgments

This work has been done in 2009 year under financial support the Polish Ministry of Sciences and Higher Education Statutory Activity PBS-768.

6 References

1. Jędrzejewski, K (2000) Biconical fused taper – a universal fiber devices technology. Opto-Electr. Rev. 8: 153-159
2. K.A. Stasiewicz, K, A, Jaroszewicz, L, R (2008) Photonic crystal fiber coupler. Elektronika, 6: 208-210
3. Birks, T, A, Li, Y, W (1992) The shape of fiber tapers. J. of Lihtwave Techn. 10: 432-438
4. Ahmad, M, Hench, L, L (2005) Effect of taper geometries and launch angle on evanescent wave penetration depth in optical fibers. Biosensors and Bioelectronics 20: 1312-1319
5. Wadsworth, W, J, Birks, T, A, Russell, P, St, J (2000) Super-continuum generation in tapered fibers. Opt. Lett, 25: 1415-1417
6. Krajewski, R, et all (2006) Design, modeling, and prototyping of microinterferometric tomography system for optical fiber inspection. SPIE, 6188**:** 61880J
7. Robinson, D,W, Reid G, T (eds) (1998) *Interferogram analysis for optical testing*. Marcel Drekker Inc, New York
8. Krajewski, R, et all (2005) Low-cost microinterferometric tomography system for 3D refraction index distribution measurements in the optical fiber splices. SPIE, 5855: 347-350
9. Kniazewski, P, Gorski, M, Kujawinska, M (2003) Microinterferome-tric tomography of photonics phase elements. SPIE, 5145: 107-116

Prosthodontic crown mechanical integrity study using Speckle Interferometry

Pierre Slangen, Stephane Corn, Michel Fages*, Frederic J.G. Cuisinier*
Ecole des Mines d'Alès, ILOA
6 Avenue de Clavieres F-30319 Ales Cedex
France
*Université Montpellier Sud de France, EA 4203
545 Avenue Prof. Viala, F-34193 Montpellier Cedex5
France

1 Introduction

New trends in dental prosthodontic interventions tend to reach biomimetic behaviour. Evolutions of CAD-CAM techniques enable to build ceramic prosthetic crowns and, above all, to set the cement joint thickness that links crown and remaining dental tissues. CAD is based on "in-mouth" optical print (i.e. shape on which the clone is glued and contact surface of the opposite jaw tooth). Prosthetic crown is then manufactured, using these parameters, from a feldspathic ceramic rod. In this study, the cloning process gives two samples with identical shape for further use: clone and tooth displacements are measured by speckle interferometry.

2 Design and goals

Several theories [1] discuss the glue thickness and its formulation, acting as a crucial interface that accomodates the different stresses applied to the prosthetic tooth. Moreover this biomechanical analysis tries to reproduce the natural behaviour of the dentine-enamel joint (DEJ). In order to validate these new concepts and materials, and to study the mechanical properties and the mechanical integrity of the prosthesis, high resolution optical measurements of the deformations of glue and crown are required [2]. In our case, samples are two intact premolars extracted for orthodontic reasons from the same patient. The reference sample is preserved while the second sample tooth is shaped to receive a feldspathic ceramic monoblock crown (clone of the reference). Vertical cuttings have also been used to allow planar object observation, and also to appreciate the differential

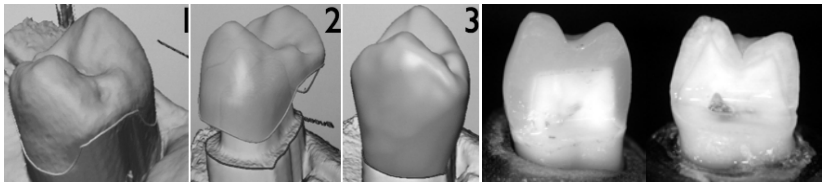

Fig. 1. Cloning process (1 ref optical print, 2 shaping, 3 CAM ready), clone and master cuts

behaviours “inside” the tooth: the crown-glue-dentine joint for the clone and the DEJ for natural tooth (Fig.1). For this study, a tooth compression test device and an optical fibers in-plane sensitive speckle interferometer have been developed. Samples are white powdered to diffuse laser light.

2.1 Mechanical set-up

The mechanical set-up is presented in Fig.2. Our compression test device fulfills the high sensitivity of speckle interferometry and also copes with the rigid body motions of the whole system. The sample tooth is placed in a dedicated mold in the lower jaw while the force transducer holder is slowly translated vertically by the stepping motor. The system can generate a „force-driven“ displacement, or just a „user“ displacement. The whole mechanical system is screwed on the holographic table top.
The force can be applied to the tooth directly with the force transducer or using a relay rod (shorter than shown Fig.2). We can point out that the force is always applied on the same part of the tooth surface for all the samples. This requires some degrees of adjustment to place the lower jaw properly. Samples have got molded jaw or have just been cemented.

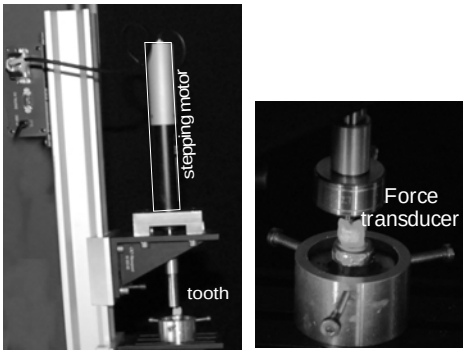

Fig. 2. Compression test mechanical set-up and dedicated molded lower jaw

2.2 Optical set-up

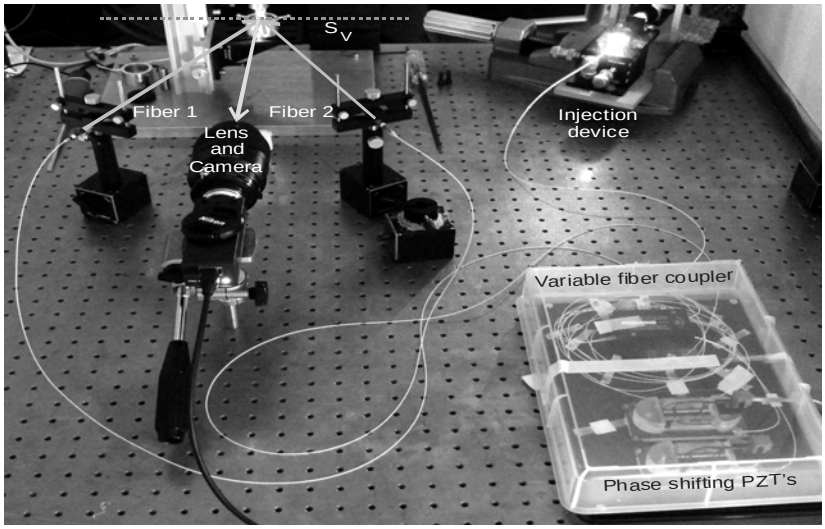

Fig. 3. In plane speckle interferometer, showing observation and illumination beams (full), sensitivity vector S_V (dashed), variable coupler, phase shifting and injection devices.

The optical set-up is presented in Fig.3. This COTS system (Canadian Instruments) offers injection, variable intensity coupling in the output fibers and also phase shifting. Parts of the output fibers are bared and wrapped around piezoelectric transducers. The phase shift is applied on any or both of the two output fibers. The system is protected from thermal and mechanical effects by a plastic box and is easily breadboardable. Phase shifts have been calibrated using common procedures [3].
Because in-plane displacements are of great interest for orthodontic measurements, an optical fibers in-plane sensitive interferometer has been designed. Horizontal sensitivity is achieved. A "4-buckets" phase shifting algorithm [4] leads to phase variations during the compression test.

3 Results and conclusion

First results have been obtained for different loads (Fig.4). In-plane displacement fields from speckle interferometry already showed interesting data concerning the mechanical behaviour of the different tooth parts. The particular behaviour of the interface joining them histologically is very important for dental aspects.

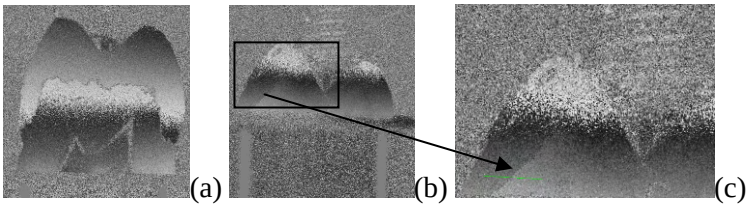

Fig. 4. Clone (a) and natural tooth (b) in-plane displacements, and (c) DEJ detection zoom

The loading range applied to the different samples are between 5 N and 120 N. Clone crown and natural tooth showed differential displacements: about 60nm for DEJ and about 100nm for the glue joint at the applied loads (20N and 40N). Each sample behaves as single solid beyond 120N.
These measurements show that the natural enamel crown moves independently from dentine. This difference is clearly delimited by a line corresponding to the anatomical location of the dentine-enamel junction (DEJ). For the ceramic clone the same kind of shift occurs at the glue junction of the ceramic crown with the dentine [5].
In further processing, optical displacements will be compared to finite elements analyses of the tooth. Mechanical sensitivity of the tooth surrounding medium will also be examinated.

4 References

1. Xu, H H, Smith, D T, Jahanmir, S, Romberg, E, Kelly, J R, Thompson, V P, Rekow, E D, (Mar 1998), Indentation damage and mechanical properties of human enamel and dentin, J.Dent.Res., 77,3:472-480
2. Zaslansky, P, Shahar, P, Barak, M M, Friesem, A A, Weiner, S (2006) Tooth and bone deformation: structure and material properties by ESPI, Proc. SPIE, 6341:6341091-6341096
3. Slangen, P, De Veuster, C, Renotte, Y, Berwart, L, Lion, Y, (1995) Computer-aided interferometric measurements of drift and phase shifter calibration for DSPI (Digital Speckle Pattern Interferometry), Opt.Eng., 34,12:3526-3530
4. Creath, K, (1988) Phase-measurement interferometry techniques, *Progress in Optics XXVI*, Elsevier Science Publisher B.V., Chapt.5, 349-393
5. Fages, M, Cloitre, T, Slangen, P, Corn, S, Cuisinier, F J G, **(**2009) Speckle Interferometry of ceramic crown deformation under loading, Joint Meeting IADR, Munich, to be published.

Monitoring of Drying Process of Paints using Lensless Fourier Transform Digital Holography

Chandra Shakher and Gyanendra Sheoran
Laser Applications and Holography Laboratory
Instrument Design Development Centre
Indian Institute of Technology, Delhi – 110016 (India)
Email id – cshakher@iddc.iitd.ac.in, cshakher1949@hotmail.com

1 Introduction

Holographic interferomtry (HI) has been widely used for NDT/ NDE of large number of components [1-2]. Recent interests in detection of de-cohesion/ failure of paint/ coating and non-contact monitoring of the state of the painted surfaces which cannot be touched is required in industries [3-5]. Tera hertz paint meter for non contact monitoring of thickness and drying process in the paint film has been proposed [6]. This method requires a special source and not suited for simple and quick testing. Very recently methods using texture analysis of speckle pattern arising from laser illumination of painted surface [7], monitoring of drying process of painted surface using digital speckle correlation [4] have been investigated. Monitoring of the state of drying of paint has been investigated from the dynamic behaviors of phase images reconstructed from phase shifting digital holography [5]. In this paper we report a new application of lenless Fourier transform digital holography (LLFTDH) to study the state of drying and flow of the paint by observing interference phase map of painted surface. The method is simple and can be used for quick practical observations.

2 Theory

In digital holography the hologram is recorded using a CCD/CMOS device and reconstructed numerically. In the specific geometry of lensless Fourier transform digital holography, the effect of the spherical phase factor associated with the Fresnel diffraction pattern of the object is eliminated by use of a spherical reference wave R with the same average curvature.

The complex amplitude at the reconstruction or image plane for the virtual image is given by [8]

$$O(X_I, Y_I) = \frac{i}{\lambda d}\exp\left[-i\frac{2\pi}{\lambda}2d\right]\exp\left[-i\frac{\pi}{\lambda d}\left(X_I{}^2 + Y_I{}^2\right)\right] \times FFT\left\{h\left(X_H, Y_H\right)\right\} \quad (1)$$

The cancellation of quadratic phase factor reduces the complexity in the algorithm for numerical reconstruction of digital holograms. The phase can be calculated from the complex amplitude as

$$\phi_I\left(X_I, Y_I\right) = \tan^{-1}\left[\frac{\mathrm{Im}\left\{O\left(X_I, Y_I\right)\right\}}{\mathrm{Re}\left\{O\left(X_I, Y_I\right)\right\}}\right] \quad (2)$$

where 'Im' and 'Re' represents the imaginary and real part of the reconstructed complex amplitude of the wave.

3 Experiment

Fig. 1 shows the schematic of the LLFTDH experimental setup employed for the study of state of drying and flow behavior of the paint. The interference pattern formed by the superposition of the reference beam and the light reflected from the coated surface was recorded by an 8-bit dynamic range CMOS sensor. The pixel size of the CMOS sensor was 6.7μm×6.7μm, the total number of pixels on CMOS chip were 1280×1022 (= 1308160). The sensor chip has an area of 8.6 mm×6.9 mm. Distance of the faceplate of the sensor was 52 cm from the plane containing the object and the reference source. The coatings were prepared by dropping of thick droplet of paint and leave it to flow itself on the horizontal cleaned surface after that it had been fixed with the stand vertically. The holograms of the painted surface were recorded at an interval of 1 minute. After acquisition of holograms, the interference phase distribution of the digitized hologram is calculated by modulo 2π subtraction

$$\Delta\Phi(X_I, Y_I) = \begin{cases} \Phi_2(X_I, Y_I) - \Phi_1(X_I, Y_I) + 2\pi & \text{if } \Phi_2(X_I, Y_I) - \Phi_1(X_I, Y_I) < -\pi \\ \Phi_2(X_I, Y_I) - \Phi_1(X_I, Y_I) - 2\pi & \text{if } \Phi_2(X_I, Y_I) - \Phi_1(X_I, Y_I) \geq +\pi \\ \Phi_2(X_I, Y_I) - \Phi_1(X_I, Y_I) & \text{else} \end{cases} \quad (3)$$

Since interference phase map provides capabilities of sensitive and precise detection of out of plane displacement, it can be used to monitor/ measure the change in thickness of the paint. Experimental results show that as paint started drying with time, the phase change will occur in the painted surface that give the information about the homogeneity of the coating and flow of the paint.

4 Results

Fig. 2 (a-f) show the variations in phase at different time interval after the drying process was started. Phase maps reveals the variation in thickness of paint with time. Fig. 2(f) show that after drying the thickness of the paint has become almost uniform. Phase maps Fig.3 (a-f) show the flow of paint in a downward direction and variation of thickness of paint with time. Fig. 3(f) show that after drying the thickness of the paint is not uniform.

5 Conclusion and Discussion

In conclusion, the difference of phase between successive holograms can provide non-contact monitoring of thickness during drying process and detection of decohesion/ failure of the paint like conventional holographic interferometry. The lenless Fourier transform digital holography (LLFTDH) technique is simple, robust and easy to implement.

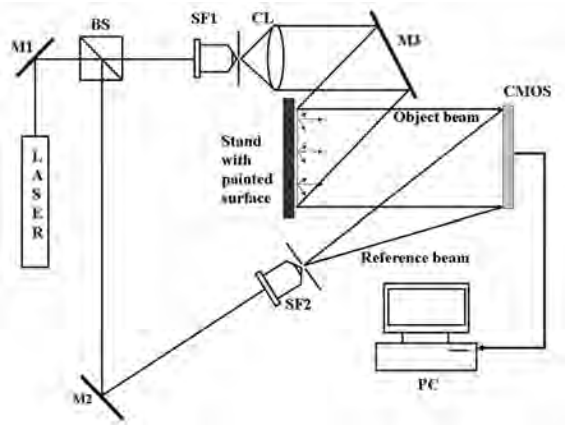

Fig. 1.– Schematic of the LLFTDH experimental setup employed for the study of state of drying

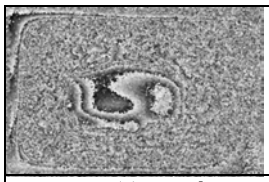

Fig. 2(a) PD between

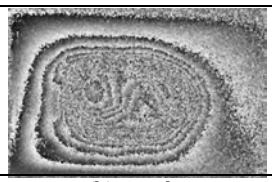

Fig. 2(b) PD between 55

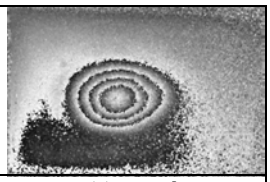

Fig. 2(c) PD between

15min. and 16min.	min. and 16min.	85min. and 86min.
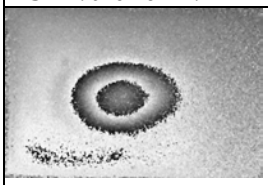	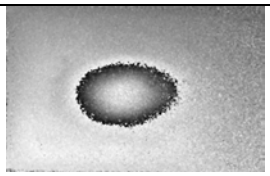	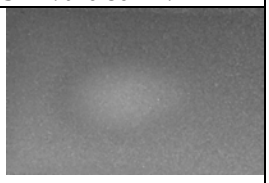
Fig. 2(d) PD between 95min. and 96min.	Fig. 2(e) PD between 105min. and 106min.	Fig. 2(f) PD between 115min. and 116min.

Fig. 2.- Phase differences (PD) of the recorded holograms of uniformly painted surface calculated at different time intervals in minutes (min.)

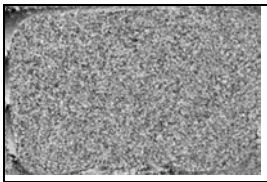	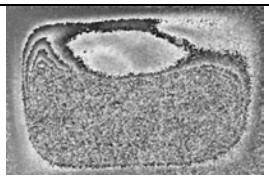	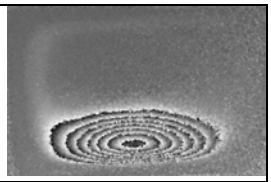
Fig. 3(a) PD between 10min. and 11min.	Fig. 3(b) PD between 40min. and 41min.	Fig. 3(c) PD between 110min. and 111min.
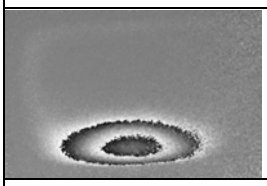	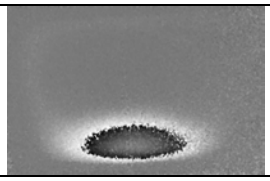	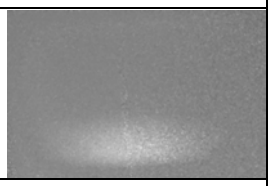
Fig. 3(d) PD between 160min. and 161min.	Fig. 3(e) PD between 190min. and 191min.	Fig. 3(f) PD between 320min. and 321min.

Fig. 3.- Phase differences (PD) of the recorded holograms of non-uniformly painted surface calculated at different time intervals in minutes (min.)

6 References

1. Champagne, E, Kersch, L, A (1969) Control of holographic fringe patterns (A). Journal of Optical Society of America (Annual meeting). ThF14, 59: 1535.
2. Shakher, C, Sirohi R, S (1980) A simple method of fringe control in holographic non-destructive testing. Journal of Physics E: Scientific Instruments 13: 284-286.
3. Raman Singh, R, K, Bayles, R, (2006) Detection of decohesion/ failure of paint/ coating using electronic speckle pattern interferometry. Journal of Engineering Failure Analysis 13: 1051-1056.
4. Yamaguchi, I, Yokota, M, Ida, T, Sunaga, M, Kobayashi, K (2007) Monitoring of paint dryness process by Digital Speckle Correlation. Journal of Optical Review 14: 362-364.
5. Yamaguchi, I, Yokota, M, Ida, T, Sunaga, M, Kobayashi, K (2007) Monitoring of paint dryness process by phase shifting digital holography. Optical Society of America Technical Digest, Paper DWC2.
6. Yasui, T, Yasuda T, Sawanaka, K, I, Araki, T (2005) Tetrahertz paint meter for non-contact monitoring of thickness and drying progress in paint film. Journal of Applied Optics 44: 6849-6856.
7. Arizaga, R, Trivi, M, Rabal, H (1999) Speckle time evolution characterization by the co-occurenece matrix analysis. Journal of Optics and Laser Technology 31: 163-170.
8. Wagner, C, Seebacher, S, Osten, W, Juptner, W (1999) Digital recording and numerical reconstruction of lensless Fourier holograms in optical metrology. Journal of Applied Optics. 38: 4812-4820.

On the Digital Holographic Interferometry of Fibrous Materials: Opto-Mechanical Properties of Fibres

Khaled Yassien,[1] Mostafa Agour,[2] and Christoph von Kopylow[2]
[1]Department of Physics, Aswan Faculty of Science, South Valley University, 81528 Aswan, Egypt
[2]Department of Optical Metrology, Bremer Institut für angewandte Strahltechnik, Klagenfurter Str. 2, D-28359 Bremen, Germany

1 Introduction

Digital holographic interferometry (DHI) has been applied in diverse fields for determining the shape, deformation and refractive index variations of transparent media [1]. In digital holography the hologram can be recorded on a CCD and the captured wavefield is also stored in a computer. The reconstruction process is performed numerically giving direct access to the intensity and phase of the stored wavefield. This process is based either on the calculation of the diffraction integral by a Fresnel-transformation method or a convolution method [2].
Orientation in polymers can be produced by several processes such as hot stretching of a molten polymer followed by rapidly cooling of the melt or by cold drawing or by cold rolling. Drawing is an important operation that improves the textile characteristics of man-made fibres [3]. In this report DHI is used to determine the opto-mechanical properties of poly (tetrafluoroethylene) (PTFE) fibres. The convolution approach is used to reconstruct numerically the recorded hologram resulting in the complex wavefield which is used to calculate the phase distribution. This phase is used to determine the refractive indices for light polarized parallel ($n^{||}$) and perpendicular ($n^{\perp}$) to the fibre axis and the birefringence B for PTFE at each draw ratio.

2 Experimental results and conclusions

A mechanical drawing system equivalent to a system utilized in [4] was used to study the opto-mechanical properties of PTFE fibre with the help

of a Mach-Zehnder interferometer. A sample of certain length is fixed at its ends with two clamps of the drawing system and put in one path of the interferometer perpendicular to its optical axis and it is immersed in a suitable liquid with a refractive index quite close to the refractive index of the fibre. The immersion liquid refractive index is measured by an Abbe refractometer with an accuracy of ±0.0001. The used refractive index of the immersion liquid is 1.398 at room temperature. The investigated fibre sample is drawn using the mechanical drawing system at draw ratios D= 1, 1.5, 2, 2.5, 3, 3.5, 4. The reference mirror of the interferometer is mounted on a Piezo-transducer PZT which is used to vary the phase difference between the two interfering beams. The PZT shifter was calibrated to minimize systematic phase shifting errors [5]. The phase shifting can be determined with an accuracy of ±3°.

A set of four holograms for light polarized parallel to the optical axis of the sample with a draw ratio D=1, with phase shifts 0, π/2, π and 3π/2 were obtained see Fig. 1(a-d). The recorded holograms have been combined to gain the complex wavefield. The convolution approach was used to reconstruct numerically the resulting wavefield and the phase distribution (φ) was calculated from it [1]:

$$\varphi(\xi,\eta) = \arctan\left\{\mathrm{Im}\left[U(\xi,\eta)\right] / \mathrm{Re}\left[U(\xi,\eta)\right]\right\}, \tag{1}$$

where;

$$U(\xi,\eta) = \int_{-\infty}^{\infty}\int_{-\infty}^{\infty} h(x,y)E_R^*(x,y)g(\xi,\eta,x,y)dxdy. \tag{2}$$

The parameters (x,y) and (ξ ,η) are the coordinates at the CCD and the reconstructed planes respectively. $h(x,y)$ is the wavefield obtained from the combination of four phase shifted holograms, $E_R^*(x,y)$ is the conjugated reference beam and $g(\xi,\eta,x,y)$ is the impulse response. The wrapped and unwrapped phases were determined and were given in Fig. 1(e,f), respectively.

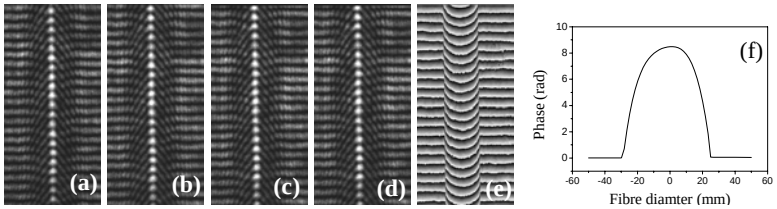

Fig. 1. (a-d) Recorded holograms (φ= 0, π/2, π, 3π/2, 2π) for light polarized parallel to the optical axis, e) Wrapped phase and f) Unwrapped phase of the recorded holograms.

The same process was used to determine the unwrapped phases of the PTFE fibre at different draw ratios for light polarized parallel and perpendicular to the fibre axis. Using the obtained unwrapped phases of the investigated sample, the refractive indices of the fibres at different draw ratios can be calculated using the following equation [6]:

$$n^i = n_L \pm \frac{\varphi^i \lambda}{2\pi t} \tag{3}$$

where i denotes to the polarization state (parallel || or perpendicular ⊥), n and n_L are the refractive indices for the fibre and the surrounding liquid, respectively, φ is the unwrapped phase at the centre of the fiber samples, λ is the wavelength of the used light and t is the fiber thickness. Positive and negative signs are used when the mean refractive index of the fiber n is greater or less than the refractive index of the immersion liquid n_L. In addition the optical birefringence B can be calculated from the difference between the measured values of refractive indices $n^{||}$ and $n^{\perp}$ ($B = n^{||} - n^{\perp}$) [6]. The relationship between the refractive indices $n^{||}$, $n^{\perp}$ and the birefringence B with the draw ratio for PTFE fibres are determined as shown in Fig. 2.

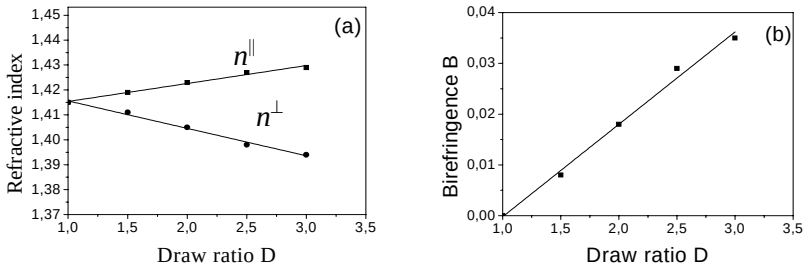

Fig. 2: The relationship between the refractive indices $n^{||}$ and $n^{\perp}$ with the draw ratio D (a) and the relationship between birefringence B with D (b) for PTFE samples

It is clear from figure 2a that the refractive index $n^{||}$ of the investigated sample increased with increasing of draw ratios and the refractive index $n^{\perp}$ decreased with increasing of draw ratios. Hence the birefringence B increases with increasing draw ratio (fig. 2b). The increasing birefringence indicates a high orientation of the fibre [3]. The refractive indices and the resulting birefringence at different draw ratios measured by DHI are in good agreement with those reported previously by literature [7].

The phase-sifting digital holography and the convolution approach for the reconstruction process were selected in order to investigate the opto-mechanical properties of fibre instead of other holographic techniques because of the following:
1) In contrast to all methods that are based on the evaluation of intensity distributions, Digital holography (DH) allows a direct access not only to the intensity but also to the phase of the wave front, which means it is entirely exhibiting such three dimension effects as depth of field [1]. 2) Digital focusing of the reconstructed wavefield emulates the manual focusing control of conventional microscopes and overcomes the limitations of the focusing (working) distance of their objectives. 3) The resolution and the accuracy of the determined interference phase are very high and found to be more than $\pi/50$. The accuracy in the measurement of the refractive index is better than 4.5×10^{-4} and this value is found to be in agreement with that obtained by literature [8].

3 References

1. Schnars, U., Jüptner, W.: Digital Holography; Springer-Verlag, Berlin, 2005
2. Schnars, U, Jüptner, W.: Direct recording of holograms by a CCD target and numerical reconstructionL; Appl. Opt. 33: 179-181, 1994
3. Zbigniew K. W.: Formation of Synthetic Fibers. Ch 7, Gordon and Breuch Science Publishers, New York, 1977
4. Hamza, A., Sokkar, T., El-Bakary, M.: Detection of the variation of the optical and geometrical parameters of fibres due to the cold drawing process; Meas. Sci. Technol. 15: 831-838, 2004
5. Chengand, Y., Wyant, J.: Phase shifter calibration in phase-shifting interferometry; Appl. Opt. 24: 3049-3052, 1985
6. Barakat, N., Hamza, A.: Interferometry of Fibrous Materials; Adam Hilger, Bristol, 1990
7. El-Dessouky, H. M., Lawrence, C. A., Voice, A. M., Lewis E. L. V., Ward, I. M.: An Interferometric Prediction of the Intrinsic Optical Properties for Cold-drawn iPP, PTFE and PVDF Fibres; J. Opt. A: Pure & Appl. Opt. 9:1041-1047, 2007
8. Benjamin, R., Pierre, M., Etienne, C., Yves, E., Christian, D., Pierre, J. M.: Measurement of the integral refractive index and dynamic cell morphometry of living cells with digital holographic microscopy; Optics Express 13: 9361-9373, 2005

Geometrical camera calibration using lasers and diffractive optical elements

M. Bauer1, D. Grießbach1, A. Hermerschmidt2, S. Krüger2, M. Scheele1, A. Schischmanow1
1German Aerospace Center (DLR), Institute of Robotics and Mechatronics, Rutherfordstraße 2, 12489 Berlin, Germany
2HOLOEYE Photonics AG, Albert-Einstein-Str. 14, 12489 Berlin, Germany

1 Introduction

For using digital cameras for quantitative measurements of angles, distances, or object sizes, a precise geometrical calibration of the whole camera as a unit, including optical system and sensor, is required. Traditional methods for geometrical camera calibration are based on calibration grids or on single-pixel illumination by collimated light. In this paper, a new method for geometrical sensor calibration by means of a well-collimated laser beam with precisely known wavelength and a tailored diffractive optical element (DOE) is presented. This method is mainly dedicated to calibration of 2D-sensor array systems, but in principle also usable for linear array sensors.

2 Description of the method

In our method, geometrical calibration of the camera is achieved by the determination of the parameter set of a pinhole camera model, incorporating the radial distortion model by Brown [1], from a single test image.
Our approach uses custom-made diffractive optical elements as beam-splitters for an incident laser beam, thus producing beams at precisely known diffraction angles which serve as virtual objects at infinite distance. Because in this configuration the recorded image is invariant against translation of the camera, a complete camera calibration #is possible with a single image avoiding complex bundle adjustments.

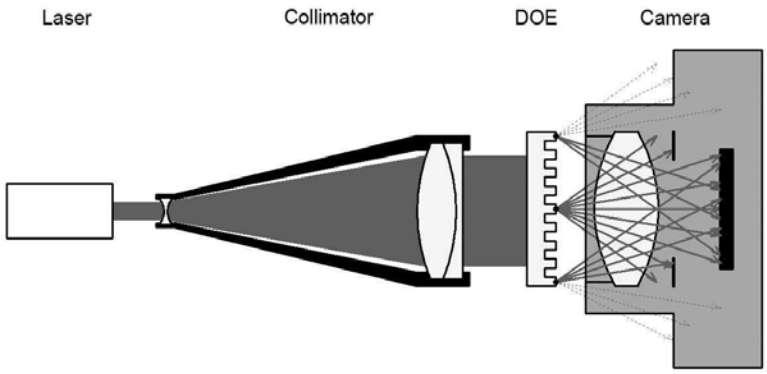

Fig. 1. Experimental set-up used for the camera calibration.

The experimental setup is shown in fig.1. A mixed-gas argon/krypton ion laser (MellesGriot 643 series) was used which offers a selection of wavelengths in the visible spectral range.
The laser, the collimator and the DOE together form the object. The camera takes an image of this object which consist of spots corresponding to diffraction orders of the DOE. The recorded image is used to determine the direct correlation between incidence angles and sensor pixels. After the spots in the image have been assigned to the diffraction orders by an iterative procedure, a numerical fit procedure can be applied to the data to determine the unknown parameters of camera and set-up.
The DOE used is a crossed grating. The incidence of the laser beam to the DOE is described by two angles α and β in a spherical coordinate system, with the zenith direction being given by the normal of the DOE surface. These angles account for the finite alignment accuracy that can be achieved in a real setup and the diffraction directions can be expressed in terms of these angles [2].
The external orientation of the camera in the coordinate system of the DOE is described by the Euler angles denoted as ω, φ and κ. The internal parameters of the camera which we want to determine by the calibration procedure are the focal length f, the principal point $[u_0,v_0]$ and the radial distortion parameters k_1, k_2 and k_3.
The quantities treated as constants are the laser wavelength and the grating periods in the two spatial directions of the DOE. The desired orders of the DOE were chosen so that an equidistant grid of spots was obtained on the sensor when illuminated with a wavelength of 632.8nm. The element was

designed using an iterative numerical procedure and fabricated as an amplitude mask of Chromium on a fused silica substrate using electron-beam writing.
Details about the design and fabrication of the DOE and the analysis procedure of the obtained images to determine the unknown parameters of the camera and the set-up are given in [3].

3 Results and Discussion

The results shown here were obtained during the calibration of a monochrome Dalsa 1M28-SA camera with a CMOS sensor of 10.6µm pixel size and a focal length of 4.8mm at the wavelength of 676.4nm. The results are given in table 1 below.

Table 1. Calibration results for Dalsa 1M28-SA camera

	#1	#2	#3	#4
u_0	521.8	521.9	521.9	521.3
v_0	482.1	482.1	482.0	481.2
f	459.6	459.9	459.9	460.4
k_1	-0.2202	-0.2220	-0.2223	-0.2349
k_2	0.0650	0.0664	0.0672	0.0826
k_3	-0.0094	-0.0094	-0.0100	-0.0147
α	-0.04°	-0.07°	-0.06°	n/a
β	0.04°	0.04°	0.01°	n/a
ω	0.11°	-3.63°	3.10°	n/a
φ	-0.03°	-8.64°	4.95°	n/a
κ	2.04°	0.04°	0.5°	n/a

The achieved results with DOE calibration (measurements #1 to #3, in which only the exterior orientation of the camera was changed) are well comparable with a photogrammetric calibration of the same camera (measurement #4). Moreover, the internal camera parameters were reproduced well in the different measurements with the DOE, with no significant dependence on the external orientation. In figure 2, the effect of

distortion correction is visualized for the chessboard image used for the photogrammetric calibration.

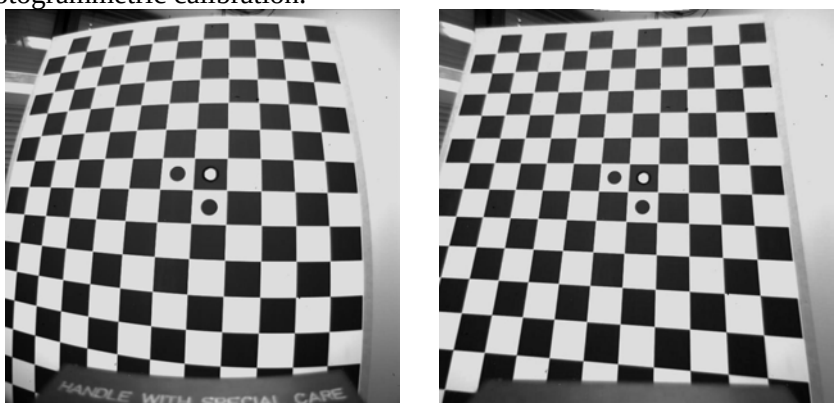

Fig. 2. Uncorrected (left) and corrected (right) image taken with the Dalsa 1M28-SA

4 Summary

It was shown that a reliable calibration can be obtained which allows separating the parameters of the interior orientation of the camera from the orientation parameters of the DOE with respect to the laser and the exterior orientation of the camera. Hence, the alignment requirements of the calibration setup components are reduced to a rather moderate level, which simplifies the calibration procedure and in principle allows in-the-field calibration. A limiting factor for the accuracy is the determination of the sub-pixel position for each diffraction spot, therefore further investigations on shape and intensity distribution are intended.

5 References

1. Brown, D C (1971) Close-range camera calibration. Photogrammetric Engineering 37, 855-866
2. McPhedran R C, Derrick G H, Brown L C (1980) “Theory of crossed gratings, ” in R. Petit (ed.), “Electromagnetic theory of gratings, ” Springer Verlag Berlin, 227–275
3. Bauer M, Grießbach D, Hermerschmidt A, Krüger S, Scheele M, Schischmanow A (2008) Geometrical camera calibration with diffractive optical elements. Optics Express 16(25), 20241-20248

Measurement of the local displacement field produced by a microindentation using speckle interferometry. Its application to analyse coating adhesion

A. E. Dolinko and G. H. Kaufmann
Instituto de Física Rosario (CONICET – UNR)
Blvd. 27 de Febrero 210 bis, S2000EZP Rosario
Argentina

1 Introduction

The definition of adhesion is not a simple issue and its characterization generates considerable debate in the technical literature [1]. Many of the existing tests to determine the adhesion of a given coating-substrate combination are qualitative or semi-quantitative and the adhesion is assessed from the appearance of the fracture surface [2].
In this work we present a technique to investigate coating adhesion based on digital speckle pattern interferometry (DSPI), which is used to measure the out-of-plane deflections of the buckling generated by the introduction of a conical microindentation. The buckling generates a circular delamination, whose magnitude is directly related to the strain energy release rate that is a parameter that can be used to evaluate the adhesion. Experiments performed in coated specimens with different interface conditions demonstrate that DSPI enables the measurement of the tiny buckling generated in the coating after the introduction of a microindentation and allows the determination of the radius of the delaminated region, which is related to the adhesion of the coating.

2 Experimental procedure and data analysis

The DSPI system used to measure the deflections of the coating due to the introduction of the microindentation was a conventional speckle interferometer designed to measure the out of plane displacement component w at the coated surface of the specimen. The microindentation was introduced using a scratch tester device (Teer coatings ST30) without

displacing the specimen, located outside of the optical bench. For this reason, the specimen was repositioned into the same position that had during the recording of reference speckle interferogram using a specially designed specimen holder with high stability.
The substrate of the specimens was a steel plate with a rectangular cross-section and as coating we used a bronze sheet with a thickness of 0.25 mm, which was glued to each steel plate by means of an epoxy resin. Different interface conditions were obtained by polishing the surface of the steel substrates using sandpapers with different grain sizes. It was supposed that the different depths of the parallel microgrooves that were generated in the polished substrate surfaces will change the effective adherence.
The wrapped phase distribution was evaluated using the Carré phase-shifting technique. The unwrapped phase was obtained using an iterative robust unwrapping algorithm based on the minimum L0-norm solution [3]. Additionally, all phase maps were processed with a method to remove spurious rigid body displacements that can be introduced during the repositioning [4].

3 Experimental results

Figure 1(a) shows a typical phase map produced by a microindented specimen. The radius R of the circular delamination was determined by the buckled region and it was estimated from the unwrapped phase maps by plotting the out of plane displacement component w measured along a radial direction r, with the origin of the coordinate system located at the indentation centre, as shown in Fig. 1(b). The distance l between both minima displayed by this curve was taken as the diameter of the buckled region. The radius R of the buckled region that can be used to characterise the adhesion of the substrate-coating system is given by $R=l/2$. In this figure, d_i denotes the diameter of the indentation mark.

3.1 Delamination radius for specimens with different interface conditions

The radius R of the buckled region was measured in three specimens with different interface conditions, which where obtained by polishing the substrate of each specimen with sandpapers having different grain sizes. The tests were performed using an indentation load of 30 N and the speckle interferograms were acquired 24 hours after the coating was glued.

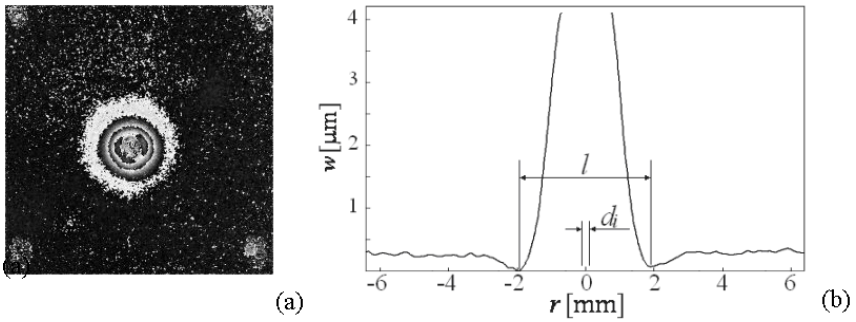

Fig. 1. (a) Wrapped phase map of one of the specimens analysed and (b) out of plane displacement component measured along a line obtained from the phase map showed in (a).

Each specimen was polished with sandpapers number 80, 240 and fine grain alumina, respectively. The radius R of the buckled region produced by each specimen was 0.9, 1.3 and 3.1 mm, respectively. These results show that the radius of the delaminated region increases as the grain size of the sandpaper was reduced.

3.2 Delamination radius as a function of the adhesive curing time

The effect of the curing time of the epoxy resin could also be analysed by measuring the radius R of the buckled region generated by various microindentation tests performed at different times after the coating was glued to the substrate. To make sure that the same interface conditions were used in all tests, all microindentations were introduced at different places over the coated surface of a single specimen.

Figure 2 shows the out of plane displacement component w measured along the radial direction r when the microindentation was introduced at 30, 90 and 150 minutes after the coating was glued. In these tests, the substrate was polished with sandpaper number 80 and the indenter load was 30 N. The radius values R of the buckled regions that were determined at 30, 90 and 150 minutes after the coating was glued were 2.1, 1.2 and 1.0 mm, respectively. As the radius of the buckled region is inversely proportional to the adhesion strength, as expected, these results confirm that the adhesion of the epoxy resin increases with the curing time. Additional tests carried out at times longer than 3 hours after the coating was glued did not show any change in the measured displacements. Therefore, these results suggest that the technique proposed in this paper confirm that the epoxy resin used to glue the coating cures completely at times longer than 3 hours.

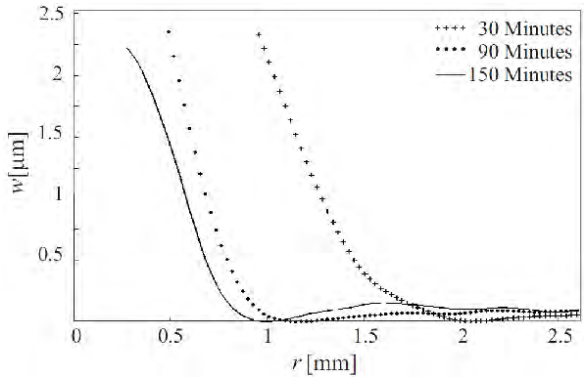

Fig. 2. Out of plane displacement component *w* measured along a radial direction at 30, 90 and 150 minutes after the coating was glued.

4 Conclusions

This paper presents the evaluation of a technique based on DSPI and a microindentation test to investigate the adhesive performance of coatings. The experiments performed on coated specimens with different interface conditions demonstrate that the proposed technique allows measuring the delamination radius produced by specimens with different interface conditions. The change in adhesion could also be successfully monitored as a function of the adhesive curing time.

5 References

1. Lacombe R. (2006) Adhesion Measurement Methods. Boca Raton: Taylor & Francis.
2. Broek D (1984) Elementary Engineering Fracture Mechanics. 3rd ed. Boston: Martinus Nijhoff Publishers.
3. Ruiz PD, Kaufmann GH, Galizzi GE (1998) Unwrapping of digital speckle-pattern interferometry phase maps by use of a minimum L0-norm algorithm. Applied Optics 37:7632-7644.
4. Dolinko A, Kaufmann GH (2006) A least-squares method to cancel rigid body displacements in a hole drilling and DSPI system for measuring residual stresses. Optics and Lasers in Engineering 44:1336–1347.

Space-Time Multiplexing in a Stereo-photogrammetry Setup

M. Große, R.Kowarschik
Friedrich-Schiller-University Jena, Institute of Applied Optics
Froebelstieg 1, 07743 Jena
Germany

1 Introduction

At the Institute of Applied Optics (IAO) a photogrammetric stereo setup was realised in 2005. The goal was to provide a fast measurement method for human faces in the context of surgical operation planning. As commercial stripe projection systems were not capable of realising data acquisition within or below one second, the maximum time frame considered tolerable for younger patients, we were looking for an alternative structured light method. The so called time-correlation technique introduced [1] was chosen, which uses a sequence of statistical, binary patterns to code the objects surface. This paper presents an enhancement of the well-known time-correlation technique which combines spatial and temporal properties of a sequence of stereo-image pairs in order to find correspondences.

2 Improvement of the statistical pattern

In [2], [3] Wiegmann showed that the transition from a pure statistical black-white pattern (BP) to a bandlimited statistical pattern (*BLP*) improved the result of the 3D reconstruction. One advantage of these *BLP* is that the size of the structure brought onto the object is optimized for detection with the used CCD-cameras. The quality of the reconstruction was further improved by binarising the bandlimited statistical pattern used by Wiegmann, as it is possible to realize a better contrast when using binarised patterns. As demonstrated in [4] the binarised bandlimited statistical patterns (BBLP) deliver the most point-matches as well as the lowest noise level. The evolution of the used statistical patterns is shown in figure 1.

3 Solution of the correspondence problem

In order to create a 3D reconstruction of different views of an object it is mandatory to find so called homologous points: n-tuples of image points which are the images of one object point. Structured light methods enable dense object reconstructions although it is usually necessary to project multiple different structures onto the object to code it appropriately. Therefore these techniques often analyse the temporal grey value sequence of every pixel or a batch of pixels to find homologous points.
In our setup an object is illuminated with a sequence of N patterns similar to the one shown in fig. 3c. Two cameras are synchronously capturing images of the object for every projected pattern. After the measurement process is finished, there are N greyvalues for every pixel of every camera. To find the homologous point for an arbitrary pixel of camera K1 the temporal grey value sequence is correlated with the temporal grey value-sequence of every pixel of camera K2 according to the usual normalized one dimensional cross correlation. Two pixels are set to be homologous to each other if the correlation is a global maximum and exceeds a certain threshold. This approach delivers a dense and outlierfree 3D reconstruction when using N>20 projected patterns. As the number of projected patterns is decreased the probability increases that two temporal grey value-sequences correlate above the set threshold although they are not physically homologous, which leads to outliers in the measurement volume (fig. 2). Increasing the threshold is not a solution as outlier arise from correlations covering the whole interval from [threshold, 1]. Therefore it is necessary to find another or additional criterion for selecting homologous points. In [5] the authors point out that there are techniques analysing temporal properties and that there are methods dealing with spatial features, but only a few which analyse a combination of temporal and spatial features. Thus it was our idea to widen the correlation technique as follows: When a pair of homologous points was found using the temporal correlation of the grey value-sequences, it is checked whether the areal properties around the pixel from K1 is similar to the areal properties around the pixel from K2. To test this approach a simple area-window correlation centered at the pixels of the homologous pair was

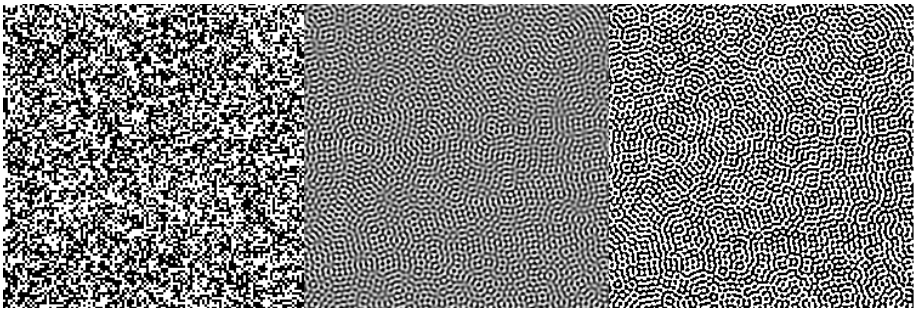

Fig. 1. a) normal statistical binary pattern – BP, b) bandlimited statistical pattern [3] – BLP, c.) binarised bandlimited statistcal pattern [4] – BBLP

implemented. If the areas are similar the potential homologous pair will be accepted as valid otherwise the homologous pair is dismissed and no 3D point calculated (fig 3).

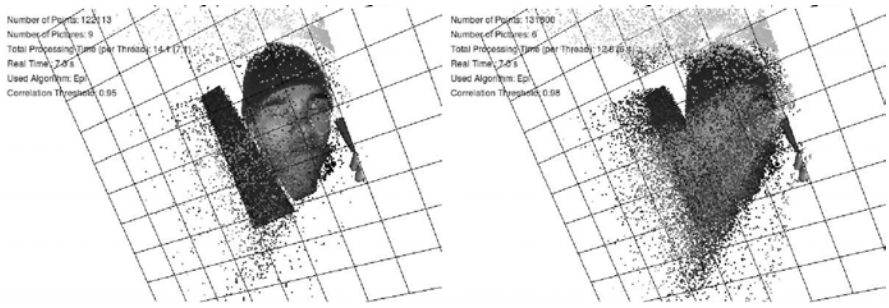

Fig. 2. Two reconstructions of a human face using less than 20 pattern images (left: 9 patterns, right: 6 patterns)

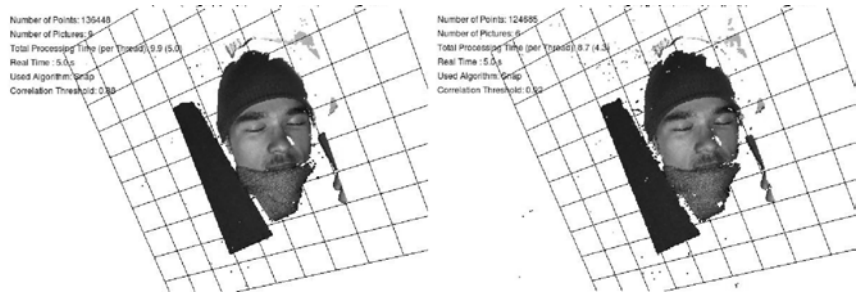

Fig. 3. Results of a face reconstruction using temporal and areal properties (left: 9 patterns, right: 6 patterns), compare with figure 2

4 Experimental results

Two calibrated cameras are looking convergently at an object. Along with a standard DLP-Beamer they are attached to a computer which synchronizes pattern projection and image capturing, realizing an image stream of about 28 pattern images per second. After the image data has been transferred to the computer homologous points are searched and the 3D points are calculated.
In order to determine the accuracy of the setup using BBLP two different measurements were conducted. [3] made use of a calibrated height-step normal. The normal consisted of several height steps in the range of five to 50 microns. Height deviations of 20 microns were detected. Furthermore a reference plane was captured and reconstructed. The peak to valley value and the standard-deviation of the point cloud to a fitted plane were calculated. The results are shown in figure 4. The measurement volume was about 20cm x 20cm x 30cm.

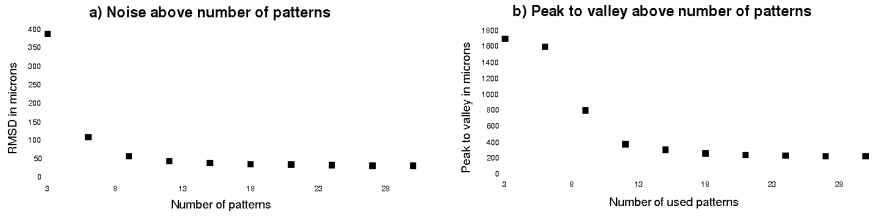

Fig. 4.a) noise values b) peak to valley values (shown is the change above the number of projected pattern)

5 Conclusion

An improved version of the BLP was presented. Furthermore it was shown that it is feasible to combine areal and temporal features of a structured light setup to reduce the number of projected patterns, which can yield a dense outlier free 3D reconstruction. The rough determination of points may be accurate enough to replace gray-code images in stripe projection systems which may lead to a shorter measurement time. With our current setup it is possible to capture all data for 3D reconstruction as fast as 0.2 seconds. Additionally there is much room to improve the way the areal features are compared as there exist several scale, rotation and affine transformation invariant methods.

6 References

1. Albrecht, P, Michaelis, B (1998) Stereophotogrammetry with Improved Spatial Resolution, 14th International Conference on Pattern Recognition
2. Wiegmann, A 2005 Gesichtsvermessung mittels Stereophotogrammetrie, Master Thesis
3. Wiegmann, A, Wagner, H 2006 Human face measurement by projecting bandlimited random patterns, Optical Express 7692
4. Große, M 2008 Untersuchungen zur korrelationsbasierten Punktzuordnung in einem Stereophotogrammetriesystem, Master Thesis
5. Davis, J, Ramamoothi, R, Rusinkiewicz, S 2003 Space-Time-Stereo: A Unifying Framework for Depth from Triangulation, IEEE Comp. Soc. Conf. on Computer Vision and Pattern Recognition (CVPR)

Interference Investigation of Concrete Structure and Dynamics During Hydration.

Mykhaylo P.Gorsky, Peter P.Maksimyak, Andrew P.Maksimyak
Correlation Optic Dept., Chernivtsi national university,
2 Kotsybunska str, 58012 Chernivtsi
Ukraine

1 Introduction

Concretes are basic materials of modern building industry and basic backfill materials for oil-and-gas industry. Concrete formation passes the process of hydration – cement and water interaction. According to existing models, concrete induration occurs due to enlargement and accretion of cement powder particles [1]. For cement crystal growth forecasting it is important to know cement powder distribution by particles sizes. For this aim method of particles size distribution using shearing interferometer was suggested. The beginning and the end of concrete solution induration determine usually [3] using Vicat apparatus. It measures immersion depth of needle in normal cement solution, poured into special taper. But this method does not allow impartially judge early hydration stages. That's why we proposed method of earlier hydration stages diagnostics by means of speckle field dynamics investigation.

2 Measurement of cement particles size distribution

Cement is a complicated mixture of particles with different sizes and forms. For calculations execution of concrete optical properties it is very important to know size distribution function of particles. This opportunity realizes by laser radiation diffraction method [2], but it essentially depends on refractive index of particles. As cement is a mixture of particles with different chemical composition, each particle could have its own refractive index value, which considerably complicates using of this method.

Method of particles size distribution measurement using shearing interferometer does not have such imperfection. For measurements we used polarization interferometer (Fig 1.) It consists of two identical wedges, which form plane-parallel plate and are situated between crossed

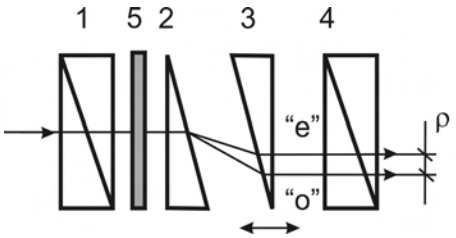

Fig. 1. Optical scheme of experimental setup.

polarizers. Principal optical axes of wedges 2 and 3 form 45^0 angle with plane of polarization of polarizers 1 and 4. Sample 5 (thin layer of cement powder, deposited on glass) is situated between polarizer 1 and wedge 2. Wedge motion causes longitudinal displacement between ordinary "o" and extraordinary "e" bundles. Transverse displacement calibration is made by extreme values of result field intensity (disparity move multiply on λ). In our experimental setup each extreme value corresponds to transverse displacement of 3.36 μm. While transverse displacement, particle images superposition is happen and intensity extremes depend on particles size. Procedure of maximum $I_{\max}(\rho, x)$ and minimum $I_{\min}(\rho, x)$ intensity values definition by this method with displacement ρ for particle's diameter d described in [4]. If in image formation ensemble of particles with different sizes is taking part, with corresponding distribution $p(x)$, then summary maximum and minimum intensity could be written as:

$$I_{\max}^{total}(\rho, \rho_s) = \int p(x) I_{\max}(\rho, x) dx \tag{1}$$

$$I_{\min}^{total}(\rho, \rho_s) = \int p(x) I_{\min}(\rho, x) dx \tag{2}$$

Distribution function definition from these equations is very complicated. But if we know function $p(x)$ appearance, we could find its parameters. Our investigation shows, that cement particles distribution by sizes is good approximated by Rayleigh distribution:

$$p\ (d, \sigma) = \frac{d}{\sigma^2} Exp(-\frac{d^2}{2\sigma^2}) \tag{3}$$

Where σ - the most probable value of d. By received from experiment extreme values of intensity (Fig. 2a), functions (1) and (2) fitting to minimum values of mean-square distance could be made (Fig. 2b).

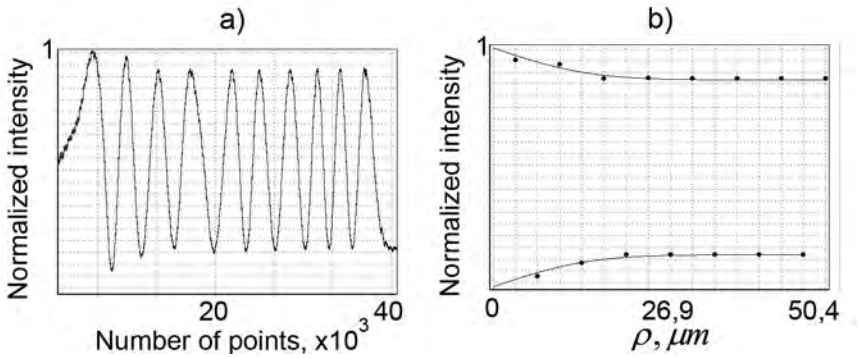

Fig. 2. Intensity, received from experiment (a), and results of fitting by extreme values of intensity (b).

By results of 10 measurements we received $\sigma = 19.5$, which good correlates with data from microscope images analysis.

3 Speckle field dynamics during concrete hydration

During hydration there are dissolutions of a crystalline system of cement, formation of new crystals and an amorphous phase. While irradiating the cement surface with coherent beam, the composite field with random amplitudes, phases and polarizations is formed. The modification of optical properties of a cement stone during hydration and induration results in redistribution of intensity of a leakage field. So, the time profile of intensity of scattered coherent beam represents the information on processes which happen in cement slurry. In experiment linearly polarized beam from He-Ne laser hits the cement paste. Filing of fluctuations of intensity is carried out by CCD. For separation of the scattered radiation from depth of a sample the polarizer, which plane of the skip is orthogonal to polarization of a laser, before CCD is used.

Received intensity fluctuations from part of image were showed on Fig.3a. Image part size was chosen to be smaller than average speckle size. Let's analyze square derivative of intensity (Fig.3b). The first part is characterized by the highest peaks. Probably, it is caused by intensive chemical reactions of cement with water (hydration). Such supposition coordinates with existing theories [1]. The second part does not contain considerable peaks. In this period of time do not contain considerable changes during hours. Vicat apparatus shows that induration time begins at 3 hours and ends at 3.2 hours. The third part contains peaks that begins at 3 hours and ends at 7 hours.

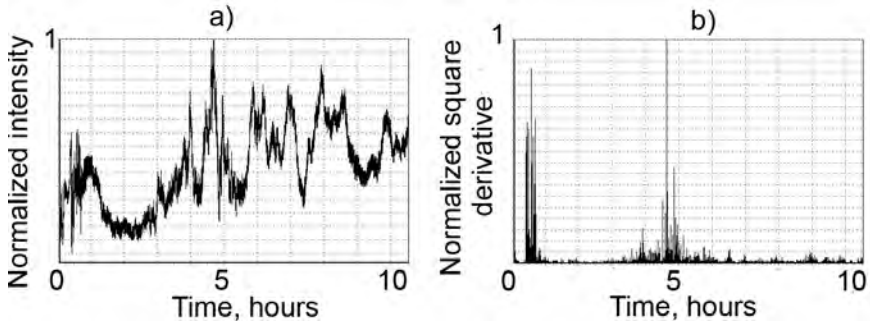

Fig. 3. Intensity of part of speckle field dependence vs. time (a) and normalized square derivative of this intensity.

In this time crystal splicing and concrete induration are happen.

4 Conclusions

Interference method of size particles distribution definition is more independent from single particles parameters then laser diffraction method.

Presented method of speckle field dynamics optical diagnostics allows doing earlier and late stages of hydration diagnostics of concrete hardening process in comparison with Vicat apparatus.

5 References

1. Ramachandran, V, Beaudoin, J (2000) Handbook of Analytical Techniques in Concrete. National Research Council of Canada, Ottawa, Canada
2. Ferraris, C, Hackley, V, Aviles, A (2004) Measurement of Particle Size Distribution in Portland Cement Powder: Analysis of ASTM Round Robin Studies. Cement, Concrete and Aggregates, Vol.26, No. 2
3. GOST 310.3-76, (1976) Cements. Methods of definition of normal density, terms of harden and uniformity of change of volume. (in Russian)
4. Maksimyak, P, Angelsky, V (1994) Optical correlation method for measuring particle size and concentration. Proc. SPIE, Vol. 1991, 260

Off-axis Reconstruction Method for Displacement and Strain Distribution Measurement with Phase-Shifting Digital Holography

Motoharu FUJIGAKI*, Kohei SHIOTANI**, Riku NISHITANI**,
Akihiro MASAYA*, Yoshiharu MORIMOTO*
*Department of Opto-mechatronics, Faculty of Systems Engineering,
Wakayama University, fujigaki@sys.wakayama-u.ac.jp
**Graduate School of Systems Engineering, Wakayama University
Sakaedani 930, Wakayama, 640-8510
Japan

1 Introduction

Inspection is very important for health monitoring and life lengthening of infrastructures such as steel bridges. An efficient measurement method of strain distribution is required to find cracks. Development of a compact and conventional strain distribution measurement equipment for practical use is required.
Phase-shifting digital holography[1] is a convenient method to measure displacement and strain distributions on the surface of an object. Many researchers are studying this method and several compact equipments are developed[2]. We also developed compact equipments for strain measurement[3]. In these equipments, several object waves are necessary to measure the in-plane displacement and strain distribution. To simplify the optical setup is required for producing more compact equipment.
In this paper, we propose an off-axis reconstruction method for displacement and strain distribution measurement with a phase-shifting digital holography.

2 Off-axis reconstruction method with two CCD sensors

Figure 1 shows an off-axis setup for displacement distribution measurement using two CCD sensors. A collimated object wave is illuminated onto an object from the front of an object. The two sensors are placed beside the incident object wave. The directions of the optical axes

of the sensors are parallel with the incident object beam. The object waves scattered on the surface of the object reach CCD sensor 1 and CCD sensor 2 with angles of θ_1 and θ_2, respectively.

In the case of CCD sensor 1, digital holograms produced with the scattered object wave and a reference wave which comes to the sensor perpendicularly can be obtained. The reconstructed image of the object appears as the object is located in front of CCD sensor 1. Phase difference $\Delta\phi_1$ can be obtained from the reconstructed image before and after deformation. In the same way, phase difference $\Delta\phi_2$ can be obtained from the reconstructed image appearing as the object is located in front of sensor 2. The in-plane displacement for the *x*-direction, d_x, and the out-of-plane displacement for the *z*-direction, d_z, are calculated by Eq. (1) and Eq. (2), respectively, where λ is a wavelength.

$$d_x = \frac{\lambda}{2\pi} \cdot \frac{(\cos\theta_2 + 1)\Delta\phi_1 - (\cos\theta_1 + 1)\Delta\phi_2}{(\cos\theta_2 + 1)\sin\theta_1 + (\cos\theta_1 + 1)\sin\theta_2} \tag{1}$$

$$d_z = \frac{\lambda}{2\pi} \cdot \frac{\sin\theta_2\Delta\phi_1 - \sin\theta_1\Delta\phi_2}{(\cos\theta_1 + 1)\sin\theta_2 + (\cos\theta_2 + 1)\sin\theta_1} \tag{2}$$

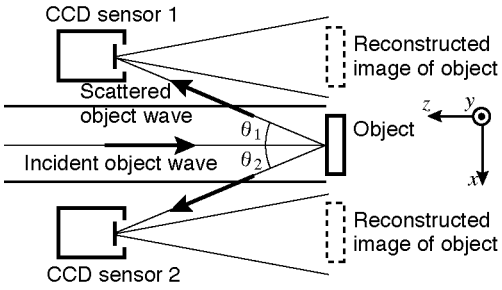

Fig. 1. Off-axis setup for displacement distribution measurement using two CCD sensors

3 Experiment for displacement and strain distribution measurement

Figure 2 shows an experimental setup for displacement and strain distribution measurement using two CCD sensors. Reference waves reach the CCD sensors as shown in Fig. 2.

A cantilever is used as an object. The part near the free end is displaced for the upper direction. Figure 3 and Fig. 4 show reconstructed images

obtained from both the sensor 1 and the sensor 2 before and after deformation, respectively. These images are reconstructed as the object is located in front of the CCD sensors. Minor adjustment of the position between the reconstructed image obtained from CCD sensor 1 and CCD sensor 2 is performed with moving the center position of the hologram[4]. The phase differences obtained from Fig. 3 and Fig. 4 are shown in Fig. 5. These phase differences are obtained by Windowed PSDHI[5] for reducing speckle noise. The displacement distribution for the *x*-direction shown in Fig. 6 is obtained from Fig. 5 using the Eq. (1). The strain distribution for the *x*-direction shown in Fig. 7 is obtained from Fig. 6 with spacial differentiation for the *x*-direction. Positive and negative strain appear at the lower and upper sides near the fixed end of the cantilever, respectivery.

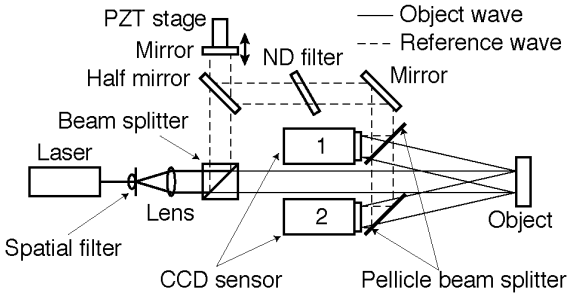

Fig. 2. Displacement and strain distribution measurement setup using two CCD sensors.

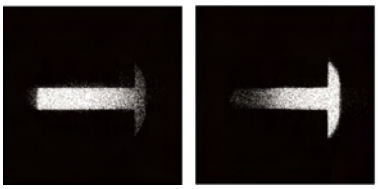

(a) Sensor 1 (b) Sensor 2

Fig. 3. Reconstructed images before deformation

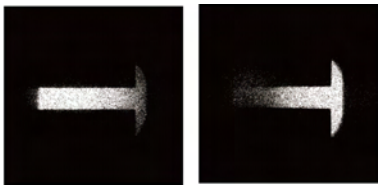

(a) Sensor 1 (b) Sensor 2

Fig. 4. Reconstructed images after deformation

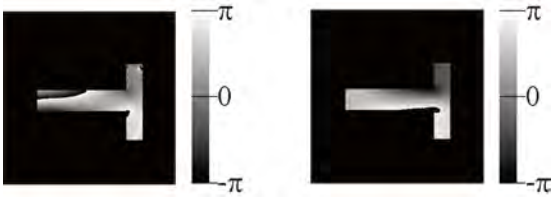

(a) Sensor 1 (b) Sensor 2

Fig. 5. Phase difference

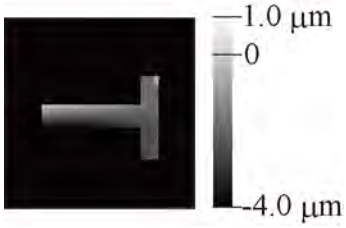

Fig. 6. Displacement distribution for the *x*-direction

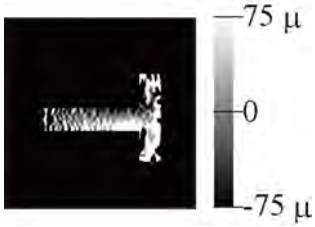

Fig. 7. Strain distribution for the *x*-direction

4 Conclusions

We proposed an off-axis reconstruction method for displacement and strain distribution measurement with a phase-shifting digital holography. An experiment of displacement and strain distribution measurement was performed with this method using two CCD sensors.

5 References

1. Yamaguchi, I., and Zhang, T. (1997) Phase-shifting Digital Holography. Optics Letters 22-16:1268-1270
2. Kujawinska, M., Michalkiewicz, A. (2008) New Approaches and Concepts for Engineering Objects Monitoring and Measurements Based on Digital Holography and Interferometric Principles. Proceedings of the International Symposium to Commemorate the 60th Anniversary of the Invention of Holography :81-88
3. Fujigaki, M., Kido, R., Shiotani, K., Morimoto, Y. (2008) High-speed and Compact Strain Measurement System by Phase-shifting Digital Holography. Proceedings of the International Symposium to Commemorate the 60th Anniversary of the Invention of Holography :316-323
4. Matsui, A., Fujigaki, M., Morimoto, Y. and Matui, T. (2006) Optical Axis Adjustment Method by Software in Multi Beam Phase-shifting Digital Holography. Proceedings of 11th Intelligence Mechatronics Workshop (in Japanese) :10-13
5. Morimoto, Y., Matsui, T., Fujigaki, M. and Kawagishi, N. (2007) Subnanometer Displacement Measurement by Averaging of Phase-difference in Windowed Digital Holographic interferometry. Optical Engineering, 46-2:025603

“Flying Triangulation”: A motion-robust optical 3D sensor principle

Svenja Ettl, Oliver Arold, Peter Vogt, Ondrej Hybl, Zheng Yang,
Weiguo Xie, and Gerd Häusler
Institute of Optics, Information and Photonics, University of Erlangen-Nuremberg, Staudtstr. 7/B2, 91058 Erlangen
Germany

1 Introduction

The complete and precise acquisition of a complex object surface can be an elaborate or even impossible task with existing sensors. First, to entirely measure the surface the sensor needs to acquire partial 3D views from different positions. Thus, the sensor has to be moved, sometimes hundreds of times or even more (e.g. for measuring sculptures or architecture). Second, sometimes a motion of the object relative to the sensor is unintended but inevitable (e.g. for medical purposes). Thus, the sensor has to acquire the single 3D views fast enough to avoid a loss of precision caused by motion. So far, most existing optical 3D sensors lack this property.

We present a new optical 3D measurement system we call "Flying Triangulation" that overcomes the mentioned difficulties. It combines a simple sensor with sophisticated algorithms. The handheld sensor can be freely moved around the object while acquiring 3D information “on the fly”. Each 3D view is acquired with one single shot which guarantees the demanded motion robustness. This has a price: We can only acquire sparse 3D data from each single shot instead of full-field data. The challenge was here to choose a light pattern which yields as much information in a single 3D view as possible but that simultaneously assures a unique identification of the pattern in the camera image.

The complete surface information is obtained by taking a “movie” of data while freely moving the sensor around the object. However, the single 3D views then need to be registered to each other to yield a dense surface model. This requires proper registration methods since conventional methods are not applicable for such sparse data [1, 2].

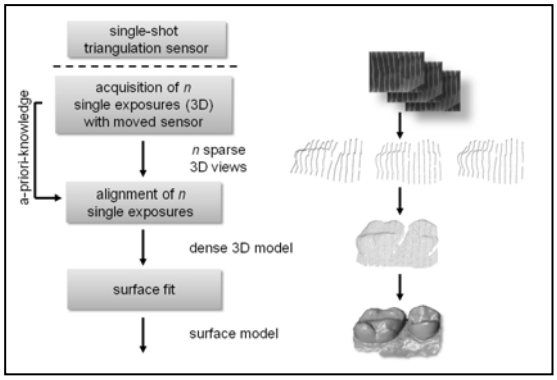

Fig. 1. Measurement principle of "Flying Triangulation".

2 Sensor principle

Our measurement system (Fig. 1) is based on an active-triangulation sensor to generate 3D views with sparse data. For this purpose, a line pattern is projected onto the object under test and the distorted pattern is observed by a camera under a fixed triangulation angle. After calibration, from each single camera image a sparse 3D view can be calculated. In order to obtain a dense 3D model all sparse 3D views are aligned to each other. Optimally, surface fitting procedures can be applied to retain a surface model of the object.

2.1 Single-shot sensor

The measurement uncertainty of an active-triangulation sensor mainly depends on the speckle noise, which is given by

$$\delta z_{\text{speckle}} = \frac{C}{2\pi} \frac{\lambda}{\sin u_{\text{obs}} \, \sin \theta}, \tag{1}$$

where C is the speckle contrast, λ is the wave length, u_{obs} is the observation aperture, and θ is the triangulation angle [3]. Most of these parameters are determined by the application requirements – we can only reduce the speckle contrast in order to minimize the measurement uncertainty. As the speckle contrast itself is a function of the spatial and temporal coherence of the illumination, we have reduced it by using a white light source and by choosing an optimal illumination aperture without losing the required

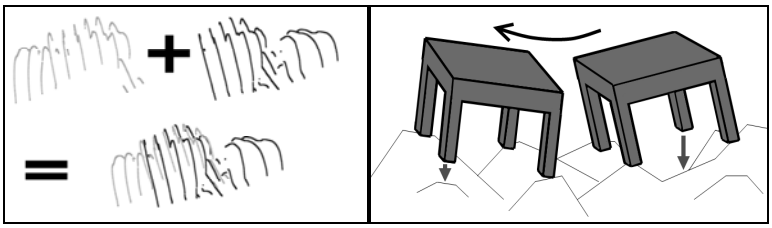

a) b)

Fig. 2. a) Alignment of two 3D views to lie in one common coordinate system. b) Illustration of a single registration step: Find optimal table position, where the distance of all legs (arrow) to the heaps is minimal.

depth of field.
Additionally, employing a high-power light source enables an acquisition of up to 30 images per second and thereby permits a free motion of our sensor around the object under test while measuring.
To gain as much information as possible from each single camera image we use a new structured light pattern with an elaborate decoding method that demands only grayscale information. Hereby we can distinguish a large number of lines and achieve a high robustness in the following registration process.

2.2 Registration of 3D views

In a first step, consecutive 3D views are aligned successively (Fig. 2a) until all views lie in one common coordinate system. The approach focuses on detecting corresponding points instead of surface features as commonly done. The idea of our sparse data registration is illustrated in Fig. 2b. One 3D view is represented by a table with N legs, the other 3D view by a rough surface with M heaps. Goal of the registration is to find the position

a) b) c)

Fig. 3. a) Measurement uncertainty (in µm) over the entire depth of field (in mm). b) Dental cast with measured area highlighted in black. c) Reconstructed surface model.

where the distance (arrow) of the legs to the heaps is minimal.
However, the successive registration leads to an accumulation of the error along the series of views. We apply outlier elimination and multi registration approaches to reconstruct the complete movement of the sensor and thereby improve the registration result.

3 Results and conclusion

Typical applications like the intraoral measurement of teeth demand a measurement uncertainty of less than 30 µm (in a single 3D view) and a depth of field of at least 15 mm. We measured a planar object and calculated the maximal standard deviation of the obtained height values. As Fig. 3a displays, we can achieve the above demand over the entire depth of field.
Further, we performed a complete measurement of a part of a dental cast (Fig. 3b). We acquired 500 images in 17s while freely moving the sensor by hand, resulting in about 3 million 3D points. The single 3dD views were registered as described above, and the surface model is reconstructed using MountainsMap (Fig. 3c). The average run time of the registration was below 30ms per 3D view (QuadCore 2.83GHz CPU, 8GB RAM), hence allowing real-time performance.
In conclusion, we have shown that our novel measurement system enables a motion-robust acquisition of surfaces with low measurement uncertainty. This system has the potential to be adapted to rough surfaces of variant sizes.

4 References

1. N. Schön, G. Häusler: “Automatic coarse registration of three-dimensional surfaces by information theoretic selection of salient points”, Applied Optics, Vol. 45, Issue 25, pp. 6539-6550 (2006)
2. T. Maier, G. Häusler: “Segmentation based fast registration of free form surfaces in the euclidean space“, Proceedings of VMV, pp. 17-24 (2006)
3. R. G. Dorsch, G. Häusler, J. M. Herrmann: "Laser triangulation: Fundamental uncertainty in distance measurement", Applied Optics, Vol. 33, Issue 7, pp. 1306-1314 (1994)

Laser direct writing of high resolution structures on curved substrates: evaluation of the writing precision

Matthias Häfner, René Reichle, Christof Pruss, Wolfgang Osten
Institut für Technische Optik – Universität Stuttgart
Pfaffenwaldring 9, 70569 Stuttgart
Germany

1 Introduction

The efficient fabrication of diffractive optics is of growing interest for many applications. Laser direct writing of such structures has proven to be a flexible, fast and cost-effective approach. In this contribution we present a direct laser writing system, that, in the final stage, will allow the fabrication of diffractive optics with sub-micrometer resolution on aspheric surfaces. High throughput for grating-like nano scale structures is obtained by means of an intrinsically parallel writing approach based on *scanning beam interference lithography (SBIL)* [1].
The combination of diffractive and refractive functions in one single optical element provides additional degrees of freedom enhancing the possibilities in the design process of specialised optical systems, e.g. imaging systems for time of flight (TOF) cameras [2], optics for laser beam shaping, or reference structures for asphere metrology. High resolution rotational symmetric periodic structures are of high interest e.g. for intra cavity polarisation control [3], interferometry [4] or novel optical micro system based approaches for rotary encoders.

2 The direct laser writing system

Efficient micro structuring of non flat surfaces still means a big effort, since existing systems suffer from low flexibility (nano imprint systems) and relatively low throughput (i.e. e-beam writers, other direct laser writing approaches). Thus, we are developing a direct laser writing system that, in the final stage, will be able to structure rotational symmetric

aspheric surfaces with a speed comparable or even higher than available with existing state of the art writing systems.
Our system writes in cylindrical coordinates on substrates spinning with constant angular velocity. In contrast to Cartesian approaches, this allows us to realise a continuous high scanning speed and intrinsically provides high accuracy for rotational symmetric structures.
One of the main challenges in such a laser based, high resolution, high accuracy system is to ensure tight focusing on the tilted surface of a curved substrate. Focussing is realized via a composition of two linear stages that move parallel to the optical axis of the curved substrate. For high speed and high accuracy displacement of the focussing optics we use a directly piezo driven objective actuator from *Physik Instrumente (PI)* with a working range of 20µm. This device is mounted onto a vertical direct drive air bearing stage from *Aerotech* which extends the operation range of the system to approx. 50mm. At the final stage, both stages will be controlled via a DSP-based real-time controller. As a consequence of the on axis approach, we do not expose perpendicular to the substrate surface. Non perpendicular focusing is made possible by a novel autofocus approach we are currently integrating into the system. This setup will allow us to maintain high accuracy virtually independent from the surface angle.
In order to enhance resolution and writing speed, we implemented a scanning beam interference lithography (SBIL) setup. In this scheme, two crossing coherent laser beams form an interference pattern, which replaces the conventional Gaussian writing spot. The grating period of this several micrometer wide pattern can be varied by adjusting the angle between the two beams.

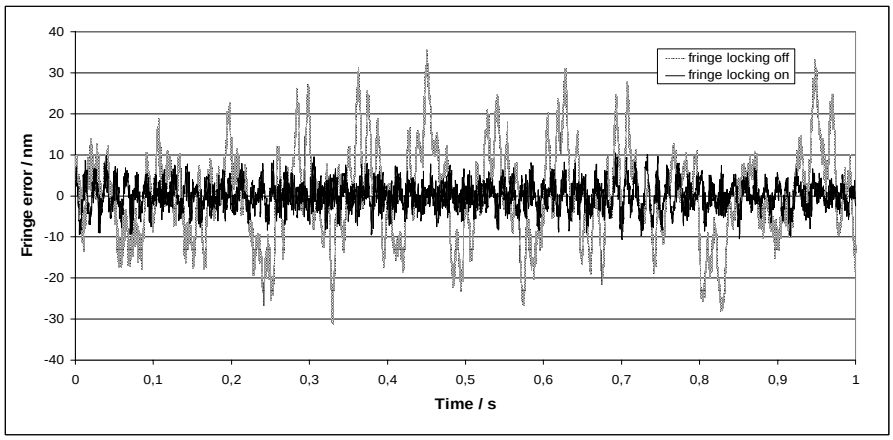

Fig. 1. Fringe error over time. Without stabilisation the 3σ-error was measured at 33.8 nm, which could be reduced to 9.9 nm by the fringe locking system

Large area grating structures are realised through phase locked pattern stitching. The pattern phase is controlled via a fringe locking system which consists of a phase measuring interferometer and a piezo actuated grating phase shifter. This arrangement allows the compensation of stage positioning errors and pattern displacement caused by turbulences in the path of the separated beams. By means of this special spot shaping the overall writing speed and the resolution of the desired structures could be significantly increased.

3 Results

The fringe locking system was characterized regarding its stabilization abilities and temporal response. Figure 1 shows the results of the fringe position error measurements. Without any fringe stabilisation the 3σ position error was measured at 33.8 nm, which is mainly caused by movements of the writing head. By means of the fringe locking system this error could be reduced to a value of 9.9 nm. The actual performance of the system is basically limited by mechanical boundary conditions. We expect to improve the stabilisation capability by further optimisation of the mechanical design. So far we have produced rotational symmetric axicon elements with feature sizes of less than 500 nm and a diameter of 16 mm.

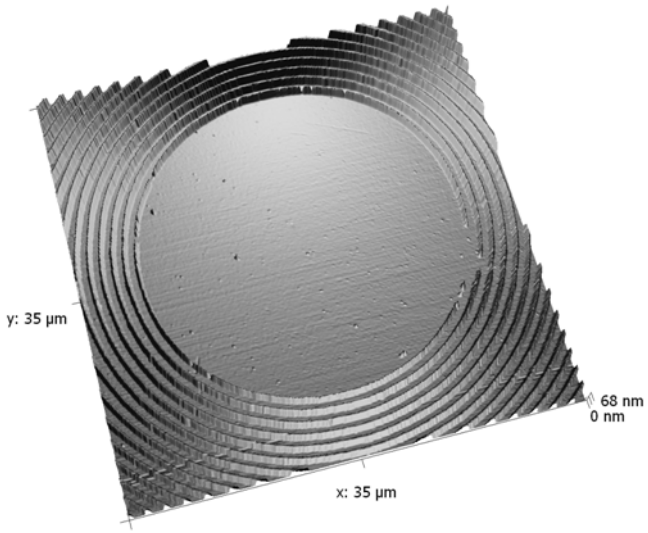

Fig. 2. AFM scan of a circular chromium structure fabricated with scanning beam interference lithography, period 951 nm

Figure 2 shows an AFM scan of a written structure. It consists of a fused silica substrate with a chromium layer as etch stop. The grating was exposed into a 150 nm thick resist layer (Shipley S1805) using an AR+-Laser operating at 457,9 nm. The resist structure serves as mask for the chromium wet etch process. In this particular case the writing time for the whole grating was approx. 16 min. We can pattern substrates with a diameter of up to 200 mm and a thickness of up to 40 mm. The overall speed is basically limited by the available laser power. In the current configuration we are able to structure a 4 inch circular area in less than 90 min. We are currently targeting smaller structure periods and expect to realise patterns with critical dimensions of 250 nm with our current setup.

4 Acknowledgements

The presented work has been funded by the German “Federal Ministry of Education and Research” (FKZ 16SV2309) and the “Landesstiftung Baden-Württemberg”, (project “Polgit”). We thank the “Institut für Strahlwerkzeuge” (IFSW) for the pleasant corporation within the project “Polgit”. The authors are responsible for the content of the publication.

5 References

1. Chen, CG, Konkola, PT, Heilmann, RK, Joo, C; Schattenburg, ML (2002), Nanometer-accurate grating fabrication with scanning beam interference lithography. Proc. SPIE, Vol. 4936, pp. 126-134
2. Reichle, R, Pruss, C, Osten, W (2007), Hybrid (diffractive/refractive) objectives for 3D-PMD-measurement cameras, Annual Report 2005/2006, Institut für Technische Optik, Stuttgart, ISBN 978-3-923560-55-4
3. Abdou Ahmed, M; Voss, A; Vogel, MM, Graf, T (2007), Multilayer polarizing grating mirror used for the generation of radial polarization in Yb:YAG thin-disk lasers. Optics Letters, Vol. 32, Issue 22, pp. 3272-3274
4. Viotti, MR; Kapp, W; Albertazzi A. (2009), Achromatic digital speckle pattern interferometer with constant radial in-plane sensitivity by using a diffractive optical element. Applied Optics, Vol. 48, Issue 12, pp. 2275-2281

TUTORIAL

Scanning Holography – A tutorial

Given by

Ting-Chung Poon
Blacksburg
(USA)

Scanning Holography – A tutorial

Ting-Chung Poon
Bradley Department of Electrical and Computer Engineering
Virginia Tech
Blacksburg, Virginia 24061, USA

1 Introduction

Optical scanning holography (OSH) is a real-time holographic recording technique in that holographic information of a 3-D object can be acquired by a single 2-D active optical scan [1]. The technique has been around for quite some time for researchers to investigate such areas as optical scanning microscopy, 3-D pattern recognition, 3-D holographic display as well as 3-D optical remote sensing [2]. The purpose of this talk is first to review the basic principles of holography using the concept of Fresnel zone plates [3,4] and then to review optical scanning holography so that new researchers in holography become aware of this modern holographic technique that is unconventional. The two holographic techniques will be compared. We hope that it will aid in the process of promoting holography.

2 Principle of Holography

For conventional holographic recording, we have the recorded hologram as

$$H(x,y) = |\psi_r + \psi_0|^2, \tag{1}$$

where ψ_r and ψ_0 are the reference wave and the object wave on the recording medium, respectively. Figure 1 shows the holographic recording of a point source. The point source, modelled as a delta function, $\delta(x,y;z_0)$, is located z_0 away from the recording film. For this example, we can write $\psi_r = a\exp(-ik_0 z_0)$, i.e., it is a plane wave of amplitude of a and k_0 is the wave number of the laser. The object wave is a spherical wave which can be written as

$$\psi_0(x,y;z_0) = \exp(-jk_0z_0)\frac{jk_0}{2\pi z_0}\exp[\frac{-jk_0}{2z_0}(x^2+y^2)].$$

Hence, the hologram of the point source, according to Eq. (1), is given by

$$\begin{aligned} H(x,y) &= |a + \frac{jk_0}{2\pi z_0}\exp[\frac{-jk_0}{2z_0}(x^2+y^2)]|^2 \\ &= a^2 + (\frac{k_0}{2\pi z_0})^2 + a\frac{-jk_0}{2\pi z_0}\exp[\frac{jk_0}{2z_0}(x^2+y^2)] + a\frac{jk_0}{2\pi z_0}\exp[\frac{-jk_0}{2z_0}(x^2+y^2)] \\ &= A + B\sin[\frac{k_0}{2z_0}(x^2+y^2)], \end{aligned} \tag{2}$$

where $A = a^2 + (k_0/2\pi z_0)^2$ and $B = ak_0/\pi z_0$. The expression in Eq.(2) is called the sinusoidal Fresnel zone plate (FZP), which is the hologram of the point source object. A typical display of the FZP is shown in Fig. 2. The center of the zone tells us the transverse location of the point object, and the "fringe density" tells us how far the point object is away from the hologram, i.e., the depth location. Hence all the 3-D location of the point object is known from the hologram. Note that by the "fringe density", we actually meant the spatial rate of change of the phase of the Fresnel zone plate, say, along the x-direction is given by

$$f_{local} = \frac{1}{2\pi}\frac{d}{dx}(\frac{k_0}{2z_0}x^2) = \frac{k_0 x}{2\pi z_0}. \tag{3}$$

f_{local} has units of inverse length and is called a local fringe spatial frequency, which increases linearly with the spatial coordinate x. In other words, the further from the zone's center, the higher the local spatial frequency within the FZP.

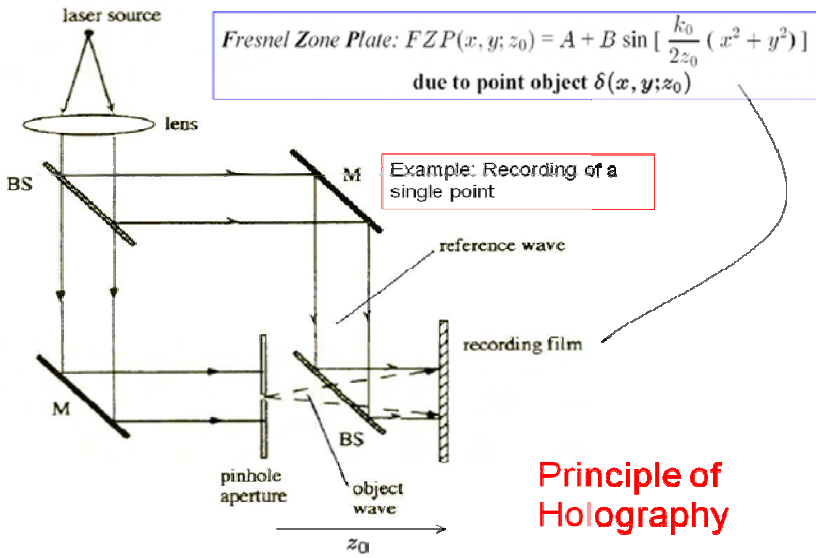

Fresnel Zone Plate: $FZP(x, y; z_0) = A + B \sin [\frac{k_0}{2z_0}(x^2 + y^2)]$

due to point object $\delta(x, y; z_0)$

Fig. 1. Holographic recording of a point source object. The point source is located z_0 away from the recording film.

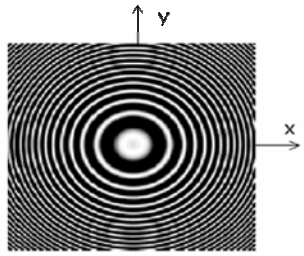

Fresnel Zone Plate = hologram of point source object

Fig. 2. Typical Display of Fresnel Zone Plate

To reconstruct the original light field from $H(x, y)$ we can illuminate the hologram with a plane wave with amplitude ψ_{rec} (called the reconstruction wave in holography), which gives, according to Fresnel diffraction,

$$\psi_{rec}H(x,y)\otimes h(x,y;z)=\psi_{rec}\{A+a\frac{-jk_0}{2\pi z_0}\exp[\frac{jk_0}{2z_0}(x^2+y^2)] +a\frac{jk_0}{2\pi z_0}\exp[\frac{-jk_0}{2z_0}(x^2+y^2)]\}\otimes h(x,y;z), \tag{4}$$

where $\otimes$ denotes convolution and $h(x,y;z)$ is the free-space impulse response function given by [5]

$$h(x,y;z)=\exp(-jk_0z)\frac{jk_0}{2\pi z}\exp[\frac{-jk_0}{2z}(x^2+y^2)].$$

The evaluation of Eq. (4) gives three light fields emerging from the hologram. The light field due to the first term in Eq. (4) is a plane wave because $\psi_{rec}A\otimes h(x,y;z)\propto\psi_{rec}A$. This plane wave is called a zeroth-order beam. The field due to the second term is

$$\psi_{rec}\frac{-jk_0}{2\pi z_0}\exp[\frac{jk_0}{2z_0}(x^2+y^2)]\otimes h(x,y;z) \propto\frac{-jk_0}{2\pi z_0}\frac{jk_0}{2\pi z}\exp[\frac{jk_0}{2(z_0-z)}(x^2+y^2)]. \tag{5}$$

Equation (5) represents a converging spherical wave if $z<z_0$. If $z>z_0$, the wave is diverging. For $z=z_0$ the wave focuses to a real point source z_0 away from the hologram and is given by a delta function, $\delta(x,y)$. For the last term in Eq. (4) we have

$$\psi_{rec}\frac{jk_0}{2\pi z_0}\exp[\frac{-jk_0}{2z_0}(x^2+y^2)]\otimes h(x,y;z) \propto\frac{-jk_0}{2\pi z_0}\frac{-jk_0}{2\pi z}\exp[\frac{-jk_0}{2(z_0+z)}(x^2+y^2)], \tag{6}$$

which is a diverging wave with its virtual point source appearing to come from a distance z_0 behind the hologram. This reconstructed point source is at the location of the original point source object. The situation is illustrated in Fig. 3. The real point source is called the twin image of the virtual point source.

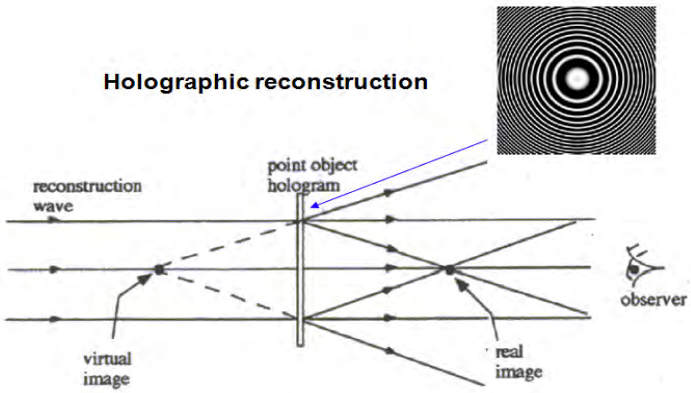

Fig. 3. Holographic recosntuction of a point souce hologram

2 Optical scanning holography

2.1 Basic Principle

Optical scanning holography (OSH) [5] is a holographic recording technique that is a radical departure from conventional holographic recording technique discussed in the last section. It uses 2-D scanning to record 3-D information. The idea is to use a time-dependent Fresnel zone plate (TDFZP) to 2-D scan over a 3-D object. The situation is shown in the optical part of Fig. 4. The 3-D object shown is a thick specimen, which is on an x-y scanning platform. The TDFZP consists of a plane wave and a spherical wave of different temporal frequencies. Hence, the scanning TDFZP z from the point source is given by

$$\mathrm{TDFZP}(x,y;t) = |\, a\exp[\,j(\omega_0+\Omega)t] + \frac{jk_0}{2\pi z}\exp[\frac{-jk_0}{2z}(x^2+y^2)]\exp(j\omega_0 t)]\,|^2$$

$$= A + B\sin[\frac{k_0}{2z}[(x^2+y^2)+\Omega t]], \qquad (7)$$

Note that for t = 0 Eq. (7) is identical to the expression in Eq. (2). As an example, let us see how this scanning beam could record a hologram of a point object. Assuming we place a pin hole z away from the point source of the scanning TDFZP as shown in Fig. 4, and upon 2-D scanning the current coming from the photo-detector is given by

$$i(x,y) = a + b\sin[\Omega t + \frac{k_0}{2z}(x^2 + y^2)],$$

where $x(t) = vt$, $y(t) = vt$ and v is the scanning speed of the TDFZP. a and b are some constants, representing the magnitude of the DC and the AC (heterodyne) current of $i(x,y)$, respectively. The bandpass filter centered at the heterodyne frequecny Ω will block the DC current and only allow the heterodyne current to go through, giving its output proportional to

$$\sin[\Omega t + \frac{k_0}{2z}(x^2 + y^2)].$$

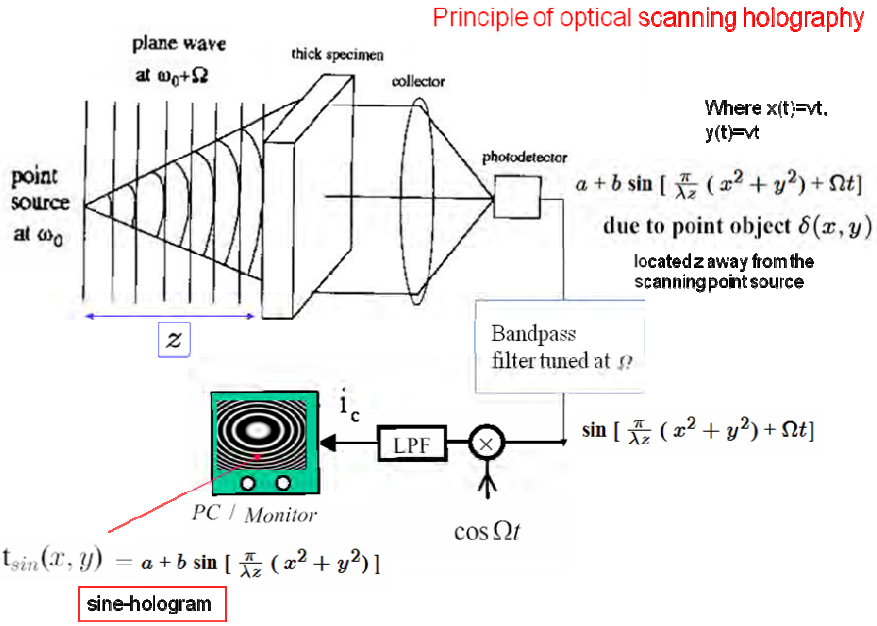

Fig. 4. Principle of optical scanning holography

This banpassed cuurent is then electronically processed by first multiplying the bandpassed cuurent by $\cos(\Omega t)$ and subsequently by lowpass filtering (LPF) to give the final current,

$$i_c(x,y) \propto \sin[\frac{k_0}{2z}(x^2 + y^2)],$$

to be stored in a PC or displayed on a 2-D monitor as a hologram:

$$H_s(x,y) \propto \text{bias} + c\sin[\frac{k_0}{2z}(x^2+y^2)]. \qquad (8)$$

Note that in order to display on a 2-D monitor or some kind of spatial light modultor (SLM), some bias should be added to $i_s(x,y)$ as shown in the above equaton. Equation (8) is the hologram of a point object as is Eq. (2) in standard holography.

2.2 Practical Implementation

Figure 5 shows a pratical implemenation of optical scanning holography. $\Gamma_0(x,y;z)$ is the transverse amplitude distribution of the 3-D object with z denoted as a depth parameter. To realize optical scanning holography, we need the object scanned by the TDFZP. We note from Fig. 5 that the object is indeed scanned by the TDFZP. The spherical wave on the object comes from the lower arm of the Mach-Zehnner interferometer formed by mirrors M and M1, and beamsplitters BS and BS1, where one of the pupils $p_1(x,y)=1$ has been chosen. The plane wave on the object comes form the upper arm of the interferometry and the other pupil $p_2(x,y)=\delta(x,y)$ has been chosen. Note that also in the upper arm, the laser frequency has been up-shifted by an acousto-optic frequency shifter AOFS at frequency Ω. Hence we now have the TDFZP on the object. Lens L3 is used to collect all the transmitted light onto the photodetector, which gives $i(x,y)$ as its current output. The function of electronic processing shown in the figure should be clear when it is compared with Fig. 4. However, on Fig. 5 , there are two electronic processing arms, one using $\cos(\Omega t)$ for the multiplication (as in Fig 4) and the other using $\sin(\Omega t)$. The use of $\cos(\Omega t)$ leads to $i_c(x,y)$ given by Eq. (8). And the use of $\sin(\Omega t)$ leads to $i_s(x,y)$, which gives a cosine hologram, $H_c(x,y) \propto \text{bias} + c\cos[\frac{k_0}{2z}(x^2+y^2)]$. Hence, the hologram in Eq. (8) is called the sine hologram. The sine and cosine holograms are on-axis holograms. However, using optical scanning holography we can acquire the two holograms simultaneously and from the two on-axis holograms, we can form a complex hologram that would reconstruct without a twin-image. The complex hologram is given by [5]

$$H_{\pm}^{c}(x,y) = H_c(x,y) \pm jH_s(x,y). \qquad (9)$$

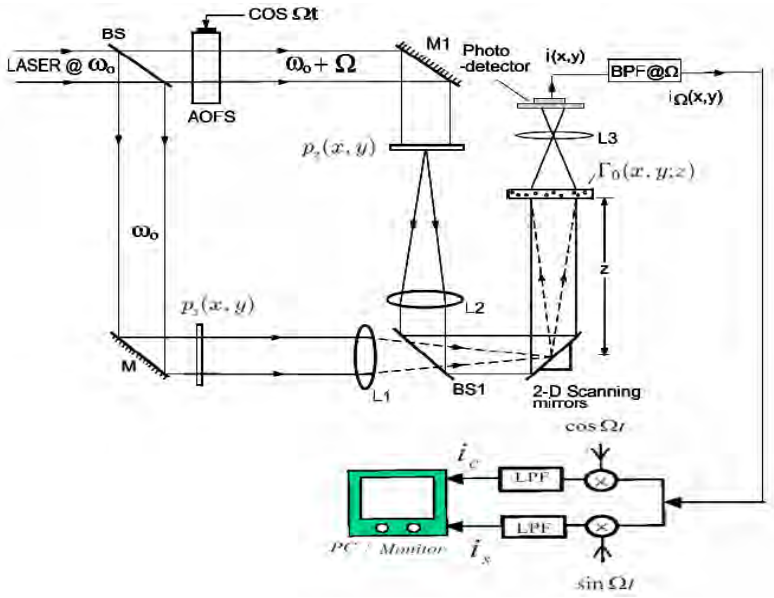

Fig. 5. Practical implementation of optical scanning holography [Adapted from T.-C.Poon, Optical scanning Holography with MATLAB, Springer 2007].

3 References

1. Poon, T.-C. (1985) Scanning holography and two-dimensional image processing by acousto-optic two-pupil Synthesis. J. Opt. Soc. Am. 2: 521-527.
2. Poon, T.-C. (2004) Recent Progress in Optical Scanning Holography," Journal of Holography and Speckle 1: 6-25.
3. Parker Givens, M. Introduction to holography. American Journal of Physics 35: 1056-1064.
4. Poon,T.-C. (2008) On the Fundamentals of Optical Scanning Holography," American Journal of Physics 76: 738-745.
5. Poon, T.-C. (2007) Optical Scanning Holography with MATLAB, Springer

APPENDIX

New Products

Pico DLP Projection - the professional way

GFM's Pico Developer Kit provides OEM's as well as laboratories with an easy access to Texas Instrument's new pico display technology, for projection tasks in measurement and numerous other applications requiring more than video playing.

The kit consists of

- the pico projector by Texas Instruments in a special version,
- a versatile microprocessor box driving the projector,
- and GFM's software interfaces for Visual Studio and LabVIEW.

TI Pico Light Engine

Unique highlights of the GFM pico kit are:

- **Synchronization with other devices**
- **Pixel accurate projection**
- **API for Visual Studio**
- **LabVIEW interface**

The matchbox sized Pico projector delivers precise images with excellent brightness. The Beagle processor box with dedicated software by GFM provides an easy-to-use connection between the Pico projector and a PC. Image sequences can be projected at up to 60 full frames/second, in color or black-and-white.

The Kit is controlled by it's versatile programming toolbox or the LabVIEW interface, enabling the integration into laboratory or automation tasks with real-time controlling, by means of an easy to use graphical interface.

pico kit

http://www.gfmesstechnik.com

info@gfmesstechnik.com

GFMesstechnik GmbH · Warthestrasse 21 · D-14513 Teltow · Germany · t.+49(3328)9360-0

DLP
TEXAS INSTRUMENTS

Your fast lane to high performance DLP projection

GFM

GFM's Alligator board offers all driving capabilities for a high speed, high power optical projection with Texas Instrument's micro mirror displays (DLP), fully controlled by the operator or application.

Single board solution, PC interface included

This highly economical solution contains everything developers and OEM customers require for DLP applications, on one single board !
The board includes a high performance processor that serves as a display controller, pattern generator and versatile interface to user control via PC.

Ultra fast pattern generator

The on-board controller can automatically assemble images with repetitive patterns from small samples freely defined by the API. This allows complex, ultra fast image sequences to be generated and controlled by USB interface.

Available as a kit with Software, DLP and optics

No necessity for shopping around - from GFM, you can get the board complete with a fitting DLP display, software, and projection optics as well.

Features:

- 0,7"XGA DLP resolution
- High frame rates:
  - 200Hz Grayscale
  - 8kHz binary
- Absolutely flexible:
  - Frame rate, bit depth
- Master/slave triggering
- 2GBit RAM memoryr
- Esaily programmable, via API and USB port
- Flexible pattern generator

Alligator

http://www.gfmesstechnik.com

info@gfmesstechnik.com

GFMesstechnik GmbH · Warthestrasse 21 · D-14513 Teltow · Germany · t.+49(3328)9360-0

NMM-1

NANOPOSITIONING AND NANOMEASURING MACHINE

The Nanopositioning and Nanomeasuring Machine NMM-1 allows the positioning, manipulation, processing and measurement of objects in the fields of micromechanics, microelectronics, optics, molecular biology genetics and microsystems engineering with a resolution of

0,1 nm

in a measuring range of

25mm x 25mm x 5mm

Various probe systems can be implemented, e.g. Scanning Probe Microscopes, Atomic Force Microscopes, Autofocus and Fixfocus Systems, White Light Interferometers, capacitive and inductive 3D probe systems.

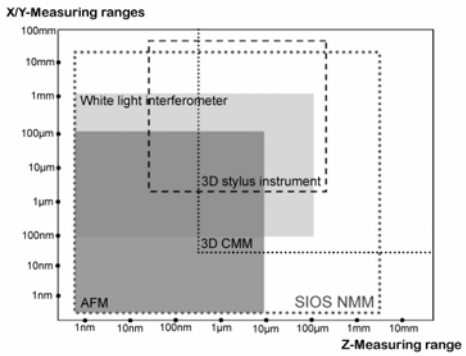

Working ranges of typical measuring systems

SAMPLE APPLICATION:

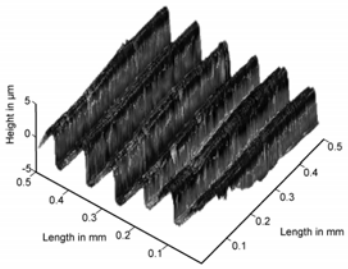

Roughness measurement standard

SIOS Meßtechnik GmbH Ilmenau, Germany
Phone: +49-(0)3677-64470 - www.sios.de

SIOS Meßtechnik GmbH